Karlsruhe Institute of Technology

First Principle Investigations of the Activity of Pd and Pt Noble Metals in Varying Sizes Supported on Ceria

Zur Erlangung des akademischen Grades einer

DOKTORIN DER NATURWISSENSCHAFTEN
(Dr. rer. nat.)

von der KIT-Fakultät für Chemie und Biowissenschaften
des Karlsruher Instituts für Technologie (KIT)

genehmigte

DISSERTATION

von

Sarah Bernart, M.Sc.

Tag der Abgabe:	Karlsruhe, den 11.03.2024
Tag der mündlichen Prüfung:	Karlsruhe, den 22.04.2024

Erster Referent:	Prof. Dr. Felix Studt
Zweite Referentin:	Prof. Dr. Karin Fink

Karlsruher Institut für Technologie
KIT-Fakultät für Chemie- und Biowissenschaften
Kaiserstraße 12
76131 Karlsruhe

Hiermit versichere ich guten Gewissens, dass ich diese Arbeit selbstständig verfasst habe. Alle benutzten Quellen und Hilfsmittel sind vollständig und genau angegeben worden. Sowohl wörtlich als auch inhaltlich übernommene Stellen, die nicht von mir stammen, sind als solche kenntlich gemacht worden. Ich habe die Satzung des Karlsruher Instituts für Technologie zur Sicherung guter wissenschaftlicher Praxis in der jeweils gültigen Fassung beachtet.

. . . . . .

Sarah Bernart
Karlsruhe, 11.03.2024

Mit Logik allein kann man sich über die Natur nicht hinwegsetzen! Die Logik rechnet mit drei Möglichkeiten, aber deren gibt es eine Million!

Rasumichin, in 'Verbrechen und Strafe' von Fjodor M. Dostojewskij[1]

Abstract

In this theoretical study, we investigated the dynamic structural changes of active species under diverse operating conditions and their impact on catalytic activity using Density Functional Theory (DFT) methods. Through structural optimization employing quantum chemical techniques, we identified the most stable structures of the heterogeneous catalyst as the active centers at the atomic level under reaction conditions. Validation of the identified species under reaction conditions was achieved by comparing the spectroscopic properties of different sizes of noble metals palladium (Pd) and platinum (Pt) with experimental investigations. In internal combustion engines, contrasting reaction conditions such as "rich phase" with low oxygen (O_2) pressures and high hydrocarbon pressures, or "lean phase" with high O_2 pressures and low hydrocarbon pressures, lead to reducing or oxidizing reaction conditions for the heterogeneous catalysts. The catalyst, used for exhaust gas treatment in internal combustion engines, actively involved in complete carbon monoxide (CO) oxidation to reduce methane (CH_4) emissions, comprises Pd or Pt noble metals as the active centers supported on cerium oxide (CeO_2 or ceria) for industrial use. Hence, in this study, we examined the oxidation states of the heterogeneous catalyst, where the metal was either reduced and covered by CO molecules or oxidized by O atoms. By conducting structural optimization, phase diagrams indicating the relative stabilities of coverage by CO molecules and O atoms were constructed. Moreover, the potential energies of reaction mechanism steps during the combustion of hydrocarbons, such as CO oxidation and O_2 dissociation, were determined, enabling the assessment of the activity of the catalyst through Gibbs free energy diagrams. Both CO oxidation and O_2 dissociation can occur via Langmuir-Hinshelwood (LH) or Mars-van-Krevelen (MvK) mechanisms. LH mechanisms involve reactions without affecting the crystal lattice of Pd or Pt noble metals and ceria, while MvK mechanisms involve the consumption of O atoms from the ceria surface lattice during CO oxidation or regenerating O defects (V_O) on the ceria surface during O_2 dissociation. Additionally, we investigated the reducibility of the support material by forming V_O, which were generated either by MvK mechanisms during CO oxidation for the generation of carbondioxide (CO_2) or by successive O atom removal, examining their relative stabilities. Furthermore, we investigated the activities of Pd and Pt noble metals across different size scales, including single-atom catalysts (SACs), subnanometer clusters (3 to 10 noble metal atoms), and extended noble metal surfaces (approaching nanometer cluster surfaces),

in terms of activity towards CO oxidation and O_2 dissociation. To probe the chemical environment of supported Pd and Pt noble metals, we investigated them as SACs on ceria surfaces, establishing an analogy between heterogeneous and homogeneous catalysis via complex chemistry. We focused on the most stable ceria surface facets (111), (110), and (100). We established a correlation between the oxidation state and CO stretching vibrational frequency, as well as the adsorption energy on SACs. This was accomplished through a systematic examination of the species and could be beneficial for future studies at the electronic level. Additionally, we conducted a study on ceria surface defects through cerium (Ce) surface lattice defects (V_{Ce}), where Pd and Pt noble metal atoms were adsorbed, evaluating their stabilities concerning surface structures (110) and (111), as well as their reducibility and oxidizability. The formation of larger agglomerates reduces the surface-to-volume ratio, resulting in increased inaccessibility to a significant portion of the metal, thereby significantly reducing resource utilization, leading to greater exploitation of natural resources and increased costs. By adsorbing single-atom noble metals into V_{Ce}, we induced nucleation, favoring agglomeration through the adsorption of the noble metal atoms Pd and Pt from the gas phase, a phenomenon confirmed by our calculations. To enhance overall catalytic performance, a higher dispersion of metal particles is preferred, as it increases surface area exposure and avoids the inefficiencies caused by the formation of larger agglomerates of noble metals. It is of particular interest to maintain the activity of the catalyst for exhaust gas treatment to a maximum, while still significantly reducing noble metal consumption by minimizing the number of atoms. Ultimately, the reduced species by CO adsorption were analyzed for their spectroscopic properties regarding CO vibrational spectra to provide validation by parison to infra red (IR) spectroscopy measured by collaborating experimenters. Furthermore, we compared our results with Extended X-ray Absorption Fine Structure (EXAFS) investigations measured by collaborating experimenters to determine the morphology of subnanometer-sized clusters and oxidation through oxygen adsorption. By computing activities at various sizes of noble metals, a substantial amount of potential energy diagrams (PEDs) was generated, serving as the basis for correlating activities with reactant adsorption strength in the form of a scaling relation. Indeed, linear scaling relations were established, indicating a dependence of activities on reactant adsorption strength resulting from the size scale of the noble metal as the active center for CO oxidation and O_2 dissociation. By conducting a systematic examination of the activities across the catalyst size scales as well as the activities towards the reaction mechanism, future investigations can benefit from these determined trends and limitations, which could provide guidance. Furthermore, the new approaches to the stabilities of subnanometer clusters can provide clues for further studies and achieve control over the agglomeration and dispersion effects.

Zusammenfassung

In der vorliegenden theoretischen Studie wurden die dynamischen strukturellen Veränderungen aktiver Spezies unter verschiedenen Betriebsbedingungen und deren Auswirkungen auf die katalytische Aktivität unter Verwendung von Dichtefunktionaltheorie (DFT) Methoden untersucht. Durch eine Strukturoptimierung der aktiven Zentren des heterogenen Katalysators wurden basierend auf quantenchemischen Methoden die stabilsten Strukturen ermittelt, die ein Katalysator unter Reaktionsbedingungen besitzt. Durch den Vergleich der spektroskopischen Eigenschaften verschiedener Größen von Edelmetallen Palladium (Pd) und Platin (Pt) mit experimentellen Untersuchungen wurde eine Validierung der gegenwärtigen Konfigurationen erreicht. In einem Verbrennungsmotor können zwei zueinander gegensätzliche Reaktionsbedingungen bestehen. Es könnte entweder eine "rich phase"mit niedrigen Sauerstoffdrücken (O_2) und hohen Kohlenwasserstoffdrücken oder eine "lean phase"mit hohen Sauerstoffdrücken und niedrigen Kohlenwasserstoffdrücken vorliegen. Abhängig von diesen Betriebsphasen ergeben sich reduzierende oder oxidierende Reaktionsbedingungen für die heterogenen Katalysatoren. Der heterogene Katalysator, der zur Abgasnachbehandlung der Verbrennungsmotoren aktiv gegenüber einer vollständigen Kohlenstoffmonoxid (CO) Oxidation zur Reduktion der Methanabgase industriell verwendet wird, besteht unter anderem aus Pd oder Pt Edelmetallen als das aktive Zentrum, das auf einem Oxiden Ceroxid (CeO_2 oder ceria) geträgert wird. In dieser Arbeit betrachteten wir daher die Oxidationszustände des heterogenen Katalysators, indem das Edelmetall durch die Adsorption von CO Molekülen reduziert wird oder durch Adsorption von Sauerstoffatome (O_2) oxidiert wird. Dadurch konnten Phasendiagramme erstellt werden, die die relativen Stabilitäten der Bedeckung durch CO Moleküle und O Atome aufzeigten. Durch die ermittelte Oberflächenbedeckung konnte eine Berechnung der potenziellen Energien der Intermediate in Hinsicht der Elementarschritte während eines O_2 Dissoziationsmechanismus und eines CO Oxidationsmechanismus erfolgen, wodurch bei einer Auftragung der freien Gibbs Energien eine Betrachtung der Aktivität des vorliegenden Katalysators erfolgte. Sowohl die CO Oxidation als auch die O_2 Dissoziation konnten entweder durch einen Langmuir-Hinshelwood (LH)- oder einen Mars-van-Krevelen (MvK) Mechanismus erfolgen. Bei einem LH Mechanismus erfolgte die Reaktion ohne Beeinflussung des Kristallgitters des Pd- oder Pt-Edelmetalls und des CeO_2. Bei einem MvK Mechanismus wurden bei einer CO Oxidation O Atome der CeO_2-Oberfläche konsumiert; bei einer O_2 Dissozia-

tion wurden diese durch den MvK Mechanismus gebildeten Sauerstoffdefekte (V_O) der CeO_2-Oberfläche wieder regeneriert. Des Weiteren wurde die Reduzierbarkeit des Trägermaterials durch Bildung von Sauerstoffdefekten untersucht. Diese wurden bei einer Untersuchung der Aktivität gegenüber der CO Oxidation zum einen durch einen Mars-van-Krevelen Mechanismus gebildet oder durch sukzessive Sauerstoffentfernung auf ihre relative Stabilitäten untersucht. Zusätzlich wurde die V_O-Migration in das Kristallgitter des Trägermaterials auf relative Stabilitäten untersucht. Es wurden zudem die Aktivitäten der Pd- und Pt-Edelmetallen in verschiedenen Größenskalen analysiert. Dazu haben wir Single-Atom-Katalysatoren (SACs), Subnanometer-Cluster der Größe von 3 bis 10 Edelmetallatomen sowie die Edelmetalloberflächen von Pd und Pt, die eine theoretische Näherung zu nanometergroßen Edelmetallkristallen darstellen, in Bezug auf die Aktivität zur CO Oxidation und O_2 Dissoziation untersucht. Zur Untersuchung der chemischen Umgebung der geträgerten Pd- und Pt-Edelmetalle wurden diese als SACs auf der CeO_2-Oberfläche untersucht. Dadurch konnte eine Analogie zwischen heterogener Katalyse und homogener Katalyse über die Komplexchemie hergestellt werden. Es wurden hierzu die stabilsten CeO_2 Oberflächen (111), (110) und (100) betrachtet. Wir haben eine Korrelation zwischen dem Oxidationszustand und der CO-Schwingungsfrequenzen sowie der Adsorptionsenergie auf SACs festgestellt. Dies wurde durch eine systematische Untersuchung der Spezies erreicht und könnte für zukünftige Studien auf elektronischer Ebene von Nutzen sein. CeO_2 ist zudem als ein "non-innocent"Trägermaterial bekannt, das nicht nur der Stabilisierung der Edelmetalle als aktive Zentren für die Katalysereaktion dient, sondern auch als Teilnehmer an den Reaktionen fungiert, indem es als Sauerstofflieferant und -speichermaterial agiert. Zur Untersuchung der Aktivitäten an der Grenzfläche zwischen dem Edelmetall und der CeO_2 Oberfläche wurden die CO Oxidations- und O_2-Dissoziationsaktivitäten an subnanometergroßen Edelmetallclustern geträgert auf CeO_2 hinsichtlich des MvK Mechanismus untersucht. Für den Vergleich wurden auch die Aktivitäten auf der durch Adsorption von Sauerstoffatomen sowie von Kohlenstoffmonoxidmolekülen auf den Edelmetalloberflächen der Subnanometergröße hinsichtlich des LH Mechanismus untersucht. Um einen Referenzwert der Aktivitäten zu Nanometer-großen geträgerten Edelmetallen auf CeO_2 gegenüber den Aktivitäten zur CO Oxidation und O_2 Dissoziation zu erhalten, wurden schließlich auch reine Edelmetalloberflächen untersucht. Zusätzlich wurde eine Untersuchung der CeO_2-Oberflächendefekte durch Cer-Fehlstellen (V_{Ce}) durchgeführt. Dabei wurden Edelmetallatome Pd und Pt in die Fehlstellen adsorbiert, und ihre Stabilitäten relativ zur Oberflächenstruktur (110) und (111) sowie ihre Reduzierbarkeit und Oxidierbarkeit betrachtet. Da ein zu größeren Agglomeraten gewachsener Edelmetallkristall ein reduziertes Oberflächen-Volumenverhältnis aufweist und dadurch eine erhöhte Unzugänglichkeit eines beträchtlichen Anteils des Edelmetalls zeigt, ist die Ressourcennutzung erheblich gemindert,

was zu einer größeren Ausbeutung der natürlichen Ressourcen und erhöhten Kosten führt. Durch die Adsorption eines Einzelatom-Edelmetalls in einer V_{Ce} haben wir eine Keimbildung hervorgerufen, die eine Agglomeration durch Adsorption der Edelmetallatome aus der Gasphase begünstigt. Dies konnte durch unsere Berechnungen durchaus bestätigt werden. Im Kontrast zu einer erzeugten Ineffizienz durch größere Agglomerate steht eine erhöhte Dispersion des Edelmetalls auf der Oxidoberfläche. Hier ist von besonderem Interesse, die Aktivität des Katalysators nach bekanntem Maß zur Abgasnachbehandlung im minimalen Maß zu erhalten, aber dennoch eine erhebliche Minderung des Edelmetallverbrauchs zu erzielen, indem die Anzahl der Atome in den aktiven Zentren möglichst gering gehalten wird. Letztendlich wurden alle betrachteten Spezies auch auf ihre spektroskopischen Eigenschaften der CO Schwingungsspektren berechnet, um für Experimentatoren eine Validierung der durch infrarot (IR) Spektroskopie gemessenen Spezies bieten zu können. Des Weiteren wurde ein Vergleich mit Extended X-ray Absorption Fine Structure (EXAFS) Untersuchungen zur Ermittlung der Morphologie der subnanometergroßen Cluster sowie der Oxidation durch Sauerstoffadsorption betrachtet. Durch die Berechnung der Aktivitäten an einer Variation der Edelmetallgrößen konnte eine erhebliche Menge an Potenzialenergiediagrammen (PEDs) erstellt werden, die als Basis für eine Korrelation zwischen den Aktivitäten und der Adsorptionsstärke der Reaktanden in Form einer Scaling-Relation ermittelt wurden. Tatsächlich konnten lineare Scaling-Relationen erstellt werden, die eine Abhängigkeit der Aktivitäten gegenüber der Adsorptionsstärke der Reaktanden resultierend auf der Größenskala des aktiven Zentrums, des Edelmetalls, ermittelt hatten. Durch eine systematische Betrachtung der Aktivitäten in Bezug auf die Größenskalen der Katalysatoren sowie der Reaktionsmechanismen könnten zukünftige Untersuchungen von den ermittelten Trends und Limitierungen profitieren, da sie wegweisend sein könnten. Zudem können die neuen Betrachtungsansätze zu den Stabilitäten der Subnanometercluster Anhaltspunkte für weitere Studien bieten und eine Kontrolle über die Agglomerations- und Dispersionseffekte ermöglichen.

Contents

List of Tables

List of Figures

Acronyms

(100), (110), (111), (211)	Crystallographic surface orientations
Å	Ångstrom
$\tilde{A}$ and $\tilde{B}$	Plane wave coefficients
A and B	Wave function constants
a	Lattice constant
AIMD	*Ab initio* Molecular Dynamics Simulations
Al	Aluminium
Al_2O_3	Aluminium oxide (alumina)
ASE-GUI	Atomic Simulation Environment Graphical User Interface
BEEF-vdW	Bayesian Error Estimation Functional with van-der-Waals correction
BEP	Brønsted-Evans-Polanyi
c	Speed of light
ccp	Cubic Close-Packed
CCSD(T)	Coupled Cluster Single Double (Triple) excitations
Ce	Cerium
Ce^{+III}	Cerium in the +III oxidation state
Ce^{+IV}	Cerium in the +IV oxidation state
CeO_2	Cerium (+IV) oxide (ceria)
CeO	Cerium (+III) oxide (reduced Ceria)
CH_4	Methane
CO	Carbonmonoxide
CO_2	Carbondioxide
$C_p(T)$	Heat capacity
δ	Free energy per unit area
DFT	Density Functional Theory
DRIFTS	Diffuse Reflectance Infrared Fourier Transform Spectroscopy
ε	Eigenstate
ER	Eley-Rideal (Mechanism)
EXAFS	Extended X-ray Absorption Fine Structure
ΔF	Helmholtz free energy
F_{HK}	Hohenberg-Kohn functional
fcc	Face-centered cubic
Fe	Iron
$Fm\bar{3}m$	Space group of cubic ceria
F_s	Exchange enhancement factor
γ	Free energy per unit area

ΔG	Differential Gibbs free energy
GGA	Generalized Gradient Approximation
GTO	Gaussian-type Orbitals
$\hbar$	Planck constant
ΔH	Differential Enthalpy
$\hat{H}$	Hamilton operator
HF	Hartree-Fock
HERFD	High Energy Resolution Fluorescence Detected
hcp	Hexagonal close-packed
HK	Hohenberg-Kohn
HOMO	Highest occupied molecular orbital
IKFT	Density Functional Theory
IR	Infrared Spectroscopy
J_{ij}	Coulomb operator
k	Wave vector
K	Kelvin
K_{ij}	Exchange operator
k_B	Boltzmann constant
k^+	Forward rate constant
KS	Kohn-Sham
λ	Vibrational frequency correction factor
La	Lanthanum
LDA	Local Density Approximation
LH	Langmuir-Hinshelwood (mechanism)
μ	Chemical potential
m	Mass
M	Noble metals as palladium or platinum
MAE	Mean Absolute Error
MD	Molecular dynamics simulations
MEP	Minimum energy path
ML coverage	Monolayer coverage
M_{PW}	Number of plane waves
MvK	Mars-van Krevelen (Mechanism)
ν	Stoichiometric coefficient
nn	nearest-neighbor
nnn	next nearest-neighbor
∇	Laplacian operator
NAP-XPS	Near Ambient Pressure X-ray Photoelectron Spectroscopy
Ni	Nickel
O	Oxygen atom
O_l	Ceria lattice oxygen
O_2	Dioxygen
Φ	Plane wave functions for periodical systems
p	Pressure

P	Probability
Pd	Palladium
Pd_1	Palladium single-atom catalyst
Pd_n	Palladium cluster consisting of n Atoms
$Pd^{-\delta}$	Palladium in the undefined negative -δ oxidation state
Pd^{0}	Palladium in the 0 oxidation state
Pd^{+II}	Palladium in the +II oxidation state
Pd^{+IV}	Palladium in the +IV oxidation state
PED	Potential energy diagram
PP	Precipitation Method
Pt	Platinum
Pt_1	Platinum single-atom catalyst
Pt_n	Platinum cluster consisting of n Atoms
$Pt^{-\delta}$	Platinum in the undefined negative -δ oxidation state
Pt^{0}	Platinum in the 0 oxidation state
Pt^{+II}	Platinum in the +II oxidation state
Pt^{+IV}	Platinum in the +IV oxidation state
$P4_2/mnm$	Tetragonal space group of ceria
q	Partition function
ρ	Density
r	Vector of position for an electron
R	Vector of position for a nucleus
R^2	Coefficient of determination
s	Density gradient
ΔS	Entropy
SE	Schroedinger equation
STO	Slater-type orbitals
t	Translation vector
T	Temperature
$\hat{T}$	Kinetic energy operator
TEM	Transmission Electron Microscopy
Ti	Titanium
TiO_2	Titanium oxide (titania)
U(T)	Internal energy, dependent on the temperature
U	Hubbard-like U term
UHV-IR	Ultra-High Vacuum Infrared Spectroscopy
$\hat{V}$	Potential energy operator
V	Volume
VASP	Vienna Ab initio Simulation Package
vdW	van-der-Waals
ω	Harmonic oscillator vibrational mode
nV_O	n oxygen lattice defects
$\chi_k(r)$	Plane wave orbital
XANES	X-ray Absorption Near Edge Structure

Xe	Xenon
XC	Exchange-Correlation
Ψ	Wavefunction
θ	Coverage
ZPE	Zero Point Energy
Zr	Zirconium
ZrO_2	Zirconium oxide (zirconia)

1. Introduction

1.1. Deciphering the Optimized Catalyst: A Challenge in Overarching Interdisciplinary Research

At the beginning of the last century, a significant industrial breakthrough was achieved in catalysis research technology. Fritz Haber and his colleagues successfully synthesized ammonia at temperatures around 823.15 K and a pressure of 175 bar, employing osmium as a catalyst.[2] The robust reactor designed to withstand these challenging conditions is illustrated in Figure 1.1. Fritz Haber and Carl Bosch pioneered the technical implementation for synthesizing ammonia from its elemental components.[3] Subsequently, Alvin Mittasch refined the catalyst to achieve essential properties of the resulting α-Fe phase, which remains in industrial use today. In routine operations, temperatures typically hover around 500 degrees Celsius with pressures reaching approximately 200 bar, leading to ammonia concentrations in the exhaust gas of up to 18 vol%.[4] The discovery of the optimal catalyst, however, required numerous trial-and-error attempts, resulting in a significant atom ecological footprint. Even today, the systematic discovery of an optimized catalyst remains a challenge. Due to the immense energy demand of modern society, optimizing catalysts for emission control and energy efficiency is more crucial than ever before. Today, internal combustion engines, particularly in the automotive industry, including heavy-duty transport vehicles, marine propulsion, and stationary large-scale industrial installations, are still in use and cannot be replaced in the foreseeable future. In addition to the unidirectional nature of the carbon cycle resulting from the combustion of fossil Earth reserves and the absence of a closed-loop system, CH_4 as a greenhouse gas poses an additional threat. As early as the 1970s, the scientific community strongly warned about CH_4 emissions, as CH_4 was recognized as a greenhouse gas 20-30 times more potent than CO_2.[5] In addition to reducing greenhouse gases, there is an interest in decreasing the use of precious metals. This goal is pursued not only to lower the costs of catalysts but also to promote a more sustainable consumption of precious metals and decrease the exploitation of the materials of the Earth. Given the pressing climate concerns, the treatment of exhaust gases in combustion engines appears outdated amidst the shift toward innovations like batteries and hydrogen as energy resources. This shift is underscored by the continued reliance on fossil fuels as a carbon hydrate source alongside the utilization of combustion engines. However, effective climate policy hinges not just on

groundbreaking technologies but also on an array of innovative solutions. While historic breakthroughs like the Haber-Bosch process[2,6] revolutionized our world as a key innovation, the current challenge demands a series of incremental yet transformative advancements. To explain this in quantitative terms, one could say that starting today, a reduction in emissions and the demand for precious metals leads to cumulative mitigation over time, resulting in a significant decrease in greenhouse gases and resource usage when integrated over time. In pursuit of these objectives, German research funds have been allocated to integrate cutting-edge technologies through close collaborations and establish robust interdisciplinary research aimed at taking a further step towards optimizing catalysts for emission control.[7] In the future, chemical catalysts must adapt to the variability in energy and raw material supply, driven by the fluctuating nature of renewable energies. This shift, especially in power-to-chemical processes, necessitates moving from steady-state to dynamic reaction conditions. The design of catalysts and reactors faces new challenges due to the dynamic nature of catalyst structures. Recent efforts have begun exploring catalysts and reactors under transient conditions, requiring advancements in operando spectroscopy, predictive theory, kinetic modeling, catalyst design methods, and innovative reactor designs.[8] A markedly enhanced catalyst for emission control would efficiently function across a broad spectrum of reaction conditions, notwithstanding the highly dynamic nature of the catalytic material. This enhancement aims to significantly reduce the overall use of precious metals while boosting activity, thereby ensuring optimal performance. However, whether we can develop this dream of a catalyst depends on our readiness to deeply draw from our technologies in all disciplinary fields and unite collaboratively. The application of quantum chemical theories represents a groundbreaking leap, made feasible within a viable timeframe by revolutionary progress in high-performance computing. This technological advancement stands as a crowning achievement in the domain of ancient natural sciences. Generating a corresponding pool of candidate structures is inherently complex, particularly

Figure 1.1.: High-pressure reaction furnace on an industrial scale around 1920. Reprinted with permission from[2]. ©2024 American Chemical Society.

for dynamic operation, adding to the existing challenges observed in steady-state conditions. Currently, candidate structures are predominantly derived from chemical intuition and available experimental information.[9] These candidates undergo iterative refinement and validation through a comparison of computed and measured spectroscopic signatures.[10] Future research should aim to augment this process with more automated approaches, potentially incorporating global geometry optimization techniques.[11,12] To achieve predictive modeling in materials science with a microscopic understanding, it is essential to employ a description that considers the statistical interplay of numerous well-described elementary processes at the microscopic level.[13,14] This process is influenced not only by the specific stabilization of free energies at the active site but also by the chemical potential in its surroundings, dictated by the reaction environment. The pursuit of a predictive understanding of reaction processes at surfaces stands as a key goal and challenge within modern theoretical surface science. Recent years have witnessed notable progress in this endeavor, driven by enhanced computational capabilities and methodological advancements.[15] Within this work, the entire dedication revolves around utilizing density functional theory (DFT) methods. This methodology grants an unprecedented opportunity to meticulously explore catalytic reactions, operating at the core of the electronic-atomic level. Constructing structural models for presumed active sites involves considering morphological, compositional, and structural changes induced by the reactive atmosphere, including factors such as composition, surface coverage, temperature, and pressure.

1.2. Optimizing Size and Shape of Emission Control Catalysts for Sustainability

The removal of CH_4 by low-temperature combustion[16] plays a pivotal role in emission control strategies. During CH_4 oxidation, a crucial step involves investigating CO oxidation using Pt and/or Pd as the active centers supported on ceria, where ceria serves as a non-innocent support acting as an O reservoir and stabilizing material.

$$Nk_3^+\theta_{CO}\theta_O = \frac{Nk_3^+ K_{CO}\sqrt{K_{O_2}}p_{CO}\sqrt{p_{O_2}}}{1+\sqrt{K_{O_2}p_{O_2}}+K_{CO}p_O} \tag{1.1}$$

Several studies[17–19] have demonstrated the high catalytic activity of Pt and Pd supported on ceria for CO oxidation on ceria surfaces in emission control processes. The forward rate constant of the reaction of CO and O to CO_2 as shown in 1.1 is rate-limiting and depends on both, the number of adsorption sites N and the coverage of the respective reactants, θ_O and θ_{CO}. k_3^+ is the forward rate constant of the surface reaction between CO and O to

form CO_2. K is the equilibrium constant of adsorption and p the partial pressure of the indicated reactant in the gas phase. The back reaction has been neglected in Equation 1.1, excluding the consideration of a CO_2 coverage. A typical potential energy diagram depicts exothermic adsorption of the reactants, a reaction barrier for the activation of CO oxidation, followed by slightly endothermic desorption of the product, the CO_2 molecule.[20] Figure 1.2 depicts the temperature dependence of the CO oxidation rate on a Pd(111) surface as investigated by Engel and Ertl et al. through molecular beam experimentation.[21,22]

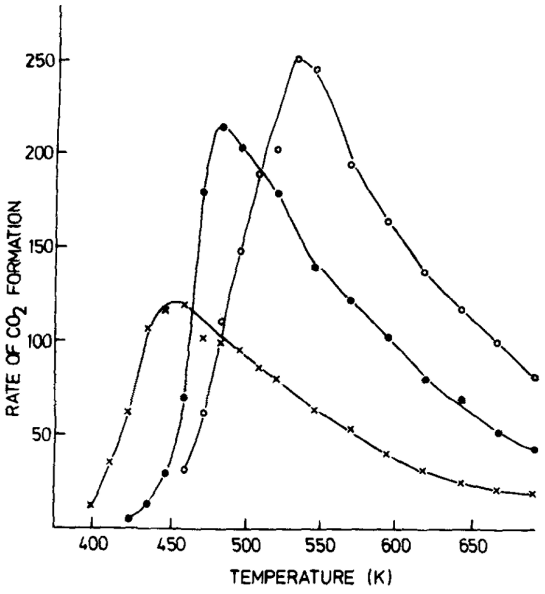

Figure 1.2.: Steady-state CO_2 formation rate as a function of temperature for an O_2 beam and CO pressures. Reprinted with permission from[22]. ©2024 American Chemical Society.

They showed that the CO_2 formation rate reaches its maximum when the coverage of the reactants CO and O is maximized, indicating a competitive process. At low temperatures, there is a deficiency in O coverage, whereas at higher temperatures, there is a deficiency in CO coverage due to the adsorption/desorption equilibrium shifting towards the gas phase side.[20,22,23] As large amounts of CO can poison the surface and inhibit O adsorption, the rate-limiting effect can be considered as the desorption of CO, needed to generate enough adsorption sites for co-adsorption. As a step toward optimizing the catalyst for emission control, the challenge lies in minimizing noble metal loading while maintaining a low operating temperature for economic feasibility in terms of precious metal loading, highlighting the importance of highly dispersed noble metals.[24] In recent years, several studies have focused on the detailed examination of noble metal catalysts composed of Pd and Pt supported on oxides such as ceria and alumina (Al_2O_3), with the aim of optimizing exhaust gas after-treatment catalysts for combustion engines. The surface coverage of reactants on the noble metal depends not only on the reaction conditions but also on the oxidation state and size of the noble metal particles. For instance, Gaenzler, Casapu, Deutschmann, and Grunwaldt et al. investigated the reaction mechanism pathway by spatially resolved operando high energy resolution fluorescence detected X-ray absorption near edge structure (HERFD-XANES), in combination with CO concentration gradient profiles along the catalyst bed, to determine the primary reaction pathways for low and high-temperature CO oxidation on Pt/CeO_2 and Pt/Al_2O_3 catalysts.[25] They found that CO was converted at a similar rate at all positions along the catalyst bed, with a linearly

increasing CO conversion corresponding to a reaction order of zero for Pt/CeO_2. In the case of a LH mechanism, a maximum slope of -1 would be expected due to strong CO poisoning. The HERFD-XANES data showed that CO adsorption on Pt/Al_2O_3 nanoparticles at all catalyst bed positions has a strong poisoning effect. Only at higher temperatures of about 423,15 K the CO would desorb to active the Pt/Al_2O_3 nanoparticles. In contrast to that, Pt/CeO_2 nanoparticles showed that CO was already significantly converted at lower temperatures of about 373,15 K. They proved that the Pt surface gets covered by CO at lower temperatures and the oxidation reaction on the Pt surface is inhibited, the Pt/CeO_2 interface still provides O from the support to the CO covered surface. Su and Hensen et al. examined the growth of stable $Pd_{1\text{-}21}$ clusters through Ostwald ripening and coalescence.[26] They found that Ostwald ripening is the preferred mechanism for the growth of the clusters. They also investigated detachment energies by migration of the $Pd_{1\text{-}21}$ clusters and found that the highest detachment energies 1.70 eV are for Pd_{10}, Pd_{14}, and Pd_{19} clusters. They also found that CO adsorption lowers the detachment energy for clusters with more than 4 Pd atoms. It has been calculated, that the stronger binding of a CO molecule on a single Pd atom, as former studies by Liu et al. on a single gold atom have shown,[27] with -2.40 eV than on clusters larger than Pd_4 as the CO binding on these are about -2.00 and -2.40 eV. Thus, they suggest that this results in the formation of isolated CO-Pd species on ceria. The study conducted by Spezzati et al. involved a thorough investigation of the thermodynamic stability of various Pd_n clusters in the size range of 2 to 21 atoms, as well as Pd and PdO_2 on the $CeO_2(111)$ surface.[28] The findings revealed that under reducing conditions, Pd_n clusters exhibit greater stability compared to isolated Pd. Conversely, in the presence of O, the dispersion of Pd_n clusters into isolated PdO_2 species becomes favorable. This observation provides an explanation for the notable Pd dispersion discussed in the study. Eliasson et al. investigated metal-support interactions between Pt nanoparticles and CeO_2 surfaces, revealing facet-dependent behavior and Pt cluster sizes.[29] Scanning transmission electron microscopy unveiled how the interaction dictated the dimensionality of Pt particles on CeO_2 facets: particles smaller than about 130 atoms preferred 3D shapes on $CeO_2(111)$, while 2D raft structures were favored on $CeO_2(100)$. Time-resolved measurements tracked the migration of a particle from $CeO_2(111)$ to $CeO_2(100)$, transitioning from 3D to 2D, showcasing the intricate transformation mechanism. DFT calculations supported these observations and highlighted the thermodynamic driving force behind the small particle migration. Boronin et al showed in their study that isolated ionic Pd species on CeO_2 nanorods rapidly reduce and agglomerate into metallic clusters during CO oxidation.[30] Their analysis of CO oxidation kinetics, along with *in situ* Near-Ambient Pressure X-ray Photoelectron Spectroscopy (NAP-XPS), Diffuse Reflectance Infrared Fourier Transform Spectroscopy (DRIFTS), and EXAFS, indicates that isolated Pd^{+II} sites are responsible for low-temperature CO oxidation

in both catalysts, with reduced $Pd^{+\delta}$ species becoming active at higher temperatures. They showed that doping CeO_2 with Pd ions activates lattice O, facilitating reverse O spillover at the Pd–O–Ce interface. The mobility of O at the metal–support interface significantly impacts the Pd stability and reactivity of single-atom catalysts. These findings suggest an alternative approach for designing active and stable single-atom catalysts by activating lattice O through support doping with transition metals. During CO oxidation, a decrease in the coordination number of Pd to O and the appearance of clusters with coordination of Pd to Pd indicate partial reduction and clustering of initially atomically dispersed Pd species. Conrad et al. examined O and CO co-adsorption on metallic Pd(111).[31] They found that O_2 adsorption is inhibited when the pre-adsorbed CO exceeds 0.33 ML coverage. This inhibition is not observed when oxygen is adsorbed first, enabling oxidation at 200 K.[32] Engel and colleagues conducted molecular beam studies of CO oxidation on Pd(111) under various conditions.[21–23] They proposed the LH mechanism where CO molecules adsorb on the surface and react with chemisorbed oxygen. The activation energy decreases from low CO coverage to medium coverage. Salo et al. established an atomic-scale mechanism through *ab initio* theoretical studies, suggesting that the reaction prefers the fcc-fcc channel.[33] They showed that CO oxidation follows the LH mechanism, with the desorption of CO, influenced by CO blockage, serving as the rate-limiting step. However, it becomes very clear here that the complexity of the catalyst, along with its properties being dependent on various reaction conditions, highlights the need for a thorough interdisciplinary investigation to optimize this catalyst.

1.2.1. Varying Sizes

The size and morphology of the noble metal clusters are highly under investigation. Varying the crystalline shape of metallic nanocrystals alters their surface facets, consequently affecting their catalytic properties. Kochubey et al. investigated the sizes and morphology by TEM and EXAFS techniques of small Pd clusters supported on oxides.[34] They found narrow size distributions of 15 to 25 Å with distinct morphologies across supports. Disordered Pd surface structures suggested new defect centers from CO and O adsorption. This distortion varied based on support and adsorbate, influencing the reactivity of adsorbed CO by forming new active centers. In a study by Kaden et al., the size-dependent activity of Pd clusters was closely tied to O adsorption for most cluster sizes.[35] They showed that CO_2 production correlated with higher-temperature CO binding sites, indicating efficient CO conversion when O was available. The manipulation of O_2 exposure and temperature on the Pd_n/TiO_2 system with titania (TiO_2) as the support led to a shift from O-limited to CO-limited kinetics, a transition heavily reliant on cluster size. n is an integer representing the number of Pd atoms in a cluster. Consequently, the size dependence of activity was significantly influenced by

O_2 exposure conditions. Smaller clusters exhibited less efficiency in O activation, likely due to their fewer highly coordinated sites compared to single crystals. Furthermore, fluctuations in Pd 3d binding energies, closely correlated with activity, suggest that variations in electron structure based on size may contribute to differences in O activation efficiency. The reaction on subnanometer clusters presents new challenges, as the ceria can as well participate in the reaction. Numerous studies in the past have investigated subnanometer clusters of noble metals supported by pristine and defective $CeO_2(111)$ surfaces. Cargnello et al. conducted a study exploring the impact of ceria-metal interactions on catalytic rates.[36] They established direct links between catalyst structure and function by tailoring the ceria-metal interface length using monodisperse Ni, Pd, and Pt nanocrystals. The researchers observed a significant enhancement in CO oxidation at the ceria-metal interface sites for various group VIII metal catalysts. This finding elucidates the crucial role played by the support in influencing catalytic activity. The frontier of the smallest possible catalysts is represented by single-atom catalysts. These have been extensively explored in the past due to their potential for minimizing resource consumption through highly dispersed active centers. Furthermore, they exhibit interactions with the O atoms of the oxide support, resembling properties known from complex chemistry. However, these catalysts are susceptible to agglomeration, transitioning from subnanometer clusters to nanometer clusters.[26] Any catalysts migrating into the bulk or synthesized to rest in the bulk are lost resources without the possibility of catalytic activity. Besides the trapping on the surface, it has also been shown that Pt_1/CeO_2 single-atoms are stable on the surface and do not migrate into the bulk.[37] Additionally, other studies[38,39] have shown successful atom-trapping to stabilize single Pt atoms on ceria surfaces, enhancing their exposure during the operational conditions and enforcing dynamic changes in the catalysts. The structure-activity relationship of highly dispersed Pt on Ceria showed that the aggregation into nanoparticles leads to the wanted low-temperature CO oxidation enhancement of activity. Re-dispersible subnanometer clusters created by reductive pre-treatment of highly dispersed single-atom catalysts show high activity.[40–44] Considering these contrasting statements, it can be speculated that the active species might not be as dispersed as single-atom catalysts but may consist of just a few atoms, similar to subnanometer clusters. Studies comparing the two well-known active noble metals concerning carbonhydrates and CO oxidation could serve as a basis for the optimized catalyst, possibly consisting of a metal alloy composed of both Pd and Pt. Moreover, a tendency observed through comparison can be attributed to the elemental properties. The relationship between the dispersion of Pd and of Pt on Ceria and their activity dependence upon dispersion and agglomeration in CO oxidation has been elucidated in several studies, emphasizing consequent activity.[45]

1.2.2. Varying Oxidation States

It has been established that Pt and Pd adopt square-planar or octahedral structures on ceria surfaces,[46] which bear resemblance to their crystal structures, particularly the noble metal monooxides PdO and PtO, with square planar coordination of four oxygens and octahedral coordination in the noble metal dioxides PdO_2 and PtO_2 crystal structures. The information on the crystal structures was provided by Shaplygin et al.[47] The lattice constants given by this literature were used as a basis for optimization in this work. For PdO and PtO, it was from Moore et al.,[48] for PdO_2 from Jain et al.[49] and for PtO_2 from Range et al.,[50] In PdO, the Pd^{+II} ions arrange themselves in a square co-planar pattern, forming strong bonds with four equivalent O^{-II} atoms, each bond measuring precisely at 2.03 Å. Conversely, in PtO, the Pt^{+II} ions adopt a comparable square co-planar geometry, engaging in bonding interactions with four equivalent O^{-II} atoms, but with a slightly longer bond length of 2.07 Å for each Pt-O bond. Additionally, the O^{-II} ions in PtO establish connections with four equivalent Pt^{+II} ions, generating a structural combination of corner and edge-sharing PtO_4 tetrahedra. This particular mixture of tetrahedral arrangements contributes significantly to the overall

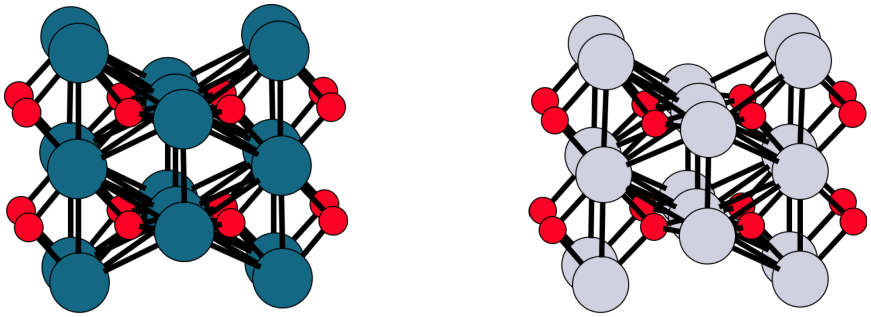

Figure 1.3.: Visualisation of the crystal structures of $Pd^{+II}O$ and $Pt^{+II}O$ crystals.

stability and structural characteristics of PtO. PtO_2 and PdO_2 exhibit distinctive structural arrangements within the tetragonal $P4_2/mnm$ space group. PtO_2 adopts the hydrophilite structure, where Pt^{+IV} ions are intricately bonded to six equivalent O^{-II} atoms. These bonds form a unique combination of both edge and corner-sharing PtO_6 octahedra, featuring corner-sharing octahedral tilt angles at 53°. Within this structure, there are two Pt-O bond lengths measuring shorter at 2.01 Å, and four others at longer lengths of 2.04 Å. Furthermore, the O^{-II} ions exhibit a trigonal planar geometry, engaging with three equivalent Pt^{+IV} atoms. PdO_2 as well shares the hydrophilite structure and crystallizes in the tetragonal $P4_2/mnm$ space group. In PdO_2, Pd^{+IV} ions bond with six equivalent O^{-II} atoms to create a mixture of edge and corner-sharing PdO_6 octahedra. The corner-sharing octahedral tilt angles measure at 52°in this structure. Pd-O bond lengths include two shorter bonds, measuring 1.97 Å, and four longer bonds at 2.00 Å. Similarly, O^{-II} ions in PdO_2 are bonded in a trigonal planar geometry, establishing connections with three equivalent Pd^{+IV} atoms. Some researchers

suggest that partially oxidized Pd serves as a poor CO oxidation catalyst, proposing that Pd dispersion might not primarily control the activity of supported Pd catalysts. Satsuma et al. analyzed using Temperature Programmed Reduction with CO (CO-TPR) that the catalytic activity order aligns quite well with the reduction temperature of supported Pd to metallic species.[51] Additionally, they suggest that there is an assertion that a lower dispersion of Pd tends to enhance activity to some extent. They noted that highly dispersed Pd particles are inclined to oxidize to Pd^{+II} ions often denoted as PdO atoms, which are from some groups assumed to be less active than metallic Pd. Thus, the metallic state of Pd is presumed to be more crucial than Pd dispersion in enhancing catalytic activity. There is a controversial assumption that the partially oxidized noble metal atoms may indeed be the active species. Further investigations concerning the contribution of the support reveal that the O storage property of the samples corresponds well with their catalytic activity for CO oxidation. This implies that the O storage of the support is another pivotal factor for CO oxidation. Both CeO_2 and TiO_2 possess remarkable O release and storage capacities, resulting in improved activities of Pd/CeO_2 and Pd/TiO_2. The currently strongest assumption is that two factors significantly influence CO oxidation over supported Pd catalysts: the reducibility of PdO to Pd and the O storage capacity of the support. The reducible support of CeO_2 particularly plays a crucial role in catalyzing the oxidation of CO due to its notable redox properties. While the metal-support interface is commonly believed to be the site of the reaction, there is no definitive conclusion regarding the nature of the active sites or phases. Regarding Pd/CeO_2 supported catalysts, the PdO species are considered the active sites for CO oxidation.[52–55] As nanometer clusters of noble metals can be approximated on pristine metal surfaces, studies concerning the catalytic activity of pure noble metals have been made, both theoretically[56–61] and experimentally[62–66]. To reduce the noble metal loading the cluster sizes can be reduced to subnanometer-size clusters or, in extreme cases, even dispersed down to single atoms. Fu et al. conducted a study on downsizing Pt nanoparticles to Pt_1 single atoms on CeO_2 using a laser ablation strategy.[67] Enhancing dispersion allows for a reduction in the quantity of noble metal since it increases the surface-to-volume ratio. Heterogeneous catalysts exhibit activity solely at their surface, hence, loading high amounts of noble metals leading to larger particles results in a significant portion that remains inaccessible to the reactants. Bruix et al. investigated the widespread use of Pt in catalysis despite its high-cost limitation.[68] This emphasizes the need for more efficient utilization of noble metal single-atoms on catalyst surfaces. One of the most promising approaches is to identify ceria dioxide 'nano pockets' that stabilize Pt^{+II} ions,[69,70] thus resisting sintering and diffusion. This discovery has the potential to reduce the use of precious metals in catalyst materials, thereby benefiting fuel cell applications.

1.3. Ceria as the non-innocent Support

There has been considerable attention paid to understanding the role of ceria in well-established industrial processes such as fluid catalytic cracking and three-way catalysts, where CeO is a crucial component in catalyst formulation.[71] Ceria is employed in automotive exhaust after treatment as support of noble metals as the active center for emissions treatment.[18] Ceria-zirconia, with zirconia (ZrO_2) as a second oxide, is one of the main components in the CO oxidation under dynamic/pulse mode.[72] Extensive research by the use of first principal methods has been conducted in the past on the ceria surface,[46,73–83] as well as experimentally[84–88] investigating their electronic properties and corresponding catalytic activities. Ceria has a non-innocent role in heterogeneous catalysis.[89] Numerous studies employing first principles methods[26,90–94] and experimental approaches[24,25,41,42,95–102] to name just a few have been conducted in this regard. Three-way catalysts aim at treating noxious pollutants from car exhausts.[103] The catalyst used in treating auto exhaust comprises noble metals and metal oxides dispersed on alumina pellets or a ceramic substrate coated with alumina. The crucial role of ceria involve O buffering during the fluctuating rich-to-lean gas phases at temperatures around 1000-1100 K. Efforts aim to optimize the thermal stability of ceria without compromising its unique properties like redox capabilities and O and V_O mobility. Researchers focus on ceria combined with thermally stable support, like CeO_2, for efficient O exchange during CO and hydrocarbon removal in O-deficient phases.[76,104–106] As ceria remains a solid crystal during the operation conditions for emission control the atomistic model can be built using pertinent crystallographic data. Simulations have revealed, that the lowest energy pathway for O atoms to move in a ceria lattice is from one site to a neighboring defect which reflects the experimentally proven property of ceria as an ion conductor.[107–111] During exhaust after-treatment, an internal combustion engine alternates between rich exhaust stoichiometry (deficient in O_2) and lean exhaust stoichiometry (excess of O_2).[106] Under these reaction conditions, ceria is subjected to an alternating cycle of reduction and oxidation.

$$4CeO_2 + 2CO \rightarrow 2Ce_2O_3 + 2CO_2 \tag{1.2}$$

$$2Ce_2O_3 + O_2 \rightarrow 4CeO_2 \tag{1.3}$$

Equation 1.2 represents reduction through the oxidation of CO molecules, while Equation 1.3 illustrates oxidation through O_2 molecules, both in consideration of stoichiometry. The transition between these two favored oxidation states is a property of the oxide that imparts its catalytic activity as an O reservoir.[112] The activity of ceria changes drastically due to the change of oxidation state on the surface.[113,114] Ceria behaves as an n-type semiconductor

as it has modified defects that introduce additional negatively charged electrons into the crystal structure. As Ceria gets reduced, it changes to be an n-type semiconductor and its transmission decreases due to the large absorption as the number of conduction electrons increases by reduction.[115] The introduction of V_O in the crystal structure of ceria reduces the bandgap and affects the way the material interacts with light. As the bandgap of ceria decreases, it can absorb longer wavelengths of light, which can fall into the black part of the visible spectrum. After reduction, the color changes successively towards grey. The element Ce in the lanthanide series exhibits both the oxidation states +IV and +III[116] as showed in the formal reaction scheme 1.4.

$$2Ce^{+IV}O_2 \rightarrow Ce_2^{+III}O_3 + 0.5O_2 \tag{1.4}$$

Numerous O atoms can be removed from the crystal lattice without altering the crystal structure.[76,81,116,117] This unique property of ceria has given this oxide significant importance in industrial applications.[76,106] Formally, this changes the composition of ceria from CeO_2 to Ce_2O_3. These two structures possess different crystal structures that can be examined by DFT methods. The corresponding oxide to these two oxidation states has the chemical structural formulas $Ce^{+IV}O_2$ and $Ce^{+II}{}_2O_3$. The change in the oxidation state of the Ce ion between +IV and +III is key to the catalytic properties of this oxide.[117] In the fully oxidized oxide $Ce^{+IV}O_2$, continuous reduction to $Ce^{+III}{}_2O_3$ is possible. The description of the content of CeO_2 and Ce_2O_3 in ceria-based catalytically active applications is of importance for a fundamental understanding of the catalytic active material. An accurate calculation of the CeO_2 and Ce_2O_3 properties demands to account for strong localization of the Ce f electron in the formal oxidation state +III.[118] Libuda et al. devised an experimental approach based of physical vapor deposition for creating a stable phase of normally polymorphic Ce_2O_3, referred to as bulk-truncated epitaxial cubic c-Ce_2O_3. This method allows precise measurements of CeO_2 surface properties under extreme conditions. By this method, a perfectly ordered arrangement of surface and subsurface defects at a total concentration of 25 % compared to CeO_2 is exhibited.[119] The reducible nature of ceria oxide renders it a non-innocent support, poised to substantially enhance the efficacy of the catalyst in fully oxidizing exhaust after-treatments. Consequently, the electronic properties of ceria are also a focal point of numerous studies aimed at better comprehending the characteristics of this oxide. A study by Kopelent et al showed that, utilizing time-resolved resonant X-ray emission spectroscopy, quantitatively correlated the initial rate of Ce^{+III} formation under transient conditions with the overall rate of CO oxidation under steady-state conditions.[120] They demonstrated that ceria reduction is a kinetically relevant step in CO oxidation, with an fraction of Ce^{+III} present as spectators. The study provided quantitative evidence for the formation of active Ce^{+III} species during CO oxidation on a platinum-promoted ceria-based

catalyst. The study of Kopelent et al. is an investigation into Ce^{+III} as an intermediate in CO oxidation and revealed a direct correlation between its formation rate under transient conditions and the steady-state CO conversion rate. They estimated initial CO_2 formation rates over a Pt/CeO_2 catalyst during transient conditions and comparing them with steady-state rates indicated a proportional relationship, validated by mass spectrometric data. This supports Ce^{+III} as an active species in CO oxidation, with O atoms between Pt and CeO_2 interfaces playing a crucial role. The analysis suggests that only O and cerium atoms near the metal–support interface contribute to CO oxidation at low temperatures, aligning with experimental findings.

1.3.1. Crystal Structure of Ceria from a theoretical Perspective

During the transitions between O-rich and O-poor cycles in a process, there is a dynamic interplay of O atoms or V_O defects induced by material reduction. The dual redox behavior of ceria stems from a mechanism in which it acts both as an O donor and acceptor. However, the exact nature of this mechanism and the involvement of Ce atoms remain not fully understood. Numerous studies have been conducted in the past on the electronic properties of ceria. One approach involves examining the ceria surface under reaction conditions, focusing on the formation and repair of O defects, as well as the subsequent generation and relaxation of these defects on the surface through polaron hopping.[71,121] Studies by Sauer and Ganduglia-Pironova et al. and other groups[80,82,88,122] have shown, that when forming O surface lattice defects, the position of the reduced Ce^{+III} ions is stabilized at a next-nearest position to the O lattice defect. In a stoichiometric (111) surface of ceria, all Ce ions are in the +IV oxidation state. The f-band is entirely empty in this oxidation state, located within an energy gap between the occupied O 2p states and the unoccupied Ce 5d states. In the partially reduced form, the removal of O results in the creation of two Ce^{+III} ions, with the remaining electrons localizing on the Ce^{+IV} f orbitals of the atoms after the removal of a neutral O atom due to the high electron negativity of the O atoms. This results in a valence change $Ce^{+IV} \rightarrow Ce^{+III}$ of formally two cations per defect.[123,124] These highly localized partially occupied f orbitals are present split from the unoccupied f states. The structure of CeO_2 oxide can have a cubic fluorite structure (CaF_2) with a space group of $Fm\bar{3}m$ as shown in Figure 1.4 a) and four tetragonal phases, all belonging to the $P4_2/nmc$ space group[125–127].[116,128] The Ce atoms are located at the 4 a 0,0,0 sites, and the O atoms at the 8c 1/4,1/4,1/4 sites.[76] The fluorite structure of CeO_2 consists of a cubic closed-packed (ccp) array of metal atoms with all tetrahedral holes filled by O. Ceria as an oxide with an elemental electron configuration $[Xe]4f^26f^2$ for the Ce atom has one $4f^1$ left in the valence shell. The energy cost for the removal of an O atom has been calculated by Zhang et al. to be 2.23 eV using GGA + U with U = 5 eV. It has been found, that O

defects are much more facile to form than Ce defects as the excess charge by the removal of a neutral O can be compensated on the ceria surface while the removal of Ce atoms leads to a significant charge depletion on the surrounding O atoms.[129] In a reducing atmosphere CeO_2 forms continously non-stoichiometric CeO_{2-x} (α phase $0<x\leq0.5$) oxides due to the formation of O-defects. The fluorite structure remains even after a higher loss of O atoms forming O defects in the lattice. The so-formed suboxides are likely to be reoxidized by exposure to an oxidizing environment. All structures are considered to be fluorite-related and anion-deficient. The fcc array of metal atoms has all tetrahedral interstitial positions filled with O atoms. The metal atoms are eight coordinated with O atoms at the corners of the coordination cube. The four-coordinated O atoms are at the center of a tetrahedron with metal atoms at the corners. The homologous series of fluorite-related O-deficient structures have the generic formula Ce_2O_{2n-2}.[130] The CeO crystal has a cubic crystal system and the space group $Fm\bar{3}m$. The reducibility and the O transport capacity are coupled with the

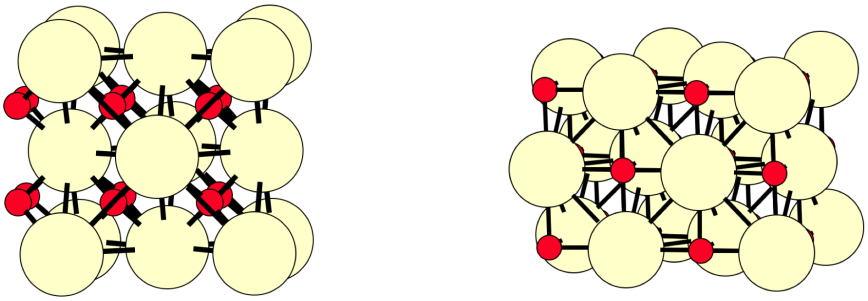

Figure 1.4.: Visualisation of the crystal structure of CeO_2[128] in the bulk phase (left) and (right) crystal structure of CeO[131] in the bulk phase (right).

facile shift between the two oxidation states of the Ce atom. Several theoretical studies have been conducted to explore the reducibility and structural effects of ceria from a theoretical perspective. The LDA and the GGA approach give a wrong metallic ground state for Ce_2O_3 arising from the narrow band character of the partially occupied 3d states. Neyman et al. investigated the strongly correlated insulator Ce_2O_3 which shows limits in the accurate description by the electronic structure calculations based on standard DFT.[132] Kresse et al showed that the GGA description of Ce_2O_3 is incorrect.[133] This has led to the improvement of the DFT methods and to go beyond the GGA and LDA approach to the GGA + U and LDA + U approaches to localize the 4f electrons properly. The electron correlations in narrow bands were initially developed to describe partially filled d- and f-bands in transition and rare earth metals. The correlation effects in narrow bands lead to atomic behavior. The electron charge density is then concentrated near the nuclei of the solid and sparse between the atoms.[134] It has been assumed, that a retro-donation from the ion to the CO molecules results in a stronger adsorption.[106] The approach of Hubbard to the collective motion problem, expanded to encompass both collective and internal electron plasma motions,

and extended to non-uniform gases,[134–136] significantly enhanced accuracy in electron localization, proving beneficial for material design purposes.[137] Electron correlations in narrow bands were originally designed to characterize partially filled d- and f-bands in transition and rare earth metals. These correlations mimic atomic behavior by concentrating electron charge density around solid nuclei while keeping it sparse between atoms.[134] This method allows the localization of an electron on a specific atom, as observed in the reduction from Ce^{+IV} to Ce^{+III} in ceria. To optimize the applied DFT method, the impact of the U value was investigated by Zhang et al. and found to be in good agreement with a Hubbard U-term of U = 5 eV.[129] Su et al. conducted a study on charge transport in defective $CeO_2(111)$.[138] First-principles calculations were employed to investigate the charge transport process. Two possible mechanisms were considered: direct migration of the O anion (defect diffusion) and a polaron-hopping-assisted mechanism. Through DFT + U calculations, it was found that the polaron-hopping is significantly more favorable than direct migration. The overall barrier for charge transport involving polaron migration, followed by O diffusion, is determined by the barrier for polaron hopping, amounting to 0.18 eV. A careful analysis of magnetization density, density of states, and reaction pathway trajectory revealed that this process is phonon induced. Since the calculation of the positions of the reduced Ce_{+III} ions alone by GGA + U methods does not lead to an optimization of the positioning, post-DFT methods are necessary to calculate the stabilization of polarons on the ceria surface. In the investigation led by Wang et al., concise molecular dynamics (MD) simulations were employed to explore the dynamic behavior of surplus electrons. At a room temperature of 300 K, electrons initially situated in the bulk layer, second or third layer, exhibited vertical hopping to the surface layer and lateral mobility within the surface layer. The electrons transition from the second Ce layer to the surface Ce layer is about 1.5 ps through a delocalization process at both layers. Upon reaching the surface Ce layer, electrons predominantly moved freely without returning to the second Ce layer. Additional 300 K *ab initio* molecular dynamics (AIMD) simulations, commencing with electrons localized at the surface Ce layer, did not observe 4f electron penetration into the bulk throughout the entire simulation duration of about 10ps. This behavior is attributed to increased elastic strain on the surface layer induced by creating a subsurface Ce^{+III} defect. In summary, AIMD results indicate a preference for electron localization at the surface, and charge transport within the initial Ce layer is facile.[139]

1.3.2. Surface Facets of Ceria

Ceria surfaces exhibit distinctive facets: octahedra with (111) surfaces, cubes exposing (100) facets, and rods with (100) and (110) terminations. The choice of the support material and its surface structures plays a crucial role as they can influence the chemical environment

of the individual catalyst atoms. Investigating the various facets of the ceria support (100), (110), and (111) aims to understand how the surface structure affects the interaction between the support material and the individual catalyst atoms. Different facets may exhibit distinct binding properties and surface reactivities, subsequently impacting the catalytic activity of single-atom catalysts as illustrated in Figure 1.5. Throughout the work, we will delve into the bonding relationships and configurations for CO oxidation in more detail. There have been numerous experimental studies in the past that demonstrate the activities of noble metals supported on different ceria surface facets. Castanet et al. conducted studies on ceria surfaces and their influence on catalytic activity, focusing on surface facets (100), (110), and (111).[140] They synthesized cubic CeO_2 nanoparticles via microwave-assisted hydrothermal synthesis in highly alkaline conditions. High-resolution transmission electron microscopy (HRTEM) revealed truncation of cube edges by CeO_2(110) surfaces and cube corners by CeO_2(111) surfaces. Adjusting synthesis conditions increased particle size, notably affecting the CeO_2(100) facets while maintaining constant sizes for CeO_2(110) and CeO_2(111). MD simulations supported this observation, indicating that (111) and (110) surfaces truncated cube edges and corners, respectively, to stabilize the nanocube. The findings highlighted surface facet balancing and the distinct behavior of (100), (110), and (111) surfaces, shedding light on nanoceria surface chemistry and potential catalyst design at the nanoscale. Song et al. synthesized ultra-low loading Pt/CeO_2 catalysts and investigated their behavior under reduction.[141] They showed that at 423.15 K, Pt atoms remain isolated on all facets. Pt_1/CeO_2 catalysts under CO oxidation conditions showed

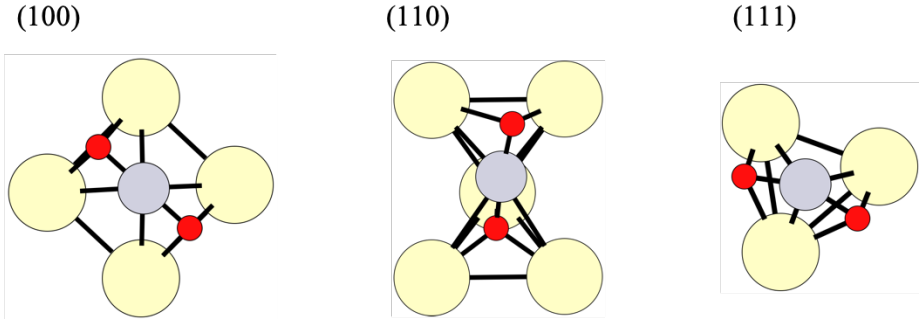

Figure 1.5.: Visualization of the bond coordination of the Pt single site adsorbed on the (100), (110), and (111) surface facets as optimized in this work. Red circles represent O, yellow circles denote Ce atoms, and gray circles indicate Pt atoms.

facet-dependent behaviors. Pt on octahedra and cubes demonstrated lower activity due to CO blocking active sites and limited O supply. Conversely, Pt supported on rods exhibited higher activity attributed to weaker Pt-CO bonds and easier O spillover from defect-rich surfaces, proving more stable over time. This study underscores the significance of low metal loadings and well-defined oxide supports in uncovering metal-support interactions

at an atomic level and their influence on catalytic activity. The study by Spezziati et al. investigates the impact of CeO_2 in rod and cube configurations on the reactivity of Pd.[142] They found that Pd supported on CeO_2 rods facilitates CO oxidation at room temperature via a LH mechanism involving isolated Pd_1O and Pd_1O_2 species. Additionally, Pd/CeO_2 cubes also contain isolated Pd_1O, demonstrating CO oxidation through a MvK pathway. The research highlights higher energy barriers in the catalytic cycle on $Pd/CeO_2(100)$ compared to $Pd/CeO_2(111)$. EXAFS measurements indicate varying responses of active Pd phases to different environmental conditions, especially significant redispersion for Pd/CeO_2 rods after oxidative treatment, which leads to heightened reactivity. Single-atom catalysts consist of individual noble metal atoms placed on a support material such as ceria. In contrast to larger metal nanoparticles in nanometer size, individual atoms in single-atom catalysts directly interact with the reactant molecules. Single-atom catalysts represent the frontier between homogeneous and heterogeneous chemistry, bridged by the field of complex chemistry. An investigation of single-atom catalysts on heterogeneous

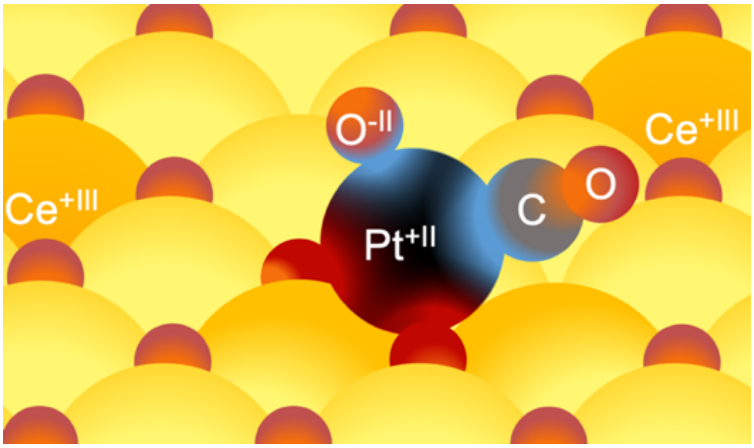

Figure 1.6.: Schematic representation of a Pt single-atom catalyst supported on the ceria (111) facets. The contextual environment is elucidated by Ce^{+IV} ions (pale yellow), Ce^{+III} ions (orange), the $Pt^{+II}O$ ion (black), O ions (red), and a carbon (gray). The color transitions signify the electronic effect exchange between the ions.

catalysts allows for targeted insights into the electronic properties of the catalyst, which can lead to further discoveries. In the past, there have been numerous experimental and theoretical investigations that have focused on the properties of single-atom catalysts. A highly dispersed noble metal is economically of particular interest, as resources can be minimized through low noble metal consumption while maintaining equivalent activity. Furthermore, the surface facets of the support can be examined more closely, allowing for a comparison of activity and stability. A schematic illustration in Figure 1.6 depicts the electronic interplay among the elements of a heterogeneous catalyst. Neitzel et al. showed, that Pt cations are stable on the surface rather than in the ceria bulk. Pd cations

show a high tendency to stabilize not only on the surface but also in the ceria bulk.[143,144] Jones et al. investigated catalysts utilizing single atoms of rare precious metals, aiming to enhance reactivity and selectivity. They employed ceria powders with distinct surface facets, observing that polyhedral ceria and nanorods effectively anchored platinum compared to ceria cubes. Their synthesis method at elevated temperatures ensured stable binding sites, resulting in a sinter-resistant catalyst with atomically dispersed metal.[38] The (100) surface is the most under-coordinated. It has the particular ability to stabilize single-atom catalysts by adsorbing them into these 'pockets'. These 'pockets' are indentations on the surface that form between four adjacent Ce atoms. Additionally, due to the stoichiometric ceria, there are two O atoms present that enable the anchoring of the single atoms. Bruix et al. suggested, and Maurer et al. support the assumption of four-fold-hollow sites/square O pockets provided by $CeO_2(100)$ to stabilize Pt^{+II} by bonding to O^{2-} in square pockets. The study of Maurer et al. has shown that a single-atom Pt catalyst supported on reductive oxides such as ceria and alumina is not active within the operating temperature for emission control.[68,69] In a study by Figueroba et al.,[145] they conducted density-functional calculations on different transition metal atoms interacting with nanoparticulate CeO_2. Investigating the (100) nanofacets of CeO_2, the research demonstrated a strong capacity of these surfaces to oxidize the interacting transition metals. Notably, metals anchored as cations on the (100) facets of nanostructured ceria exhibited remarkable stability, resisting agglomeration into metal particles. This suggests the potential for designing stable single-atom catalysts with high metal efficiency in nanocatalysis. The (110) surface forms rows of Ce atoms on the surface, alternating in height. One could also refer to this as a kind of 'tunnel'. The 'tunnel' facilitates the stabilization of noble metals by embedding them between two prominent rows of Ce and anchoring the noble metal with two O atoms at the bottom of the 'tunnel'. Unlike the (100) surface where there is a 'pocket' between four Ce atoms, a linear row exists, allowing the noble metal atom to move more freely within the tunnel. In the investigation by Fu et al., it was observed through Laser ablation and DFT calculations that Pt nanoparticles served as the primary active center for CO oxidation. Concurrently, Pt single-atom catalysts supported on a (110) surface facet of ceria altered the chemical potential of lattice O on ceria, thereby lowering the energy barrier necessary for CO oxidation by lattice O, leading to an overall enhancement in performance.[146] The (111) surface of ceria is the most densely packed ceria surface. Su et al. conducted theoretical density functional theory (DFT) calculations examining Pd cluster ripening on $CeO_2(111)$.[26] They observed that Ostwald ripening is the primary sintering mechanism, as Pd atoms possess greater mobility than Pdn clusters on the $CeO_2(111)$ surface. Coalescence occurs for clusters comprising fewer than 5 Pd atoms, facilitated by adsorbed CO, which reduces barriers for cluster diffusion and the detachment of Pd atoms, transforming initial planar clusters. On the topmost layer,

numerous O atoms are present, offering binding sites for noble metals. Spectroscopic analyses of single-atom catalysts supported on ceria reveal unique peaks across diverse temperature ranges, distinguishing them from extended metal surfaces or subnanometer-sized clusters. The gas phase vibrational frequency of CO serves as a crucial probing tool, offering unmistakable signatures in infrared spectra. The collective interplay of adsorption energies and vibrational frequencies provides insights into the electronic environment. The size distribution of the noble metal could alternate during the reaction between single-atom catalysts or subnanometer clusters, and nanometer clusters. Given that a weighting of size scales can occur, and it is also likely that several facets exist simultaneously at different size scales, the separate investigation of size scales is significant. As described in the past, there have been several approaches. Lou et al. compared Pt nanoparticles to single-atom catalysts supported on ceria.[147] They highlighted the remarkable activity of low Pt-loaded Pt_1/Fe_2O_3 and Pt_1/CeO_2 for high-temperature CO oxidation, demonstrating comparable performance to 1.0 wt% nano-Pt/Fe_2O_3 at 623.15 K. Using DFT calculations, they identified the role of the Pt_1–O_4 configuration in catalyzing CO oxidation through a non-classical MvK pathway while ensuring Pt_1 atom stability.

1.4. Distinct CO Oxidation Pathways on noble Metals as Active Centers supported by Ceria

The active species undergo dynamic structural changes under varying operational conditions characterized by lean and rich environments at different temperatures, impacting the oxidation state and dispersion of noble metals. These conditions can cause oxidation or reduction of the species, which can exist as single atoms, subnanometer-sized clusters, or larger nanometer-sized clusters. Each of these species demonstrates distinct activity levels for CH_4 and CO oxidation. In Figure 1.7, a schematic representation of an elementary reaction step for CO oxidation, catalyzed by a heterogeneous catalyst, is depicted. The potential energies of the respective reaction steps are influenced by electronic and morphological interactions with the heterogeneous catalyst. The reaction depicted here for CO oxidation presents a favorable reaction mechanism based on the relative Gibbs free energies. However, depending on the constitution at the electronic and morphological levels of the catalyst surface, the relative Gibbs free energies can adversely affect the relative energies. This could result in inhibition of CO_2 molecule desorption or insufficient adsorption strength of the reactants, leading to an increase in the reaction barrier relative to the reactants in the gas phase. The activities of the heterogeneous catalysts are assessed by evaluating their performance in CO oxidation, O_2 dissociation, and CO_2 desorption, considering both the LH and MvK mechanisms. Numer-

ous theoretical[148] and experimental[36,149–152] studies have focused on the two reaction mechanisms.

The actual underlying reaction mechanism in the CO oxidation catalyzed by noble metals Pd and Pt supported on ceria remains unknown.[68] Some studies postulate, that the lattice O can be activated under the reaction conditions.[153] However, this is questionable due to assumed poisoning by CO_2 molecules, as the desorption energy is considered too high. The Mars-van-Krevelen (MvK) mechanism is named after the scientists (J.H. de Boer), A.J. Mars, and J. van Krevelen, who made significant contributions to catalysis research and proposed this mechanism. The MvK mechanism postulates that the lattice components of the catalyst are present in the reaction products.[154] An oxidation mechanism involving lattice O that becomes part of the desorbing products was explicitly formulated by Kroeger et al.,[155] and experimental studies supported this assumption.[156,157] Several studies assume, that introducing noble metal ions as Pd activates the lattice O of ceria.[30,142] Boreskov et al. conducted an investigation into the MvK mechanism using isotopic exchange in molecular O_2. This method aids in studying the catalytic oxidation reaction mechanisms by revealing details about the nature of O_2 bonds on oxidation catalyst surfaces. Catalytic reactions take place through interactions between adsorbed molecules, adsorbed radicals, or fragments of the reactant molecules in the adsorption mechanism. The Eley-Rideal (ER) mechanism suggests that a reaction by collision of molecules from the gas phase with the adsorbed species is feasible. The ER mechanism has been indirectly confirmed through reaction kinetics.[158] A study conducted by Kumar et al. examines the LH and the ER mechanisms. The investigation focuses on catalytic CO oxidation on Pt(111). The study finds that reaction barriers for LH mechanisms tend to be higher than those for ER mechanisms. Despite this higher barrier, experimental evidence still favors the LH mechanism for this system. The critical contrast between these mechanisms is rooted in the behavior of chemisorbed CO on the surface. In the LH mechanism, chemisorbed CO establishes a bond with the surface. In contrast, in the ER mechanism, the CO molecule does not form a chemical bond with the surface. The study by Kumar indicates that the unique energy characteristics of the

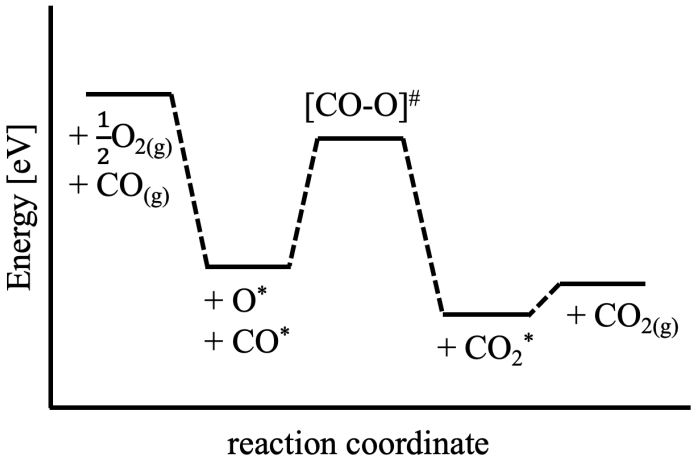

Figure 1.7.: Schematic representation of an elementary reaction step for CO oxidation, catalyzed by a heterogeneous catalyst.

system hinder the likelihood of a collision between the CO molecule and the adsorbed O atom.[159] In his studies he explains, as a CO molecule approaches an O-covered surface, it typically enters the chemisorption unless precisely above the adsorbed O atom. Given that O atoms occupy only a small part of the surface, the chance of CO aligning directly above O at the outset is relatively low. Even if CO is placed directly above O and approaches it, the ER mechanism might not progress due to encountering a substantial reaction barrier. He concludes that repulsive forces are more likely to guide the CO molecule towards the chemisorption well rather than surmounting the barrier.

1.4.1. Langmuir-Hinshelwood Mechanism

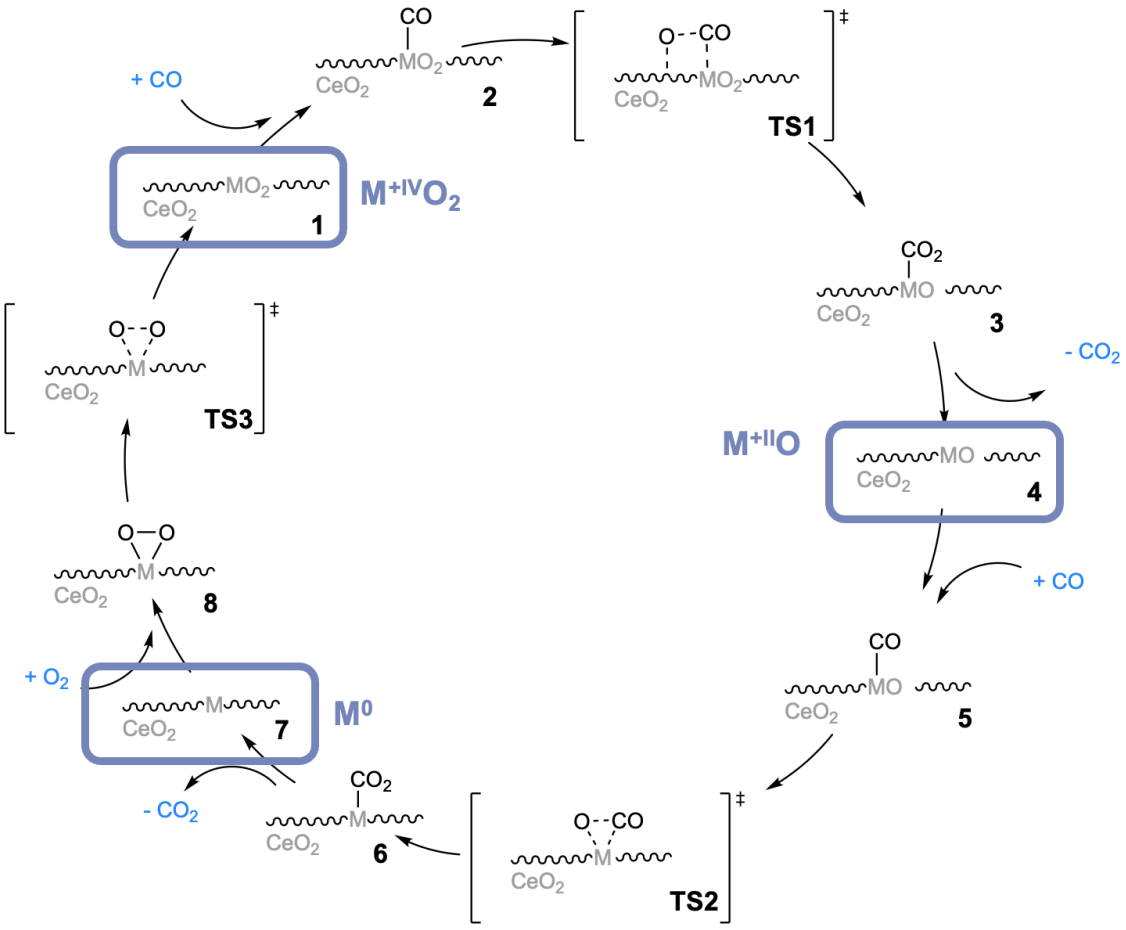

Figure 1.8.: Reaction mechanism cycle of the LH mechanism conducted on the ceria support (curved lines) and a noble metal M (Pd or Pt) as the active center. For simplicity, M is represented here as a SAC. However, it could also be located at an interface between the support material ceria and the noble metal cluster. The reactants in the gas phase are depicted in blue. The intermediate oxidation states of the noble metals are highlighted in pale blue.

Unlike the MvK mechanism, the LH mechanism does not utilize the oxygen atoms from the crystal lattice for CO oxidation. Instead, these O atoms are adsorbed onto the noble metals Pd or Pt without impacting its crystal structure or converting the crystal structure of the noble metal into oxides. The reaction mechanism cycle depicted in Figure 1.8 initiates with the active site species $M^{+IV}O_2/CeO_2$ (1). This involves a noble metal M (Pt or Pd) supported on the ceria surface, additionally featuring two adsorbed O atoms in a vicinal position to the noble metal. Consequently, the noble metal is oxidized, resulting in a formal oxidation state of +IV for an individual noble metal atom. In the subsequent step, a CO molecule adsorbs linearly onto a noble metal atom, forming the spezies CO-$M^{+IV}O_2/CeO_2$ (2), which then undergoes a transition state $[CO\text{-}O\text{-}M^{+II}O/CeO_2]^{\ddagger}$ (TS1) for CO oxidation. The resulting CO_2 molecule initially remains adsorbed on the surface CO_2-$M^{+II}O/CeO_2$ (3). The adsorbed CO_2 molecule is bent at an angle and anchored to the surface by one oxygen atom. Desorption leads to the creation of the $M^{+II}O/CeO_2$ species (4), incorporating an additional O atom adsorbed in a vicinal position to the noble metal atom of interest. This adsorbed O atom further facilitates CO oxidation. Subsequently, another CO molecule adsorbs onto the noble metal atom in a vicinal position to the O atom, forming CO-$M^{+II}O/CeO_2$ (5). The CO oxidation proceeds through a transition state denoted as $[CO\text{-}O\text{-}M^{0}/CeO_2]^{\ddagger}$ (TS2). The resulting CO_2 molecule initially remains adsorbed on the noble metal, bent at an angle and anchored to the surface by one oxygen atom as CO_2-M^{0}/CeO_2 (6). Upon the desorption of the CO_2 molecule, the Pt^{0}/CeO_2 species (7) is created, representing a noble metal supported on the stoichiometric ceria surface with no additional O atoms. In a subsequent step, an O_2 molecule can adsorb, forming O_2-M^{0}/CeO_2 (8). The dissociation of the O_2 molecule proceeds through a transition state $[O\text{-}O\text{-}M^{0}/CeO_2]^{\ddagger}$ (TS3). After dissociation, two O atoms are adsorbed in a vicinal position to the noble metal, creating the $MO_2{}^{+IV}/CeO_2$ (1) species, which marks the starting point of the reaction mechanism cycle.

1.4.2. Mars-van Krevelen Mechanism

In a MvK mechanism an O lattice atom (O_l) is utilized, which is characterized by its integration into the crystal structure of the heterogeneous catalyst.[154] This means that the removal of this O_l will require the expenditure of lattice energy. This O_l atom can be a part of both the support and the noble metal. In any case, the prerequisite is that the O_l atom is explicitly integrated into the crystal structure and is part of the lattice structure, such that its removal would reduce the stoichiometric formula of the crystal structure by one O atom. The resulting oxygen lattice defect, V_O, therefore represents a structural defect. In this work, it is considered that the MvK mechanism explicitly takes place at the interface between M and the support. The reaction mechanism illustrated in Figure 1.9 commences

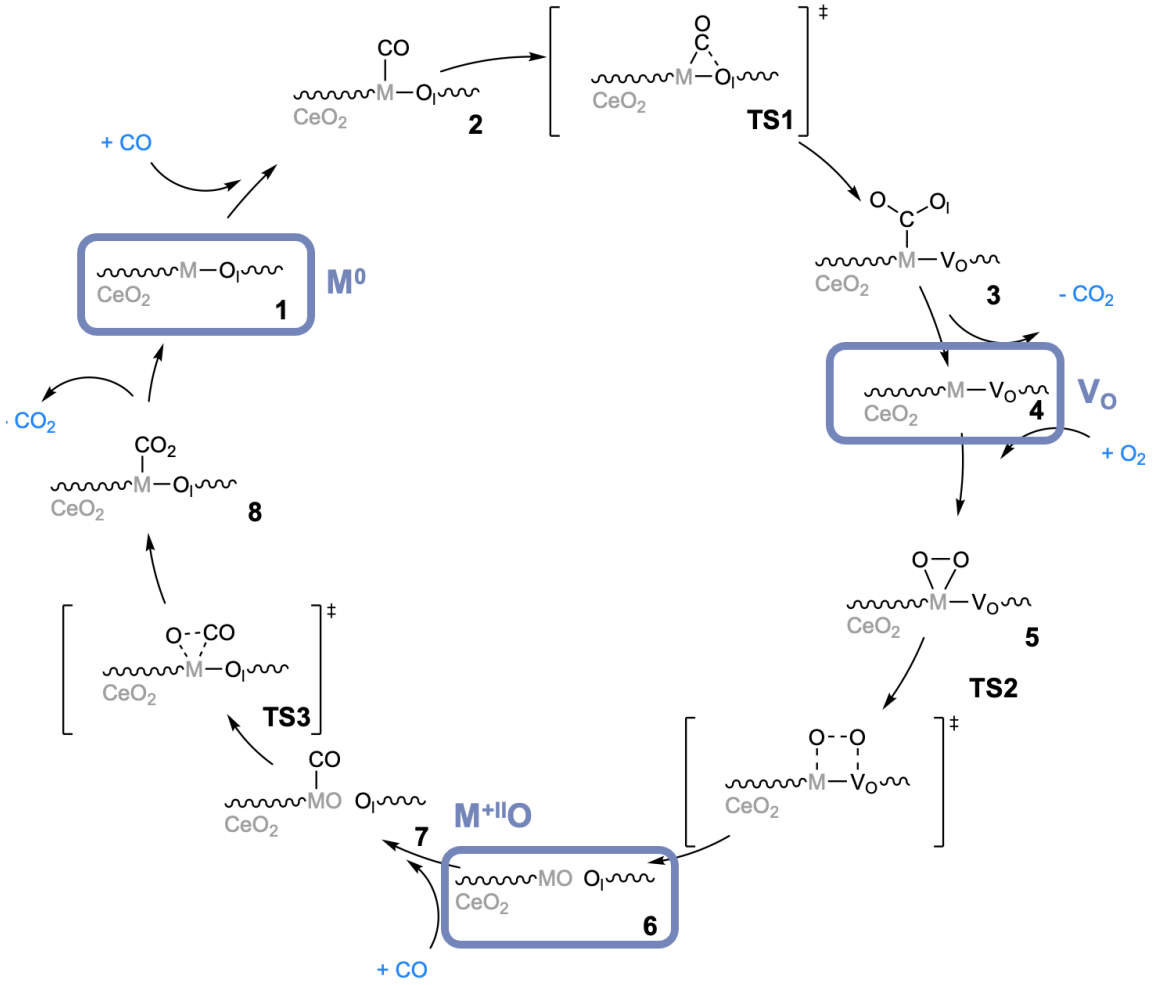

Figure 1.9.: Reaction mechanism cycle of the MvK mechanism conducted on the ceria support (curved lines) and a noble metal M (Pd or Pt) as the active center. For simplicity, M is represented here as a SAC. However, it could also be located at an interface between the support material ceria and the noble metal cluster. The reactants in the gas phase are depicted in blue. The intermediate oxidation states of the noble metals are highlighted in pale blue.

with the species Pt^0/CeO_2 (1) which is a noble metal supported on the stoichiometric ceria surface and no oxidation of the noble metal by additional O atoms. In the subsequent step, a CO molecule adsorbs linearly onto a noble metal atom, $CO\text{-}M^0/CeO_2$ (2), which then undergoes a transition state $[CO\text{-}O\text{-}V_O\text{-}M^{-\delta}/CeO_2]^{\ddagger}$ (TS1) for CO oxidation. The oxidation state is undetermined but negative. Therefore, $-\delta$ was chosen to denote this oxidation state. The resulting CO_2 molecule initially remains adsorbed on the surface, $CO_2\text{-}M^{-\delta}/CeO_2$ (3). The adsorbed CO_2 molecule can be either bent at an angle or linear, and is anchored to the surface by the oxygen atom O_l to replace the oxygen defect V_O. This situation is particularly significant in the MvK mechanism, as the desorption of the CO_2 molecule must overcome lattice energy to remove this oxygen atom. Desorption leads to the formation of the $V_O\text{-}M^{-\delta}/CeO_2$ species (4), containing an O lattice defect V_O. In a subsequent step, the

defect V_O is regenerated by the adsorption of an O_2 molecule, O_2-V_O-$M^{-\delta}/CeO_2$ (5). If V_O is filled by the adsorption of an O_2 molecule, the oxidation state of the noble metal is neutral 0 and no longer negative -δ. The dissociation of the O_2 molecule proceeds through a transition state $[O\text{-}O\text{-}V_O\text{-}M^{-\delta}/CeO_2]^{\ddagger}$ (TS2), resulting in an $M^{+II}O/CeO_2$ species (6), where the noble metal holds an adsorbed O atom in a vicinal position. This adsorbed O atom can further be utilized for CO oxidation. For this purpose, another CO molecule adsorbs onto the noble metal atom that is in a vicinal position to the O atom, $M^{+II}O/CeO_2$ (7). A transition state $[CO\text{-}O\text{-}M^0/CeO_2]^{\ddagger}$ (TS3) is involved in the CO oxidation process. The resulting CO_2 molecule remains initially adsorbed on the noble metal, CO_2-M^0/CeO_2 (8). After desorption of the CO_2 molecule, the reaction mechanism cycle returns to its initial state. It should be noted that the illustrated reaction mechanisms LH and MvK shown here are schematic and may deviate in the case of specific noble metal and support configurations. For instance, the formed CO_2 molecule may desorb spontaneously (with a minor energy barrier) without anchoring to the surface of the heterogeneous catalyst in an intermediate step. Conversely, it is worth mentioning that during the formation of an O defect on the surface, an O atom from the CO_2 molecule can indeed coordinate to this defect. Therefore, the depictions in Figure 1.8 and 1.9 are not static but can be adjusted to the specific situation characteristic of the catalyst being considered.

1.5. Deciphering activities through Scaling Relations

The quest for an optimized catalyst for industrial purposes is until today an odyssey of trial-and-error processes. Analytical concepts, coupled with the chemical intuition of chemists, have the potential to expedite the search for a catalyst with enhanced catalytic performance. Rather than relying solely on one chemist, interdisciplinary collaborations among research

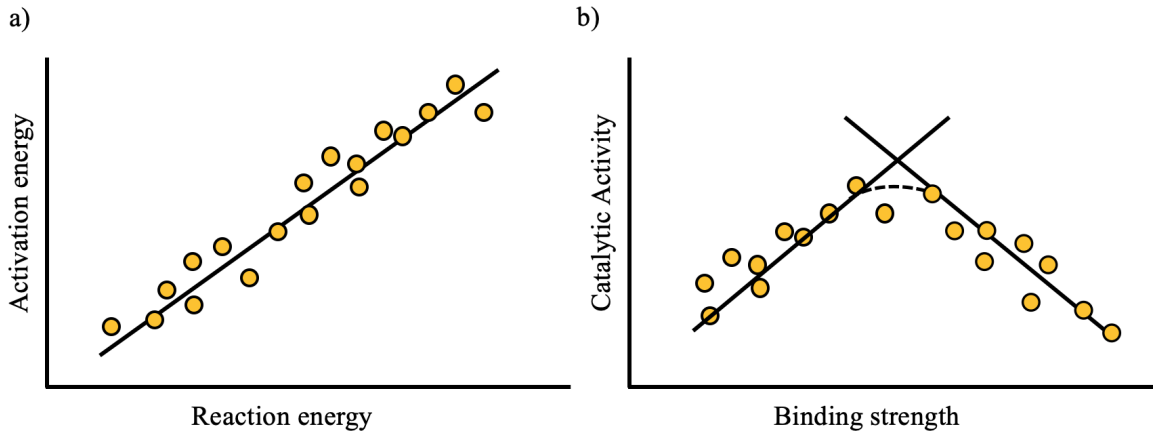

Figure 1.10.: Schematic representation of scaling relations (a) and volcano plots (b). Reproduced from the cited literature sources in this section.

institutions represent a modern approach to broaden the perspective on the challenge of finding the optimized catalyst, enabling the brightest minds to collaborate. One possible perspective on an atomic level is facilitated by methods based on quantum chemistry. Contrary to the commonly mentioned belief that first-principle methods represent a more sustainable approach without the use of chemicals, the computational power required, along with the associated time and electrical energy, makes it nevertheless a resource-intensive endeavor. Analytical concepts provide possible guidance in the trial-and-error process, narrowing down the search for the optimized catalyst. One of these concepts is the development of scaling relations. This concept is rooted in the idea that certain properties of catalysts, such as binding energies of reaction intermediates or transition states, are interconnected. Brønsted fixed a conception of acidity and basicity by a theoretical definition determining an activity concept that is used for reactions catalyzed by acids and basics.[160] The influence of a catalyst is described by Evans and Polanyi to be able to

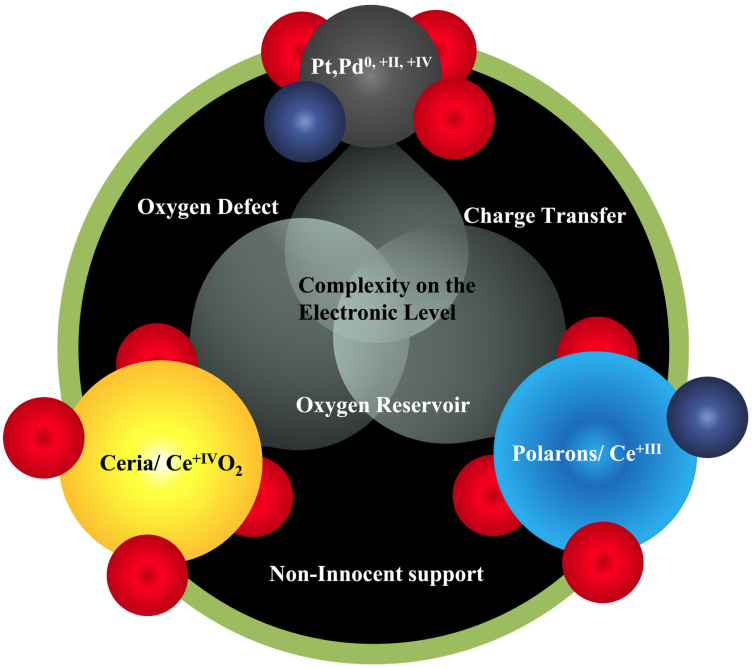

Figure 1.11.: Schematic illustration of $Ce^{+IV}O_4$ (yellow), $Ce^{+III}O_4$ (bright blue), and a noble metal $Pd^{0,+II,+IV}O_4$ (black). These are surrounded by O atoms as they are embedded in the crystal structure of the heterogeneous catalyst. The O atoms are schematically represented in each species as 4 (red) or may be absent as O lattice defects (dark blue). Orbital clouds between these three species are depicted in transparent gray, indicating electronic interferences.

break (inertia) and to form (driving force) bonds due to its electron properties. A driving force is referred to as the formation of a bond that occurs in the reaction and causes a lowering of the activation energy.[161] The theories were combined into the Brønsted-Evan-Polyani Principle describing the relationship between the activation energy for dissociation in the case of oxidation reactions, as in this work for CO oxidation, and the surface bond

energy which depends on the surface structure. This linear relationship can be translated into a volcano-shaped dependence of the catalytic activity on the adsorption energy.[162] In Figure 1.10, a schematic representation of the scaling relations and volcano plots is depicted. A linear scaling relation illustrates the correlation between two descriptors. A volcano plot illustrates two correlations that unify the surface properties of the heterogeneous catalyst.An ascending curve can represent the increasing binding strength of the surface, while a descending one can represent a surface with increasing binding weakness. And as the transition state geometries are similar for different reactants, the relationship is considered to be adsorbate-independent.[162] Zhao et al. reviewed the challenges in identifying active sites in heterogeneous catalysts, highlighting two decades of scaling relationships. Reactivity descriptors, scaling linearly with other properties, facilitate predicting catalytic performance. Using these descriptors enables rational catalyst design and efficient screening of the activities.[163] The endeavor of fundamental understanding of the electronic structure of an ensemble of surface atoms and its relationship with the energetics of adsorbate-surface interactions is part of a long history of research that has concentrated on unraveling the electronic structure of functional materials, particularly in the context of their catalytic performance.[164–167] Xin et al. investigated the influence of d-band shape on local electronic structure to understand the intricate link between electronic structure and chemical reactivity on metal surfaces by utilizing the upper d-band edge.[168] Khorshidi et al. broke linear scaling relationships with single-atom alloys, and illustrated how strain can effectively overcome this limitation by employing a mechanics-based eigenstress model to rationalize the influence of strain on the bonding between adsorbates and catalysts. This model suggests that the direction of the binding-energy response to strain relies on the interplay between the eigenstress induced by the adsorbate and the applied strain. Therefore, under tensile strain, the binding can be either strengthened or weakened, depending on the specific eigenstress characteristics of the adsorbate on the surface.[169] Figure 1.11 encapsulates the fundamental properties of the catalysts, necessitating a meticulous, multi-perspective examination that unveils intricate interconnections between these attributes. Thus far, the majority of reactivity descriptors have been confined to a specific class of catalyst materials, such as metal surfaces or metal-oxide surfaces. The formation energy of active sites can be readily adjusted by altering the physical properties of the catalysts. In this work, an ensemble of size-varying noble metals supported on the non-innocent reducible oxide ceria is generated and their activities in CO oxidation are investigated. By this, the intrinsic chemical and physical properties of these ceria-supported noble metals are examined by establishing scaling relations. An ordered sequence of noble metal surfaces, influenced by size differences through a size-effect, can demonstrate a correlation with activity at the electronic level in interaction with ceria.

1.6. Validation of the Active Species through Spectroscopic Investigations

To experimentally validate the vibrational frequencies calculated through DFT methods, a comparison is commonly made with spectroscopic techniques such as DRIFTS and Ultrahigh Vacuum Fourier Transform Infrared Spectroscopy (UHV-FTIR). These methods leverage the unique vibrational frequency of CO in an isolated environment, confirming the accuracy of the theoretical predictions. Furthermore, the structural validation of the catalysts is enhanced through EXAFS measurements, adding depth to the understanding of their composition and behavior. In recent years, numerous studies have once again turned their attention to catalytic converters. The current technologies have reached a new standard, encouraging renewed research investments. The interdisciplinary interplay of innovations can provide insights into catalysts that may lead to optimization, significantly impacting the cost-effectiveness of the catalysts. Spezzati et al. undertook an extensive exploration of the CO oxidation reaction mechanism, employing a blend of experimental methodologies, including aberration-corrected TEM to elucidate Pd site structures and CO-FTIR for characterizing adsorbed CO.[28,142] Theoretical calculations, utilizing DFT, allowed for precise assignment of each infrared band, facilitating a comprehensive assessment of the entire catalytic mechanism and validating the presence of single Pd sites in the catalyst. Selected spectroscopic data extracted from the literature are presented in Table 1.1. Spezzati et al. investigated individual Pd sites play a pivotal role in promoting low-temperature CO oxidation. The identification of single sites in the Pd/CeO_2-rod sample, confirmed through AC-TEM and FTIR, explains the enhanced activity of the catalyst in CO oxidation at temperatures where metallic Pd remains inactive due to CO poisoning. In the study of single-atom catalysts, Boronin et al. compare two Pd/CeO_2 catalysts synthesized through different methods.[30] The catalysts, active in low-temperature CO oxidation, exhibit varying structural dynamics during the reaction. The impregnated catalyst faces reduction and sintering of oxidized Pd atoms, while the flame spray pyrolysis-derived catalyst maintains Pd atom integrity on the CeO_2 surface. *In situ* characterization links Pd single atom stability to the Pd-CeO_2 the reducibility of the interface and the extent of reverse O spillover, highlighting the importance of understanding metal–support interactions for rational catalyst design. In their investigation, they discovered three major CO infrared bands for the Pd-rods catalyst under reaction conditions. The band at 2143 cm^{-1} corresponds to CO adsorbed on Pd single atoms bound to CeO_2 through two bridged O atoms (Pd_1O_2). Another band at 2096 cm^{-1} is attributed to Pd single atoms bound to CeO_2 via one O atom (Pd_1O_2). As CO oxidation progresses, additional carbonyl bands at about 2060 and about 1900 cm^{-1} emerge, indicating the presence of semi-oxidized and metallic Pd clusters, respectively. The

Table 1.1.: Assembly of experimental and theoretical vibrational frequencies of the CO molecule adsorbed on Pd as single-atom catalysts and in several cluster sizes supported on ceria in recent literature.

Species	Experimental f [cm^{-1}]	Theoretical f [cm^{-1}]
Spezzati et al.[28,142]		
$Pd^{0}/CeO_2(111)$		2048
$Pd^{+II}O/CeO_2(111)$	2098	2099
$Pd^{+IV}O_2/CeO_2(111)$	2143	2137
$Pd_3/CeO_2(111)$, 1-fold		2062
$Pd_3O/CeO_2(111)$, 2-fold	1907	1912 (1900-1950)
$Pd_{n,small}O_{x,partial}/CeO_2(111)$	$\sim$ 1900	
Spezzati et al.[28,142]		
Pd(111), 1-fold		2056
Pd(111), 2-fold		1868
Pd(111), 3-fold		1789
Boronin et al, on nanorods with (111) and (110) surface facets[30]		
$Pd^{+II}O/CeO_2$	2143	
$Pd^{+IV}O_2/CeO_2$	2096	
$Pd_{n,small}O_{x,partial}/CeO_2$	2060	
$Pd_{n,small}O_{x,partial}/CeO_2$	$\sim$1900	
Maurer et al.[69]		
$Pd^{+II}O/CeO_2(100)$		2092
$Pd^{+II}O/CeO_2(110)$		2043
$Pd^{+II}O/CeO_2(111)$		2090
Salcedo et al.[10]		
$Pd_{13}/CeO_2(111)$, 1-fold		2043
$Pd_{13}/CeO_2(111)$, 2-fold		1900
$Pd_{13}/CeO_2(111)$, 3-fold		1868

study by Maurer et al. successfully identified platinum-induced restructuring on the CeO_2 surface, precisely locating platinum single sites, and monitoring changes in their active state during reactions.[69] Utilizing a combination of density functional theory calculations, *in situ* infrared spectroscopy, operando high-energy-resolution fluorescence detected X-ray absorption spectroscopy, and catalytic CO, C_3H_6, and CH_4 oxidation, the research reveals that the initiation of CO oxidation corresponds to the migration of platinum single sites from four-fold hollow positions to form small clusters with a few platinum atoms. This emphasizes the pivotal role of operando studies in assessing the fate and resulting catalytic properties of single sites. Salcedo et al. investigated the limitations of extended flat surface models in capturing essential features unique to nanoparticles.[10] These include lower metallic coordination, edges, kinks, interaction with the support, and the finite nature of nanoparticles. They created a model by adsorbing CO exclusively on bridge sites at edges, revealing a spectrum devoid of peaks corresponding to linear and hollow CO. This underscores the importance of considering strong vibrational coupling between various CO

adsorbates at high coverage, spreading the CO stretching vibrational region into several IR active bands. Through preceding experimental studies, this work aims to validate our purely theoretical models developed through first principle methods and proceed to investigate their activities. Since catalytic species cannot be unequivocally assigned under spectroscopic investigations, and depending on the method, only a vague assumption is possible, DFT methods provide an opportunity to make a clear conjecture about the species by optimizing the structures quantum chemically. In Table 1.1, experimentally determined vibrational spectra are listed, as presented in the literature. Through continuous comparison between experimental and our theoretically determined investigations conducted here, an attempt can be made to validate the species.

1.7. Scope of this Work

The active species undergo dynamic structural changes during operating conditions, as lean and rich conditions at varying temperatures affect the oxidation state and dispersion of noble metals. Depending on the conditions, the species can be oxidized or reduced as single atoms, subnanometer-sized clusters, or larger nanometer-sized clusters. Each of these species exhibits different activity levels for CH_4 and CO oxidation.[170] Previous studies from Li et al.[171] on the size effect of clusters in the gas phase have revealed that the electronic structure of clusters approaches that of a crystal as their size increases beyond a critical threshold. Up to this critical size, the electronic impact on reactant adsorption converges. This work provides an overview across several distinguished size scales of active species, varying the oxidation states, and compares them with experimental studies to validate the species present under reaction conditions. By examining the associated activities, our aim is to investigate a size effect concerning the size of noble metals on the support. The activities are compared through CO oxidation, O_2 dissociation, and CO_2 desorption, considering both the LH and the MvK mechanisms. Additionally, the reducibility of the ceria surface in the vicinity of the noble metal catalyst was assessed, and the activity dependent on the oxidation state of the cerium ions was calculated. Due to the ability of single-atom catalysts to rapidly explore surface structures of ceria and oxidation states through computationally expensive DFT calculations, a comprehensive case study is conducted on the most prominently exposed surface facets of ceria (100), (110), and (111), along with the stable oxidation states of the single-atom catalysts +II and +IV that the catalyst transitions through during a reaction. Subsequently, the configurations of selected subnanometer-sized clusters are examined as a function of coverage by the reactants O and CO. Furthermore, spectroscopic properties of the size scales were examined to provide a wide range of possibilities for subsequent experimental investigations, aiming to better distinguish the species. Upon exploring these

size regimes of the active center, namely the noble metal supported on the non-innocent support ceria as single-atom catalysts, as subnanometer clusters in the size range of 3 to 10 atoms, and as nanometer clusters (approached theoretically by extended metal surfaces), scaling relations have been identified that elucidate the correlations between activities in CO oxidation via the LH and MvK mechanisms and the interaction of the catalyst as a function of size scales. Utilizing these scaling relations, one can compare and reconcile the activities across various size scales, the oxidation states of noble metals, and the support materials. Insights into the correlation between the electronic and morphological properties of the catalyst and its activity could serve as a guide for future investigations.

2. Computational Chemistry of Heterogeneous Catalysts

2.1. Quantum Chemistry of Multi-Atomic Systems

2.1.1. The Electronic Problem

The application of quantum chemical methods plays a crucial role in understanding and predicting the behavior of molecules and materials at the atomic and electronic levels. By solving the time-independent, non-relativistic Schrödinger equation, quantum chemical calculations provide valuable insights into molecular energies, electronic structures, and chemical properties. In 1926, Louis de Broglie introducing the Hamiltonian analogy between mechanics and optics, which laid the foundation for the subsequent development by Schrödinger of the wave equation, a pivotal concept in quantum mechanics.[172,173] Schrödinger developed in this, and in the subsequent writings, a theory that is now known as the Schrödinger equation for describing the motion of particles. The time-dependent Schrödinger equation is used to describe the motion of nuclei and electrons. The interactions in their stationary states can be represented by the time-dependent Schrödinger equation 2.1.[174]

$$i\hbar\frac{\partial}{\partial t}\Psi(r,t) = \left(-\frac{\hbar^2}{2m}\nabla^2 + V(r,t)\right)\Psi(r,t) = (\hat{T}+\hat{V})\Psi(r,t) = \hat{H}(r,t)\Psi(r,t) \qquad (2.1)$$

$\hat{\mathrm{H}}$ is the Hamilton operator, and Ψ the wave function to describe the state of the system, i is the imaginary number unit, $\hbar$ is the reduced the Planck constant with $\hbar = \frac{\mathrm{h}}{2\pi}$, t is the time, r the vector of position including all the positions of particles in the system, ∇ is the spatial differential operator, m is the particle mass. The energy of the system can be determined by applying the Hamiltonian operator, which comprises both the potential operator $\hat{\mathrm{V}}$ and the kinetic operator $\hat{\mathrm{T}}$. When the potential remains constant or changes slowly over time, the Hamiltonian is considered time-independent, allowing the Schrödinger equation to be expressed by equation 2.1 with $\mathrm{E_n}$ as the Eigenenergies of the system calculated from the operations on the wave function.

$$\Psi(r,t) = \Psi(r)\cdot e^{\frac{-iE_n}{\hbar}t} \qquad (2.2)$$

The energy of a multi-atomic system consisting of nuclei and electrons with vector positions of R and r, respectively, can be found by applying the time-independent Hamiltonian on the wave function $\Psi(\mathrm{r},\mathrm{R})$. The distance between the i^{th} and the A^{th} nucleus is given as $\mathrm{r_{iA}} = |\mathrm{r_{iA}}| = |\mathrm{r_i} - \mathrm{R_A}|$ and the distance between the i^{th} and the j^{th} electron is given as $\mathrm{r_{ij}} = |\mathrm{r_i} - \mathrm{r_j}|$. The distance between the i^{th} nucleus is $\mathrm{R_{AB}} = |\mathrm{R_A} - \mathrm{R_B}|$. The Hamiltonian $\hat{\mathrm{H}}_{\mathrm{nucl}}$ for a system of N electrons and M nuclei is expressed as the sum of the kinetic energy operators for the electrons and nuclei, the potential energy interactions between electrons and nuclei, and the electron-electron interactions, given by equation 2.3 and 2.4.[175]

$$\hat{H}_{nucl} = -\sum_{i=1}^{N} \frac{1}{2}\nabla_i^2 - \sum_{A=1}^{M} \frac{1}{2M_A}\nabla_A^2 - \sum_{i=1}^{N}\sum_{A=1}^{M} \frac{Z_A}{r_{iA}} + \sum_{i=1}^{N}\sum_{j>i}^{N} \frac{1}{r_{ij}} + \sum_{A=1}^{M}\sum_{B>A}^{M} \frac{Z_A Z_B}{R_{AB}} \tag{2.3}$$

In Equation 2.3 $\mathrm{M_A}$ symbolizes the ratio between the mass of nucleus A to the mass an electron, while $\mathrm{Z_A}$ denotes the atomic number of the nucleus A. The Laplacian operators ∇_{i}^2 and ∇_{A}^2 involve the differentiation with respect to the coordinates of the i^{th} electron and the A^{th} nucleus. The components outlined in Equation 2.3 correspond to the operators regulating the kinetic energies of the electrons, which can be designated as $\mathrm{T_e}$, and the nuclei, $\mathrm{T_N}$, the coulomb attraction between nuclei and electrons, $\mathrm{V_{Ne}}$, is represented in the third term. The fourth and fifth terms elucidate the potential energies stemming from electron-electron repulsion, $\mathrm{V_{ee}}$, and nucleus-nucleus repulsion, $\mathrm{V_{NN}}$, respectively. Thus, Equation 2.3 can be succinctly summarized as shown in Equation 2.4.[175]

$$\hat{H} = \hat{T}_e + \hat{T}_N + \hat{V}_{Ne} + \hat{V}_{ee} + \hat{V}_{NN} \tag{2.4}$$

Once the electronic problem is solved, the motion of the nuclei can then be determined using the same assumptions that were applied to formulate the electronic problem. The mass of a nucleus is typically 10^4 times heavier than an electron. This ansatz is called the Born-Oppenheimer approximation and can serve as the foundation for an approximation, under the assumption that the electrons promptly enter a stationary state upon the movement of a nucleus. By applying the Born-Oppenheimer approximation to the interactions between nuclei and electrons, which are described by the Hamiltonian operator $\hat{\mathrm{H}}$, the kinetic energy of the nuclei and the potential energy due to nuclei are neglected, while the core repulsion is treated as constant. Equation 2.3 can be reduced to the terms describing the electronic contributions, which can be associated with the electronic Hamiltonian operator, denoted as $\hat{\mathrm{H}}_{\mathrm{elec}}$.[175]

$$\hat{H}_{elec} = -\sum_{i=1}^{N} \frac{1}{2}\nabla_i^2 - \sum_{i=1}^{N}\sum_{A=1}^{M} \frac{Z_A}{r_{iA}} + \sum_{i=1}^{N}\sum_{j>i}^{N} \frac{1}{r_{ij}} \tag{2.5}$$

Hence, the solution to a Schrödinger equation governed by the Hamiltonian yields the electronic wave function, denoted as Ψ_{elec}, as depicted in Equation 2.6. This function delineates the electron dynamics, explicitly contingent upon electronic coordinates with $\Psi_{\text{elec}} = \Psi_{\text{elec}}(\{\text{r}_\text{i}\}, \{\text{R}_\text{A}\})$ and parametrically influenced by nuclear coordinates, akin to the electronic energy E_{elec}. The parametric dependence means that a different arrangement of the nuclei results in a different function of the electronic coordinates.[175]

$$\hat{H}_{elec}\Psi_{elec} = E_{elec}\Psi_{elec} \tag{2.6}$$

Upon solving the electronic problem, it becomes feasible to address the motion of the nuclei utilizing the same assumption employed in formulating the electronic problem. The solution to the Schrödinger equation involves the electronic Hamiltonian and is the electronic wave function which describes the motion of the electrons as shown in equation 2.7.[175]

$$\Psi_{elec} = \Psi_{elec}(\{r_i\};\{R_A\}) \tag{2.7}$$

r_i denotes the vector position of the electron i, and R_i the vector position of the nucleus i. The electronic wave function depends explicitly on the electronic coordinates but parametrically on the nuclear coordinates just as the electronic energy does as shown in equation 2.8.[175]

$$E_{elec} = E_{elec}(\{R_A\}) \tag{2.8}$$

The parametric dependence of the nuclei in different arragements is refered to a different function of coordinates Ψ_{elec} where the nuclear coordinates are not explicitly included. To describe the total energy for fixed nuclei the constant nuclear repulsion must be included as shown in equation 2.9.[175]

$$E_{total} = E_{elec} + \sum_{A=1}^{M}\sum_{B>A}^{M}\frac{Z_A Z_B}{R_{AB}} \tag{2.9}$$

Equations 2.5 and 2.9 are developed to constitute the electronic problem. This generates a nuclear Hamiltonian H_{nucl} for the motion of the nuceli in the average field of the electrons as shown in Equation 2.10, which is the shorter version of Equation 2.3, to calculate the total energy $\text{E}_{\text{total}}(\{\text{R}_\text{A}\})$.[175]

$$\hat{H}_{nucl} = \sum_{A=1}^{M}\frac{1}{2M_A}\nabla_A^2 + E_{total}(\{R_A\}) \tag{2.10}$$

The total energy, denoted as $E_{total}(\{R_A\})$, serves as a potential for the nuclear motion, constituting what is known as a potential energy surface. Within the framework of the Born-Oppenheimer approximation, the nuclei traverse this surface, which arises from the solution to the electronic problem. This approach is instrumental in theoretical catalysis for assessing the relative stabilities of states within the chemical system.[175]

$$\hat{H}_{nucl}\Psi_{nucl} = E\Psi_{nucl} \tag{2.11}$$

The solution to a nuclear Schrödinger equation, as shown in equation 2.11, describe the vibration, rotation and translation of a molecule and can be described by equation 2.12.[175]

$$\Psi_{nucl} = \Psi_{nucl}(\{R_A\}) \tag{2.12}$$

Here, E as the total energy of the Born-Oppenheimer approximation includes the electronic, vibrational, rotational and translational energy. Thus, the corresponding approximation to the total wave function of the time-independent Schrödinger equation $\hat{H}|\Psi_{nucl}\rangle = E|\Psi_{nucl}\rangle$ is as shown in eqution 2.13.[175]

$$\Psi(\{r_i\};\{R_A\}) = \Psi_{elec}(\{r_i\};\{R_A\})\Psi_{nucl}(\{R_A\}) \tag{2.13}$$

The concept known as Hess's Law will be described in Section 2.24, named after the chemist Germain Henri Hess, describes a fundamental principle in thermodynamics. It states that the total enthalpy change of a chemical reaction remains constant regardless of the pathway taken from the initial to the final state. This allows chemists to determine the overall enthalpy change by summing the enthalpy changes of individual steps, regardless of their observability.[176,177]

2.1.1.1. The Hartree-Fock Approximation

The first publication on the Hartree-Fock (HF) method was authored by Douglas Hartree in 1928.[178] The work of Hartree laid the foundation for what became known as the Hartree-Fock method, which is a widely used approximation method in quantum mechanics for solving the electronic structure of atoms and molecules. In his work, he discusses the potential application of the wave mechanics by Schrödinger to refine the atomic structure model of Niels Bohr. He suggests using wave functions to describe charge density within atoms, aiming to improve upon the classical approach Bohr. In the HF method, the wave function is represented as a Slater determinant Ψ^{SD} composed of single-particle wave functions, with each orbital describing one electron. The aim is to minimize the total energy of the system by applying the principle of variation within a self-consistent field

framework. In variational theory, the wave function of the system is varied by adjusting certain parameters within this wave function. These parameters are chosen in such a way that they minimize the energy of the system. The exact energy determined by the HF method is inherently limited by the approximations made within the method itself rather than solely by the broader theoretical frameworks like the Born-Oppenheimer approximation and the non-relativistic condition. The HF method approximates the many-body wave function by neglecting electron correlation effects beyond the mean-field approximation, which treats electron-electron interactions as an average field. To accomplish this, the HF method employs operators such as the Coulomb operator J_{ij} and the exchange operator K_{ij}. K_{ij} has a minus sign from the factor of $(-1)^p$ in the antisymmetrizing operator. These operators act on pairs of electrons i and j. The Coulomb operator accounts for the classical electrostatic repulsion between electrons, while the exchange operator ensures the antisymmetry of the wave function due to the Pauli exclusion principle. Together, these operators are utilized to construct the Fock operator, which is then diagonalized to solve the Hartree-Fock equations. Equation 2.14 presents the symmetrical form, incorporating the self-interaction correction for an electron interacting with itself within an orbital. The factor of 1/2 ensures that the double sum accounts for all electron pairs without double-counting.[179]

$$E_{el} = \langle \Psi^{SD} | \hat{H}_{el} | \Psi^{SD} \rangle = \sum_{i=1}^{N} h_i + \frac{1}{2} \sum_{i=1}^{N} \sum_{j=1}^{N} (J_{ij} - K_{ij}) + V_{nn} \tag{2.14}$$

The Fock operator contains terms that account for both Coulomb and exchange interactions between electrons. These interactions differ for electrons with parallel and antiparallel spin. By approximating the HF method, the ability of electrons with the same spin to avoid each other while minimizing energy is neglected, leading to the exclusion of a significant part of electron interaction known as electron correlation. This omission impacts the description of chemical systems.

2.1.2. Density Functional Theory

Constructed on the foundational theorems of Hohenberg and Kohn, DFT posits that electrons within a system respond to an external potential. The first theorem of Hohenberg and Kohn asserts that both the external potential and the total energy are uniquely determined by the electron density, forming a distinct functional relationship in their work published in 1964. This pivotal work marked the inception of DFT, a widely employed theoretical framework in fields such as condensed matter physics, chemistry, and materials science.[180] They introduced a variational principle for the ground-state energy, where the electron density as a variable. They derived a universal functional applicable to all ground states

of the electronic systems, regardless of the external potential, capturing deviations from uniform density. Their analysis included cases of slowly varying density, advancing previous refinements of the Thomas-Fermi method. However, they acknowledged the limitations of the gradient expansion in describing certain oscillations in electronic density. Additionally, they examined a collection of arbitrary electrons influenced by external potential and mutual Coulomb repulsion, assuming nondegenerate ground states denoted. DFT differs from HF fundamentally by relying on the electron density of the quantum chemical system rather than wave functions. According to the first Hohenberg-Kohn theorem, the ground state energy can be directly derived from the electron density. This energy is expressed as a functional of the electron density and is calculated as a numerical value from the function. However, the exact functional remains unknown. One approach is to compute the kinetic energy using an auxiliary set of orbitals, while the remaining, relatively small portion is attributed to the exchange-correlation energy, obtained through uniform functional distribution for specific chemical systems. The energy functional is divided into three functionals: the kinetic energy T[ρ], the attraction between nuclei and electrons $E_{eN}[\rho]$, and the electron-electron repulsion $E_{ee}[\rho]$. The nuclear-nuclear repulsion $E_{NN}[\rho]$ is considered constant within the Born-Oppenheimer approximation. The $E_{ee}[\rho]$ functional can be further split into two components: the Coulomb and exchange-correlation xc parts, represented as J[ρ] and K[ρ], respectively.[179]

$$\hat{H} = \hat{T} + \hat{V}_{ee} + \hat{V}_{ext} \tag{2.15}$$

These enable the calculation of the ground-state energy directly from the electron density F[ρ(r)], obviating the need for a wave function. The first Hohenberg-Kohn theorem establishes a connection between the exact ground state energy and an unknown functional F[$\rho(\tilde{r})$] of the electron density. This functional is universal, applying equally to every system. With this functional, the relationship between density and energy can be described. The external potential is determined by the exact density of the ground state and depends on the number of electrons N, the core coordinates A(R_A), and the charge of the nucleus Z_A. Consequently, the Hamilton operator $\hat{H}$ is uniquely determined by the density of the ground state. The Hamilton operator is characterized by the kinetic energy $\hat{T}$, the electron-electron interaction $\hat{V}_{ee}$, and the interaction with the external potential defined as $\hat{V}_{ext}$ according to equation 2.15. $\hat{T}$ and $\hat{V}_{ee}$ are independent of N, R_A, and Z_A, giving them universal validity. The system-independent terms are summarized in the Hohenberg-Kohn functional $F_{HK}[\rho]$ as shown in equation 2.16.[179]

$$F_{HK}[\rho] = \hat{T}[\rho] + E_{ee}[\rho] \tag{2.16}$$

This approach allows for the determination of the ground-state energy E_0 as a functional of the ground-state density ρ_0. The number of electrons in the system can be determined through integration via the density. An advantage of calculating with the electron density is that, unlike the wave function, it is observable and can be measured experimentally. As the functional is universal, according to the first theorem, it holds true for all systems. The second theorem states that the principle of variation also applies to the electron density. Consequently, the universal functional calculates energies for test densities that are higher than or equal to the exact ground-state energies. By calculating the minimum of the functional of the electron density, the ground-state energy is determined.[179]

$$E_0[\rho_0] = \int \rho_0(\vec{r}) V_{ext}(\vec{r}) d\vec{r} + F_{HK}[\rho_0] \tag{2.17}$$

However, the exact expression for the exchange-correlation functional that links electron density and energy remains unknown. To address this, Kohn and Sham proposed an alternative approach by defining an exchange-correlation functional, which is still unknown but can be approximated.[181] This significantly reduces the complexity of DFT compared to wave functional theory. Orbitals are reintroduced, making the energy dependent on the number of electrons in the system. The kinetic energy term is split into an exact calculable term and a correction term. In the Kohn-Sham theory, the kinetic energy is calculated considering the approximation where electrons do not interact with each other. The missing portion of the exact kinetic energy, namely the electron correlation and exchange energy, is accounted for as an additional term. As no exact expression for the exchange-correlation functional is known, approximations are developed. By considering electron correlation, the DFT method can yield better results than the Hartree-Fock (HF) method. The accuracy of electron correlation depends on the specific functional used and is often adjusted accordingly. Various approaches are employed to calculate the exchange and correlation energies, leading to system-specific impacts on the results. A significant improvement is achieved by incorporating information about the gradient of the charge density $\nabla\rho(\tilde{r})$, which allows for considering the inhomogeneity of the exact electron density. Generalized gradient-corrected correlation functionals. GGA functionals are computationally efficient compared to other functionals and offer a better description of chemical systems and their properties compared to HF. They are particularly suitable for the calculation of solids and large systems. On the other hand, hybrid functionals are more computationally demanding than GGA functionals. The ability to choose different functionals provides a characteristic flexibility of the DFT method, allowing researchers to select the most appropriate approach for their specific system and research objectives.[179]

2.1.3. Bayesian Error Estimation Functional with van der Waals correlation

The Bayesian Error Estimation Functional with van der Waals correlation (BEEF-vdW) functional is based on the Bayesian statistics, which is an approach to data analysis and parameter estimation and is based on Bayes' theorem named after Thomas Bayes.[182,183] The typical Bayesian workflow, also used in the BEEF-vdW functional parametrization, is divided into three main steps; the prior distribution, the likelihood function, and the posterior distribution. Characteristical for Bayesian statistics is updated knowledge in the posterior distribution used to conduct inferences which are optimized by averaging over the joint probability distribution based on the conditional distribution given by the prior distribution over the observed data.[184,185] The group of Nørskov developed particularly well-suited functionals for surface science and catalysis studies. The Exchange-correlation model development with Bayesian error estimation is a methodology for semiempirical density functional optimization using regularization and cross-validation methods from machine learning.[186] The Bayesian error estimation takes advantage of the ability of machine learning methods to generate accurate density functionals, as former studies have shown.[187,188] In the BEEF-vdW class of functionals machine learning is combined with a Bayesian point of view to generalize a fitting procedure for the exchange-correlation functionals by estimating the errors of the given calculated quantities. The method is developed for a set of systems that are meant to be transferable to systems not included in the fitted data set. The transferability is gained as the errors on the fitted data set can be used to estimate the errors of the systems under investigation. The ensemble of exchange-correlation functionals is constructed using Bayesian statistics.[189] The ensemble is applied non-selfconsistently on the electron density resulting from the optimally fitted functional. Figure 2.1 provides an illustration of the BEEF-vdW ensemble as given in the literature from Nørskov et al.[186] Each data point within the datasets is applied to BEEF-vdW electron densities in a non-self-consistent manner. The standard deviation predictions of the ensemble for a given quantity serve as an estimate of the standard deviation expected from BEEF-vdW. The exchange enhancement ensemble expands around 2, by which time much of the chemistry and solid-state physics processes have occurred. To evaluate its effectiveness, the ensemble has been tested using 20 000 ensemble functionals. Here, it is worth mentioning that the DFT method used significantly affects the calculated bond lengths. In summary, it is important to highlight that the BEEF-vdW method's reliability concerning the calculated bond lengths is subject to some controversy whilst improvement has been established in a mBEEF-vdW functional.[190] However, studies have shown that the obtained energies are within an acceptable chemical accuracy.[186,191]

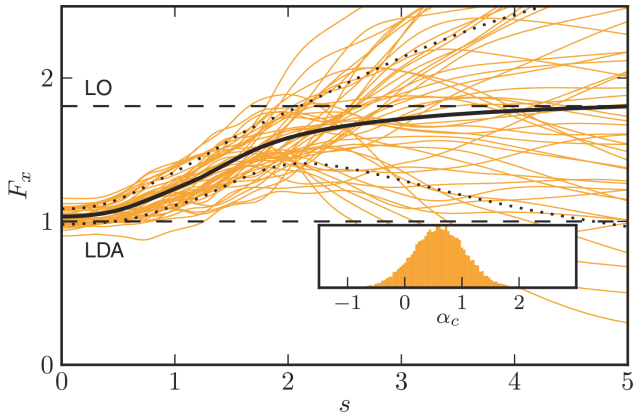

Figure 2.1.: Bayesian ensemble of exchange-correlation functionals centered around BEEF-vdW. The black solid line represents the BEEF-vdW exchange enhancement factor, while the orange lines show 50 samples randomly selected from the ensemble. Dashed black lines mark the exchange model perturbations leading to DFT results ±1 standard deviation away from BEEF-vdW. The predictive performance of the ensemble has been evaluated using 20 000 ensemble functionals. $F_x(s)$ represents the exchange enhancement factor, which depends on both the local electron density and its gradient as indicated by the reduced density gradients denoted as s. LO is the Local Orbital and LDA the Local Density Approximation. Reprinted with permission from[186]. ©2024 American Physical Society.

2.1.4. Plane Waves

Basic functions used in quantum chemistry include Slater-type orbitals (STOs) and Gaussian-type orbitals (GTOs), which describe the electronic orbitals of a closed system by linear combinations of atomic orbitals. These localized basis functions are particularly suitable for describing molecules and systems with localized electrons. In contrast, plane wave basis functions take a different approach and describe the entire system as an infinite system with periodic boundary conditions. In this method, the unit cell of the crystal or solid receives periodic boundary conditions through functions with an infinite range. This allows for the description of extended systems, such as crystals and periodic solids, where electrons are not confined to localized regions. The periodicity of plane wave functions Φ is reflected in their solutions to the Schrödinger equation, where they are expressed as complex exponentials or combinations of cosine and sine functions. The periodicity and completeness of these plane waves enable efficient calculations for a wide range of materials, including metals, semiconductors and insulators. However, plane wave basis sets require careful consideration of the energy cutoff and k-point sampling to accurately describe the electronic structure of the system. $\tilde{A}$ and $\tilde{B}$ are coefficients. A and B are constants.

$$\Phi = \tilde{A}e^{ikx} + \tilde{B}e^{-ikx} \tag{2.18}$$

$$\Phi = Acos(kx) + Bsin(kx) \tag{2.19}$$

The energy E depends quadratically on the k-factor:

$$E \propto k^2 \tag{2.20}$$

Molecular orbitals with clearly vanishing energy gaps are described together as a band model. The electrons of a band are described by plane wave orbitals $\chi_{\mathrm{k}}(\mathrm{r})$ which are developed by plane waves.

$$\chi_k(r) = e^{ikr} \tag{2.21}$$

k represents the wave vector. The allowed k-values are given by the translation vector of a unit cell t, m is a positive integer.

$$k \cdot t = 2\pi m \tag{2.22}$$

M_{PW} represents the number of plane waves by the highest energy of the k-vector and thus also defines the maximum kinetic energy and the volume V of the unit cell.

$$M_{PW} = \frac{1}{2\pi^2} V E_{max}^{\frac{3}{2}} \tag{2.23}$$

The parameter E_{max} plays a crucial role in determining the size of the plane wave basis set and, consequently, the quality of the calculations. As the value of E_{max} increases, the basis set size also increases, leading to improved accuracy in the results. The size of the plane waves is determined by the combination of E_{max} and the size of the periodic cell, but it is independent of the actual size of the system being described within that cell. This feature makes plane waves particularly advantageous for large systems, such as zeolites or metallic catalysts. The Kohn-Sham density functional theory (DFT) in describing a wide range of systems has its limitations in accurately accounting for certain interactions, particularly dispersion effects. The dispersion energy, which arises from attractive van-der-Waals interactions, as well as electrostatic and repulsive Pauli interactions between electrons, poses challenges when applying DFT to systems with weakly bonded or non-bonded interactions. As the size of the molecule increases, the limitations of DFT become more apparent, leading to deviations from experimental values. These deviations can be both quantitative and qualitative, impacting the overall reliability of the calculated results. Efforts to improve the treatment of dispersion forces within DFT have led to the development of various correction schemes and dispersion-corrected functionals. These methods aim to enhance the accuracy of DFT calculations for systems with weak interactions, bridging the gap between theory and experiment and providing more reliable predictions for a wide range of molecular and materials properties. The error considered due to a poor description of the exchange-correlation of the electrons can be compensated by the correction of dispersion by the use of a vdW correction. An application by the D3 Functional of Grimme leads to

the replacement of some terms by non-local, long- and medium-range electron correlation effects in conventional gradient-corrected electron densities.[192] Higher accuracy is achieved by adapting short-range terms of the density functional to a long-range correction and avoiding double counting effects. However, even then the energy barriers would still be systematically underestimated.[192] In order to achieve better results and to be able to estimate the errors better, further calculations should be performed using a periodic model or a cluster model with a particularly complex method such as Coupled Cluster with Single, Double, and perturbative Triple excitations CCSD(T) focused on the active center.

2.1.5. Smearing Scheme

DFT methods are used to calculate the ground-state total energy, electronic charge density, and Born-Oppenheimer forces of a system with N electrons in a given ionic potential. Energy-dependent occupation numbers in density-functional theory have the purposes of simulating the canonical ensemble for electrons at non-zero temperatures and improving convergence in the number of electronic wave vectors sampling the Brillouin zone. The smearing method is employed to approximate the Fermi-Dirac distribution function, which characterizes the occupancy of electronic states at finite temperatures.[193] In the case of the purpose to simulate the canonical ensemble for electrons at non-zero temperature the Fermi-Dirac occupation numbers broaden the electronic occupations, leading to the partial occupation of energy levels near the Fermi level for the Kohn-Sham eigenstates. With that, the Fermi surface of a metal is not a sharp feature in the Brioullin zone. Although at 0 K the system is formally at its ground state and the thermal smearing should not be necessary, the choice of a smearing method can still affect the accuracy of the calculation. A study by dos Santos and Marzari showed by enhancing the accuracy of DFT calculations using the smearing technique. They discuss advanced smearing methods like Methfessel-Paxton and cold smearing, which, while effective for metallic systems, pose challenges in semiconductors and insulators. The nonmonotonic occupation functions and non-uniquely defined chemical potential in these materials are addressed. The authors highlight potential errors induced by incorrect Fermi energy in both crystal structure and bandgap, emphasizing the relevance for insulators, where relative errors can be significant, reaching up to 50%.[194] To treat metals a 0 K, smearing schemes can be used to improve the convergence with respect to the number of electronic wave vectors sampling the Brillouin zone and to delocalize electronic occupations properly. For insulating systems or systems with a finite band gap a small smearing with a small width of the smearing function prevents the electronic occupations from being stuck at the gap.

2.1.6. Hubbard-like U Term

Ceria as an oxide with an elemental electron configuration [Xe]$4f^2 6f^2$ for Ce^{+III} has one $4f^1$ left in the valence shell. The characteristic of this oxide, due to the high electron negativity of the oxygen atoms is a high localization of the valence electron. This states an additional difficulty for the calculation methods to represent the oxide as GGA methods are based on DFT and the functionality developed for metal surfaces with large overlapping valence orbitals representing conducting bands. The electron correlations in narrow bands were initially developed to describe partially filled d- and f-bands in transition and rare earth metals. The correlation effects in narrow bands lead to atomic behavior. The electron charge density is then concentrated near the nuclei of the solid and sparse between the atoms.[134] With that, an electron can be localized on a specific atom, which is the case for reduced Ce^{+IV} to Ce^{+III} in ceria. The approach to the collective motion problem divided into a collective motion and an internal motion of the electron plasma and extended to the theory to the non-uniform gas by Hubbard[134–136] also showed a high gain in accuracy by localizing electrons specifically for the use of material design.[137] The interaction parameter U can be determined empirically by fitting the theoretically reproduced band gap to the experimental band gap or theoretically, by the linear response method proposed by Cococcioni and de Gironcoli which does not depend on experimental results and places an *ab initio* approach.[195]

2.2. Thermodynamics

As described in Section 2.1.1, the calculation of total energy, based on quantum chemistry theories, enables the determination of a potential energy surface. This methodology is crucial in theoretical catalysis for evaluating the relative stabilities of states within chemical systems. Hess's Law as described in Equation 2.24, named after chemist Germain Henri Hess, elucidates a fundamental thermodynamic principle. It asserts that the total enthalpy change of a chemical reaction remains constant irrespective of the pathway taken from initial to final states. This facilitates the determination of overall enthalpy change by aggregating individual step enthalpy changes, regardless of observability.[176,177]

$$\Delta_r H = \sum_{products} \nu_i H_i - \sum_{educts} \nu_j H_j \tag{2.24}$$

H is the enthalpie and ν the stoichiometric coefficient. The indices i and j represent the number of species. In basic literature, H refers to standard enthalpies, which exist under standard conditions defined as 1 bar and 298.15 K. However, when working with catalysts, neither molecules in the adsorbed state nor molecules in the gas phase under artificial reaction conditions have standard enthalpies. Consequently, catalyzed reactions

are analyzed in terms of intrinsic enthalpies, specific to the reaction using a catalyst. The potential energy diagram (PED) describes potential energies within a reaction between atoms and molecules along a reaction coordinate. Along the reaction coordinate, the movement of atoms and molecules results in a change of the potential energy, while local and global minimum shows the metastable and stable states of the chemical system. A minimum energy path (MEP) is created along the reaction coordinates, which has the constraint of the lowest energy pathway between the potential minima and therefore represents the most probable reaction path. At the maximum, the MEP has a unique hessian with only one negative eigenvalue, which relates to the single negative curvature along the MEP. This results in a single imaginary vibration mode in normal mode analysis.

2.2.1. Zero Point Energy

The zero point energy (ZPE) correction has an impact on the thermodynamics of the investigated reaction mechanism, as the vibrational frequencies of the reactants play a crucial role in the potential energies. At the limiting case T $\rightarrow$ 0 the system maintains according to the concept of ZPE[196] at the energy of a one-dimensional harmonic oscillator vibrating with the energy E_n and frequency ω and is given by

$$E_n = (n + \frac{1}{2})\hbar\omega. \tag{2.25}$$

n is the quantum number which are integer numbers with n = 0, 1, 2, ... and h is the Planck constant. In the case of DFT structure optimizations, the systems are at the ground state, thus n = 0. The contribution of the different vibrational modes are additive.

$$ZPE = \sum_{i}^{N_{modes}} \frac{1}{2}\hbar\omega_i \tag{2.26}$$

The ZPE is obtained with the harmonic approximation as a sum over the harmonic oscillators of all M fundamental modes ω_i of the particle.[197]

$$\mu_{vib} = ZPE + \Delta\mu_{vib} = \sum_{i=1}^{M}\left[\frac{\hbar\omega_i}{2} + k_B T ln(1 - e^{\frac{\hbar\omega_i}{k_B T}})\right] \tag{2.27}$$

k_B is the Boltzmann constant, T the Temperature, and μ^{vib} is the chemical potential of the molecule by the vibrational contribution. The contribution of the vibrational degrees of freedom is accounted for using a harmonic approximation and is described by the vibrational free energy, F^{vib}.

$$F^{vib}(T,\omega) = \frac{\hbar\omega}{2} + k_B T ln(1 - e^{-\frac{\hbar\omega}{k_B T}}) \tag{2.28}$$

To obtain the entropy $S^{vib}(T,\omega)$ equation 2.28 must be divided by the Temperature T.

$$S^{vib} = \frac{F^{vib}(T,\omega)}{T} = \frac{\frac{\hbar\omega}{2} + k_B T ln(1 - e^{-\frac{\hbar\omega}{k_B T}})}{T} \tag{2.29}$$

The unit of the entropy contribution is eV/K. The vibrational modes given by the VASP calculations have the units cm^{-1}. For the conversion to the unit of 1/s the velocity of light must be multiplied by a factor of 100 and divided by $\lambda = 1$.

$$\omega_i[\frac{1}{cm}] = \frac{c[\frac{m}{s}]}{\lambda[m]} * 100 = \frac{2.99 * 10^8 \frac{m}{s} * 100}{1m} = 2.99 * 10^{10} \frac{1}{s} \tag{2.30}$$

The conversion of ω_i into $1/s$ can be used as a factor.

$$\frac{c[\frac{m}{s}] * 100 * 4.13 * 10^{15[eVs]}}{2} * \omega_i[\frac{1}{cm}] = 6.199 * 10^{-5} * \omega_i[\frac{1}{s}] \tag{2.31}$$

With with ω_i inserted into equation 2.26 the ZPE is obtained with a unit of eV. The ZPE is the summation of all vibrational modes ω_i. The summation of the ZPE-corrected ground-state energy E_0 and the heat capacity $C_p(T)$ prescribes the internal energy U(T) of a chemical system, which is a function of the given temperature of the reaction. As the heat capacity changes within an increasing temperature, an integration up to the relevant temperature leads to the actual internal energy with consideration of Boltzmann statistical changes of the distribution of quantum-states due to higher temperatures.

$$U(T) = E_0 + \int_{T=0}^{T} C_p(T')dT' \tag{2.32}$$

The internal energy defines the enthalpy H by an additional term due to the volumetric changes, which itself defines the Gibbs free energy G.

$$H = U - pV \tag{2.33}$$

$$G = H - TS \tag{2.34}$$

Gibbs free energy G determines the stability of states at constant pressure and temperature.

2.2.2. Phasediagrams

The Gibbs free energy is calculated as supposed by Reuter and Rogal as shown in the following equations. The phase diagrams plotted in this work refer to a static model system of surface determination. The surface is considered homogeneous, thus the Gibbs

free energy will scale linearly. With this, the surface free energy per unit area, γ, can be introduced.[197]

$$\gamma(T,p) = \frac{1}{A}(G - G_{solid} - G_{gas}) \tag{2.35}$$

The computation of the solid phase Gibbs free energy can be divided into several contributing terms:

$$G = E^{total} + F^{vib,ad} + F^{conf} + pV \tag{2.36}$$

The total energy E^{total} is the dominant term calculated by DFT calculations.

$$\delta G = E_{PdO_x/CeO_2} - (E_{CeO_2} + E_{Pd_{bulk}} + 0.5x\mu(O_2)) \tag{2.37}$$

2.2.3. Collision Theory

In heterogeneous catalysis, the focus is on surface reactions. The Arrhenius equation can generally be split into two factors: the pre-exponential factor, describing the energy brought by atoms or molecules, and the exponential factor, indicating the chance of the reaction occurring.[20,198]

$$k = ve^{\frac{-G_a}{k_B T}} \tag{2.38}$$

v is the prefactor, k_B the Boltzmann constant and T the absolute temperature. The pre-exponential factor was introduced by Trautz[199] and Lewis[200] through the kinetic theory of collision as an initial treatment of reaction rates. In the gas phase, a reactant always possesses a certain translational energy. The magnitude of translational energy follows a statistical distribution. The average velocity $\bar{v}$ can, in turn, be characterized by a Maxwell-Boltzmann distribution.[20,198]

$$\bar{v} = \sqrt{\frac{8k_B T}{\pi m}} \tag{2.39}$$

The particles in the gas phase have an eigenstate ε_i, and the probability P of finding a particle i in a specific eigenstate is as follows:[20,198]

$$P_i = \frac{e^{-\frac{\varepsilon_i}{k_B T}}}{q} \tag{2.40}$$

With:[20,198]

$$\varepsilon_i = \frac{i^2 h^2}{8ml^2} \tag{2.41}$$

l is the length of the box. And q is the translational partition function in one dimension:[20,198]

$$q_{translational} = \frac{l\sqrt{2\pi k_B m T}}{h} \tag{2.42}$$

Considering the average velocity, the number of collisions between two reactants A and B with a certain mass m and the kinetic (translational) energy can be determined, taking into account the temperature.[20,198]

$$r_{collision} = \pi d^2 \sqrt{\frac{8k_BT}{\pi m}} \frac{P_A P_B}{(k_BT)^2} \tag{2.43}$$

The collision rate is, therefore, the number of collisions between A and B, which is multiplied by the reaction probability. For a reaction to take place upon collision with another reactant, the translational energy must be sufficiently high to surpass the activation energy.

2.2.4. Transition State Theory

The energetic states of particles involve more than just translational energy. Therefore, additional states must also be considered in the analysis of activation energies to calculate reaction rates. To derive this, the transition state itself must first be defined first. Following approaches by Perrin[201,202] and others regarding the 'radiation theory of chemical action' and the spirited discussion leading to Lindemann's[203] theory, the Transition State Theory by Eyring[204,205], Evans, and Polanyi[206,207] was eventually introduced. Eyring described the concept of the activated complex, describing it as a critical configuration with the highest potential energy that the system must traverse during a reaction. The metastable activated complex, akin to reactants or products, exhibits an average energy that rises with temperature. The resulting surface exhibits low valleys or basins representing chemical compounds separated by mountain ranges. As the valleys, basins, and passes align with stationary points in potential energy, the theory of small vibrations becomes applicable. This theory allows us to derive the frequencies essential for calculating the probability of these critical configurations for any change in arrangement. A classical chemical system is in the absolute ground state with the potential energy $E_{pot}{}^{min}$ at a global or a local minimum. As the exact position of a particle and its momentum is uncertain due to the Heisenberg uncertainty principle,[198]

$$\Delta x \Delta p \geq \frac{\hbar}{2} \tag{2.44}$$

the actual energy at the ground state E_n of a quantum system is described by a correction term with h as Planck's constant, n as the quantum number, and an approximation of the harmonic oscillator. For that reason, a particle is not perfectly at rest in the ground state and has a contribution of the angular frequency w_i. In the ground-state n = 0, thus, the following equation:[198]

$$E_n = E_{pot}^{min} + (n + \frac{1}{2})\hbar\omega_i \tag{2.45}$$

becomes:[198]

$$E_0 = E_{pot}^{min} + \frac{1}{2}\hbar\omega_i. \tag{2.46}$$

During a reaction, bonds are broken and formed, with the transition state representing a condition where these bonds are neither broken nor formed, forming a complex. The rate at which bonds are broken and formed equals the vibrational frequency hν. Since this frequency is relatively small compared to $k_B T$, the partition function can be described by a classical limit with $k_B T/h\nu$. To incorporate the eigenstates that give the reaction a probability to proceed, partition functions are introduced. The energy difference between the ground state and the transition state is the energy barrier ΔE_a, referring to the activation energy.[198] By calculating the potential energies in the ground state using quantum chemical methods, the total energies can be computed at 0 K which can be approximated to be equal to the enthalpy H. The calculation of temperature-dependent entropy components like the heat capacity $C_p(T)$ which is part of the enthalpy H, is feasible for gas-phase molecules. However, for a heterogeneous catalyst represented by periodic calculations with a slab, the effort is greater than the gain in accuracy. Calculating the entropy S at a given temperature allows for the calculation of the Gibbs free energy G. The reaction rate represents the difference between an initial state and a transition state Gibbs free energy, with the Gibbs free energy complemented by a double dagger for the calculation of the reaction rate. Translated into the thermodynamic relations shown in equation 2.34, the rate of reaction can be calculated as follows:[198]

$$k = \nu e^{\frac{-G_a^{\ddagger}}{k_B T}} \tag{2.47}$$

and equivalently:[198]

$$k = \frac{k_B T}{h} e^{-\Delta S_{TS}^{\ddagger}/k_B} \cdot e^{-\Delta H_{TS}^{\ddagger}/k_B T} \tag{2.48}$$

Additionally, the zero-point energies at the ground state and the transition state shall be included by adding to the Gibbs free energy. The catalyst functions by altering the activation barrier through its intrinsic electronic and morphological properties, reducing the activation energy and, consequently, lowering the Gibbs free energy difference between the initial state and the transition state.

3. Computational Methodology

The DFT calculations were performed using the Vienna Ab initio Simulation Package (VASP)[208,209] in connection with the Atomic Simulation Environment Graphical User Interface (ASE-GUI)[210]. A plane-wave basis set with a cut-off energy of 415 eV,[30] the projector augmented wave method[211,212] and the Bayesian error estimation functional with van-der-Waals exchange-correlation (BEEF-vdW) functional[186] was used. For the description of localized Ce 4f electrons, the GGA + U with U = 4.5 eV method was applied. The slabs were separated by more than 15 Å of vacuum. Atoms in the top two layers were allowed to relax during geometry optimizations while the bottom two were kept fixed to present in the bulk phase of ceria. The Brillouin zones were sampled using only the gamma point. The Brillouin zones were sampled using a (3 × 6 × 1) Monkhorst-Pack k-point grid for the (100) surface facet of ceria, (4 × 6 × 1) for (110) and (4 × 5 × 1) for (111) and a (1 × 1 × 1) Monkhorst-Pack k-point grid for the subnanometer cluster on the (111) surface. For the extended Pd and Pt metal surface a (4 × 4 × 1) Monkhorst-Pack k-point grid for the (100) surface, (3 × 4 × 1) for (110), (4 × 4 × 1) for (111), and (5 × 6 × 1) for (211). A Fermi smearing with a width of 0.1 eV has been used. The convergence criterion for geometry optimizations was a maximum force of $1e^{-7}$ eV/Å. Spin polarization was considered in all calculations. Vibrational analyses were carried out in the harmonic approximation using finite difference with displacements of magnitude 0.01 Å. The size of the unit cells is 2 × 2 for (111) and (110), and $2\sqrt{2} \times 2\sqrt{2}$ for (100). The (111) and the (110) slabs are not polar. Cleaving the (100) surface of ceria induces a perpendicular dipole moment, necessitating reconstruction due to the instability of dipolar surfaces.[213] The infinite slab models consist of four layers for all systems but in section 4.3.2. For the stability of the size and shape of subnanometer clusters on ceria, only two layers were necessary.

3.1. Convergence of the Lattice Constant

To show the optimization process of the calculated lattice constant used for the structure optimization of the slabs, the convergence of the lattice constant of Pt for different cut-off energies $E_{cut\text{-}off}$ and densities of the k-point sampling is shown in Figure 3.1. In Figure 3.1, the relative variation of the potential energy in percent [%] for the used parameters is plotted against a varying lattice constant a. It can be seen, that for a (7,7,7) k-point sampling the

lattice constant is converged for $E_{cut\text{-}off}$ 415 eV. Using $E_{cut\text{-}off}$ 415 eV for different k-point samplings shows the convergence in the k-point density for (7,7,7) and higher. The given $E_{cut\text{-}off}$ 415 eV and k-point density for (7,7,7) is used to optimize the lattice constant of bulk Pt. The lattice constants were optimized manually for Pd and Pt bulk. The oxides PdO and

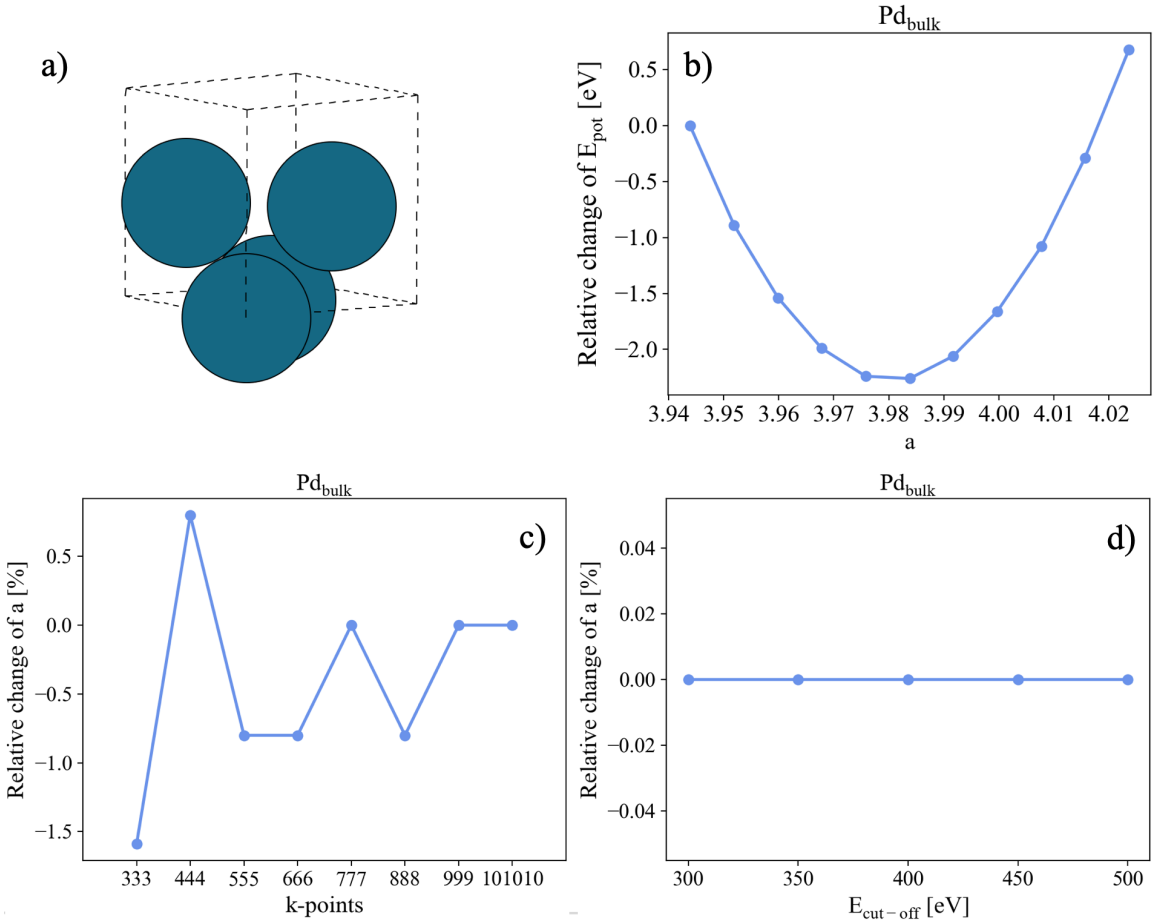

Figure 3.1.: Lattice constant optimization of the Pd pristine crystal in the bulk phase. Upper left: the unit cell optimized of the octahedral crystal structure of Pd in the bulk phase. a) Structure of the bulk Pd. b) Lattice constant optimization, with a change of potential energy relative to a starting point plotted against a varying lattice constant. c) A relative change of the lattice constant in % plotted against varying k-points. d) A relative change of the lattice constant in % plotted against varying cut-off energy.

PtO, and CeO_2 were adapted from previous works within this group and reoptimized within this work.[24,69,214] The lattice parameter for the Pd bulk was optimized to 3.984 Å, Pt bulk to 4.010 Å. CeO_2 was previously optimized to 5.519 Å, PdO to 3.069 Åand PtO to 3.086 Å. As illustrated in Figure 3.1, the lattice parameter shows a minimum in the potential energy for the structure optimized value. Under the increase of the k-points and the cut-off energy, convergence is observed at around (7,7,7) k-points. Varying the cut-off energy resulted in a wide range of consistency, around 400 eV.

3.2. Hubbard-like U Term

An electron can be localized on a specific atom, which is the case for reduced Ce^{+IV} to Ce^{+III} in ceria. The approach to the collective motion problem divided into a collective motion and an internal motion of the electron plasma and extended to the theory to the non-uniform gas by Hubbard[134–136] also showed a high gain in accuracy by localizing electrons specifically for the use of material design.[137] Still, care must be taken by using this method.[215] In former studies of Fabris et al. the Hubbard-like U Term choice of the parameter U was investigated for ceria surface facets[216] and single-atom catalysts supported on ceria.[217] Loschen et al. chose a Hubbar-U parameter to provide a balanced description between CeO_2 and Ce_2O_3, whereas Ce_2O_3 is much more sensitive to the choice of the U parameter.[218] Castleton et al. showed, that an accurate description may require different U parameters.[219] Jiang et al. used the GGA + U(J) method to study several surface facets of CeO_2.[220] The optimal parameter of U = 7 eV and J = 0.7 eV was found to improve the on-site Coulomb correlation and exchange interaction due to the strongly localized 4f electrons of the cerium atom. Nolan et al. investigated the low-indexed surface with increased surface energies in the order (111) > (110) > (100) and used a U value of 5 eV.[109] For the ceria surface, it was suggested, that a lower Hubbard-like U Term is recommended as the used value of 5 eV tends to overestimate the binding energy of CO. Fabris and Kresse optimized a U parameter to 4.5 eV in their research.[79,123,133,217] Cococcioni and de Gironcoli implemented U = 4.5 eV for the 4f electron of ceria.[73,195,221] In general, the interaction parameter U can be determined empirically by fitting the calculated band gap to the experimental band gap or theoretically, by the linear response method proposed by Cococcioni and de Gironcoli which does not depend on experimental results and places an *ab initio* approach.[195]

3.3. Unit Cell of the Slabs

It should be emphasized that the approach used in this work to simulate the heterogeneous catalysts, Pd and Pt noble metals supported on ceria, represents an idealized catalytic system. Particular care was taken to consider special edge cases throughout. In a real system, there would be a statistical distribution of the edge cases presented. In the case of single-atom catalysts, a larger unit cell of doubled size (4×4) was calculated, but we chose to use the 2×2 unit cell size for analysis. However, since we are paying particular attention to the oxidation states and specific configurations of the single-atom catalysts, we have chosen to avoid using larger unit cells. There were some complications encountered when using larger unit cells. The noble metal atom and the O atoms are prone to movement on the ceria surface into the bulk as the ceria surface is reduced by the formation of O defects.

Due to this dynamic, certain reduced oxidation states may not be achieved. For this reason, we opted for the smallest unit cell size consisting of 2 × 2 large unit cells to minimize the number of neighboring oxygen atoms, considering that the adjacent unit cell already represents the subsequent single site. With that, O diffusion from a near neighbor or next near neighbor position is regulated, as the number of O atoms is limited to the vicinal O atoms of the metal atom. An interaction between the neighboring active sites is not seen, but the polaron formation by O lattice removal and the reduced ceria atoms on the surface due to charge transfer can not undergo an electronic relaxation. The polaron distribution is in the case of the single-atom catalysts not relaxed during structure optimization with the chosen unit cell size as the number of neighboring cerium atoms is limited to the vicinal atoms. Nearest neighbors and next-nearest neighbors are in the direct vicinity of the next single atom already. Former studies have shown, that the polarons distribute to the next nearest neighbor of the lattice O defect[80,121,138,222–228] and it is assumed that the negative charge distributes naturally due to repulsion. Four layers thick 2 × 2 large unit cells with the bottom two layers fixed were used to represent $CeO_2(111)$ infinite slab models with single Pd atoms being either adsorbed on the stoichiometric ceria surface or the defective V_{Ce} ceria surface. For section 4.3.1, 4.3.6 and 6.2.4, where the O defects were farther migrated into

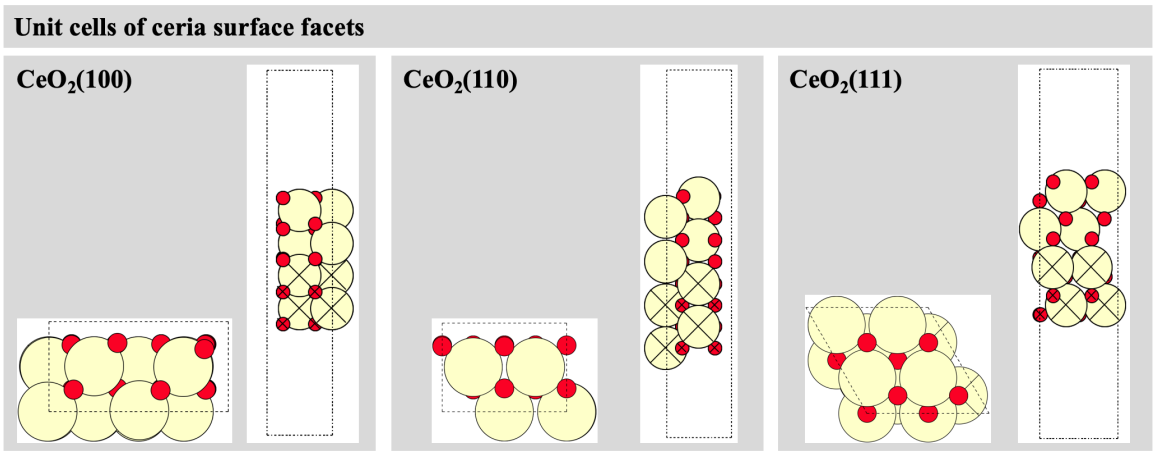

Figure 3.2.: Visualization of the supercells for calculating the heterogeneous catalyst surfaces. The ceria surface facets (100), (110), and (111) are depicted. Red circles represent O, and yellow circles denote Ce atoms. Other surfaces are shown in the Appendix in Section A.35.

the bulk phase of the ceria surface and the resulting reduced Ce^{+III} ions play a crucial role in the study. For this reason, it was of utmost importance in these sections to use four layers, even though the calculations became extremely demanding. With around 500 atoms, the DFT method reached its performance limit, considering the time constraints of this study.

3.4. Surface Energies

Surface energy refers to the energy change associated with the relaxation or structural rearrangement of atoms at the surface of a material. It represents the difference in energy between the relaxed surface structure and the unrelaxed surface structure. In DFT calculations, the surface relaxation energy can be computed by comparing the total energies of the relaxed and unrelaxed surface configurations. Different crystal facets can have different relaxed surface energies. The surface energy is required to create one unit of surface area. Surface energy represents the energy needed to generate one unit of surface area in a material. Mathematically, the surface energy $E_{surf.}$ is defined as the difference between the total energies of two systems: System 2, where an additional surface area A is created. The surface facet structures are (100), (110) and (111) $E_{total,surface}$. For System 1, the initial state is the bulk phase of ceria $E_{total,bulk}$. $E_{total,surface}$ is the relaxed structure, and $E_{total,bulk}$ the unrelaxed structure. By relaxation, a new structure is created due to a change in the configuration of the crystal surface under the conservation of the number of atoms. $E_{total,surface}$ is the total energy of the calculated surface faces of ceria (100), (110), and (111). $E_{total,bulk}$ is the total energy of the bulk.[229–231] A formula to calculate the surface relaxation energy is given by Equation 3.1.

$$E_{surf.} = \frac{1}{A} * \frac{1}{n}(E_{total,surface} - E_{total,bulk}) \tag{3.1}$$

In this case, we consider the whole surface slab. Since we are dealing with an oxide with differing ratios of O to cerium atoms, we normalize by considering each unit as comprising two O atoms paired with one cerium atom. For this, n is the number of CeO_2 units.

3.5. Defect formation Energies and Adsorption Energies

The formation of surface lattice O vacancies is calculated as follows:

$$E_{form.}(V_O) = E_{total,surface} - (E_{total,surface}(V_O) + \frac{1}{2}E_{total}(O_2)_{(g)}) \tag{3.2}$$

$E_{total,surface}$ represents the total energy of the surface slab, $E_{total,surface}(V_O)$ denotes the total energy of the surface slab with one O defect V_O, and $E_{total}(O)_{(g)}$ signifies the total energy of a single O atom in the gas phase. The latter is computed based on an O_2 molecule in the gas phase, subsequently divided by two. The adsorption energy E_{ads}(Pd) and E_{ads}(Pt) for Pd and Pt, respectively, has been calculated using Equation 3.3.

$$E_{ads}(Pd,Pt) = E_{total,ads}(Pd,Pt) - (E_{total,surface} + E_{total}(Pd,Pt)_{(g)}) \tag{3.3}$$

$E_{total,ads}$(Pd,Pt) represents the total energy of the surface slab with a single atom of the noble metals Pd or Pt. $E_{total,surface}$ denotes the total energy of the plain surface facet, while $E_{total}(Pd,Pt)_{(g)}$ signifies the total energy of Pd and Pt in the gas phase, respectively.

3.6. Vibrational Frequency Correction Factor

Free energies were computed using the harmonic approximation. The vibrational frequencies were calculated from the finite difference method including only the adsorbed CO. The calculated frequency of the CO molecule in the gas phase using DFT methods has a smaller deviation in accuracy compared to larger systems with a higher number of atoms. To systematically approach experimental frequencies, the calculated vibrational frequencies of the adsorbed CO molecule are multiplied by a correction factor by equation 3.4.

$$\lambda = \frac{\nu_i^{exp}}{\omega_i^{calc}} \tag{3.4}$$

The experimental vibrational frequency of the CO molecule in its gaseous form is commonly found to be 2143.2 cm^{-1}.[232] The theoretically calculated vibrational frequency at 0 K in this work is 2124.5 cm^{-1}. The theoretical vibrational frequencies calculated on the catalyst, determined using quantum chemical methods, can be improved in accuracy by multiplying with a vibrational scale factor, represented by the quotient of the experimentally determined value ν_i^{exp} and the theoretical value ω_i^{calc} (Equation 3.4). The calculated λ factor for the used method is found to be 1.00847.

3.7. *Ab initio* Thermodynamics

The coverage degree can be computed as a function of temperature using *ab initio* thermodynamics. To achieve this, we have plotted the successive coverage by CO molecules or O atoms through the differential energy G_{diff}.

$$\Delta G_{diff} = G_{cluster+CO_{ads}} - (G_{cluster} + G_{CO_{(g)}}) \tag{3.5}$$

The ground state energies are calculated by the use of DFT methods at 0 K (-273.15°C) and are increased by the use of *ab initio* thermodynamics in 100°C steps starting from 423.15 K (150°C) to 723.15 K (450°C). The differential adsorption energy is ZPE-corrected. ΔG, as already explained in Chapter 2.2.1 of the Theory section, includes an entropy term that depends on temperature. The ZPE is added to ΔG. The temperature dependency is included based on the calculated total energies, according to the theory of *ab initio*

Thermodynamics, which is explained by Scheffler and Reuter et al.[197] The catalytic cycle is plotted in a potential Energy diagram that takes the Pt^0/CeO_2 species as a reference as the starting point of the reaction mechanism circle. The potential energy diagrams are ZPE corrected for the molecules in the gas phase, adsorbed gas phase molecules, and the O_2 dissociated chemisorption of O atoms for the PtO oxide. According to former studies of Niemandsverdriet et al., it is crucial to include ZPE corrections in reactions involving species that contain hydrogens. It has been reported, that the methanation process the successive addition of hydrogen to atomic carbon is endothermic up to the addition of the third hydrogen atom, but exothermic in the final hydrogenation step, leading to the product methane.[233] In this work, the first H dissociation of CH_4 is investigated and corrected by adding the ZPE. For the LH and the MvK mechanisms including CO oxidation, O_2 dissociation, and CO_2 desorption all vibrational frequencies of the surface species that are involved in the reaction mechanism as reactants are calculated, and corrected by adding the ZPE. The vibrational modes of the CO molecules and O atoms in the gas phase, after adsorption, during the reaction, and after desorption were computed to calculate the differential energy. Subsequently, the calculated ZPE and entropy S were averaged over the number of adsorbed species. Since each adsorption considers only one adsorbate in the differential adsorption energy, the ZPE correction and S are applied to both the adsorbed phase and the gas phase for each adsorption.

4. Stability of Pd and Pt noble metal Species supported on Ceria

4.1. Pd and Pt single-atom Catalysts adsorbed on stoichiometric Ceria Surface Facets

These surfaces offer significant advantages in controlling emissions through the complete combustion of CH_4, owing to their distinctive properties.[100] Hence, exploring these surfaces in-depth for their role as supports for Pd and Pt, acting as active catalyst centers, becomes crucial. This Section delves into the examination of the three most stable surfaces (100), (110), and (111) loaded with Pd and Pt single-atom catalysts. The presence of these surfaces is contingent upon the ceria crystal structures, with the (111) surface being the most prevalent. Surfaces showcasing defects leading to kinks and edges encompass the under-coordinated (110) and (100) surfaces. Figure 4.1 illustrates the three surfaces investigated in this study, showing plain ceria surfaces in the upper row and surfaces with adsorbed Pd and Pt single-atoms in the rows below. In Table 4.1 the surface energy after relaxation of the interface relative to the bulk phase of ceria $E_{surf.}$, and the adsorption energies of the Pd and Pt single-atoms E_{ads}(Pd) and E_{ads}(Pt) are listed. $E_{surf.}$ is calculated as presented in Section 3. $E_{surf.}$ for the (100) surface is calculated to be $1.28 \cdot 10^{-2}$ eV/Å^2, for (110) it is $0.79 \cdot 10^{-2}$ eV/Å^2, and for (111) it is $0.45 \cdot 10^{-2}$ eV/Å^2. A study about the surface energy of the ceria surface facets demonstrates that the surface stability order is (111)>(110)>(100) for the relaxed structures, while the extent of surface relaxations follows the opposite sequence.[109,234] The trend of surface relaxation observed here is analogous to several studies about the surface energies.[109,235,236] Experimental observations corroborate these findings,[237,238] revealing that the (111) surface is observed to be stable and undergoes little surface relaxation, whereas the (110) and (100) surfaces have been observed to undergo surface relaxation.[239] Notably, the (100) surface is the least stable one and has been the subject of comprehensive study. The surface energy increases as the surface becomes more undercoordinated, while the adsorption energy for Pd and Pt single-atoms follows an inverted trend. The higher the surface density, resulting in a lower coordination to an adsorbate, the lower the adsorption energy. Conversely, for more open surfaces, higher coordination for an adsorbate is facilitated as the surface atoms are already under-coordinated. Consequently,

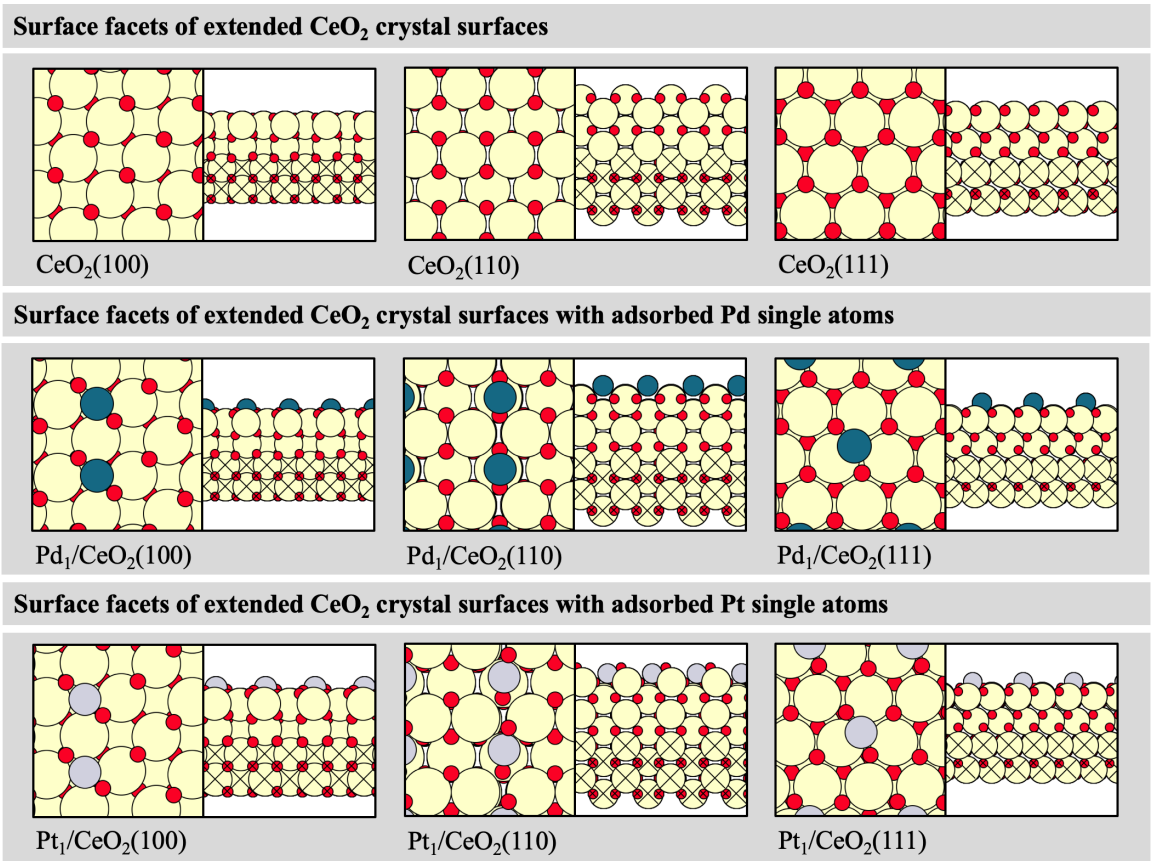

Figure 4.1.: Stoichiometric Surface facets of ceria, showcasing all three surface facets from left to right: (100), (110), and (111). Both the top and side views of the entire slab are presented. The upper row displays plain ceria surface facets, while the middle and bottom rows exhibit ceria surfaces with adsorbed single-atom catalysts of Pd and Pt, respectively. Red circles represent O, yellow circles Ce atoms, petrol circles Pd atoms, and gray circles indicate Pt atoms. The total energies are listed in the Appendix in Table A.2.

the adsorption energy for a Pd atom from the gas phase on the (100) surface is -3.00 eV, on the (110) surface it is -2.10 eV, and on the (111) surface it is -1.45 eV. The adsorption energy for a Pt atom from the gas phase is higher than that of Pd, with -5.58 eV on the (100) surface, -4.73 eV on the (110) surface, and -3.33 eV on the (111) surface. The difference is greater, the more open the surface, with a variance of 2.58 eV for the (100) surface, a lower variance of 2.63 eV for (110), and the smallest variance of 1.88 eV for (111). Su et al. discovered that the binding energy of a Pt atom at the ceria step edge is significantly higher with -5.54 eV compared to that of (111) with -3.21 eV.[240] Figueroba investigated the adsorption energies of several noble metals on a (100) edge, showing that Pt with -7.03 eV binds stronger than Pd with -5.22 eV. These binding energies are similar to those identified in this study. This indicates that atomically dispersed Pt can be stabilized on a ceria step edge as the undercoordinated surface facets (100) and (110) over a significantly broader range of operating temperature conditions than on the (111) surface. According to Nie and

Jones, due to similar stability observed between Pt(CO) complexes on the $CeO_2(111)$ step and $CeO_2(100)$, it is expected that single-atoms of Pt can persist across a wide range of conditions on the more open $CeO_2(100)$ surface.[38,153] Experimental observations support this prediction.[145,241] Our results align with these findings.

Table 4.1.: Calculated surface energies $E_{surf.}$ in eV/Å^2 of the surface area (s.a.) in Å^2 for one unit cell of the noble metal slabs at 0 K. Adsorption Gibbs free energies of one Pd atom E_{ads}(Pd) and one Pt atom E_{ads}(Pt) referenced to one Pd and Pt atom in the gas phase on the stoichiometric surface of the ceria surface facets (100), (110) and (111) in eV at 423.15 K.

	s.a. [Å^2]	$E_{surf.}$ [eV/Å^2]	E_{ads}(Pd) [eV]	E_{ads}(Pt) [eV]
Extended surface facets of ceria				
$CeO_2(100)$	60.48	$1.28 \cdot 10^{-2}$	-3.00	-5.58
$CeO_2(110)$	42.77	$0.79 \cdot 10^{-2}$	-2.10	-4.73
$CeO_2(111)$	52.38	$0.45 \cdot 10^{-2}$	-1.45	-3.33

4.2. Nanometer Cluster theoretically approached by extended Metal Surfaces

Figure 4.2 depicts the extended noble metal surfaces, as calculated in this work using supercell slabs. The fixed atoms are marked with a cross and represent a lattice constant in the bulk phase, while the surface atoms whose relaxation was allowed are unmarked. The investigation of the extended surface facets of the noble metals Pd and Pt serves

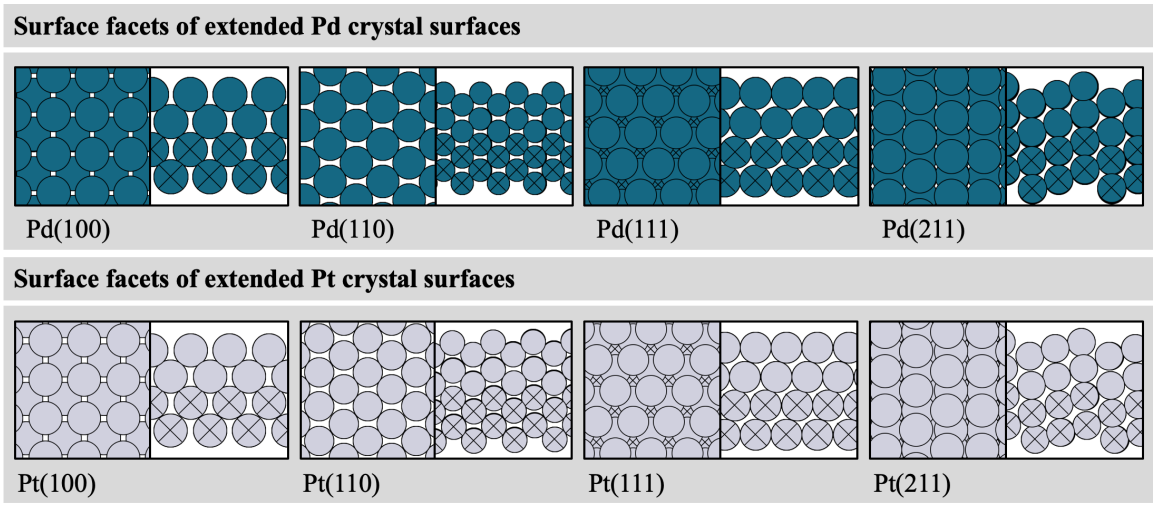

Figure 4.2.: Stoichiometric extended noble metal surfaces, showcasing all four surface facets from left to right: (100), (110), (111), and (211). Both the top and side views of the entire slab are presented. The upper row displays Pd surface facets, while the middle and bottom rows exhibit Pt surfaces. Petrol circles represent Pd atoms, and gray circles indicate Pt atoms. The total energies are listed in the Appendix in Table A.3.

as an approach to represent nanometer-sized clusters supported on ceria. By comparing

single-atom catalysts, sub-nanometer clusters, and nanometer-sized clusters (represented by extended surface facets), we aim to conduct a systematic investigation of size effects. Former studies have shown that only the first row at the very interface with the ceria surface exhibits charge transfer from the noble metal cluster. Since a nanometer-sized cluster consists of several hundred noble metal atoms, the charge transfer effect on all surfaces far from the interface is negligible or even nonexistent.[70,242–244] Due to the significant variability in adsorption sites and subsequent transition states, it is crucial to establish correlations between equivalent adsorption sites among the noble metal species in this study. This ensures valid comparisons and prevents comparing dissimilar scenarios. The pristine surfaces of Pd and Pt noble metals are used in this study as a reference for the active sites on a nanometer scale. Nanometer-sized clusters can be approximated by considering slabs

Table 4.2.: Calculated surface energies $E_{surf.}$ in eV/Å^2 of the surface area (s.a.) in Å^2 for one unit cell of the noble metal slabs at 0 K. Adsorption Gibbs free energies on the ceria surface facets (100), (110) and (111) in eV at 423.15 K of the first O atom $G_{ads}(O^*_{low})$, the second O atom $G_{ads}(O^*_{high})$ referenced to O in the gas phase and adsorption Gibbs free energies of the CO adsorption close to the first adsorbed O atom $G_{ads}(CO^*_{low})$ and the CO adsorption close to the second adsorbed O atom $G_{ads}(CO^*_{high})$ referenced to CO in the gas phase. The corresponding structures of O adsorptions can be found in Section 6.3.2 for high loading and Section 6.3.3 for low loading.

	$E_{surf.}$ [eV/Å^2]	s.a. [Å^2]	$G_{ads}(O^*_{low})$	$G_{ads}(O^*_{high})$	$G_{ads}(O^*_{low})$	$G_{ads}(O^*_{high})$
Exdended surface facets of Pd						
Pd(100)	$1.25 \cdot 10^{-2}$	31.74	-0.63	0.19	-0.38	0.07
Pd(110)	$1.34 \cdot 10^{-2}$	44.89	-0.53	-0.03	-0.43	-0.04
Pd(111)	$1.16 \cdot 10^{-2}$	27.49	-0.65	0.12	-0.13	0.10
Pd(211)	$0.86 \cdot 10^{-2}$	38.87	-0.66	-0.13	-0.43	-0.17
Exdended surface facets of Pt						
Pt(100)	$1.42 \cdot 10^{-2}$	32.16	-0.14	-0.95	-0.97	0.23
Pt(110)	$1.53 \cdot 10^{-2}$	45.48	-0.68	-0.56	-0.57	0.29
Pt(111)	$1.23 \cdot 10^{-2}$	27.85	-0.72	0.57	-0.36	-0.30
Pt(211)	$0.86 \cdot 10^{-2}$	39.39	-0.50	-0.57	-0.52	-0.17

of extended noble metal surfaces. At the nanometer cluster size, the most exposed surface is not the boundary line with the support but rather the pure noble metal surface facets. The surface facets in nanometer clusters vary in proportion to each other depending on the cluster structure and size as studies of Vogt[245,246] and Hamilton[247] et al. investigated, showing particle size-activity relationships. The interfacial area relative to the extended metal surface facets of the clusters increases as the cluster size decreases. In addition to the question regarding the electronic effect[171,248], therefore, it raises the question of whether the pure noble metal is indeed the most active species, or if subnanometer clusters, which exhibits a larger boundary-line-to-noble-metal ratio, can compete against it. The noble metal surface facets (111), (110), (100), and (211) and their activity towards O_2 dissociation and CO oxidation are depicted in the following sections. These surfaces, in the mentioned

order, provide an increasing terrace space. Specifically, (110) offers an additional row, (100) provides two, and (211) offers three rows forming a terrace. The adsorption of reactants such as O and CO is favored by adsorption at one of the edges or kinks, as the under-coordination of the surface leads to higher coordination of the adsorbates. However, regarding the chosen adsorption sites and the according structures, we rely on the aforementioned literature and do not conduct in-depth investigations of these surfaces.[56] Nevertheless, we did perform a variation of the adsorption sites and focused on the more stable as well as systematic ones. In Table 4.2, the surface energies $E_{surf.}$, calculated as explained in Section 3.4. The surface energies of the pristine noble metal surfaces are very similar to each other. Pd ranges between $0.86 \cdot 10^{-2}$ and $1.34 \cdot 10^{-2}$ eV/Å, and Pt between $0.86 \cdot 10^{-2}$ and $1.53 \cdot 10^{-2}$ eV/Å. The surface energy of Pt is on average around $0.05 \cdot 10^{-2}$ eV/Å higher than for Pd. The adsorption energies considered are calculated for a temperature of 423.15 K and stay in line with the literature, as Su et al. have shown in the investigation of the surface energies of Pt(111) and Pt(100) with $1.37 \cdot 10^{-2}$ eV/Å and $1.61 \cdot 10^{-2}$ eV/Å, respectively.[240] The temperature for the adsorption energies is accounted by the use of *ab initio* thermodynamics, including the contributions of ZPE and entropy, as discussed in Section 3.7. Additionally, the adsorption energies G_{ads} of the reactants are listed for the O^* (* as a superscript next to the element indicates the adsorbed state on a heterogeneous catalyst.) adsorption $G_{ads}(O^*_{low})$ leading to a low O^* coverage and the CO^* adsorption on a low O^* coverage $G_{ads}(CO^*_{low})$, as well as the counterparts with a high O^* coverage $G_{ads}(O^*_{high})$ and $G_{ads}(CO^*_{high})$. The CO adsorption is stronger for the Pt pristine surface than for the Pd surface with around -0.50 to -1.00 eV for Pt and around -0.10 to -0.40 eV for Pd for $G_{ads}(CO^*_{high})$. $G_{ads}(O^*_{high})$ is around 0 eV between slightly endothermic and slightly exothermic adsorption energies.

4.2.1. Ceria surface facets as the non-innocent Support for Pd and Pt as the Active Center

To investigate the reducibility and the oxidation of the ceria surface facets as the support for the active species as Pd and Pt noble metals, we removed and added one and two O atoms on all three stable ceria surfaces (100), (110), and (111). In this work, we refrain from using Kroger-Vink notation. Instead, we focus solely on the number of V_O defects or adsorbed O atoms, considering either one or two of these, and provide a detailed figure illustrating the configuration in each case. V_O defects are denoted by V_O and adsorbed O atoms are denoted by O^*, preceded by an integer indicating the quantity 1 or 2. The ceria surfaces depicted in Figure 4.3 illustrate surface facets with a reduction of either 1 or 2 O atoms, leading to $1V_O$ or $2V_O$ surface defects, as well as oxidation by O atoms leading to $1O^*$ or $2O^*$ adsorbed O atoms. The (100) surface offers several favorable V_O defect positions and adsorption sites for O atoms. This surface is composed of Ce atoms

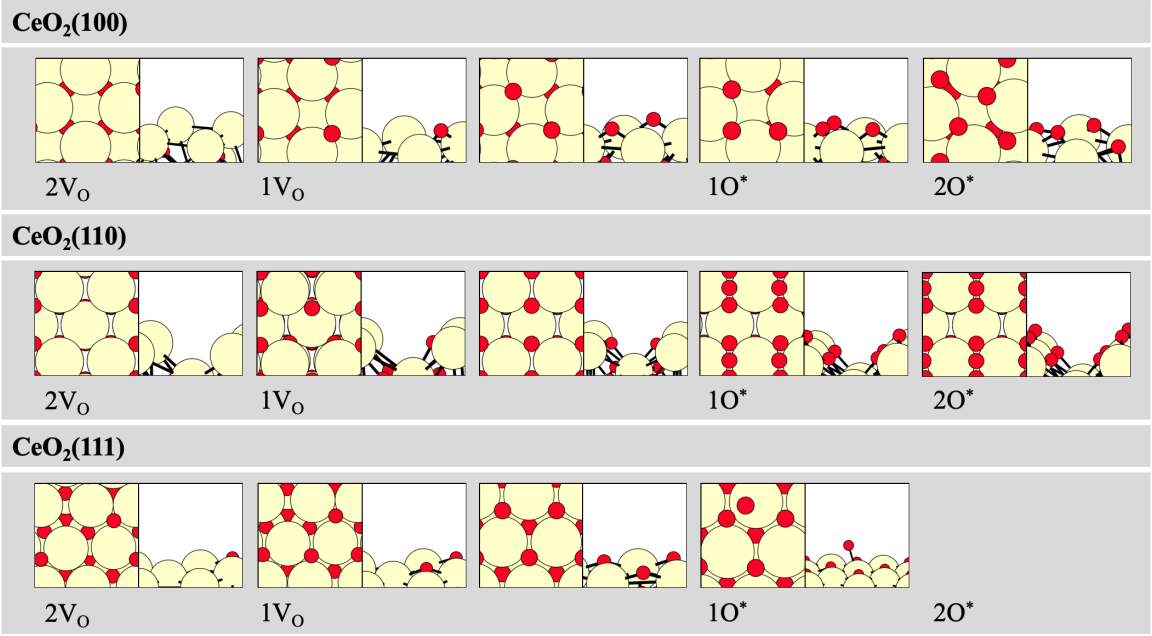

Figure 4.3.: Ceria surface facets (100), (110), and (111) with varying O adsorption and defect formation leading to $2V_O$, $1V_O$, the stoichiometric surface, $1O^*$, $2O^*$. The total energies are listed in the Appendix in Table A.4.

forming a "pocket". O atoms can adsorb on these highly under-coordinated Ce atoms in bridge positions between two Ce atoms or create defects, thereby anchoring the Ce atoms to the O atoms of the lower layer. This "pocket" structure is a specific feature of the (100) surface. The (110) surface also exhibits a structure that offers advantages for V_O defects and adsorption. This structure resembles a "tunnel", formed by alternating rows of Ce atoms that are raised and lowered. Consequently, the lower Ce rows create a "floor", while the raised ones form a "ridge". It stands to reason that within these "tunnels", adsorbates can also be embedded. Due to the low coordination of the Ce rows, O atoms have the opportunity to bind either in hollow sites within the "tunnel" or in bridge sites on the upper Ce rows. The (111) surface, being the most densely packed surface, is unfavorable for additional O adsorptions. It leads to oversaturation, making it difficult to optimize the structure for adsorption by 2 O atoms. The higher coordination of the Ce atoms by anchoring O atoms on the surface and the layers beyond, allows for forming V_O defects, providing various positioning of the defects around the Ce atoms. The calculated Gibbs free energies by structure optimization for O adsorption and V_O defect formation are listed in Table 4.3 and visualized in Figure 4.4. The first removal of an O atom results in the formation of one $1V_O$ defect. The corresponding Gibbs free energy is denoted here as $\Delta G_{des}(1V_O)$. The formation of two $2V_O$ defects is referenced to the first defect or adsorbed O atom. The adsorption of n O atoms results in the formation of nO^* species on the heterogeneous catalyst. The corresponding Gibbs free energy is denoted as $\Delta G_{ads}(nO^*)$, where n represents either 1 or 2

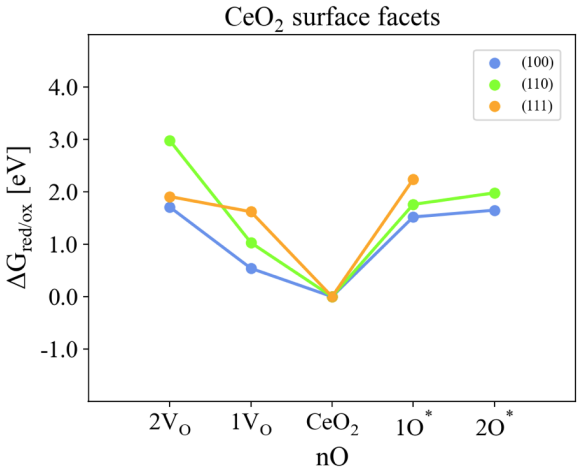

Figure 4.4.: Gibbs free energies of oxidation and reduction $\Delta G_{red/ox}$ on the stoichiometric ceria surface on the three surface facets of ceria (100), (110) and (111) in eV at 423.15 K. The Gibbs free energy of the second O removal or adsorption is relative to the first, respectively. And the first O removal or adsorption is relative to the stoichiometric surface. The (100) surface is marked in blue, the (110) in green, and the (111) in red.

oxygen atoms The energies associated with the desorption and adsorption of O atoms on the surfaces suggest that the (100) surface exhibits the lowest energies, with values of 0.54 eV for the first $\Delta G_{des}(1V_O)$, 1.71 eV for the subsequent second $\Delta G_{des}(2V_O)$, 1.52 eV for the first $\Delta G_{ads}(1O^*)$, and 1.65 eV for the subsequent second $\Delta G_{ads}(2O^*)$. The (110) surface demonstrates Gibbs free energy values of 1.03 eV for $\Delta G_{des}(1V_O)$, 2.98 eV for $\Delta G_{des}(2V_O)$, 1.76 eV for $\Delta G_{ads}(1O^*)$, and 1.98 eV for the subsequent second O adsorption $\Delta G_{ads}(2O^*)$. The values for the (110) surface are about 0.50 higher for the first V_O defect formation and 1.00 eV higher for the second V_O defect formation than for the (100) surface facet of ceria. The first O adsorption is about 0.25 eV higher for the first O adsorption and 0.30 eV higher for the second O adsorption than for the (100) surface facet of ceria. The (111) surface shows slightly elevated values for the first O defect $\Delta G_{des}(1V_O)$ formation with 1.62 eV than the other two surface facets, first O adsorption $\Delta G_{ads}(1O^*)$ with 2.24 eV. The second O defect $\Delta G_{des}(2V_O)$ formation is lower with 1.91 eV. In general, it can be observed that

Table 4.3.: Adsorption energies of the O atom $\Delta G_{ads}(1O^*)$, the two O atoms $\Delta G_{ads}(2O^*)$, one O surface defect formation $\Delta G_{des}(1V_O)$ and two O surface defect formation $\Delta G_{des}(2V_O)$ on the ceria surface facets (100), (110) and (111) in eV at 423.15 K. The Gibbs free energy of the second O removal or adsorption is relative to the first, respectively. And the first O removal or adsorption is relative to the stoichiometric surface.

	$\Delta G_{des}(2V_O)$	$\Delta G_{des}(1V_O)$	stoichiometric	$\Delta G_{ads}(1O^*)$	$\Delta G_{ads}(2O^*)$
Reducibility and oxidation of extended ceria surface facets					
$CeO_2(100)$	1.71	0.54	0	1.52	1.65
$CeO_2(110)$	2.98	1.03	0	1.76	1.98
$CeO_2(111)$	1.91	1.62	0	2.24	-

both the first and second formation of V_O defects and the first and second adsorption of

O on a stoichiometric ceria surface are endothermic. The surface facets of ceria exhibit slightly different Gibbs free energies for removal and adsorption, but there are no significant differences between the surface facets in reduction and oxidation. As already outlined in the motivation 1.3, there is a considerable amount of literature on V_O defect formation on ceria surfaces. The values determined here are consistent with those compiled in the literature and summarized by Sauer and Ganduglia-Pirovano et al. in a review.[80,81]. As the surface energy increases and the surface becomes more undercoordinated, The Gibbs free energy for O defect formation $\Delta G_{des}(1V_O)$ increases with surface density in the sequence (100) < (110) < (111). For the (100) surface, it is 0.46 eV, for (110) it is 0.92 eV, and for (111) it is 1.52 eV at 423.15 K. Nolan et al. found 2.27 eV for the (111) surface and 1.99 eV for (110) and 2.60 eV for (111).[74,81,249] This trend is proportional to the surface density. Experimentally, O can be removed from the bulk either by annealing[250] with subsequent diffusion to the surface or directly from the surface through annealing, sputtering[251–254], electron irradiation[255], exposure to X-rays[256], or chemical reduction[257,258]. The trend of (100) < (110) < (111) with increasing $\Delta G_{des}(nV_O)$ shows, that it is more demanding to remove an O atom from the surface, the higher the surface coordination is. And it is less demanding, the more open the surface structure is due to the lower coordination of surface atoms.

4.2.2. O defective and oxidized Pd and Pt single-atoms adsorbed on Ceria surface facets

To investigate the reducibility and the oxidation of the single-atom catalysts the noble metal atoms Pt and Pd are adsorbed on the surface facets (100), (110), and (111) of ceria. The structures are depicted in Figure 4.5 for Pd and 4.6 for Pt, the V_O defects, and O adsorption in the vicinity of the single-atom catalysts. After structure optimization, it became evident that the single-atom catalysts aim for a square-planar configuration. The ceria surface offers opportunities for a square-planar configuration across all three facets. However, while the "pocket" of the (100) facet is optimal for a square-planar configuration and the "tunnel" of the (110) surface can also form a square-planar structure, the (111) surface does not provide adequate anchoring possibilities. In this scenario, the Pd and Pt atoms can only anchor to two O atoms on the surface, forming corners of the square-planar structure, while an additional two O atoms are located at a distance from the surface, pointing into the z-direction. It is noteworthy that the small size of the unit cell used to form the slab supercell results in a high density of V_O defects and a high O loading on the heterogeneous catalyst. Consequently, the surface coverage by a single noble metal atom is high, as each unit cell contains one of these noble metal atoms. Furthermore, it should be noted that the expansion of the lattice constant was excluded due to the fixation of the bulk phase in the lower two

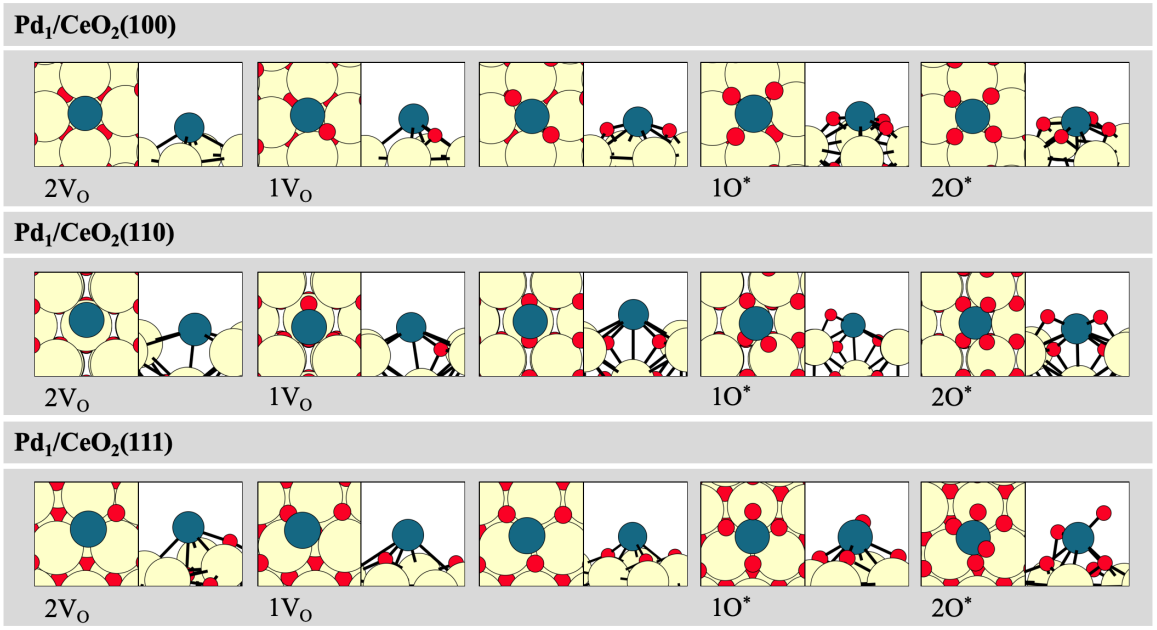

Figure 4.5.: Ceria surface facets (100), (110), and (111) with varying O adsorption and defect formation of two $2V_O$ defects, one $1V_O$ defect, the stoichiometric surface, one $1O^*$ adsorption, two $2O^*$ adsorption at the vicinity of a Pd single-atom catalyst. Red circles represent O, large yellow circles denote Ce atoms, and petrol circles represent Pd atoms. The total energies are listed in the Appendix in Table A.5.

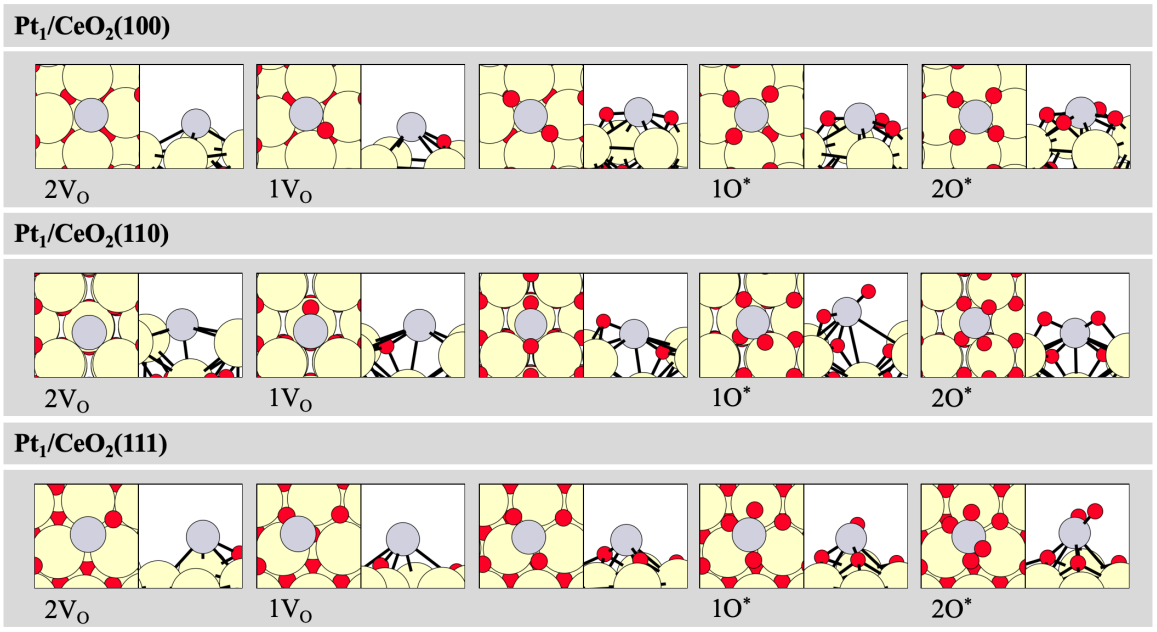

Figure 4.6.: Ceria surface facets (100), (110), and (111) with varying O adsorption and defect formation of two $2V_O$ defects, one $1V_O$ defect, the stoichiometric surface, one $1O^*$ adsorption, two $2O^*$ adsorption at the vicinity of a Pt single-atom catalyst. Red circles represent O, large yellow circles denote Ce atoms, and gray circles represent Pt atoms. The total energies are listed in the Appendix in Table A.5.

layers, the relaxation of only two layers on the surface, and the size of the unit cell. In a real situation, it is likely that the single noble metal atoms, due to the absence of the

necessary O atoms to anchor them on the surface, are drawn into the bulk to integrate into the ceria crystal structure. This results in the noble metal atom, acting as a cation, occupying a position of the Ce cation to lower the enthalpy of the lattice structure and find a more stable configuration. It would seek coordination through O atoms. The crystal structures of ceria and the Pd and Pt noble metal oxides were presented in the Introduction in Section 1.3, crystal structures of the oxides by Pd, Pt, and Ce oxides. By fixing the lower two layers and the small number of relaxing upper two layers, any migration into the lower layers of the single-atom catalysts has been artificially prevented. However, this may lead to experimental deviations. We have not corrected these deviations at this point, as a relevant investigation should lead to a systematic examination to categorize the oxidation states and the associated physical and chemical properties. Based on this, future studies can systematically investigate deviations as well. In future investigations, it is recommended to consider Frenkel and Schottky defects in the event of migration of the noble metal atom into the lower layers. A migration of a noble metal atom into the boundary layer within the ceria crystal or the bulk phase of the ceria crystal results in the atom either occupying a lattice site (Schottky defect) or being positioned between lattice sites (Frenkel defect). The latter is more unstable as it does not require lattice energy and is problematic due to the different ion sizes. The former requires lattice energy since the ceria structure must be rearranged to make room for the Pd atom. After integration into the crystal structure, a stable state should be achieved. Schottky defects require charge compensation, which is achieved by substituting a Pd atom. A deficiency of O on the surface causes the single-atom catalysts Pd and Pt to migrate into the interface (Frenkel defect). A substituted ceria surface (Schottky defect) refers to a Pd or Pt atom occupying a lattice site in the ceria crystal and therefore does not diffuse further. Figure 4.7 illustrates a comparison of O removal and

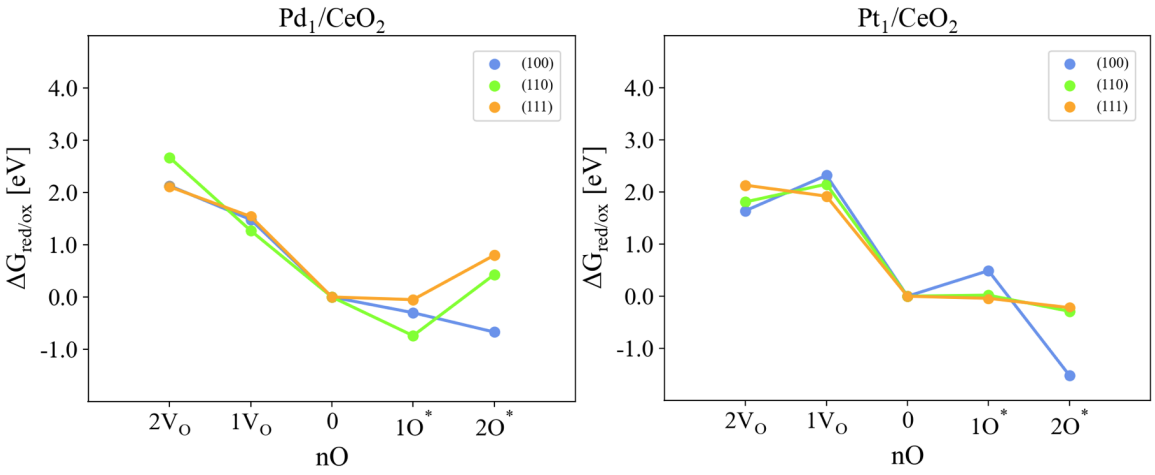

Figure 4.7.: Gibbs free energies of reduction by V_O defect formation and oxidation by O adsorption $\Delta G_{red/ox}$ relative to the stoichiometric ceria surface of single Pd or Pt atoms on the surface facets of ceria (100), (110) and (111) in eV at 423.15 K.

addition concerning the stoichiometric surface facet with Pd or Pt single-atom dopants. The Gibbs free energies are listed in Table 4.4. The reaction temperature was calculated at 423.15 K. The desorption of O atoms leading to the formation of ordered two $1V_O$ surface defect and $2V_O$ surface defects, respectively, is consistently endothermic. These are for the first removal of an O atom in a vicinal position to a Pd single-atom 1.48 eV for the (100) surface, 1.27 eV for (110), and 1.54 eV for (111). Thus, a tendency towards denser packed surfaces is observed as the desorption energy increases, the denser the ceria surface is packed. The second O removal in a vicinal position to Pd single-atoms is 2.13 eV for the (100) surface, 2.67 eV for (110), and 2.11 eV for (111). Therefore, removing another O atom is significantly more endothermic than the first O atom. The first removal of an O atom in a vicinal position to a Pt single-atom is 2.30 eV for the (100) surface, 2.15 eV for (110), and 1.92 eV for (111). For the Pt single-atom catalyst, therefore, O removal is more endothermic for the (100) and (110) surfaces, but nearly the same for the (111) surface as with a Pd single-atom catalyst. In contrast, the removal of a second O atom has a lower difference with 1.64 eV for the (100) surface, 1.81 eV for (110), and 2.13 eV for (111) than the removal of a second O atom in the vicinity of a Pd single-atom catalyst. The first

Table 4.4.: Adsorption energies of the O atom $\Delta G_{ads}(1O^*)$, the two O atoms $\Delta G_{ads}(2O^*)$, one O surface defect formation ΔG_{1V_O} and two O surface defect formation ΔG_{2V_O} on the ceria surface facets (100), (110) and (111) with one Pd or Pd single-atom adsorbed in eV at 423.15 K.

	$2V_O$	$1V_O$	stoichiometric	$1O^*$	$2O^*$
Reducibility and oxidation of Pd single-atom catalysts					
$Pd_1CeO_2(100)$	2.13	1.48	0	-0.30	-0.67
$Pd_1CeO_2(110)$	2.67	1.27	0	-0.74	0.43
$Pd_1CeO_2(111)$	2.11	1.54	0	-0.05	0.80
Reducibility and oxidation of Pt single-atom catalysts					
$Pt_1CeO_2(100)$	1.64	2.32	0	0.49	-1.52
$Pt_1CeO_2(110)$	1.81	2.15	0	0.02	-0.29
$Pt_1CeO_2(111)$	2.13	1.92	0	-0.04	-0.22

adsorption of an O atom in a vicinal position to a Pd single-atom is -0.30 eV for the (100) surface, -0.74 eV for (110), and -0.05 eV for (111). Hence, for the Pt single-atom catalyst, O adsorption is exothermic at the reaction temperature of 423.15 K for the (110) and (111) surfaces. The adsorption of a second O atom is -0.67 eV for the (100) surface, 0.43 eV for (110), and 0.80 eV for (111). The first adsorption of an O atom in a vicinal position to a Pt single-atom is 0.48 eV for the (100) surface, 0.02 eV for (110), and -0.04 eV for (111). Hence, for the Pt single-atom catalyst, O adsorption is endothermic at the reaction temperature of 423.15 K for the (100) and (110) surfaces and just slightly exothermic for the (111) surface. The adsorption of a second O atom is -1.52 eV for the (100) surface, -0.29 eV for (110), and -0.22 eV for (111). The Pd and Pt single-atom catalysts, as introduced

in the Introduction in Section 1.3, prefer oxidation to higher oxidation states. Adsorption by an O atom leads to a formal oxidation state of +II, and a second O atom to +IV of the noble metal atom. However, a Bader charge analysis can demonstrate that these are partial oxidation states. This is detailed in Section 5.1. The general trend is that the more closed the ceria surface on which the single-atom catalyst is adsorbed, the more endothermic the O adsorption becomes. A second O adsorption is more endothermic than the first. The (100) surface is the most closely packed and provides an optimal adsorption site for additional O atoms for both a Pd and a Pt single-atom catalyst due to its pocket structure. In general, it can be observed here that a formal oxidation state of +II is preferred for the Pd single-atom catalyst, while an oxidation state of +IV for the Pt single-atom catalyst is favored after the first oxidation to +II.

4.2.3. Migration of O defect Formation into the Sublayer of Ceria

The surface lattice V_O defects, due to maintaining the crystal lattice, are particularly migratory, allowing O ion transport, thereby providing ceria with an ion conductivity as explained in the Introduction in Section 1.3. In this section, we examine the migration of an V_O defect into the sublayer of the ceria surface. Figure 4.8 illustrates the positions of the V_O defects. The defect on the top layer, directly at the surface of the heterogeneous catalyst, is in a vicinal position to a single-atom catalyst Pd or Pt. All three stable ceria surface structures (100), (110), and (111) are considered. Upon migration into the second layer, an

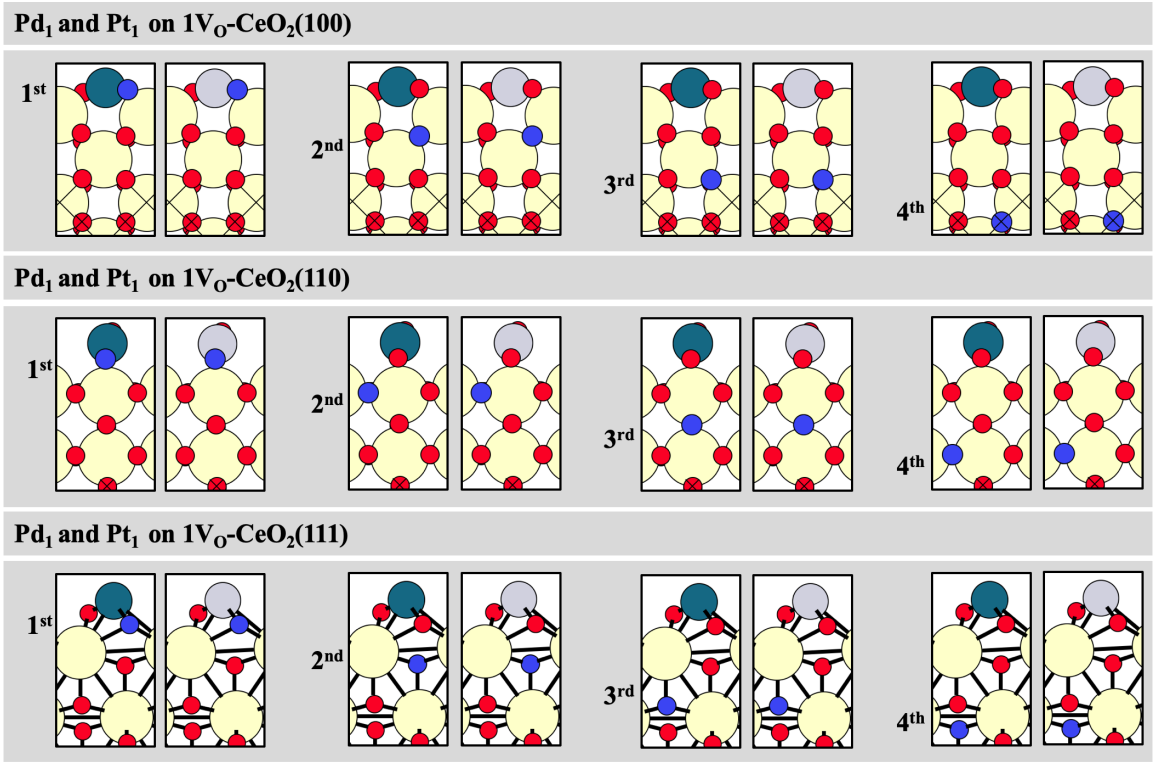

Figure 4.8.: Ceria surface facets with migrating V_O defects starting at the vicinity of Pd and Pt single-atom catalyst on the surface facets of ceria (100), (110), and (111) towards the bulk phase of the surfaces. The numbering refers to the O layers of the ceria surface, with the first layer denoted as 1^{st}, the second layer as 2^{nd}, the third layer as 3^{rd}, and the fourth layer as 4^{th}. Dark blue circles represent V_O defects, red circles O, large yellow circles denote Ce atoms, petrol circles Pd atoms, and gray circles represent Pt atoms. The total energies are listed in the Appendix in Table A.6.

O atom migrates into the upper layer. This propagation continues into the lower layers. It can be observed that the surface structure of ceria (100) facilitates a straightforward linear migration of the V_O defect in the negative z-direction. On the (110) surface, these are diagonal to each other. On the (111) surface, the two upper O layers were found to be quite close to each other, while the two lower layers were found at a greater distance from the upper two but close to each other again. In each case, we made sure to proceed as straight

as possible in the negative z-direction. This approach enables tracking the Gibbs free energy associated with the movement of the oxygen atom as it migrates towards the bulk. The Gibbs free energies at an ambient temperature of 423.15 K are depicted in a potential energy diagram in Figure 4.9 and listed in Table 4.5. The temperature is accounted by the use of *ab initio* thermodynamics, including the contributions of ZPE and entropy, as discussed in Section 3.7. The oxygen defect in the top layer, located adjacent to the single noble metal atom, is used as the reference point, with its Gibbs free energy set to zero. The migration of the V_O defects is relative to the previous position. The migration into the second O layer is

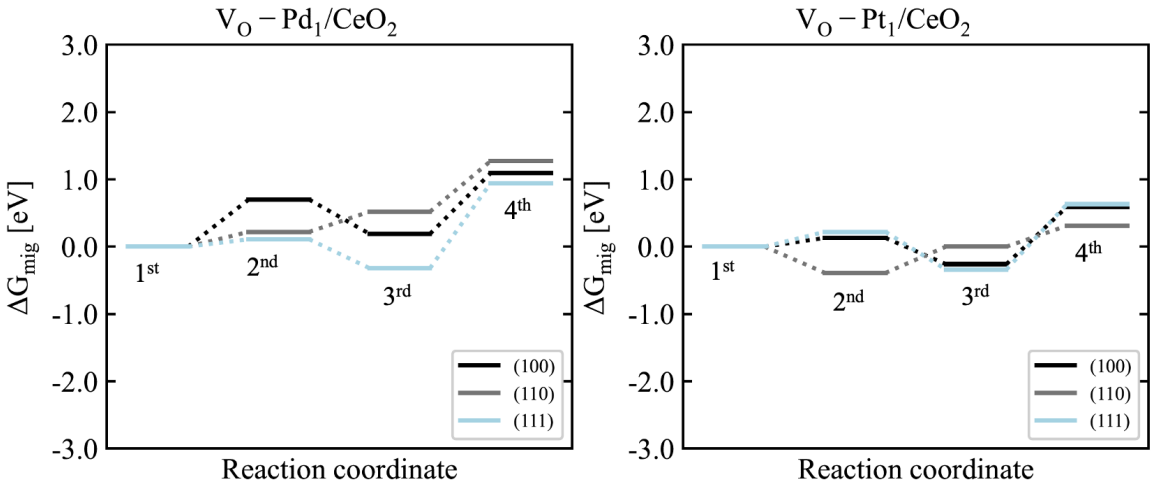

Figure 4.9.: Gibbs free energy diagram of the O defect V_O migration ΔG_{mig} relative to the V_O in the first layer in the vicinity of single Pd or Pt atom adsorbed on the two surface facets of ceria (100), (110) and (111) in eV at 423.15 K after structure optimization.

endothermic for the Pd single-atoms, with 0.70 eV for the (100) surface, 0.22 eV for (110), and 0.11 eV for (111). For the Pt single-atoms, it is 0.13 eV for the (100) surface, -0.39 eV for (110), and 0.22 eV for (111). Therefore, the energetic cost to perform the first migration is endothermic except for the (110) surface with a Pt single-atom catalyst, which presents a barrier to migration into the lower layers. The (111) surface has a low Gibbs free energy for migration for both Pd and Pt single-atom catalysts. The migration into the third layer is 0.19 eV for Pd for the (100) surface, 0.52 eV for (110), and -0.32 eV for (111), and for Pt, it is -0.26 eV for the (100) surface, 0.00 eV for (110), and -0.34 eV for (111). Thus, the most stable position for the V_O defect is in the third layer on the (111) surface, as it is exothermic for both Pd and Pt single-atom catalysts. Migration into the third layer on the (110) surface is also exothermic with a Pt single-atom catalyst. However, all other cases in the third layer are neutral or endothermic. Migration into the fourth layer is endothermic in all cases, with 1.09 eV for Pd for the (100) surface, 1.27 eV for (110), and 0.94 eV for (111), and for Pt, it is 0.59 eV for the (100) surface, 0.31 eV for (110), and 0.63 eV for (111). Migration to this position is unfavorable in all cases, as our bulk situation represents

a fixed structure within the supercells of the slabs. The most stable crystal structure of ceria is in the bulk phase. Therefore, O removal closest to the bulk phase logically results in the highest energy cost, unlike the surface layers. Overall, it can be stated that in the case of a Pd single-atom catalyst, the migration of the V_O defects towards the bulk phase is most stable when they are located in what we refer to as the third layer of the (111) surface. For a Pt single-atom catalyst, stability is achieved when the V_O defects reach the second layer on the (110) surface. If a (111) surface is considered, stabilization in the same third

Table 4.5.: Gibbs free energies of the O defect V_O migration, ΔG_{mig}, relative to the V_O in the first layer in the vicinity of single Pd or Pt atoms adsorbed on the two surface facets of ceria (100), (110), and (111) in eV at 423.15 K after structure optimization. The numbering refers to the O layers of the ceria surface, with the second layer denoted as 2^{nd}, the third layer as 3^{rd}, and the fourth layer as 4^{th} relative to the first layer.

	2^{nd}	3^{rd}	4^{th}
V_O migration at Pd single-atom catalyts			
$Pd_1/1V_OCeO_2(100)$	0.70	0.19	1.09
$Pd_1/1V_OCeO_2(110)$	0.22	0.52	1.27
$Pd_1/1V_OCeO_2(111)$	0.11	-0.32	0.94
V_O migration at Pd single-atom catalyts			
$Pt_1/1V_OCeO_2(100)$	0.13	-0.26	0.59
$Pt_1/1V_OCeO_2(110)$	-0.39	0.00	0.31
$Pt_1/1V_OCeO_2(111)$	0.22	-0.34	0.63

layer can also be found for Pt. We would like to emphasize that we may have assigned the layers differently from other studies in the literature. Therefore, it is always important to refer to the configurations and examine them to make a direct comparison. In the study by Ganduglia-Pirovano et al.[80], a pure ceria (111) surface without Pd or Pt single-atoms is considered. There, the position of the V_O defect, which we refer to as the second O layer, is labeled as a sublayer. According to the study, stabilization of the V_O defects occurs in the second layer. Here, we observe that migration of the V_O defects into the bulk phase, induced by the adsorption of a noble metal atom on the ceria surface, leads to altered stabilization. In general, it can be said that migration is not completely inhibited, but there is a tendency towards the third layer instead of the second.

4.2.4. Reduced and oxidized Pd and Pt atoms as Substitutes for Ce Surface Atoms

If a Ce atom on the ceria surface is substituted by a Pd or Pt single-atom catalyst, it results in the replacement of a Ce cation in the ceria crystal lattice, which is described as a Schottky defect, as discussed in the previous section. The ceria surface thus effectively acquires a Ce defect which is described by V_{Ce}. To investigate the reducibility and oxidation of the single-atom catalysts as substitutes for a Ce atom, we performed these experiments on all three ceria surfaces (100), (110), and (111). The structure-optimized configurations are depicted

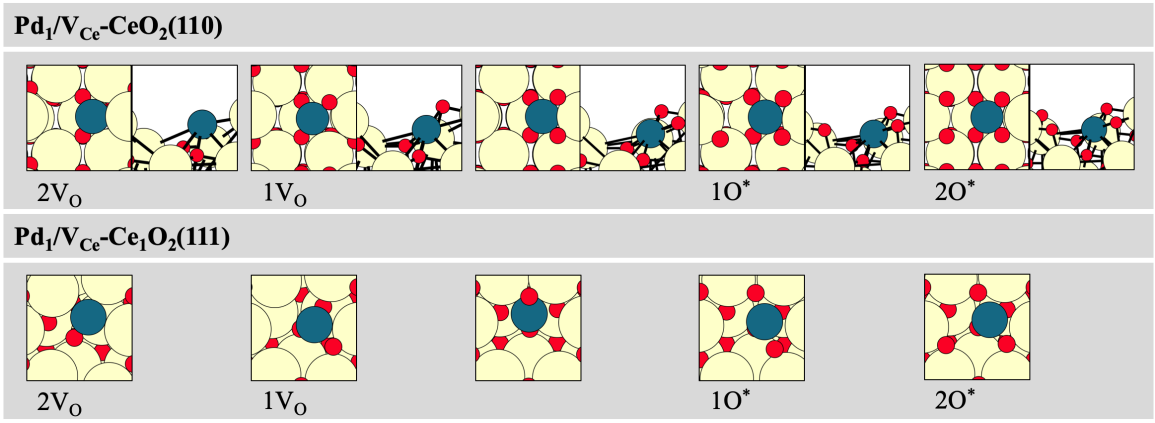

Figure 4.10.: Ceria surface facets (110) and (111) with defect formation and varying O adsorption at the vicinity of a Pd single-atom catalyst as substitutes for Ce surface atoms on the two surface facets of ceria with two $2V_O$ defects, one $1V_O$ defect, the stoichiometric surface, one $1O^*$ adsorption, two $2O^*$ adsorption. Red circles represent O atoms, large yellow circles denote Ce atoms, and petrol circles represent Pd atoms. The total energies are listed in the Appendix in Table A.7.

in Figures 4.10 for Pd and 4.11 for Pt. Because visualizing the "holes" on the (111) surface from a lateral perspective to demonstrate binding relationships is inapt, we have opted not to include it here. In a stoichiometric exchange, a substitution of a Ce cation on the ceria

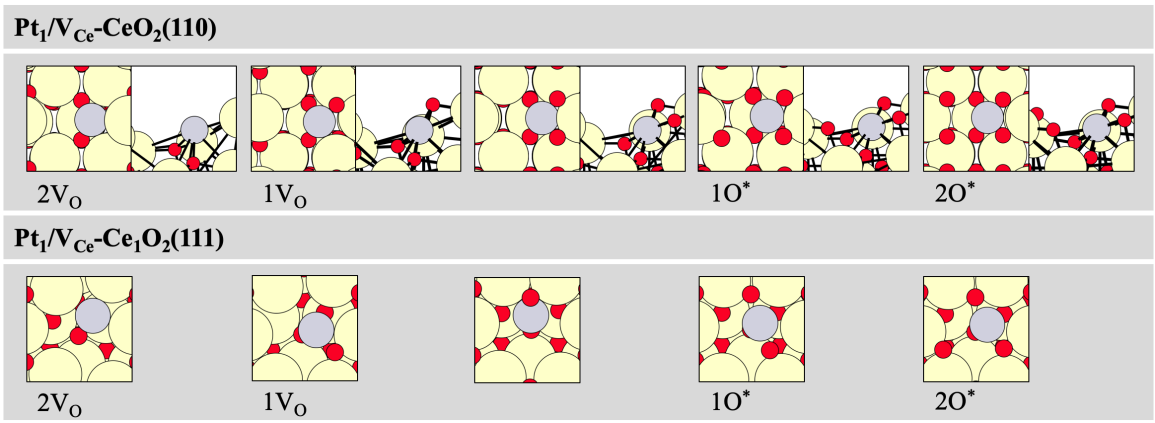

Figure 4.11.: Ceria surface facets (110) and (111) with defect formation and varying O adsorption at the vicinity of a Pt single-atom catalyst as substitutes for Ce surface atoms on the two surface facets of ceria with two $2V_O$ defects, one $1V_O$ defect, the stoichiometric surface, one $1O^*$ adsorption, two $2O^*$ adsorption. Red circles represent O atoms, large yellow circles denote Ce atoms, and gray circles represent Pt atoms. The total energies are listed in the Appendix in Table A.7.

surface results in the Pd or Pt atom being consequently oxidized to a formal oxidation state of +IV. When substituting a Ce cation on the (110) surface, one of the Ce atoms from the row forming the sides of the "tunnel" is removed and replaced by a Pd or Pt single-atom catalyst. On a stoichiometric ceria surface, the Pd and Pt single-atoms are embedded in a square planar configuration by anchoring onto 4 O atoms, with two additional O atoms remaining on the opposite side. By reducing these two O atoms, a stoichiometric ceria surface is

obtained, but a noble metal atom with a formal oxidation state of 0 is retained. Further reduction removes the two O atoms positioned in a vicinal position to the noble metal atom and adsorbs them onto the upper Ce row concerning the ceria surface. When substituting a Ce cation on the (111) surface, one of the Ce atoms is removed from the surface. The (111) surface is the most densely packed and by removing a surface Ce atom, a surface defect is created, forming a deep hole. The noble metal atom can adsorb at various sites within this

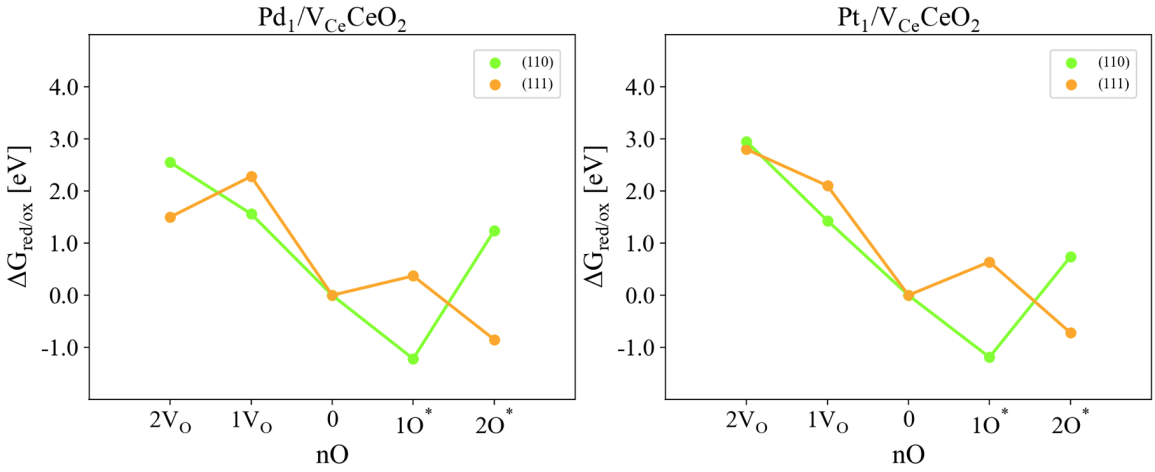

Figure 4.12.: Gibbs free energies of reduction by V_O defect formation and oxidation by O adsorption $\Delta G_{red/ox}$ relative to the stoichiometric but Ce defective ceria surface of single Pd or Pt atom as substitutes for Ce surface atoms on the two surface facets of ceria (110) and (111) in eV at 423.15 K.

surface defect to find a stable configuration. On a stoichiometric ceria surface, the Pd and Pt single-atoms can exist in an octahedral or square planar configuration. In the octahedral configuration, the noble metal atom would occupy the same center as the Ce atom that was replaced and would be coordinated by all neighboring O atoms. For the investigation of oxidation states, we have chosen a novel structure previously identified by Hensen and Su et al.[259], which represents an active catalyst. Another square planar structure would embed the noble metal further down into the "hole" of the Ce defect. However, this makes it inaccessible for reactants such as CO molecules. Therefore, this "novel" structure as already suggested by Hensen and Su et al., with adsorption on the upper O atoms of the"hole", is the accessible configuration for the reactants for CO oxidation. During reduction by removal of the O atoms, initially, the O atoms located on the top layer of the ceria surface were removed. Then, the O atoms in a vicinal position to the single-atom catalyst, which are highest in the next layer, were removed. After the removal of two O atoms following the stoichiometric ceria surface and achieving a formal oxidation state of 0 for the single-atom catalyst, only one O atom remains at the bottom of the "hole". In Figure 4.12, the Gibbs free energies for reduction are illustrated. The temperature of 423.15 K is accounted by the use of *ab initio* thermodynamics, including the contributions of ZPE and entropy, as discussed in Section

Table 4.6.: Adsorption energies of the first O atom $E_{ads}(1^{st}O)$, the second O atom $E_{ads}(2^{nd}O)$, the first O lattice defect formation $E_{form.}(V_O{}^{1st})$ and second O lattice defect formation $E_{form.}(V_O{}^{2nd})$ on the ceria surface facets (100), (110) and (111) with a single Pd or Pt atom adsorbed on the surface in eV at 423.15 K.

	$2V_O$	$1V_O$	stoichiometric	$1O^*$	$2O^*$
Reducibility and oxidation of Pd substitutes					
$Pd_1CeO_2(110)$	2.55	1.56	0	-1.22	1.24
$Pd_1CeO_2(111)$	1.50	2.22	0	0.37	-0.85
Reducibility and oxidation of Pt substitutes					
$Pt_1CeO_2(110)$	2.95	1.43	0	-1.19	0.74
$Pt_1CeO_2(111)$	2.80	2.10	0	0.64	-0.72

3.7. The corresponding Gibbs free energies are listed in Table 4.6. To facilitate direct comparison with the previous chapters, we assume a stoichiometric surface of ceria, and the Pd or Pt single-atom catalyst is formally adsorbed into the Ce defects V_{Ce}. Therefore, the adsorption of one or two O atoms causes oxidation of the Pd or Pt single-atom catalyst. Removal of the O atoms starting from the stoichiometric ceria surface, which holds a Pd or Pt single-atom, results in reduction. The first removal of an O atom in a vicinal position to a Pd single-atom is 1.56 eV for the Ce defective (110) surface and 2.22 eV for (111). For Pt, it is 1.43 eV for the Ce defective (110) surface and 2.10 eV for (111). The second removal of an O atom in a vicinal position to a Pd single-atom is 2.55 eV for the Ce defective (110) surface and 1.50 eV for (111). For Pt, it is 2.95 eV for the Ce defective (110) surface and 2.80 eV for (111). These are all endothermic. For the adsorption of one O atom in a vicinal position to a Pd single-atom, it is -1.22 eV for the Ce defective (110) surface and 0.37 eV for (111). For Pt, it is -1.19 eV for the Ce defective (110) surface and 0.64 eV for (111). Thus, adsorption on the (110) Ce defective surface is exothermic, while on the (111) Ce defective surface, it is endothermic. For the adsorption of the second O atom in a vicinal position to a Pd single-atom, it is 1.24 eV for the Ce defective (110) surface and -0.85 eV for (111). For Pt, it is 0.74 eV for the Ce defective (110) surface and -0.72 eV for (111). Thus, the adsorption of the second O atom on the (110) Ce defective surface is endothermic, while on the (111) Ce defective surface, it is exothermic. The second O atom results in inverted signs. Since the selection of O atoms for removal on the (111) surface includes several variants, we refrain from making definitive statements about the signs of reduction and oxidation caused by O atoms here. A more detailed examination is needed to determine which O atoms would need to be removed to enable a systematic investigation of stabilities. In this work, we are more interested in tendencies. It has been found that oxidation through adsorption of O atoms to increase the oxidation state of the single-atom noble metal is exothermic, while removal leading to reduction of the ceria surface is endothermic. Furthermore, this provided insight into how the migration of a noble metal atom into the ceria surface would occur in the case of a Schottky defect. It was observed here that integrated noble metal atoms

exhibit comparable reducibility and oxidation to those of surface-bound noble metal atoms. However, it is generally expected that diffusion of the embedded noble metal atoms into the ceria surface is more challenging, and subsequent agglomeration is anticipated. Further investigations into this have been conducted in the literature and are out of the scope of this work.

4.3. Structural Dynamics of Subnanometer Clusters

4.3.1. Nucleation Process onto Pd and Pt atoms as Substitutes for Ce Surface Atoms

In Section 4.2.1, we have previously investigated a surface defect involving Ce on a ceria (111) surface. Furthermore, in Section 4.2.4, we have explored the affinity of noble metals for adsorption on a ceria surface. In this section, we will delve into the process of induced nucleation of Pd_{10} and Pt_{10} clusters, which are adsorbed on noble metal atoms $Pd_{nuc.}$ or $Pt_{nuc.}$ that themselves are substitutes for ceria surface atoms. The $Pd_{nuc.}$ or $Pt_{nuc.}$ are Pd and Pt single-atom nuclei inducing the nucleation to form subnanometer cluster. To accomplish this, we initially introduce one to three noble metal atoms into the same number of Ce defects on the ceria surface. In each case, we assume adsorption from the gas phase. A further step for future investigations could be to use this as an example and focus on the species present under reaction conditions, as well as investigate the diffusion of noble metals for agglomeration, induced by noble metal nuclei on the surface. All calculated values presented here are listed in Table 4.7 and are computed according to Equation 4.1 Pd and Pt are denoted here as M.

$$E_{ads} = \frac{E_{total}(M_{10}V_{nO}) - E_{total}(M_{10}V_{nO}) + 10 \cdot E_{total}(Pd_{10(g)})}{10} \tag{4.1}$$

In Figure 4.13, the structure-optimized noble metals with an oxidation state of +IV and in Figure 4.14 and oxidation state 0 adsorbed into the Ce defective (111) ceria surface are depicted. In Figure 4.15, the subnanometer clusters Pd_{10} and Pt_{10} are adsorbed on a stoichiometric ceria surface, with the noble metal nuclei having an oxidation state of +IV. In Figure 4.16, they are reduced to an oxidation state of 0. In Figure 4.18, the subnanometer clusters are oxidized with an adsorption of 7 O atoms, but the nuclei are reduced to 0. In Figure 4.17, both the subnanometer clusters with an adsorption of 7 O atoms and the nuclei are oxidized to +IV. Overall, the intention here is to consider not only the number of nuclei but also the dependence of adsorption energy on the existing oxidation state. In the diagram 4.19, all these forms of nucleation are depicted and the adsorption energies are listed in Table 4.7. If noble metal atoms are already adsorbed on the surface, the adsorption energies for Pd_{10} and Pt_{10} subnanometer cluster become -2.61 eV for one Pd substitute, -2.79 eV for

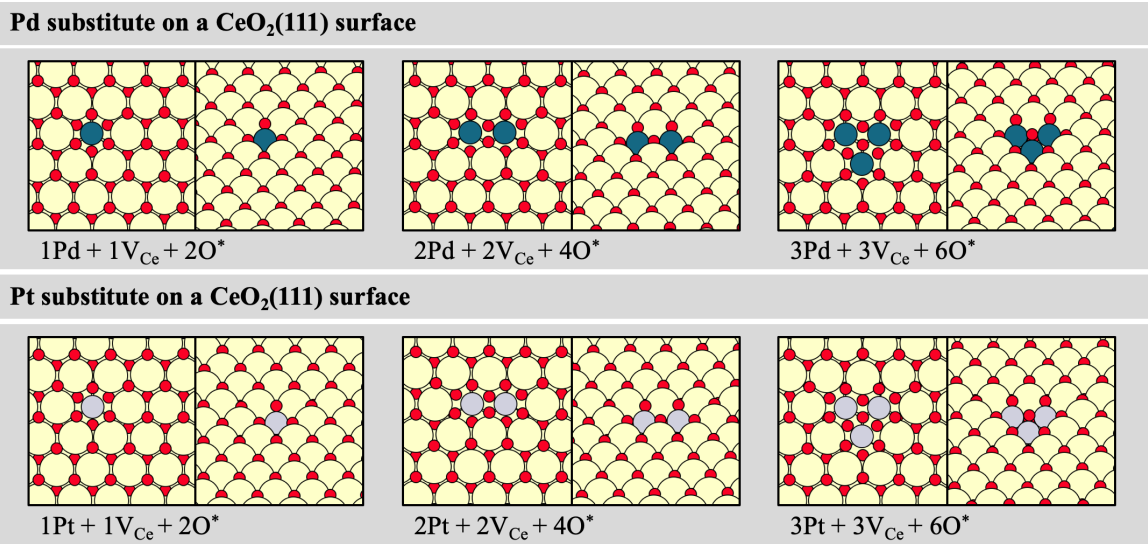

Figure 4.13.: Structure-optimized configurations of $Pd^{+IV}{}_{nuc.}$ or $Pt^{+IV}{}_{nuc.}$ atoms as substitutes for ceria surface atoms representing the nuclei inducing the nucleation in eV and at 0 K. Red circles represent O, yellow circles Ce, petrol circles Pd atoms, and gray circles indicate Pt atoms. The total energies are listed in the Appendix in Table A.8.

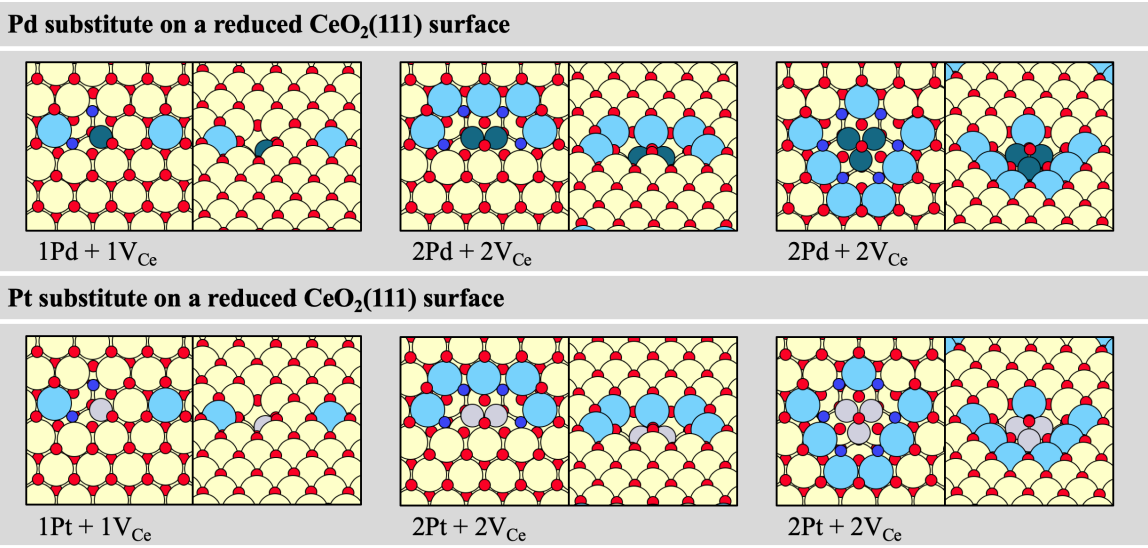

Figure 4.14.: Structure-optimized configurations of $Pd^{0}{}_{nuc.}$ or $Pt^{0}{}_{nuc.}$ atoms as substitutes for ceria surface atoms representing the nuclei inducing the nucleation in eV and at 0 K. Red circles represent O atoms, large yellow circles denote Ce atoms, blue circles represent the reduced Ce^{+III} ions, petrol circles Pd atoms, and gray circles indicate Pt atoms. The total energies are listed in the Appendix in Table A.8.

two, and -2.94 eV for three in the case the nuclei are oxidized to the oxidation state +IV and -2.29 eV for one Pd substitute, -2.17 eV for two, and -2.46 eV for three in the case the nuclei are reduced. For Pt, the adsorption on the oxidized nuclei is -4.50 eV for one Pt substitute, -4.72 eV for two, and -4.82 eV for three and on reduced nuclei -4.19 eV for one Pt substitute, -4.11 eV for two, and -4.45 eV for three. If the subnanometer cluster

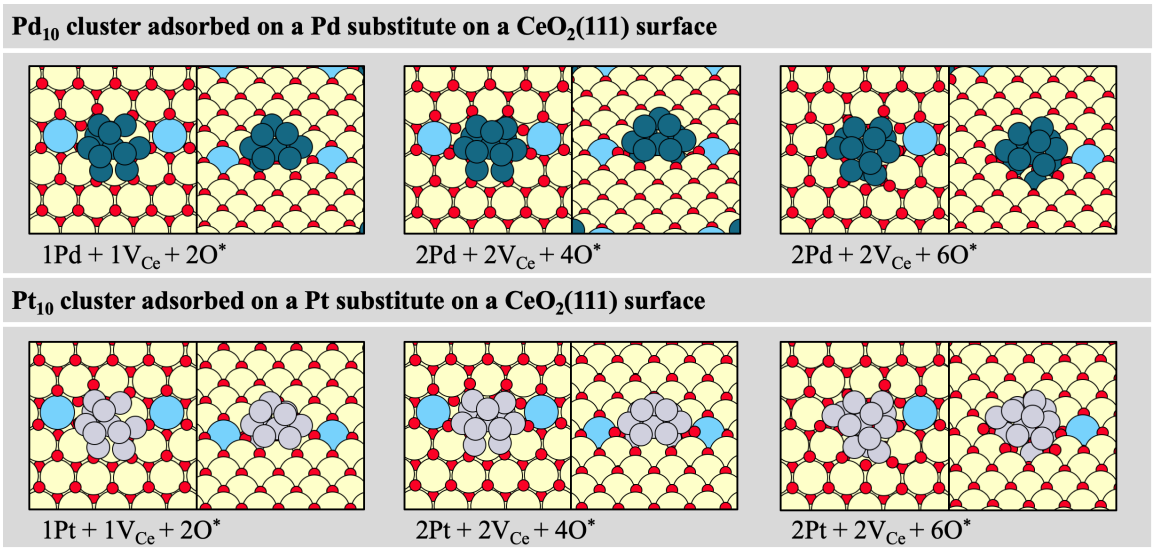

Figure 4.15.: Structure-optimized configurations of Pd_{10} and Pt_{10} subnanometer cluster adsorbed onto $Pd^{+IV}{}_{nuc.}$ or $Pt^{+IV}{}_{nuc.}$ atoms in eV and at 0 K. Red circles represent O atoms, large yellow circles denote Ce atoms, blue circles represent the reduced Ce^{+III} ions, petrol circles Pd atoms, and gray circles indicate Pt atoms. The total energies are listed in the Appendix in Table A.8.

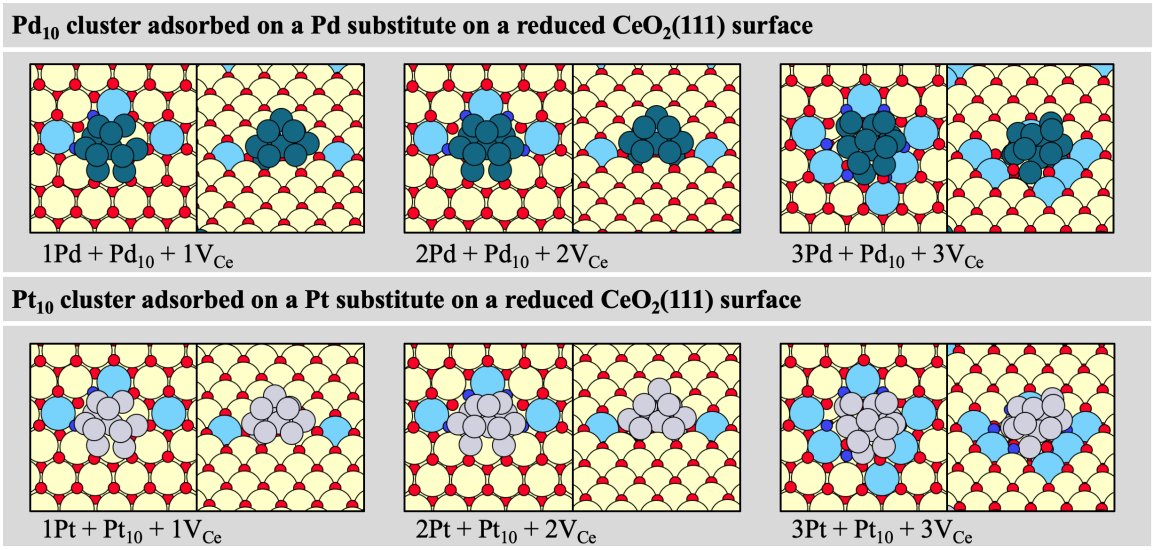

Figure 4.16.: Structure-optimized configurations of Pd_{10} and Pt_{10} subnanometer cluster adsorbed onto $Pd^{0}{}_{nuc.}$ or $Pt^{0}{}_{nuc.}$ atoms in eV and at 0 K. Red circles represent O atoms, large yellow circles denote Ce atoms, blue circles represent the reduced Ce^{+III} ions, petrol circles Pd atoms, and gray circles indicate Pt atoms. The total energies are listed in the Appendix in Table A.8.

is considered to be oxidized with $7O^{*}$, the adsorption energy on reduced nuclei is -3.30 eV for one Pd substitute, -3.42 eV for two, and -3.63 eV for three and -5.19 eV for one Pt substitute, -5.40 eV for two, and -5.44 eV for three. If the subnanometer cluster Pd_{10} and Pt_{10} is considered to be oxidized with $7O^{*}$, the adsorption energy on oxidized nuclei is -2.99 eV for one Pd substitute, -3.18 eV for two, and -3.18 eV for three and -4.93 eV

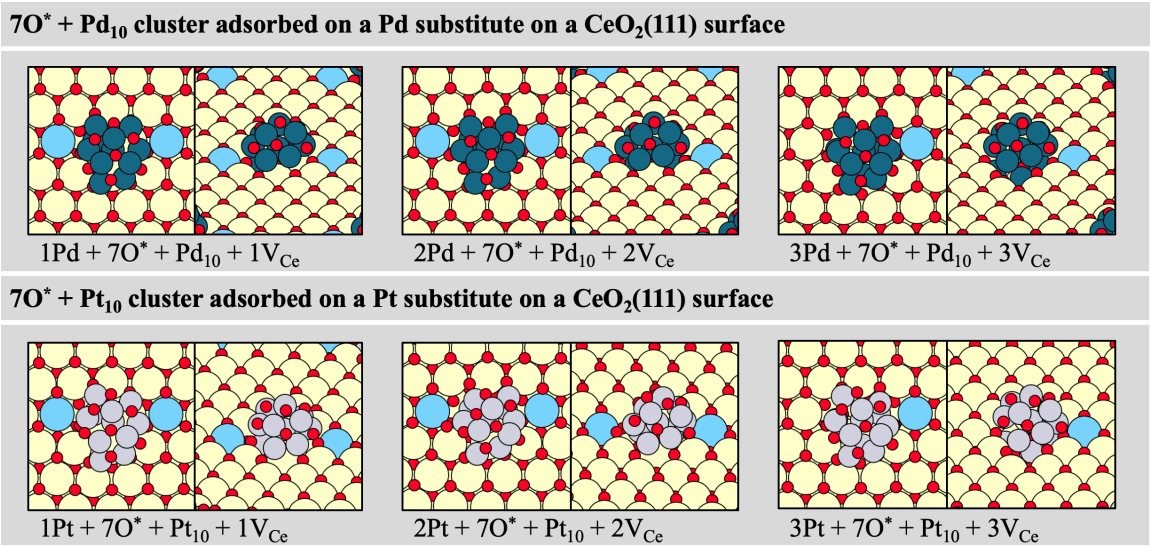

Figure 4.17.: Structure-optimized configurations of $7O^{*}$ + Pd_{10} and $7O^{*}$ + Pt_{10} subnanometer cluster adsorbed onto $Pd^{+IV}{}_{nuc.}$ or $Pt^{+IV}{}_{nuc.}$ atoms in eV and at 0 K. Red circles represent O, yellow circles Ce, petrol circles Pd atoms, gray circles indicate Pt atoms, and sky blue circles reduced Ce^{+III} ions. The total energies are listed in the Appendix in Table A.8.

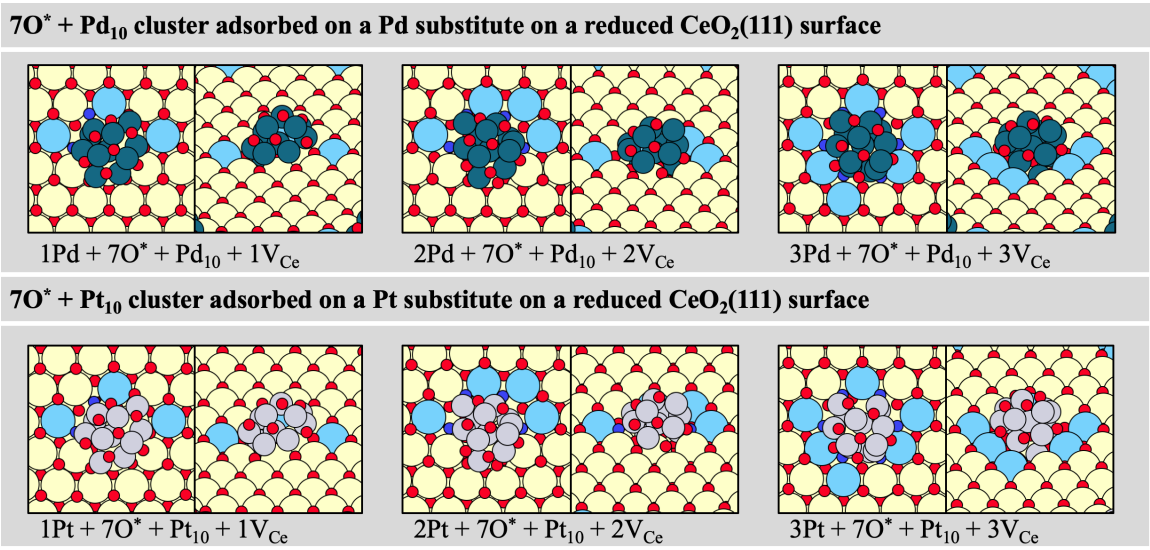

Figure 4.18.: Structure-optimized configurations of $7O^{*}$ + Pd_{10} and $7O^{*}$ + Pt_{10} subnanometer cluster adsorbed onto $Pd^{0}{}_{nuc.}$ or $Pt^{0}{}_{nuc.}$ atoms in eV and at 0 K. Red circles represent O atoms, large yellow circles denote Ce atoms, blue circles represent the reduced Ce^{+III} ions, petrol circles Pd atoms, and gray circles indicate Pt atoms. The total energies are listed in the Appendix in Table A.8.

for one Pt substitute, -5.09 eV for two, and -5.18 eV for three. Overall, the adsorption energy for the cluster increases by 0.20 eV for both Pd and Pt clusters when a noble metal atom is adsorbed into a Ce surface defect of ceria. The adsorption energy of subnanometer clusters by individual noble metal atoms from the gas phase on a reduced ceria surface with $6V_O$ is -2.01 eV for a Pd_{10} cluster and -3.87 eV for a Pt_{10} cluster. These are marked as a

reference for nucleation by the dashed blue line in Figure 4.19. The adsorption energy on a stoichiometric ceria surface with $6V_O$ is -2.46 eV for a Pd_{10} cluster and -4.30 eV for a Pt_{10} cluster, marked as a reference for nucleation by the dashed black line. In the case of oxides with $7O^*$ adsorbed O atoms, it is -3.14 eV for the Pd cluster and -5.02 eV for the Pt cluster, marked with a red dashed line. It is evident that in all cases, the adsorption energies are slightly more positive than those for nucleation-induced adsorption energies of the clusters by noble metal atoms (and O atoms for the oxidized clusters) from the gas phase. In general, it can also be stated that any adsorption energy of the Pt clusters and through nucleation by Pt substitutes is stronger than that of the Pd counterparts. With an increased number

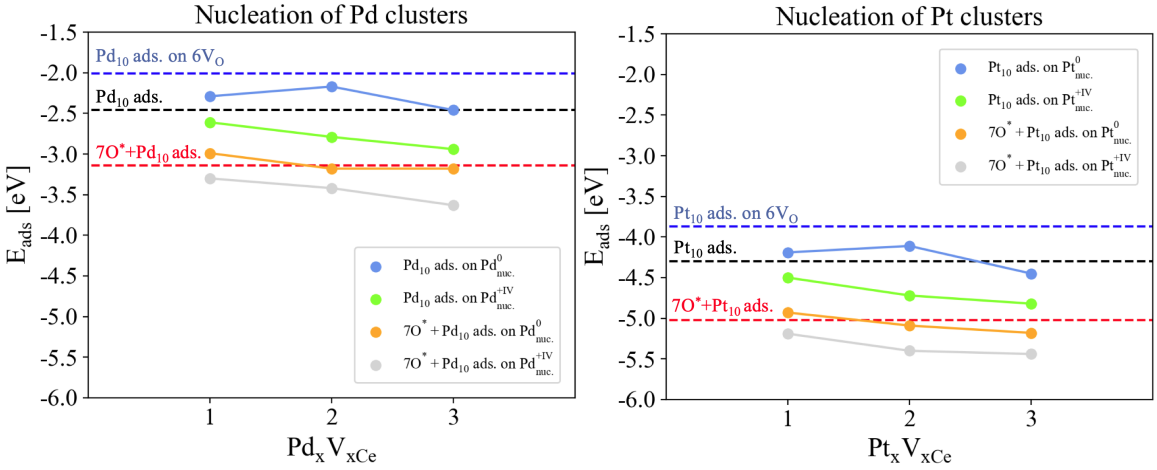

Figure 4.19.: Adsorption energies E_{ads} of noble metal atoms from the gas phase forming Pd_{10} or Pt_{10} subnanometer clusters plotted against the number of $Pd_{nuc.}$ or $Pt_{nuc.}$ atoms. The subnanometer clusters are adsorbed on the $Pd_{nuc.}$ or $Pt_{nuc.}$ atoms, which represent the nuclei and act as substitutes for Ce atoms on the ceria (111) surface. The dashed lines represent: $6V_O$ at the nn position to Pd_{10} or Pt_{10} clusters adsorbed onto a ceria (blue) corresponding to oxidized clusters mentioned in Section 4.3.1, as depicted in Figure 4.16 for Pd and for Pt clusters. Pd_{10} or Pt_{10} adsorbed on a stoichiometric ceria surface (black) corresponding to Figure 4.20 for Pd and 4.21 for Pt in Section 4.3.2. $7O^*$ adsorbed onto a Pd_{10} or Pt_{10} subnanometer clusters (red) corresponding to oxidized clusters Figure 5.23 for Pd and 5.24 for Pt in Section 5.4. The species for the oxidation state 0 are shown in 4.14 (blue), 4.15 (green), 4.18 (orange), and 4.17. The total energies are listed in the Appendix in Table A.9 for Pd and A.10 for Pt.

of already adsorbed noble metal atoms in the Ce surface defects of ceria, the adsorption of Pd_{10} and Pt_{10} increases by approximately 0.10 eV to 0.20 eV. Therefore, nucleation is indeed favored over a pure ceria surface. The magnitudes of the increased adsorption energies are around 0.10 to 0.30 eV at 0 K. This also accounts for the oxidized subnanometer clusters. The noble metal atoms from the gas phase forming Pd_{10} or Pt_{10} subnanometer clusters onto $Pd_{nuc.}$ or $Pt_{nuc.}$ atoms which represent the nuclei and act as substitutes for Ce atoms on the ceria (111) surface show stronger adosorption energies than onto a plain ceria (111) surface facet. Thus, they can trigger agglomeration of other noble metal atoms, either from the gas phase or diffusing on the ceria surface, by coordinating to the noble metal atoms embedded in the ceria surface, which are particularly stable as they are part of the

previously defective ceria crystal lattice. Additionally, it becomes evident that there is a tendency towards more stable nucleation with higher oxidation states of both the nuclei and the subnanometer clusters. The number of nuclei on the ceria surface is less influential in this regard. In summary, it can be said that diffusion of the noble metal atoms on an extended, plain ceria surface will always result in a Ce defective surface V_{Ce} contributing to nucleation. Oxidized noble metal atoms possibly originating from the gas phase are favored to contribute to nucleation and agglomerate into larger clusters. However, it is noted that these structures were calculated only at 0 K. The influence of temperature can be explored, for instance, through post-DFT methods, to consider the agglomeration of clusters originating from a gas phase or the diffusion of noble metals in a reduced atmosphere. The structures presented here were computationally demanding, serving as initiating structures for subsequent post-DFT methods. A realistic catalyst exhibit numerous Ce surface defects. Therefore, it can be assumed that noble metal atoms adsorbing on a pure ceria surface will invariably find stabilization within the defects. This alters the perception of a real catalyst in such a way that a crystalline mixture of noble metal atoms is more likely to be found on the surface rather than a distribution of clusters or single-atoms. Hence, the surfaces considered in first principles studies should be significantly diversified, and always regarded as an idealized scenario among a vast ensemble of possibilities.

Table 4.7.: Adsorption energies E_{ads} of reduced and oxidized Pd_{10} and Pt_{10} subnanometer cluster on the noble metal nuclei $Pd^{0}{}_{nuc.}$, $Pt^{0}{}_{nuc.}$ in the reduced state and $Pd^{+IV}{}_{nuc.}$, $Pt^{+IV}{}_{nuc.}$ in the oxidized state from the gas phase in eV at 0 K. The number of nuclei are referred as adsorption energies on one $E_{ads}(1)$, two $E_{ads}(2)$, and three $E_{ads}(3)$ in the Ce defects V_{Ce} on the (111) ceria surface. Here, M is either Pd or Pt.

	M_{10} + $M^{0}{}_{nuc.}$	M_{10} + $M^{+IV}{}_{nuc.}$	$7O^{*}$ + M_{10} + $M^{0}{}_{nuc.}$	$7O^{*}$ + M_{10} + $M^{+IV}{}_{nuc.}$
Nucleation at $Pd^{+IV}{}_{nuc.}$				
$E_{ads}(1M_{nuc.})$	-2.29	-2.61	-2.99	-3.30
$E_{ads}(2M_{nuc.})$	-2.17	-2.79	-3.18	-3.42
$E_{ads}(3M_{nuc.})$	-2.46	-2.94	-3.18	-3.63
Nucleation at $Pt^{+IV}{}_{nuc.}$				
$E_{ads}(1M_{nuc.})$	-4.19	-4.50	-4.93	-5.19
$E_{ads}(2M_{nuc.})$	-4.11	-4.72	-5.09	-5.40
$E_{ads}(3M_{nuc.})$	-4.45	-4.82	-5.18	-5.44
Adsorption at extended ceria (111) surface				
$6V_O$ + Pd_{10}	-2.01			
Pd_{10}	-2.46			
$6O^{*}$ + Pd_{10}	-3.14			
$6V_O$ + Pt_{10}	-3.87			
Pt_{10}	-4.30			
$6O^{*}$ + Pt_{10}	-5.02			

4.3.2. Size and Shapes of subnanometer Clusters

The main decision-making to come to five categorizations was the formation of Pd and Pt subnanometer clusters adsorbed on a ceria (111) surface by hand by the use of intuition. Plenty of the categorized structures resemble Wulff structures and aim to represent different angles and facet exposure. After an Odysse of trial-and-error to form several cluster shapes starting with just a few atoms and followed by increasing sizes six cluster categorizations are made in this work. The structural optimization of the subnanometer clusters takes place in the ground state, which is reached at 0 K. In this case, no ab initio thermodynamics are used to account for temperatures. All subnanometer clusters were investigated in varying sizes. The largest subnanometer cluster created in this way is the Pd_{61} and Pt_{61} Heart-like structure. Analogous structures for all subnanometer clusters between Pd and Pt were created. The structurally optimized clusters are shown in Figure 4.20 for the Pd clusters and 4.21 for the Pt clusters. The Flower-like structure inherently has an immediate coordination of noble

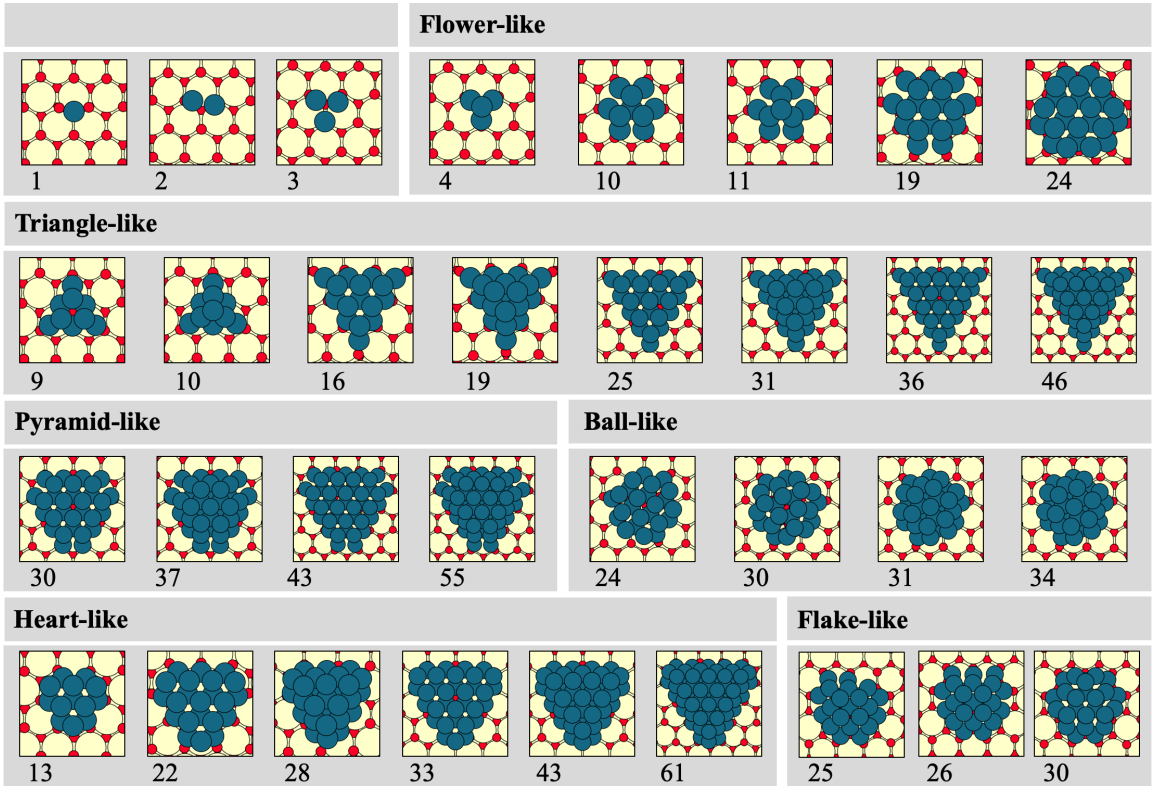

Figure 4.20.: Structure-optimized Pd subnanometer clusters supported on the (111) surface of ceria, increasing in size from 1 atom to 61 atoms and categorized into shape classes. The number of noble metal atoms in the subnanometer clusters is indicated as an index below the images. Red circles represent O atoms, large yellow circles Ce atoms, and petrol circles Pd atoms. The total energies are listed in the Appendix in Table A.9.

metals at the interface with the O atoms on the surface of the support. The Triangle-like structures mimic the surface structure of the oxide. The specific interface differs based on

the orientation of the triangles. The Pyramid-like structure is derived from the Triangle-like structures, with the distinction that they are flattened at the corners. Several atoms were removed from the corners of the triangles, exposing an additional surface facet of the cluster. The assumption here was that the surface enthalpy could be reduced, making the clusters potentially more stable than the Triangle-like structures. The Heart-like structures are derived from the Pyramid-like structures. Here, the intention was to alter the angle in the opposite direction. While the angles between the cluster and the ceria surface are significant in the Triangle and Pyramid-like structures, they are smaller in the Heart-like structures. The Ball-like structure arose from the consideration that the entire cluster has the smallest possible angle, resembling a droplet settling on a surface with high surface enthalpy. The surface area of the cluster is minimized to balance this enthalpy. The flake-like structure emerged as corners and edges were cut from the previous structures.

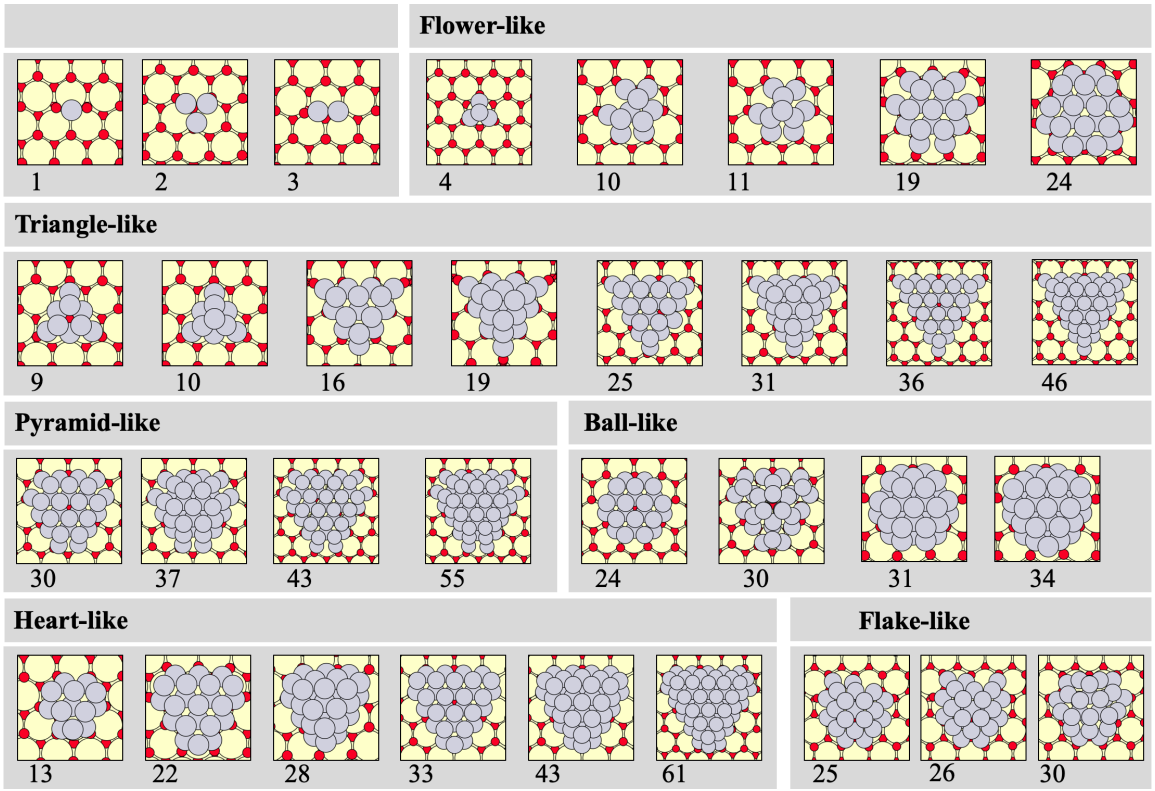

Figure 4.21.: Structure-optimized Pt subnanometer clusters supported on the (111) surface of ceria, increasing in size from 1 atom to 61 atoms and categorized into shape classes. The number of noble metal atoms in the subnanometer clusters is indicated as an index below the images. Red circles represent O atoms, large yellow circles Ce atoms, and gray circles Pt atoms. The total energies are listed in the Appendix in Table A.10.

4.3.3. Stability of Pd and Pt Clusters Supported on Ceria

The atom energy, E_{atom}, denotes the energy of a noble metal atom within the cluster relative to its most stable configuration, which is the bulk atom in a crystalline lattice. Consequently, it is expected that each Pd and Pt atom within the clusters experiences a progressively more stable environment as the cluster size increases and approaches the crystalline lattice structure. The atom energy E_{atom} for each noble metal atom is calculated using the equation 4.2. E_{atom} is calculated as shown in equation 4.2. This is done by summing $E_{support}$, which represents the total energy of the support, and nE_{bulk}, representing the total energy of n noble metal atoms (Pd or Pt) in the bulk phase. The sum is then subtracted from the total energy of the subnanometer cluster supported on the ceria surface. Since E_{atom} reflects the energy of each individual noble metal atom relative to the bulk phase, the result is then divided by the number of noble metal atoms.

$$E_{atom} = \frac{E_{cluster+support}(Pd/Pt) - (E_{support} + nE_{bulk}(Pd/Pt))}{n(Pd/Pt)} \tag{4.2}$$

With that, a correlation can be established by plotting the atom energy E_{atom} against the number of noble metal atoms present in the cluster, as shown in Figure 4.22. It is expected and has been validated that as the cluster size increases, E_{atom} converges towards the bulk phase, approaching the bonding environment of a bulk atom. In the plot 4.22, it is evident that different morphologies have a significantly smaller impact on E_{atom} relative to the cluster size. This suggests that small deviations, due to the absence of only a few atoms from a specific cluster shape, have only a minor effect on the stability. The greater impact on stability comes from the shape rather than the number of atoms that form a specific size of the structure. As a result, when comparing different studies, even a difference of only a few atoms in cluster size should not necessarily be disregarded. If an experimental expectation of cluster size differs by just one or two atoms, the theorist should aim to use the most stable shape of the subnanometer cluster possible to make a direct comparison. The fundamental morphology is likely comparable to that of the experiment. In Figure 4.22, it is evident that the stability of the shapes only occurs through a significant change in surface enthalpy. For example, pyramid and flower structures have similarly large angles relative to the ceria surface and differ only slightly in their stability. However, ball and heart shapes have a smaller angle to the surface, making them noticeably less stable, as the atom energies deviate from the convergence towards the bulk situation with lower E_{atom} values compared to the pyramid and flower shapes. Pd and Pt clusters generally exhibit the same morphological stability relative to each other. Overall, Pd converges more quickly towards higher E_{atom} values and has higher values overall. This suggests that the crystal structure of Pd tends to approach that of a crystalline lattice more strongly. Further investigation is

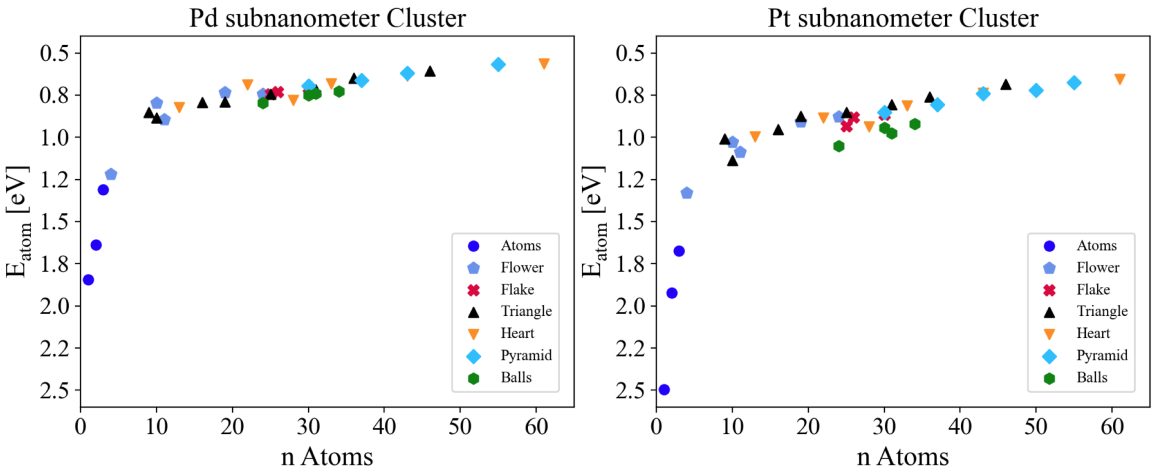

Figure 4.22.: The atom energy E_{atom} of each Pd bulk atom for different cluster shapes plotted against the cluster size. The categorizations are shown in the legend and classified by atoms with only a few (1 to 3) atoms forming a cluster (dark blue), flower (blue), flake (red), triangle (black), heart (yellow), pyramid (sky blue), balls (green). The atom energies are listed in the Appendix in Table A.9 for Pd and A.10 for Pt.

needed by considering the adsorption energy to incorporate the interaction with the support into the analysis to make a statement about the relative stabilities of the clusters depending on the noble metal, which will be discussed in the next section. Upon detailed examination of the diagrams, it is evident that the flower structure with a size of 10 noble metal atoms for a Pd cluster is the first cluster size to converge to a crystalline lattice structure. For Pt, this is the triangle structure with 9 atoms. However, the triangle structure with 10 atoms is also less stable for Pt compared to the flower structure with 10 atoms. The flower structure with 11 atoms is less stable for both Pd and Pt clusters. In this case, only one atom is placed on the apex of the flower cluster consisting of 10 atoms. This logically leads to a reduction in atom energy since the top atom has the fewest coordination possibilities, which can become similar to a crystalline lattice structure. Through the considerations of relative stabilities in this section, we have found that the smallest cluster size exhibiting significant stability is the Pd_{10} and Pt_{10} flower clusters, as convergence towards the bulk environment is close. The choice of the smallest possible, yet representative, subnanometer cluster is necessary due to the immense computational costs by the use of DFT methods in the GGA + U level of theory. Therefore, in the subsequent analyses of this work, we will use these clusters to investigate activities towards O_2 dissociation and CO oxidation. To explore activities regarding a possible size effect of cluster size, we will use, in addition to the configuration of the Pd_{10} and Pt_{10} clusters of flower structure, which consist of two layers with five noble metal atoms in the first layer and three atoms in the third layer, also the Pd_3 and Pt_3 clusters that reflect the same structure as the apex of the Pd_{10} and Pt_{10} clusters, with three noble metal atoms ordered in a triangle. In the Pd_3 and Pt_3 clusters, the cluster consists of only one layer on the support. These chosen clusters for subsequent studies are small enough to conduct quantum

chemical calculations with reasonable time and effort. A third layer, which could represent a ball-like cluster of size 31 noble metal atoms, is not useful since only the first layer of the clusters exhibits charge transfer to the support, as previous studies have recognized and can also be confirmed here and is shown in Scetion 4.3.5.[70,242–244] The second layer behaves more like a pure metal surface. Therefore, as a third step towards nanometer-sized clusters, the extended noble metal surfaces of Pd and Pt were considered to enable a size effect in four stages: the single-atom catalysts, Pd_3 and Pt_3 clusters consisting of one layer of noble metal atoms, Pd_3 and Pt_3 clusters consisting of two layers of noble metal atoms, and the extended noble metal surfaces, reflecting the nanometer clusters with sizes from 100 noble metal atoms upwards with 4 layers. When considering the angles between the clusters and the ceria surface, the flower structures are provided with a flat angle. A narrower angle could affect the reactivities at the interface. It is advisable to consider including the heart structure consisting of 13 noble metal atoms in future investigations. A larger angle could represent the pyramid structure with 9 atoms. An investigation of activities depending on the interface structure and the associated surface enthalpies is unfortunately out of the scope of this work but is strongly recommended. Larger clusters, as can be seen in Figure 4.22, exhibit the lowest E_{atom} values for ball structures, while pyramid and triangle structures show higher stability against the crystalline structure. The differences are minor and can be attributed to the internal interactions of the noble metal atoms within the cluster, which in this configuration resemble the crystalline structure less than in the case of triangle and pyramid structures. Heart structures consistently exhibit high crystalline lattice stability.

4.3.4. Integral Heat of Adsorption

The integral heat of adsorption E_{heat} from the gas phase is the energy released when noble metal atoms, such as Pd or Pt, are adsorbed from the gas phase onto the ceria surface forming subnanometer clusters. Therefore, the calculated energies have a negative sign, indicating the energy released from the system, which can be measured in experiments. To avoid confusion regarding the chosen signs, we have opted to use the integral heat of adsorption instead of the adsorption energy to obtain a comparable plot for direct comparison with experimental studies.[260] E_{heat} is calculated as shown in equation 4.3. This is done by summing $E_{support}$, which represents the total energy of the support, and nE_{gas}, representing the total energy of n noble metal atoms (Pd or Pt) in the gas phase. The sum is then subtracted from the total energy of the subnanometer cluster supported on the ceria surface. Since E_{heat} reflects the energy of each individual noble metal atom relative to the gas phase,

the result is then divided by the number of noble metal atoms.

$$E_{heat} = \frac{E_{cluster+support}(Pd/Pt) - (E_{support} + nE_{gas}(Pd/Pt))}{n(Pd/Pt)} \tag{4.3}$$

The integral heat of adsorption provides insights into the adsorption strength of the noble metal on the ceria surface. A lower value indicates weaker interaction with the surface. Consequently, dispersion and agglomeration will be affected by the interaction strength towards the surface. Based on the comparison between Pt and Pd, it can be concluded that Pd is more prone to agglomeration, while Pt tends to disperse more readily. Lu and Yang examined the adsorption energies of Rh, Pd, and Pt as single-atoms and as subnanometer clusters consisting of 4 atoms adsorbed on the ceria (111) surface by first principle methods. They found that the adsorption energy follows this order: Rh < Pd < Pt, with clusters adhering more strongly than individual atoms.[261] Our finding, that Pt adsorbs stronger to the ceria surface than Pd, is in line with the literature.[260] Therefore, similar to the previous

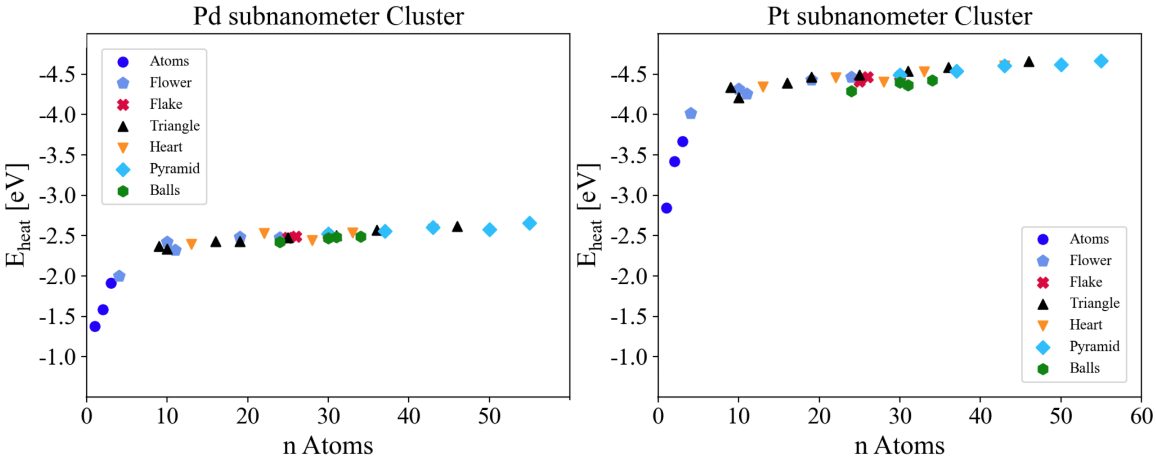

Figure 4.23.: The Integral Heat of Adsorption E_{heat} plotted against increasing cluster size. The categorizations are shown in the legend and classified by atoms with only a few (1 to 3) atoms forming a cluster (dark blue), flower (blue), flake (red), triangle (black), heart (yellow), pyramid (sky blue), balls (green). The energies are listed in the Appendix in Table A.9 for Pd and A.10 for Pt.

section, we plotted E_{heat} against the increasing cluster size. Since the assumption here is that a cluster forms upon the adsorption of a noble metal atom, both the interaction with the ceria surface and the lattice energy contribute to the integral heat of adsorption. In the previous section, we thoroughly examined the lattice energy. As evident in Figure 4.23, the convergence towards more stable clusters that converge towards a lattice structure of the bulk phase is similar to that observed in a plot of E_{atom} against cluster size. Since the ball structure exhibits lower integral heat of adsorption energies compared to the other structures, it can be assumed that the interaction with the surface is minimal due to the limited surface area of the ball clusters in contact with the ceria surface. Therefore, it can be inferred that

the atom energy is lower than that of other structures because the morphology of the ball structure does not allow for a stabilizing lattice structure. A significant difference, however, is that the deviations of the individual structures are in general lower here. This suggests the influence of the interaction with the surface, as it should be continuous due to the uniform (111) surface of ceria. An important observation is that Pt exhibits significantly higher integral heat of adsorption while having lower atom energies. A higher value indicates a stronger interaction with the surface in the case of integral heat of adsorption, and a lower value in atom energy indicates lower lattice structure stability. Pd behaves inversely. Therefore, the formation of the lattice structure, as mentioned in the previous section, is more pronounced for Pd cluster formation, while the interaction with the ceria surface, as evident here, is lower. Whether the driving force is to form the most stable crystal structure within the cluster or to coordinate with the ceria surface remains to be elucidated and can only be determined through further investigations on the binding energies based on the electronic properties governing the binding of the two noble metals Pd and Pt. In the following sections of this work, an attempt will be made to investigate the electronic properties of the ceria surface through the process of polaron hopping initiated by reduction and O removal from the ceria surface or through charge transfer upon the adsorption of the noble metals.

4.3.5. Charge Transfer forming Ce^{+III} Cations

The adsorption of a noble metal with a preferred positive oxidation state induces a charge transfer from the cluster to the support, leading to the reduction of ceria on the surface. Negreiros and Fabris utilized DFT calculations to identify both stable and metastable morphologies of Pt_3 to Pt_6 clusters.[90] Their research revealed that the charge of the supported cluster, its interaction with the substrate, and the extent of ceria reduction are contingent on the metal/oxide interface area and the specific morphology of the cluster. They also discovered a notable energy preference for the Ce^{+III} ions induced by the cluster to be close to the cluster, either directly below it or near an interfacial atom. Interfacial effects in catalyzed CO oxidation by noble metals as Pd and Pt supported on ceria (111) catalysts arise from both geometric and electronic properties. Upon transition metal adsorption, electron transfer to the interfacial Ce^{+IV} cation occurs, leading to the formation of Ce^{+III} at the interface. Adsorbed O_2 at the dual sites promotes the generation of active O species essential for CO oxidation. In Figure 4.24 for Pd subnanometer clusters and 4.25 for Pt subnanometer clusters, the resulting Ce^{+III} ions on the ceria (111) surface are visualized. To investigate the dependence of charge transfer on the examined cluster shapes and sizes, as already introduced in Section 4.3.2 and depicted in Figure 4.20 for the Pd clusters and Figure 4.21 for the Pt clusters, we established according to Equation 4.4 a relationship

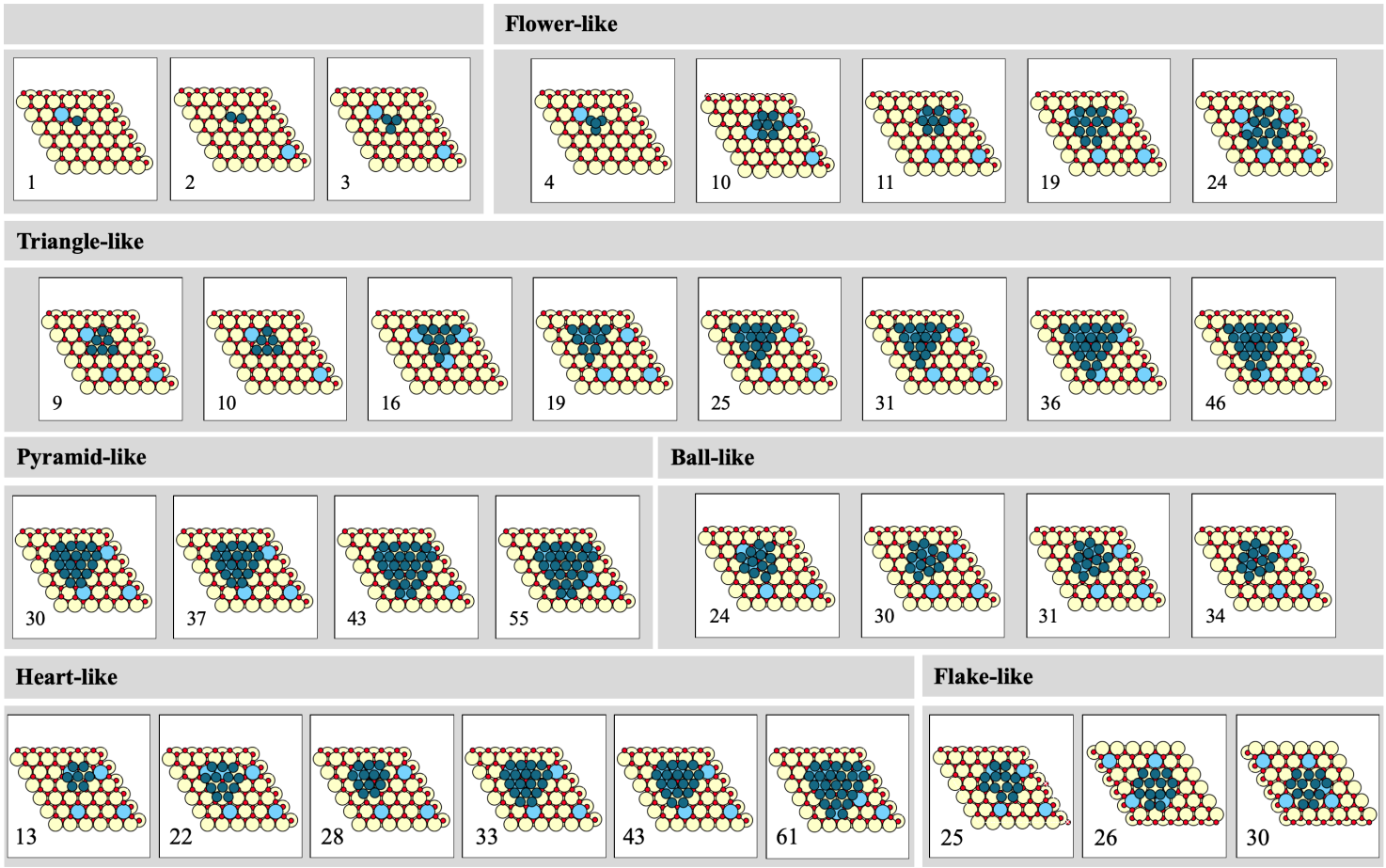

Figure 4.24.: Structure-optimized subnanometer clusters supported on the (111) surface of ceria, increasing in size from 1 atom to 61 atoms and categorized into shape classes. In this figure, the unit cell in the x and y directions is additionally highlighted, along with reduced Ce^{+III} ions. The subnanometer clusters are visually condensed to the interface layer, although the complete cluster structures have been optimized. These clusters correspond to those depicted in Figure 4.20. Red circles represent O, large yellow circles denote Ce atoms, petrol circles indicate Pd atoms, blue circles represent the reduced Ce^{+III} ions. The total energies are listed in the Appendix in Table A.9.

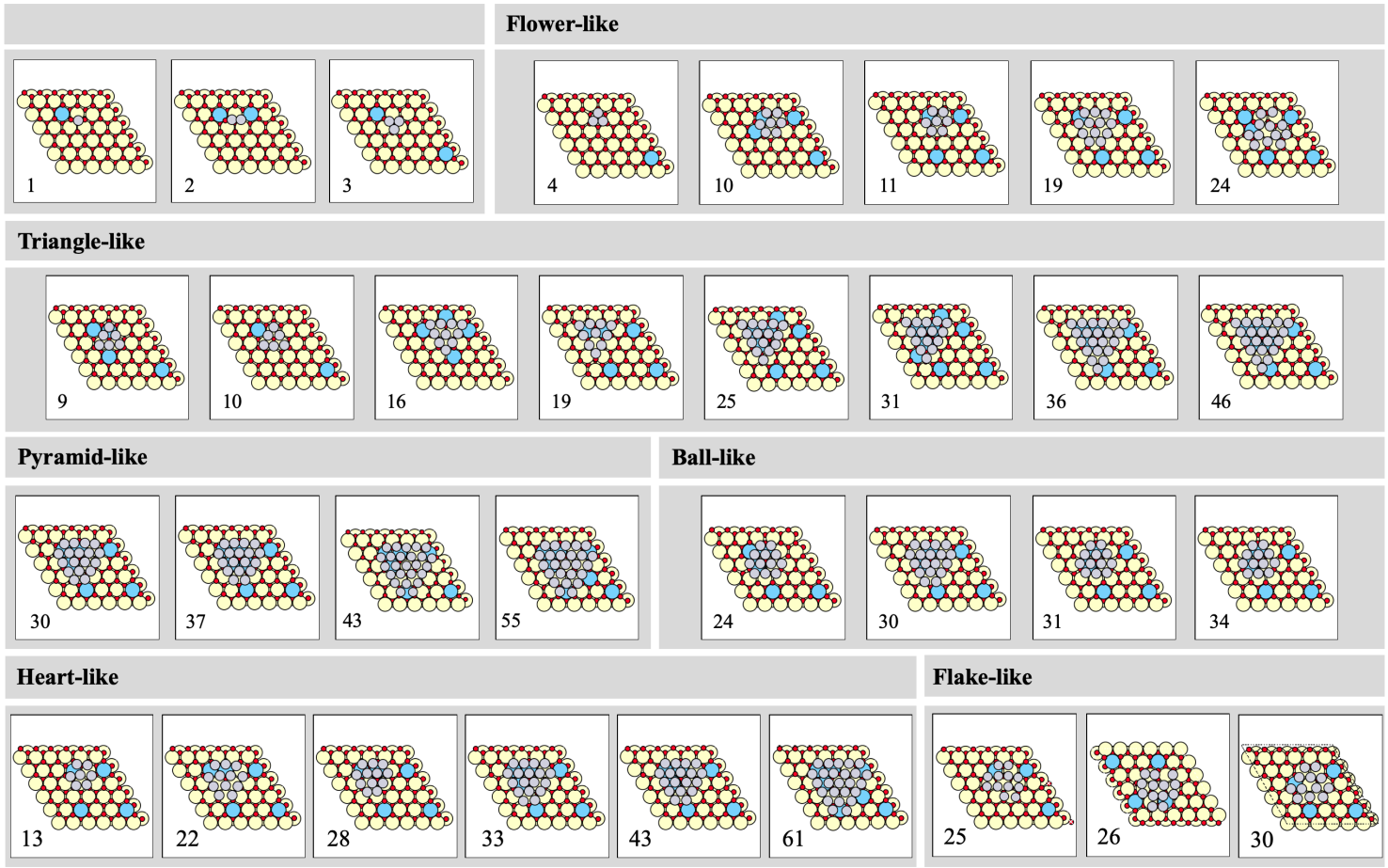

Figure 4.25.: Structure-optimized subnanometer clusters supported on the (111) surface of ceria, increasing in size from 1 atom to 61 atoms and categorized into shape classes. In this figure, the unit cell in the x and y directions is additionally highlighted, along with reduced Ce^{+III} ions. The subnanometer clusters are visually condensed to the interface layer, although the complete cluster structures have been optimized. These clusters correspond to those depicted in Figure 4.21. Red circles represent O, large yellow circles denote Ce atoms, gray circles indicate Pt atoms, blue circles represent the reduced Ce^{+III} ions. The total energies are listed in the Appendix in Table A.10.

between the reduced Ce^{+III} cations and the noble metal atoms of the clusters at the interface between the ceria (111) surface and the cluster. This quotient is formed by the number of formed Ce^{+III} cations per number of interface noble metal atoms $n_{interface}$ of the Pd or Pt clusters.

$$q_{chg} = \frac{n_{Ce^{+III}}}{n_{interface}} \tag{4.4}$$

Figure 4.26 illustrates the number of Ce^{+III} atoms generated by the interaction between the cluster and the ceria surface, plotted against the cluster size. This process demonstrates the electron donation of the noble metal to the ceria surface, leading to the reduction of Ce atoms from +IV to +III oxidation states. Figure 4.26 illustrates that as the cluster size

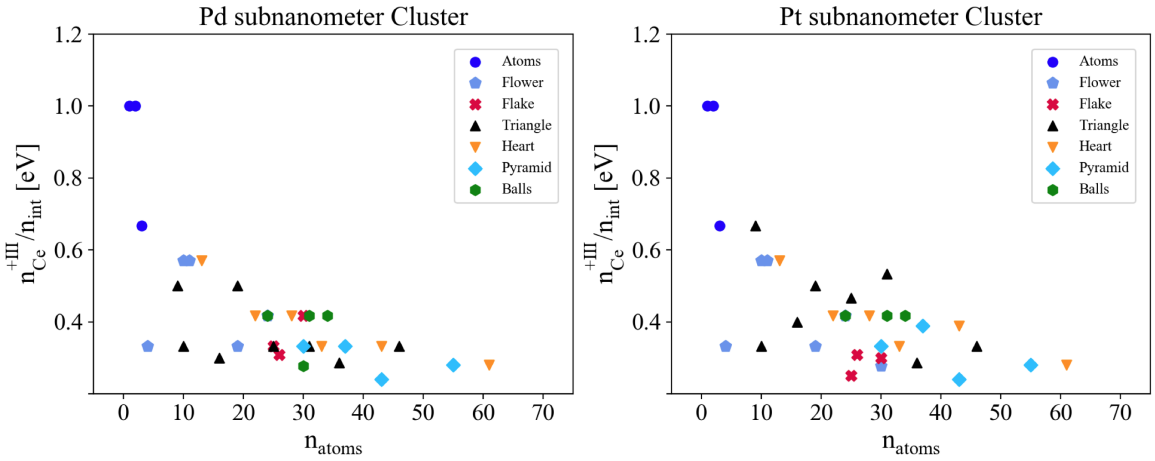

Figure 4.26.: The quotient formed by the number of formed Ce^{+III} cations per number of interface noble metal atoms q_{chg}, plotted against cluster size. The total energies are listed in the Appendix in Table A.9 for the Pd cluster and A.10 for the Pt cluster. The energies, the number of reduced Ce^{+III} cations, and the number of interface noble metal atoms are listed in the Appendix in Table A.9 for Pd and A.10 for Pt.

increases, the number of reduced Ce^{+III} ions also increases, and the quotient continuously decreases due to the simultaneous increase in the number of interface noble metal atoms. The Pd and Pt subnanometer clusters do not differ significantly from each other. A linear correlation cannot be observed, as the noble metal atoms on the interface do not increase linearly with size. This is because higher layers, starting from the second layer, do not facilitate the transfer of electrons from the clusters to the ceria surface. Therefore, only the first layer, which represents the interface between the noble metal cluster and the ceria surface, exhibits a charge transfer. Furthermore, it can be stated that the charge transfer of Pd and Pt within the applied DFT methods shows no differences in the choice of noble metal. However, the methodology further restricts the distribution of the localization of the reduced Ce^{+III} ions artificially. The positions of the reduced Ce^{+III} ions, as determined by the applied method, did not reach stable states through manual adjustments to their localization. These adjustments aimed to reduce the expected repulsion between the reduced Ce^{+III} cations and

the higher oxidized Ce^{+IV} ions. Efforts could be made manually to stabilize the system by either increasing the distance between the reduced cations with an oxidation state of +III to mitigate repulsive interactions or by finding a logical structure that could achieve symmetry based on the pattern of the ceria surface, thereby leading to a more stable state. It appears, as shown in Figure 4.24 for the Pd clusters and Figure 4.25 for the Pt clusters, that the positioning of the Ce^{+III} ions on the surface is influenced by both the limitations imposed by the size and shape of the unit cell and potentially by the historical context of the calculations. In earlier studies by Ganduglia-Pirovano,[80,82] it was shown that simulating a reduced oxidation state Ce^{+III} could be achieved by initially performing a brief single-point calculation with a substituted Ce atom replaced by a La atom. Subsequently, convergence at a lower level of theory would be attained, and the charge information files could then guide a full convergence at a higher level of theory using the GGA + U method, with the Ce atom re-substituted. This procedure alters the position of the Ce^{+III} ion. However, as our primary objective was to demonstrate the number of resulting Ce^{+III} ions rather than undertaking this time-consuming manipulation, likely, the positions of the Ce^{+III} ions obtained in our study may not correspond accurately to reality. For future investigations, it would be beneficial to explore alternative computational methods beyond the commonly used DFT approach to achieve a more relaxed distribution of Ce^{+III} ions within a reasonable timeframe. We recommend the development of alternative algorithms that take into account statistical distributions and physical parameters. Since experimental studies have already utilized the property of ceria to generate Ce^{+III} ions as a spectroscopic probing tool, gaining further insights into the formation and distribution of these ions is of paramount importance. Our DFT calculations provide initial insights into this matter, serving as a foundation for stimulating ideas based on the sizes and shapes of the clusters we have identified. Neyman et al. and others suggested that the strength of adsorption bonds depends on three key factors: the polarization of adsorbates at the surface in an electrostatic field, the overlap of d and O_2p orbitals of the metals, and Pauli repulsion resulting from filled electronic shells.[262–265] These contributions collectively determine the bonding strength in adsorption processes. In general, 5d-metal complexes exhibit the strongest binding, while their 4d-metal counterparts tend to form weaker bonds, with a few exceptions. This interplay of factors governs the strength of adsorption bonds on surfaces. In this study, these assumptions could be observed and confirmed.

4.3.6. Reducibility of the Ceria Surface at the Interface to the subnanometer Pd_{10} and Pt_{10} Cluster

Since the previous chapter examined the formation of reduced Ce^{+III} atoms induced by a charge transfer from the adsorbed clusters, considering the relaxation of only the top layer

of the ceria (111) facet, we will now conduct a more comprehensive study. In this study, we will represent the ceria surface using a supercell with 4 layers and will relax the top two layers. Given the possibility that the distribution of reduced Ce^{+III} ions on the ceria interface may extend into the sublayers, it is pertinent to consider relaxing the sublayers through structural optimizations. We use the smallest cluster that converges to the bulk phase of Pd and Pt as shown in Section 4.3.3, which is shown to be the Pd_{10} and Pt_{10} clusters in figure 4.22. As discussed in the Introduction in Section 1.3.1, the removal of O atoms on the ceria surface leads to a reduction of the surface Ce^{+IV} ions to the oxidation state Ce^{+III}. In this chapter, we investigate the reducibility of the ceria surface and along the interface of the Pd_{10} and Pt_{10} clusters, both in the nearest neighbor position to the cluster, as depicted in Figure 4.28 for the Pd clusters and Figure 4.29 for the Pt clusters, and in the sublayer nearest neighbor position to the cluster as depicted in Figure 4.30 for the Pd clusters and Figure 4.31 for the Pt clusters. The O atom being removed is analogous to those in the structures we considered in Section 4.2.3. It is located similarly to the O layer we examined there, in the second layer toward the bulk phase of the ceria surface. For direct comparability of the reducibility of the ceria surface depending on the noble metal adsorbed and its positioning relative to the noble metals, we ensure that the successive removal of O atoms occurs directly at the interface of the Pd_{10} and Pt_{10} clusters and the ceria surface. However, initially, we remove the O atoms from the plain ceria surface as shown in Figure

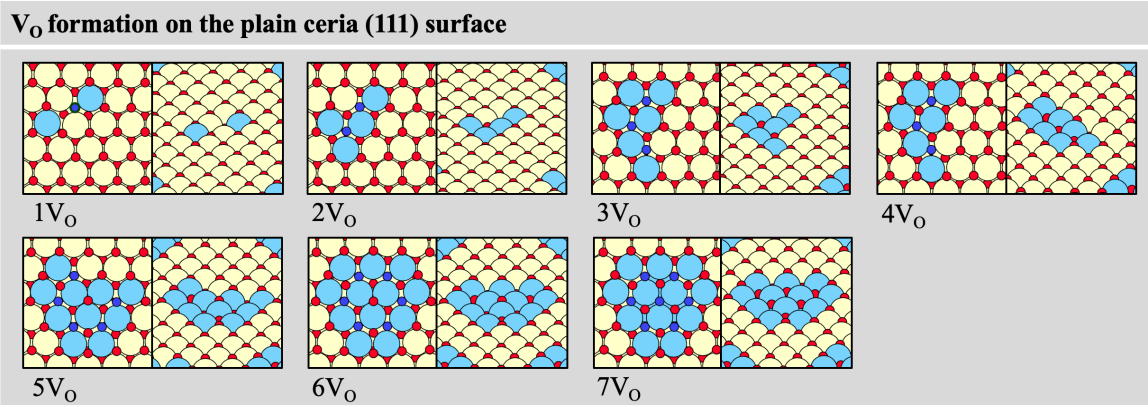

Figure 4.27.: Structure-optimized configurations of successive O defect formation (1-7)V_O atoms on the ceria surface at the interface to the subnanometer Pd_{10} and Pt_{10} cluster in eV and at 0 K. Red circles represent O, yellow circles Ce, dark blue circles V_O defects, and sky blue circles reduced Ce^{+III} ions. The total energies are listed in the Appendix in Table A.11.

4.27, which can serve as a reference to evaluate the influence of the noble metals on the reducibility. By counting the formed reduced Ce^{+III} ions, it can be inferred from Figure 4.27 on the extended ceria (111) surface that for each created O lattice defect V_O, two reduced Ce^{+III} ions are formed. An exception is observed with the removal of the seventh O atom, positioned in the middle of the other six O atoms; in this case, three reduced Ce ions Ce^{+III}

are generated. This anomaly may be attributed to an electronic effect stemming from the subnanometer cluster, as the noble metal atoms of the second layer are concentrated above this position. As we also allow a side view of the ceria (111) surface, it is evident that the crystal structure undergoes slight changes, with the reduced Ce^{+III} atoms highlighted on the surface and O atoms migrating from the sub-layers to the surface to stabilize the crystal structure. This raises the question of whether the localized removal of several O atoms in one area of the ceria surface leads to a transition from the CeO_2 crystal structure to the CeO structure. This topic was discussed in the Introduction in Section 1.3.1 based on existing literature and illustrated in Figure 1.4. In the CeO crystal structure, O ions arrange linearly with the Ce ions, with angles of 90°and evenly distributed distances typical of a cubic crystal structure.[266] The structurally optimized reduced ceria surface here demonstrates a tendency to transition to the CeO crystal structure as reduction becomes predominant. In

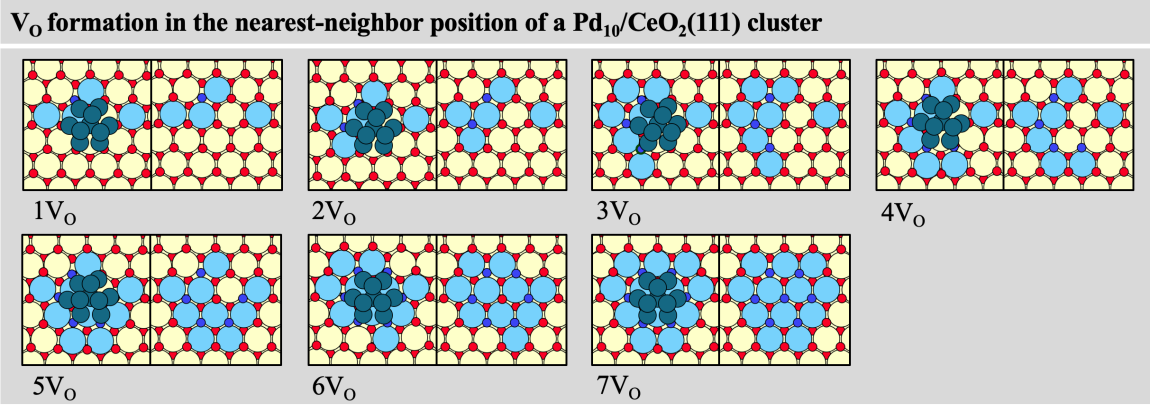

Figure 4.28.: Structure-optimized configurations of a Pd_{10} subnanometer cluster adsorbed onto successive O defect formation (1-7)V_O atoms in the nearest neighbor position to the cluster in eV and at 0 K. Red circles represent O atoms, large yellow circles Ce atoms, petrol circles Pd atoms, dark blue circles V_O defects, and sky blue circles reduced Ce^{+III} ions. The total energies are listed in the Appendix in Table A.11.

Figures 4.28 and 4.29, we depict O surface defects positioned in the nearest neighbor to the adsorbed noble metal clusters, which induce a reduction of the ceria surface by forming two reduced Ce^{+III} ions. The Pt_{10} clusters did not receive sufficient anchoring on an increasing V_O defect ceria surface for $3V_O$ and $5V_O$ defects, resulting in a significant configuration change of the cluster structure. Therefore, they are not utilized in this study as the systematic relation to the other structures has been lost. However, a statement that can be made here is that the Pt-Pt binding strength appears to be stronger than the Pd-Pd binding strength, leading to a preference for Pt_{10} to contract itself to a hemisphere towards lower surface enthalpy. As can bee seen in, each O desorption does not invariably yield two reduced Ce^{+III} ions, resulting in an irregular increase in their count with increasing O removal. From the observed data, no precise regularity can be deduced. Bruix et al. found in a first-principle investigation of a Pt_8 cluster supported on a (111) ceria surface that the analysis of the

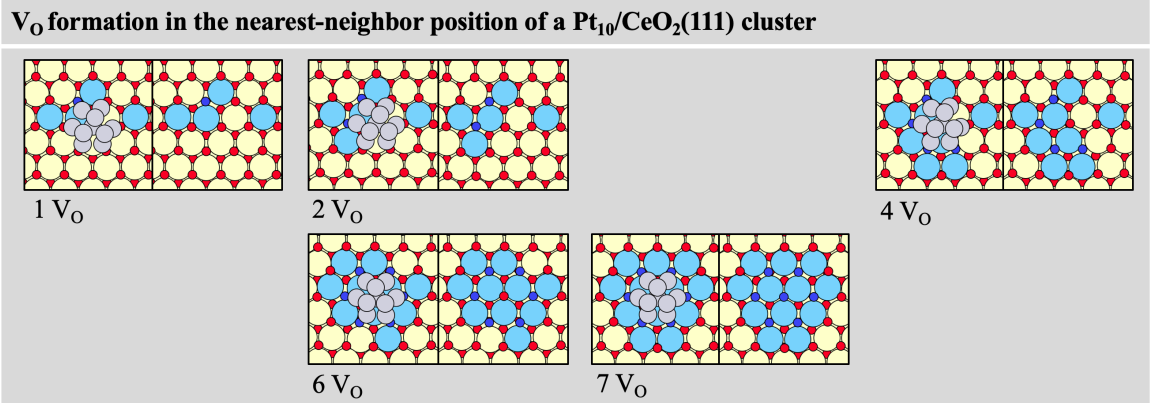

Figure 4.29.: Structure-optimized configurations of a Pt_{10} subnanometer cluster adsorbed onto successive O defect formation (1-7)V_O atoms in the nearest neighbor position to the cluster in eV and at 0 K. Red circles represent O, yellow circles Ce, gray circles indicate Pt atoms, dark blue circles V_O defects, and sky blue circles reduced Ce^{+III} ions. The total energies are listed in the Appendix in Table A.11.

electronic structure reveals the formation of only three Ce^{+III} cations.[267] They demonstrated that the removal of O reduces the formal charge of the supported metal particle from +II to formally +I. Thus, the interaction of a Pt subnanometer subnanometer cluster with an V_O defect site on the ceria (111) surface also leads to an oxidation of the Pt cluster, although less pronounced than for the interaction with the oxidized surface. This indicates that the reduction of the ceria surface in our work may not be linear, as a Pd or Pt subnanometer cluster participates in charge transfer. This explains the irregularity that we can observe here. The resulting reduced Ce^{+III} ions consistently emerge on the surface through the removal of surface O atoms, with no instances observed in the sublayers. The configuration of the noble metal clusters remained surprisingly stable, even though the anchoring O atoms were removed from the surface. In Figure 4.30 for Pd and Figure 4.31 for Pt, we illustrate the

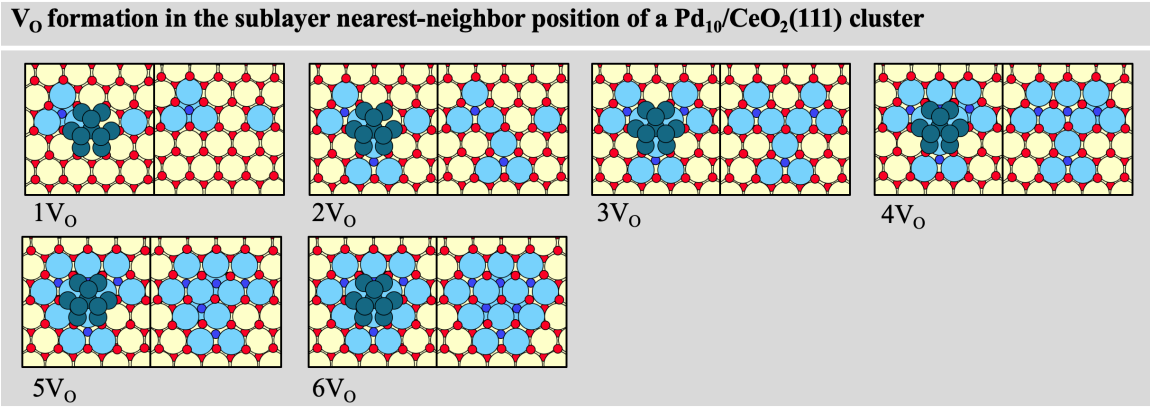

Figure 4.30.: Structure-optimized configurations of a Pd_{10} subnanometer cluster adsorbed onto successive O defect formation (1-7)V_O atoms in the sublayer nearest neighbor position to the cluster in eV and at 0 K. Red circles represent O, yellow circles Ce, petrol circles Pd atoms, dark blue circles V_O defects, and sky blue circles reduced Ce^{+III} ions. The total energies are listed in the Appendix in Table A.11.

reduction of O atoms in the sublayer nearest neighbor positions. The removed O atoms are

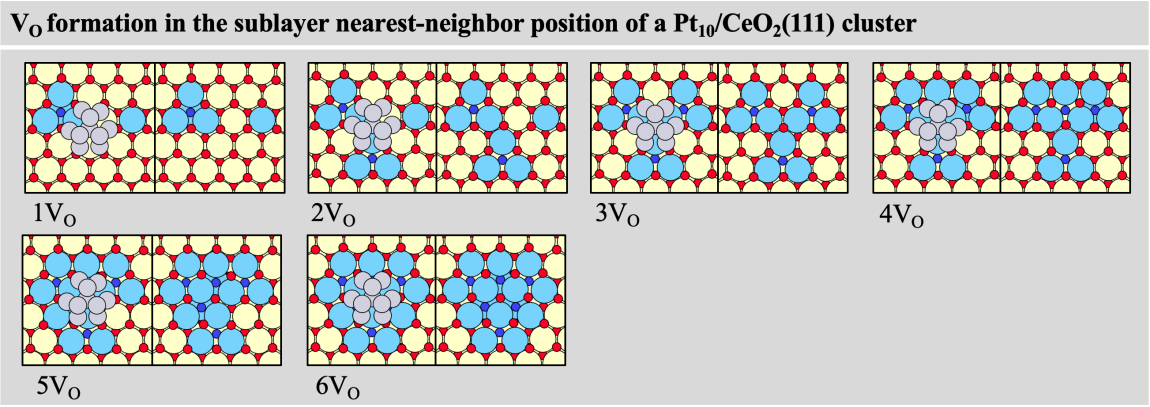

Figure 4.31.: Structure-optimized configurations of a Pt_{10} subnanometer cluster adsorbed onto successive O defect formation (1-7)V_O atoms in the sublayer nearest neighbor position to the cluster in eV and at 0 K. Red circles represent O, yellow circles Ce, petrol circles Pt atoms, dark blue circles V_O defects, and sky blue circles reduced Ce^{+III} ions. The total energies are listed in the Appendix in Table A.11.

positioned as close as possible to the cluster. The resulting removal of all selected O atoms exhibits a triangular positioning relative to each other, rather than the flower-like shape of the adsorbed noble metal clusters. This provides insight into the configuration of the O layer of the ceria surface, which directly interacts with the adsorbed cluster. However, no further interpretation can be made at this point. After the removal of all O atoms, the positioning of all resulting reduced Ce^{+III} ions adopts the same configuration as the previous reduced pure ceria surface and the removal of all nearest neighbor O atoms at the interface with the adsorbed cluster. As in this case, the directly anchoring O atoms were not affected by the removal, the Pd and Pt clusters remained unchanged in their configuration due to the reduction. To evaluate the reducibility of the ceria (111) surface concerning the chemical environment and the position of removed O atoms, the desorption energy ΔG_{des} is computed using Formula 4.5. ΔG_{des} of O atoms is plotted against the number of O atoms removed in Figure 4.32. ΔG_{des} is calculated for a reaction temperature of 423.15 K and were averaged over the number n of desorbed O atoms V_{nO}. The temperature of 423.15 K is accounted by the use of *ab initio* thermodynamics, including the contributions of ZPE and entropy, as discussed in Section 3.7.

$$\Delta G_{des} = \frac{(E_{total}(V_{nO} - species) + nE_{total}(\frac{1}{2}O_2)) - E_{total}(species)}{n} \tag{4.5}$$

$E_{total}(V_{nO}\text{-species})$ represents the calculated total energy of the considered species on the $CeO_2(111)$ surface by the use of DFT methods. This can occur without an adsorbed noble metal cluster on the pure ceria surface (V_{nO}-$CeO_2(111)$), or with an adsorbed noble metal subnanometer cluster (Pd_{10} or Pt_{10}) on the ceria surface (V_{nO}-$Pd_{10}/CeO_2(111)$ for

a Pd cluster or V_{nO}-Pt_{10}/CeO_2(111) for a Pt cluster). The indices (nn) and (sub) denote desorption in the nearest neighbor position to the subnanometer cluster or in the nearest neighbor sub-position to the subnanometer cluster, respectively. Plotting the desorption

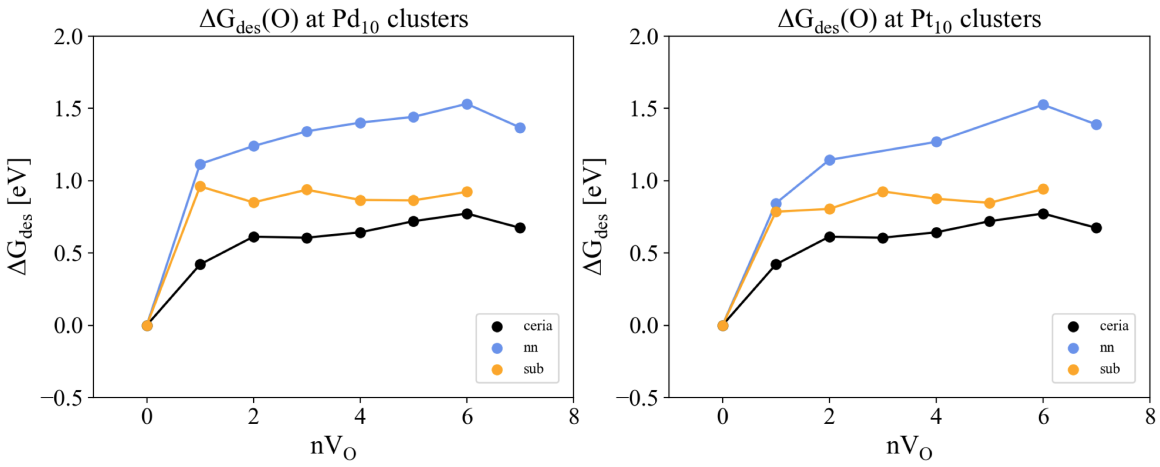

Figure 4.32.: Desorption energies ΔG_{des} of successive formation of O lattice vacancies V_O in the interface of the cluster and the ceria surface (blue), in the sub-layer close to the cluster (orange) as well as the plain ceria surface (black) on the same positions. The desorption energies ΔG_{des} are listed in the Appendix in Table A.11.

energies of individual O atoms in Figure 4.32 reveals that, on average, these energies are 0.14 eV lower for the pure ceria (111) surface compared to those of O atoms in the sublayer, and 0.71 eV lower than those in the nearest neighbor position. This indicates that the desorption energies of an O atom at the interface with a subnanometer cluster on a ceria (111) surface are endothermic, especially when directly coordinated with noble metal atoms. However, even in the sublayer without direct coordination with noble metal atoms, this effect significantly impacts desorption energies. Thus, the noble metal cluster has an electronic effect on its immediate surroundings. In summary, in both cases of O removal on the extended ceria surface and in the nearest neighbor position to an adsorbed subnanometer cluster, it is observed that the reduction of sublayer Ce ions occurs only in the final stages of removing the last O atom, which is centrally located on the already quite reduced surface. However, this is not the case during O removal in the sublayer nearest neighbor position close to the adsorbed subnanometer cluster, as reduction occurs in the sublayer as well, induced by the presence of the V_O defect. This suggests that reduction is preferentially localized close to the V_O defect in the case of the used DFT methods. This result contradicts the findings of Ganduglia et al. as discussed in the Introduction in Section 1.3.1, who determined that the next nearest neighbor positions to the V_O defects are preferred. Additionally, the literature suggests that the distribution of the reduced Ce^{+III} ions is primarily on the surface. As mentioned earlier, the determination of the positions of the reduced Ce^{+III} ions by the DFT method used is not reliable enough to make a definitive

statement. It is strongly recommended in this work to develop or refine post-DFT methods to realistically simulate the distribution of the reduced Ce^{+III} ions.

5. Spectroscopy Analysis of varying Pd and Pt Active Site Sizes supported on Ceria

5.1. Correlation of Oxidation State and CO stretching Vibrational Frequency on Pd_1 and Pt_1 Species

The adsorption of a noble metal onto the ceria surface induces a charge transfer from the noble metal to the ceria surface.[80] This phenomenon has been extensively studied in the literature, as mentioned in the Introduction in Section 1.3. Pt and Pd can have the formal oxidation states of 0, +II, and +IV, representing the number of electron losses due to charge transfer from adsorbed O atoms which have an oxidation state of -II per O atom. In a bulk phase within a Pd or Pt crystal, they exhibit a formal oxidation state of 0, while the crystals of the oxides PdO and PtO have a +II oxidation state, and +IV for PdO_2 and PtO_2 oxides have a +IV oxidation state. In this Section, we focus on the oxidation states of the single-atom catalysts. When considering reduction and oxidation by varying the number of adsorbed O atoms in the vicinity, a formal oxidation state is assigned to the noble metal atom instead of the ceria surface. However, it is known that the cerium atoms on the surface undergo reduction due to the adsorption of the noble metal atom, as the charge transfer from the noble metal promotes oxidation of the noble metal and reduction of the cerium atoms. Therefore, it can be assumed that no formal integer electron charges are present, but rather partial oxidation states. The charge transfer can be calculated using Bader analysis[134] on the electron density distribution between the accounted atoms, yielding Bader charges that reflect the partial oxidation state of the single-atom catalysts. In addition to the oxidation state, the CO vibration frequency can serve as a characteristic parameter for single-atom catalysts, as the harmonic oscillation of a CO molecule is narrow and thus isolated from its chemical environment. We aimed to adsorb CO molecules as linearly as possible on the single-atom catalysts, avoiding coordination with neighboring O and Ce atoms. By comparison of the structures of the single-atom catalysts in Figure 4.5 for Pd and 4.6 for Pt without the CO molecule adsorbed and Figure 5.1 for Pd and 5.2 for Pt with the CO molecule adsorbed, it can be seen that the single-atom catalyst can undergo structure configuration changes by the adsorption of the CO molecule. However, this rearrangement was only permitted for the (110) surface in the case of two adsorbed

O atoms $2O^*$. For the (111) surface, we adopted a structure in which the square planar arrangement of the Pd or Pt atoms is facilitated by anchoring with four O atoms, analogous to that of the (100) surface. This allowed us to ensure a continuous increase in the oxidation state with the exception of one case on the (111) surface, enabling systematic analysis through correlations of the physical parameters for forthcoming investigations. Upon

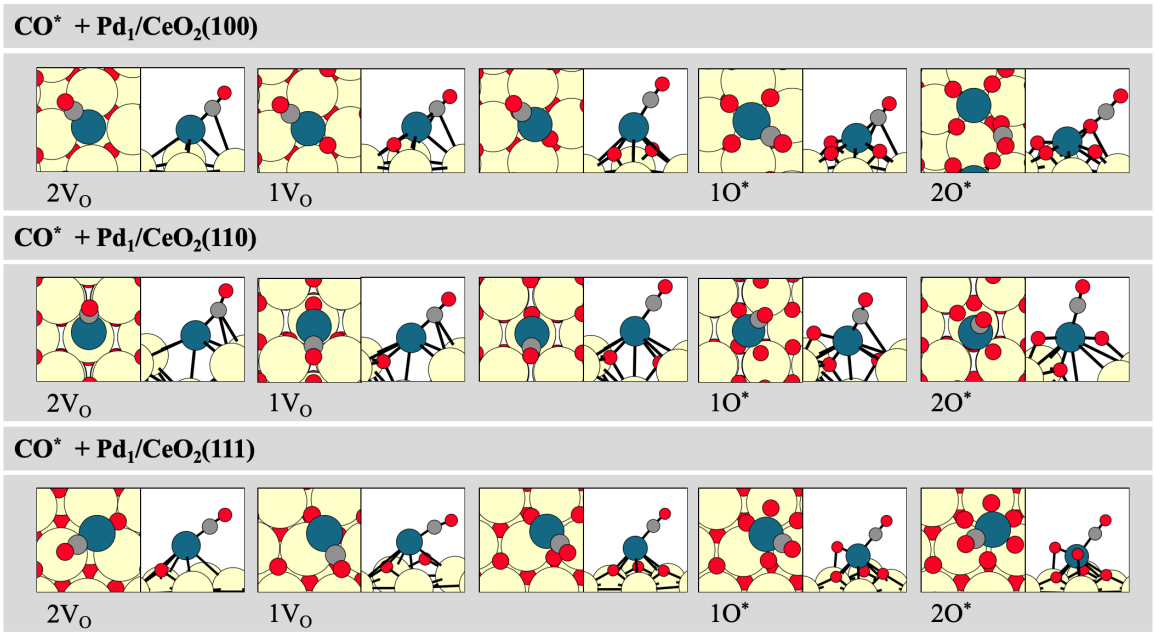

Figure 5.1.: Ceria surface facets with varying O adsorption and defect formation at the vicinity of a Pd_1 single-atom catalyst. From left to right: two $2V_O$ defects, one $1V_O$ defect, the stoichiometric surface, one $1O^*$ adsorption, two $2O^*$ adsorption. From top to bottom: the (100), the (110), and the (111) surface facets of ceria. Red circles represent O atoms, large yellow circles Ce atoms, dark gray circles C atoms, and petrol circles Pd atoms. The total energies are listed in the Appendix in Table A.15.

plotting the CO vibration frequency against the partial oxidation states determined via Bader analysis, we observed a scattering of vibration frequencies towards lower frequencies, indicating higher coordination of the CO molecules. Consequently, we chose to use the partial oxidation states of the noble metal atoms before CO adsorption as one descriptor and the vibration frequencies after CO adsorption as the second descriptor. As illustrated in Figure 5.3, a scaling relation was observed through the linear correlation between the vibration frequencies and the partial oxidation states of the noble metal atoms. According to a review conducted by Shenjun et al., the described selection of descriptors may have led to a linear scaling relation or potentially a broken scaling relation, as explained in the introduction in Section 1.5.[163] In the case of an O reduction with two $2V_O$ surface defects, the correlation partially deviates from a linear scaling relation, resulting in higher vibrational modes for the CO stretching vibration than a linear correlation would anticipate. It is possible to consider a minimum in the case of a single $1V_O$ surface defect or on the

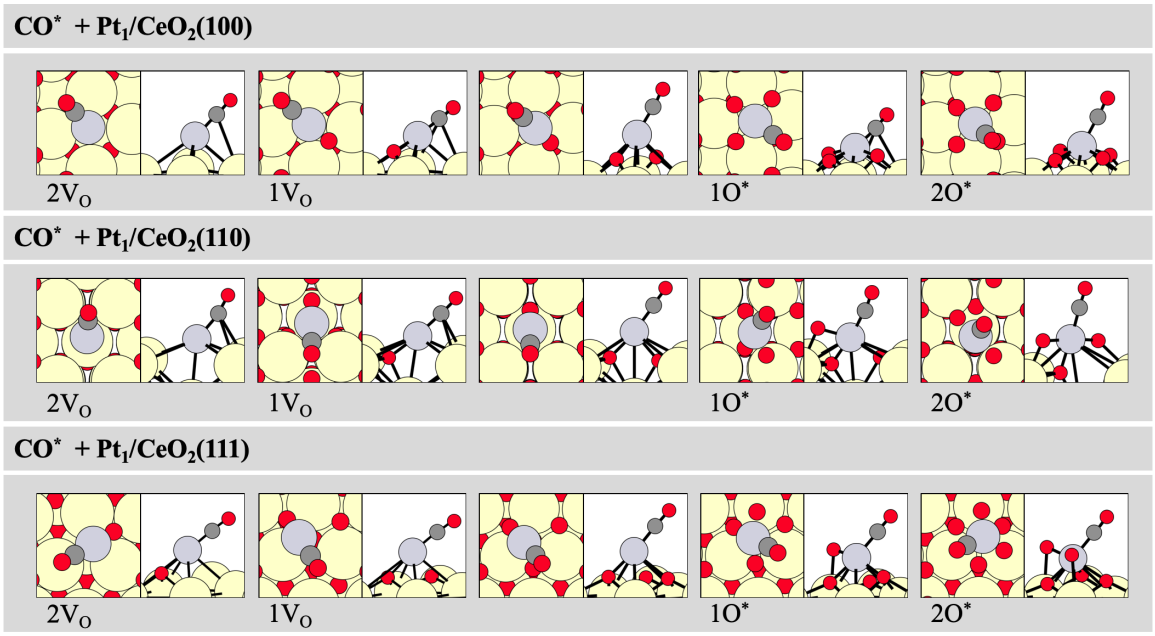

Figure 5.2.: Ceria surface facets with varying O adsorption and defect formation at the vicinity of a Pt_1 single-atom catalyst and an adsorbed CO molecule. From left to right: two $2V_O$ defects, one $1V_O$ defect, the stoichiometric surface, one $1O^*$ adsorption, two $2O^*$ adsorption. From top to bottom: the (100), the (110), and the (111) surface facets of ceria. Red circles represent O atoms, large yellow circles Ce atoms, dark gray circles C atoms, and gray circles Pt atoms. The total energies are listed in the Appendix in Table A.15.

stoichiometric ceria surface. In order to obtain such a scaling relation, consistent reduction or oxidation of the single-atom catalysts in the direct vicinity of the Pd and Pt atoms was ensured. The mean absolute error (MAE) values of 0.26 for the Pd single-atom catalyst and 0.30 for Pt represent the average deviation between the predicted and actual CO vibrational frequencies across the three ceria surfaces. The vibrational frequencies are denoted as wavenumbers in spectroscopy and are measured in cm^{-1}. They are denoted as $\tilde{\nu}$ in the Tables. These values are within the expected range given the complexity of the system being studied. Regarding the coefficient of determination R^2 with a value of 0.75 for Pd and 0.72 for Pt indicates that approximately 75% and 72%, respectively, of the variability in CO vibrational frequencies can be accounted for by changes in the Bader charge. The patterns refer to the systematic changes or trends observed in the CO vibrational frequencies in response to variations in the Bader charge. These may include shifts in vibrational modes, changes in bond strengths, or alterations in molecular interactions, all of which are reflected in the measured frequencies. Additionally, we have plotted the adsorption energies of the CO molecule against the vibrational frequencies in Figure 5.5. Here, a direct correlation between the adsorption energy and the vibrational frequencies is also noticeable. However, we observe a greater deviation here with an increased MAE of 0.39 for Pd and 0.72 for Pt single-atom catalysts. The proportion of variability R^2 in CO vibrational frequencies

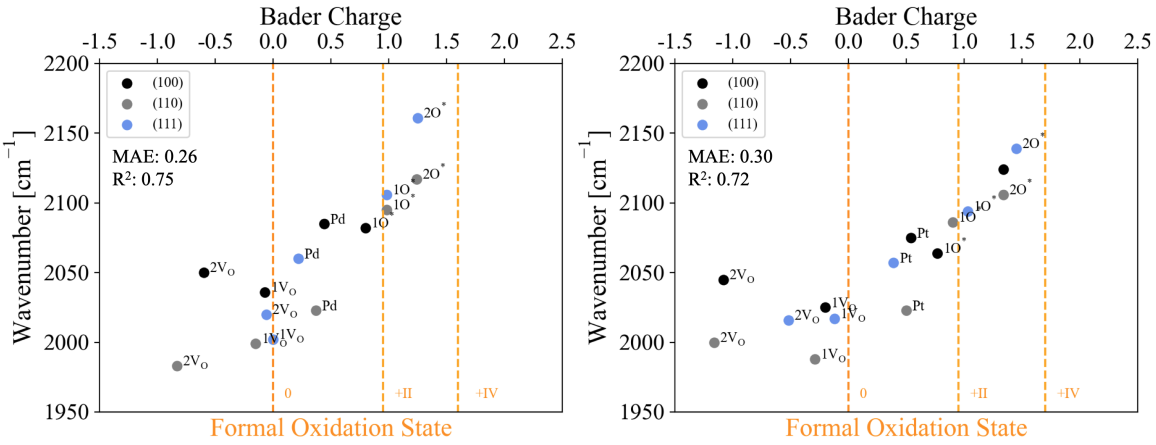

Figure 5.3.: The correlation between CO vibrational frequencies in cm^{-1} and Bader charge for Pd (left) and Pt (right) single-atom catalysts depicted in a scaling relation diagram. Additionally, the calculated Bader charges of the noble metals in the bulk phase, with 0 representing a noble metal crystal, +II for PdO and PtO oxides, and +IV for PdO_2 and PtO_2 oxides, are depicted as dashed orange lines along the x-axis. These correspond to their formal oxidation states. The noble metal atoms Pd and Pt are adsorbed on the surface facets (100) (black), (110) (gray), and (111) (blue). The oxidation state ranges from two $2V_O$ defects, one $1V_O$ defect, stoichiometric surface denoted with Pd or Pt, one O atom adsorbed $1O^*$, and two O atoms adsorbed $2O^*$. The vibrational frequencies and the Bader charges are listed in Table 5.1, the total energies and the Bader analysis in Table A.15 in the Appendix.

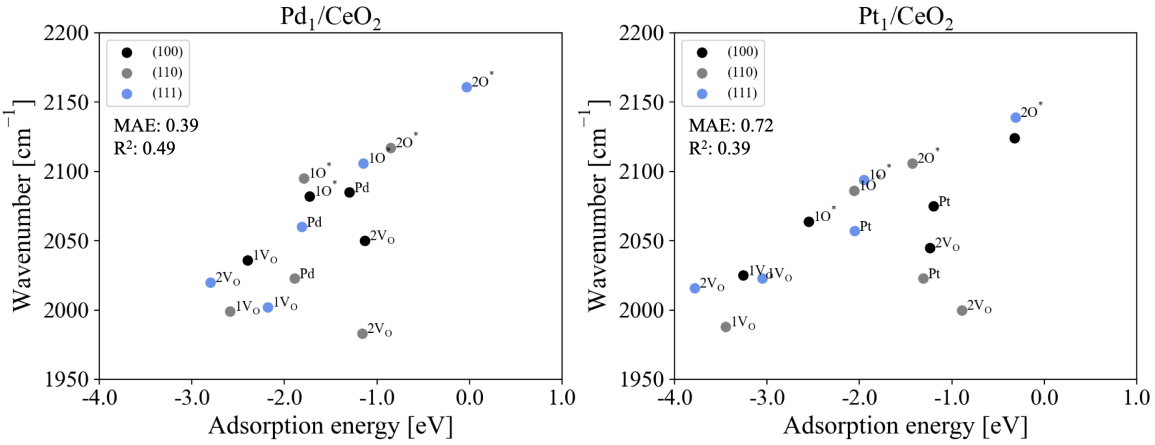

Figure 5.4.: The correlation between CO adsorption energies in eV at 0 K and vibrational frequencies denoted as wavenumbers in cm^{-1} for Pd (left) and Pt (right) single-atom catalysts depicted in a scaling relation diagram. The noble metal atoms Pd and Pt are adsorbed on the surface facets (100) (black), (110) (gray), and (111) (blue). The oxidation state ranges from two $2V_O$ defects, one $1V_O$ defect, stoichiometric surface denoted with Pd or Pt, one $1O^*$ adsorbed, and two $2O^*$ adsorbed. The vibrational frequencies are listed in Table 5.1, and the CO adsorption energies are listed in the Appendix in Table A.15.

is smaller, with values of 0.49 and 0.39. This suggests that only about half of the data points can be attributed to a correlation. This may be because the adsorption energies in this case do not represent broken scaling relations. Therefore, a higher scattering of vibrational frequencies towards lower frequencies is observed, likely due to additional coordination of the CO molecule to the chemical environment of the single-atom catalysts, such as

coordination with cerium ions. It is conceivable that single-point calculations, where the CO molecules are removed but the potential energy of the structure is calculated without structure optimization, could yield only the adsorption energy without capturing additional configuration changes induced by CO molecule adsorption. We opted not to pursue this method because the correlation and the observed scattering are readily apparent and can be explained. Further evaluation of the spectroscopic data can be performed through the

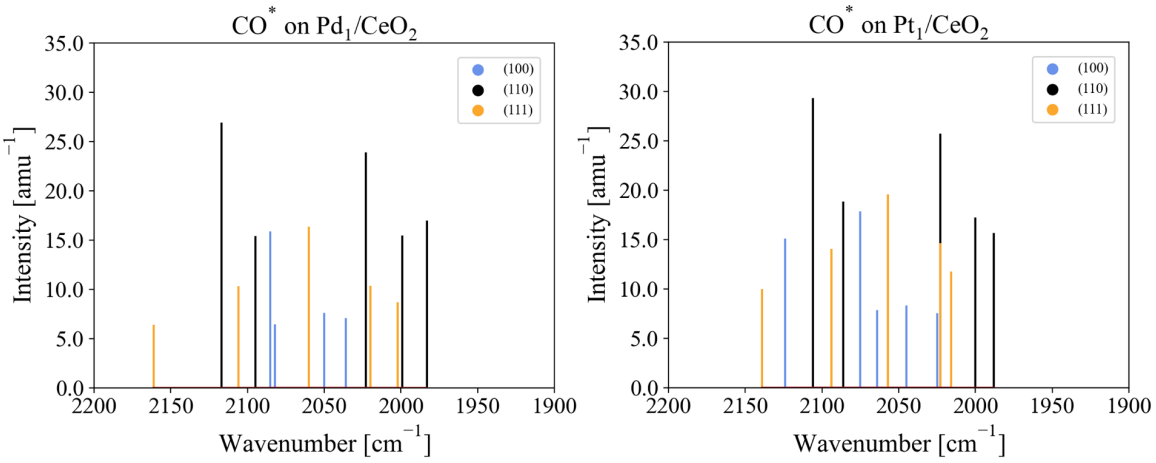

Figure 5.5.: Plot of the intensities in amu^{-1} of CO vibrational frequencies denoted as wavenumbers in cm^{-1}. Pd single-atom catalysts (left) and Pt single-atom catalysts (right) are plotted. The noble metal atoms are adsorbed on the (100) surface facet (blue), (110) surface facet (black), and (111) surface facet (orange). All oxidation states ranging from two $2V_O$ defects, one $1V_O$ defect, stoichiometric surface, one $1O^*$ adsorbed, and two $2O^*$ adsorbed are included. The vibrational frequencies and the according intensities are listed in Table 5.1.

calculated intensities of the CO vibrational frequencies. By visualizing them in a plot, as shown in Figure 5.5, the vibrational frequencies relative to each other can be examined more closely. Here, they have been categorized according to the surface facets of ceria. While the overall trends are subtle, some observations can still be made. The vibrational frequencies of CO molecules adsorbed on a noble metal atom Pd or Pt on the (100) surface are found in a narrower spectrum. Those on the (110) surface tend towards lower frequencies, while those on the (111) surface tend towards higher ones. A more precise explanation can be attributed to the coordination. On a dense surface like (111), additional coordination of the CO molecule is minimal, and the CO molecule tends to adsorb linearly on the surface. In contrast, the (110) surface, with its surface structure formed by staggered cerium rows, presents several possibilities for additional coordination. The (100) surface, on the other hand, offers only selected adsorption sites due to its characteristic "pocket" structure. General trends can be observed through a closer examination of the vibrational frequencies under a dependence on the oxidation states, as listed in Table 5.1. Around 2110-2120 cm^{-1}, the oxidation states of +IV resulting from the adsorption of two O atoms in the vicinity of

Table 5.1.: Spectroscopic data obtained through DFT calculations. The species under investigation here refer to the structures of single-atom catalysts given in 4.5 for Pd and 4.6 for Pt, each possessing different oxidation states. The stretching vibrations of the CO molecule and their corresponding intensities were determined based on dipole moments. Additionally, a Bader charge (B.C.) analysis was conducted. The oxidation states, denoted here by superscripts 0, +II, and +IV, refer to the formal oxidation states resulting from the counting of electrons involved in bonding with O atoms.

	B.C.	$\tilde{\nu}$[cm^{-1}]	I [amu^{-1}]		B.C.	$\tilde{\nu}$[cm^{-1}]	I [amu^{-1}]
Spectroscopic data of CO adsorbed on of Pd_1 and Pt_1							
$Pd_1CeO_2(100)$				$Pt_1CeO_2(100)$			
$2V_O$	-0.60	2050	7.61	$2V_O$	-1.08	2045	8.35
$1V_O$	-0.07	2036	7.07	$1V_O$	-0.20	2025	7.54
Pd^O	0.44	2085	15.89	Pd^O	0.54	2075	17.87
$Pd^{+II}O$	0.80	2082	6.44	$Pd^{+II}O$	0.77	2064	7.89
$Pd^{+IV}O_2$	1.18	-	-	$Pd^{+IV}O_2$	1.34	2124	15.11
$Pd_1CeO_2(110)$				$Pt_1CeO_2(110)$			
$2V_O$	-0.83	1983	16.97	$2V_O$	-1.16	2000	17.26
$1V_O$	-0.15	1999	15.46	$1V_O$	-0.29	1988	15.68
Pd^O	0.37	2023	23.91	Pd^O	0.50	2023	25.72
$Pd^{+II}O$	0.98	2095	15.44	$Pd^{+II}O$	0.90	2086	18.85
$Pd^{+IV}O_2$	1.24	2117	26.94	$Pd^{+IV}O_2$	1.34	2106	29.30
$Pd_1CeO_2(111)$				$Pt_1CeO_2(111)$			
$2V_O$	-0.06	2020	10.35	$2V_O$	-0.52	2016	11.77
$1V_O$	0.00	2002	8.69	$1V_O$	-0.12	2023	14.65
Pd^O	0.22	2060	16.35	Pd^O	0.39	2057	19.57
$Pd^{+II}O$	0.98	2106	10.33	$Pd^{+II}O$	1.03	2094	14.05
$Pd^{+IV}O_2$	1.25	2161	6.39	$Pd^{+IV}O_2$	1.45	2139	10.00

the single-atom catalysts can be identified. Similarly, frequencies around 2080-2090 cm^{-1} correspond to oxidation states of +II caused by the adsorption of one O atom, while those in the range of 2050-2070 cm^{-1} are associated with oxidation states of 0. The spectroscopic data obtained aligns with previous experimental and theoretical studies on single-atom noble metals supported on ceria, as will be discussed in Section 5.2, which is the next Section. The stabilization of surface facets and its correlation with activity could serve as a reference in future experimental measurements. The bond strength resulting from CO adsorption in single-atom catalysts is reflected in individual stretching vibrational frequencies.

5.2. Validation of the Structures of Pd_1 and Pt_1 Species by Collaboration with Experimentalists

The in-situ spectroscopic investigations by Sarma et al. were conducted under CO and CO + O_2 reaction conditions, employing continuous gas flows.[268] The objective was to comprehend the binding of CO to catalysts synthesized through wet impregnation and precipitation

methods. The examination of catalysts utilizing DRIFTS spectroscopy offers the opportunity to explore both the charged states and their associated coordination environments. Here, isolated supported noble metals and CO adsorption are considered as the probing molecule. CO exhibits strong reducing properties on the catalyst, prompting an investigation into how the local structure of the isolated active sites undergoes structural and electronic alterations upon CO adsorption. To unravel these dynamics, they conducted a series of *in-situ* XAS and DRIFTS experiments in reducing conditions (1% CO) and oxidizing environments (1% CO + 1% O_2) at room temperature over a time of 1 hour. The temporal evolution of various species in the DRIFTS spectra for the Pd and Pt single-atom catalysts was extracted from the literature[268] and reconstructed for visualization. Figure 5.6 illustrates the spectra under reaction conditions with only CO in the atmosphere, while Figure 5.7 shows the spectra with both CO and O_2 present in the atmosphere. The vibrational spectra we calculated in this work are listed in Table 5.1. It can be observed that the given vibrations in the DRIFTS spectra exhibit analogous vibrations as discussed in the collaborative work with experimental data. The collaboration between experimentalists and our first principles investigations provided crucial insights into CO adsorption behaviors on various Pd and Pt sites. However, caution is warranted as the size of the noble metal significantly influences

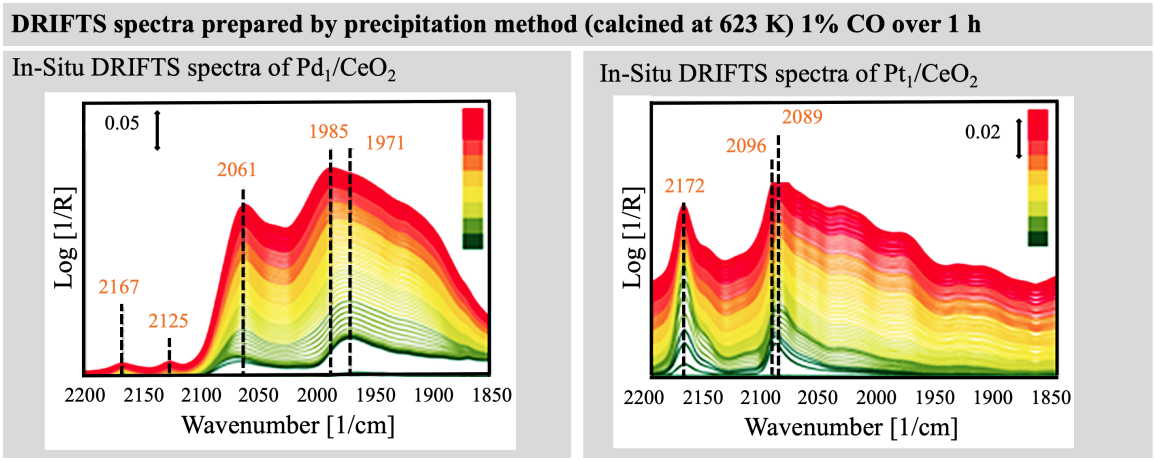

Figure 5.6.: DRIFTS spectra derived from Sarma et al. of Pd (left) and Pt (right) noble metals supported on ceria and calcined at 623 K depict CO adsorption at room temperature over catalysts prepared via the precipitation (PP) method. The spectra showcase the evolution of species over time in DRIFTS spectra for Pd and Pt under a reaction environment with CO in the gas phase. The color bar in the Figure denotes spectra collected over 1 hour. The time increases from green to red. Reprinted and adapted with permission from[268] ©2024 American Chemical Society.

the vibrational spectra. In the case of single-atom catalysts, species can be assigned based on Table 5.1. The frequencies at 1985 and 1971 cm^{-1} for the Pd catalysts and 2089 cm^{-1} for the Pt catalysts cannot be assigned to either the pristine noble metal surfaces in Table 5.32 in Section 5.6 or the single-atom catalysts in Table 5.1 in Section 5.1. The frequencies

around 2061 cm^{-1} for Pd and 2096 cm^{-1} for Pt can be assigned to the vibrational frequencies of single-atom catalysts, specifically to Pd single-atom on the (111) surface with a formal oxidation state of 0 and Pt single-atom on the (111) surface with a formal oxidation state of +II. The vibrational spectra above 2100 cm^{-1} are attributed to the formal oxidation states of +IV for both Pd and Pt single-atom catalysts in our work. Accordingly, two O atoms are adsorbed in a vicinal position to the noble metal atoms. In Figure 5.6, the frequencies around 2125 and 2167 cm^{-1} for Pd and 2172 cm^{-1} for Pt could be assigned to these. In Figure 5.7,

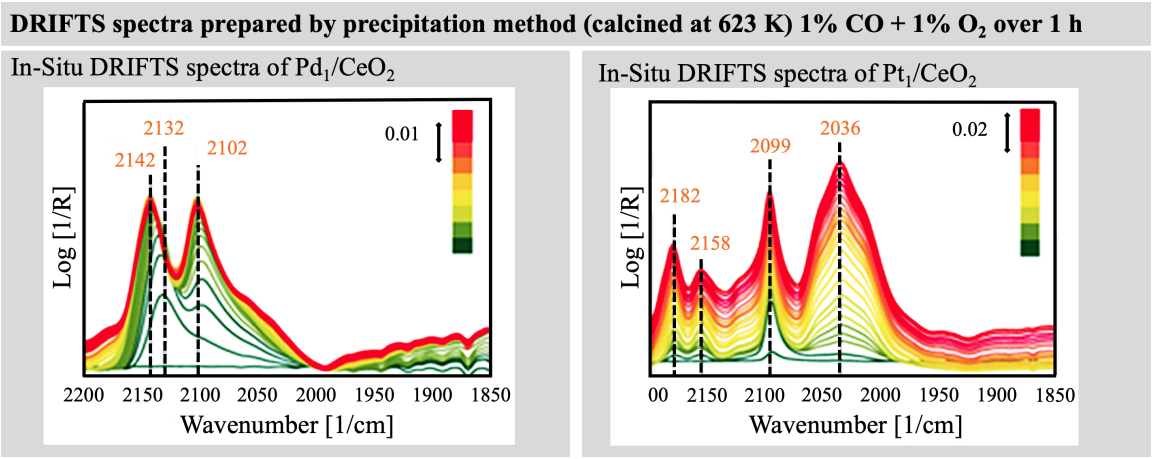

Figure 5.7.: DRIFTS spectra derived from Sarma et al. of Pd (left) and Pt (right) noble metals supported on ceria and calcined at 623 K depict CO adsorption at room temperature over catalysts prepared via the precipitation PP method. The spectra showcase the evolution of species over time in DRIFTS spectra for Pd and Pt under a reaction environment with CO + O_2 in the gas phase. The color bar in the Figure denotes spectra collected over 1 hour. The time increases from green to red. Reprinted and adapted with permission from[268] ©2024 American Chemical Society.

the catalysts were spectroscopically examined under oxidizing reaction conditions. The spectra shifted drastically to higher frequencies, while the lower ones, which we attribute to subnanometer clusters, are no longer present. The spectra at 2102 cm^{-1} for Pd correspond to the oxidation states +II for all ceria surface facets, with values of 2082 cm^{-1} for (100), 2095 cm^{-1} for (110), and 2106 cm^{-1} for (111), as shown in Table 5.1. The (111) surface aligns most closely with this value. Similarly, for Pt, the oxidation state +II corresponds to a vibrational frequency of 2099 cm^{-1} in Figure 5.7, matching frequencies of 2064 cm^{-1} for (100), 2086 cm^{-1} for (110), and 2094 cm^{-1} for (111) in Table 5.1. Again, the (111) surface is closest to the experimental value. The vibrational frequency at 2036 cm^{-1} for the Pt spectrum in Figure 5.7 could be attributed to single-atom catalysts in a reduced state with an O defect in vicinal position, or to stoichiometric surfaces with an oxidation state of 0, or to pure noble metal surfaces with an on-top coordination of the CO molecule. In this case, the reduced states are excluded as we are currently under oxidizing atmosphere. The formal oxidation state is also excluded, as we have observed and confirmed in previous

UHV-IR Spectra of Pt Single Sites and plain CeO_2 at 113 K in 0.01 mbar

In-Situ DRIFTS spectra of Pd_1/CeO_2

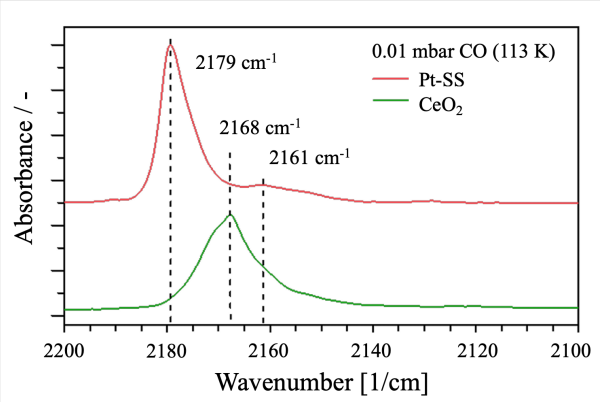

Figure 5.8.: UHV-IR spectroscopy of Pt single-atom catalysts and plain CeO_2 derived from Maurer et al. at 113 K in 0.01 mbar CO after annealing in UHV at 770 K. Reprinted and adapted with permission from[69]. ©2024 American Chemical Society.

Sections and in numerous literature sources that noble metals can indeed be oxidized under oxidizing conditions. The vibrational frequencies of the noble metal surfaces of Pt are generally higher than 2036 cm^{-1}, with values of 2075 cm^{-1} on (111), 2062 cm^{-1} for (100), and 2053 cm^{-1} for (211). The (110) surface, with a frequency of 2043 cm^{-1}, is closer to the sought-after frequency. However, it is advisable to also consider subnanometer clusters, as none of the suggested species seems to be present or are rather rarely exposed, which will be addressed in subsequent Sections of this work. All frequencies above 2100 cm^{-1} can be attributed to the higher oxidized species here. These align within a range with those of the +IV oxidation states, as depicted in Table 5.1 for single-atom catalysts. On pure noble metal surfaces, such high frequencies cannot be readily achieved. Subnanometer clusters will be addressed in the following Sections. Generally, it can already be noted here that in this regard, they can be treated similarly to the noble metal surfaces. Analogous studies conducted by Kottwitz et al.[269], Aleksandrov et al.[270], Maurer et al.[69], and Lu et al.[271] concurred with these observations, associating CO vibrational frequencies around 2095 cm^{-1} with single-site Pt species. Conversely, Resasco et al.[272] proposed CO vibrational frequencies ranging from 2090 to 2100 cm^{-1}, linked solely to CO adsorption over small PtO_x clusters. Maurer et al. observed these frequencies using UHV-IR spectroscopy of Pt single-atom catalysts and plain CeO_2 at 113 K in 0.01 mbar CO after annealing in UHV at 770 K as shown in Figure 5.8. While two major features at 2179 cm^{-1} and 2161 cm^{-1} were observed for Pt single-atom catalysts, only one peak at 2168 cm^{-1} was found for pure CeO_2. The CO vibrational frequencies found here were assigned to those of the Pt single-atom catalysts. It should be noted that the species studied in their work may have

different configurations than those considered here. In Table 5.1, the highest vibrations for the +IV oxidation state for Pt single-atoms are listed, which are 2124 cm^{-1} for the (100) surface, 2106 cm^{-1} for (110), and 2139 cm^{-1} for the (111) surface. While we cannot confirm that our species were validated by the measurements of Maurer et al., the assumption that high oxidation states correspond to higher frequencies above 2100 cm^{-1} is indeed plausible.

5.2.1. CO coverage on Pd_3 and Pt_3 subnanometer Cluster

The smallest cluster size is denoted by a Pd_3 and Pt_3 cluster, comprising only one layer of noble metal atoms with three atoms each. In contrast, the Pd_{10} and Pt_{10} clusters previously considered consist of two layers. Additionally, these larger clusters have a topmost layer

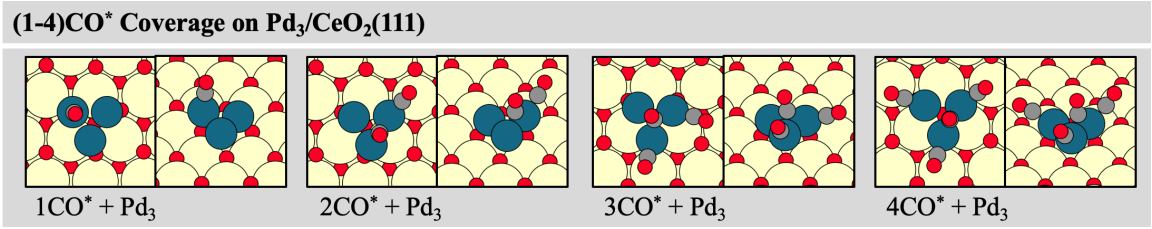

Figure 5.9.: Structure-optimized configurations of the successive adsorption of CO molecules ranging from 1 to 4 on the Pd_3 cluster. Red circles represent O atoms, dark gray circles C atoms, large yellow circles Ce atoms, and petrol circles Pd atoms. The total energies are listed in the Appendix in Table A.12.

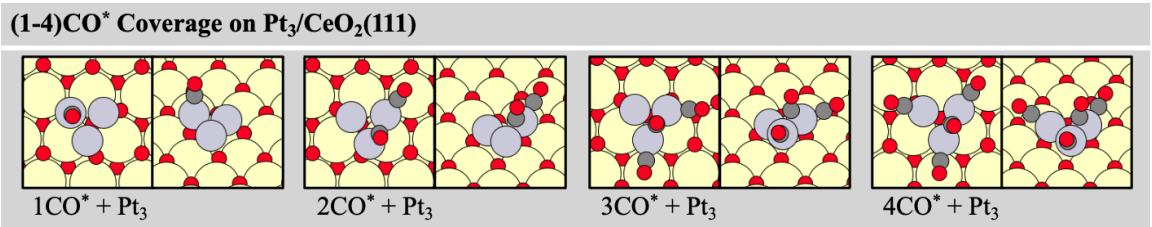

Figure 5.10.: Structure-optimized configurations of the successive adsorption of CO molecules ranging from 1 to 4 on the Pt_3 cluster. Red circles represent O atoms, dark gray circles C atoms, large yellow circles Ce atoms, and gray circles Pt atoms. The total energies are listed in the Appendix in Table A.12.

arranged similarly to the smaller clusters, forming a triangular configuration with three noble metal atoms, allowing for systematic investigations into size effects. Figure 5.9 for the Pd_3 cluster and Figure 5.10 for the Pt_3 cluster presents the structure-optimized configurations, illustrating successive CO adsorption. The CO molecule loading on the Pd_3 and Pt_3 cluster is considered to reach a maximum of 4 CO molecules. One CO molecule is located in the hollow site coordination on top of the cluster, similar to the arrangement in the Pd_{10} and Pt_{10} clusters. The remaining three CO molecules are positioned on top, bent towards the ceria surface. During the first adsorption of a CO molecule, the structure optimizations revealed that the CO molecule does not coordinate to the hollow site but instead adopts an on-top

position oriented towards the center of the cluster. Upon the adsorption of a second CO molecule, which coordinates to one of the three noble metal atoms in an on-top position, the central CO molecule migrates to a bridge position. Only with the third CO molecule does the initially centrally adsorbed CO molecule locate itself in the hollow site coordination on top of the cluster, similar to the arrangement in the Pd_{10} or Pt_{10} clusters. The remaining three CO molecules are positioned on top, bent towards the ceria surface. A comparison of the clusters presented in Section 5.3 in Figure 5.14 for the Pd_{10} cluster and in Figure 5.15 for the Pt_{10} cluster reveals that the CO molecules positioned at the edge of the Pd_3 and Pt_3 clusters are also bent towards the ceria surface, and instead of an on-top configuration, they reside on bridge positions. During the structure-finding process in this work, on-top positions were also found. However, multiple bonds lead to stronger adsorption energies. Thus, on-top configurations are naturally less stable than bridge configurations. Therefore,

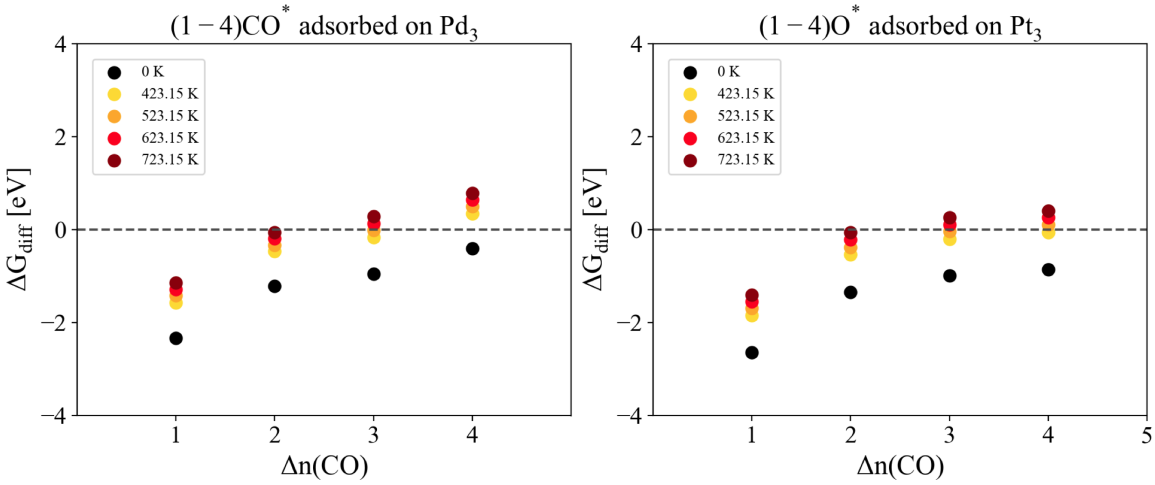

Figure 5.11.: Differential energy ΔG_{diff} of the successive adsorption of CO molecules ranging from 1 to 4 on the Pd_3 (left) and the Pt_3 (right) cluster. An increase in temperature is shown in colors ranging from yellow to dark red. The total energies, the ZPE and the entropies are listed in the Appendix in Table A.12.

it is particularly interesting to understand how a configuration where the CO molecule is in an on-top position could occur in a noble metal cluster consisting of only three atoms and one layer adjacent to the ceria surface. Both a pure noble metal surface with a (111) surface facet and a subnanometer cluster with at least two noble metal layers, such as the Pd_{10} or Pt_{10} clusters, can indeed adsorb CO molecules on hollow sites. This circumstance could be indicative of electronic effects that arise in the last layer adjacent to the ceria surface. As mentioned in the introduction in Section 1.3, a significant portion of the charge transfer occurs only at the interface between the noble metal atoms and the ceria surface. The second layer already exhibits formal oxidation states of pure noble metals, with 0. In the following course of this work, we will therefore address the specific question of how the electronic effects of the subnanometer clusters manifest through a size effect on the activity towards

CO oxidation. The differential Gibbs free energies for successive CO adsorption on the Pd_3 and Pt_3 clusters against the number of adsorbed CO molecules are plotted in a diagram, as shown in Figure 5.11 and listed in Table 5.2. It is evident that the CO coverage becomes progressively endothermic as the number increases. At 0 K, as expected, it is exothermic, but from a number of 4 CO molecules, it becomes slightly exothermic. However, the first CO adsorption is significantly exothermic with -2.33 eV for the Pd cluster and -2.64 eV for the Pt cluster. For the second CO adsorption at 0 K, the adsorption energy is already reduced by over 1.00 eV, with values of -1.22 eV for the Pd cluster and -1.35 eV for the Pt cluster. However, the decrease is less drastic for the third adsorption, with values of -0.90 eV for the Pd cluster and -0.99 eV for the Pt cluster, and even less so for the fourth adsorption, with values of -0.45 eV for the Pd cluster and -0.88 eV for the Pt cluster. The

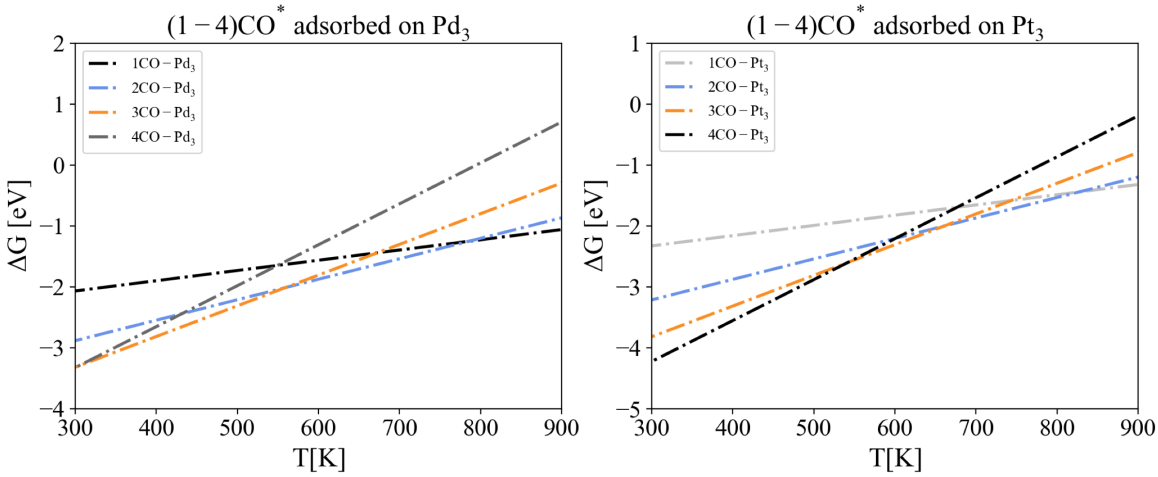

Figure 5.12.: Phase diagrams of the Gibbs free energies for the CO adsorption from the gas phase of 1 to 4 CO molecules on the Pd_3 (left) and Pt_3 (right) clusters. The Gibbs free energies for adsorption ΔG include all CO molecules being adsorbed at once. The temperature shown ranges from 0 to 800 K. The highlighted orange, blue and black dashed lines represent the number of CO molecules present within the operational temperature range of 423.15 K to 723.15 K for exhaust gas treatment. The other CO adsorptions are highlighted by increasingly darker shades of gray dashed lines as the number of adsorbed CO molecules increases. The differential Gibbs free energies are listed in Table 5.2, the total energies, the ZPE and the entropies are listed in the Appendix in Table A.12.

adsorption energy on the Pt_3 cluster is approximately 0.30 eV higher than on the Pd_3 cluster. With increasing temperature, it is noticeable that both the Pd_3 and Pt_3 clusters switch from exothermic at a coverage of up to 2 CO molecules to endothermic with a coverage of 3 CO molecules. It is therefore reasonable to assume that under reaction conditions above 423.15 K, the Pd_3 and Pt_3 clusters are found with a maximum coverage of 2 CO molecules. Below this temperature, there could potentially be 4 CO molecules adsorbed. To more precisely examine the stable species under reaction conditions with temperature dependence, we have created a phase diagram presented in Figure 5.12 to visualize this better. For the Pd_3 cluster, it is evident that a coverage of 3 CO molecules is stable from around 300 K to approximately

Table 5.2.: Differential Gibbs free energies ΔG_{diff} in eV and at the temperature range of 0 to 723.15 K in 100 K steps starting from 425.15 K of successive CO adsorption on Pd_3 and Pt_3 cluster as shown in Figure 5.9 for Pd clusters the $Pd_3/CeO_2(111)$ and 5.10 for Pt clusters the $Pt_3/CeO_2(111)$.

	0 K	423.15 K	523.15 K	623.15 K	723.15 K
CO coverage on Pd_3					
$1CO^*$	-2.33	-1.57	-1.42	-1.28	-1.15
$2CO^*$	-1.22	-0.47	-0.33	-0.19	-0.06
$3CO^*$	-0.95	-0.17	-0.01	0.13	0.28
$4CO^*$	-0.40	0.35	0.50	0.64	0.78
CO coverage on Pt_3					
$1CO^*$	-2.64	-1.85	-1.69	-1.55	-1.40
$2CO^*$	-1.35	-0.54	-0.38	-0.22	-0.06
$3CO^*$	-0.99	-0.20	-0.04	0.11	0.26
$4CO^*$	-0.86	-0.06	0.11	0.26	0.41

550 K, then transitions to a coverage of 2 CO molecules up to a temperature of about 750 K, and stabilizes at a coverage of one CO molecule from around 800 K onwards. The Pt_3 cluster, on the other hand, remains stable with a coverage of 4 CO molecules up to a temperature of 550 K. It then transitions over a small temperature range to a coverage of 3 CO molecules, from about 650 K to a coverage of 2 CO molecules, and at approximately 850 K, a coverage of 1 CO molecule becomes stable. It is important to note that this is only a theoretical consideration. At high temperatures above around 723.15 K, this catalyst is generally prone to be destroyed.

5.2.2. Spectroscopic Data of adsorbed CO Molecules on the subnanometer Cluster Pd_3 and Pt_3

In this Section, we investigate the spectroscopic properties of CO molecules successively adsorbed on the subnanometer clusters Pd_3 and Pt_3, ranging from 1 CO molecule up to 12 CO molecules. The corresponding structures for these spectroscopic data are depicted in Figure 5.9 for the Pd cluster and 5.10 for the Pt cluster in Section 5.2.1. The intensities calculated using DFT methods are plotted against the vibrational frequencies in Figure 5.13. Expressed as percentages and listed in Table 5.3 for this ensemble of CO coverages, we observe a total of 70% on-top sites, 30% bridge sites, and 10% hollow sites for the Pd cluster, and 70% on-top sites and 30% bridge sites for the Pt cluster. Most CO molecules adsorb predominantly in an ontop position for both the Pd and Pt clusters. However, the CO molecule centrally positioned on the cluster tends to preferentially coordinate in a bridge position. In general, it can be stated that the specific CO vibrational spectra vary within a narrow range depending on the coordination to the Pd_3 and Pt_3 clusters, typically falling between 2030 to 2055 cm^{-1} for both the Pd and Pt clusters.

Table 5.3.: Distribution of binding sites for CO molecules on Pd_3 and Pt_3 clusters given in percentages [%]. All species presented in the diagrams in this Section were considered.

	ontop [%]	bridge [%]	hollow [%]
Binding sites of CO on Pd_3 and Pt_3			
Pd_3	70	20	10
Pt_3	70	30	0

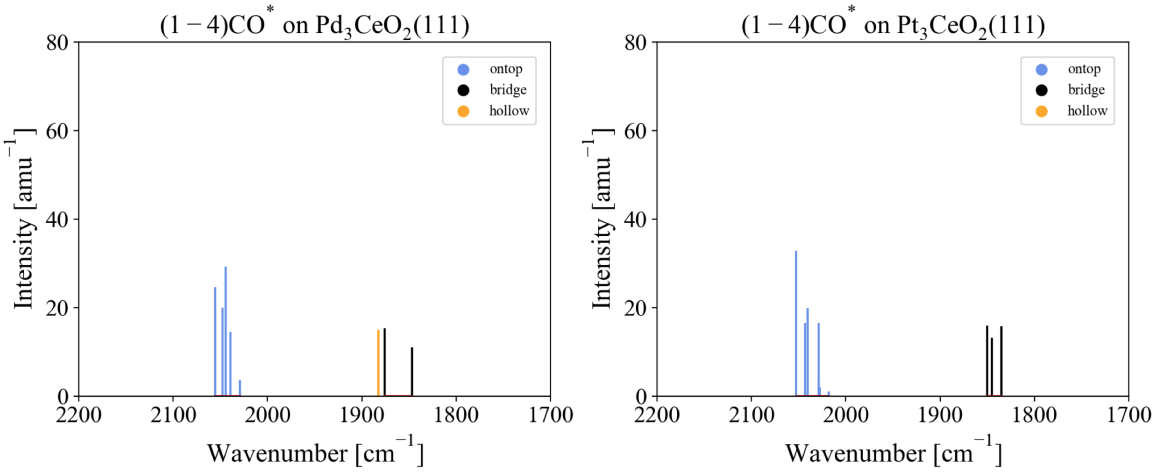

Figure 5.13.: Plot of CO intensities in amu^{-1} and of vibrational frequencies in cm^{-1} ranging from 1 to 4 CO molecules adsorbed. Pd single-atom catalysts (left) and Pt single-atom catalysts (right) are plotted. The noble metal atoms are adsorbed at ontop (blue), bridge (black) and hollow site (orange). These refer to the species shown in Figure 5.9 for Pd (left) and 5.10 for Pt cluster (right). The spectroscopic data are listed in the Appendix in Table A.12.

5.3. CO Coverage on Pd_{10} and Pt_{10} Cluster

During a rich phase in exhaust gas treatment, the noble metal supported on the ceria undergoes a phase of reduction. We conducted a coverage saturation by CO molecules in dependency of the temperature. To determine this coverage, we incrementally introduced adsorption starting from one CO molecule up to 12 CO molecules on a Pd_{10} as shown in Figure 5.14 and a Pt_{10} cluster as shown in Figure 5.15. The possible variations in coverage sites, including hollow, bridge, or ontop sites, are immense. We systematically examined some of these variations and will present here those coverage possibilities. We decided based on the energies that led to similar configurations to avoid stark fluctuations in the diagrams for the following analysis, while the noble metal cluster largely retained its configuration. As the coverage increases due to a rising number of adsorbed CO molecules, atop sites eventually emerge as a result of increasing repulsion between the adsorbed CO molecules. The on-top positions of the sites on the interface possess the characteristic of bending toward the ceria surface. Hensen and Su et al. demonstrated, through machine learning-enabled multiscale modeling, that the bridge position statistically dominates CO adsorption on

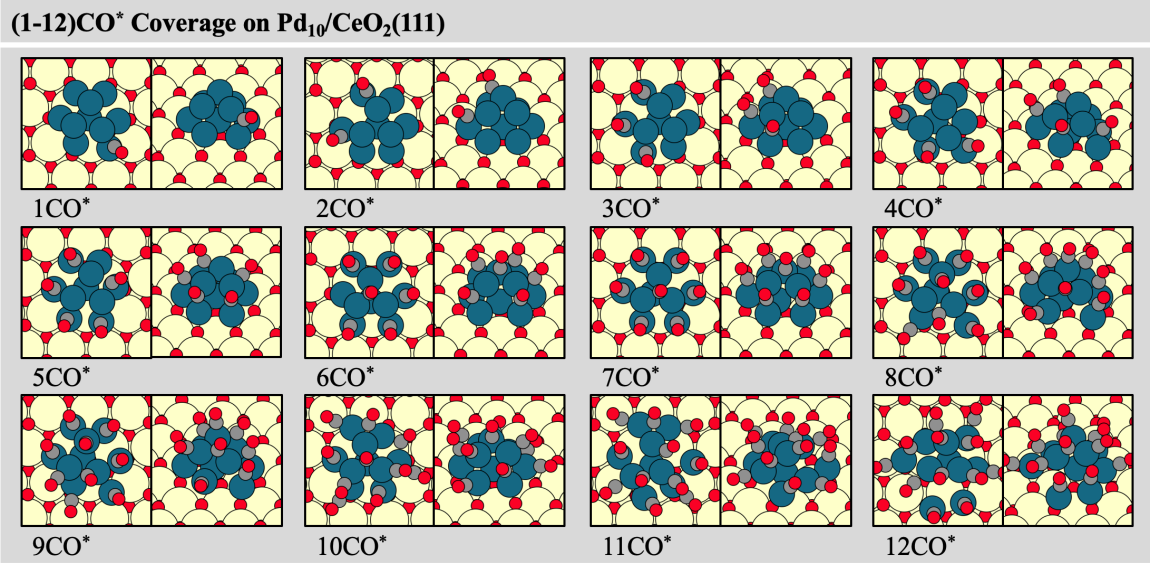

Figure 5.14.: Structure-optimized Pd_{10} clusters adsorbed on a $CeO_2(111)$ surface with a successive CO molecule adsorption ranging from 1 to 12 molecules. Red circles represent O atoms, dark gray circles C atoms, large yellow circles Ce atoms, and petrol circles Pd atoms. The total energies are listed in the Appendix in Table A.14.

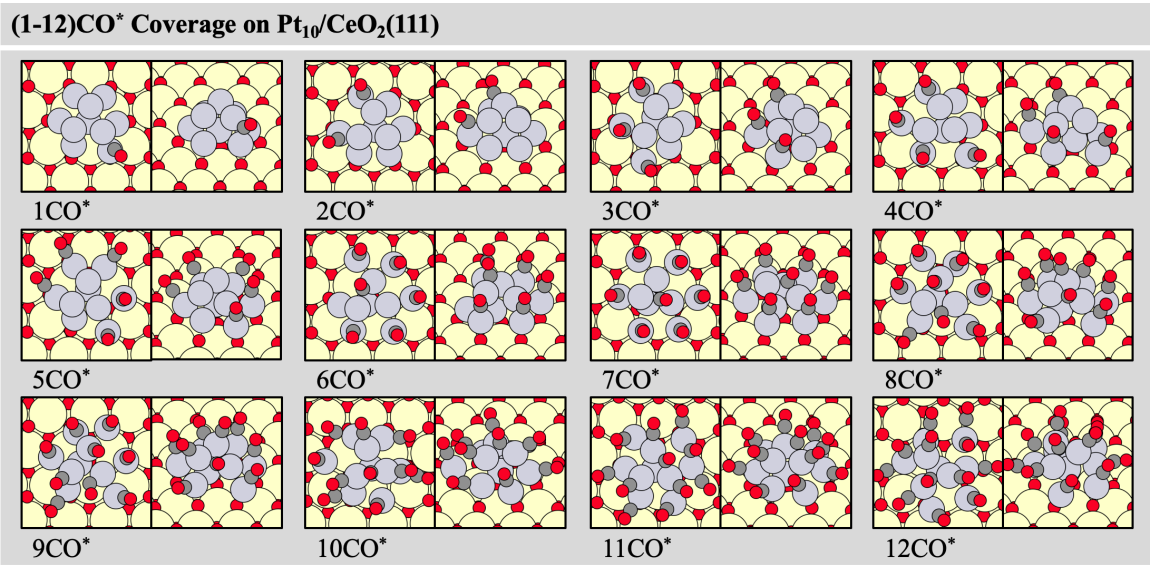

Figure 5.15.: Structure-optimized Pt_{10} clusters adsorbed on a $CeO_2(111)$ surface with a successive CO molecule adsorption ranging from 1 to 12 molecules. Red circles represent O atoms, dark gray circles C atoms, large yellow circles Ce atoms, and gray circles Pt atoms. The total energies are listed in the Appendix in Table A.14.

subnanometer clusters.[273] This observation also holds true for the flower-like structure of Pd_{10} and Pt_{10} as the structure inherently possesses a substantial number of bridge sites. The structural optimizations through DFT methods have revealed that up to 7 adsorbed CO molecules, the bridge sites are a preferred adsorption site for the Pd_{10} cluster. On the other

hand, the Pt_{10} cluster more frequently favors on-top positions than a Pd_{10} cluster overall. This slight distortion led to a preference for on-top positions by the Pt_{10} cluster overall. At a coverage of 8 CO molecules, both the Pd_{10} and Pt_{10} clusters bent CO molecules at

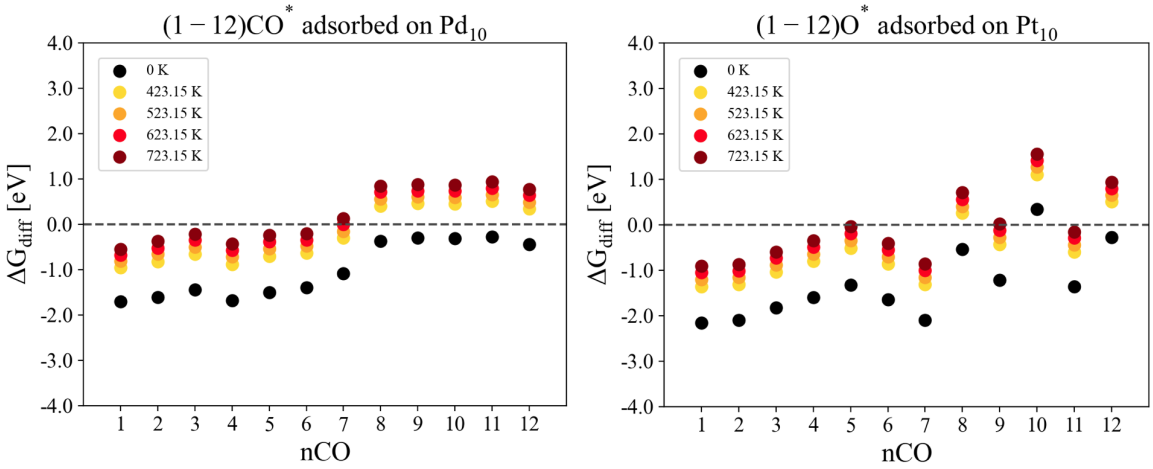

Figure 5.16.: Differential energies ΔG_{diff} of the adsorbed CO molecules on the subnanometer cluster Pd_{10} and Pt_{10} in eV and at the temperature range of 423.15 K to 723.15 K in 100 K steps and 0 K of successive CO adsorption on the clusters as shown in Figure 5.14 for Pd_{10} clusters and 5.15 for Pt_{10} clusters. The number of adsorbed CO molecules ranges from 1 to 12 molecules. The differential energies are listed in 5.4, the total energies, the ZPE and the entropies are listed in the Appendix in Table A.14.

the outer edge of the clusters to on-top positions. This ultimately led to the cluster being unable to maintain its structure at a coverage of 11 CO molecules and being torn apart into individual atoms at 12 CO molecules. With Pd, a CO molecule could consistently remain on the apex of the Pd_{10} cluster up to a coverage of 11 CO molecules. However, with Pt, this CO molecule on the apex of the Pt_{10} cluster began to squeeze into the middle of the cluster already at 6 CO molecules, but it became pronounced at 7 CO molecules, leading to a heavily distorted structure of the cluster. In a plot of the differential Gibbs free energies per adsorbed CO molecule against the number of adsorbed molecules as depicted in Figure 5.16, the differential Gibbs free energies of successive coverages by CO molecules on the Pd_{10} and Pt_{10} clusters at 0K were examined. Additionally, the temperature was increased in increments of 100 K from 423.15 K to 723.15 K. It can be observed that Pd exhibits a continuous increase in Gibbs free energy with increasing CO coverage towards endothermic adsorption energy. At 0K, as expected, this is exothermic in every case, albeit slightly endothermic at a coverage of 8 CO molecules. As the temperature rises, a coverage of 7 CO molecules emerges as the boundary between exothermic and endothermic. Around 623.15 K, this coverage begins to become unfavorable, and a coverage of 6 CO molecules is preferred. Since in the following part of the work we aim to examine the activities of CO-covered Pd_{10} and Pt_{10} clusters in CO oxidation via the MvK mechanism, this observation suggests that a coverage of 7 CO molecules should provide a starting point for the successive consumption

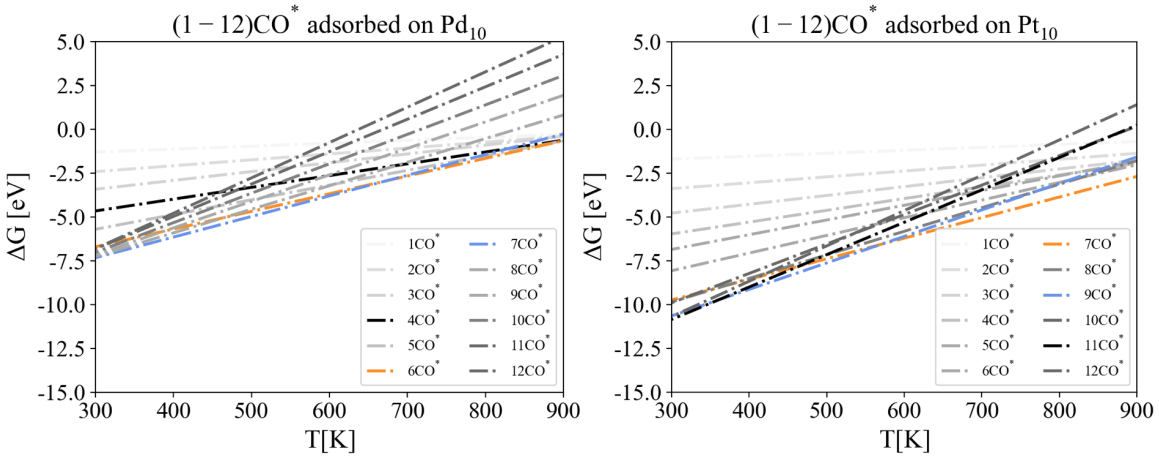

Figure 5.17.: Phase diagrams of the Gibbs free energies for the CO adsorption from the gas phase of 1 to 12 CO molecules on the Pd_{10} (left) and Pt_{10} (right) clusters. The Gibbs free energies for adsorption correspond to all CO molecules being adsorbed. The temperature shown ranges from 0 to 800 K. The highlighted orange, blue, and black dashed lines represent the number of CO molecules present within the operational temperature range of 423.15 K to 723.15 K for exhaust gas treatment. The other CO adsorptions are highlighted by increasingly darker shades of gray dashed lines as the number of adsorbed CO molecules increases. The differential energies are listed in 5.4. The total energies, the ZPE and the entropies are listed in the Appendix in Table A.14.

of CO molecules. In the case of the Pt_{10} cluster, the differential Gibbs free energies with increasing coverage and temperature dependence are not observed to be as continuous. Fluctuations were strongly observed starting at a coverage of 5 CO molecules, which could not be smoothed out with a more systematic choice of configurations. This is due in part to the significantly stronger interaction between the CO molecules and the Pt_{10} cluster. The adsorption strength is overall stronger, and therefore, the impact of the CO molecule adsorptions on the structure of the cluster is more pronounced, leading to more frequent distortions of the configuration compared to a Pd_{10} cluster. In addition to the differential Gibbs free energy diagram, we also presented a phase diagram to visualize the temperature dependence of the CO coverages in Figure 5.17. It is evident that for the Pd_{10} cluster, the coverage of 7 CO molecules transitions to a coverage of 6 CO molecules starting from low temperatures, reaching approximately 700 K. On the other hand, the Pt_{10} cluster prefers a coverage of 11 CO molecules up to about 200 K, then transitions to 6 CO molecules around 550 K, and switches to 7 CO molecules at higher temperatures, remaining stable at this coverage over a wide temperature range, even at very high temperatures. It is noteworthy that the coverage of 11 CO molecules led to a fragmentation of the clusters. Therefore, it cannot be unequivocally stated that there is a surface coverage of 11 molecules; rather, the stability of smaller subnanometer clusters down to single noble metal atoms on the ceria surface with adsorbed CO molecules can be observed.

Table 5.4.: Differential energies ΔG_{diff} of the adsorbed CO molecules on the subnanometer cluster Pd_{10} and Pt_{10}. ΔG_{diff} in eV and at the temperature range of 423.15 K to 723.15 K in 100 K steps and 0 K of successive CO adsorption on the clusters as shown in Figure 5.14 for Pd clusters and 5.15 for Pt clusters. The number of adsorbed CO molecules ranges from 1 to 12 molecules.

	0 K	423.15 K	523.15 K	623.15 K	723.15 K
CO coverage on Pd_{10}					
$1CO^*$	-1.70	-0.95	-0.81	-0.68	-0.55
$2CO^*$	-1.61	-0.82	-0.66	-0.52	-0.37
$3CO^*$	-1.44	-0.67	-0.52	-0.38	-0.24
$4CO^*$	-1.68	-0.88	-0.73	-0.58	-0.44
$5CO^*$	-1.50	-0.70	-0.54	-0.38	-0.24
$6CO^*$	-1.39	-0.63	-0.48	-0.34	-0.20
$7CO^*$	-1.08	-0.30	-0.15	0.00	0.13
$8CO^*$	-0.37	0.41	0.56	0.71	0.85
$9CO^*$	-0.30	0.46	0.61	0.74	0.88
$10CO^*$	-0.31	0.45	0.60	0.74	0.87
$11CO^*$	-0.27	0.51	0.66	0.80	0.94
$12CO^*$	-0.44	0.34	0.49	0.64	0.77
CO coverage on Pt_{10}					
$1CO^*$	-2.16	-1.36	-1.20	-1.05	-0.91
$2CO^*$	-2.10	-1.31	-1.16	-1.01	-0.87
$3CO^*$	-1.76	-0.98	-0.82	-0.67	-0.53
$4CO^*$	-1.67	-0.88	-0.72	-0.57	-0.43
$5CO^*$	-0.42	0.36	0.52	0.67	0.81
$6CO^*$	-2.54	-1.76	-1.61	-1.46	-1.32
$7CO^*$	-2.09	-1.31	-1.15	-1.00	-0.86
$8CO^*$	-0.53	0.26	0.41	0.56	0.71
$9CO^*$	-1.21	-0.43	-0.27	-0.12	0.02
$10CO^*$	0.34	1.11	1.27	1.42	1.56
$11CO^*$	-1.36	-0.59	-0.44	-0.29	-0.15
$12CO^*$	-0.27	0.51	0.66	0.80	0.94

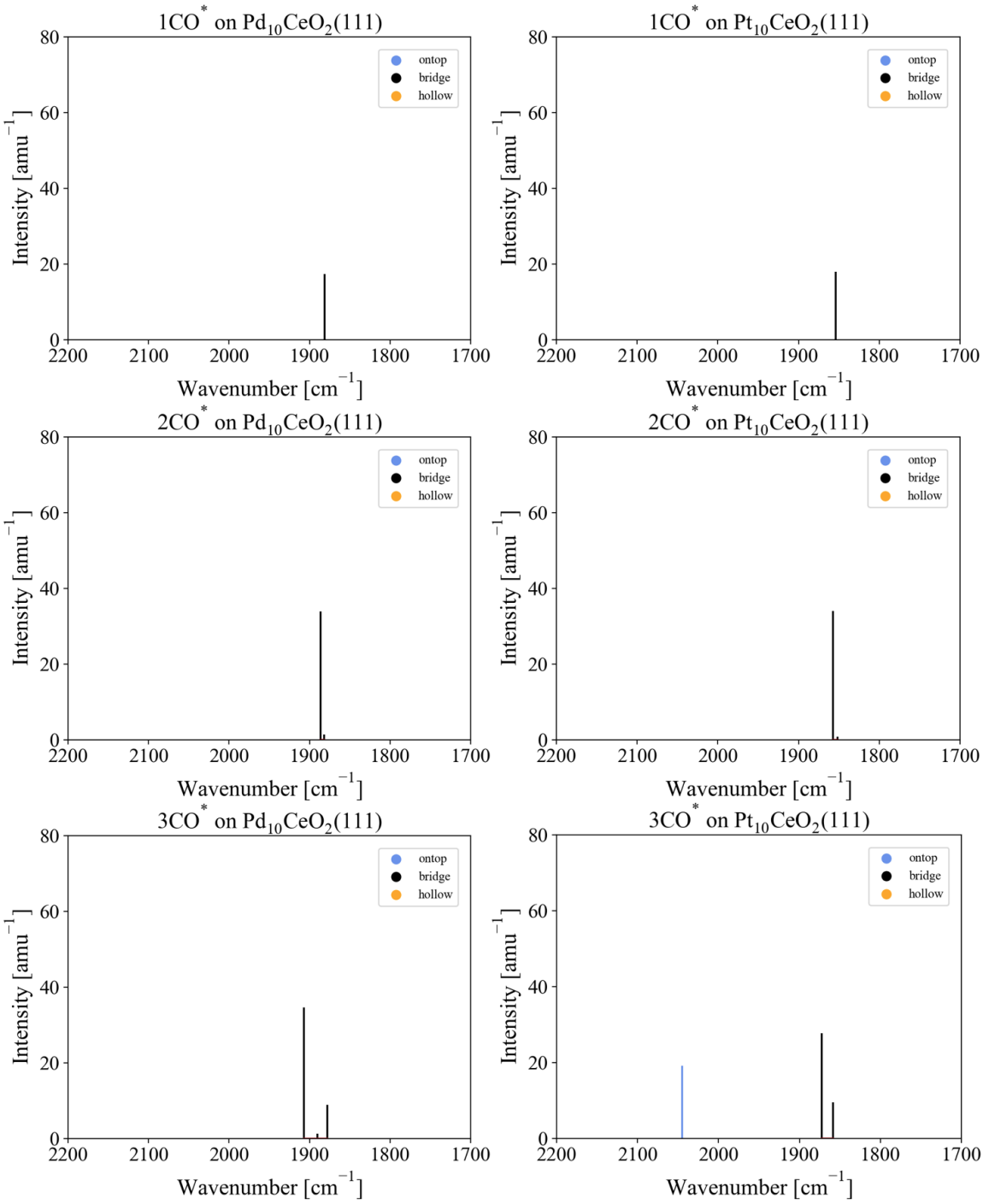

Figure 5.18.: Plot of the CO vibrational frequencies cm^{-1} and the according intensities in amu^{-1} ranging from 1 to 3 CO molecules adsorbed on Pd_{10} (left) and Pt_{10} (right) cluster. The noble metal atoms are adsorbed at ontop (blue), bridge (black) and hollow site (orange). These refer to the species shown in Figure 5.14 for Pd and 5.15 for Pt cluster. The vibrational frequencies and the according intensities are listed in the Appendix in Table A.14.

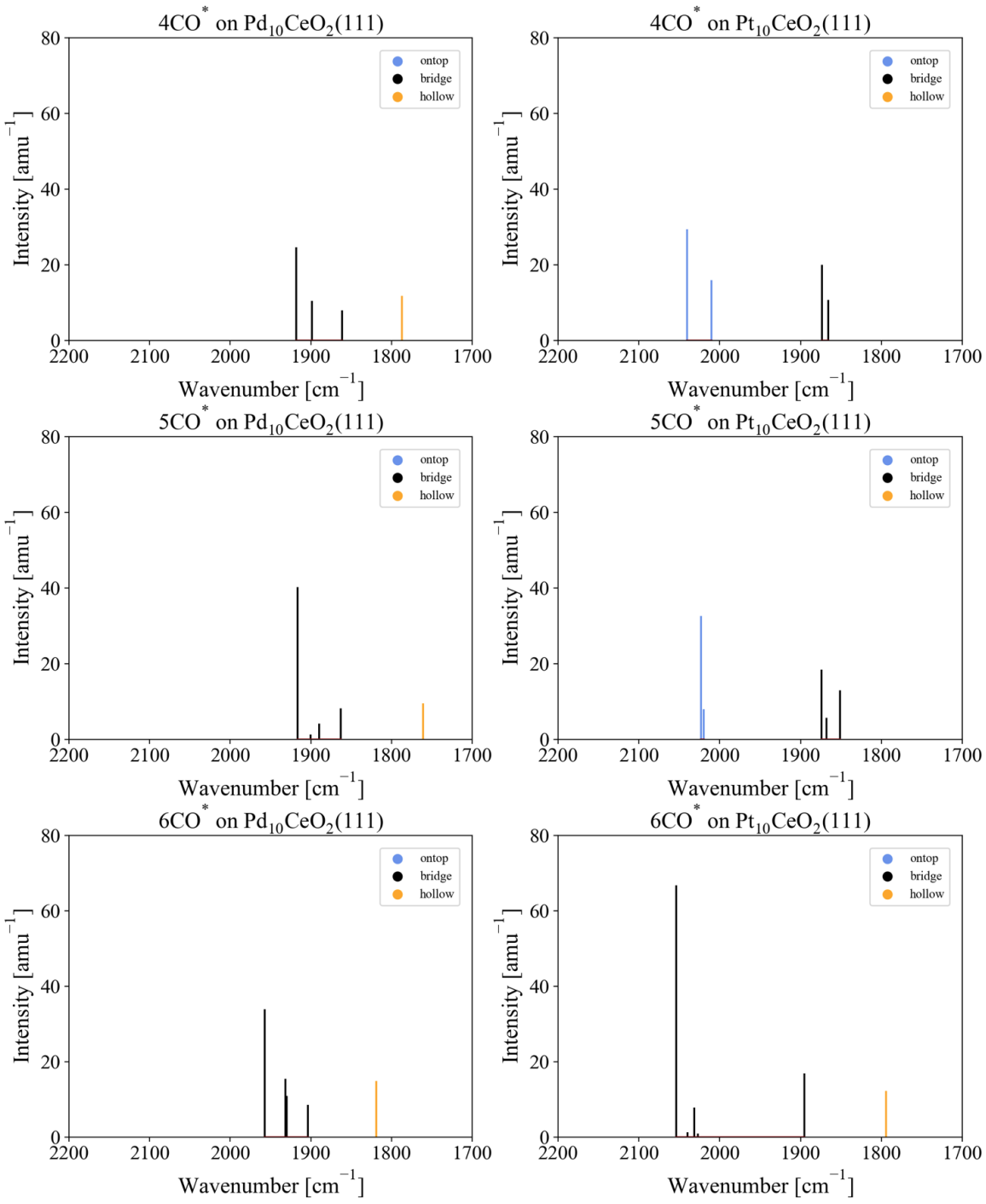

Figure 5.19.: Plot of the CO vibrational frequencies cm^{-1} and the according intensities in amu^{-1} ranging from 4 to 6 CO molecules adsorbed on Pd_{10} (left) and Pt_{10} (right) cluster. The noble metal atoms are adsorbed at ontop (blue), bridge (black) and hollow site (orange). These refer to the species shown in Figure 5.14 for Pd and 5.15 for Pt cluster. The vibrational frequencies and the according intensities are listed in the Appendix in Table A.14.

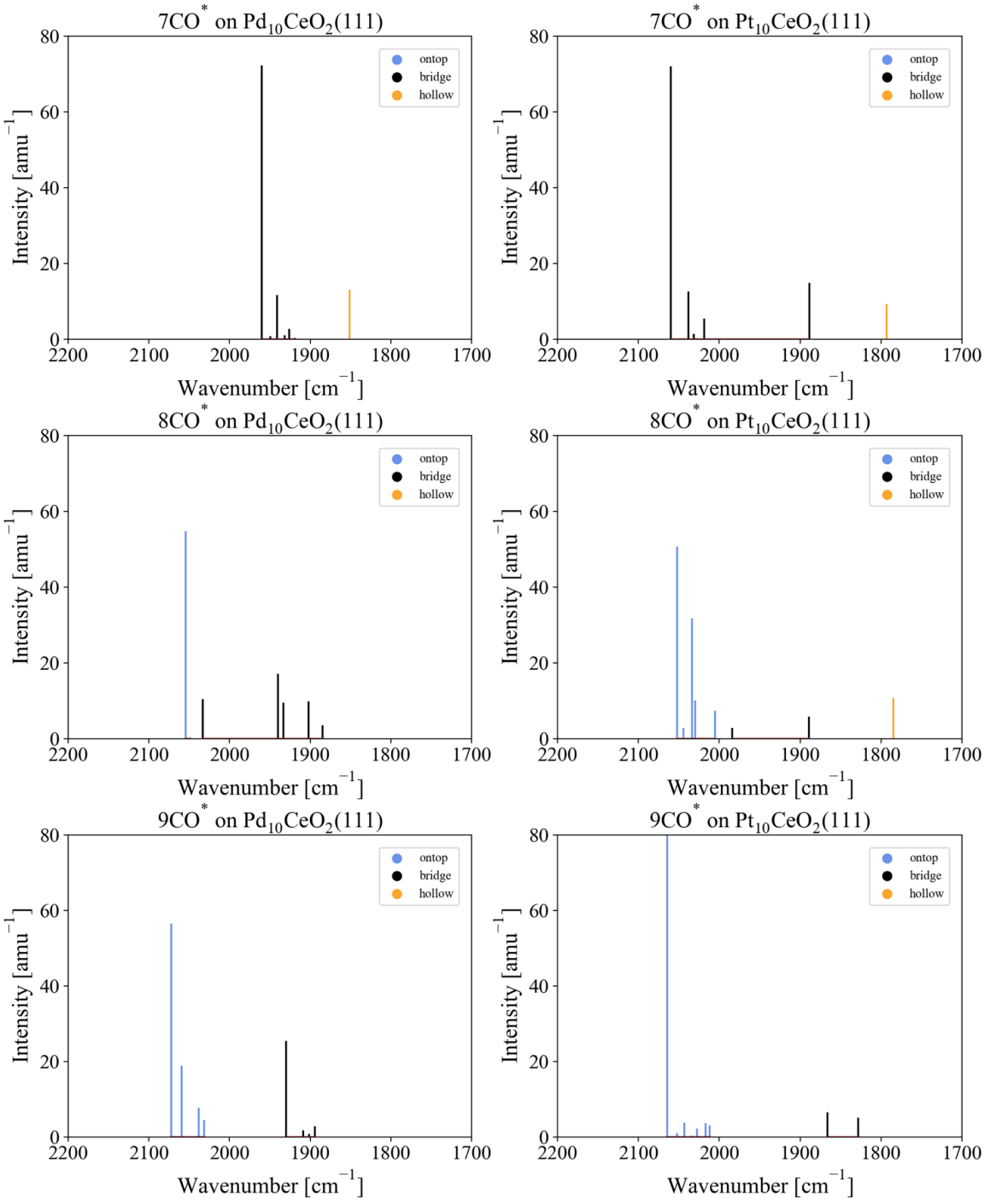

Figure 5.20.: Plot of the CO vibrational frequencies cm^{-1} and the according intensities in amu^{-1} ranging from 7 to 9 CO molecules adsorbed on Pd_{10} (left) and Pt_{10} (right) cluster. The noble metal atoms are adsorbed at ontop (blue), bridge (black) and hollow site (orange). These refer to the species shown in Figure 5.14 for Pd and 5.15 for Pt cluster. The vibrational frequencies and the according intensities are listed in the Appendix in Table A.14.

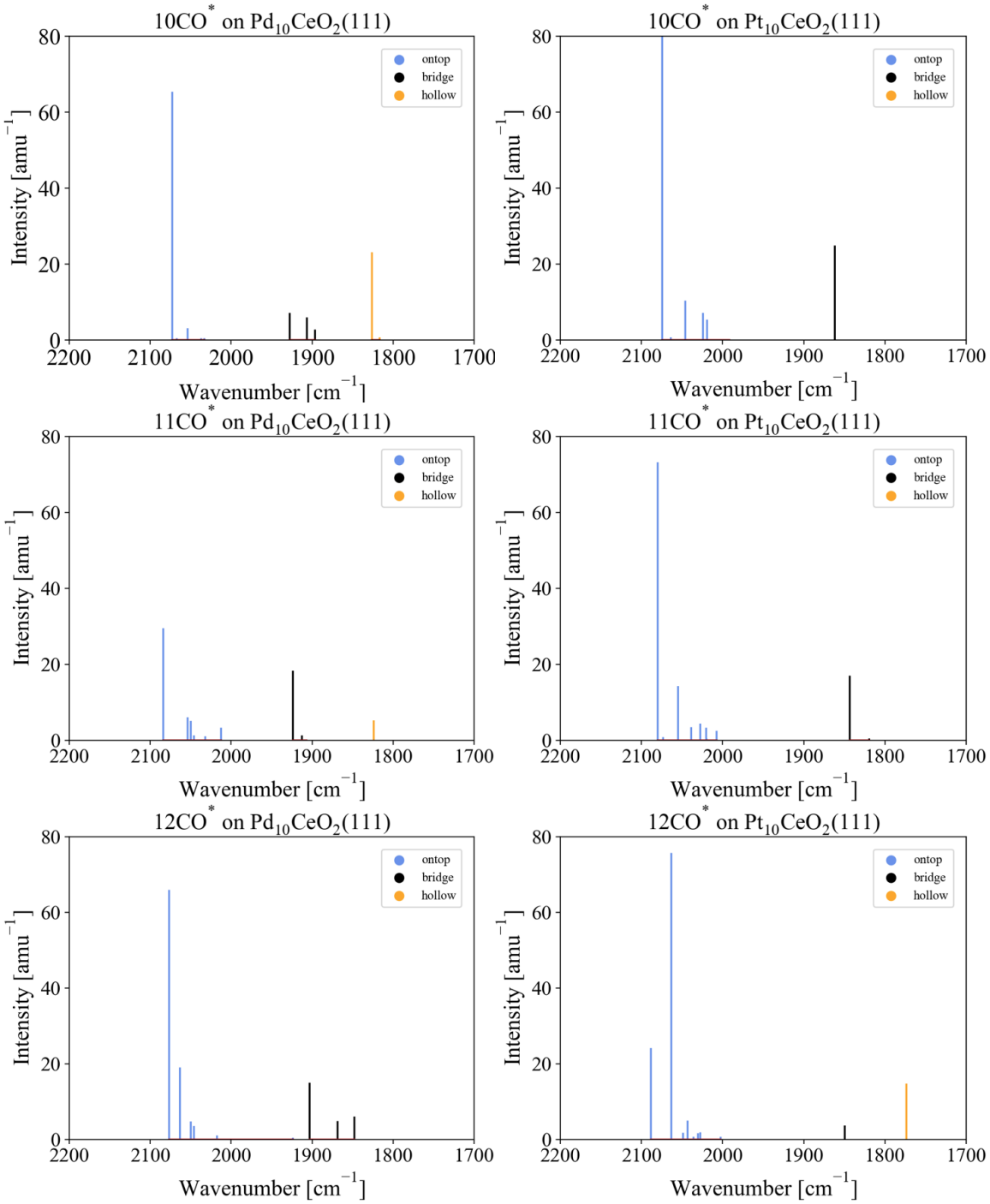

Figure 5.21.: Plot of the CO vibrational frequencies cm^{-1} and the according intensities in amu^{-1} ranging from 10 to 12 CO molecules adsorbed on Pd_{10} (left) and Pt_{10} (right) cluster. The noble metal atoms are adsorbed at ontop (blue), bridge (black), and hollow site (orange). These refer to the species shown in Figure 5.14 for Pd and 5.15 for Pt cluster. The vibrational frequencies and the according intensities are listed in the Appendix in Table A.14.

5.3.1. Spectroscopic Data of adsorbed CO Molecules on Pd_{10} and Pt_{10} Cluster

In this Section, we explore the spectroscopic properties of CO molecules successively adsorbed on the subnanometer clusters Pd_{10} and Pt_{10}, ranging from 1 CO molecule up to 12 CO molecules. The corresponding structures of these spectroscopic data are depicted in Figure 5.14 for Pd and Figure 5.15 for Pt in Section 5.3. In Figures 5.18, 5.19, 5.20 and 5.21, by the use DFT methods calculated intensities are plotted against the vibrational frequencies. The coverage of CO molecules on the Pd_{10} and Pt_{10} clusters under consideration here are statistically just one possible ensemble among countless others. The spectroscopic properties are classified according to the coordination number of the CO molecule adsorbed on the noble metals, enabling differentiation between an on-top site, a bridge site, and a hollow site. The stretching vibration modes of the CO molecule are influenced by the loading of CO molecules on the subnanometer cluster. As the proximity to other CO molecules increases, it affects both adsorption and vibrations. In Table A.14 in the Appendix, all spectroscopic data associated with the species of this Section are listed. The CO loadings onto the Pd_{10} and Pt_{10} clusters range from 1 to 12 CO molecules. Below 4 molecules, the neighbor effect is minimal, while above 9 molecules, the structure of the cluster is disrupted and dispersed into smaller fractions of noble metals with CO molecules adsorbed, owing to the strong interaction with numerous CO molecules. The general trend is a decreasing vibration frequency with increasing coordination. The vertical arrangement of the successively increasing number of adsorbed CO molecules in the diagrams visually demonstrates a shift from lower frequencies to higher frequencies from the top to the bottom diagrams as the coverage by CO adsorption onto the subnanometer clusters Pd_{10} and Pt_{10} increases. This can be explained by the neighbor effect, where vibrations intensify with the growing number of neighbors due to a stronger interaction between adjacent CO molecules on the subnanometer clusters Pd_{10} and Pt_{10}. Since both the coordination of CO molecules and the neighbor effect influence the "redshift" (referring to the tendency towards higher wavenumbers) simultaneously, comparisons between loadings should be made while considering both of these factors. It should be noted that only similar coordination numbers should be compared to reflect the neighbor effect. Another effect that can be observed here

Table 5.5.: Distribution of binding sites for CO molecules on Pd_{10} and Pt_{10} clusters given in percentages [%]. All species presented in the diagrams in this Section were considered.

Species	ontop [%]	bridge [%]	hollow [%]
Binding sites of CO on Pd_{10} and Pt_{10}			
Pd_{10}	35	56	9
Pt_{10}	59	36	5

and listed in table 5.5 is the distribution of binding sites for the CO molecules. Expressed

in percentages for this ensemble of CO coverages, we have a total of 35% ontop sites and 56% bridge sites for the Pd cluster, and 59% ontop sites and 36% bridge sites for the Pt cluster. Additionally, there are 9% hollow sites for the Pd cluster and 5% for the Pt cluster. Interestingly, this shows that for Pd sites, bridge sites dominate, followed by ontop sites, while for Pt, the distribution is inverted, with a predominance of ontop sites followed by bridge sites. Hollow sites are present in both noble metal clusters, but with a relatively low percentage. An additional peculiarity worth mentioning is the co-adsorption of two CO

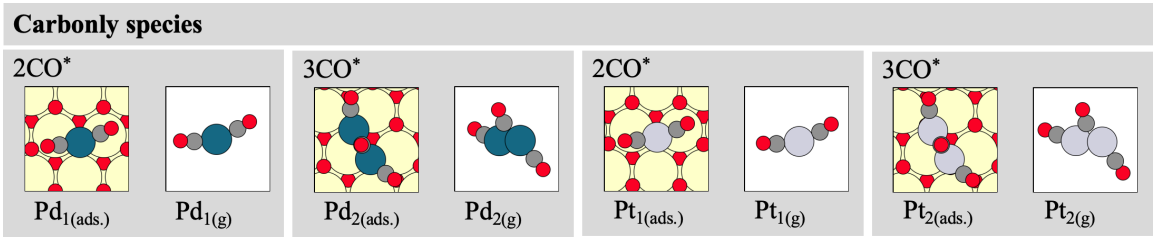

Figure 5.22.: Total energies and spectroscopic data of the structure-optimized mono- and dimer Pd and Pt species with two or three co-adsorbed CO molecules forming adsorbed carbonyl species on the (111) ceria surface and gas phase species (white background). Red circles represent O atoms, dark gray circles C atoms, large yellow circles Ce atoms, petrol circles Pd atoms, and gray circles Pt atoms. The total energies are listed in the Appendix in Table A.19.

molecules on a single noble metal atom or three CO molecules adsorbed on two noble metal atoms, as shown in Figure 5.22. In this study, we observed that with high CO coverage, individual noble metal atoms detach from the subnanometer cluster due to the interaction of adsorbed CO molecules. This phenomenon is illustrated in Figures 5.14 for the Pd cluster and 5.15 for the Pt cluster in Section 5.3. Out of curiosity and for completeness, we also calculated the vibrational frequencies and the corresponding intensities of these species adsorbed onto the ceria (111) surface and in the gas phase and gained the spectroscopic data as listed in Table 5.6. A carbonyl species of this kind is known in the literature to be highly unstable.[274] Stable $Pd(CO)_4$ and $Pt(CO)_4$ carbonyls have a tetrahedral structure,[275–278] which could only be stabilized in low-temperature matrices.[279–281] However, there are also studies that show square-planar structures.[282,283] A dinuclear complex of these noble metals would result in a $[\{Pt(CO)_3\}_2]^{+II}$ complex with carbonyl ligands.[283,284] Several of the mentioned studies have investigated the configurations of the carbonyls at a dinuclear center formed by Pd or Pt. Two limiting structures are conceivable: two carbonyls could each form a bridging function at the Pd and Pt center, or alternatively, three carbonyls could be bound in a planar arrangement at one center. As discussed within these studies, Pd and Pt as metal centers are considered non-classical metal carbonyls because they primarily exhibit σ-donor bonding. The π-backbonding from the noble metals to the CO molecule is minimal.[274] In this work, we have chosen the gas-phase carbonyls that are analogous to those of the adsorbed carbonyls on ceria in order to maintain consistency. It is important to

emphasize that a thorough understanding of the bonding situation of the carbonyls is crucial for gaining a fundamental understanding of their stability. In this study, the vibrational

Table 5.6.: Spectroscopic data obtained through DFT calculations of the structures of carbonyl species given in 5.22 for Pd and for Pt. The stretching vibrations of the CO molecule and their corresponding intensities were determined based on dipole moments.

	$\tilde{\nu}$[cm^{-1}]	$\tilde{\nu}$[cm^{-1}]	$\tilde{\nu}$[cm^{-1}]		$\tilde{\nu}$[cm^{-1}]	$\tilde{\nu}$[cm^{-1}]	$\tilde{\nu}$[cm^{-1}]
Supported on CeO_2(111)							
$2CO^* + Pd_1$	2005	2033		$2CO^* + Pt_1$	1988	2022	
$3CO^* + Pd_2$	1867	2029	2038	$3CO^* + Pt_2$	1814	2019	2032
Gas phase							
$2CO^* + Pd_{1(g)}$	2021	2085		$2CO^* + Pt_{1(g)}$	2016	2099	
$3CO^* + Pd_{2(g)}$	1906	2035	2058	$3CO^* + Pt_{2(g)}$	1886	2037	2062

frequencies of the adsorbed single Pd atom were calculated to be 2005 and 2033 cm^{-1}, and 2021 and 2085 cm^{-1} for Pt. The vibrational spectra on the dimer show peaks at 1867 cm^{-1} for Pd and 1906 cm^{-1} for Pt in the bridge position, and 2029 and 2038 cm^{-1} for Pd, and 2019 cm^{-1} and 2032 cm^{-1} for Pt. Overall, it can be stated that the CO molecules adsorbed on top of a noble metal atom or dimer, with a significant majority, exhibit vibrational frequencies around 2030 cm^{-1} for Pd and 2020 cm^{-1} for Pt. These are characteristic for these species. In contrast, in the gas phase, they result in 2021 and 2085 cm^{-1} for Pd single-atoms, 1906 cm^{-1} for bridge, 2035 and 2058 cm^{-1} for the on-top position, and in 2016 and 2099 cm^{-1} for Pt single-atoms, 1886 cm^{-1} for bridge, 2037 and 2062 cm^{-1} for the on-top position. The gas-phase species show smaller differences between the Pd and Pt noble metal atoms than when adsorbed on the ceria surface. Upon adsorption, these frequencies generally decrease. Decomposition of a noble metal under strong CO adsorption, leading to the adsorption of single noble metal atoms and dimers on the ceria surface, results in specific vibration spectra. If these are observed in experimental spectra, carbonyl species could be considered.

5.4. O Coverage on Pd_{10} and Pt_{10} subnanometer Cluster

During a lean phase in exhaust gas treatment, the noble metals on the ceria surface are exposed to oxidizing reaction conditions. Under these conditions, the noble metal cluster begins to adsorb and dissociate O_2 molecules. In a later Section, we will examine the dissociation energies. In this Section, we will first consider oxidation of the subnanometer cluster Pd_{10} and Pt_{10} through surface coverage with O atoms from one to seven atoms to evaluate at an increasing reaction temperature. The cluster configuration remains metallic during the adsorption of O atoms and does not transform into a PdO or PdO_2 crystal structure. The adsorption of O atoms has only a minor impact on the configuration of the PdO or PdO_2. Figure 5.23 for Pd and 5.24 for Pt depict the structures of successively adsorbed O atoms.

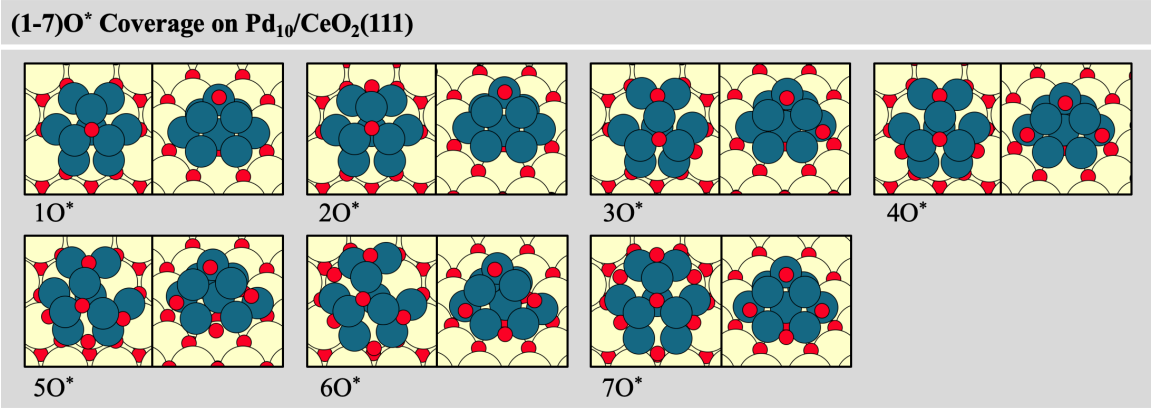

Figure 5.23.: Structure-optimized Pd_{10} clusters adsorbed on a $CeO_2(111)$ surface with successive O adsorption ranging from 1 to 7 O atoms. Red circles represent O atoms, dark gray circles C atoms, large yellow circles Ce atoms, and petrol circles Pd atoms. The total energies are listed in the Appendix in Table A.13.

In this study, we aim to examine the degree of O coverage under temperature dependence. We start with adsorption on the second layer in the z-direction, thereby occupying a hollow site on the apex of the cluster. The following three atoms each adsorb on one of the "leaves". These are also adsorbed on a hollow site. To fully oxidize the cluster through O atom adsorption, the connections between the "leaves" are successively covered up to a total of 5 O atoms. These O atoms adsorb on the cluster at a bridge position. Full coverage is considered achieved with a total of 7 O atoms adsorbed on the Pd_{10} and Pt_{10} clusters. Pd and Pt behave similarly in their configurations. Figure 5.25 displays the plot of the

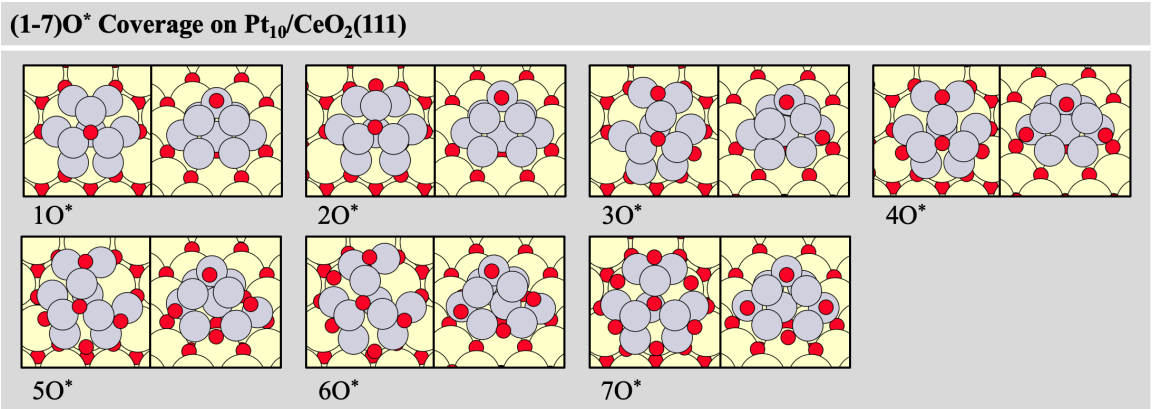

Figure 5.24.: Structure-optimized Pt_{10} clusters adsorbed on a $CeO_2(111)$ surface with successive O adsorption ranging from 1 to 7 O atoms. Red circles represent O atoms, dark gray circles C atoms, large yellow circles Ce atoms, and gray circles Pt atoms. The total energies are listed in the Appendix in Table A.13.

differential adsorption energy ΔG_{diff} in eV and at the temperature range of 0 to 723.15 K in 100 K steps starting from 425.15 of successive O adsorption on the clusters as shown in Figure 5.23 for Pd and 5.23 for Pt. The differential Gibbs free energies depicted in plot 5.25 are listed in Table 5.7. To calculate the differential Gibbs free energy, with each

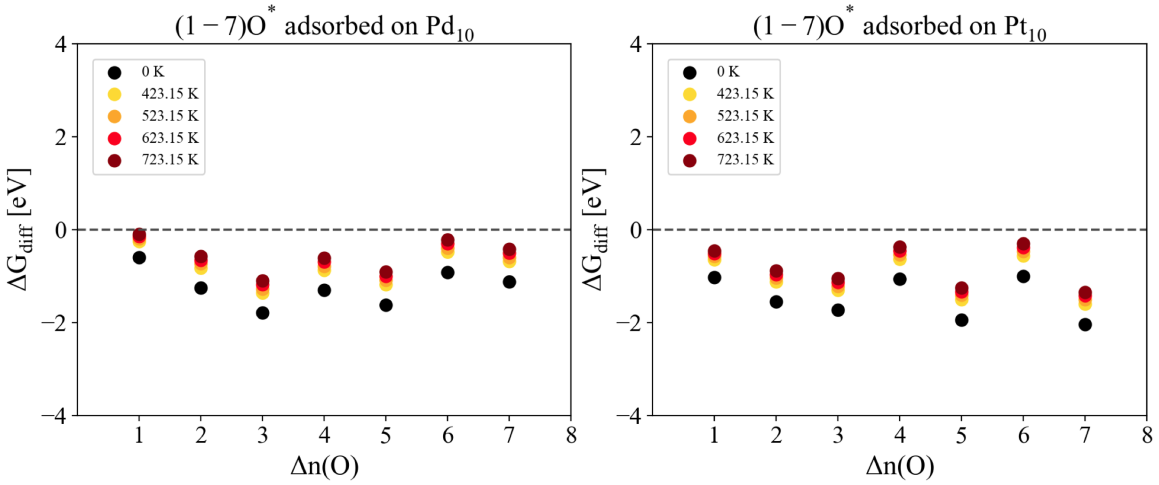

Figure 5.25.: Differential energies of structure-optimized Pd_{10} (left) and Pt_{10} (right) clusters adsorbed on a CeO_2(111) surface with successive O adsorption ranging from 1 to 7 O atoms is plotted against the number of adsorbed O atoms. The temperature is considered to increase in 100 K steps starting from 425.15 K and ending in 724.15 K. The colors range from yellow, over orange to bright red to dark red for each step, respectively. The differential energies are listed in Table 5.7, the ZPE and the entropies are listed in the Appendix in Table A.13.

new coverage by the next O atom, the Gibbs free energy is computed for each additional adsorption. The adsorption energies at 0 K for the first O atom are -0.60 eV for the Pd cluster and -1.02 eV for the Pt cluster. With each subsequent O atom, the adsorption energy at 0 K increases by approximately 0.50 to 1.00 eV for both noble metals. Overall, the adsorption energies at 0 K are approximately 0.50 eV higher for Pt. At 423.15 K, the adsorption energy for each O atom on both noble metal clusters has decreased by about 0.40 eV. As the temperature increases by 100 K up to 723.125 K, the adsorption energy for each O atom on both Pd and Pt clusters decreases by approximately 0.05 to 0.10 eV. The plots of the differential adsorption energy show that even with increasing temperatures, oxidation through adsorption on the surface sites of the subnanometer clusters is largely exothermic. The adsorption of O atoms on the Pd cluster is slightly less exothermic than on the Pt cluster. To visualize the surface coverages present under reaction conditions, a phase diagram was created in Figure 5.26 at a reaction temperature of 423.15 K. The Pd_{10} cluster is stable with a coverage of 7 O atoms up to temperatures of about 600 K. With further increasing temperature, the coverage decreases to 5 O atoms. However, the Pd_{10} cluster adsorbs more strongly overall and theoretically remains covered with 7 O atoms up to temperatures over 850 K. It should be noted here that reaction temperatures above this temperature pose a challenge to the stability of the catalyst in general. It is assumed that the catalyst is not stable at these high temperatures. It is also worth mentioning that the configurations chosen here represent only a snapshot of an ensemble that should undergo dynamic changes between the possibilities. Thus, it can be generally summarized that a surface coverage of up to 7

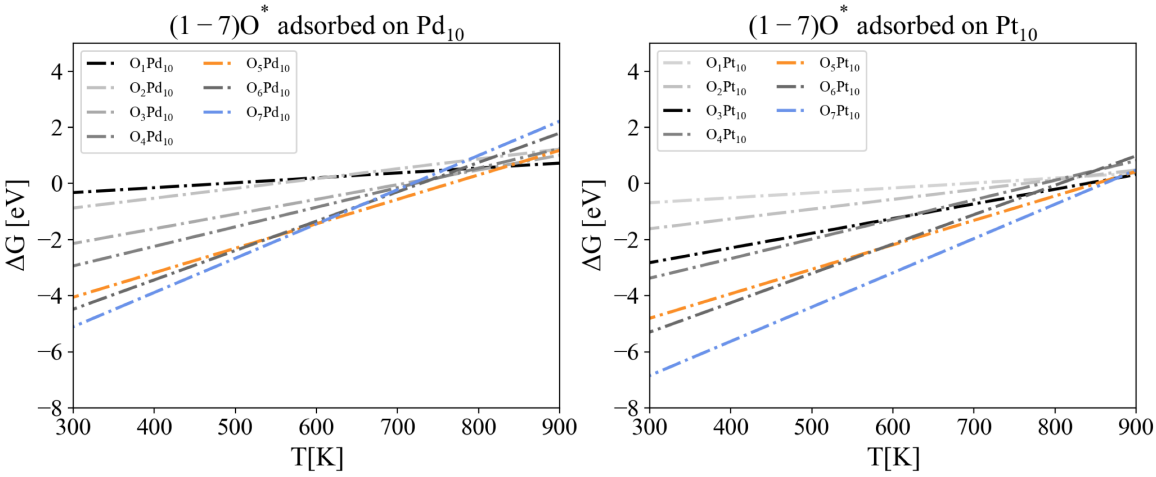

Figure 5.26.: Phase diagrams of the Gibbs free energies for the O adsorption from the gas phase of 1 to 7 O atoms on the Pd_{10} (left) and Pt_{10} (right) clusters. The Gibbs free energies for adsorption correspond to all O molecules being adsorbed. The temperature shown ranges from 0 to 800 K. The highlighted orange, blue and black dashed lines represents the number of O molecules present within the operational temperature range of 423.15 K to 723.15 K for exhaust gas treatment. The other CO adsorptions are highlighted by increasingly darker shades of gray dashed lines as the number of adsorbed CO molecules increases. The differential energies are listed in Table 5.7, the ZPE and the entropies are listed in the Appendix in Table A.13.

Table 5.7.: Differential energies ΔG_{diff} of the adsorbed O molecules on the Pd_{10} and Pt_{10} cluster. ΔG_{diff} in eV and at the temperature range of 423.15 K to 723.15 K in 100 K steps and 0 K of successive O adsorption on the clusters as shown in Figure 5.23 for Pd clusters the $Pd_{10}/CeO_2(111)$ and 5.23 for Pt clusters the $Pt_{10}/CeO_2(111)$. The number of adsorbed O molecules ranges from 1 to 7 molecules.

	0 K	423.15 K	523.15 K	623.15 K	723.15 K
O coverage on Pd_{10}					
$1O^*$	-0.60	-0.26	-0.20	-0.14	-0.09
$2O^*$	-1.25	-0.82	-0.74	-0.65	-0.58
$3O^*$	-1.79	-1.36	-1.27	-1.18	-1.10
$4O^*$	-1.30	-0.87	-0.78	-0.69	-0.61
$5O^*$	-1.62	-1.18	-1.09	-1.00	-0.92
$6O^*$	-0.92	-0.48	-0.39	-0.31	-0.22
$7O^*$	-1.12	-0.68	-0.59	-0.50	-0.42
O coverage on Pt_{10}					
$1O^*$	-1.02	-0.64	-0.58	-0.51	-0.45
$2O^*$	-1.55	-1.12	-1.04	-0.96	-0.88
$3O^*$	-1.73	-1.30	-1.21	-1.13	-1.05
$4O^*$	-1.06	-0.63	-0.54	-0.46	-0.38
$5O^*$	-1.94	-1.50	-1.42	-1.33	-1.25
$6O^*$	-1.00	-0.56	-0.47	-0.38	-0.30
$7O^*$	-2.03	-1.59	-1.50	-1.42	-1.34

O atoms leads to a stable configuration. Other reaction conditions, such as reducing CO molecules, have not been considered here. The oxidation of Pd_{10} and Pt_{10} determined here

can be used in later Sections to examine the activity of oxidized subnanometer clusters in CO oxidation via the LH mechanism.

5.5. Investigation of Sizes and Shapes of Subnanometer Clusters

As the exhaust gas after-treatment reaction cycles alternate between O-rich and O-lean conditions, it tests the resilience of cluster shapes. Surface oxidation of subnanometer-sized clusters might occur during this process. However, the precise structure and size of the oxidized noble metals remain unclear. This raises questions about whether the crystal structure of the clusters remains intact while forming an oxide layer on the surface through O atom adsorption or if the surface structure emerges with an oxidized crystal structure layer. A thorough oxidation process would entail a change in the crystal structure of the cluster, potentially leading to a PdO_2 or PtO_2 lattice where each Pd atom seeks to form a square planar structure with four O atoms at each corner. To investigate the size, shape, and

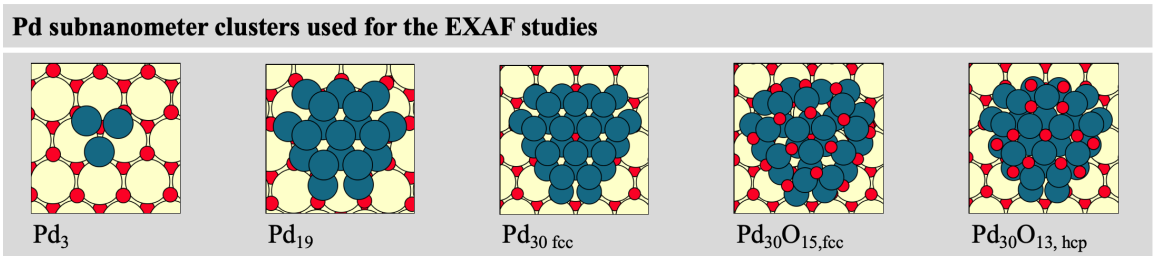

Figure 5.27.: Subnanometer Pd cluster structure-optimized by DFT methods conducted by us and used for fitting to the EXAFS studies conducted by Gashnikova.[285,286] The total energies are listed in the Appendix in Table A.20.

O coverage, we aim to determine the shape, size, and adsorption sites of the O atoms on exposed noble metal surfaces in both nanometer and subnanometer clusters by comparing structures obtained through DFT methods with EXAFS studies. In the following discussion, the subnanometer clusters depicted in Figure 5.27 are analyzed in a study by Gashnikova et al., conducted in collaboration with our research.[285,286] The collaborative investigation by Gashnikova et al., conducted within our network, employed various in situ/operando methodologies to monitor active Pd clusters within a 0.5% Pd/5% CeO_2-Al_2O_3 catalyst during CO oxidation. Through X-ray absorption spectroscopy (XAS), they estimated the active Pd cluster size ranging from 10 to 30 Pd atoms based on structures calculated by our work. Operando XAS and diffuse reflectance infrared Fourier transform spectroscopy (DRIFTS) revealed the dependency of Pd subnanometer cluster stability on temperature and reaction conditions. The Pd clusters Pd_3, Pd_{10}, Pd_{19}, and Pd_{30} were utilized for fitting, as depicted in Figure 5.28. However, they explained that the fitting failed to replicate the first Pd-O coordination shell at 1.5 Å, leading to the inclusion of a hybrid model integrating Pd

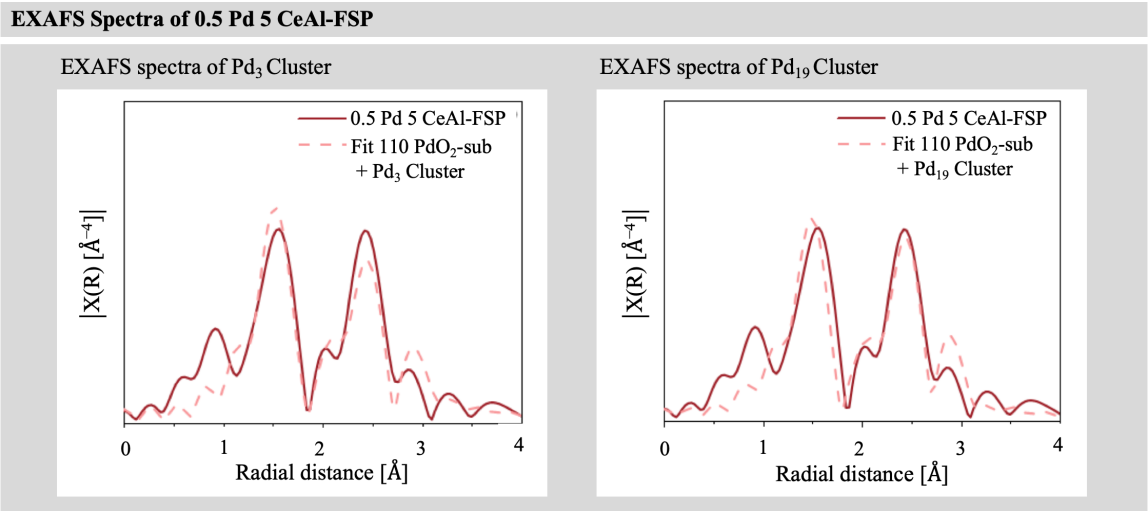

Figure 5.28.: Results of Gashnikova et al.[285,286] extracted from the Manuscript with permission about EXAFS data analysis of 0.5 Pd and 5CeAl-FSP using a fit model of Pd_3 cluster (left) and Pd_{19} (right) or combination of two structure models (Pd cluster and a Pd single-atom substituting one cerium atom of the ceria (110) surface, here assigned as PdO_2-sub for EXAFS fitting. The experimental spectrum was recorded under reaction conditions at 70 DC after reductive treatment at 200 DC in 2% H2/He.

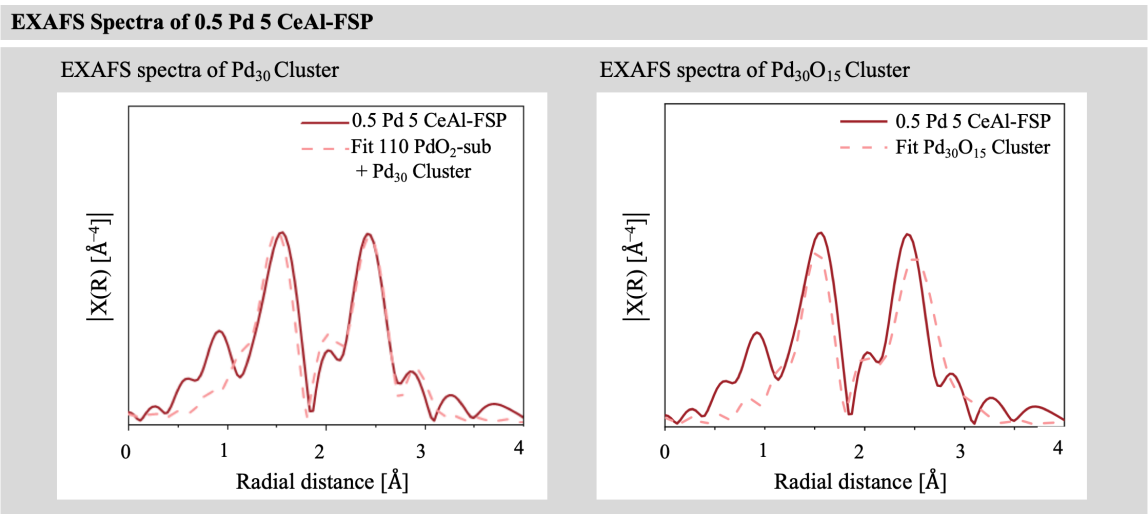

Figure 5.29.: Results of Gashnikova et al.[285,286] extracted from the Manuscript with permission about EXAFS data analysis of 0.5Pd 5CeAl-FSP using a fit model of Pd_{30} cluster (left) and $Pd_{30}O_{15}$ oxidized cluster by O adsorption onto the surface (right) or combination of two structure models (Pd cluster and a Pd single-atom substituting one cerium atom of the ceria (110) surface, here assigned as PdO_2-sub for EXAFS fitting. The experimental spectrum was recorded under reaction conditions at 70 DC after reductive treatment at 200 DC in 2% H_2/He.

single-atoms adsorbed on CeO_2 surface facets into the fitting, as shown in Figure 5.28 for the Pd_3 and Pd_{19} cluster and in Figure 5.29 for the $Pd_{30}O_{15,fcc}$ and $Pd_{30}O_{13,hcp}$ cluster. It is assumed that Pd single-atom catalysts and subnanometer clusters may coexist under the examined reaction conditions. The fittings demonstrated a good agreement between the experimental spectra and theoretical structures, taking single-atom catalysts into account.

Upon comparing the structures optimized using DFT methods with those obtained from the EXAFS study conducted by our experimental collaborators conducted by Gashnikova, it was found that the $Pd_{30}O_{15,fcc}$ cluster with face-centered cubic (fcc) adsorption sites represents the most stable structure, while the hexagonal close-packed (hcp) adsorption sites $Pd_{30}O_{13,hcp}$ exhibited a less favorable fitting, indicating a distinct preference for O atom adsorption on fcc sites. In a broader context, Feibelman et al. investigated H atom adsorption, noting minimal binding energy variations between fcc and hcp sites on closely packed metal surfaces, typically less than 0.2 eV.[287] However, the calculations of Stampfl and Scheffler for O adsorption on close-packed transition-metal surfaces revealed significant energy differences between fcc and hcp sites, ranging from 0.4 to 0.5 eV.[288] Feibelman further explained the O-site preference on Pt(111), attributing it to electrostatic repulsion between highly electronegative O adatoms and neighboring first-layer Pt atoms, as well as the inverse correlation between d-band filling and inter-Pt atom bond strength. This analysis sheds light on the intricate interplay between adsorbate-substrate interactions and surface geometry in determining adsorption preferences.[289]

5.6. Spectroscopic Data of CO molecules adsorbed on the extended Pd and Pt surface facets

The spectroscopic data regarding the stretching vibration spectra of adsorbed CO molecules on the (111), (110), (100), and (211) surfaces of the pure noble metal crystals Pd and Pt yield specific spectra. These can be compared with the experimental vibration spectra data available in the existing literature. The CO molecule is a particularly adsorption site-sensitive probing molecule, as its stretching vibration mode can be considered in isolation from the chemical environment. For this purpose, the adsorption sites on the metal surface were utilized, facilitating screening of the surface, as illustrated in Figure 5.30 for Pd surfaces and Figure 5.31 for Pt surfaces. The vibration spectra are detailed in Table 5.32 and visualized in diagrams in Figure 5.32. We have sorted them into three categories highlighting the coordination of the CO molecule to the noble metal surface. The CO molecule can be bound on top (1-fold), bridge (2-fold), or hollow (3-fold, with an exception at the (100) surface 4-fold). Some of these adsorption sites, however, could not be generated for Pt surfaces. The absence of certain adsorption sites in Table 5.32 indicates that the CO molecule could not be optimized at a minimum of the potential energy structure on these adsorption sites. Instead, in these cases, it migrated from hollow to bridge in the case of the (110) and the (211) surface facets and bridge to hollow in the case of the (111) surface facet during the course of the structure optimization. The missing pictures in Figure 5.31 refer to these cases. Gajdovs et al. have already made these observations in their studies.[290]

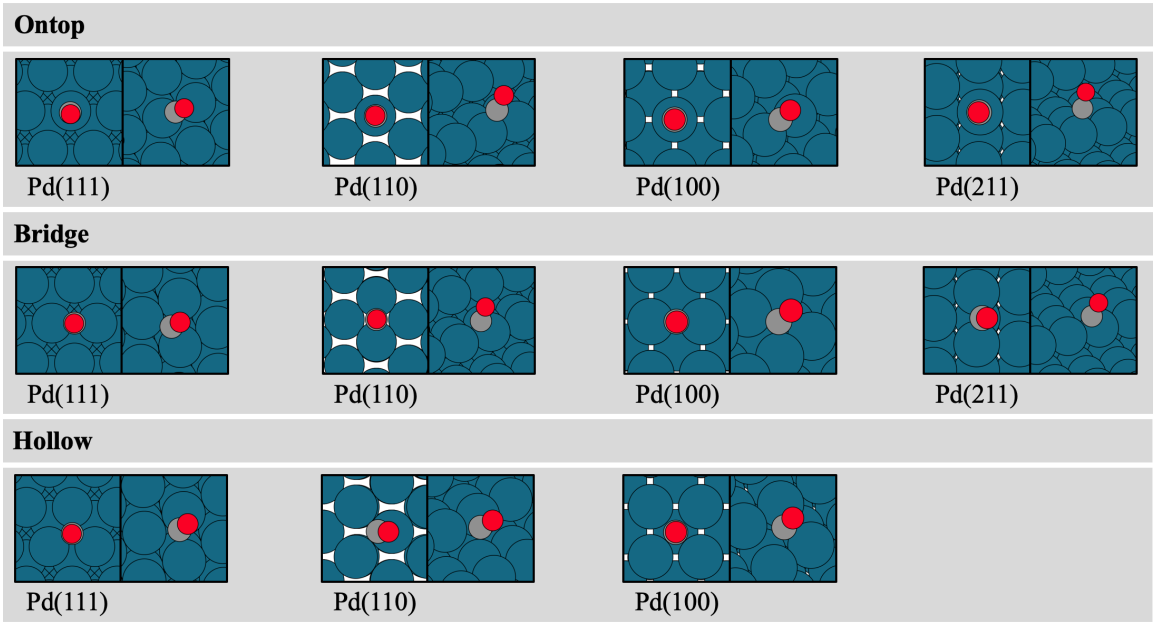

Figure 5.30.: CO molecules adsorbed on the (111), (110), (100), and (211) pristine surface facets of Pd crystals with one molecule in one unit cell of the slab. Red circles represent O atoms, dark gray circles C atoms, large yellow circles Ce atoms, and petrol circles Pd atoms. The total energies are listed in the Appendix in Table A.21.

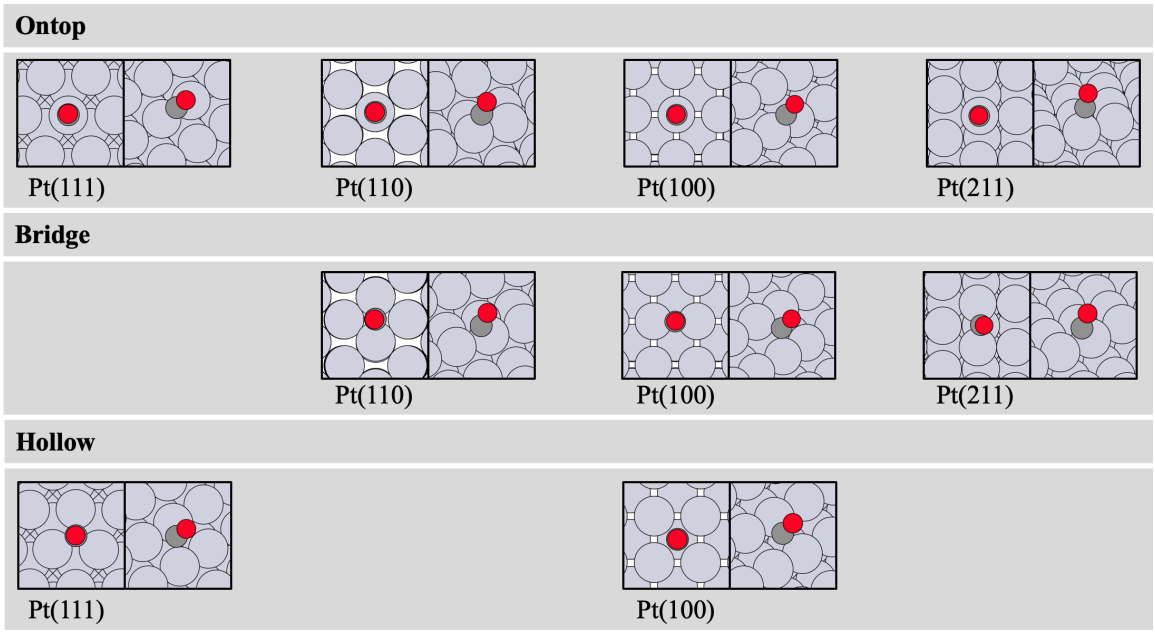

Figure 5.31.: CO molecules adsorbed on the (111), (110), (100), and (211) pristine surface facets of Pt crystals with one molecule in one unit cell of the slab. Red circles represent O atoms, dark gray circles C atoms, large yellow circles Ce atoms, and gray circles Pt atoms. The total energies are listed in the Appendix in Table A.21.

He elucidates the energy gap between the HOMO (highest occupied molecular orbital) 5σ and LUMO (lowest unoccupied molecular orbital) 2π orbitals significantly influences

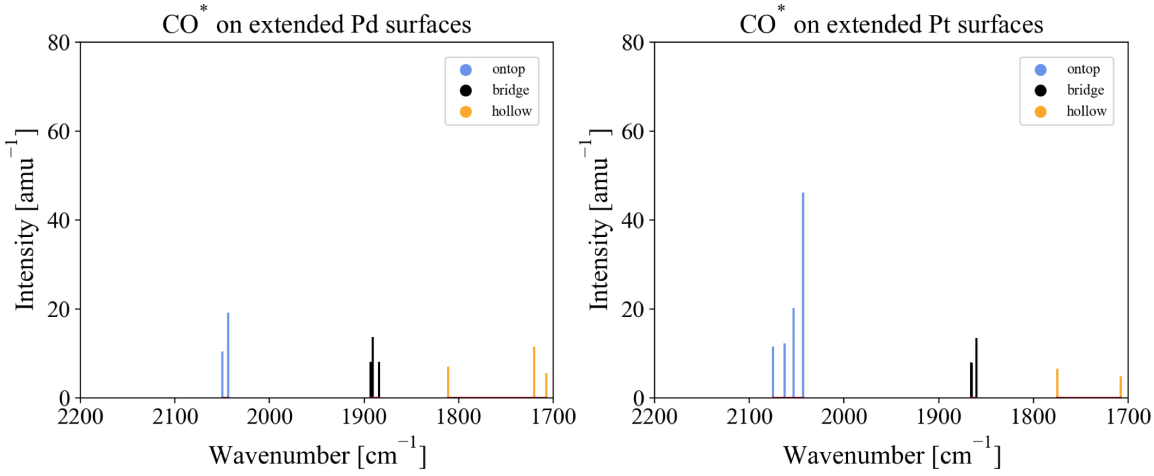

Figure 5.32.: Plot of the intensities in amu^{-1} of the CO vibrational frequencies in cm^{-1} against the CO vibrational frequencies wavenumber in cm^{-1} at 0 K. The CO molecules are adsorbed on Pd surfaces (left) and Pt surfaces (right). These refer to the species shown in Figure 5.30 for the Pd surfaces and Figure 5.31 for the Pt surfaces. The frequencies are differentiated between the adsorption sites by on top (blue), bridge (black), and hollow (orange). The vibrational frequencies and the according intensities are listed in Table 5.8.

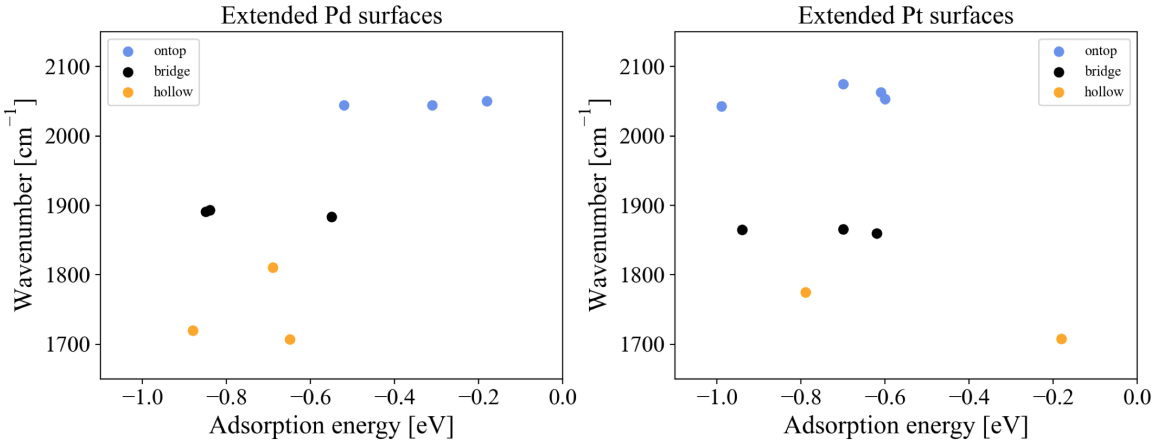

Figure 5.33.: Plot of the CO vibrational frequencies in cm^{-1} against CO adsorption energies in eV at 0 K. The CO molecules are adsorbed on Pd surfaces (left) and Pt surfaces (right). These refer to the species shown in Figure 5.30 for the Pd surfaces and Figure 5.31 for the Pt surfaces. The frequencies are differentiated between the adsorption sites by ontop (blue), bridge (black), and hollow (orange). The adsorption energies are listed in the Appendix in Table A.21 and the vibrational frequencies in Table A.21.

CO binding. Upon adsorption, the peak broadens towards the higher energy levels up to the Fermi level, forming what is commonly termed the $d_{\tilde{\pi}}$ orbital. Interactions with the 1π orbital, located below the Fermi level, exhibit a repulsive nature. Furthermore, he explains that the heat of adsorption diminishes as the d band fills up. Notably, computational models tend to favor adsorption sites with higher coordination, leading to mispredictions, particularly for Rh, Pt, and Cu surfaces, favoring hollow sites over top sites. The bonding situation of the CO molecule exhibits peculiar characteristics. The frontier orbitals of the CO molecule, including the HOMO and the LUMO, $2p^*$, engage with metal states of s

symmetry to establish a dative bond. This leads to the transfer of charge from the metal to the CO molecule, which is counterbalanced by a return transfer into the CO $2p^*$ orbital. This interplay results in the formation of a synergistic π bond, causing the internal C-O bond to weaken as a consequence of the increased presence of the antibonding CO $2p^*$ orbital during the return transfer.[291] The vibration spectra obtained in Figure 5.32 show that on-top bound CO molecules exhibit spectra in the range of 2040-2075 cm^{-1}, bridge at 1860-1895 cm^{-1}, and hollow at 1750-1800 cm^{-1}, both in Pd and Pt. However, Pt displays slightly higher frequencies for on-top by approximately 10-25 cm^{-1}, while bridge and hollow show around 30 cm^{-1} lower frequencies. The vibrational spectra determined here are consistent

Table 5.8.: Spectroscopic data obtained through DFT calculations of CO molecules adsorbed on structure-optimized pristine metal surfaces given in 5.30 for Pd and 5.31 for Pt in the appendix. The stretching vibrations of the CO molecule and their corresponding intensities were determined based on dipole moments. These can be compared with IR spectroscopic values.

	$\tilde{\nu}$[cm^{-1}]	I [amu^{-1}]	E_{ads}		$\tilde{\nu}$[cm^{-1}]	I [amu^{-1}]	E_{ads}
Spectroscopic data of CO adsorbed on of Pd and Pt							
Pd(111)				Pt(111)			
ontop	2050	10.5	-0.18	ontop	2075	11.6	-0.70
bridge	1884	8.1	-0.55	bridge	-	-	-
hollow	1811	7.0	-0.69	hollow	1775	6.5	-0.79
Pd(110)				Pt(110)			
ontop	2025	40.9	-0.39	ontop	2043	46.2	-0.99
bridge	1874	30.5	-0.70	bridge	1865	7.9	-0.94
hollow	1720	11.6	-0.70	hollow	-	-	-
Pd(100)				Pt(100)			
ontop	2044	11.4	-0.31	ontop	2063	12.3	-0.61
bridge	1893	8.1	-0.84	bridge	1866	8.0	-0.70
hollow	1707	5.6	-0.65	hollow	1708	4.9	-0.18
Pd(211)				Pt(211)			
ontop	2044	19.2	-0.52	ontop	2053	20.2	-0.60
bridge	1891	13.7	-0.85	bridge	1860	13.4	-0.62
hollow	1779	9.69	-0.83	hollow	-	-	-

with those experimentally determined by Spezziati et al., as listed in Section 1.6.[28,142] The vibration spectra obtained here are intended to serve as a reference for nanometer clusters, as these can be approximated with noble metal surfaces. The adsorption energies depicted in Figure 5.33 show that the adsorption sites are found within a range, depending on the adsorption site where the CO is located. For the Pd surface facets, the hollow sites are at approximately -0.80 eV, indicating the strongest binding. The bridge sites range from -0.60 to -0.80 eV, and the on-top sites range from -0.10 to -0.50 eV, with the latter binding the weakest. The Pt sites exhibit overall stronger binding. Here, the on-top site is the strongest, ranging from approximately -0.60 to -1.00 eV, the bridge site ranges from -0.60

to -0.90 eV, and the hollow site is the weakest, ranging from -0.20 to -0.80 eV. The binding relationships in Pt are thus inverted, and neither show a scaling relation. The investigation of Sadek and Wang, as confirmed by our study, reveals significant variations in the vibrational behavior and bonding attributes of CO depending on the adsorption site.[292] Moreover, their results did not conclusively demonstrate a direct correlation between the adsorption energy and the vibrational properties of the CO bond. Nonetheless, they observed a consistent trend showing a decrease in the frequency of CO vibrations as the length of the CO bond decreased.

6. Catalytic Activity of noble metal Catalysts towards O_2 Activation and CO Oxidation

6.1. Catalytic Activity of Pd_1 and Pt_1 Single-Atom Catalysts

Single-atom catalysts offer a unique paradigm as the ceria support acts as a multidentate ligand providing multiple binding sites for the oxygen atoms on the ceria surface. In this analogy to complex chemistry, O atoms function as coordination sites for the noble metal atom, acting as the active center of the catalyst. This concept can be further explained by considering the disassociation of a ligand, resulting in a change in the oxidation state. This process opens up an available adsorption site for a reactant to coordinate. The remaining ligands, represented by the O atoms, can then interact with the reactant, serving as superior leaving groups. This dynamic framework sheds light on the intriguing behavior of these catalysts during reactions, exhibiting parallels with principles observed in homogeneous catalysis within complex chemical systems. In this Section about single-atom catalysts, we examine the elementary reaction of CO oxidation on a partially oxidized single-atom catalyst featuring Pd or Pt as the active centers supported on all three pertinent ceria surface facets, (100), (110), and (111). During the lean phase of catalysts used in exhaust gas after-treatment, the catalyst operates under oxidative conditions due to the increased concentration of O_2 in the atmosphere. $O_{2(g)}$ molecules adsorb onto the heterogeneous catalyst and are dissociated by the active centers of noble metal atoms such as Pd and Pt, which can exist in the form of single-atom catalysts denoted as Pd_1 and Pt_1. The activated, adsorbed $O_2{}^*$ molecules subsequently become available for CO oxidation through either an LH mechanism or an MVK mechanism. In the LH mechanism, activated $O_2{}^*$ molecules lead to two dissociated $2O^*$ atoms, which are adsorbed in the at the single-atom catalysts. For the MVK mechanism, we assume that the consumed O atom for CO oxidation is part of the ceria crystal structure as an lattice O_l atom and is positioned adjacent to the activating noble metal atom. During the rich phase of exhaust gas after-treatment, hydrocarbons are oxidized, leading to the formation of CO molecules, which are pivotal in determining the reaction mechanisms until complete oxidation to the inert CO_2 molecule occurs. The activation of the CO molecule upon adsorption onto the single-atom catalyst is facilitated by electronic interactions, as introduced in Section 1.2.1 of the Introduction. The reactants

adsorb onto the heterogeneous catalyst, undergo activation, and traverse a transition state where the heterogeneous surface stabilizes them. The reaction mechanisms for CO oxidation on reduced single-atom catalysts of Pd and Pt species are considered to undergo the MvK mechanism. The reaction mechanisms of the LH and MVK mechanisms have already been discussed in the introduction in Section 1.4. The interaction with the non-innocent support is addressed in Section 1.3, and the activation by the noble metal atoms is discussed in Section 1.2.2. As demonstrated in Section 5.1 a charge transfer occurs between the noble metal atoms and the ceria surface, leading to the partial oxidation state of the noble metal. We will use the formal oxidation states, which can be assigned to the partial oxidation states through Figure 5.3, in the subsequent course of the work. In the following Sections, we examine these reaction mechanisms on the single-atom catalysts adsorbed on all three ceria surface facets, thereby experiencing different chemical environments. The ceria surface facets were introduced in the Introduction in Section 1.3.2. These surface facets possess different coordination possibilities.

6.1.1. O_2 Dissociation on Pd_1^0 and Pt_1^0 via LH Mechanism

The O_2 dissociation mechanism occurs according to the optimized structures as depicted in Figure 6.1 and 6.2. The O_2 dissociation on the stoichiometric surface of ceria takes place on top of the single-atom catalysts, which have a formal oxidation state of 0. The structure-optimized reaction mechanism steps as depicted in Figure 6.1 for the Pd_1 and in Figure 6.2 for the Pt_1 catalysts. On the (100) surface, the single-atom catalysts are embedded within a "pocket". These are shown in figure 6.1 and 6.2 in the respective upper rows. This represents the particularly stable configuration and is characteristic of this surface. In this "pocket", the Pt and Pd atoms are in a square-planar configuration, anchored by O atoms. On a stoichiometric surface, two O atoms are present diagonally to each other. The adsorbed O_2^* molecule on the Pt^0 and Pd^0 species, which is supported on a stoichiometric ceria surface, is adsorbed on top of the single-atom. The adsorption causes a bond elongation from 1.23 Å at 0 K in the gas phase to 1.31 Å for the adsorption on a Pd and 1.35 Å on a Pt single-atom catalyst. The transition state of the dissociation causes a bond extension into 1.88 Å for the adsorption on a Pd and 1.74 Å on a Pt single-atom catalyst. After the O_2 dissociation, a species standing upright on the ceria surface is considered, in which two O atoms point in the z-direction. This configuration is just one possibility among many possible ensembles of configurations. We have chosen this configuration to have an initial structure of $2O^*$ in case of a reverse reaction involving the formation of an O_2^* molecule, ensuring consistency between the forward and reverse reactions. As the reaction mechanism cycle progresses, the $2O^*$ atoms dissociated here will adopt a more stable configuration to undergo subsequent CO oxidation. These $2O^*$ atoms will then be

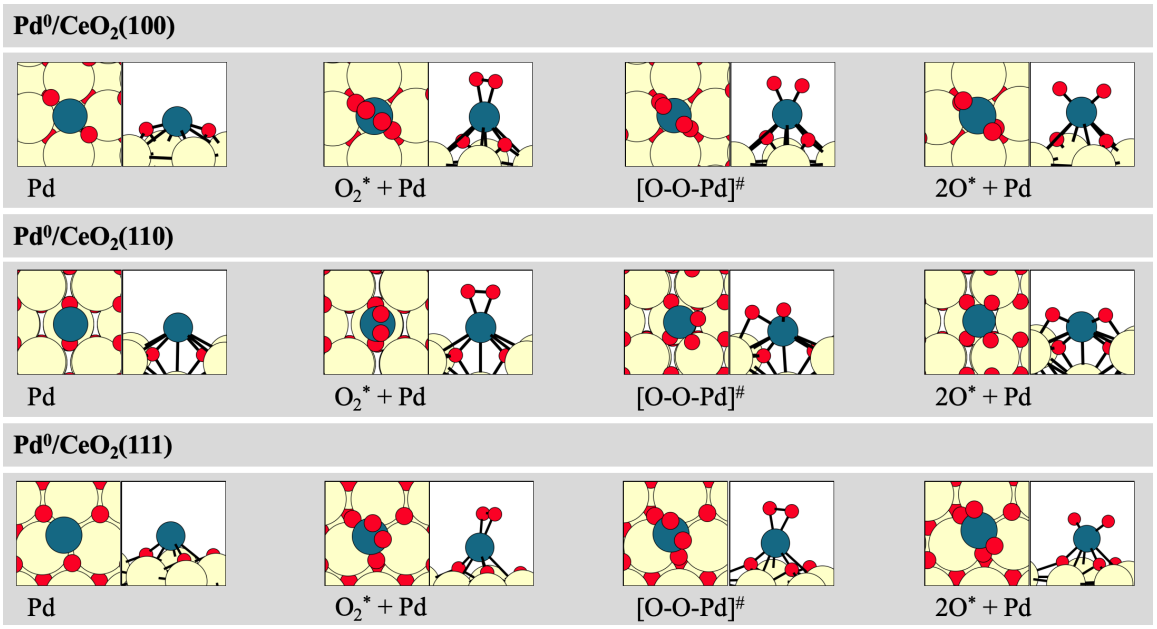

Figure 6.1.: Reaction mechanism of an O_2 dissociation on a structure-optimized Pd_1 single-atom catalyst adsorbed on the stoichiometric (100), (110) and (111) ceria surface facets. Red circles represent O atoms, large yellow circles Ce atoms, and petrol circles represent Pd atoms. The total energies are listed in the Appendix in Table A.22.

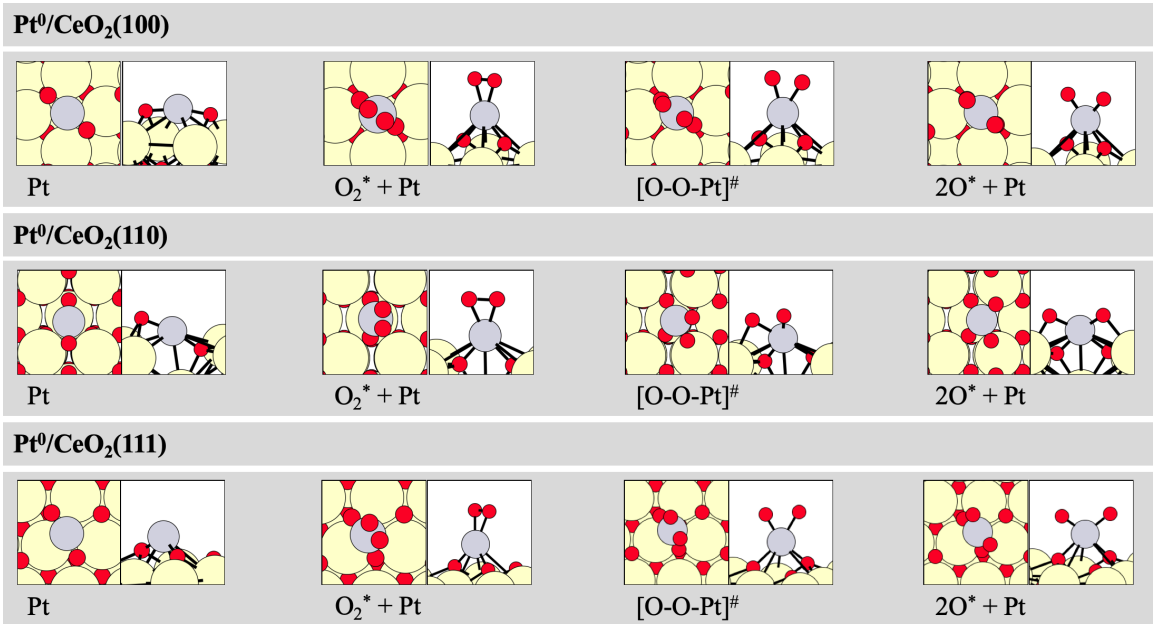

Figure 6.2.: Reaction mechanism of an O_2 dissociation on a structure-optimized Pt_1 single-atom catalyst adsorbed on the stoichiometric (100), (110) and (111) ceria surface facets. Red circles represent O atoms, large yellow circles Ce atoms, and gray circles indicate Pt atoms. The total energies are listed in the Appendix in Table A.22.

located in the opposite corner of the "pocket", surrounding the noble metal atom on the (100) surface. This will be further elaborated in the following Section. The (110) surface

configuration presents a "tunnel" structure that facilitates the adsorption of a single-atom between two Ce rows. The formation of this "tunnel" structure occurs due to the alignment of two parallel rows of cerium atoms, with an additional row of cerium atoms comprising the base of the tunnel. This surface structure of ceria provides a stable adsorption position for noble metal atoms. The single-atom catalyst is positioned within this "tunnel" structure, adopting a square-planar arrangement while anchored to the available two O atoms on the base of the "tunnel" on the stoichiometric surface of ceria. $O_{2(g)}$ adsorption takes place directly on top of the noble metal atom. During the dissociation process, the transition state involves anchoring to a third corner of the square-planar structure of the noble metal atom, with this O atom resting on a row of ceria atoms. Following the O_2 dissociation, both O atoms are situated on opposing cerium rows. This square-planar configuration on the surface includes two O atoms occupying the lower corners within the "tunnel" and two additional O atoms positioned at the corners above the ceria rows. Consequently, the noble metal atom is precisely anchored between the two cerium rows by four O atoms serving as anchoring sites. The adsorption causes a bond elongation from 1.23 Å at 0 K in the gas phase to 1.33 Å for the adsorption on a Pd and 1.37 Å on a Pt single-atom catalyst. The transition state of the dissociation causes a bond extension into 1.84 Å for the adsorption on a Pd and 1.84 Å on a Pt single-atom catalyst. The (111) surface represents the most

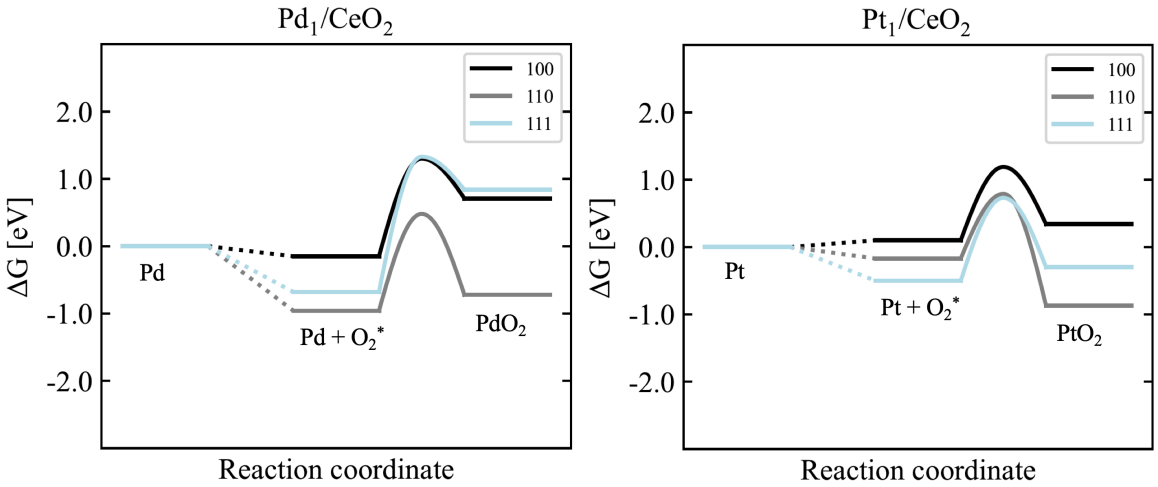

Figure 6.3.: Calculated Gibbs free energies of the structure-optimized O_2 dissociation elementary reaction steps on single-atom catalysts supported on stoichiometric ceria as depicted in Figure 6.1 for Pd and Figure 6.1 for Pt plotted against the reaction coordinate in a potential energy diagram. The Gibbs free energies are referenced to single-atom catalyst adsorbed on the stoichiometric ceria ceria surface facets (100), (110) and (111) in eV at 423.15 K. The total energies, the ZPE and the entropies are listed in the Appendix in Table A.22.

densely packed surface of ceria, providing limited space for the noble metal atoms to anchor within its surface structure. In this configuration, two O atoms serve as anchoring sites for the noble metal atom, as evidenced by prior research. A third O atom on this surface

structure is nearby and could also contribute to anchoring during a reaction mechanism. The $O_{2(g)}$ molecule adsorbs directly atop the noble metal atom. Following dissociation, a square-planar structure is established. However, unlike the more open surfaces, this square-planar configuration cannot lie flat on the surface and be embedded within a "pocket" as observed on the (100) surface or a "tunnel" as seen on the (110) surface. Instead, the noble metal atom is positioned "upright", supported by two O atoms while aligned with two additional O atoms in the z-direction. The adsorption of the $O_{2(g)}$ molecule causes a bond elongation from 1.23 Å at 0 K in the gas phase to 1.31 Å for the adsorption on a Pd and 1.35 Å on a Pt single-atom catalyst. The transition state of the dissociation causes a bond extension into 1.93 Å for the adsorption on a Pd and 1.89 Å on a Pt single-atom catalyst. This arrangement results in a square-planar structure with four anchoring O atoms. In this upright position, both the adsorption and the transition state and the dissociated state of the O_2^* molecule occur. This configuration is not the most stable, but it certainly represents a plausible reaction pathway. We opted for this configuration to maintain consistency in structure with other surfaces and to align with those observed in the O_2^* dissociation on sub-nanometer clusters as well as pristine metal surfaces, approximating the nanometer clusters. This approach is essential for subsequent analysis employing scaling relations, ensuring comparable transition state configurations to avoid generating inexplicable outliers by comparing apples with oranges. The potential energy diagrams for O_2 dissociation on

Table 6.1.: Calculated Gibbs free energies of the O_2 dissociation elementary reaction referenced to the single-atom catalyst supported on the stoichiometric ceria surface facets (100), (110) and (111) in eV and at 423.15 K of the structure-optimized elementary steps depicted in Figure 6.1 for Pd and Figure 6.2 for Pt. The Gibbs free energies are plotted in the potential energy diagrams 6.3. The bond lengths after adsorption and during the transition state are described as b.l. in Å at 0 K and included in gray letters.

	O_2^* [eV]	b.l. [Å]	$[O\text{-}O]^\#$ [eV]	b.l. [Å]	$2O^*$ [eV]
O_2 dissociation via LH Mechanism					
$Pd_1/CeO_2(100)$	-0.15	1.31	1.30	1.88	0.71
$Pd_1/CeO_2(110)$	-0.95	1.33	0.48	1.84	-0.72
$Pd_1/CeO_2(111)$	-0.68	1.31	1.33	1.93	0.84
$Pt_1/CeO_2(100)$	0.10	1.35	1.19	1.74	0.34
$Pt_1/CeO_2(110)$	-0.17	1.37	0.79	1.84	-0.87
$Pt_1/CeO_2(111)$	-0.50	1.35	0.73	1.89	-0.30

the stoichiometric ceria surface facets (100), (110), and (111), where a noble metal atom acts as the active center, are depicted in Figure 6.3. The reaction temperature is calculated at 423.15 K, and the associated energies are listed in Table 6.10. The temperature of 423.15 K is accounted by the use of *ab initio* thermodynamics, including the contributions of ZPE and entropy, as discussed in Section 3.7. At this temperature, the adsorption energies on the Pd single-atom catalyst for all surfaces are exothermic, ranging from -0.15 eV on the (100) surface, -0.95 eV on (110), and -0.68 eV on (111). Conversely, adsorption on the

Pt single-atom catalysts is consistently more positive. On the (100) surface, it is slightly endothermic at 0.10 eV, slightly exothermic on (110) at -0.17 eV, and notably exothermic on the (111) surface at -0.50 eV. The (100) surface structure exhibits the lowest adsorption energy for the $O_{2(g)}$ molecule on an embedded noble metal atom. Despite the structural similarities between Pd and Pt, significant differences between the surface facets (110) and (111) are evident. The adsorption energies exhibit a significantly different behavior compared to the resulting bond lengths. The associated bond lengths are approximately the same across all surfaces and both noble metals, with a difference of merely 0.02 Å on the surfaces on a metal atom of Pd or Pt, and a discrepancy of +0.04 Å for Pt compared to Pd. The reaction energy barriers following $O_{2(g)}$ adsorption on the Pd single-atom catalyst are 1.45 eV for the (100) surface, 1.43 eV for (110), and 2.01 eV for (111). For Pt, they are 1.08 eV on the (100) surface, 0.96 eV on (110), and 1.23 eV on the (111) surface. In Table 6.10, the energy barriers relative to $O_{2(g)}$ in the gas phase are listed. The reaction barriers following $O_{2(g)}$ adsorption are overall higher for the Pd single-atom catalysts compared to the Pt single-atom catalysts, with a difference of 0.37 eV on the (100) surface and 0.48 eV on the (110) surface, and 0.78 eV on the (111) surface. The reaction barriers before O_2 molecule adsorption relative to the gas phase are slightly higher for Pd on the (100) surface, with a difference of 0.11 eV, and significantly higher on the (111) surface, with a difference of 0.60 eV compared to Pt. However, on the (110) surface, due to the stronger adsorption energy on Pd, this difference is lower by 0.31 eV compared to Pt. In general, a comparison of the activation of O_2 dissociation across different surface facets of ceria in terms of reaction barriers relative to the gas phase reveals that the (100) surface exhibits the highest barriers, with 1.19 eV for Pd and 1.30 eV for Pt during O_2 dissociation. Conversely, the (110) surface displays the lowest barriers, measuring 0.48 eV for Pd and 0.79 eV for Pt. When utilizing a Pd single-atom catalyst, the latter presents the lowest barrier, thus representing the most strongly activating surface for O_2 dissociation. The (111) surface demonstrates significantly higher barriers of 1.33 eV for Pd, akin to the level observed on the (100) surface for dissociation energy, whereas Pt, at 0.73 eV, aligns more with the range of activation observed on the (110) surface for O_2 dissociation. The overall reaction energy represents the energy after O_2 dissociation with the formation of two adsorbed $2O^*$ atoms relative to the initial state with $O_{2(g)}$ in the gas phase. Interestingly, the O_2 dissociation on the (100) surface, for both Pd and Pt single-atom catalysts, proves to be an endothermic reaction process. On the (110) surface, this reaction process is notably exothermic, registering at -0.72 eV for Pd and -0.87 eV for Pt. Conversely, on the (111) surface, Pd exhibits a significant difference compared to the Pt single-atom catalyst. The reaction mechanism is markedly endothermic for Pd at 0.84 eV and exothermic for Pt at -0.30 eV. In summary, it can be concluded that the (100) surface is the least active for O_2

dissociation on the stoichiometric ceria surface activated by a single-atom catalyst, whereas the (110) surface is the most active. Additionally, the (111) surface is unreactive for Pd and active for Pt.

6.1.2. O_2 Dissociation on $1V_O$-$Pd_1^{-\delta}$ and $1V_O$-$Pt_1^{-\delta}$ via MvK Mechanism

Regeneration of the surface defect on the ceria support occurs through O_2 dissociation with the adsorption of an O^* atom from the O_2 molecule onto the V_O position. The single-atom catalysts as shown in figure 6.4 for Pd and 6.5 for Pt. In this deliberately simplified reaction cycle, assuming a single defect, after dissociation, another O^* atom remains adsorbed vicinal to the single noble metal atom, thereby oxidizing it to a formal oxidation state of +II forming the PdO and PtO species. In the case of the (100) surface, the $O_{2(g)}$ molecule adsorbs at one of the O sites, anchoring the noble metal atom. The dissociation occurs at a potential site, allowing the second O atom to migrate in the z-direction. After dissociation, this atom remains atop the noble metal atom, forming a square-planar structure with the two O atoms anchoring the surface, creating a square-planar configuration around the noble metal atom, with one corner remaining vacant. The $O_{2(g)}$ molecule adsorbs in vicinal position to the $Pt^{-\delta}$ and $Pd^{-\delta}$ species, which is supported on an V_O-defective (100) ceria surface facet. The adsorption causes a bond elongation from 1.23 Å at 0 K in the gas phase to 1.40 Å for the adsorption on a Pd and 1.42 Å on a Pt single-atom catalyst. The transition state of the dissociation causes a bond extension into 1.86 Å for the adsorption on a Pd and 1.76 Å on a Pt single-atom catalyst. At the (110) surface, the O_2^* molecule is not adsorbed onto the defect V_O due to steric hindrance caused by the noble metal atom. Because of the defect, the noble metal atom has migrated closer to it, obstructing accessibility. Nonetheless, the $O_{2(g)}$ molecule adsorbs further upwards along the z-axis, over the defect, lying not on the lower cerium row of the "tunnel" but on the upper cerium row. Upon dissociation, a configuration emerges where a square-planar structure is formed by only three O atoms: two O atoms situated at the bottom of the "tunnel" anchoring the Pd or Pt atom, and one O atom lying further along the upper row of cerium atoms. One O site of this square-planar structure represents a defect for the noble metal atom. The $O_{2(g)}$ molecule adsorbs in vicinal position to the $Pt^{-\delta}$ and $Pd^{-\delta}$ species, which is supported on an V_O-defective (110) ceria surface facet. The adsorption causes a bond elongation from 1.23 Å at 0 K in the gas phase to 1.40 Å for the adsorption on a Pd and 1.41 Å on a Pt single-atom catalyst. The transition state of the dissociation causes a bond extension into 1.83 Å for the adsorption on a Pd and 1.71 Å on a Pt single-atom catalyst. At the (111) surface, although two possible O sites are available for anchoring, for the sake of consistency, we"ve chosen to anchor the noble metal atom to only one O atom on the surface, creating an O surface lattice defect V_O. Consequently, the $O_{2(g)}$ molecule adsorbs onto this V_O defect and dissociates along the

single-atom catalyst in the z-direction, similar to the other surfaces. Following dissociation, an upright square-planar structure is formed, akin to the other surfaces, where two O atoms anchor the noble metal atoms, and a third O atom is oriented in the z-direction. This also results in a V_O defect at one corner of the square-planar configuration due to the missing O atom. The $O_{2(g)}$ molecule adsorbs in vicinal position to the $Pt^{-\delta}$ and $Pd^{-\delta}$ species, which is supported on an V_O-defective (111) ceria surface facet. The adsorption causes a bond elongation from 1.23 Å at 0 K in the gas phase to 1.45 Å for the adsorption on a Pd and 1.49 Å on a Pt single-atom catalyst. The transition state of the dissociation causes a bond extension into 1.86 Å for the adsorption on a Pd and 1.86 Å on a Pt single-atom catalyst. The potential energy diagrams for O_2 dissociation on the O-defective ceria surface facets

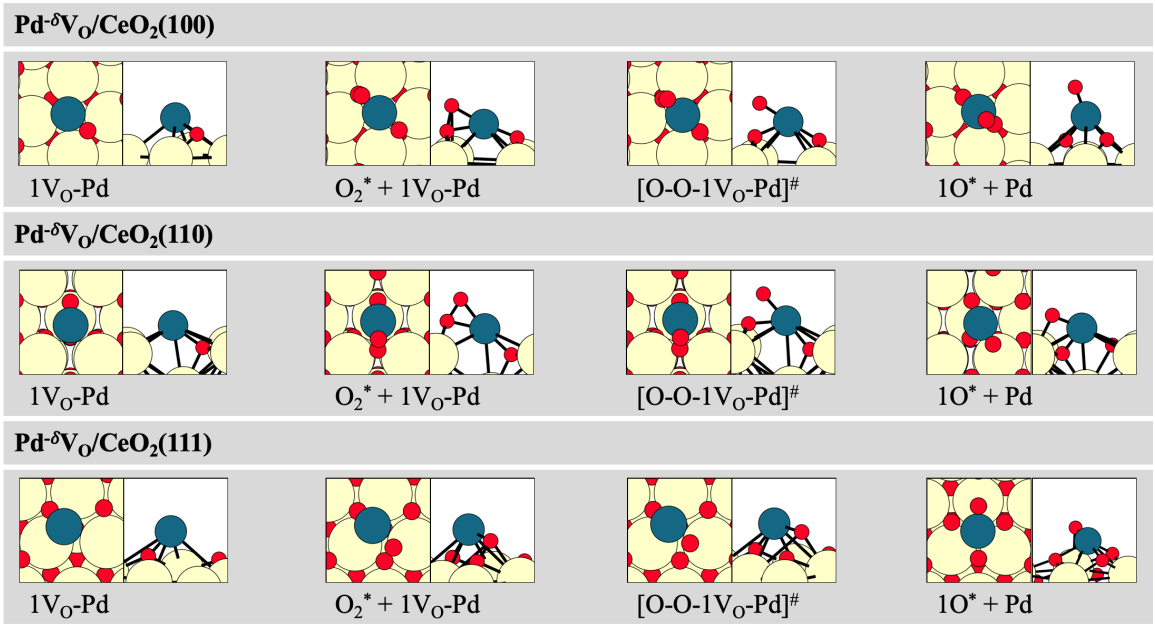

Figure 6.4.: Reaction mechanism of an O_2 dissociation on a structure-optimized V_O-Pd_1 single-atom catalyst adsorbed on the V_O-defective (100), (110) and (111) ceria surface facets. Red circles represent O atoms, large yellow circles Ce atoms, and petrol circles represent Pd atoms. The total energies are listed in the Appendix in Table A.23.

(100), (110), and (111), where a noble metal atom acts as the active center, are depicted in Figure 6.6. The reaction temperature is calculated at 423.15 K, and the associated energies are listed in Table 6.2. The temperature of 423.15 K is accounted by the use of *ab initio* thermodynamics, including the contributions of ZPE and entropy, as discussed in Section 3.7. At this temperature, the adsorption energies on the noble metal single-atom catalyst for all surfaces are strongly exothermic, ranging from -1.72 eV for Pd and -2.18 eV for Pt on the (100) surface, -0.86 eV for Pd and -1.21 eV for Pt on (110), and -1.43 eV for Pd and -1.55 eV for Pt on (111). The (100) surface structure exhibits the highest adsorption energy for the $O_{2(g)}$ molecule on an embedded noble metal atom. The associated bond lengths

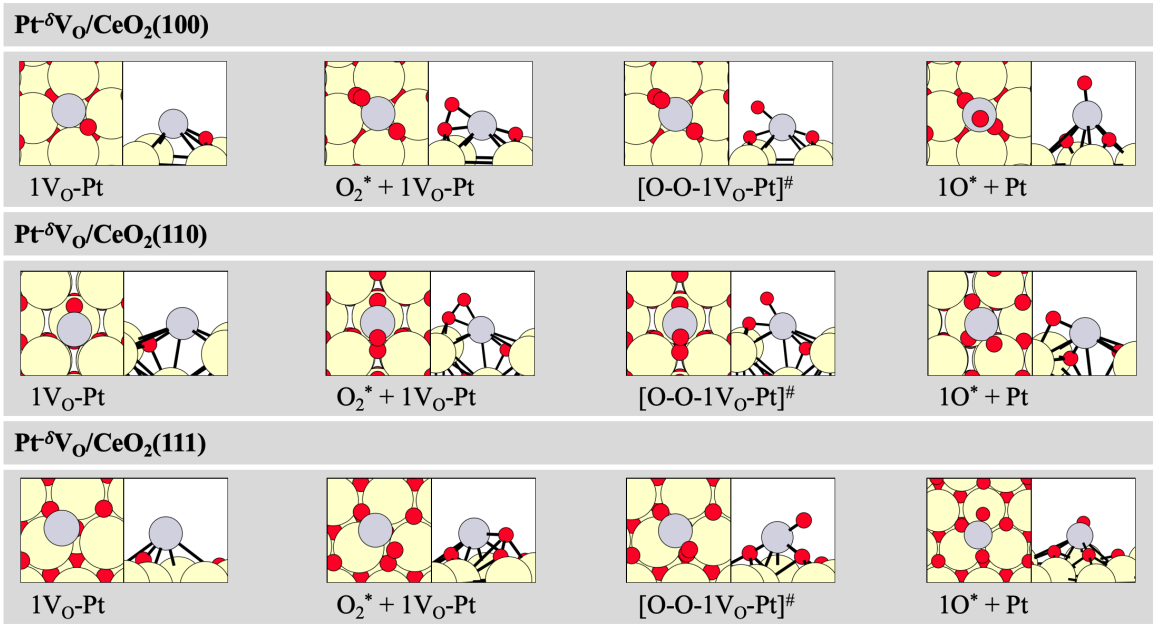

Figure 6.5.: Reaction mechanism of an O_2 dissociation on a structure-optimized V_O-Pt_1 single-atom catalyst adsorbed on the V_O-defective (100), (110) and (111) ceria surface facets. Red circles represent O atoms, large yellow circles Ce atoms, and gray circles indicate Pt atoms. The total energies are listed in the Appendix in Table A.23.

are approximately the same across all surfaces and both noble metals, with a difference of maximum 0.08 Å on the surfaces on a metal atom of Pd or Pt, and a discrepancy of + 0.04 Å for Pt compared to Pd. Again, it is worth mentioning that the DFT method used significantly affects the calculated bond lengths. The reaction energy barriers following $O_{2(g)}$ adsorption on the Pd single-atom catalyst are 0.90 eV for the (100) surface, 0.75 eV for (110), and 0.58 eV for (111). For Pt, they are 0.69 eV on the (100) surface, 0.60 eV on (110), and 0.63 eV for the (111) surface. However, the temperature influence is negligibly small, with a maximum difference of only 0.02 eV compared to 0 K. In Table 6.2, the energy barriers relative to $O_{2(g)}$ in the gas phase are listed. The reaction barriers following $O_{2(g)}$ adsorption are higher on the (100) and (110) surface facets for the Pd single-atom catalysts compared to the Pt single-atom catalysts, with a difference of 0.21 eV on the (100) surface and 0.15 eV for the (110) surface. For the (111) surface the barrier is lower for the Pd single-atom catalyst with a difference of 0.05 eV. The reaction barriers before $O_{2(g)}$ molecule adsorption relative to the gas phase are significantly lower for Pt on the (100) surface, with a difference of 0.67 eV, and slightly lower on the (111) surface, with a difference of 0.07 eV compared to Pd. On the (110) surface, the reaction barrier relative to $O_{2(g)}$ in the gas phase is the highest for both noble metal atoms, and it is higher for Pd with a difference of 0.50 eV compared to Pt. All reaction barriers relative to the initial state with the $O_{2(g)}$ molecule in the gas phase are exothermic during O_2 dissociation on the O surface lattice defect. A comparison of the

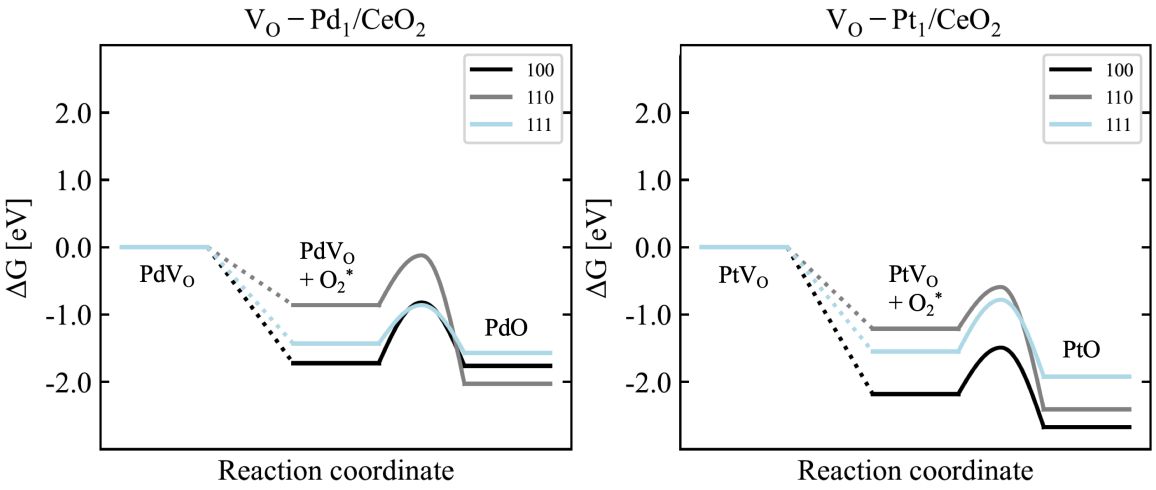

Figure 6.6.: Calculated Gibbs free energies of the structure-optimized O_2 dissociation elementary reaction steps on single-atom catalysts supported on V_O-defective ceria as depicted in Figure 6.4 for Pd and Figure 6.5 for Pt plotted against the reaction coordinate in a potential energy diagram. The Gibbs free energies are referenced to single-atom catalyst adsorbed on the single V_O-defective $1V_O$-CeO_2 surface facets (100), (110) and (111) in eV at 423.15 K. The total energies, the ZPE and the entropies are listed in the Appendix in Table A.23.

activation of O_2 dissociation across different surface facets of ceria in terms of reaction barriers relative to the gas phase reveals that the (100) surface exhibits the lowest barrier for the Pt single-atom catalyst, with -1.49 eV. Conversely, the Pd single-atom catalyst on the (110) surface displays the highest barriers, measuring -0.12 eV eV. Thus, the Pt single-atom

Table 6.2.: Calculated Gibbs free energies of the O_2 dissociation elementary reaction step referenced to the single-atom catalyst supported on the V_O-defective ceria surface facets (100), (110) and (111) with one defect V_O in eV and at 423.15 K of the structure-optimized elementary steps depicted in Figure 6.4 for Pd and Figure 6.5 for Pt. The Gibbs free energies are plotted in the potential energy diagrams 6.6. The bond lengths after adsorption and during the transition state are described as b.l. in Å at 0 K and included in gray letters.

	O_2^* [eV]	b.l. [Å]	$[O\text{-}O]^\#$ [eV]	b.l. [Å]	$2O^*$ [eV]
O_2 dissociation via LH Mechanism					
$1V_O$-Pd_1CeO_2(100)	-1.72	1.40	-0.82	1.86	-1.76
$1V_O$-Pd_1CeO_2(110)	-0.86	1.40	-0.12	1.83	-2.03
$1V_O$-Pd_1CeO_2(111)	-1.43	1.45	-0.86	1.86	-1.57
$1V_O$-Pt_1CeO_2(100)	-2.18	1.42	-1.49	1.76	-2.67
$1V_O$-Pt_1CeO_2(110)	-1.21	1.41	-0.62	1.71	-2.41
$1V_O$-Pt_1CeO_2(111)	-1.55	1.49	-0.78	1.86	-1.92

catalyst on a (100) surface facet with V_O defects in the vicinal position presents the lowest barrier, representing the most strongly activating surface for O_2 dissociation on O-defective surfaces. The overall reaction energy represents the energy after O_2 dissociation with the formation of one adsorbed O^* atom and one filled surface lattice O_l atom relative to the initial state with $O_{2(g)}$ in the gas phase and the V_O-defective surface. In all cases, this

process is exothermic, being the lowest at -1.57 eV for Pd on the (111) surface and the highest at -2.67 eV for Pt on the (100) surface. In summary, it can be concluded that the (111) surface is the least active for O_2 dissociation on the O-defective ceria surface activated by a single-atom catalyst, whereas the (100) surface is the most active. It can be stated that O_2 dissociation is favored on the O-deficient surface, whereas on the stoichiometric surface, it is significantly exothermic only on the (110) surface.

6.1.3. CO Oxidation at $2O^* + Pd_1^{+IV}$ and $2O^* + Pt_1^{+IV}$ via LH Mechanism

The formal oxidation states of the Pd and Pt noble metal atoms are determined by the two additionally adsorbed O^* atoms in the vicinal position. Despite this, there is still a charge transfer from the noble metal to the ceria surface. Hence, the actual oxidation state is partial, as discussed before in Section 5.1. The structure-optimized configurations are presented in Figure 6.7 for Pd and 6.8 for Pt, showing almost identical structures with two exceptions. One exception lies in the CO adsorption on the Pd single-atom catalyst embedded in a "pocket" on a (100) ceria surface. According to the DFT methods, this configuration is highly unstable and spontaneously reacts via CO oxidation to form a CO_2 molecule. Therefore, a prior adsorption of the CO molecule could not be generated. The noble metal atom does not provide an obvious adsorption site for the CO molecule, given its existing coordination with 4 O atoms forming a square-planar structure. Another less stable configuration that the noble metal can adopt is an octahedral configuration, coordinated with 6 O atoms. On the (100) surface, a distorted square pyramidal structure was generated for the Pt noble metal atom by adsorbing the CO molecule in a manner akin to an octahedral structure but tilted towards the ceria surface. On the (110) surface, the embedded square-planar Pd noble metal atom needed to be displaced from its four-coordinated position with 4 vicinal O atoms by one O atom. In the case of the Pt single-atom catalyst, a square pyramidal structure is generated on the (110) surface. In general, the CO molecule adsorbs in linearly to the Pd^{+IV} and Pt^{+IV} species. The transition state causes a bond elongation of the $CO_2{}^*$ molecules between one O^* and the C^* atom from 1.17 Å at 0 K in the gas phase to 1.93 Å during the CO oxidation on a Pd and 1.77 Å on a Pt single-atom catalyst on the (110) surface facet of ceria and to 2.20 Å on Pd and 2.03 Å on Pt on the (111) surface facet. This creates a vacant adsorption site, which, upon CO adsorption, regains a square-planar configuration with 3O atoms and one CO molecule. Conversely, on the Pt single-atom catalyst, a square pyramidal structure was achieved. Here, 4 O atoms form the square-planar structure, while the CO molecule constitutes the apex of the pyramid. On the (111) surface, a configuration was obtained where the CO molecule adsorbs in a square pyramidal fashion. Similar to previous structures, 4 O atoms form the square-planar structure, and the CO molecule comprises the apex of the pyramid. This structure may be one of the most unstable

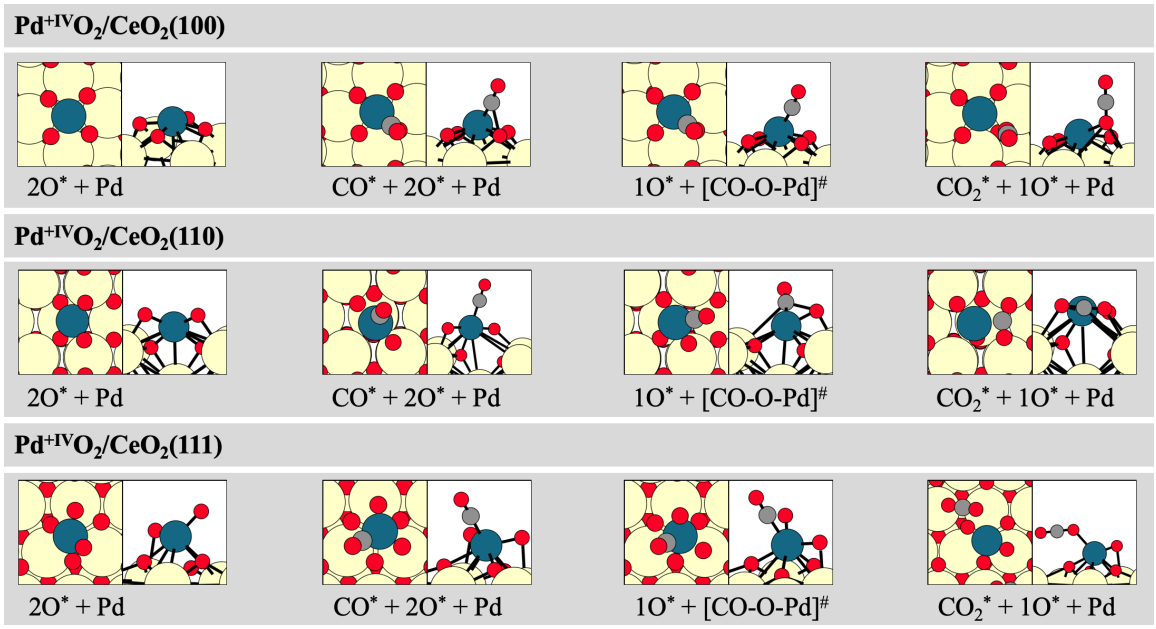

Figure 6.7.: Reaction mechanism of an CO oxidation on a structure-optimized $Pd_1{}^{+IV}$ single-atom catalyst adsorbed on the (100), (110) and (111) ceria surface facets with two $2O^*$ atoms adsorbed. Red circles represent O atoms, dark gray circles C atoms, large yellow circles Ce atoms, and petrol circles indicate Pd atoms. The total energies are listed in the Appendix in Table A.24.

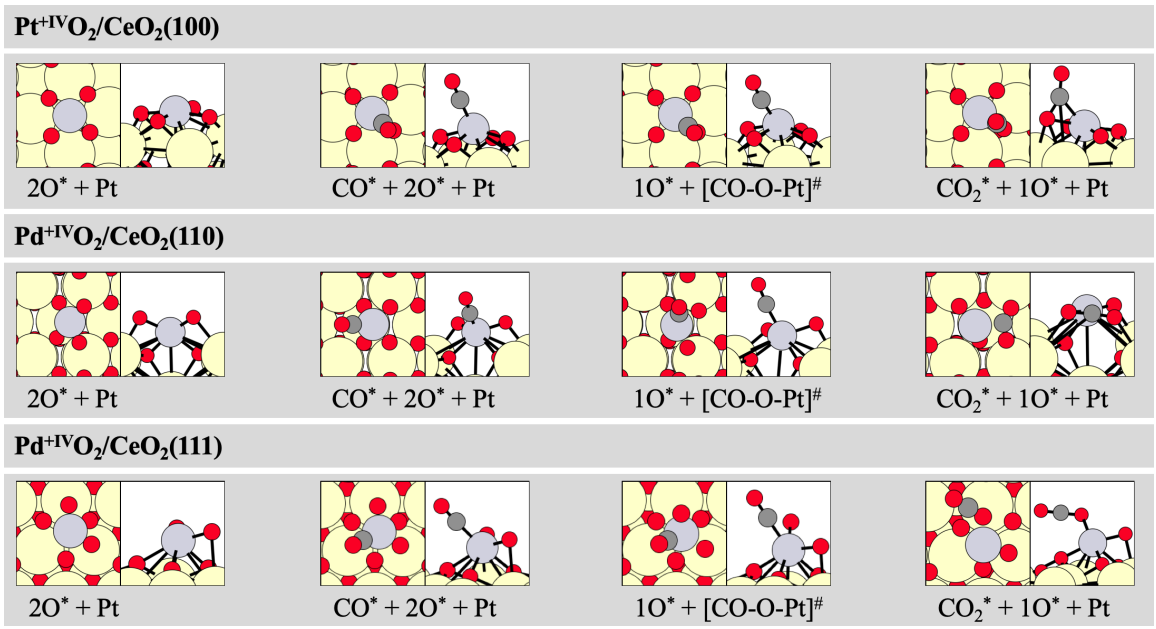

Figure 6.8.: Reaction mechanism of an CO oxidation on a structure-optimized $Pt_1{}^{+IV}$ single-atom catalyst adsorbed on the (100), (110) and (111) ceria surface facets with two $2O^*$ atoms adsorbed. Red circles represent O atoms, dark gray circles C atoms, large yellow circles Ce atoms, and gray circles indicate Pt atoms. The total energies are listed in the Appendix in Table A.24.

configurations possible. However, we chose this configuration to maintain consistency in the transition state configuration relative to the subnanometer clusters and the pristine noble

metal surfaces, which approach nanometer clusters. While on the (100) and (110) surfaces, the CO molecule migrates towards the O atom for CO oxidation, on the (111) surface, the O atom migrates towards the CO molecule for CO oxidation. The resulting CO_2^* molecule is adsorbed on the (100) and (110) surfaces before desorption. On the (100) surface, one of the O atoms of the CO_2^* molecule coordinates into a corner of the square-planar single noble metal atom. For Pd, it is already linear, whereas for Pt, it is still angled. On the (110) surface, the CO_2^* molecule remains angled for both Pd and Pt, coordinating with the C atom to the noble metal. On the (111) surface, one of the O atoms of the CO_2^* molecule coordinates to a corner of the square-planar noble metal atom, but for both noble metals, it is already linear. The bond angles of the formed CO_2^* molecules in the vdW-bound state to the surface are nearly 180°. For the (110) surface, the angle is significantly reduced to 145° on the Pd single atom and 141° on the Pt single atom. Overall, it can be concluded that the Pd single-atom catalyst allows for fewer configurations than Pt. The computation of

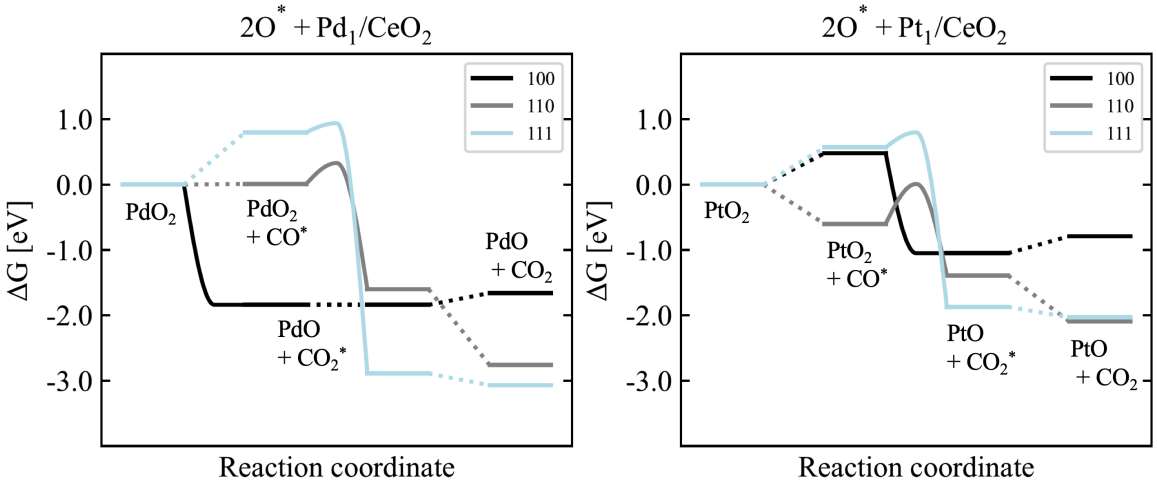

Figure 6.9.: Calculated Gibbs free energies of the structure-optimized CO oxidation elementary reaction steps on single-atom catalysts with the formal oxidation state of +IV as depicted in Figure 6.7 for Pd and Figure 6.8 for Pt plotted against the reaction coordinate in a potential energy diagram. The Gibbs free energies are referenced to single-atom catalyst adsorbed on the ceria surface facets (100), (110) and (111) with two O atoms $2O^*CeO_2$ in eV at 423.15 K. The total energies, the ZPE and the entropies are listed in the Appendix in Table A.24.

the Gibbs free energies of these configurations is depicted in a potential energy diagram as shown in Figure 6.9 and calculated at a reaction condition temperature of 423.15 K. The temperature of 423.15 K is accounted by the use of *ab initio* thermodynamics, including the contributions of ZPE and entropy, as discussed in Section 3.7. The $CO_{(g)}$ adsorption on the (100) surface leads to spontaneous oxidation with an adjacent O atom for Pd, forming a CO_2 molecule. On the Pt single-atom catalyst, initial adsorption occurs, eventually leading to spontaneous oxidation and the formation of an $CO_{2(g)}$ molecule. Adsorption on the (110) surface is slightly endothermic for Pd at this temperature, with 0.01 eV, while exothermic

for Pt with -0.60 eV. On the (111) surface, both are quite endothermic, reaching 0.80 eV for Pd and 0.57 eV for Pt. The latter is attributed to the unfavorable configuration chosen to maintain consistency with the transition state between the species. The reaction barrier is the smallest for the spontaneous CO oxidation reactions occurring on the (100) surface. Comparatively, the barriers on the (111) surface are lower at 0.14 eV for Pd and 0.22 eV for Pt, similar to those on the (110) surface which measure 0.33 eV for Pd and 0.62 eV for Pt. Therefore, in all cases, the barrier for Pt is slightly higher by approximately 0.29 eV compared to Pd. The $CO_2{}^*$ desorption under the operating temperature of 423.15 K is only slightly endothermic for the (100) surface with 0.18 eV for Pd and 0.25 eV for Pt. For the (110) surface it is significantly exothermic with -1.15 eV for Pd and -0.70 eV for Pt on the (110) surface. It is slightly exothermic for the (111) surface with -0.18 eV for Pd and -0.16 eV for Pt. The reaction energy of the elementary step remains exothermic in all cases. For Pd, the (100) surface exhibits much more exothermicity at -1.66 eV, while for Pt, it is much less at -0.79 eV. Both are the least exothermic among the surface facets. Additionally, both the (110) and (111) surfaces are significantly more exothermic for Pd at -2.76 eV and -3.07 eV, respectively, compared to Pt at -2.09 eV and -2.03 eV. The barriers

Table 6.3.: Calculated Gibbs free energies of the CO oxidation elementary reaction step referenced to the single-atom catalyst supported on the ceria surface facets (100), (110), and (111) with the formal oxidation state of +IV in eV and at 423.15 K of the structure-optimized elementary steps depicted in Figure 6.8 for Pd and Figure 6.8 for Pt. The Gibbs free energies are plotted in the potential energy diagrams 6.9. The Bond length between the C^* and the O^* atom during the transition state is described as b.l. in Å at 0 K and included in gray letters. The bond angles in degree of the formed CO_2 molecules are given in gray letters. Non-optimizable structures with very low barriers are considered spontaneous reactions and are denoted as sp.

	CO^* [eV]	$[CO\text{-}O]^\#$ [eV]	b.l. [Å]	$CO_2{}^*$ [eV]	CO_2 [eV]	angle [°]
CO oxidation via LH Mechanism						
$2O^*$ + $Pd_1/CeO_2(100)$	sp.	sp.	-	-1.84	-1.66	173
$2O^*$ + $Pd_1/CeO_2(110)$	0.01	0.33	1.93	-1.60	-2.76	149
$2O^*$ + $Pd_1/CeO_2(111)$	0.80	0.94	2.20	-2.89	-3.07	178
$2O^*$ + $Pt_1/CeO_2(100)$	0.48	sp.	-	-1.05	-0.79	172
$2O^*$ + $Pt_1/CeO_2(110)$	-0.60	0.01	1.77	-1.39	-2.09	141
$2O^*$ + $Pt_1/CeO_2(111)$	0.57	0.80	2.03	-1.87	-2.03	178

relative to the initial state with $CO_{(g)}$ in the gas phase are 0.33 eV for Pd and 0.01 eV for Pt on the (110) surface, while on the (111) surface they are 0.94 eV for Pd and 0.80 eV for Pt, which is quite endothermic. Generally, it can be stated that CO oxidation under fully oxidized Pd and Pt single-atom catalysts is favored as the entire reaction is exothermic, and $CO_2{}^*$ desorption poses no inhibition. The reactions are even spontaneous for the (100) surface, although the barrier due to low adsorption is endothermic. The (111) surface would require a different configuration to achieve a lower oxidation state, creating a more stable configuration, resulting in barriers relative to the initial state with $CO_{(g)}$ in the gas phase

becoming exothermic. A similar situation was attempted for Pd on the (110) surface, yet it did not yield a lower barrier. For Pt, this configuration was not attempted, resulting in nearly neutral barriers. In general, regarding the surfaces and oxidation state, it can be stated that a lower coordination possibility to the surface but higher coordination to the reactants and O atoms results in higher barriers because the metal atom does not allow further coordination. On the (110) surface, which is slightly less densely packed than the (111) surface, the movement of the single-atom catalyst within the "tunnel" while retaining the oxidation state provides an alternative reaction path. However, the (100) surface proves to be the most reactive. The CO molecule adsorption on the Pt single-atom catalyst embedded in the (100) surface should be regarded as an artificial fragment, and the spontaneous reaction should be considered as given.

6.1.4. CO Oxidation at $1O^*$ + $Pd_1{}^{+II}$ and $1O^*$ + $Pt_1{}^{+II}$ via LH Mechanism

Within the typical temperature range found in lean-burn gas engine exhaust, existing research suggests that the active phase of the catalyst is a single-atom catalyst with an oxidation state of +II, as one O atom is adsorbed onto the vicinity of the noble metal atom. The structures

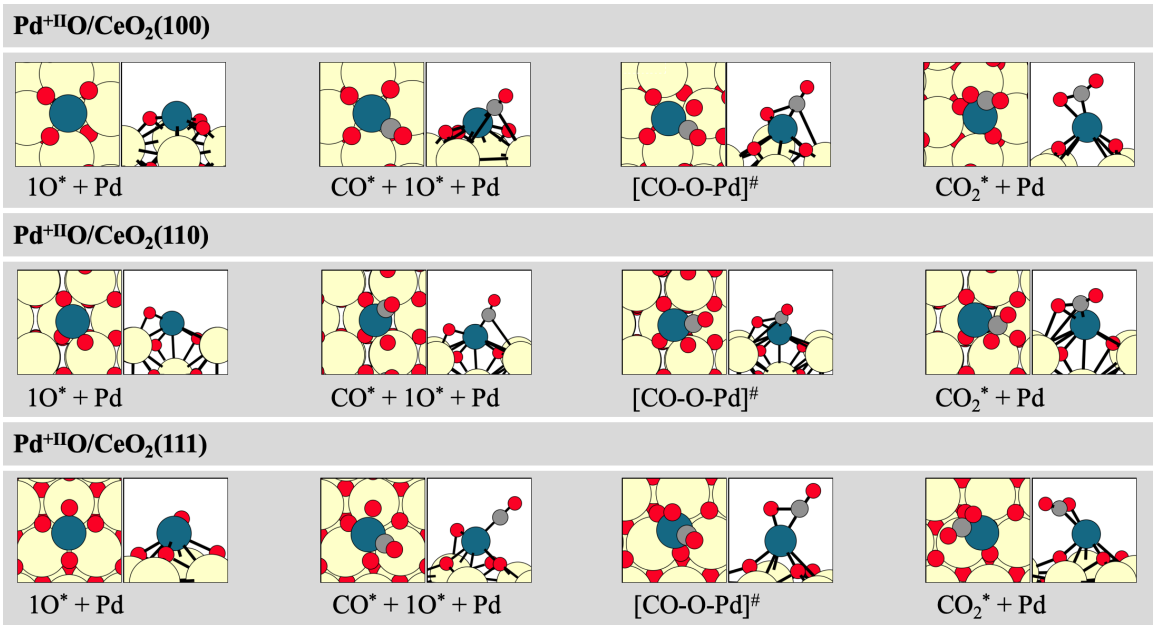

Figure 6.10.: Reaction mechanism of an CO oxidation on a structure-optimized $Pd_1{}^{+II}$ single-atom catalyst adsorbed on the (100), (110) and (111) ceria surface facets with one $1O^*$ atoms adsorbed. Red circles represent O atoms, dark gray circles C atoms, large yellow circles Ce atoms, and petrol circles indicate Pd atoms. The total energies are listed in the Appendix in Table A.25.

of Pd and Pt single-atom catalysts under the formal oxidation states of +II are depicted in Figure 6.10 and 6.11. This selection of configurations represents a possible ensemble that these single-atom catalysts may adopt under reactive conditions. The chosen configurations

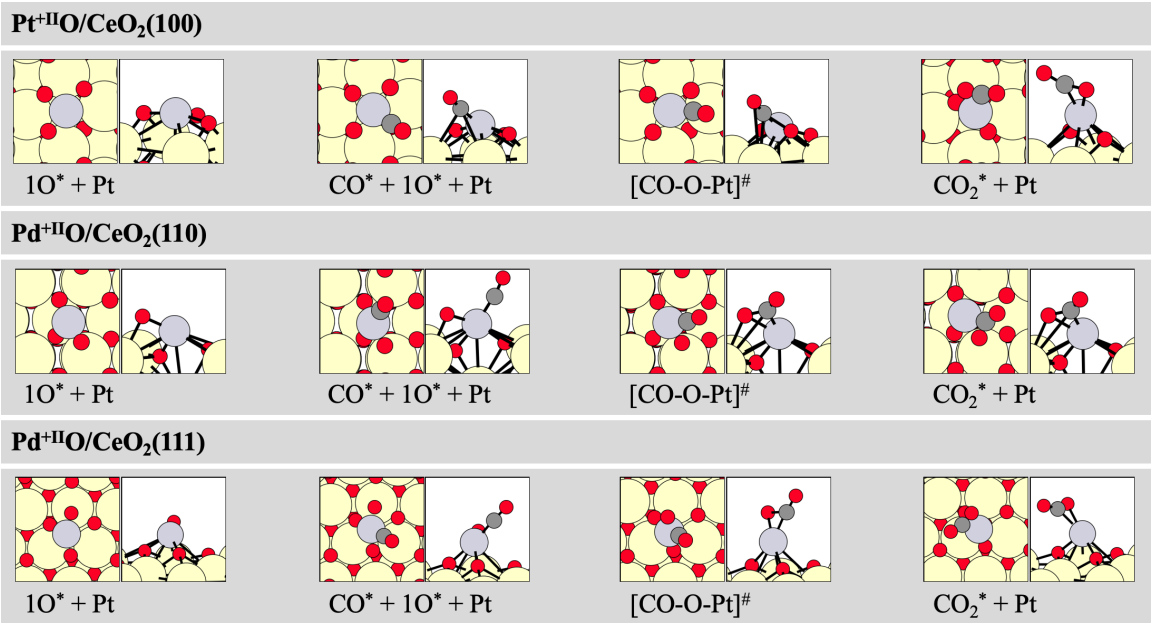

Figure 6.11.: Reaction mechanism of an CO oxidation on a structure-optimized $Pt_1{}^{+II}$ single-atom catalyst adsorbed on the (100), (110) and (111) ceria surface facets with one $1O^*$ atoms adsorbed. Red circles represent O atoms, dark gray circles C atoms, large yellow circles Ce atoms, and gray circles indicate Pt atoms. The total energies are listed in the Appendix in Table A.25.

aimed to maintain high consistency with other elementary reactions such as CO oxidation and preceding O_2 dissociation. Additionally, a general consistency with subnanometer clusters and pristine noble metal surfaces, which closely resemble nanometer clusters, was taken into account. The structures of the Pd and Pt single-atom catalysts are nearly identical. The partially oxidized PdO and PtO species exhibit a square-planar configuration on all three ceria surfaces, with two O atoms from the stoichiometric ceria surface and an additional O atom coordinated at all three corners. One corner remains uncoordinated, allowing CO adsorption to occur. This leads to a complete square-planar configuration, anchoring the noble metal atom to the ceria surface through four ligands. During CO oxidation on the (100) surface, the reactants must migrate towards each other. However, the "pocket" structure of the surface generates steric hindrance, requiring the reactants to migrate across one of the cerium atoms. In the stoichiometric ceria (100) surface, where a noble metal atom is adsorbed within one of the "pockets", diagonal O atoms in vicinal positions to the noble metal atom provide a stable configuration. This stable configuration is initially not achieved through CO oxidation. During migration, while one of the three O atoms moves towards the CO molecule over a cerium atom, the remaining two O atoms are localized on one side, here on the left. As this configuration is highly unstable, structural optimizations using DFT methods did not yield a metastable configuration of the CO_2 formation, where the two O atoms are still localized on one side. Instead, it was inevitable for them to take

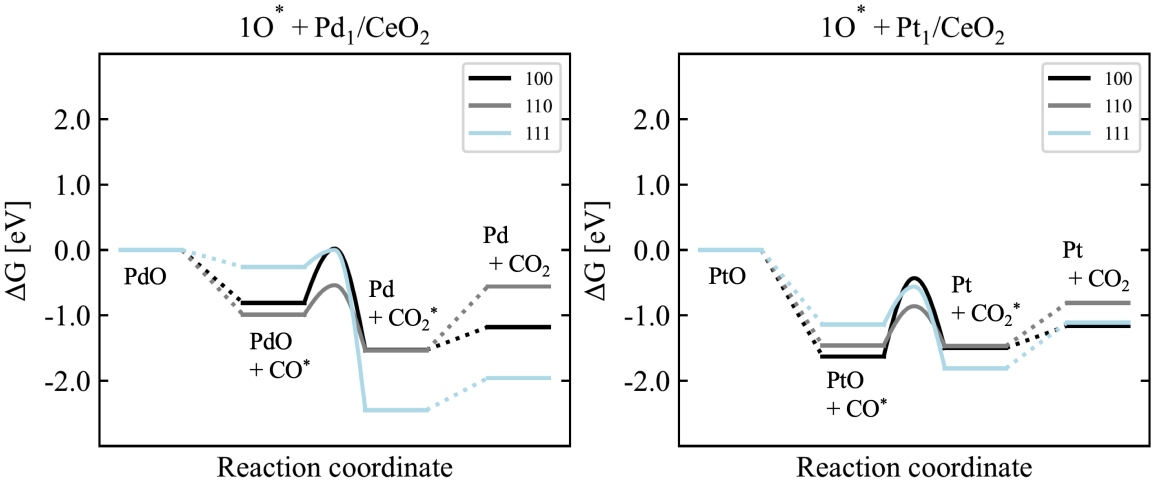

Figure 6.12.: Calculated Gibbs free energies of the structure-optimized CO oxidation elementary reaction steps on sinle-atom catalysts with the formal oxidation state of +II as depicted in Figure 6.10 for Pd and Figure 6.11 for Pt plotted against the reaction coordinate in a potential energy diagram. The Gibbs free energies are referenced to single-atom catalyst adsorbed on the ceria surface facets (100), (110) and (111) with one O atom O^*CeO_2 in eV at 423.15 K. The total energies, the ZPE and the entropies are listed in the Appendix in Table A.25.

the diagonal configuration towards each other. The resulting $CO_2{}^*$ molecule, adsorbed via a carbon atom on top of the noble metal atom Pd or Pt, is initially present in an angled state before ultimately desorbing. The CO oxidation on the (110) surface proceeds quite straightforwardly. The noble metal atom is anchored by two O atoms at the bottom of the "tunnel", along with a third O atom in a square-planar configuration. The fourth vacant position is occupied by a CO molecule. CO oxidation proceeds via the third O atom, which rests on one of the cerium rows, as the CO molecule migrates towards this O atom. The resulting $CO_2{}^*$ molecule is initially adsorbed via the carbon atom in an angled state before ultimately desorbing. The CO oxidation process on the (111) surface involves the adsorption of a CO molecule onto the available site within the square-planar configuration formed by two O atoms from the stoichiometric ceria surface and an additional O atom. The reactants, oriented perpendicular to the surface, migrate towards each other, forming a CO_2 molecule. Initially, this $CO_2{}^*$ molecule, coordinated through an O atom and the carbon atom atop the Pd and Pt metal atoms, remains in a bent conformation before eventually desorbing. The Gibbs free energies of the reactions are depicted in Figure 6.12 in potential energy diagrams. The associated Gibbs free energies of the individual steps are listed in Table 6.4. The Gibbs free energies are calculated at 423.15 K. The temperature of 423.15 K is accounted by the use of *ab initio* thermodynamics, including the contributions of ZPE and entropy, as discussed in Section 3.7. The CO adsorption on the Pd noble metal atoms is notably less exothermic at -0.81 eV for the (100) surface, -0.99 eV for the (110) surface, and only -0.26 eV for the (111) surface. In contrast, for Pt, the values are approximately 1

eV higher: -1.63 eV for the (100) surface, -1.46 eV for the (110) surface, and -1.14 eV for the (111) surface. However, the reaction barrier after CO adsorption is consistently slightly lower on the Pd single-atom catalyst, measuring 0.84 eV for the (100) surface, 0.45 eV for the (110) surface, and 0.26 eV for the (111) surface. This indicates a difference from Pt, with a range of about 0.20 to 0.40 eV, where Pt presents higher reaction barriers after CO adsorption, reaching 1.20 eV for the (100) surface, 0.60 eV for the (110) surface, and 0.57 eV for the (111) surface. The reaction barriers relative to the initial state with $CO_{(g)}$

Table 6.4.: Calculated Gibbs free energies of the CO oxidation elementary reaction step referenced to the single-atom catalyst supported on the ceria surface facets (100), (110), and (111) with the formal oxidation state of +II in eV and at 423.15 K of the structure-optimized elementary steps depicted in Figure 6.10 for Pd and Figure 6.11 for Pt. The Gibbs free energies are plotted in the potential energy diagrams 6.12. The Bond length between the C^* and the O^* atom during the transition state is described as b.l. in Å at 0 K and included in gray letters.

	CO^* [eV]	$[CO\text{-}O]^\#$ [eV]	b.l. [Å]	$CO_2{}^*$ [eV]	CO_2 [eV]	angle [°]
CO oxidation via LH Mechanism						
O^* + $Pd_1/CeO_2(100)$	-0.81	0.02	1.80	-1.53	-1.18	179
O^* + $Pd_1/CeO_2(110)$	-0.99	-0.54	1.70	-1.54	-0.56	149
O^* + $Pd_1/CeO_2(111)$	-0.26	0.00	1.98	-2.45	-1.96	178
O^* + $Pt_1/CeO_2(100)$	-1.63	-0.43	1.83	-1.50	-1.16	153
O^* + $Pt_1/CeO_2(110)$	-1.46	-0.86	1.70	-1.47	-0.81	141
O^* + $Pt_1/CeO_2(111)$	-1.14	-0.56	1.79	-1.81	-1.11	150

in the gas phase are mostly exothermic to nearly neutral at the given reaction temperature of 423.25 K. For Pd, this translates to 0.02 eV for the (100) surface, -0.54 eV for the (110) surface, and 0.00 eV for the (111) surface. Conversely, for Pt single-atom catalysts, all reaction barriers relative to $CO_{(g)}$ in the gas phase are exothermic, with -0.43 eV for the (100) surface, -0.86 eV for the (110) surface, and -0.56 eV for the (111) surface. The barriers for CO oxidation on the partially oxidized single-atom catalysts are consistently about 1 eV lower relative to the initial state with $CO_{(g)}$ in the gas phase, both for Pd and Pt as the active center, owing solely to CO adsorption. The barriers after CO adsorption are comparably high. This emphasizes the significance of systematically investigating configurations for elementary steps to facilitate direct comparison between oxidation states. The bond distances during the transition state for CO oxidation range approximately from 1.70 to 1.98 Å, as listed in table 6.4. These distances are quite similar between Pd and Pt. The differences are primarily observed among the different surfaces, yet they are also relatively minor. The overall lowest barrier is represented by CO oxidation on both Pd and Pt on the (110) surface. It is about 0.30 eV lower relative to the gas phase than CO oxidation on the other two surfaces. However, after CO adsorption, the (111) surface exhibits the lowest barrier, approximately 0.20 eV lower than the barriers of the other surfaces. The significant loss of activity is primarily attributed to the (100) surface, largely owing to

steric hindrance. The CO_2^* desorption, at the given reaction temperature of 423.15 K, is endothermic in all cases. The desorption energies for a Pd single-atom catalyst are 0.35 eV on the (100) surface, 0.97 eV on the (110) surface, and 0.49 eV on the (111) surface. In contrast, for Pt, the desorption energies are 0.34 eV on the (100) surface, 0.66 eV on the (110) surface, and 0.71 eV on the (111) surface. Generally speaking, it can be stated that the desorption energies are comparably high and not drastically elevated. The reaction energy of the elementary steps are exothermic in all cases, indicating the plausibility of CO_2^* desorption. The bond angle of the adsorbed CO_2^* molecules is approximately 150° if it does not transition into a vdW-bound state. Across Pd and Pt, these energies exhibit similar levels depending on the surface structures. On the (100) surface, the disparity is minimal, with -1.18 eV for Pd and -1.16 eV for Pt. On the (110) surface, Pd displays a slightly higher overall reaction energy at -0.56 eV, while Pt demonstrates a marginally more exothermic reaction at -0.81 eV. Conversely, on the (111) surface, Pd exhibits a lower overall reaction energy at -1.96 eV, while Pt shows a significantly more endothermic reaction at -1.11 eV.

6.1.5. CO Oxidation at Pd_1^0 and Pt_1^0 via MvK Mechanism

This Section delves into the MvK mechanism, considering a stoichiometric ceria surface on all three pertinent facets (100), (110), and (111). The CO oxidation process utilizes one of the O atoms from the ceria surface, which is an integral part of the crystal structure of ceria. Removing this O atom necessitates additional lattice energy to extract it from the crystal lattice. The structurally optimized configurations obtained through DFT methods are depicted in Figure 6.13 for Pd and 6.14 for Pt single-atom catalysts. The CO adsorption on the noble metal atom embedded within a "pocket" on a (100) surface occurs through coordination with one of the diagonally coordinated O atoms in vicinal proximity to the noble metal atom. This results in a standing square-planar configuration around the noble metal atom, leaving one corner uncoordinated. The transition state for CO oxidation occurs as the CO molecule migrates toward the O atom on the surface. Upon successful formation of CO_2, the O atom is slightly raised out of the crystal surface in the z-direction but remains notably integrated into the crystal structure. The resultant CO_2^* molecule is thus anchored and angled with a surface lattice O_l atom. After CO_2^* desorption, an the surface remains with a V_O defect. The CO oxidation on the (110) stoichiometric surface with a Pd metal atom adsorbed is hindered by steric constraints. The two remaining O atoms are positioned at the bottom of a "tunnel", while the adsorption of the CO molecule, leading to a square-planar configuration of the noble metal atom, occurs on the upper cerium rows. For Pt, the same configuration could not be achieved. In that case, structural optimization through DFT methods was necessary to obtain the stoichiometric surface, indicating that for Pd, a

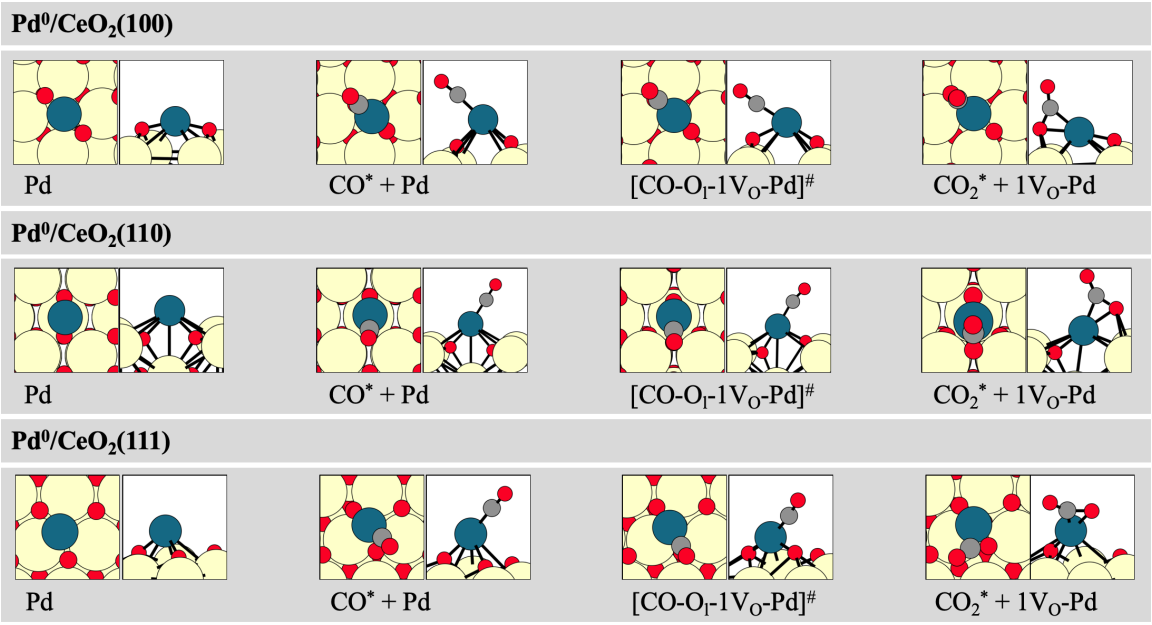

Figure 6.13.: Reaction mechanism of the CO oxidation on a structure-optimized $Pd_1{}^0$ single-atom catalyst adsorbed on the stoichiometric (100), (110) and (111) ceria surface facets. Red circles represent O atoms, dark gray circles C atoms, large yellow circles Ce atoms, and petrol circles indicate Pd atoms. The total energies are listed in the Appendix in Table A.26.

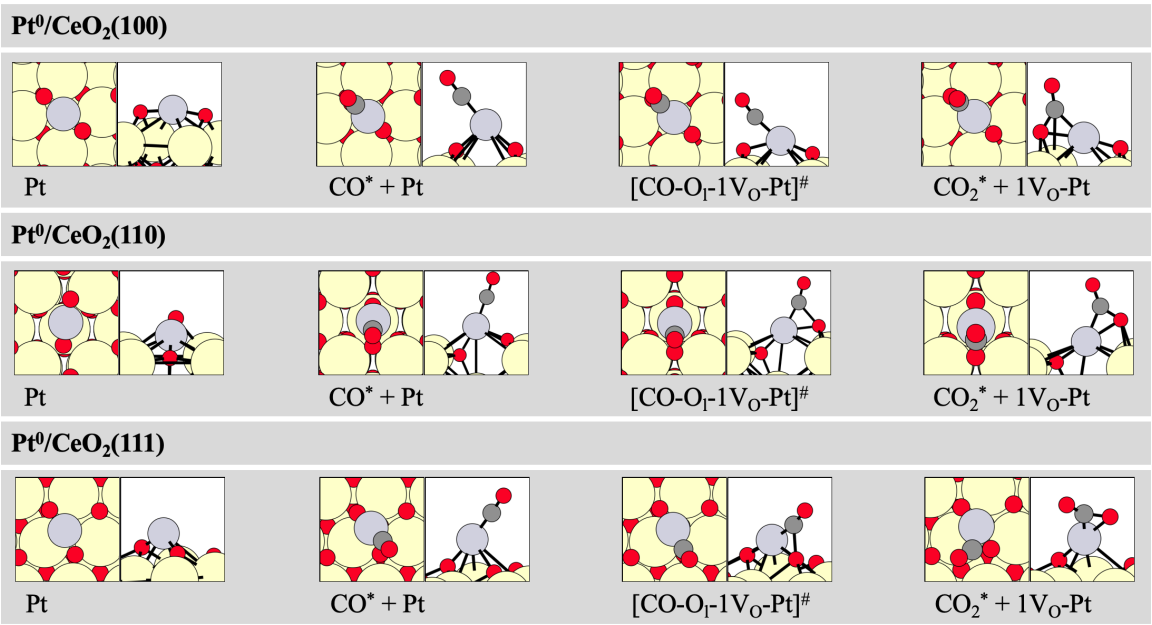

Figure 6.14.: Reaction mechanism of the CO oxidation on a structure-optimized $Pt_1{}^0$ single-atom catalyst adsorbed on the stoichiometric (100), (110) and (111) ceria surface facets. Red circles represent O atoms, dark gray circles C atoms, large yellow circles Ce atoms, and gray circles indicate Pt atoms. The total energies are listed in the Appendix in Table A.26.

configuration with two O atoms at the bottom of the "tunnel", anchoring the noble metal atom, might not be the more stable configuration. Hence, the energetic cost for O migration

can potentially be disregarded here. Upon successful CO oxidation, a CO_2 molecule is formed, anchored through an O atom at its previous position. The crystal structure of the ceria surface appears to be minimally affected after the prior O migration in the z-direction. The CO oxidation on the stoichiometric (111) ceria surface proceeds as a standing CO molecule adopts a square-planar configuration in the z-direction. This CO molecule migrates toward the anchoring O atoms of the surface, coordinated with the noble metal atom. During the transition state, a bond length of 1.81 to1.92 Å for Pd and 1.72 to 1.93 Å for Pt is achieved between the O_l atom and the CO molecule. The bond length according on the surfaces are listed in Table 6.5. Upon the successful formation of CO_2, an O atom remains in square-planar coordination with the noble metal atom, while the adsorbed $CO_2{}^*$ molecule is angled. Following the desorption of the $CO_2{}^*$ molecule, a V_O-$Pd^{-\delta}{}_1$ species for Pd and the V_O-$Pt^{-\delta}{}_1$ species for Pt is present on the (111) surface. The Gibbs free energies of

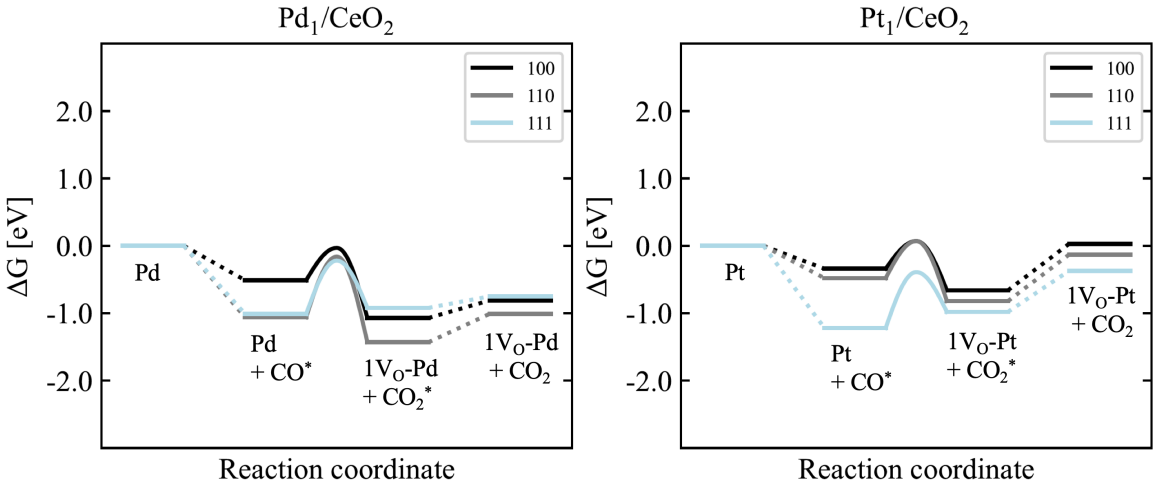

Figure 6.15.: Calculated Gibbs free energies of the structure-optimized CO oxidation elementary reaction steps on single-atom catalysts with the formal oxidation state of 0 as depicted in Figure 6.13 for Pd and Figure 6.14 for Pt plotted against the reaction coordinate in a potential energy diagram. The Gibbs free energies are referenced to single-atom catalyst adsorbed on the stoichiometric ceria CeO_2 surface facets (100), (110) and (111) in eV at 423.15 K. The total energies, the ZPE and the entropies are listed in the Appendix in Table A.26.

the structurally optimized elementary reactions for CO oxidation at 423.15 K, depicted in Figure 6.13 for Pd and Figure 6.14 for Pt, are presented in a potential energy diagram shown in Figure 6.15. The temperature of 423.15 K is accounted by the use of *ab initio* thermodynamics, including the contributions of ZPE and entropy, as discussed in Section 3.7. The corresponding Gibbs free energies are listed in Table 6.5. The CO adsorption occurs exothermically in all cases and is -0.51 eV for the (100) surface, -1.05 eV for (110) and -1.01 eV for the (111) surface for the Pd single-atom catalyst. The CO adsorption onto the Pd single-atom catalyst is stronger, with values of -0.51 eV and -1.05 eV, respectively. In contrast, the adsorption energies for Pt are -0.34 eV for the (100)surface, -0.48 eV for

(110) and -1.22 eV for (111). The subsequent reaction barriers relative to the adsorbed CO molecule are 0.47 eV on the (100) surface, 0.90 eV on the (110) surface, and 0.78 eV on the (111) surface for Pd. For the Pt noble metal atom, the barriers for catalyzed CO oxidation are 0.40 eV on the (100) surface, 0.55 eV on the (110) surface, and 0.82 eV on the (111) surface. Hence, the barriers on the (100) and (110) surfaces for Pd are slightly higher by 0.07 eV and 0.34 eV, respectively. Conversely, on the (111) surface, the barrier for Pt is 0.04 eV higher. Overall, it can be inferred that these differences are negligibly high and fall within the error tolerance of DFT methods. The reaction barrier relative to the initial state with the CO molecule in the gas phase is exothermic in all cases for the Pd single-atom catalyst, with values of -0.03 eV on the (100) surface, -0.16 eV on the (110) surface, and -0.22 eV on the (111) surface. On the Pt surface, the barriers relative to $CO_{(g)}$ in the gas phase are slightly endothermic, at 0.07 eV for both the (100) and (110) surfaces, but significantly exothermic at 0.39 eV on the (111) surface. Generally, it can be inferred that the barriers relative to $CO_{(g)}$ in the gas phase are almost neutral when the reaction temperature is at 423.15 K. At higher temperatures, an increase in these barriers can be expected due to the decrease in CO molecule adsorption energies. In the case of the (110) surface, the formation of the CO_2 molecule is endothermic relative to the adsorbed CO molecule, unlike the (100) and (111) surfaces. This suggests that CO_2 dissociation is more favorable on the (110) surface than CO oxidation. Subsequently, all $CO_2{}^*$ desorptions are endothermic under the given reaction temperature at 423.15 K, with values of 0.26 eV on the (100) surface for Pd and 0.69 eV for Pt, 0.41 eV on the (100) surface for Pd and 0.69 eV for Pt, 0.17 eV on the (100) surface for Pd and 0.61 eV for Pt. Thus, $CO_2{}^*$ desorption in Pt is notably more endothermic, approximately 0.50 eV higher than in Pd. The distance between the C atom and the O atom during the transition state of CO oxidation is approximately between 1.70 and 1.90 Å. The bond angle of the adsorbed $CO_2{}^*$ molecules is approximately 150°. It has also been shown that the lower the oxidation state of the single-atom catalyst, the smaller the angle. In an MvK mechanism, this angle consistently remains around 150°. The reaction energy of the elementary step is exothermic for Pd as a single-atom catalyst, with values of -0.81 eV on the (100) surface, -1.01 eV on (110), and -0.75 eV on (111). However, for Pt, the reaction is notably less exothermic. On the (100) surface, it is even slightly endothermic at 0.03 eV, slightly exothermic at -0.13 eV on (110), and more exothermic at -0.37 eV on the (111) surface. In general, it can be inferred that an MvK mechanism exhibits barriers relative to the initial state with $CO_{(g)}$ in the gas phase that is low enough for the reaction to occur only at low temperatures. As the temperature rises, $CO_2{}^*$ desorptions become less of a hindrance and are not significantly high for Pd at low temperatures but notably higher for Pt. Overall, an MvK mechanism is more probable on a Pd single-atom catalyst than on a Pt single-atom catalyst. After $CO_2{}^*$ desorption, an O-deficient surface V_O remains, which

Table 6.5.: Calculated Gibbs free energies of the CO oxidation elementary reaction step referenced to the single-atom catalyst supported on the stoichiometric ceria surface facets (100), (110) and (111) in eV and at 423.15 K of the structure-optimized elementary steps depicted in Figure 6.13 for Pd and Figure 6.14 for Pt. The Gibbs free energies are plotted in the potential energy diagrams 6.15. The Bond length between the C^* and the O^* atom during the transition state is described as b.l. in Å at 0 K and included in gray letters. The bond angles in degree of the formed CO_2 molecules are given in gray letters.

	CO^* [eV]	$[CO\text{-}O]^\#$ [eV]	b.l. [Å]	$CO_2{}^*$ [eV]	CO_2 [eV]	angle [°]
CO oxidation via MvK Mechanism						
$Pd_1/CeO_2(100)$	-0.51	-0.03	1.92	-1.07	-0.81	147
$Pd_1/CeO_2(110)$	-1.05	-0.16	1.84	-1.43	-1.01	147
$Pd_1/CeO_2(111)$	-1.01	-0.22	1.81	-0.92	-0.75	148
$Pt_1/CeO_2(100)$	-0.34	0.07	1.93	-0.66	0.03	141
$Pt_1/CeO_2(110)$	-0.48	0.07	1.94	-0.82	-0.13	142
$Pt_1/CeO_2(111)$	-1.22	-0.39	1.72	-0.98	-0.37	145

can be regenerated through O_2 dissociation, as elaborated in Section 6.1.2, to restore the oxidation state of the active species PdO or PtO.

6.2. Catalytic Activity of subnanometer Clusters

Subnanometer clusters represent an intermediate species between single-atom catalysts and nanometer-sized clusters. While single-atom catalysts and nanometer-sized clusters (which can be approximated by extended surfaces) have a lower variety of reaction positions, not only various positions on the cluster but also various electronic states come into play in the case of subnanometer clusters. Due to computational limitations, we must constrain ourselves to a specific number of reaction sites and a low cluster size of the subnanometer clusters. After identifying the smallest possible subnanometer clusters that converge in stability relative to the noble metal atoms in the bulk phase, the configurations of the adsorbates onto the clusters towards CO oxidation were investigated. In the following Sections, we will examine the O_2 dissociation on varying noble metal sizes as the Pd_3, Pt_3 and Pd_{10} and Pt_{10} subnanometer clusters to investigate a size-effect. We will compare these single-atom catalysts Pd and Pt to the subnanometer clusters. The Pd_{10} and Pt_{10} subnanometer clusters exhibit the same adsorption configuration concerning the O_2 activation among three noble metal atoms at the apex of the cluster as the Pd_3 and Pt_3 clusters. The comparative analysis conducted in this work will also extend to include the pristine metal surfaces of Pd and Pt. Additionally, both, the LH and the MvK mechanisms are investigated. In the case of an LH mechanism, the reaction occurs on the top surface of the Pd_3, Pt_3 and Pd_{10} and Pt_{10} subnanometer clusters. In the MvK mechanism, the reaction takes place at the interface between the subnanometer cluster and the ceria surface. The CO oxidation via the MvK mechanism is situated at the outer boundary of the adsorption surface of the cluster. Here,

an O atom from the ceria surface is consumed during the CO oxidation. The lattice O_l atom of the ceria surface is coordinated in the direct vicinity of a Pd or Pt atom of the cluster. In this study, a CO loading of $4CO^*$ molecules is considered for the Pd_3 and Pt_3 subnanometer clusters, and $7CO^*$ molecules for the Pd_{10} and Pt_{10} subnanometer clusters, gradually reducing the number of CO molecules successively. The O atoms are considered to be stoichiometric at each elementary CO oxidation reaction. For kinetic investigations, it is advisable to gradually reduce the O lattice defects and take into account the vibrational modes of the O atoms involved in the reaction on the ceria surface. This allows for the calculation of entropies at the reaction temperature to ensure thermodynamic consistency. However, as our focus is solely on the activity of noble metal sizes and we confine ourselves to elementary steps in this work, achieving thermodynamic consistency during the investigation of subnanometer cluster activity becomes challenging due to the complexity arising from the multitude of O species to be considered and is therefore excluded. Furthermore, care has been taken throughout this work to ensure that the selection of active sites and the configurations of the adsorbed reactants enable a meaningful comparison between single sites, subnanometer clusters, and nanometer-sized clusters. The configurations chosen in this work are thus similar for the pristine metal surfaces of Pd and Pt, the Pd_3 and Pt_3 subnanometer clusters, and the Pd_{10} and Pt_{10} subnanometer clusters, offering a comparable setup for subsequent analysis. Efforts have been made to ensure that the structures between Pd and Pt are nearly identical. The Pd_{10} flowerlike and Pt_{10} flowerlike clusters, each in a subnanometer size, chosen for further analysis of CO oxidation in this work, were selected for several reasons. It is likely that this is due to the proportional number of anchor positions provided by the O atoms on the (111) ceria surface to the resting Pd or Pt atoms. Secondly, they represent the next smallest size after the Pd_3 and Pt_3 clusters that exhibit stable configurations. This cluster is also interesting because, compared to the smaller cluster with only 3 noble metal atoms, it features a second row in the z-direction while simultaneously having the same reaction surface, a 3-atom second layer, as the small Pd_3 and Pt_3 clusters. This enables an initial exploration of size effects due to a second layer and a systematic increase in the number of atoms. This cluster was fully oxidized in a previous Section in this work through successive O adsorption, ranging from 1 to 7 O atoms on the surface. However, EXAFS studies have suggested that the existence of partially oxidized clusters due to O adsorption on the cluster surface is more likely.[285] In this Section, to investigate configurations during CO oxidation via an LH mechanism, we will use a range of O atoms from 1 to only 4 to simulate partial oxidation. The LH mechanism investigated on the Pd_{10} and Pt_{10} clusters is thermodynamically consistent and can thus serve as a basis for kinetic simulations, provided that successive O oxidation, up to partial oxidation with 4 O atoms, is considered. In this work, CO oxidation via an MvK mechanism is also investigated. In this

case, a CO^* coverage of up to $7CO^*$ molecules is considered. The rationale for this coverage stems from the temperature dependence, which was determined in Section 5.3.1 through *ab initio* calculations. It is likely that under rich reaction conditions, with a maximum temperature of 623.15 K, a coverage of approximately 6 to $7CO^*$ atoms can be assumed. In this Section, we assume that this CO^* coverage reacts successively through an MvK mechanism. This mechanism should occur under rich conditions since no O atoms adsorb on the now exposed surface sites of the clusters, preventing an LH mechanism. However, this is a simplifying assumption made to separate an LH and an MvK mechanism. Under real conditions, intermediate stages could exist where both reactions occur simultaneously, or the competition between these two mechanisms becomes significant, and only one of them dominates. Therefore, we aim to use DFT methods to shed light on an atomic level and provide a guiding idea to support these assumptions.

6.2.1. O_2 Dissociation on Pd_3 and Pt_3 Clusters via the LH and the MvK mechanism

The smallest cluster that can still be referred to as a "cluster" both topologically and electronically, is a subnanometer cluster consisting of 3 atoms. The elementary reactions for O_2 dissociation on the Pd_3 and Pt_3 subnanometer clusters were depicted in Figure 6.16 and 6.17, respectively, after structural optimization using DFT methods. The dissociation of

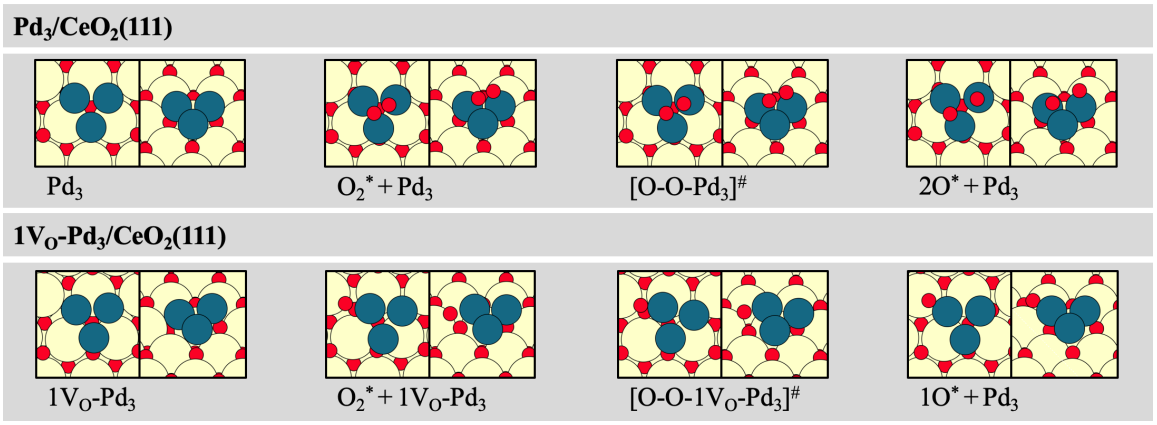

Figure 6.16.: Reaction mechanism of a O_2 dissociation on a structure-optimized Pd_3 clusters adsorbed on a stoichiometrc $CeO_2(111)$ surface. Red circles represent O atoms, large yellow circles Ce atoms, and petrol circles indicate Pd atoms. The total energies are listed in the Appendix in Table A.27.

O_2 on the Pd_3 and Pt_3 subnanometer clusters, supported on the stoichiometric (111) surface of ceria, involves all three noble metal atoms. One O atom of the adsorbed O_2^* molecule is adsorbed on top of one of the noble metal atoms, while the other is in a bridge position between the other two noble metal atoms. The adsorption on the Pd_3 and Pt_3 subnanometer cluster induces a bond elongation, increasing from 1.23 Å at 0 K in the gas phase to 1.40 Å for the adsorption on the Pd cluster and 1.52 Å on the Pt cluster. The transition state of the

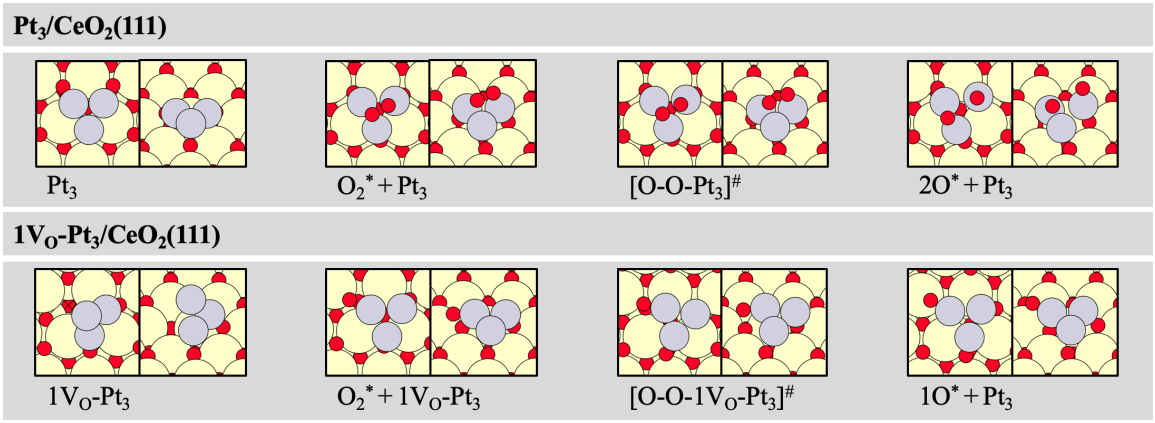

Figure 6.17.: Reaction mechanism of a O_2 dissociation on a structure-optimized Pt_3 clusters adsorbed on a stoichiometrc $CeO_2(111)$ surface. Red circles represent O atoms, large yellow circles Ce atoms, and gray circles indicate Pt atoms. The total energies are listed in the Appendix in Table A.27.

dissociation leads to a bond extension, measuring 1.62 Å on the Pd cluster and 1.71 Å on the Pt cluster. After dissociation, an O atom is located in the bridge position on the cluster, and another O atom is in an on-top position opposite the third noble metal atom of the cluster. The dissociation of O_2 on the $1V_O$-Pd_3 and $1V_O$-Pt_3 subnanometer clusters, supported on the V_O-defective (111) surface of ceria, occurs at the interface of the cluster with the ceria surface. The $O_{2(g)}$ molecule adsorbs into the V_O defect, thereby filling it through one of the O atoms. The bond length of the $O_2{}^*$ molecule extends from 1.23 Å at 0 K in the gas phase upon adsorption. The dissociation of the second O atom takes place along the side of the subnanometer cluster. For O_2 dissociation, the bond length during the transition state on the Pt cluster is longer with 1.80 Å over the LH mechanism and 1.71 Å over the MvK mechanism, compared to the Pd cluster with 1.79 Å over the LH mechanism and 1.62 Å over the MvK mechanism. The same tendencies also apply to the adsorbed $O_2{}^*$ molecules. The corresponding Gibbs free energies were computed for a reaction temperature of 423.15 K and are represented in the potential energy diagrams shown in Figure 6.18. The temperature of 423.15 K is accounted by the use of *ab initio* thermodynamics, including the contributions of ZPE and entropy, as discussed in Section 3.7. The Gibbs free energies are listed in Table 6.6. The adsorption energy of an $O_{2(g)}$ molecule is -1.82 eV on the Pd_3 cluster and -1.37 eV on the Pt_3 cluster in the case of a stoichiometric (111) surface of ceria. Thus, the adsorption energy for Pd is 0.49 eV higher than that for Pt. This difference might be attributed to structural and associated electronic considerations. The activation barrier starting from $O_{2(g)}$ adsorption is 0.23 eV for the Pd_3 cluster and 0.03 eV for the Pt_3 cluster. Relative to $O_{2(g)}$ in the gas phase, these are for the Pd_3 and Pt_3 clusters -1.59 eV and -1.34 eV, respectively. The reaction energy of the elementary step is also highly exothermic, with -1.82 eV for the Pd_3 cluster and -1.83 eV for the Pt_3 cluster. During the regeneration of an O-deficient ceria

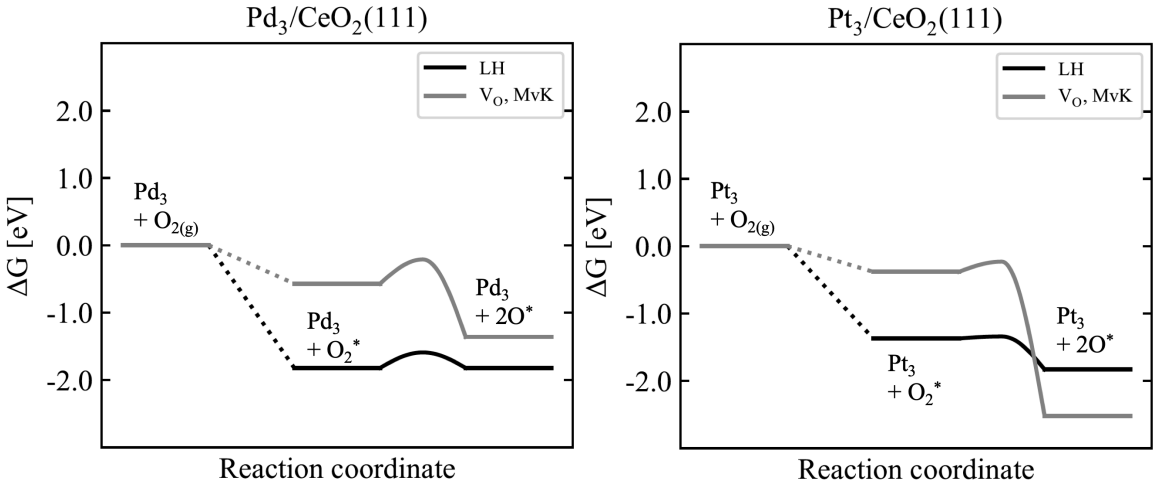

Figure 6.18.: Calculated Gibbs free energies of the structure-optimized O_2 dissociation elementary reaction steps on Pd_3 and Pt_3 clusters as depicted in Figure 6.13 for Pd and Figure 6.14 for Pt plotted against the reaction coordinate in a potential energy diagram. The Gibbs free energies are referenced to Pd_3 and Pt_3 catalysts adsorbed on the stoichiometric ceria CeO_2 surface facet (111) in eV at 423.15 K. The total energies, the ZPE and the entropies are listed in the Appendix in Table A.27.

(111) surface through O_2 dissociation, the adsorption energy is significantly lower, with approximately -0.57 eV for the Pd_3 cluster and -0.38 eV for the Pt_3 cluster. The activation barrier starting from $O_{2(g)}$ adsorption is 0.36 eV for the Pd_3 cluster and 0.15 eV for the Pt_3 cluster. These values are slightly higher than those observed on the stoichiometric surface of ceria, as described above. The reaction energies relative to $O_{2(g)}$ in the gas phase are -0.21 eV and -0.23 eV for the Pd_3 and Pt_3 clusters, respectively. These values, due to the lower adsorption strength, are significantly higher than those observed for the Pd_3 and Pt_3 clusters on the stoichiometric ceria surface. However, the reaction energy of the elementary step is exothermic with -1.36 eV for the $1V_O$-Pd_3 cluster and -2.52 eV for the $1V_O$-Pt_3 cluster. Overall, it can be concluded that the adsorption energy presents a hindrance, making these clusters less active than the subnanometer clusters supported on the stoichiometric ceria surface. This could be explained by some energy being consumed by the lattice structure that is being regenerated. However, further investigations at the electronic level are required to substantiate this claim. Nonetheless, this reaction is exothermic in both cases and on both noble metal clusters at a reaction temperature of 423.15 K.

6.2.2. CO Oxidation on $1O^*$ + Pd_3 and $1O^*$ + Pt_3 Cluster via the LH and MvK mechanism

Although we conducted O_2 dissociation in the previous Section to gain two adsorbed O^* atoms, we will limit our focus here to CO oxidation by a single O^* atom adsorbed on the Pd_3 and Pt_3 cluster. This choice is made because no significant information gain is expected

Table 6.6.: Calculated Gibbs free energies of the O_2 dissociation elementary reaction step referenced to the Pd_3 and Pt_3 clusters supported on the stoichiometric ceria surface facets (100), (110) and (111) in eV and at 423.15 K of the structure-optimized elementary steps depicted in Figure 6.16 for Pd and Figure 6.17 for Pt. The Gibbs free energies are plotted in the potential energy diagrams 6.18. The Bond length between the C^* and the O^* atom during the transition state is described as b.l. in Å at 0 K and included in gray letters.

	$O_2{}^*$ [eV]	b.l. [Å]	$[O\text{-}O]^\#$ [eV]	b.l. [Å]	$2O^*$ [eV]
O_2 dissociation via LH Mechanism					
$Pd_3CeO_2(111)$	-1.82	1.40	-1.59	1.62	-1.82
$Pt_3CeO_2(111)$	-1.37	1.52	-1.34	1.71	-1.83
O_2 dissociation via MvK Mechanism					
$1V_O\text{-}Pd_3CeO_2(111)$	-0.57	1.46	-0.21	1.79	-1.36
$1V_O\text{-}Pt_3CeO_2(111)$	-0.38	1.48	-0.23	1.80	-2.52

from two O atoms adsorbed on these clusters composed of only three Pd and Pt atoms. Figure 6.19 for Pd and 6.20 for Pt illustrate the LH mechanism for CO oxidation on a Pd_3 and a Pt_3 subnanometer cluster on the (111) surface of ceria, respectively. This elementary reaction corresponds to an LH mechanism. In this section, we have additionally considered the examination of an MvK mechanism. This allows for a direct comparison of the activity of this subnanometer cluster with respect to CO oxidation under oxidation by an O atom corresponding to an LH mechanism pathway or an MvK mechanism pathway. The oxidation of the subnanometer cluster could be compared to that of partial oxidation. This O atom

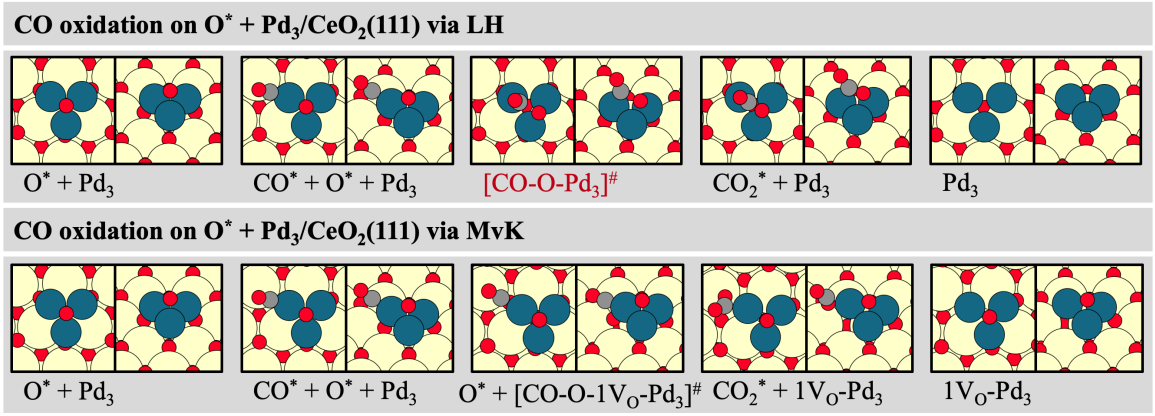

Figure 6.19.: Reaction mechanism of a CO oxidation on a structure-optimized O^* +Pd_3 clusters via the LH mechanism (upper row) and the MvK mechanism (lower row) adsorbed on a stoichiometric $CeO_2(111)$ surface. Red circles represent O atoms, dark gray circles C atoms, large yellow circles Ce atoms, and petrol circles indicate Pd atoms. The total energies are listed in the Appendix in Table A.28. The structure highlighted in red could not be structure-optimized because the reaction has such a low barrier that it can be assumed to be spontaneous. The total energies are listed in the Appendix in Table A.28.

is adsorbed on the hollow site of the cluster, coordinating with all three available noble metal atoms. The CO molecule adsorbs in both cases, the LH and the MvK mechanism. in a linear position onto one of the three noble metal atoms bent towards the ceria surface. To react with the O atom via the LH mechanism, the CO molecule consequently migrates

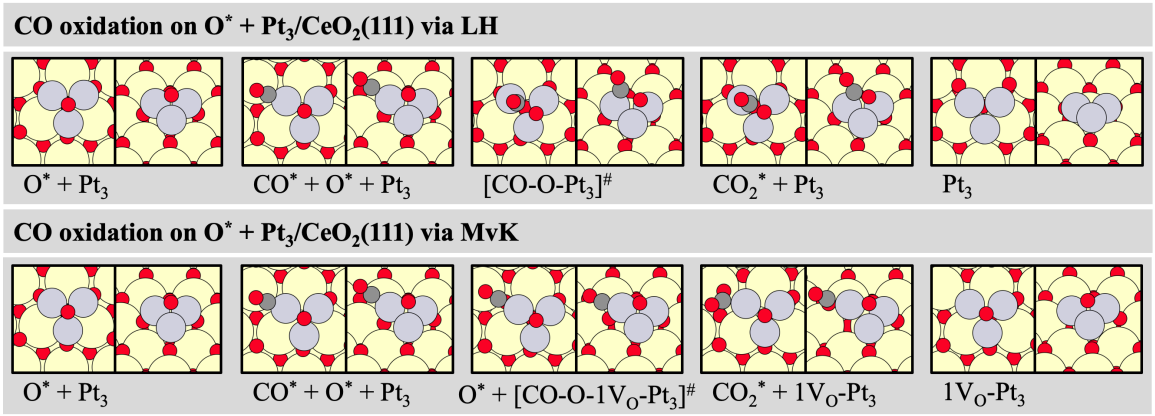

Figure 6.20.: Reaction mechanism of a CO oxidation on a structure-optimized O^* +Pt_3 clusters via the LH mechanism (upper row) and the MvK mechanism (lower row) adsorbed on a stoichiometric $CeO_2(111)$ surface. Red circles represent O atoms, dark gray circles C atoms, large yellow circles Ce atoms, and gray circles indicate Pt atoms. The total energies are listed in the Appendix in Table A.28.

towards the hollow site, while it migrates towards the ceria surface via the MvK mechanism. Upon the formation of CO_2, it becomes further angled, maintaining coordination over an O atom and the carbon atom on the hollow site, both on the Pd_3 and Pt_3 subnanometer clusters. After the desorption of the CO_2 molecule, the Pd_3 or Pt_3 subnanometer cluster returns to a stoichiometric (111) ceria surface in the case of the LH mechanism, but with an $1V_O$ defect in the case of the MvK mechanism. In the case of the LH mechanism, the cluster is reduced, whereas in the case of the MvK mechanism, the ceria gets reduced but the cluster remains oxidized. The bond length distance during the transition state for CO oxidation on the Pt_3 subnanometer cluster is 1.87 Å. The Gibbs free energies of the reaction mechanisms are

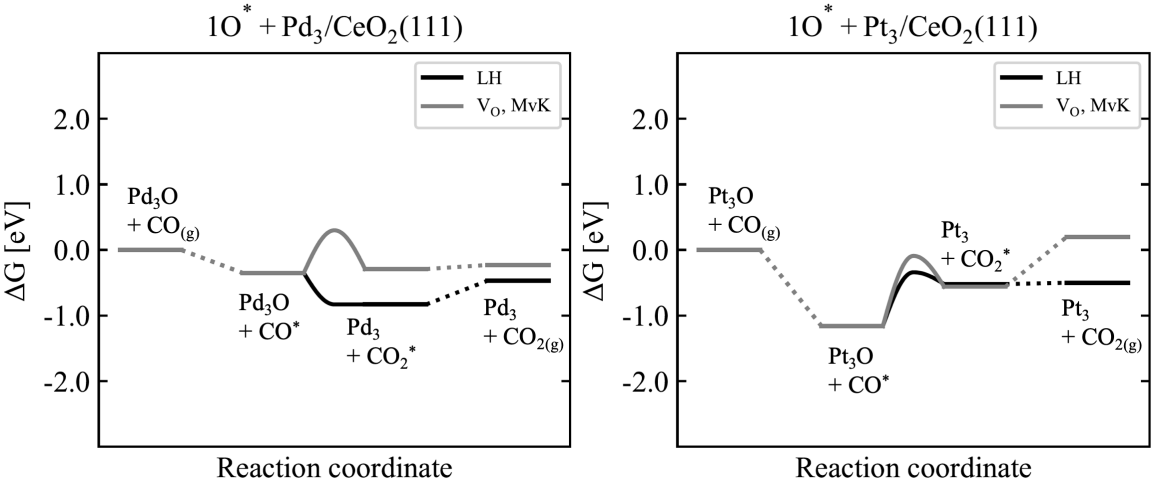

Figure 6.21.: Calculated Gibbs free energies of the structure-optimized CO oxidation elementary reaction steps on O^* + Pd_3 and O^* + Pt_3 cluster as depicted in Figure 6.19 for Pd and Figure 6.20 for Pt plotted against the reaction coordinate in a potential energy diagram. The Gibbs free energies are referenced to $1O^*$ + Pd_3 and $1O^*$ + Pt_3 catalysts adsorbed on the stoichiometric ceria CeO_2 surface facet (111) in eV at 423.15 K. The total energies, the ZPE and the entropies are listed in the Appendix in Table A.28.

depicted in Figure 6.21 and listed in Table 6.7. The adsorption energy of the CO molecule is significantly more exothermic at the Pt clusters with -1.16 eV under the reaction temperature of 423.15 K compared to Pd, which is at -0.35 eV. The CO oxidation via the LH mechanism on the $1O^*$ + Pd_3 subnanometer cluster is spontaneous, whereas on Pt_3, it encounters a reaction barrier of 0.82 eV after CO adsorption. Via the MvK mechanism, the barrier after CO adsorption is 0.65 eV for the Pd cluster and 1.08 eV for the Pt cluster. Consequently, it is clear that for the Pt cluster, the barriers differ by only 0.26 eV, while the difference for the Pd cluster between the MvK mechanism and the spontaneous LH mechanism is significantly higher at 1.03 eV. Furthermore, the reaction barrier relative to $CO_{(g)}$ in the gas phase for the Pt cluster is significantly lower, as the adsorption strength of the CO molecule is considerably greater. The reaction barrier relative to $CO_{(g)}$ in the gas phase is 0.33 eV for the Pd_3 cluster via the MvK mechanism and -0.34 eV via the LH mechanism and -0.09 eV via the MvK mechanism for the Pt_3 cluster. The desorption of CO_2 is endothermic in all cases with 0.36 eV via the LH mechanism and 0.06 eV via the MvK mechanism on the Pd_3 cluster and 0.02 eV via the LH mechanism and 0.76 eV via the MvK mechanism on the Pt_3 cluster. The reaction energy of the elementary step is exothermic via the LH

Table 6.7.: Calculated Gibbs free energies of the CO oxidation elementary reaction step referenced to the Pd_3 and Pt_3 clusters supported on the stoichiometric ceria surface facets (100), (110) and (111) in eV and at 423.15 K of the structure-optimized elementary steps depicted in Figure 6.19 for Pd and Figure 6.20 for Pt. The Gibbs free energies are plotted in the potential energy diagrams 6.21. The Bond length between the C^* and the O^* atom during the transition state is described as b.l. in Å at 0 K and included in gray letters. The bond angles in degree of the formed CO_2 molecules are given in gray letters. Non-optimizable structures with very low barriers are considered spontaneous reactions and are denoted as sp.

	CO^* [eV]	$[CO\text{-}O]^\#$ [eV]	b.l. [Å]	$CO_2{}^*$ [eV]	CO_2 [eV]	angle [°]
CO oxidation via LH Mechanism						
$1O^*$ + Pd_3	-0.35	sp.	-	-0.83	-0.47	131
$1O^*$ + Pt_3	-1.16	-0.34	1.87	-0.52	-0.50	125
CO oxidation via MvK Mechanism						
$1O^*$ + Pd_3	-0.35	0.33	1.79	-0.26	-0.23	144
$1O^*$ + Pt_3	-1.16	-0.09	1.64	-0.56	0.20	138

mechanism for both noble metal clusters, measuring -0.47 eV for the Pd_3 cluster and -0.50 eV for the Pt_3 cluster. Via the MvK mechanism the reaction energy of the elementary step is exothermic for the Pd_3 cluster with -0.23 eV but endothermic for the Pt_3 cluster with 0.20 eV. The general statement can be made here that CO oxidation via the LH mechanism on the Pd_3 and Pt_3 clusters is indeed plausible. However, the hindrance of $CO_2{}^*$ desorption is the primary factor contributing to the endothermic nature of the mechanism for the Pt cluster and an unfavorable reaction energy for the Pd cluster. Interestingly, one of the greatest influences of a partially oxidized subnanometer cluster is not the barrier for the formation of the CO_2 molecule, but rather the desorption of the formed CO_2 molecule, especially in

the case of the Pt cluster. The cause for this peculiarity of the Pt cluster lies in the strong adsorption energy of the reactants. The stronger adsorption by the Pt cluster is reflected in the shorter bond length during the transition state, which is 1.64 Å. Additionally, this is also shorter for the Pd cluster during the MvK mechanism at 1.79 Å, and longest during the LH mechanism at 1.87 Å. In contrast, a difference is observed in the case of the Pd cluster. An MvK mechanism is mainly hindered by the increased barrier, but not by the desorption of the CO_2 molecule. Through this comparison, a significant difference between the Pd and Pt clusters has now been established. However, conclusive evidence can only be obtained through the examination of experimental comparisons. The bond angle of the formed CO_2 molecules is quite small, approximately 125°, on the Pd_3 and Pt_3 subnanometer clusters via the LH mechanism. For the MvK mechanism, the angle for a carbon atom bound on top of one of the noble metal atoms is also unexpectedly small, approximately 144°. Pt and Pd differ only slightly.

6.2.3. CO Oxidation on (1-4)O^* + Pd_3 and a (1-4)O^* + Pt_3 Cluster via MvK Mechanism

In this Section, the activity of the Pd_3 and Pt_3 subnanometer clusters in CO oxidation via the MvK mechanism is examined. The corresponding structures are illustrated in Figure 6.22 for a Pd_3 cluster and Figure 6.23 for a Pt_3 cluster. The Pd_3 and the Pt_3 clusters provide four adsorption sites for the CO molecule. The ceria surface, in each elementary step we observe here, is in a stoichiometric state. The formed V_O lattice defects of one elementary step for CO oxidation are not involved in the subsequent elementary step for the CO oxidation of the next CO molecule. Thus, the elementary reactions considered here cannot be directly traversed in sequence. Our focus has been on a direct comparison between coverages by CO molecules, and hence, we have established consistency between the species considered. Thermodynamically, however, these elementary steps would not be consistent. If a kinetic investigation based on these elementary steps is conducted in the future, we would like to emphasize that consistency regarding the formed V_O species and their regeneration must be taken into account. In this study, we explore CO oxidation progressively from saturation with $4CO^*$ molecules to the complete consumption of the available CO molecules. We assumed complete saturation to simulate the MvK mechanism with the highest possible coverage by four CO molecules. Three 1-fold positions on top of the three Pd and Pt atoms are occupied, leaving a 3-fold site in the middle of the three chemisorbed Pd and Pt atoms, which can be occupied by a fourth CO molecule. All CO molecules adsorbed on the top sites of the noble metal are oriented towards the ceria surface and exhibit an angle of approximately 100° for Pd and 100° for Pt relative to the surface. Thus, considering the angle, the structures of the CO molecules at the border of the Pd and the Pt clusters are quite

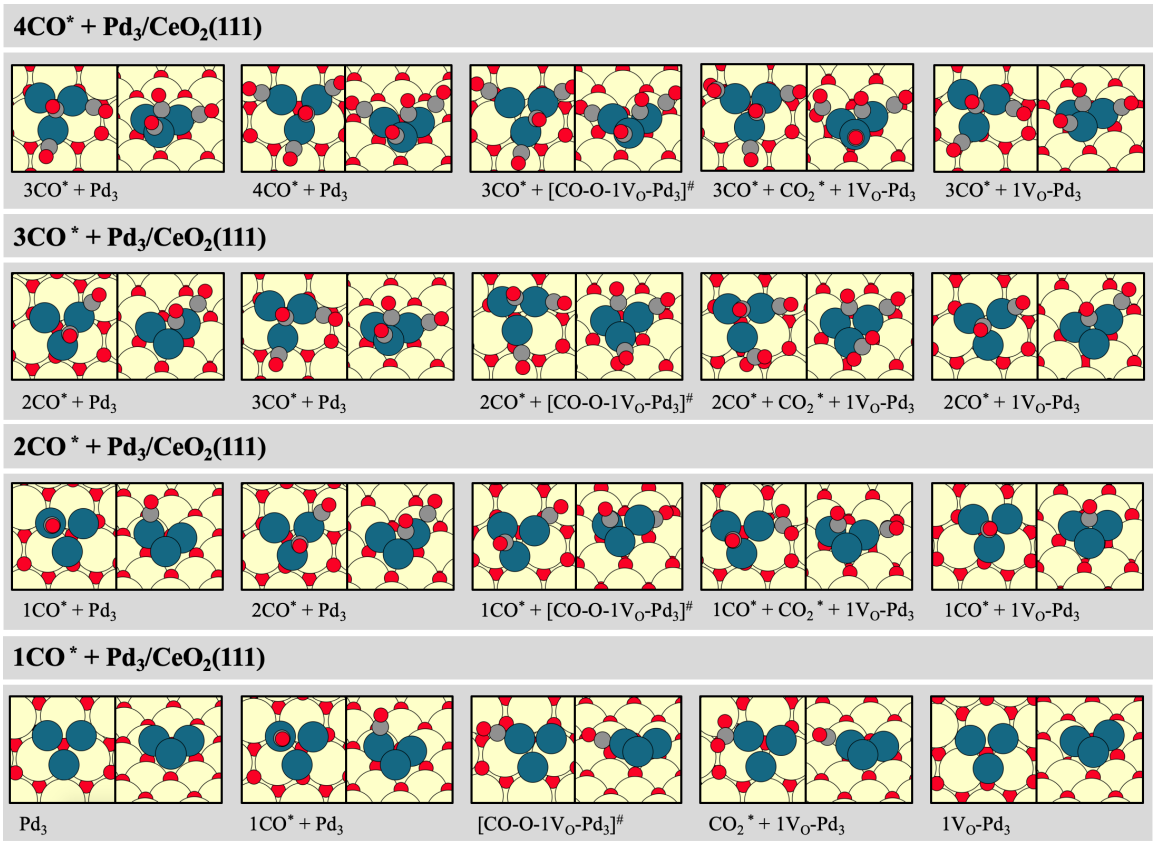

Figure 6.22.: Reaction mechanism of the CO oxidation on structure-optimized (1-4)CO^* + Pd_3 clusters via the MvK mechanism adsorbed on a stoichiometric CeO_2(111) surface. Red circles represent O atoms, dark gray circles C atoms, large yellow circles Ce atoms, and petrol circles indicate Pd atoms. The total energies are listed in the Appendix in Table A.29.

similar. This configuration is already favorable for an MvK mechanism. In the case of all the nCO^* + Pd_3 and the nCO^* + Pt_3 species (with n = 1-4), the CO molecule migrates to an O atom on the ceria (111) surface, forming a CO_2 molecule. It is assumed that the formation of the O lattice defect during the CO oxidation is more demanding than the migration of CO, as the crystal structure requires overcoming the lattice energy to remove a lattice O_l atom. The formed CO_2 molecule remains adsorbed at the same 1-fold position on one of the Pd or Pt atoms of the cluster before desorbing. The lattice O_l atom still faces the V_O lattice defect. However, in doing so, O_l vacates the position of V_O. After CO oxidation a CO_2 molecule is formed and anchored with one O atom onto the surface at the site of the generated V_O defect. Unlike the single-atom catalysts, however, the formed CO_2 molecule is not further anchored to the V_O lattice defect via an O atom. Therefore, it is expected that the $CO_2{}^*$ desorption, unlike in the case of single-atom catalysts, does not pose a significant inhibiting step. It is worth noting that, in all cases, there is an additional steric hindrance affecting the accessibility of the bent CO molecule and the O_l atom. The Pd or Pt atom where the CO molecule adsorbs for the reaction is situated on a location of the ceria surface where

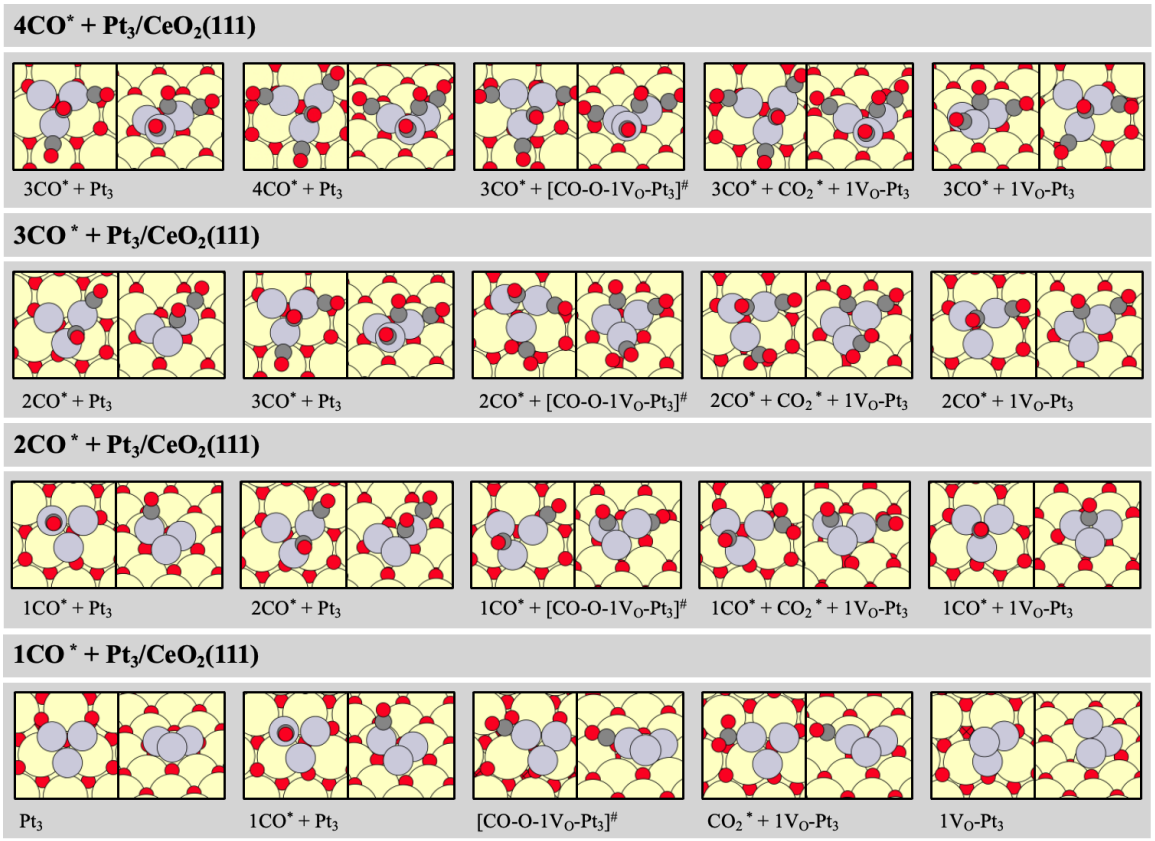

Figure 6.23.: Reaction mechanism of the CO oxidation on structure-optimized (1-4)CO^* + Pt_3 clusters via the MvK mechanism adsorbed on a stoichiometric CeO_2(111) surface. Red circles represent O atoms, dark gray circles C atoms, large yellow circles Ce atoms, and gray circles indicate Pt atoms. The total energies are listed in the Appendix in Table A.29.

it directly adsorbs to an O atom of the ceria surface. In any case, the O atoms anchor the cluster, as described earlier through the morphology of the clusters. Such steric hindrance will occur in each CO oxidation for a Pd_3 or Pt_3 cluster. The second CO oxidation by a $3CO^*$ + Pd_3 and $3CO^*$ + Pt_3 cluster, as well as the third CO oxidation by a $2CO^*$ + Pd_3 and $2CO^*$ + Pt_3 cluster depicted in Figure 6.22 in the second elementary reaction mechanism, occurs similarly to the first reaction mechanism on the $4CO^*$ + Pd_3 and $4CO^*$ + Pt_3 cluster. In the last CO oxidation on the CO^* + Pd_3 and CO^* + Pt_3 species, a change occurs. Firstly, the 3-fold bonded CO molecule has diffused to a 1-fold position to enable an MvK mechanism over an O_l atom of the ceria surface. This process is energetically more demanding than the previous reactions since diffusion must occur initially. As there is no longer a CO molecule between the three Pd or Pt atoms of the cluster and it is stabilized in its way, the formation of V_O during the CO oxidation via the MvK mechanism lifts the cluster into the z-direction from the surface. The Gibbs free energies are calculated for a reaction temperature of 423.15 K and plotted in a potential energy diagram in Figure 6.24. The temperature of 423.15 K is accounted by the use of *ab initio* thermodynamics, including the contributions of ZPE and

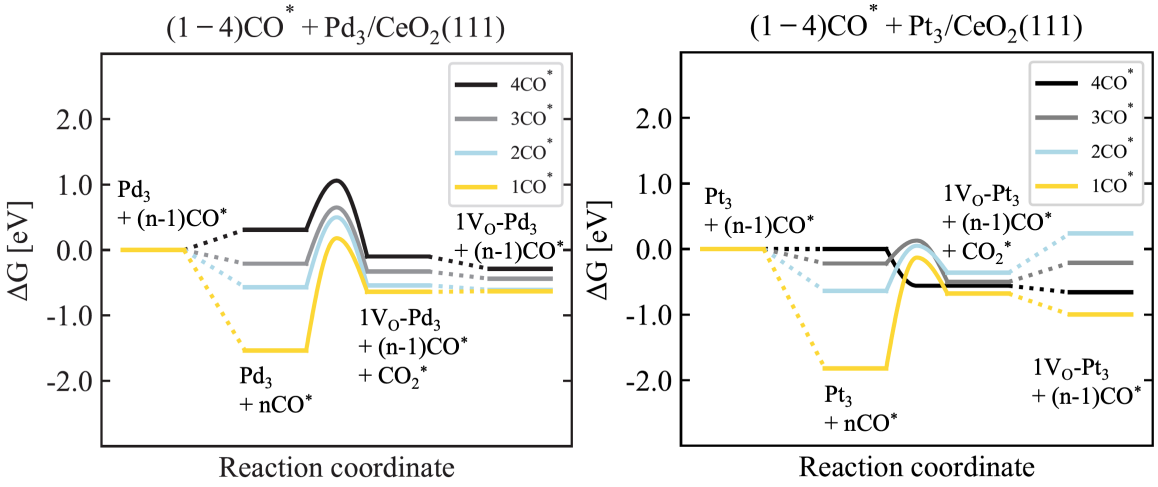

Figure 6.24.: Calculated Gibbs free energies of the structure-optimized CO oxidation elementary reaction steps on Pd_3 and a Pt_3 cluster via the MvK mechanism as depicted in Figure 6.22 for Pd and Figure 6.23 for Pt plotted against the reaction coordinate in a potential energy diagram. The Gibbs free energies are referenced to (1-4)CO^* + Pd_3 and (1-4)CO^* + Pt_3 catalysts adsorbed on the stoichiometric ceria CeO_2 surface facet (111) in eV at 423.15 K. The total energies, the ZPE and the entropies are listed in the Appendix in Table A.29.

entropy, as discussed in Section 3.7. The Gibbs free energies are listed in Table 6.8. The adsorption energies of the CO molecules continuously decrease: -1.54 eV for the first CO molecule, -0.57 eV for the second, -0.21 eV for the third, and 0.31 eV for the fourth on a Pd_3 cluster; and -1.82 eV for the first CO molecule, -1.64 eV for the second, -0.22 eV for the third, and 0.00 eV for the fourth on a Pt_3 cluster. The fourth CO molecule on the Pd_3 cluster is already endothermic at 423.15 K. The barriers after CO adsorption show a trend depending on the CO^* coverage. With the coverage of $4CO^*$ molecules, the CO oxidation barrier for one of these CO molecules is 0.75 eV, with $3CO^*$ molecules it is 0.85 eV, with $2CO^*$ molecules it is 1.06 eV, and with only $1CO^*$ molecule, it is 1.71 eV on the Pd_3 cluster. On the Pt_3 cluster, the barriers after CO adsorption with a coverage of $4CO^*$ molecule is spontaneous, with $3CO^*$ molecules it is 0.35 eV, with $2CO^*$ it is 0.69 eV, and with only $1CO^*$ molecule, it is 1.69 eV. The barriers for the Pd cluster are slightly higher than for the Pt cluster. The reaction barriers relative to the initial state with the CO molecule in the gas phase for the Pd cluster are 1.06 eV for $4CO^*$, 0.65 eV for $3CO^*$, 0.50 eV for $2CO^*$, and 0.18 eV for $1CO^*$. For Pt, the barriers relative to $CO_{(g)}$ in the gas phase is 0.05 eV for $3CO^*$, -0.13 eV for $2CO^*$, and -0.09 eV for $1CO^*$. The bond lengths of the C atom and the O atom during the transition state for CO oxidation are all in the same range, approximately 1.75 to 1.95, for both the Pd_{10} cluster and the Pt_{10} cluster. Due to the higher adsorption energy of CO molecules on the Pt cluster, the barriers relative to $CO_{(g)}$ in the gas phase are lower than those on the Pd cluster. Ultimately, a coverage of 4 CO molecules leads to a spontaneous reaction. It has also been found that for the Pt cluster, the coverage by 4 CO molecules is not significantly endothermic at the reaction temperature of 423.15 K. However, for the Pd

cluster, such coverage is already unlikely, which means that the lowered barrier compared to the low coverages will unfortunately not occur. In contrast, the Pt cluster has the general tendency to bind the reactants more strongly, allowing for high coverage at low temperatures. Additionally, the reaction barrier relative to $CO_{(g)}$ in the gas phase tends to decrease from higher CO^* coverage to lower CO^* coverage, with progressively lower barriers. This trend is exactly inverted compared to the barriers after CO adsorption. It is evident that CO adsorption and coverage both influence the barriers, complementing each other. The lowest barrier occurs with the strongest CO adsorption and minimal CO^* coverage with one CO molecule. Adsorption energies generally have a stronger impact on reaction barriers relative to the gas phase than the barriers after CO adsorption. In general, the cluster activation for

Table 6.8.: Calculated Gibbs free energies of the CO oxidation elementary reaction step referenced to the Pd_3 and Pt_3 clusters supported on the stoichiometric ceria surface facet (111) in eV and at 423.15 K of the structure-optimized elementary steps depicted in Figure 6.22 for Pd and Figure 6.23 for Pt. The Gibbs free energies are plotted in the potential energy diagrams 6.24. The Bond length between the C^* and the O^* atom during the transition state is described as b.l. in Å at 0 K and included in gray letters. The bond angles in degree of the formed CO_2 molecules are given in gray letters. Non-optimizable structures with very low barriers are considered spontaneous reactions and are denoted as sp.

	CO^* [eV]	$[CO\text{-}O]^\#$ [eV]	b.l. [Å]	$CO_2{}^*$ [eV]	CO_2 [eV]	angle [°]
CO oxidation via MvK Mechanism						
$4CO^*$	0.31	1.06	1.75	-0.10	-0.29	146
$3CO^*$	-0.21	0.65	1.94	-0.33	-0.44	149
$2CO^*$	-0.57	0.50	1.86	-0.54	-0.61	146
$1CO^*$	-1.54	0.18	1.83	-0.64	-0.63	146
$4CO^*$	0.00	sp.	-	-0.56	-0.66	132
$3CO^*$	-0.22	0.13	1.74	-0.50	-0.21	143
$2CO^*$	-0.64	0.05	1.95	-0.36	0.24	138
$1CO^*$	-1.82	-0.13	1.77	-0.68	-1.00	140

CO oxidation increases with decreasing CO^* coverage. However, it is crucial to consider the formation energies after the transition state in the overall reaction energies of the elementary reaction steps. The reaction energy of the elementary step is exothermic in all cases for the Pd cluster, with -0.28 eV for the coverage of $4CO^*$ molecules, -0.43 eV for $3CO^*$ molecules, -0.62 eV for $2CO^*$ molecules, and -0.63 eV for one $1CO^*$ molecule for the Pd_3 cluster. For the Pt_3 cluster, the reaction energy of the elementary step is -0.66 eV for the coverage of $4CO^*$ molecules, -0.21 eV for $3CO^*$ molecules, -1.40 eV for $2CO^*$ molecules, and -1.00 eV for one $1CO^*$. Generally, the overall reaction energy tends to be more exothermic with lower CO^* coverage. The $CO_2{}^*$ desorption is generally slightly exothermic to neutral at a reaction temperature of 423.15 K on the Pd cluster, with -0.19 eV, -0.10 eV, -0.07 eV, and 0.01 eV as the CO^* coverage decreases from $4CO^*$ molecules to one $1CO^*$ molecule. For the Pt cluster, the desorption energy becomes endothermic at higher CO^* coverages, with 0.29 eV, 0.60 eV, -0.32 eV, and 0.76 eV as the CO^* coverage decreases. The desorption

energies are only slightly endothermic, indicating that, especially at lower temperatures, they are unlikely to pose a significant obstacle to the CO oxidation via the MvK mechanism. The bond angles for the formed CO_2 molecules adsorbed at an ontop position onto the Pd cluster are in the range of 145°, with the angles for the Pt cluster being slightly lower, up to 132°. All Gibbs free energies were calculated at a reaction temperature of 423.15 K. With increasing temperature, all intermediates involving adsorption of reactants or products rise. However, it could be assumed that $CO_2{}^*$ desorption itself may not pose inhibition even at lower temperatures, unlike in the case of single-atom catalysts. The assumption is plausible that the subnanometer clusters should indeed be active for an MvK mechanism.

6.2.4. CO Oxidation on Pd_3 and Pt_3 cluster via MvK Mechanism including the Effect of Ceria Reduction

Charge transfer is a fundamental property of this chemical system involving noble metals and the ceria support. As shown in this work there is a common trend for Pd and Pt atoms to preferentially anchor atop on the surface lattice O_l. As already discussed in the Introduction in Section 1.3, it is expected that the reactants adsorb on the noble metals and undergo a change in electron configuration resulting from the donation and back-donation of electrons between the noble metal, which themselves are impacted electronically by the support. It is therefore suspected that the support acts non-innocently, meaning that the electronic properties of the cerium cations may interfere with the activity of the reactants. This can be explained by the orbital overlapping of the p-orbitals of the adsorbent carbon atom with the pz-orbital of the noble metal which decreases, leading to a bonding elongation. This reduction in overlapping occurs as the noble metal back-donates electrons to the surface, resulting in an increase of reduced cerium atoms on the surface. Consequently, the size of the orbital pointing out from the surface decreases, while the symmetrically opposing orbital pointing to the surface increases. As the interaction between the adsorbent and the orbital of the noble metal is pointing-out decreases, the bonding between them elongates. In this Section, particular attention is given to the effect of the reduced Ce^{+III} species of the non-innocent support $CeO_2(111)$ towards the CO oxidation via the MvK mechanism on a $1O^*$ + Pd_3 and a $1O^*$ + Pt_3 cluster. The adsorption of a Pd_3 cluster resulted in the formation of two reduced Ce^{+III} atoms. The Ce^{+III} atoms formed through charge transfer from the adsorbed cluster are highlighted in blue in Figure 6.25. The positions of the reduced Ce^{+III} atoms are calculated to be in the direct vicinity in the nearest neighbor position of the cluster and on the left-hand side at the next-nearest position on the right-hand side as shown in figure 6.25. The positioning was not manipulated by a prior substitution with Lanthanide but settled into these positions after structure optimization using the methods outlined in the methods Section. Castleton et al. addressed the question of charge localization extensively in their

research.[219] Their conclusion, based on exploration within the DFT + U framework, was that it was not possible to fully localize the Ce 4f electrons on these Ce sites while simultaneously preserving a correct description for all the other electrons. Several studies have shown that after the reduction of ceria, the remaining electrons are localized at a distance away from the defect.[88,222,223,293–297] As shown in Section 4.2.3, the migration of the V_O defect is

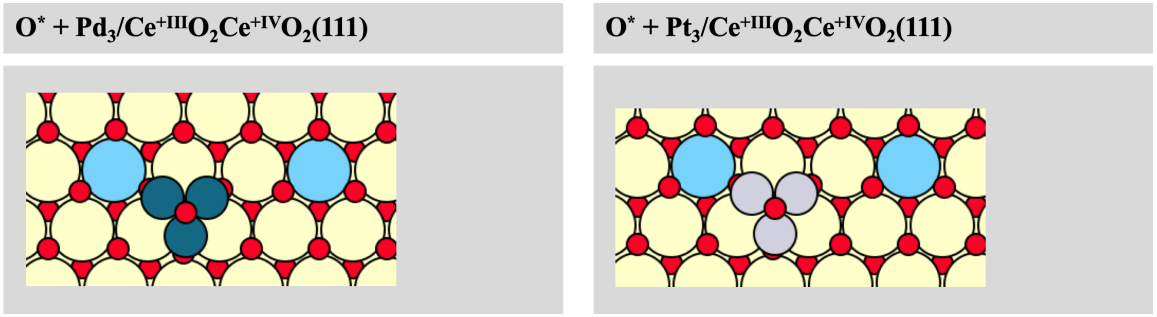

Figure 6.25.: Visualization of the positions of the reduced Ce^{+III} ions relative to the noble metal cluster Pd_3 and Pd_3. Red circles represent O atoms, large yellow circles are the Ce ions in the oxidation state +IV, large blue circles are Ce ions in the oxidation state +III, petrol circles indicate Pd atoms, and gray circles indicate Pt atoms.

slightly more favored than remaining on the top layer of the (111) surface lattice. These two charge transfer phenomena forming reduced surrounding cerium atoms in the oxidation state from +IV to +III are closely related. Naik and Tien conducted a study that combined electrical conductivity and nonstoichiometric data based on the V_O defect model with the correct ionization state.[298] The concluded, that in nonstoichiometric CeO_{2-x}, electrons are localized, and high-temperature electrical conduction occurs through a hopping mechanism where electrons jump from a Ce^{+III} ion to a neighboring Ce^{+IV} ion. They showed that upon surface reduction, excess electrons are primarily localized in empty Ce 4f orbitals at low defect concentrations and they explained that at higher defect concentrations, these excess electrons could also be localized at O defects. In defective ceria, these excess electrons lead to n-type conductivity (conductivity due to the presence of electrons), involving the motion of charge carriers in a band or through a hopping-diffusion mechanism. Under certain circumstances, this could indicate the presence of a MvK mechanism. There might potentially be an overlooked effect that renders the MvK mechanism more probable, caused by properties on the electronic level. In this Section, we aim to address this question and formulate an example mechanism by considering the surface reduction of the support. Consequently, the reduced Ce^{+III} ions could ultimately be recognized as a co-catalyst, thus functioning as a non-innocent support. We opt for the single-layered Pd_3 cluster for a couple of reasons. The 3-fold adsorption site of the Pd_3 cluster provides a direct route for simulating both, the LH and MvK mechanisms, as variations are kept to a minimum. Another advantage of selecting the minimally sized cluster Pd_3 is not only the minimal

computational effort but also the symmetry, which allows observation both to the left and right of the cluster. This is relevant because adsorption occurs at positions in the nearest neighbor (nn) and next nearest neighbor (nnn) of the reduced Ce^{+III} atoms as shown in Figure 6.25. Breaking down the O migration process into distinct stages aims to provide a detailed analysis, seeking to elucidate whether the CO oxidation mechanism is influenced by the reduced ceria surface and if the diffusion of O defects occurs favorably. Through this comprehensive examination, valuable insights into the complex dynamics of the ion conduction phenomenon can be gained. This cyclic charge transport effect could explain the mechanism behind the non-innocent support of ceria at the interface with the noble metal. The reaction mechanism considered here represents a partial segment of the overall

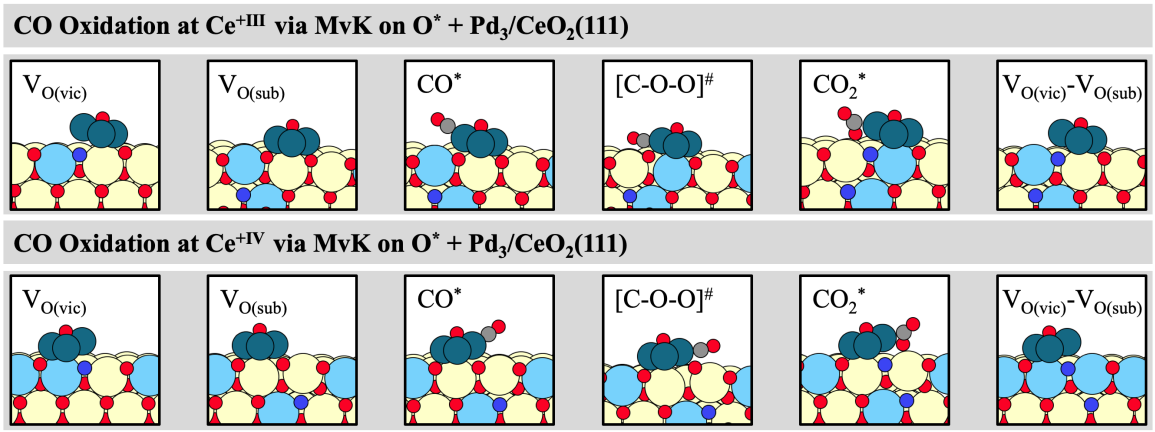

Figure 6.26.: Reaction mechanism of the CO oxidation on a structure-optimized O^* + Pd_3 clusters via the MvK mechanism adsorbed on the V_O-defective $CeO_2(111)$ surface. A reduced cerium atom with the oxidation state of +III (upper row) and +IV (lower row) in the nearest neighbor position takes part in the reaction as non-innocent support. Red circles represent O atoms, large yellow circles are the cerium ions in the oxidation state +IV, large blue circles are cerium ions in the oxidation state +III, dark gray circles represent C atoms, and petrol circles indicate Pd atoms. The total energies are listed in the Appendix in Table A.30.

reaction mechanism cycles for CO oxidation via the MvK mechanism, catalyzed by noble metals Pd and Pt supported on reducible ceria. We opted for this partial representation due to computational constraints. The calculations were performed on a 4-layer slab with a unit cell of 6x6. The two lower layers are fixed, representing the bulk, while the two upper layers are relaxed. The inclusion of a large number of atoms in the supercell results in significant computational complexity. The 4-layer configuration was chosen because V_O defect migration extends into the sublayers. A slab with only 2 layers, where one layer is relaxed and the other fixed, would lack in describing the electronic effects and lead to artificial deviations of the calculated energies. The decision to include an additional O^* atom in the chosen species stems from the aim of this study to compare the LH and MvK mechanisms. In the LH mechanism, the O atom is consumed during CO oxidation, while in the MvK mechanism, it is not. To maintain consistency and systematic approach, we

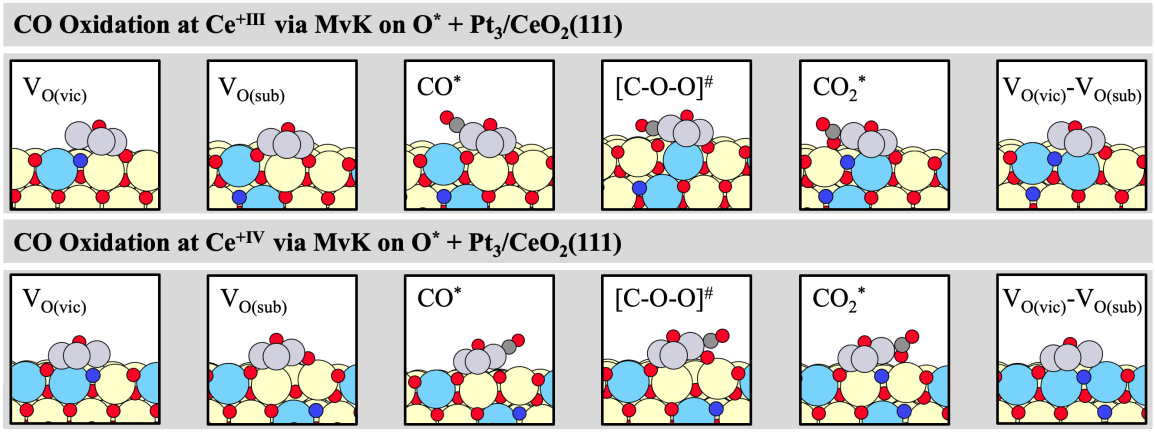

Figure 6.27.: Reaction mechanism of the CO oxidation on a structure-optimized O^* + Pt_3 clusters via the MvK mechanism adsorbed on the V_O-defective $CeO_2(111)$ surface. A reduced cerium atom with the oxidation state of +III (upper row) and +IV (lower row) in the nearest neighbor position takes part in the reaction as non-innocent support. Red circles represent O atoms, large yellow circles are the cerium ions in the oxidation state +IV, large blue circles are cerium ions in the oxidation state +III, dark gray circles represent C atoms, and gray circles indicate Pt atoms. The total energies are listed in the Appendix in Table A.30.

kept the cluster identical for this Section. Further calculations without this additional O^* atom were conducted in Section 6.2.3. The structure-optimized reaction mechanisms on the $1O^*$ + Pd_3 and the $1O^*$ + Pt_3 subnanometer clusters are nearly identical. The reaction mechanism in this Section initiates with an V_O defect in the direct vicinity of the Pd_3 and the Pt_3 subnanometer cluster formerly formed by an MvK mechanism diffusing into the sublayer. The O atom from the sublayer then moves into its place, now positioned in the direct vicinity of the cluster. The V_O is now located directly beneath the cerium atom in the direct vicinity. If the reduced cerium atom Ce^{+III} is in the nearest-neighbor position, the V_O is now directly underneath it. In the case of the next-nearest-neighbor position, the V_O is located next to a fully oxidized cerium atom Ce^{+IV}. It is positioned at the same distance from the cluster. Subsequently, a CO molecule adsorbs to the Pd or Pt atom of the cluster, which is in direct vicinity to the previously migrated O atom from the sublayer. The O atom that has migrated upward due to the migration of V_O is now going to interact with the adsorbed CO molecule. The CO oxidation proceeds through a transition state where the CO molecule aligns with the O atom in the vicinal position beneath the cluster. After CO oxidation via the MvK mechanism, two V_O defects in the ceria lattice, $V_{O(vic)}$ and $V_{O(sub)}$, are present. The formed CO_2 molecule is coordinated to $V_{O(vic)}$ at a small distance and subsequently desorbs. In the next step, O_2 dissociation occurs on the now-present $V_{O(vic)}$ and $V_{O(sub)}$ to bring about the regeneration of the surface, aiming to return the catalyst to its initial state (assuming the preceding Section conducted an initial CO oxidation via the MvK mechanism). The O_2 molecule adsorbs onto the V_O defect in the vicinal position to the cluster, $V_{O(vic)}$. A transition state for this process was

not calculated in this work, as it requires higher technical demands than would be useful for the scope of this study. It is noticeable that the cerium atom, around which the V_O defects move and exert electronic influence on CO oxidation, shifts in the z-direction and induces lattice strain due to O migration into the sublayer. Additionally, it is noteworthy that the Pd_3 and the Pt_3 subnanometer clusters, without anchoring to the ceria surface but with the formation of an V_O defect in the vicinal position, also move in the z-direction. In Figure 6.28, the potential energy diagram with the calculated Gibbs free energies at

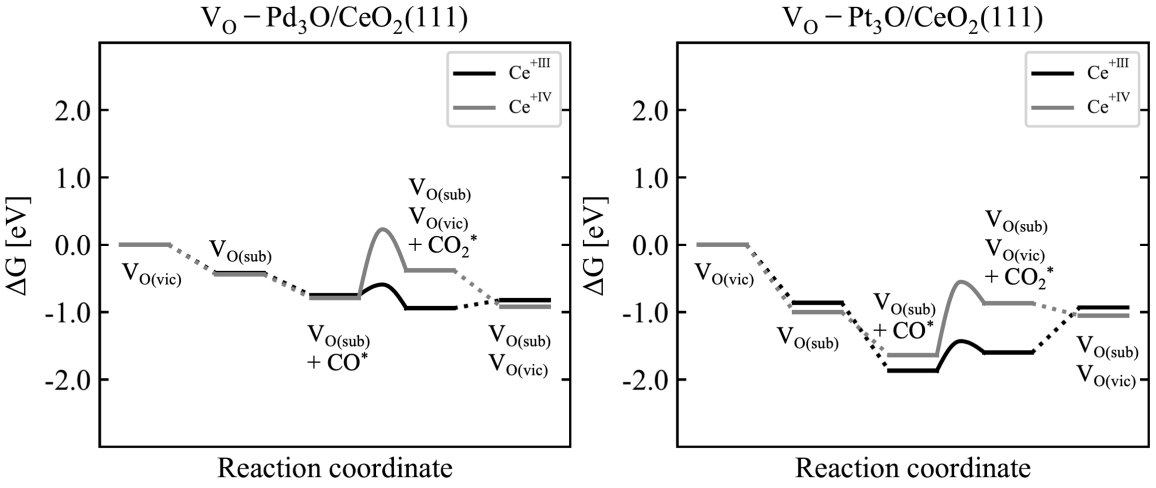

Figure 6.28.: Calculated Gibbs free energies of the structure-optimized CO oxidation elementary reaction steps on Pd_3 and Pt_3 cluster including the effect of ceria reduction as depicted in Figure 6.26 for Pd and Figure 6.27 for Pt are plotted against the reaction coordinate in a potential energy diagram. The Gibbs free energies are referenced to the Pd_3 and Pt_3 clusters supported on the stoichiometric ceria surface facet (111) in eV and at 423.15 K. The total energies, the ZPE and the entropies are listed in the Appendix in Table A.30.

423.15 K is depicted. The temperature of 423.15 K is accounted by the use of *ab initio* thermodynamics, including the contributions of ZPE and entropy, as discussed in Section 3.7. The V_O defect migration into the sublayer or equivalently, the O migration from the sublayer to the toplayer, is an exothermic process with -0.42 eV for $1O^*$ + Pd_3 at both the Ce^{+III} cerium ion in the nn position (abbreviated as nn position in the future) and -0.43 eV the Ce^{+IV} cerium ion with the Ce^{+III} cerium ion in the nnn position (abbreviated as nnn position in the future). However, for the $1O^*$ + Pt_3 cluster, this process is significantly more exothermic with -0.86 eV at the nn position and -1.00 eV at the nnn position. The CO adsorption is again exothermic in all cases, with -0.42 eV for the nn position in Pd, -0.44 eV for the nnn position, -0.86 eV at the nn position in Pt, and -1.00 eV at the nnn position. The binding strength of the reactants to the $1O^*$ + Pt_3 cluster is significantly stronger than to the $1O^*$ + Pd_3 cluster. The reaction barrier for CO oxidation after CO adsorption is 0.17 eV in the nn position and 1.03 eV in the nnn position for Pd, and 0.43 eV in the nn position and 1.09 eV in the nnn position for Pt. Therefore, the barriers for Pt are significantly higher. The bond length between the C atom and the O atom of the lattice during the transition

state of the CO oxidation is 1.64 Å for the nn position and 1.72 Å for the nnn position at the Pd cluster. However, relative to the gas-phase CO, this barrier becomes considerably lower for Pt, as its adsorption strength is stronger. The reaction barriers relative to $CO_{(g)}$ in the gas phase and before O migration are -0.59 eV in the nn position and 0.23 eV in the nnn position for Pd, and -1.43 eV in the nn position and -0.55 eV for the nnn position for Pt. In summary regarding reactivity towards CO oxidation, a Ce^{+III} cerium ion in the nn position results in a significant reduction in barriers. For $1O^*$ + Pd_3, the difference is 0.86 eV, and for $1O^*$ + Pt_3, it is 0.66 eV. Therefore, involving a reduced cerium atom Ce^{+III} in the reaction is more beneficial for the Pt cluster, but the difference is drastic in both cases. After formation, the CO_2 binds to one of the noble metal atoms on $1O^*$ + Pd_3 and $1O^*$ + Pt_3. The C atom is coordinated, and the molecule has an angle of 141° for an nn and an nnn position for Pd, and 136° for an nn position, 137° for an nnn position for Pt. Therefore, the angle with a coordination to the Pt cluster is slightly narrower. At a reaction temperature of 423.15 K, desorption of the CO_2 molecule with a Ce^{+IV} ion in vicinal position and a Ce^{+III} ion in the nnn position is exothermic with -0.54 eV for the Pd cluster and -0.19 eV for the Pt cluster. However, with a Ce^{+III} ion in the nn position, it is endothermic with 0.12 eV for the Pd cluster and 0.67 eV for the Pt cluster. The $CO_2{}^*$ desorption is endothermic with 0.12 eV for the nn position and exothermic with -0.62 eV for the nnn position at the Pd cluster. Hence, the desorption of the CO_2 molecule is favored when the reduced Ce^{+III} ion is electronically involved, coordinating directly with the O atom of the ceria surface lattice used for the CO oxidation of the CO molecule. Literature research, as shown by[120], indicates enhanced reactivity at the interface with the cluster due to the reduced support ceria. Our investigations reveal that the effect of the reduced vicinal Ce^{+III} ions significantly lowers the barrier, with this effect being more pronounced for the Pd cluster than for the Pt cluster. However, the Pt cluster still faces challenges with the significant hindrance of $CO_2{}^*$ desorption in the case of an MvK mechanism, whereas for the Pd cluster, this hindrance is

Table 6.9.: Calculated Gibbs free energies of the structure-optimized elementary steps for CO oxidation via the MvK mechanism on Pd_3 and Pt_3 cluster including the effect of ceria reduction, referenced to the O^* + Pd_3 and O^* + Pt_3 clusters supported on the O-defective ceria surface facet (111) at a vicinal position to the noble metal cluster, and measured in eV at 423.15 K. These values are depicted in Figure 6.26 for Pd and 6.27 for Pt. The potential energy diagrams are presented in 6.28. The Bond length between the C^* and the O^* atom during the transition state is described as b.l. in Å at 0 K and included in gray letters. The bond angles in degree of the formed CO_2 molecules are given in gray letters.

	$V_{O(sub)}$	CO^* [eV]	$[CO\text{-}O]^\#$ [eV]	b.l. [Å]	$CO_2{}^*$ [eV]	angle [°]	$V_{O(vic)}$,$V_{O(vic)}$
CO oxidation via MvK Mechanism							
Ce^{+III}	-0.42	-0.75	-0.59	1.64	-0.94	141	-0.82
Ce^{+IV}	-0.44	-0.79	0.23	1.72	-0.38	141	-0.92
Ce^{+III}	-0.86	-1.87	-1.43		-1.60	136	-0.93
Ce^{+IV}	-1.00	-1.64	-0.55		-0.87	137	-1.05

considerably smaller. The reaction energy of the elementary step of CO oxidation, with the presence of an V_O surface defect and thus a reduced ceria surface, is exothermic, with a total of -0.82 eV for Pd and -0.92 eV for Pt in the nn position relative to the reduced Ce^{+III} ion. The overall reaction energy for the nnn position relative to the reduced Ce^{+III} ion is not significantly different, with -0.93 eV for the Pd cluster and -1.05 eV for the Pt cluster. These studies demonstrate that a reduced Ce^{+III} ion participating in the reaction significantly lowers the barrier, while a fully oxidized cerium atom Ce^{+IV} exhibits an increased barrier.

6.2.5. O_2 Dissociation on Pd_{10} and Pt_{10} Cluster via the LH and the MvK mechanism

The investigation in this Section pertains to the dissociation process of two O_2 molecules occurring on the Pd_{10} and a Pt_{10} subnanometer cluster. The reaction is situated at the second layer atop the cluster in each case. Figure 6.29 illustrates the sequential reaction steps for the O_2 dissociation mechanism on the Pd_{10} cluster and Figure 6.30 for the Pt_{10} cluster. Initially, an O_2 molecule adsorbs with on the apex position atop one of the clusters. There, three Pd or Pt atoms form a triangular structure within the second layer of the cluster. An O atom of the O_2 molecule adsorbs in a bridge position between two of the three noble metal atoms on the cluster, with another O atom in an on-top position on the third noble metal atom. The binding length of the $O_{2(g)}$ molecule in the gas phase was calculated to be 1.23 Å at 0 K. After adsorption on the cluster, the binding length extends to 1.37 Å on the Pd cluster and 1.44 Å on the Pt cluster. During the transition state, this length further extends to 2.07 Å on the Pd cluster and 1.75 Å on the Pt cluster. After dissociation, both O atoms remain on the top layer of the cluster. The O atom of the $O_{2(g)}$ molecule that was bound on top of one of the noble metal atoms remains on top but shifts towards the outermost side of the cluster. The bridge-bound O atom also remains in its bridge position, slightly oriented outward, without significant movement. In the second O_2 dissociation, it is assumed that both O atoms from the previous O_2 dissociation are located on the sides of the cluster, freeing up an on-top adsorption site on the cluster for the next $O_{2(g)}$ molecule. The two O atoms from the first dissociation are 3-fold coordinated, each situated in one of the "leaves" of the flower-like structure of both the $2O^*$ + Pd_{10} and the $2O^*$ + Pt_{10} clusters. The binding length of the second O_2 molecule extends from 1.23 Å in the gas phase to 1.41 Å on the Pd cluster and 1.51 Å on the Pt cluster. During the transition state, this length further extends to 2.00 Å on the Pd cluster and 1.65 Å on the Pt cluster. The bond lengths are also listed in Table 6.10. The bond length after the second O_2 dissociation is slightly longer, while that of the transition state is slightly shorter. The dissociation of the second O_2 molecule leads to larger cluster deformations on both the $2O^*$ + Pd_{10} and $2O^*$ + Pt_{10} clusters compared to the first O_2 dissociation. The O atom that was initially on the on-top position on one of the three noble metal atoms forming the apex of the cluster slightly orients outward during

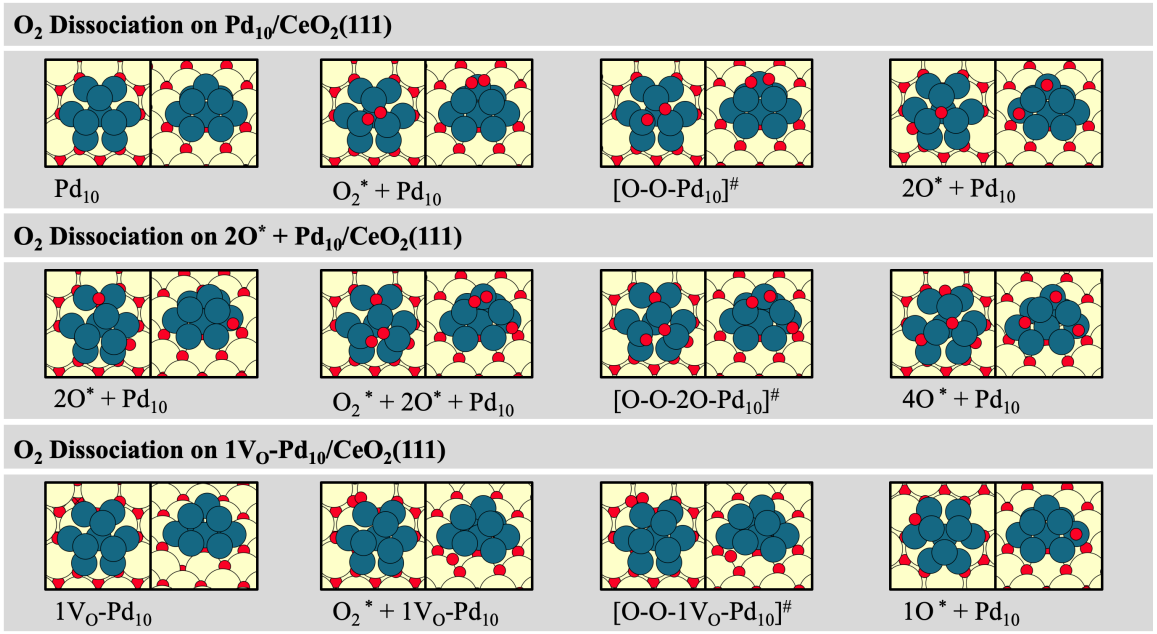

Figure 6.29.: Reaction mechanism of the O_2 dissociation on a structure-optimized Pd_{10} clusters adsorbed on a stoichiometric and V_O-defective $CeO_2(111)$ surface. Red circles represent O atoms, large yellow circles Ce atoms, and petrol circles indicate Pd atoms. The total energies are listed in the Appendix in Table A.31.

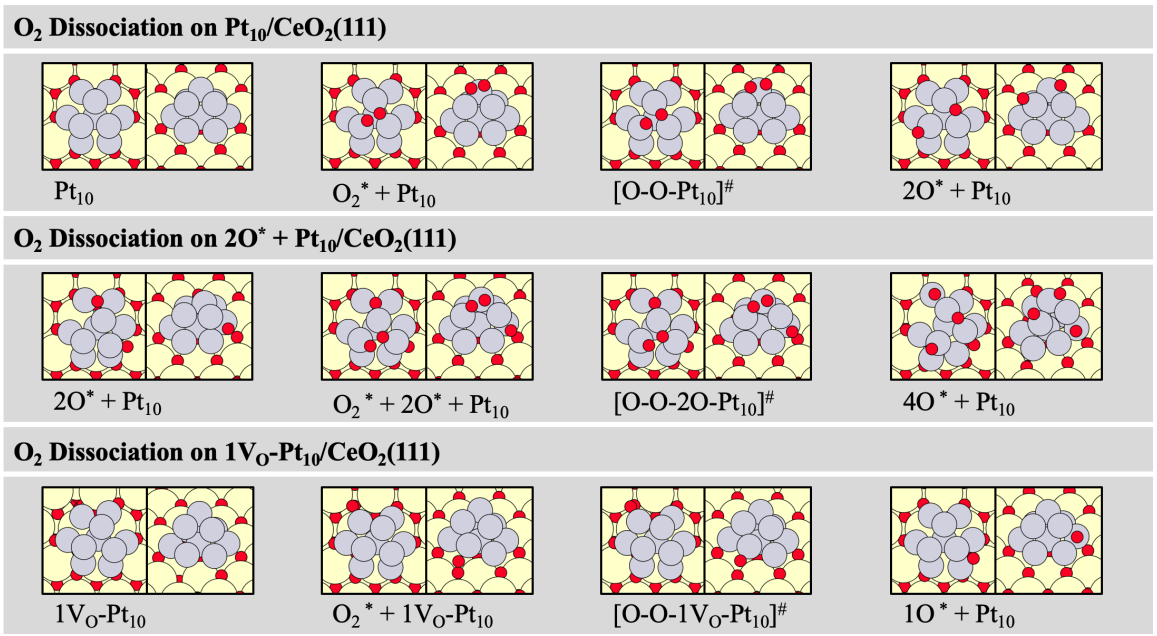

Figure 6.30.: Reaction mechanism of the O_2 dissociation on a structure-optimized Pt_{10} clusters adsorbed on a stoichiometric and V_O-defective $CeO_2(111)$ surface. Red circles represent O atoms, large yellow circles Ce atoms, and gray circles indicate Pt atoms. The total energies are listed in the Appendix in Table A.31.

the dissociation, shifting its noble metal atom in the process. After dissociation on the $2O^*$ + Pt_{10} cluster, the O atoms align similarly to the first O_2 dissociation. A significant difference in the resulting $4O^*$ + Pt_{10} cluster is a configuration change on the first layer,

where two Pt atoms are now noticeably farther apart. Notably, this increased distance is also observed in the pristine Pt_{10} cluster, whereas the pristine Pd_{10} cluster does not exhibit such a change. There could be an electronic reason for this, as a reduced Ce^{+III} ion connects these two Pt noble metal atoms. The positions of these Ce^{+III} ions are illustrated in Section 4.3.5. One of the O atoms from the first O_2 dissociation is now located at a bridge position due to the substantial configuration change. The "leaves" of the flower-like structure are no longer clearly assignable as "leaves" due to the adsorption of the four O atoms. In summary, despite the structural changes, the $4O^*$ + Pt_{10} cluster can be identified as an intact cluster in partial oxidation. The $4O^*$ + Pd_{10} cluster has also undergone a configuration change, but it is significantly less pronounced. One of the two O atoms after the second O_2 dissociation is hollow site-bound in the third "leaf" of the flower-like structure, previously unoccupied. The fourth O atom is on-top in a hollow position on the cluster. The calculated

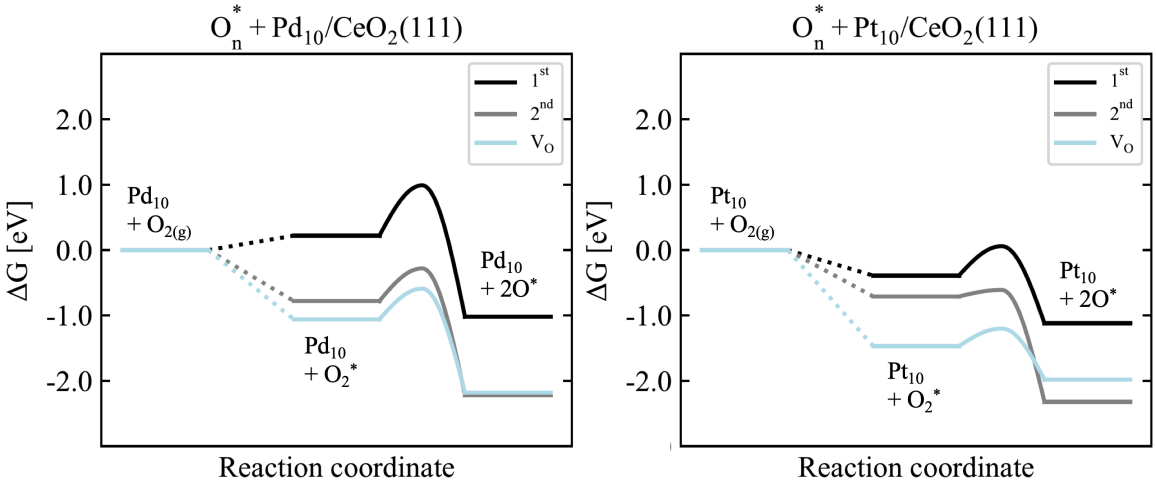

Figure 6.31.: Calculated Gibbs free energies of the structure-optimized O_2 dissociation elementary reaction steps on Pd_{10} and Pt_{10} cluster as depicted in Figure 6.29 for Pd and Figure 6.30 for Pt plotted against the reaction coordinate in a potential energy diagram. The Gibbs free energies are referenced to the Pd_3 and Pt_3 clusters, with no additional O adsorbed for the 1st O_2 dissociation and with two O pre-adsorbed for the 2nd O_2 dissociation, supported on the stoichiometric ceria surface facet (111) in eV and at 423.15 K. The total energies, the ZPE and the entropies are listed in the Appendix in Table A.31.

Gibbs free energies at a reaction temperature of 423.15 K are plotted in a potential energy diagram, as shown in Figure 6.31. The temperature of 423.15 K is accounted by the use of *ab initio* thermodynamics, including the contributions of ZPE and entropy, as discussed in Section 3.7. The corresponding energies are listed in Table 6.10. The adsorption energy of the $O_{2(g)}$ molecule on the reduced Pd_{10} cluster is slightly endothermic at 0.22 eV, while on the reduced Pt_{10} cluster, it is quite exothermic at -0.39 eV. The adsorption energies on the pre-oxidized $2O^*$ + Pd_{10} cluster and the $2O^*$ + Pt_{10} cluster are significantly more exothermic with -0.78 eV and -0.71 eV, respectively. On the reduced ceria surface with one defect $1V_O$ is the most exothermic with -1.06 for the V_O + Pd_{10} cluster and -1.47 eV for

the V_O + Pt_{10} cluster. This suggests that regeneration of the ceria surface at the interface with a noble metal cluster is indeed enhanced. The reaction barrier relative to $O_{2(g)}$ in the gas phase is 0.99 eV for the Pd_{10} cluster and 0.06 eV for the Pt_{10} cluster, -0.28 eV and -0.61 eV, respectively, if $2O^*$ is already adsorbed, and -0.59 eV and -1.20 eV when the interface is reduced, respectively. A clear tendency towards regeneration at the interface is apparent here. However, already oxidized subnanometer clusters are also inclined to have lower barriers for further O adsorptions. This is also reflected in the reaction energy of the elementary step, which is -1.02 eV for Pd and -1.12 eV for Pt on a reduced cluster but a stoichiometric ceria surface, -2.22 eV for Pd and -2.32 eV for Pt when the cluster is pre-oxidized, and -2.18 eV for Pd and -1.98 eV for Pt when an V_O defect is present. The reaction of O_2 dissociation is therefore extremely exothermic at a Pd_{10} and Pt_{10} cluster, with regeneration and a pre-oxidized cluster preferentially promoting O_2 dissociations. The latter could be due to the fact that the crystal structure tends to aim for a PdO and PtO crystal structure through pre-oxidation. However, this study is not sufficient to make a clear statement about this. Nevertheless, by observing the activities, a follow-up study can be prompted.

Table 6.10.: Calculated Gibbs free energies of the O_2 dissociation elementary reaction step referenced to the Pd_3 and Pt_3 clusters on the stoichiometric ceria surface facet (111), with two O pre-adsorbed $2O^*$, and on the $1V_O$-defective (111) ceria surface in eV and at 423.15 K of the structure-optimized elementary steps as depicted in Figure 6.19 for the Pd cluster and Figure 6.20 for the Pt cluster. The Gibbs free energies are plotted in the potential energy diagrams 6.31. The Bond length between the C^* and the O^* atom during the transition state is described as b.l. in Å at 0 K and included in gray letters.

	$O_2{}^*$ [eV]	b.l. [Å]	$[O\text{-}O]^\#$ [eV]	b.l. [Å]	$2O^*$ [eV]
O_2 dissociation via LH Mechanism					
$Pd_3/CeO_2(111)$	0.22	1.37	0.99	2.07	-1.02
$Pt_3/CeO_2(111)$	-0.39	1.44	0.06	1.75	-1.12
O_2 dissociation via LH Mechanism					
$2O^* + Pd_3$	-0.78	2.07	-0.28	2.00	-2.22
$2O^* + Pt_3$	-0.71	1.75	-0.61	1.65	-2.32
O_2 dissociation via MvK Mechanism					
$1V_O$-Pd_3	-1.06	1.79	-0.59	1.79	-2.18
$1V_O$-Pt_3	-1.47	1.97	-1.20	1.97	-1.98

6.2.6. CO Oxidation on (1-4)O^* + Pd_{10} and (1-4)O^* + Pt_{10} Cluster via LH Mechanism

After the two O_2 dissociation shown in Section 6.2.5, the partially oxidized $4O^*$ + Pd_{10} and $4O^*$ + Pt_{10} are available for CO oxidation via the LH mechanism. The four O atoms can be successively consumed through CO oxidation. In this study, we assume that CO oxidation takes place exclusively on top of the cluster. We have opted for this assumption for the sake of simplicity, as there could be numerous other adsorption configurations on the cluster.

For the sake of systematicity and comparability with other species in this work as Pd_3 and Pt_3 and the metal surfaces (111) and (211) of Pd and Pt surfaces, we made this decision to facilitate a comprehensive comparison. Potential variations could lead to an escalating complexity in this study. Therefore, care has been taken to ensure a comparable transition state among the species studied in this work by selecting an analogous reaction site for all species investigated. Figure 6.32 for Pd and 6.33 for Pt illustrate the LH mechanism for CO oxidation on a (1-4)O^* + Pd_{10} and a (1-4)O^* + Pt_{10} subnanometer cluster on the (111) surface of ceria, respectively. The adsorption of the CO molecule takes place on the (1-4)O^*

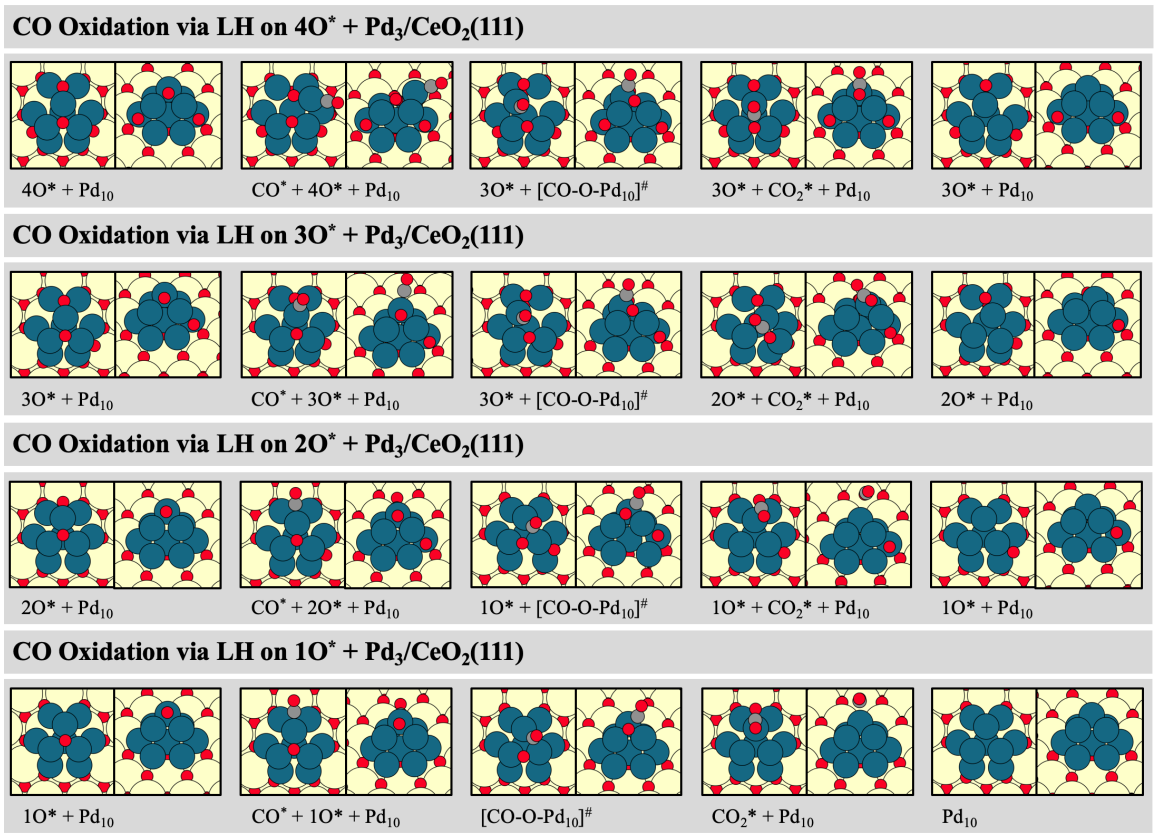

Figure 6.32.: Reaction mechanism of the CO oxidation on structure-optimized (1-4)O^* + Pd_{10} clusters via the LH mechanism adsorbed on a stoichiometric CeO_2(111) surface. Red circles represent O atoms, large yellow circles denote Ce atoms, dark gray circles represent C atoms, and petrol circles indicate Pd atoms. The total energies are listed in the Appendix in Table A.32.

+ Pd_{10} and (1-4)O^* + Pt_{10} clusters, each on the on-top position of one of the three noble metal atoms in the second layer. For the $4O^*$ + Pd_{10} and $4O^*$ + Pt_{10} clusters, CO adsorption has led to a deformation of the configuration. The coordination of the noble metal atom Pd and Pt deviates from the other two noble metal atoms due to the additional coordination to the CO molecule, in addition to the existing coordination to the 4 O atoms. The CO molecule bends strongly toward the ceria surface. For the (2-4)O^* + Pd_{10} and (2-4)O^* + Pt_{10} clusters, the cluster configuration remains largely unaffected. The CO molecule adsorbs

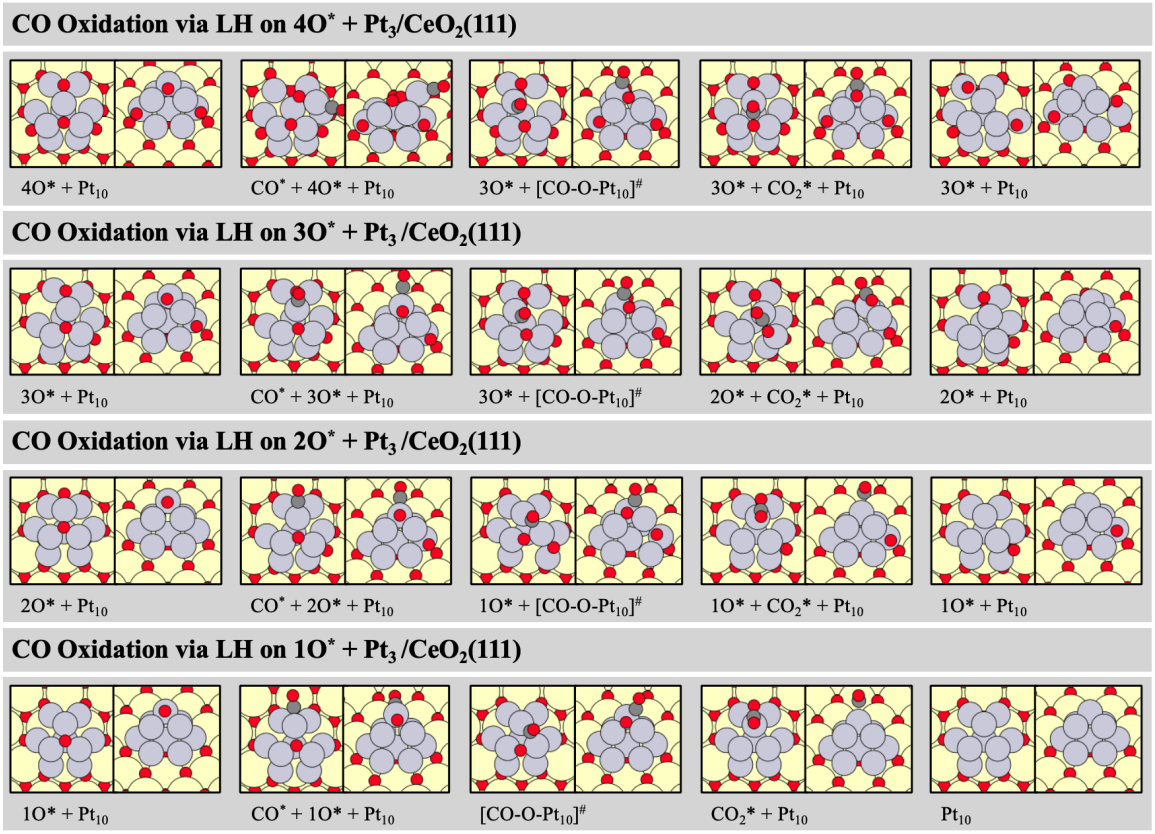

Figure 6.33.: Reaction mechanism of the CO oxidation on structure-optimized (1-4)O^* + Pt_{10} clusters via the LH mechanism adsorbed on a stoichiometric CeO_2(111) surface. Red circles represent O atoms, large yellow circles denote Ce atoms, dark gray circles represent C atoms, and gray circles indicate Pt atoms. The total energies are listed in the Appendix in Table A.32.

on top of the noble metal atom Pd or Pt, and if an O atom in the underlying "leaf" of the flowerlike structure is hollow site-bound, it bends upward toward the O atom on top of the cluster. As the hollow site of the "leaf" is vacant, the CO molecule adsorbs preferably onto this position. For the (1-2)O^*-Pd_{10} and (1-2)O^* + Pt_{10} clusters, the transition state occurs in such a way that the O molecule adsorbs on top of the cluster in a bridge position between two noble metal atoms, and the CO molecule adsorbs on the third noble metal atom of the apex of the cluster. In this process, the CO molecule approaches the O atom, with the noble metal atom on which it is adsorbed adjusting to the migration. On the (3-4)O^*-Pd_{10} and (3-4)O^* + Pt_{10} clusters, however, the CO molecule is coordinated ontop of one of the three noble metal atoms of the apex. The formed CO_2 molecule on the initial (1-2)O^*-Pd_{10} and (1-2)O^* + Pt_{10} clusters, which are now reduced by one O atom, continues to coordinate with the O atom that was previously at the bridge position between two of the three noble metal atoms on top of the cluster at the same position. For the initial (3-4)O^* + Pd_{10} and (3-4)O^* + Pt_{10} clusters, which are now reduced by one O atom, the formed CO_2 molecule is coordinated over the C atom further on the cluster with on-top coordination on one of

the three noble metal atoms on the apex of the cluster. The angles of the CO_2 molecules are 134° for the initial $4O^*$ + Pd_{10} cluster and for $4O^*$ + Pt_{10} cluster 127°, 138° for the initial $3O^*$ + Pd_{10} cluster and 132° for 3O-Pd_{10}, 130° for the initial $2O^*$ + Pd_{10} cluster and 148° for $2O^*$ + Pd_{10}, and 157° for the initial $1O^*$ + Pd_{10} cluster and 148° for $1O^*$ + Pt_{10}. After desorption, the cluster remains with the remaining O atoms at the side of the cluster, or in the latter case of CO oxidation, completely without O atoms. In the case of the $2O^*$ + Pd_{10} cluster formed after CO oxidation with the O atoms at the side, the cluster is slightly oriented towards the O atoms. The Gibbs free energies were calculated for a reaction

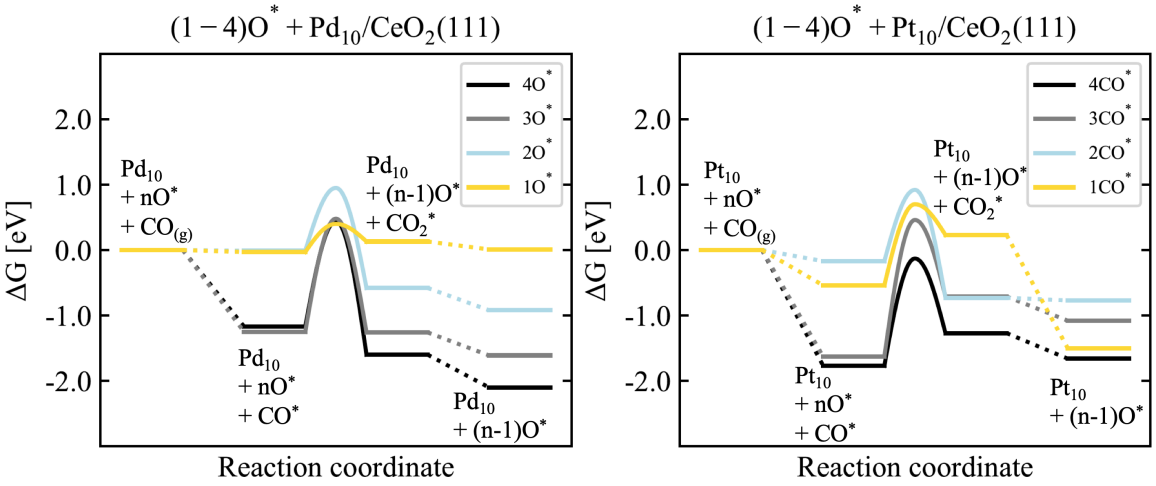

Figure 6.34.: Calculated Gibbs free energies of the structure-optimized CO oxidation elementary reaction steps on (1-4)O^* + Pd_{10} and (1-4)O^* + Pt_{10} via the LH mechanism as depicted in Figure 6.32 for Pd and Figure 6.33 for Pt plotted against the reaction coordinate in a potential energy diagram. The Gibbs free energies are referenced to (1-4)O^* + Pd_{10} and (1-4)O^* + Pt_{10} catalysts adsorbed on the stoichiometric ceria CeO_2 surface facet (111) in eV at 423.15 K. The total energies, the ZPE and the entropies are listed in the Appendix in Table A.32.

temperature of 423.15 K and are depicted in Figure 6.34 in a potential energy diagram. The temperature of 423.15 K is accounted by the use of *ab initio* thermodynamics, including the contributions of ZPE and entropy, as discussed in Section 3.7. The corresponding potential energies are listed in Table 6.11. The adsorption energies of CO molecules on the (3-4)O^* + Pd_{10} and (3-4)O^* + Pt_{10} clusters at a given reaction temperature of 423.15 K are -0.03 eV for the Pd cluster with $4O^*$ atoms, -0.01 eV for $3O^*$ atoms, -0.54 eV for the Pt cluster with $4O^*$ atoms, and -0.17 eV for $3O^*$ atoms. Thus, for partially oxidized Pd clusters, these energies are thermodynamically nearly neutral at low temperatures but become increasingly endothermic at higher temperatures. In contrast, the partially oxidized Pt cluster binds slightly exothermically. For a number of O^* atoms below 3, ranging from 1 to $2O^*$ atoms, both Pd_{10} and Pt_{10} clusters can strongly exothermically bind CO molecules with -1.25 eV for $2O^*$ atoms, -1.17 eV for $1O^*$ atom on the Pd_{10} cluster, and -1.63 eV for $2O^*$ atoms, -1.77 eV for $1O^*$ atom on the Pt_{10} cluster. The trend indicates that partially

oxidized Pt clusters overall bind more strongly than partially oxidized Pd clusters. Clusters with a low number of adsorbed O^* atoms have the ability to expose hollow site adsorption positions. The CO molecule preferably binds in a 3-fold position, leading to structural optimizations revealing the migration of the CO molecule to this position. The increased activation barriers for the lower oxidized clusters 1 and 2 can be attributed to the more strongly bound CO^* molecules. These molecules require increased energy to break the 3-fold coordinated interactions with the cluster in order to migrate to the O^* atom. For the sake of systematicity, reverse migration of the O^* atom toward the CO^* molecule was not investigated in this study. This study serves as a sort of red line through the species landscape of the highly dynamic catalyst, providing a foundation for other variants that can branch out from selected points along the trajectory of this study. The adsorption strengths and activation barriers can be collectively considered in terms of reaction energy relative to $CO_{(g)}$ in the gas phase. The potential energies referenced to the Pd_3 and Pt_3 clusters

Table 6.11.: Calculated Gibbs free energies of the CO oxidation elementary reaction step referenced to the number of adsorbed O^* on the Pd_{10} and Pt_{10} clusters before CO oxidation on the surface facet (111) of ceria in eV and at 423.15 K of the structure-optimized elementary steps depicted in Figure 6.32 for Pd and Figure 6.33 for Pt. The Gibbs free energies are plotted in the potential energy diagrams 6.34. The Bond length between the C^* and the O^* atom during the transition state is described as b.l. in Å at 0 K and included in gray letters. The bond angles in degree of the formed CO_2 molecules are given in gray letters.

	CO^* [eV]	$[CO\text{-}O]^\#$ [eV]	b.l. [Å]	$CO_2{}^*$ [eV]	$(n-1)O^*[eV]$
CO oxidation via LH Mechanism					
$4O^* + Pd_{10}$	-0.03	0.40		0.13	0.01
$3O^* + Pd_{10}$	-0.01	0.95		-0.58	-0.92
$2O^* + Pd_{10}$	-1.25	0.48		-1.26	-1.61
$1O^* + Pd_{10}$	-1.17	0.44		-1.60	-2.10
$4O^* + Pt_{10}$	-0.54	0.70		0.23	-1.50
$3O^* + Pt_{10}$	-0.17	0.92		-0.73	-0.77
$2O^* + Pt_{10}$	-1.63	0.46		-0.71	-1.08
$1O^* + Pt_{10}$	-1.77	-0.13		-1.27	-1.66

supported on the stoichiometric ceria surface facet (111) in eV and at 423.15 K of the structure-optimized elementary steps depicted in Figure 6.19 for Pd and Figure 6.20 for Pt. The Gibbs free energies are plotted in the potential energy diagrams 6.34. The Bond length between the C^* and the O^* atom during the transition state is described as b.l. in Å at 0 K and included in gray letters. The reaction barriers relative to $CO_{(g)}$ in the gas phase are as follows for the Pd_{10} cluster: $4O^*$ 0.40 eV, $3O^*$ 0.95 eV, $2O^*$ 0.48 eV, and $1O^*$ 0.44 eV. For the Pt_{10} cluster: $4O^*$ 0.70 eV, $3O^*$ 0.92 eV, $2O^*$ 0.46 eV, and $1O^*$ -0.13 eV. A maximum in reaction barriers is observed at a coverage of $3O^*$ atoms for both Pd and Pt. For the Pd cluster, all other coverages have reaction barriers approximately equal at around 0.45 eV. However, the Pt cluster exhibits a more pronounced maximum at $3O^*$, with the lowest barrier occurring at

a coverage of $1O^*$. It can be stated that, as expected, the adsorption energies and activation barriers balance out when considering the reaction barriers relative to $CO_{(g)}$ in the gas phase. Additionally, it can be noted that even the slightly oxidized Pt cluster alone shows activity in CO oxidation through the LH mechanism. The formed CO_2 molecule is exothermic relative to the adsorbed CO^* molecule as the initial state for the Pd_{10} cluster at 3O with -0.57 eV, for 1O with -0.43 eV, and for the Pt_{10} with -0.56 eV. At $4O^*$ for the Pd_{10} cluster, the formed CO_2 molecule is exothermic at 0.16 eV, neutral at $3O^*$, and endothermic at -0.43 eV for $1O^*$ atom. For the Pt_{10} cluster, at $4O^*$, it is endothermic with 0.78 eV, at $2O^*$ with 0.92 eV, and at $1O^*$ with 0.50 eV. Overall, it can be concluded that CO_2 formation is not a favored reaction on partially oxidized clusters; it may also occur reversibly in equilibrium reactions. The desorption of the CO_2 molecule poses no hindrance; at low temperatures (423.15 K), it is always slightly exothermic, around -0.40 eV. Conversely, this implies that $CO_{2(g)}$ adsorption occurs with minimal energy expenditure if temperatures are sufficiently low. All in all, the partially oxidized noble metal cluster is significantly exothermic in the overall reaction, the lower the number of adsorbed O atoms. The $1O^*$ + Pd_{10} cluster with -2.10 eV, $2O^*$ + Pd_{10} cluster with -1.61 eV, and $1O^*$ + Pt_{10} cluster with -1.66 eV seem to exhibit favorable conditions for an active species. However, the strong CO adsorption and the associated increased activation barrier may lead to CO poisoning. With increased partial oxidation of the clusters, the CO adsorption energies and the accompanying increased activation barrier are significantly reduced, ruling out CO poisoning. Additionally, these reactions, although with a moderately low reaction barrier relative to $CO_{(g)}$ in the gas phase, are exothermic. These reaction barriers are lowest for a $4O^*$ coverage, while CO_2 formation is most exothermic for a $3O^*$ coverage. The active species is not conclusively determined in this analysis. Further kinetic or analytical investigations may be required to make an accurate statement about their activities. For now, we assume that a surface coverage with $3O^*$ atoms in Pd_{10} and Pt_{10} clusters leads to a reaction that is exothermic enough (-0.92 eV and -0.77 eV) for an exothermic $CO_2{}^*$ desorption by adsorption on the second layer and no CO^* poisoning by adsorption on 1-fold adsorption sites, making it a potentially active species against CO oxidation through the LH mechanism at low temperatures. The configurations of the reactants and the electronic properties of the subnanometer cluster are crucial in this context. The calculations on the PdO and PtO (101) crystal surfaces in Section 6.3.4 also revealed that a fully oxidized cluster, adopting the crystal structure of the oxide, does not lead to a more active species. The adsorption energies of the $CO_{(g)}$ molecules are comparable, with -0.45 eV for PdO and -1.06 eV for PtO, and activation barriers at 0.59 eV for PdO and 1.62 eV for PtO. The reaction barriers relative to $CO_{(g)}$ in the gas phase are 0.14 eV for PdO and 0.56 eV for PtO, making their activities comparable to the reaction on the second layer of a partially oxidized cluster (1-4)O^* + Pd_{10} and (1-4)O^*

+ Pt_{10}. When compared to the activity of $1O^*$ + Pd_3 and $1O^*$ + Pt_3 clusters, as demonstrated in Section 6.2.3, the size effect positively influences the activity against CO oxidation. The barriers on these smaller clusters, with proximity to the support through only one layer, are significantly lower. The $1O^*$ + Pd_3 even leads to spontaneous CO_2 formation, while the $1O^*$ + Pt_3 cluster has an activation barrier of only 0.82 eV, balanced by an adsorption energy of -1.16 eV to achieve an exothermic reaction barrier relative to $CO_{(g)}$ in the gas phase at -0.34 eV. The interfacial region and an electronic effect accompanying it are therefore of particular importance in enabling an LH mechanism on partially oxidized clusters through O^* adsorption on the surface of the clusters. Nevertheless, the single-atom catalysts as shown in Section 6.1.4 shown an enhanced activity as well. The adsorption energies are all exothermic, around -1.00 eV, the activation barriers are not too high, approximately 0.75 eV, the reaction energies relative to $CO_{(g)}$ in the gas phase are exothermic, about -0.50 eV, the $CO_2{}^*$ desorptions are endothermic, with 0.70 eV, and the overall reaction energy is also exothermic, approximately -1.00 eV. In summary, it can be said here that from the second layer of a partially oxidized cluster onwards, the activity is similar to that of an oxide with partial oxidation and does not exhibit activity against CO oxidation via the LH mechanism. Single-atom catalysts are more active than these partially oxidized surfaces of subnanometer clusters and partially oxidized noble metal oxides, and can indeed represent active species. In contrast, a size-effect with subnanometer clusters, resulting in a single-layer distance from the ceria surface, presents a significantly more active species.

6.2.7. CO Oxidation on (1-7)CO^* + Pd_{10} and (1-7)CO^* + Pt_{10} Cluster via MvK Mechanism

The noble metal surfaces of subnanometer clusters can experience increased $CO_{(g)}$ adsorption under rich conditions. In this Section, we aim to illustrate the configurations of a Pd_{10} or Pt_{10} cluster occupied by CO^* molecules, which, during an MvK mechanism for CO oxidation on a ceria-supported surface, involve the consumption of O_l atoms from the surface lattice. The differential adsorption energy on the Pd_{10} and Pt_{10} clusters revealed that, at operating temperatures ranging from 423.15 K to 723.15 K, a surface coverage of $7CO^*$ molecules is expected for the Pd cluster and $9CO^*$ molecules for the Pt cluster. The temperatures are accounted by the use of *ab initio* thermodynamics, including the contributions of ZPE and entropy, as discussed in Section 3.7. Certain assumptions are being made about the coverage of CO^* molecules and their configurations during successive CO oxidation. These assumptions are necessary to simplify the study, as potential variations could lead to escalating complexity. Therefore, care has been taken to ensure a comparable transition state among the species studied in this work by selecting an analogous reaction site for all species investigated. We start with a total of 7 adsorbed CO^* molecules and

successively allow each CO^* molecule to react with a neighboring O_l lattice atom at the interface between the cluster and the ceria surface to form a CO_2 molecule per elementary step until all CO^* molecules have reacted. Certainly, in each elementary step, we assume that the O_l atom of the ceria surface adjacent to the cluster has already regenerated. The rationale here is that a formed V_O after each elementary step stabilizes in a sublayer of the (111) surface facet of ceria, causing the O_l atoms from the sublayer to move to the surface. For the sake of simplicity, in each elementary step, we assume a stoichiometric ceria surface. These calculations in this sequence are therefore not thermodynamically consistent and need modifications for a kinetic simulation. This is out of the scope of this work; hence, we restrict ourselves solely to the systematics that we will analyze the energy barriers for in the later stages of this work. In this case, it is of utmost importance to establish a systematic approach for a direct comparison between the species considering the CO^* coverage and the O^* coverage. In Section 5.3, we explored the stabilities of CO^* coverage at various temperatures in a $CO_{(g)}$ gas atmosphere. As indicated by the phase diagram in Section 5.3.1, the transition in stabilities on the Pd_{10} cluster occurs around 723.15 K, shifting from $7CO^*$ molecules to $6CO^*$ molecules. On the Pt_{10} cluster, the transition occurs around 423.15 K, shifting between 7 and $8CO^*$ molecules. Therefore, a coverage of CO^* molecules up to 7 is justified even at higher temperatures, with the maximum reaction temperature expected to be within the range of 723.15 K to ensure the stability of the catalyst under reaction conditions. The $7CO^*$ + Pd_{10} and $7CO^*$ + Pt_{10} species exhibit a particular symmetry. Starting from here, we initiate the first elementary reaction for CO oxidation via an MvK mechanism, as illustrated in Figure 6.35 for Pd and 6.36 for Pt. In the first step of the elementary reaction mechanism, initial CO adsorption takes place. In all cases, the configuration change during the reaction mechanism for the Pd_{10} and Pt_{10} clusters is minimal. The configuration changes are slightly higher for the Pt clusters than for the Pd clusters. However, the configurations remain comparable between the Pd and Pt clusters. The CO^* molecules adsorbed on the side of the cluster (excluding one CO^* molecule adsorbed on top) are preferably adsorbed in a 2-fold, bridge site configuration. Otherwise, the $CO_{(g)}$ molecule can also adsorb in a 1-fold, ontop position. The CO^* molecule migrates toward the O_l of the ceria surface during the CO oxidation. Hence, for the CO^* molecule, it is necessary to diffuse from a 2-fold position to a 1-fold position in order to reach to O_l atom. This energetic cost is not separately considered in this work. This means that this energy contributes to the activation energy barrier for the transition state. We assume here that at higher temperatures, the diffusion barrier is negligible compared to the activation energy barrier to extract an O_l from the crystal structure, which involves the effort of lattice energy. The CO oxidation via the MvK mechanism occurs in a configuration analogous for all $7CO^*$ molecules that are successively oxidized. This allows for a direct comparison of CO oxidations with decreasing

Figure 6.35.: Reaction mechanism of the CO oxidation on structure-optimized (1-7)CO^* + Pd_{10} clusters via the MvK mechanism adsorbed on a stoichiometric CeO_2(111) surface. Red circles represent O atoms, large yellow circles denote Ce atoms, dark gray circles represent C atoms, and petrol circles indicate Pd atoms. The total energies are listed in the Appendix in Table A.33.

CO^* coverage. The configuration of the transition state for the formation of a CO_2 molecule through an MvK mechanism is non-trivial and requires considerable effort to be identified.

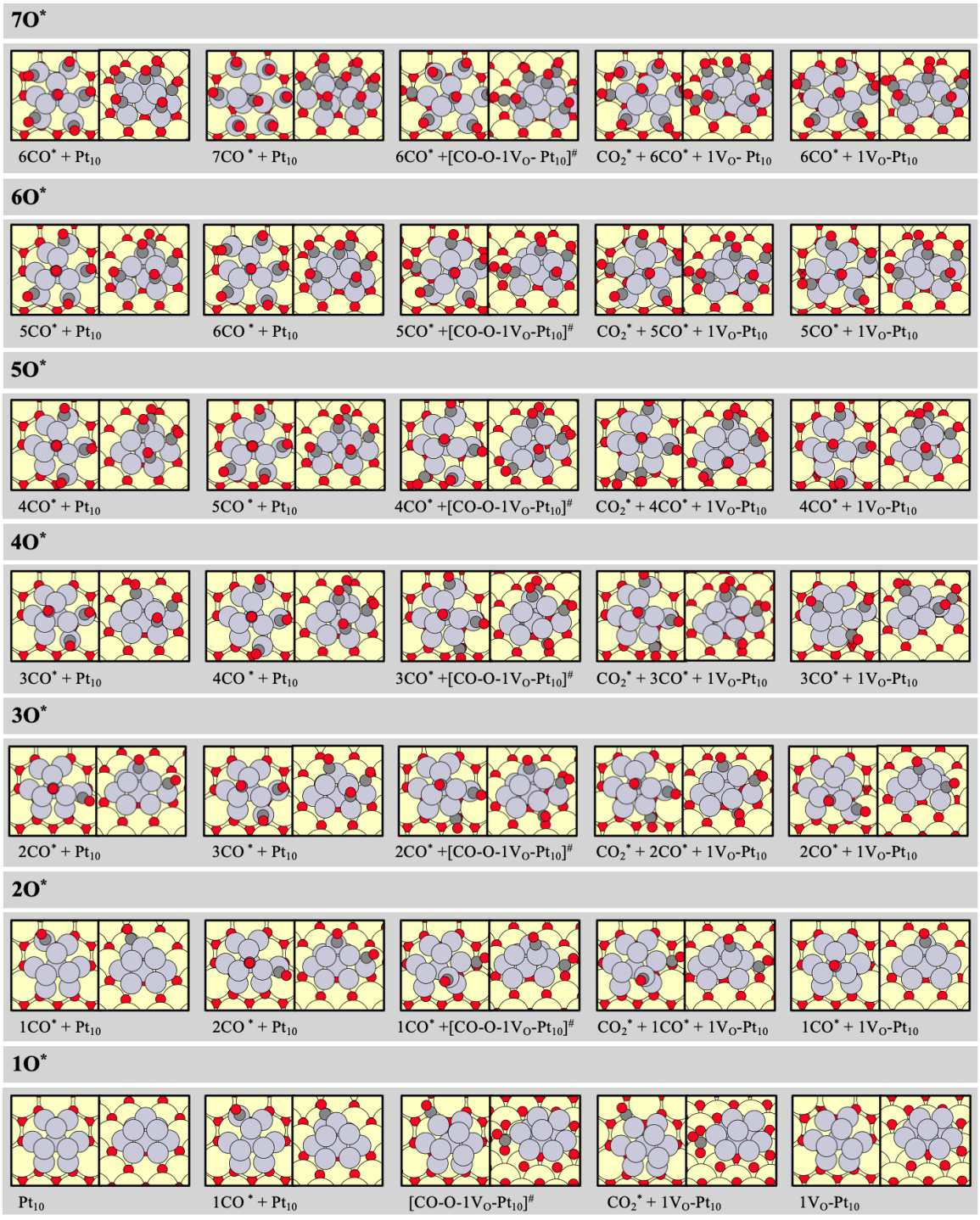

Figure 6.36.: Reaction mechanism of the CO oxidation on structure-optimized (1-7)CO^* + Pt_{10} clusters via the MvK mechanism adsorbed on a stoichiometric CeO_2(111) surface. Red circles represent O atoms, large yellow circles denote Ce atoms, dark gray circles represent C atoms, and gray circles indicate Pt atoms. The total energies are listed in the Appendix in Table A.33.

During the transition state, the O_l atom is partially detached from the surface of the ceria crystal lattice but still partially connected to it. The CO^* molecule has moved significantly

toward the ceria surface, progressively reducing the angle towards the ceria and increasingly bending towards it. The distance between the C^* atom and the O_l atom are listed in Table 6.12. After the formation of the CO_2 molecule, the O_l atom is removed from the crystal structure and forms an angled CO_2 molecule. The angles are listed in Table 6.12. After desorption of the CO_2 molecule, an V_O lattice defect remains on the ceria surface. In the next elementary step, the CO oxidation begins with a (n-1)CO^* + Pd_{10} and (n-1)CO^* + Pt_{10} species on a stoichiometric ceria (111) surface, without considering any V_O from the previous step. We maintained this systematic approach to consider these steps without the additional influence of nV_O defects. This influence would need to be separately examined in a further study. Unfortunately, this is out of the scope of this work; we highly recommend a more detailed investigation. With this study, we provide valuable and reliable configurations derived through an extensive investigation that can serve as a basis for further studies. The process of CO oxidation repeats itself starting from the 7CO^* + Pd_{10} and 7CO^* + Pt_{10} species at each step until the last CO^* molecule, which, in this case, has to diffuse from the hollow site on the apex of the cluster on the 2nd layer to the interface. For the sake of simplicity, we have omitted the investigation of diffusion energies since they do not contribute to the systematic examination of transition states and their energies. Based on the configurations presented here, it becomes apparent that the Pd_{10} and Pt_{10} structures are quite advantageous configurations to simplify such complex reaction mechanisms into essential steps. This approach aids in conducting time- and resource-intensive DFT calculations with an appropriate level of theory within a manageable timeframe and effort. Die basic configuration of the Pd_{10} and Pt_{10} structures have remained relatively unaffected by the reactants and the transition state. This suggests a particular stability of these species, providing high flexibility in the adsorption sites for the reacting species. In some elementary steps, it is observed that the structure bends particularly when there is one-sided adsorption on the cluster. However, this bending rectifies itself when symmetry in adsorption or complete desorption of the reactants is reestablished. Additionally, in the case of the formation of the V_O, it is noticeable that one of the Pd or Pt atoms moves in the z-direction due to the lack of anchoring to the surface. However, due to the specific configuration of the Pd_{10} and Pt_{10} structures anchoring perfectly to one O_l with each noble metal atom on the interface, only one noble metal atom detaches on the position of the V_O, which, upon regeneration by an O atom on this lattice site of the ceria surface, returns to its position coordinated with an O_l atom. The structures were fully structure-optimized, and the Gibbs free energies were calculated for a reaction temperature of 423.15 K. These values are depicted in Figure 6.37 in a potential energy diagram, and the calculated Gibbs free energies are listed in Table 6.12. The $CO_{(g)}$ adsorption energy is exothermic in all cases, ranging from 1CO^* to 7CO^* molecules, both on the Pd_{10} and Pt_{10} clusters. The activation barriers for CO

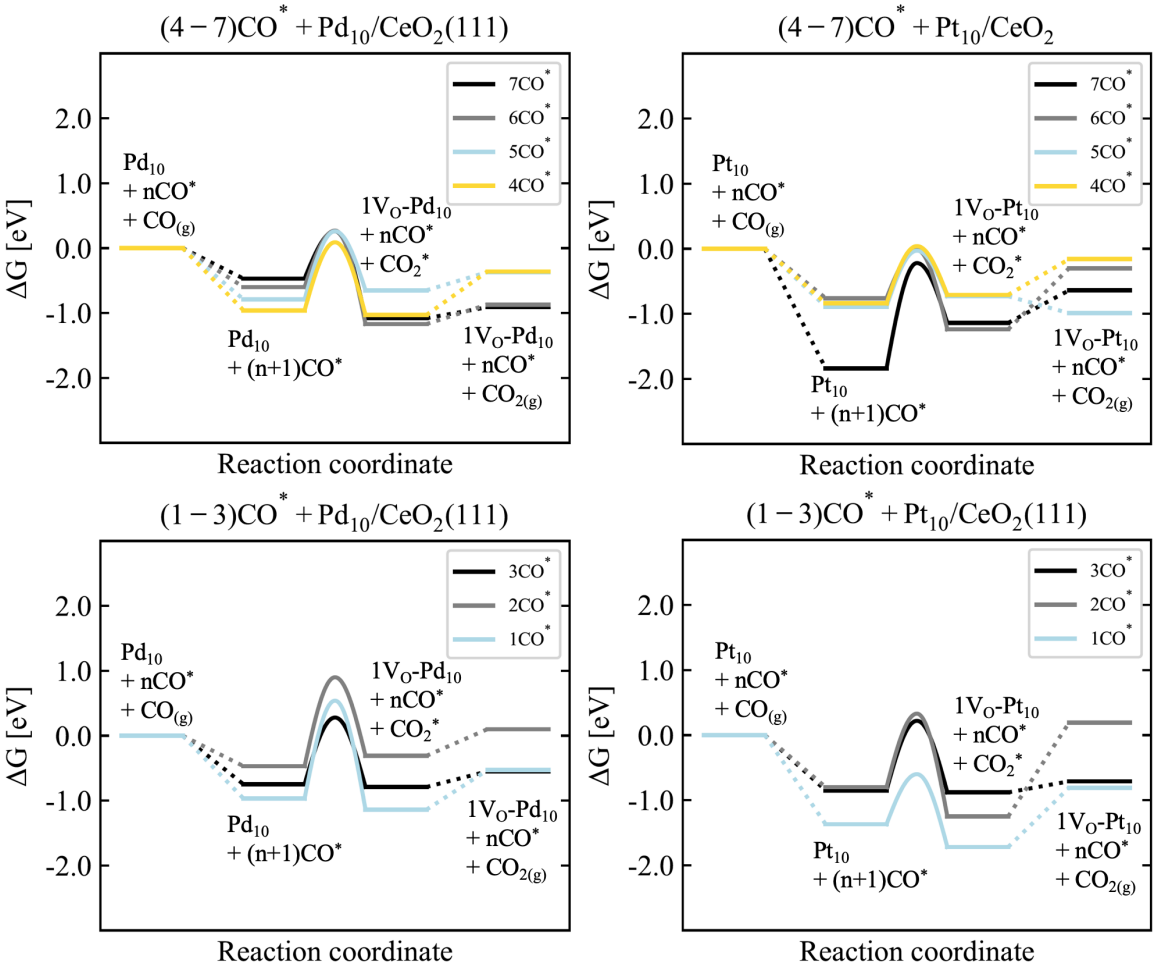

Figure 6.37.: Calculated Gibbs free energies of the structure-optimized CO oxidation elementary reaction steps on (1-7)CO* + Pd_{10} and (1-7)CO* + Pt_{10} cluster via the MvK mechanism as depicted in Figure 6.35 for Pd and Figure 6.36 for Pt plotted against the reaction coordinate in a potential energy diagram. The Gibbs free energies are referenced to (1-7)CO* + Pd_{10} and (1-7)CO* + Pt_{10} catalysts adsorbed on the stoichiometric ceria surface facet (111) in eV at 423.15 K. The total energies, the ZPE and the entropies are listed in the Appendix in Table A.33.

oxidation via the MvK mechanism on the (1-7)CO* + Pd_{10} cluster, starting with decreasing CO adsorption from 7CO* molecules, are as follows: 0.73 eV, 0.87 eV, 1.05 eV, 1.05 eV, 1.03 eV, 1.38 eV, and 1.51 eV for the last CO* molecule. On the (1-7)CO* + Pt_{10} cluster, starting with decreasing $CO_{(g)}$ adsorption from 7CO* molecules, the activation barriers are: 1.62 eV, 0.74 eV, 0.85 eV, 0.88 eV, 1.07 eV, 1.13 eV, and 0.77 eV for the last CO* molecule. Therefore, a tendency can be observed in the Pd cluster, leading to higher activation barriers with decreasing CO* coverage. The difference gradually decreases by about 0.10 eV, with the largest difference between 7CO* molecules and 1CO* molecule being 0.78 eV. For the Pd_{10} cluster, the reaction energies of the elementary step are exothermic at a reaction temperature of 423.15 K, ranging from 0.26 eV to 0.90 eV. For the Pt_{10} cluster, the reaction barriers relative to $CO_{(g)}$ in the gas phase are exothermic starting with 7CO* moleculesand

decreasing in adsorbed CO^* molecules with 0.26 eV, 0.27 eV, 0.26 eV, 0.09 eV, 0.28 eV, 0.90 eV, and 0.54 eV for the last CO^* molecule on the Pd_{10} cluster and -0.22 eV, -0.02 eV, -0.03 eV, 0.04 eV, 0.22 eV, 0.33 eV, and -0.60 eV on the Pt_{10} cluster. The $CO_2{}^*$ desorption is endothermic in all cases, with values depending on the CO^* coverage, starting from $7CO^*$ molecules and decreasing successively to end with $1CO^*$ molecule with 0.17 eV, 0.30 eV, 0.29 eV, 0.68 eV, 0.23 eV, 0.41 eV, 0.61 eV for the Pd_{10} cluster and 0.50 eV, 0.94 eV, -0.25 eV, 0.55 eV, 0.16 eV, 1.44 eV, 0.90 eV for the Pt_{10} during the decrease of adsorbed CO^* molecules starting from $7CO^*$ molecules and ending with $1CO^*$ molecule. The bond angles of the formed CO_2 molecule are interestingly once again quite small, approximately 130° for the Pd_{10} cluster and 125° for the Pt_{10} cluster. The distances between the C atom and the O atom during the transition state of CO oxidation are all in the range of 1.30 Å. In

Table 6.12.: Calculated Gibbs free energies of the CO oxidation elementary reaction step referenced to the number of CO adsorbed nO^* on the Pd_{10} and Pt_{10} clusters before CO oxidation via the MvK mechanism on the surface facet (111) of ceria in eV and at 423.15 K of the structure-optimized elementary steps depicted in Figure 6.35 for Pd and Figure 6.36 for Pt. The potential energies are plotted in the potential energy diagrams 6.37. The Bond length between the C^* and the O^* atom during the transition state is described as b.l. in Å at 0 K and included in gray letters. The bond angles in degree of the formed CO_2 molecules are given in gray letters.

	CO^* [eV]	$[CO\text{-}O]^\#$ [eV]	b.l. [Å]	$CO_2{}^*$ [eV]	$(n\text{-}1)O^*$ [eV]	angle [°]
CO oxidation via MvK Mechanism						
$7CO^* + Pd_{10}$	-0.47	0.26	1.29	-1.08	-0.91	133
$6CO^* + Pd_{10}$	-0.60	0.27	1.28	-1.17	-0.87	134
$5CO^* + Pd_{10}$	-0.79	0.26	1.30	-0.65	-0.37	131
$4CO^* + Pd_{10}$	-0.96	0.09	1.30	-1.03	-0.36	130
$3CO^* + Pd_{10}$	-0.75	0.28	1.30	-0.79	-0.55	129
$2CO^* + Pd_{10}$	-0.47	0.90	1.30	-0.31	0.10	130
$1CO^* + Pd_{10}$	-0.97	0.54	1.28	-1.14	-0.53	134
$7CO^* + Pt_{10}$	-1.84	-0.22	1.32	-1.14	-0.64	126
$6CO^* + Pt_{10}$	-0.76	-0.02	1.31	-1.24	-0.30	125
$5CO^* + Pt_{10}$	-0.89	-0.03	1.35	-0.73	-0.99	122
$4CO^* + Pt_{10}$	-0.84	0.04	1.32	-0.71	-0.16	125
$3CO^* + Pt_{10}$	-0.85	0.22	1.32	-0.88	-0.72	125
$2CO^* + Pt_{10}$	-0.80	0.33	1.34	-1.25	0.19	122
$1CO^* + Pt_{10}$	-1.37	-0.60	1.30	-1.72	-0.81	129

general, it can be observed here that depending on the CO^* coverage, a trend in activity can be observed. With low CO^* coverage, the reaction barrier is still quite high. Additionally, $CO_2{}^*$ desorption is high, indicating that low CO^* coverage does not positively affect the activity. However, with increased coverage, a reduction in reaction barriers can be observed, and $CO_2{}^*$ desorption is also lower. This is a particularly interesting insight into the activities of subnanometer clusters. In a previous study by Koleva et al.,[299] the same activities were conducted with coverages between $7CO^*$ molecules and $12CO^*$ molecules. As observed

in Section 5.3, higher coverage by CO^* molecules is not advantageous for a subnanometer cluster of small size. Firstly, the size of the cluster cannot be maintained, raising questions about whether such high coverage can still be considered. After the dissociation of the subnanometer clusters, due to their high interaction with adsorbed CO^* molecules, smaller noble metal clusters or even single atoms are formed, which, while exhibiting high coverage, do not match the coordination of $12CO^*$ molecules on a Pd_{10} cluster and Pt_{10} cluster. Furthermore, under reaction conditions, such high coverage, as discussed in Section 5.3, is not realistic. As discussed there, coverages of approximately (5-7)CO^* molecules are very interesting to consider. As observed in this section, increased activity due to higher CO^* coverage is evident.

6.3. Nanometer Clusters theoretically approached by Extended Pd and Pt noble metal Surfaces

The structures used in this study were inspired by literature, primarily by Grönbeck[300], and subsequently refined based on various investigations within the research field. After reviewing the literature, we selected configurations not based on the most stable ones but rather on those featuring a wide range of noble metal sizes supported on ceria oxide.

6.3.1. O_2 Dissociation on Pristine noble Metal Surfaces of Pd and Pt via LH Mechanism

Figure 6.38 for Pd and Figure 6.39 for Pt depict the O_2 dissociation on all four significant surfaces (111), (100), (110), and (211) of the extended metal surfaces of Pd and Pt. The elementary step of O_2 dissociation commences with the adsorption of an $O_{2(g)}$ molecule. The molecule horizontally adsorbs on the surface, attached to two or three noble metal atoms on each surface, occupying an on-top or bridge position, respectively. During dissociation the O atoms increase the distance between each other, primarily favoring the on-top or bridge positions for coordination to the noble metal atoms. After dissociation, it is assumed that the O atoms reside as single adsorbed O^* atoms on the surface. In this work, we did not prioritize seeking the most stable adsorbtion site of these two O^* atoms now adsorbed on the surface, which could be achieved through subsequent surface diffusion. It is noteworthy that this work does not primarily focus on the noble metal surfaces but on subnanometer-sized noble metal clusters supported on ceria. The noble metal surfaces are utilized here as a reference, primarily due to their resemblance to potential configurations resulting from $O_{2(g)}$ adsorptions and dissociations on the subnanometer clusters, which will be presented later in the course of this work as the dissociated O atoms presented here have an analogous structure. It is essential to note that for O_2 dissociation in this Section, a configuration

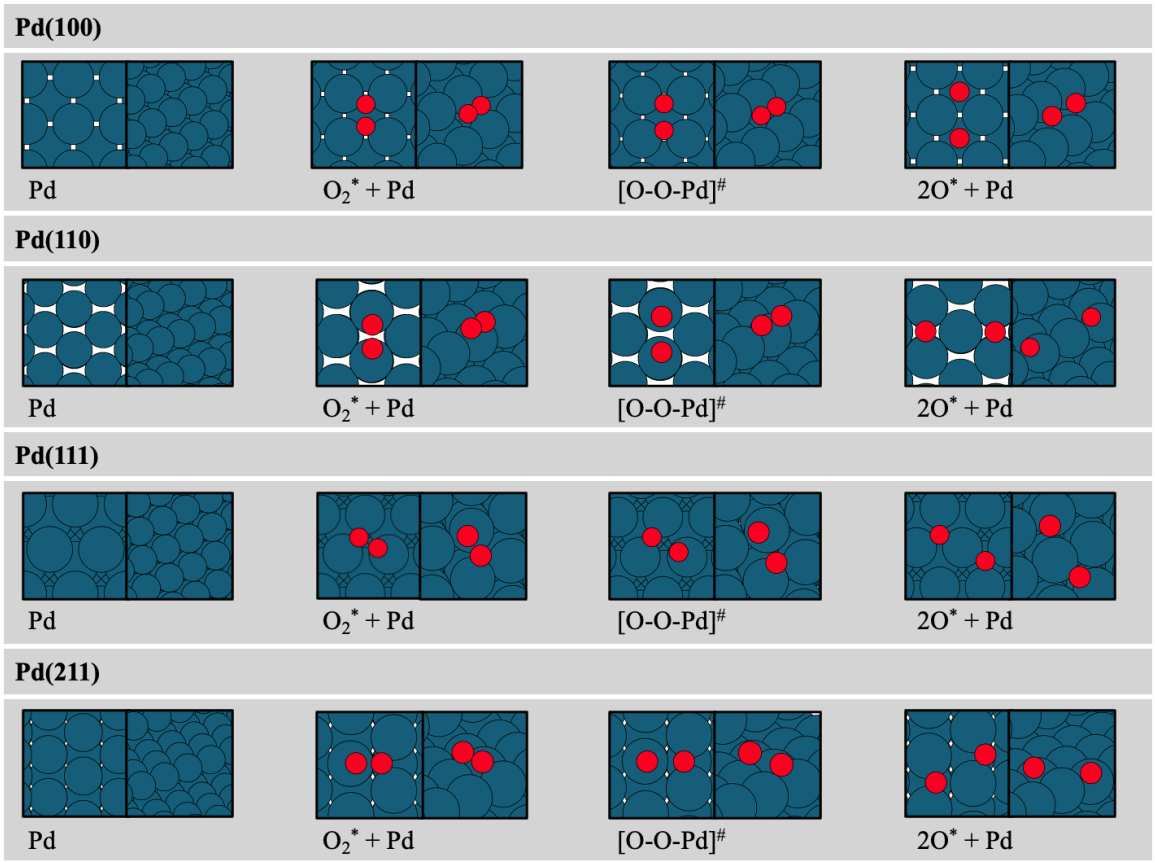

Figure 6.38.: Reaction mechanism of an O_2 dissociation on structure-optimized extended Pd surface facets (111), (110), (100), and (211) with a high loading of adsorbed O^* atoms via the LH mechanism. Red circles represent O atoms, and petrol circles represent Pd atoms. The total energies are listed in the Appendix in Table A.34.

reflecting three noble metal atoms arranged in a triangle, with one O atom of the O_2^* molecule adsorbed on an on-top position and another on a bridge position distributed over two noble metal atoms, is chosen. This configuration resembling the subnanometer cluster surfaces is selected to systematically conduct subsequent analyses through scaling relations of transition states and $O_{2(g)}$ molecule adsorptions. This circumstance is particularly true for the (111) and the (211) surface of the noble metal crystals. The O positions may differ between the Pd and Pt extended crystal surfaces. For instance, on the (100) surface of the Pd crystal, the O_2 molecule is adsorbed for each O atom of the molecule at a bridge position between two noble metal atoms each, while on the Pt surface, it is adsorbed on the ontop configuration each. After dissociation, the O atoms on the Pd surface occupy the hollow site, whereas on the Pt surface, they occupy the bridge site. On the (110) surface, the O_2 dissociation on Pd and on Pt occurs at the kink, with each atom in an on-top position. Following, the dissociated two O^* atoms on the (110) surface coordinate with the bridge site for both Pd and Pt. These circumstances emerged during the structural optimizations, even

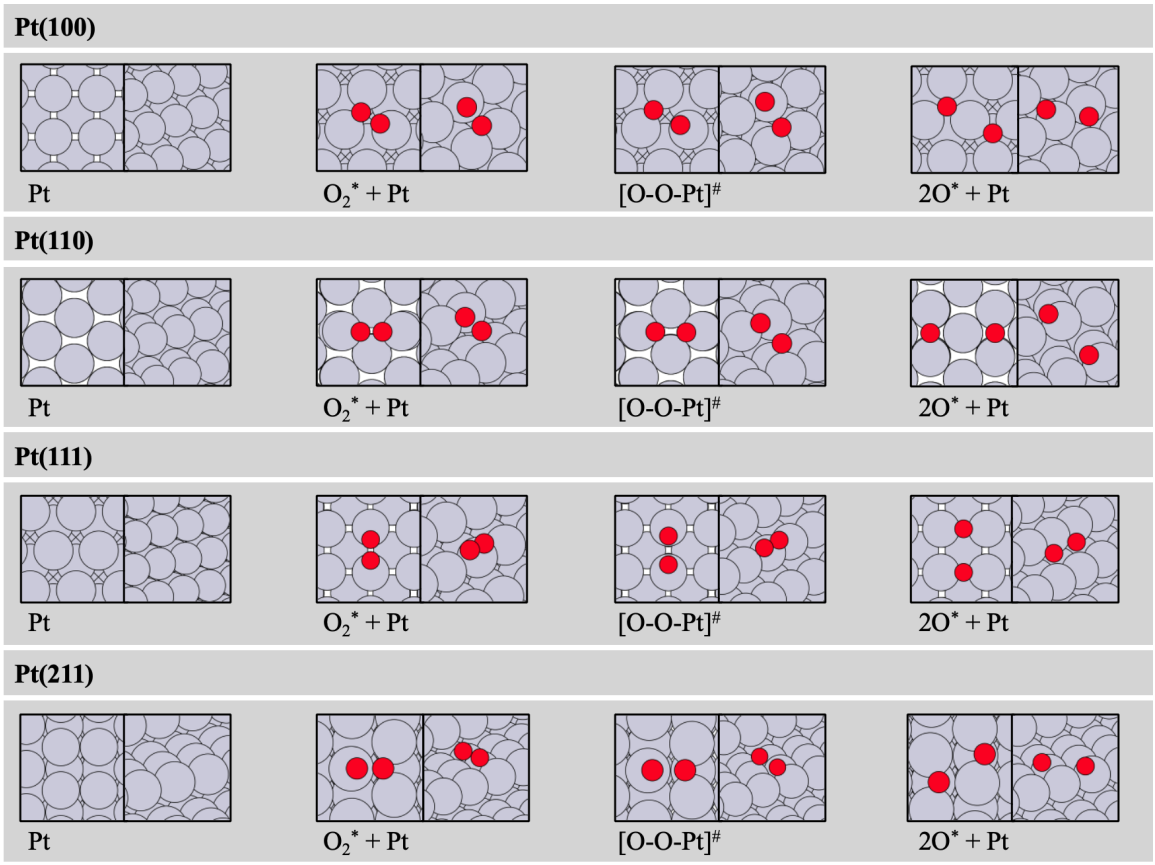

Figure 6.39.: Reaction mechanism of an O_2 dissociation on structure-optimized extended Pt surface facets (111), (110), (100), and (211). Red circles represent O atoms, and gray circles represent Pt atoms. The total energies are listed in the Appendix in Table A.34.

though initially, all configurations were systematically and consistently approached. While we won"t delve into the quantum chemical or element-specific backgrounds in this work, we wish to note them at this point. It is also noteworthy that the O^* positions differ between the Pd and Pt surfaces. For instance, on the (100) surface of the Pd crystal, the O_2 molecule is adsorbed as a bridge, while on the Pt surface, it is adsorbed as an on-top configuration. After dissociation, the O^* atoms on the Pd surface occupy the hollow site, whereas on the Pt surface, they occupy the bridge site. On the (110) surface, the $O_2{}^*$ dissociation on Pd occurs at the kink, with each atom in an on-top position, whereas on Pt, it occurs between the kink rows, with each atom in an on-top position. Following dissociation, the O^* atoms on the (110) surface coordinate with the bridge site for both Pd and Pt. The energetic differences between these configurations will not significantly impact the rest of the work, as the noble metal surfaces are solely used as a reference for the nanometer clusters. This circumstance is particularly true for the (111) surface of the noble metal crystals. The differences in adsorption sites are reflected in the potential energy diagram 6.40, illustrating the Gibbs free energies of the elementary reaction step for O_2 dissociation calculated to have a reaction

temperature of 423.15 K. The temperature of 423.15 K is accounted by the use of *ab initio* thermodynamics, including the contributions of ZPE and entropy, as discussed in Section 3.7. Different barriers arise from the possible adsorption sites. Generally speaking, the (111) surface, which corresponds to the adsorption sites of the subnanometer clusters, as will be demonstrated in the course of this work, resembles those of the (211) surface. The (211) surface offers a broad terrace where a reaction can occur either directly at the kink or on the free surface. The Gibbs free energies are depicted in a potential energy diagram in Figure 6.40. The corresponding calculated Gibbs free energies are computed for a reaction temperature of 423.15 K and listed in Table 6.13. The temperature of 423.15 K is accounted by the use of *ab initio* thermodynamics, including the contributions of ZPE and entropy, as discussed in Section 3.7. The bond lengths are included therein. The O_2 molecule in the gas phase at 423.15 K exhibits only a slight elongation of 0.001 Å compared to the respective bond lengths at 0 K. Therefore, the bond length at 0 K can be considered, and the elongation at increasing temperature can be disregarded. Upon adsorption, there is a bond elongation from 1.23 Å at 0 K in the gas phase to around 1.40 Å on the Pd and Pt surfaces. The transition state demonstrates an increasing bond elongation towards approximately 2.00 Å for both the Pd and Pt surfaces. However, it is not possible to categorically distinguish between the surfaces and the noble metals in this regard. The adsorption energy of the O_2 molecule on the pure extended noble metal surfaces is exothermic for Pd on the (100) and (110) surfaces with -0.39 eV and -0.23 eV, respectively. For Pt, only the (110) surface exhibits exothermic adsorption with -0.57 eV. On all other surfaces, the adsorption energy is endothermic, with values of 0.18 eV for (111) and 0.04 eV for (211) on the Pd surface, and 0.01 eV for (100), 0.35 eV for (111), and 0.18 eV for (211) on the Pt surface. Consequently, the adsorption energy significantly depends on the configuration of the O_2 molecule on the adsorption site which are identified as strain effects by a study of Dietze et al. affecting the reactivity. It is stated, that compressive strain leads to stronger bonding, and tensile strain reduces the bond strength.[301] A general trend that can be observed is that on the (111) and (211) surfaces, sites with densely packed configurations of surface atoms provide lower adsorption energy compared to surface defect configurations on the (110) and (100) surfaces. Pt shows a greater disparity in adsorption energies between densely packed and defective step structures. Therefore, O_2 binds weaker on densely packed surfaces but stronger on kink and edge structures. In general, it can be stated that the dissociation energy depends on the adsorption site. While the (111) and (211) surfaces offer comparable transition state configurations, significant differences are evident on the (100) and (110) surfaces. Regarding the reaction barriers relative to $O_{2(g)}$ in the gas phase, for Pd, endothermic energies are observed on the (111) and (211) surfaces, with 0.93 eV and 0.67 eV, respectively. For the (100) surface, it is exothermic with -0.24 eV, and for the (110) surface, it is considered

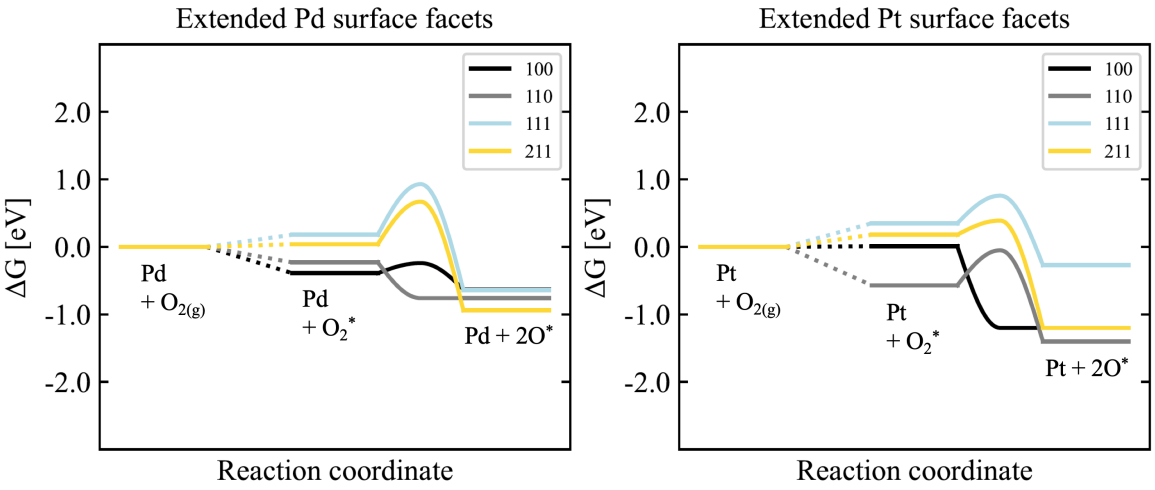

Figure 6.40.: Calculated Gibbs free energies of the structure-optimized O_2 dissociation elementary reaction steps on extended noble metal surface facets (100), (110), (111) and (211) as depicted in Figure 6.38 for Pd and Figure 6.39 for Pt plotted against the reaction coordinate in a potential energy diagram. The Gibbs free energies are referenced to single-atom catalyst adsorbed on the stoichiometric extended Pd and Pt noble metal surface facets (100), (110), (111) and (211) in eV and at 423.15 K. The total energies, the ZPE and the entropies are listed in the Appendix in Table A.34.

Table 6.13.: Calculated Gibbs free energies of the O_2 dissociation elementary reaction step on the extended noble metal surface facets (100), (110), (111) and (211) in eV and at 423.15 K of the structure-optimized elementary steps depicted in Figure 6.38 for Pd and Figure 6.39 for Pt. The Gibbs free energies are plotted in the potential energy diagram 6.40. The Bond length between the O atoms during the transition state is described as b.l. in Å at 0 K and included in gray letters. Non-optimizable structures with very low barriers are considered spontaneous reactions and are denoted as sp.

	O_2^* [eV]	b.l. [Å]	$[O\text{-}O]^\#$ [eV]	b.l. [Å]	$2O^*$ [eV]
O_2 dissociation via LH Mechanism					
Pd(100)	-0.39	1.41	-0.24	1.71	-0.63
Pd(110)	-0.23	1.34	sp.	-	-0.76
Pd(111)	0.18	1.36	0.93	1.93	-0.64
Pd(211)	0.04	1.38	0.67	2.00	-0.94
Pt(100)	0.01	1.37	sp.	-	-1.20
Pt(110)	-0.57	1.38	-0.05	2.14	-1.40
Pt(111)	0.35	1.40	0.76	1.93	-0.27
Pt(211)	0.18	1.42	0.39	1.80	-1.20

spontaneous. In contrast, for the Pt surfaces, while it is spontaneous for the (100) surface, it is significantly endothermic for all other surfaces, with -0.05 eV for (110), 0.76 eV for (111), and 0.39 eV for (211). Overall, the reaction energy depends on the adsorption sites on the noble metals. Previous studies have shown[56] that kink and corner sites with defective surface structures are the more reactive surfaces, which can be generally confirmed here. It is advisable to make a general statement about the noble metal structures for evaluating the activation barriers within this work, aiming to approximate the nanometer clusters. It can be stated that the reaction energy of the elementary reaction is exothermic in all cases, slightly

lower for the Pd surfaces, around -0.70 eV, and significantly higher for the Pt surfaces, around -1.30 eV.

6.3.2. CO Oxidation on Extended Pd and Pt noble Metal Surfaces with high O^* loading via LH Mechanism

Once an O_2 molecule is dissociated, two dissociated O^* atoms adsorbed on the heterogeneous catalyst are formed. Since the diffusion barriers of adsorbed O^* atoms on a Pd or Pt surface are small with about 0.45 eV as calculated by Bogicevic et al., the O^* atoms are expected to diffuse on the surface.[289,302,303] This implies that the adsorbed $2O^*$ atoms resulting from an O_2 dissociation within a unit cell rapidly reduce to a single adsorbed O^* atom in a real reaction such as CO oxidation, as the surface distribution of adsorbed O^* atoms quickly reaches equilibrium. Therefore, the surface coverage by $2O^*$ atoms within a unit cell can only be described under real reaction conditions when referring to an increased surface coverage. This ensures an even distribution of adsorbed O atoms across coverage

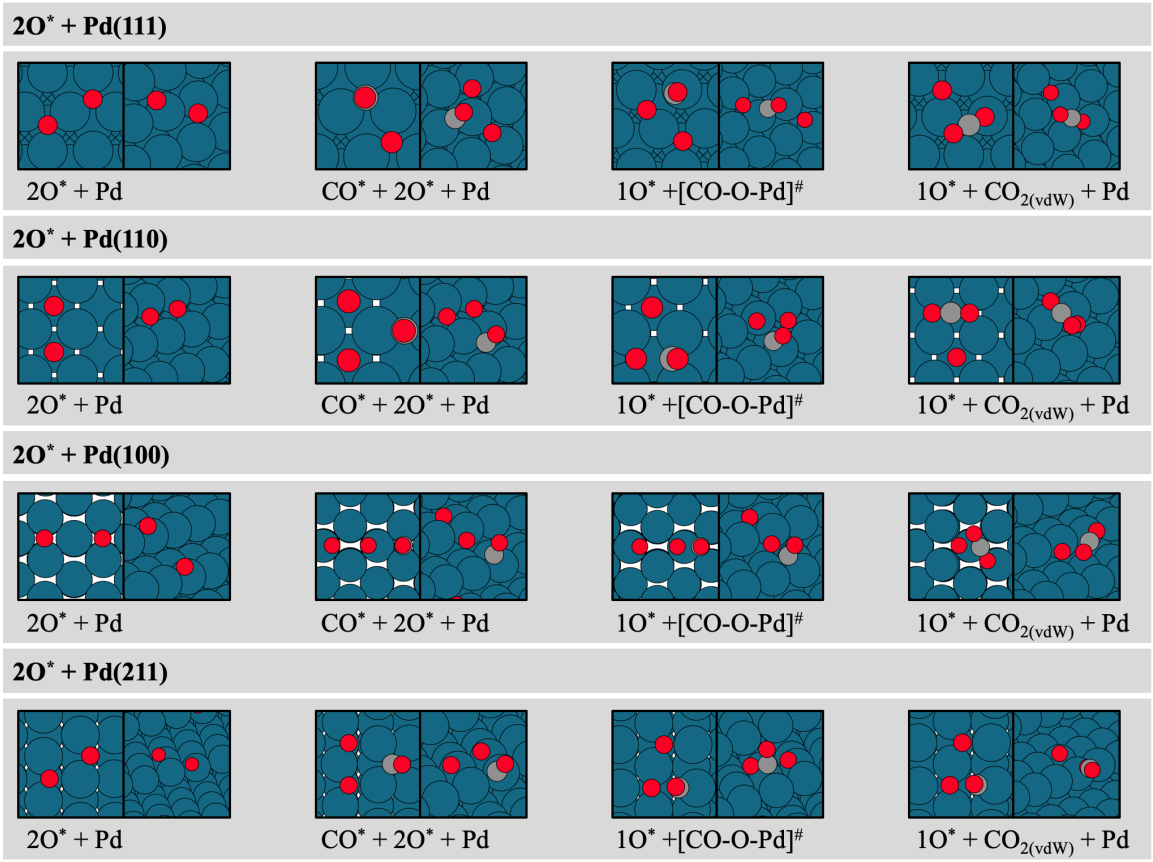

Figure 6.41.: Reaction mechanism of an CO oxidation on structure-optimized extended Pd surface facets (111), (110), (100), and (211) with high O^* loading of adsorbed O^* atoms via the LH mechanism. Red circles represent O atoms, dark gray circles represent C atoms, and petrol circles represent Pd atoms. The total energies are listed in the Appendix in Table A.35.

sites, guaranteeing their continuous availability. To assess the coverage of O^* atoms on the heterogeneous catalyst, which undergoes $CO_{(g)}$ adsorption in a neighboring position to CO oxidation, the unit cells can be reduced to calculate the surfaces through a single O atom. However, as our project collaborates with another project to conduct kinetic simulations based on our DFT calculations, we process our data in a way that provides thermodynamic consistency, targeting a surface coverage of $2O^*$ atoms resulting from O_2 dissociation in a single unit cell. For experimental comparisons, a surface coverage of $2O^*$ atoms in a unit cell is considered as a high O^* surface coverage, while a coverage of only one O^* atom is regarded as lower O^* surface coverage. Figure 6.41 for Pd and Figure 6.42 for Pt depict an LH mechanism on all four significant surfaces (111), (100), (110), and (211) of the pristine metal surfaces of Pd and Pt, where an additional O^* atom is adsorbed but does not participate in this elementary reaction step. This is considered as the high O^* surface

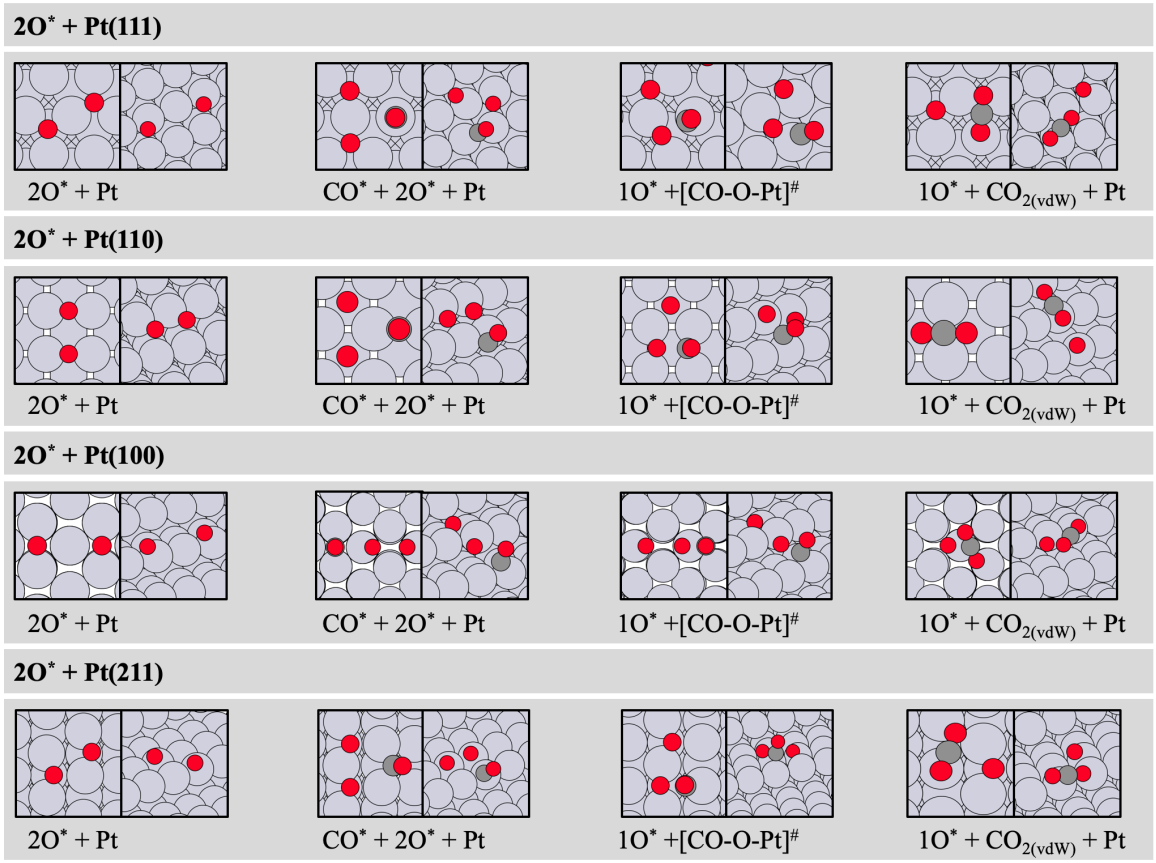

Figure 6.42.: Reaction mechanism of CO oxidation on the extended noble metal surface facets (100), (110), (111) and (211) with a high loading of adsorbed O^* atoms via the LH mechanism. Red circles represent O atoms, dark gray circles represent C atoms, and gray circles Pt atoms. The total energies are listed in the Appendix in Table A.35.

coverage. After the CO^* adsorption next to the $2O^*$ atoms the CO oxidation leads to a CO_2 formation. It is well known that, according to first-principles calculations at the level

of theory used here, the CO molecule does not predict the correct adsorption sites on a Pt surface. Experimentally, different sites have been observed. This computational issue is referred to as the CO puzzle.[304] Our studies have shown that this phenomenon indeed occurs on the Pt surface, while Pd surfaces appear to be unaffected. DFT methods tend to underestimate the binding of CO molecules to low-coordination sites on Pt(111). This lead to CO adsorbed on hollow sites rather than atop sites on Pt(111), contradicting experimental studies conducted at low temperatures.[305–309] The general trend of CO oxidation on these surfaces involves oxidation occurring at the edges of the under-coordinated surfaces (100), (110), and (211). The CO molecule binds at an angle to the terrace surface and in a bridge position directly on the last row of the edges. The (111) surface has the particularity of forming an optimal active site with the reactants adsorbed in close proximity, both on a hollow site. After CO oxidation, the resulting yet adsorbed $CO_2{}^*$ molecule is desorbed rapidly. The structure optimization by the use of DFT methods calculated that desorption of $CO_2{}^*$ molecules is highly favorable. The surfaces of noble metals offer different adsorption sites that significantly influence the configuration during CO oxidation. On the (111) and (211) surfaces, the CO^* molecule is bound atop a noble metal atom, while the O^* atom is bridge-bound to two adjacent noble metal atoms. On the (100) surface, the O^* atoms are

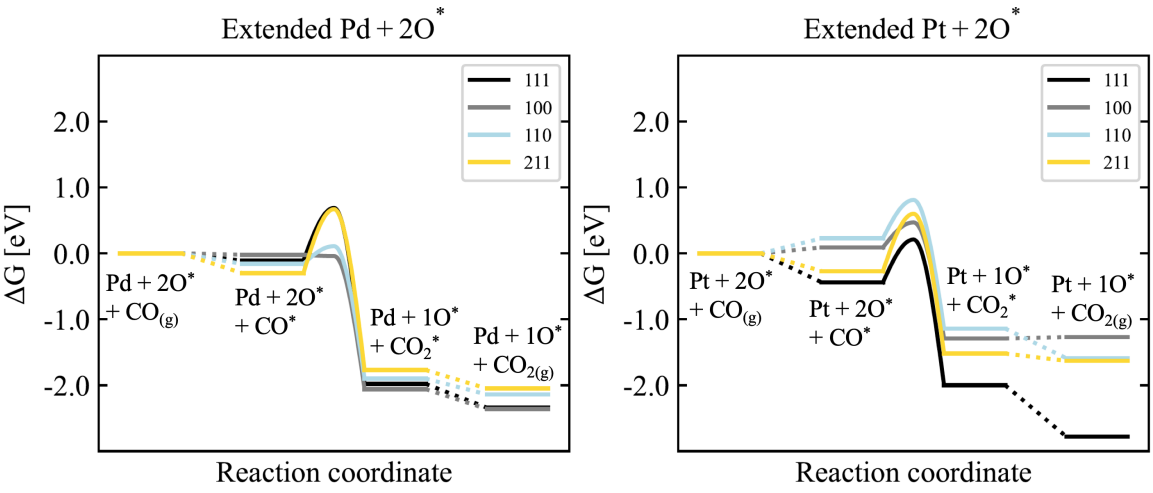

Figure 6.43.: Calculated Gibbs free energies of the structure-optimized CO oxidation elementary reaction steps on the extended noble metal surface facets (100), (110), (111) and (211) with high O^* loading of adsorbed O^* atoms via the LH mechanism as depicted in Figure 6.41 for Pd and Figure 6.42 for Pt plotted against the reaction coordinate in a potential energy diagram. The Gibbs free energies are referenced to the extended Pd and Pt noble metal surface facets (100), (110), (111), and (211) with two adsorbed $2O^*$ in eV and at 423.15 K. The total energies, the ZPE and the entropies are listed in the Appendix in Table A.35.

bound in a hollow position, while the CO^* molecule is bridge-bound. During the transition state, both the O^* atom and the CO^* molecule are bridge-bound, forming a bond through migration towards each other. The (100) surface allows for a proximity of bridge positions due to the rows of noble metals on this defective surface. In contrast, the (110) surface

offers an additional row of noble metal, resulting in the CO^* molecule being bridge-bound while the O^* atom is in a hollow site. During bond formation, the CO^* molecule migrates to the O^* atom. Furthermore, the (211) surface has the peculiarity that the CO molecule is bound at a corner and therefore must first diffuse onto the terrace during migration. After performing structural optimization for all steps of the elementary reaction of CO oxidation, the Gibbs free energies were calculated for a reaction temperature of 423.15 K and plotted in a potential energy diagram in Figure 6.43 and are listed in Table 6.14. The temperature of 423.15 K is accounted by the use of *ab initio* thermodynamics, including the contributions of ZPE and entropy, as discussed in Section 3.7. The $CO_{(g)}$ adsorption on the Pd surface, along with pre-adsorbed $2O^*$ atoms, is slightly exothermic: -0.11 eV for (111), -0.16 eV for (110), -0.02 eV for (100), and -0.30 eV for (211). Conversely, on the Pt surface, CO adsorption is slightly endothermic on (100) and (110) surfaces with 0.09 eV and 0.23 eV, respectively. For (111) and (211) surfaces, it is exothermic with -0.44 eV and -0.27 eV, respectively. After CO adsorption, the reaction barrier for CO oxidation on the Pd surfaces is 0.91 eV for (111), 1.50 eV for (110), 0.48 eV for (100), and 0.83 eV for (211). For the

Table 6.14.: Calculated Gibbs free energies of the CO oxidation elementary reaction steps on the extended noble metal surface facets (100), (110), (111) and (211) with high O^* loading of adsorbed O^* atoms via the LH mechanism in eV and at 423.15 K of the structure-optimized elementary steps depicted in Figure 6.41 for Pd and Figure 6.42 for Pt. The Gibbs free energies are plotted in the potential energy diagram 6.43. The Bond length between the C^* and the O^* atom during the transition state is described as b.l. in Å at 0 K and included in gray letters. The bond angles in degree of the formed CO_2 molecules are given in gray letters.

	CO^* [eV]	$[CO\text{-}O]^\#$ [eV]	b.l. [Å]	$CO_2{}^*$ [eV]	CO_2 [eV]	angle [°]
O_2 dissociation via LH Mechanism						
$2O^*$ + Pd(111)	-0.11	0.69	2.05	-1.98	-2.34	180
$2O^*$ + Pd(100)	-0.02	-0.04	1.89	-2.06	-2.36	180
$2O^*$ + Pd(110)	-0.16	0.11	1.84	-1.90	-2.14	180
$2O^*$ + Pd(211)	-0.30	0.67	2.01	-1.77	-2.05	180
$2O^*$ + Pt(111)	-0.44	0.21	1.87	-2.00	-2.78	180
$2O^*$ + Pt(100)	0.09	0.47	1.89	-1.29	-1.27	179
$2O^*$ + Pt(110)	0.23	0.81	1.89	-1.14	-1.59	180
$2O^*$ + Pt(211)	-0.27	0.60	1.82	-1.52	-1.63	179

Pt surfaces, it is 0.81 eV for (111), 0.27 eV for (110), -0.02 eV for (100), and 0.97 eV for (211). The reaction barriers for Pt surfaces are therefore slightly higher, ranging from approximately 0.10 to 0.30 eV, compared to Pd surfaces. The reaction barriers relative to $CO_{(g)}$ in the gas phase are quite endothermic for Pd surfaces, with values of 0.69 eV for the (111) surface and 0.67 eV for the (211) surface. For the (110) and (100) surfaces, they are relatively neutral, with values of 0.11 eV and -0.04 eV, respectively. In contrast, the Pt surface behaves differently, with all reaction barriers relative to $CO_{(g)}$ in the gas phase being endothermic. These values are 0.21 eV for (111), 0.81 eV for (110), -0.04 eV for (100),

and 0.60 eV for (211). The bond distance between the C atom and the O atom during the transition state for CO oxidation on the extended metal surfaces is around 2.00 Å for the Pd surfaces and around 1.90 Å for the Pt surfaces. The bond angles after the formation of the $CO_{2(g)}$ molecule due to spontaneous desorption are already 180°. Upon desorption into the gas phase, the reaction energy of the elementary step is exothermic in all cases, ranging from approximately -2.10 eV to -2.30 eV for Pd surfaces, and slightly less exothermic for Pt surfaces, ranging between -1.30 eV and -1.60 eV. It is noteworthy that the (111) surface for Pt exhibits a significantly more exothermic reaction energy -2.78 eV at the (111) surface compared to the others. Overall, it can be concluded that the (111) and (211) surfaces, both for Pd and Pt, exhibit relatively high reaction barriers compared to the other surfaces. Due to the endothermic adsorption of the $CO_{(g)}$ molecule at the reaction temperature of 423.15 K on the (100) and (110) surfaces for Pt, the reaction barriers relative to $CO_{(g)}$ in the gas phase are approximately at the same level as those of the other two surfaces. However, for Pd, the (100) and (110) surfaces are significantly lower, as $CO_{(g)}$ adsorption is also exothermic. The potentially decisive insight from the Gibbs free energies of CO oxidation on the Pd and Pt surfaces with high O^* coverage is that the desorption of $CO_{2(g)}$ does not present inhibition.

6.3.3. CO Oxidation on Extended Pd and Pt noble Metal Surfaces with low O^* loading via LH Mechanism

Figure 6.44 for Pd and Figure 6.45 for Pt show an LH mechanism on all four significant surfaces (111), (100), (110), and (211) of the pristine metal surfaces of Pd and Pt. Firstly, the $CO_{(g)}$ gas phase molecule adsorbs, preferably on the corners or kink sites to reach a bridge position. The structures considered here are similar to those discussed in Section 6.3.2, concerning the activities of extended noble metal surfaces with high O^* coverage, with the exception that no second O^* atom is present. In this Section, the coverage per unit cell is reduced by one adsorbed O^* atom. Hence, we refer to a lower O^* coverage here. In Figure 6.46, the Gibbs free energies are depicted in a potential energy diagram based on the structures shown in Figure 6.44 for Pd and Figure 6.45 for Pt. The reaction temperature was calculated at 423.15 K and the Gibbs free energies are listed in Table 6.15. The temperature of 423.15 K is accounted by the use of *ab initio* thermodynamics, including the contributions of ZPE and entropy, as discussed in Section 3.7. The adsorption energies of the $CO_{(g)}$ gas phase molecules remain exothermic at this reaction temperature. However, this differs significantly from an increased surface coverage by O^* atoms, as described in the previous Section. The adsorption energies on the Pd surface are -0.17 eV for (111), -0.66 eV for (100), -0.20 eV for (110), and -0.59 eV for (211). For the Pt surfaces, these are -0.45 eV for (111), -1.07 eV for (100), -0.71 eV for (110), and -0.64 eV for (211). Therefore, the adsorption energies on all surfaces are approximately in the same range, but

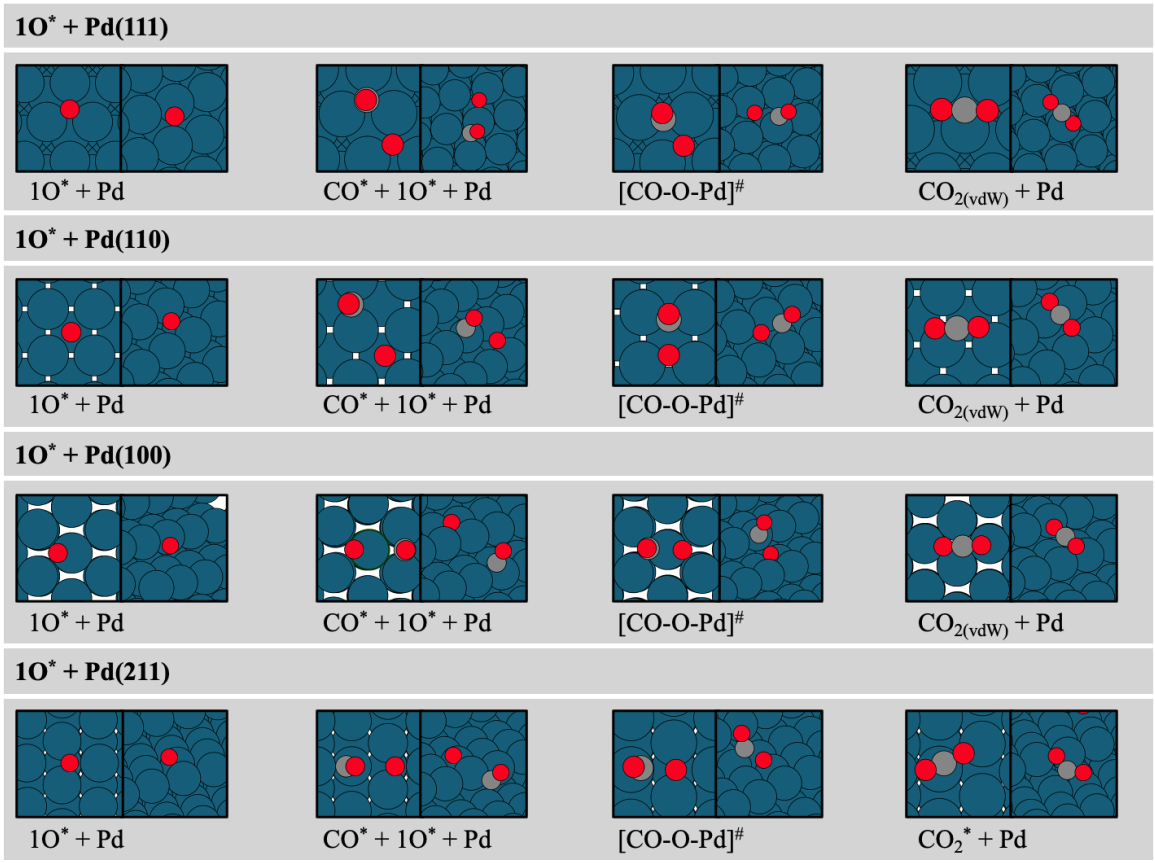

Figure 6.44.: Reaction mechanism of CO oxidation on structure-optimized extended Pd surface facets (111), (110), (100), and (211) with a low loading of adsorbed O^* atoms via the LH mechanism. Red circles represent O atoms, dark gray circles represent C atoms, and petrol circles represent Pd atoms. The total energies are listed in the Appendix in Table A.36.

stronger by about 0.10 to 0.50 eV for Pt surfaces compared to Pd surfaces. The reaction barriers after $CO_{(g)}$ adsorption on the Pd surface are 0.85 eV for (111), 0.60 eV for (100), 0.61 eV for (110), and 1.28 eV for (211). For the Pt surfaces, these values are 0.65 eV for (111), 0.38 eV for (100), 0.57 eV for (110), and 0.88 eV for (211). It is evident that both the (111) and (211) surfaces, for both Pd and Pt, exhibit higher reaction barriers of about 0.30 eV compared to the other two surfaces. The reaction barriers relative to $CO_{(g)}$ in the gas phase, due to the exothermic adsorption of the CO molecule, are significantly more endothermic, ranging from endothermic to neutral. For Pd surfaces, they are 0.61 eV for (111), 0.09 eV for (100), -0.04 eV for (110), and 0.69 eV for (211). For the Pt surfaces, these are 0.46 eV for (111), -0.60 eV for (100), 0.76 eV for (110), and 0.20 eV for (211). An exception is the (100) surface on Pt, which exhibits a noticeably more exothermic value. The bond formation during the transition state leads to a closer distance between the C^* atom of the CO^* molecule and the O^* atom adsorbed on the surface. For Pd surfaces, this distance is 1.87 Å for (111), 1.95 Å for (100), 1.78 Å for (110), and 1.77 Å for (211). For

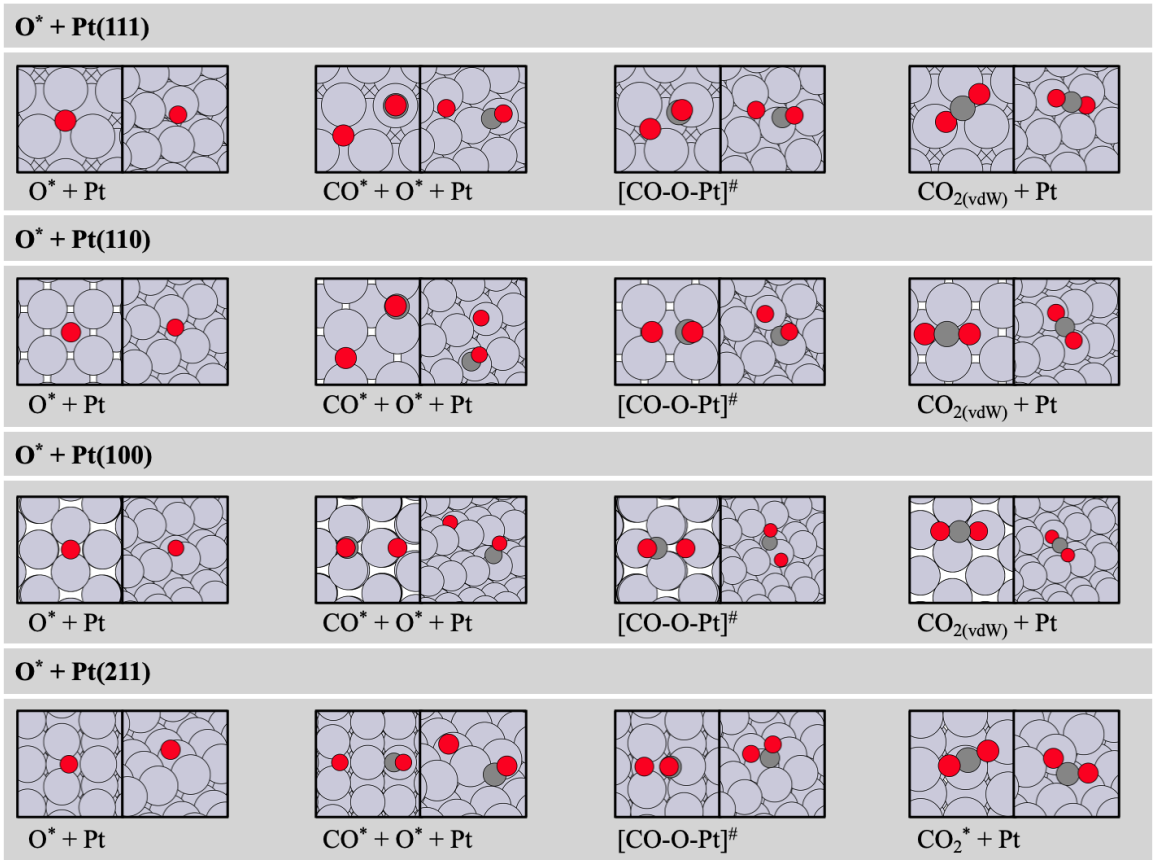

Figure 6.45.: Reaction mechanism of CO oxidation on structure-optimized extended Pt surface facets (111), (110), (100), and (211) with a low loading of adsorbed O^* atoms via the LH mechanism. Red circles represent O atoms, dark gray circles represent C atoms, and gray circles indicate Pt atoms. The total energies are listed in the Appendix in Table A.36.

the Pt surfaces, these values are 1.87 Å for (111), 1.89 Å for (100), 1.84 Å for (110), and 1.84 Å for (211). After formation, the desorption of the $CO_2{}^*$ molecule is an exothermic step, although it should be noted that the calculated values using DFT methods might be artificial, as discussed in the former Section already. The $CO_2{}^*$ molecules initially remain in van-der-Waals proximity due to long-range electron dispersion effects. Under reaction conditions, $CO_2{}^*$ desorption will likely occur spontaneously. The bond angles are 130° in exceptional cases where the $CO_2{}^*$ molecule remains adsorbed on the surface. In all other cases, desorption occurs spontaneously. It is assumed that at elevated reaction temperatures, $CO_2{}^*$ desorption proceeds rapidly. The reaction energy of the elementary step is also exothermic in all cases. For Pd surfaces, it is -1.56 eV for (111), -1.53 eV for (100), -1.67 eV for (110), and -1.55 eV for (211). For the Pt surfaces, these values are -1.50 eV for (111), -2.05 eV for (100), -1.49 eV for (110), and -1.71 eV for (211). No difference between the noble metals can be observed in this regard. However, it can generally be stated that a lower

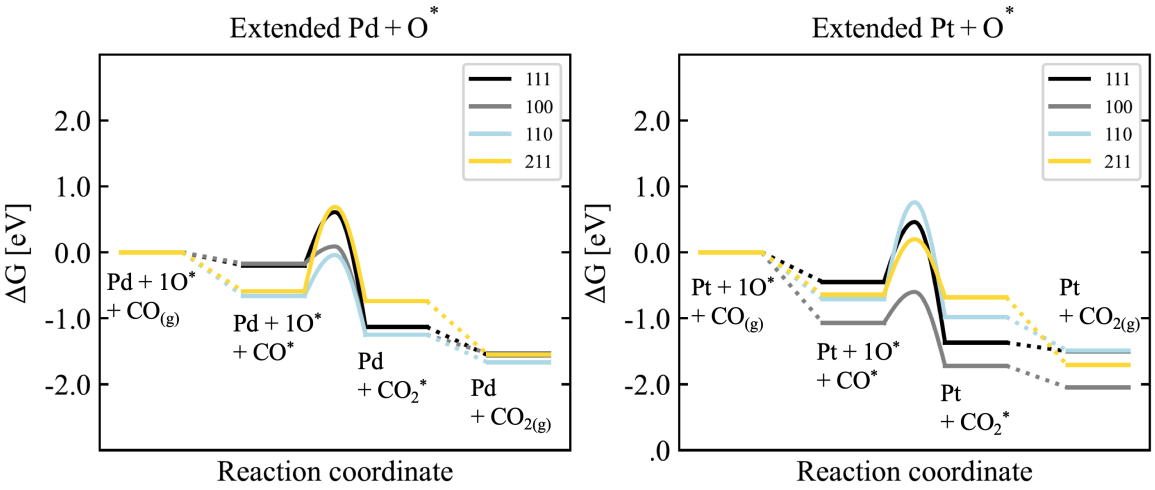

Figure 6.46.: Calculated Gibbs free energies of the structure-optimized CO oxidation elementary reaction steps on extended noble metal surface facets (100), (110), (111) and (211) with low O^* loading as depicted in Figure 6.44 for Pd and Figure 6.44 for Pt plotted against the reaction coordinate in a potential energy diagram. The Gibbs free energies are referenced to the extended Pd and Pt noble metal surface facets (100), (110), (111), and (211) with one O^* adsorbed O^* in eV and at 423.15 K. The total energies, the ZPE and the entropies are listed in the Appendix in Table A.36.

Table 6.15.: Calculated Gibbs free energies of the CO oxidation elementary reaction step on the noble metal surfaces with one additional O^* atom adsorbed on the extended noble metal surface facets (100), (110), (111) and (211) in eV and at 423.15 K of the structure-optimized elementary steps depicted in Figure 6.44 for Pd and Figure 6.45 for Pt on and all four surface facets of the noble metal surfaces (111), (110), (100) and (211), respectively, relative to the stoichiometric pristine noble metal surfaces in eV and at 423.15 K. The Gibbs free energies are plotted in the potential energy diagram 6.46. The Bond length between the C^* and the O^* atom during the transition state is described as b.l. in Å at 0 K and included in gray letters. The bond angles in degree of the formed CO_2 molecules are given in gray letters.

	CO^* [eV]	$[CO\text{-}O]^\#$ [eV]	b.l. [Å]	$CO_2{}^*$ [eV]	CO_2 [eV]	angle [°]
CO oxidation via LH Mechanism						
$1O^*$ + Pd(111)	-0.17	0.09	1.95	-1.25	-1.53	180
$1O^*$ + Pd(100)	-0.66	-0.04	1.78	-1.25	-1.67	180
$1O^*$ + Pd(110)	-0.20	0.61	1.87	-1.13	-1.56	180
$1O^*$ + Pd(211)	-0.59	0.69	1.77	-0.74	-1.55	131
$1O^*$ + Pt(100)	-1.07	-0.60	1.87	-1.72	-2.05	180
$1O^*$ + Pt(110)	-0.71	0.79	1.84	-0.98	-1.49	180
$1O^*$ + Pt(111)	-0.45	0.46	1.87	-1.37	-1.50	180
$1O^*$ + Pt(211)	-0.64	0.20	1.84	-0.68	-1.71	127

surface coverage results in an overall reaction energy that is significantly more exothermic than that of higher O^* coverage, stemming from the exothermic adsorption energy.

6.3.4. CO Oxidation on PdO and PtO Extended Metal Oxide Surfaces

In order to approach the nanometer scale clusters, we examined pure (101) oxide surfaces of PdO and PtO crystals for their activities in CO oxidation. The PdO for PtO extended surfaces

(101) are depicted in Figure 6.47. The reaction mechanism for CO oxidation is illustrated from $CO_{((g)}$ adsorption, through the transition state, to CO_2 formation. The corresponding Gibbs free energies are shown in Figure 6.48 in a potential energy diagram for PdO(101) and PtO(101) surfaces during CO oxidation. These oxides were used to approximate the partial oxidations of a nanometer cluster. The CO oxidation of a PdO_2(101) or PtO_2(101) crystal was also investigated. It was found that CO adsorption leads to a CO_3 species, exceeding the scope of investigating simple CO oxidation. The Gibbs free energies are presented in Table

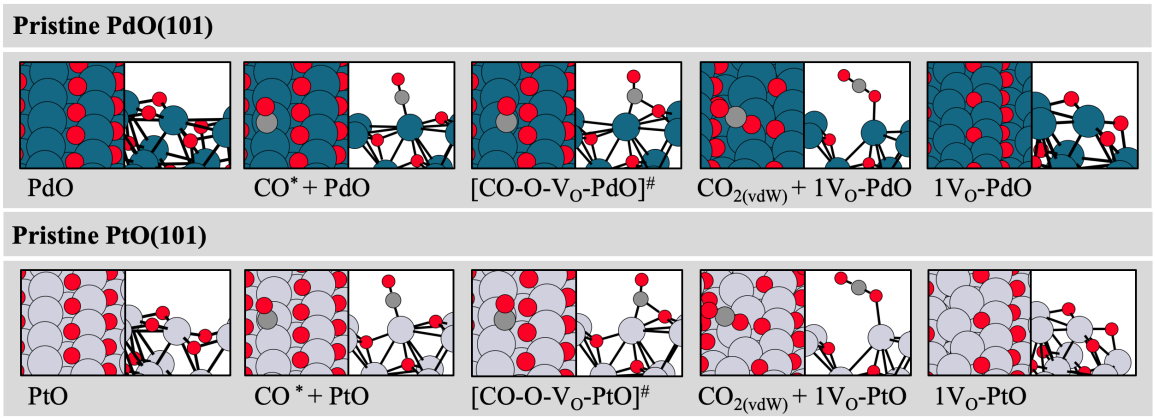

Figure 6.47.: Reaction mechanism of the CO oxidation on structure-optimized extended metal oxide PdO and PtO surfaces via the MvK mechanism. Red circles represent O atoms, dark gray circles represent C atoms, petrol circles represent Pd atoms, and gray circles indicate Pt atoms. The total energies are listed in the Appendix in Table A.37.

6.16. The (101) surface of the PdO and PtO crystals exhibit an alternating noble metal and O sequence. This arrangement creates adsorption sites on the noble metal sequence where the $CO_{(g)}$ molecule can adsorb. During the oxidation process, the CO molecule migrates to one of the O atoms within the O rows. The resulting CO_2 molecule remains adsorbed by one of the two O atoms belonging to the CO_2 molecule on the crystal surface until it eventually desorbs. The now O-deficient surface of the crystal alters the surface structure, as depicted in Figure 6.47 in the last two pictures of the rows. It is evident that the previously linear noble metal sequence now exhibits a zigzag pattern. The potential energy diagrams illustrate the progression of CO oxidation at 423.15 K relative to the starting point, which is the pure metal oxides free from adsorbates. The temperature of 423.15 K is accounted by the use of *ab initio* thermodynamics, including the contributions of ZPE and entropy, as discussed in Section 3.7. The subsequent CO adsorption is exothermic, with barriers between Pd and Pt differing by 1.03 eV in the energy barrier after $CO_{(g)}$ adsorption and 0.42 eV in the apparent energy barrier before CO adsorption. The adsorption energy of the $CO_{(g)}$ molecule on the PtO crystal is significantly stronger, by 0.61 eV, compared to that on the PdO crystal. The $CO_{2(g)}$ desorption itself should be endothermic at low temperatures. Due to the structural alteration, a change in configuration affects the Gibbs free energy, meaning

that the desorption step does not solely represent the transition of the $CO_2{}^*$ molecule into the gas phase. The Gibbs free energies of the noble metal surfaces with one additional O^*

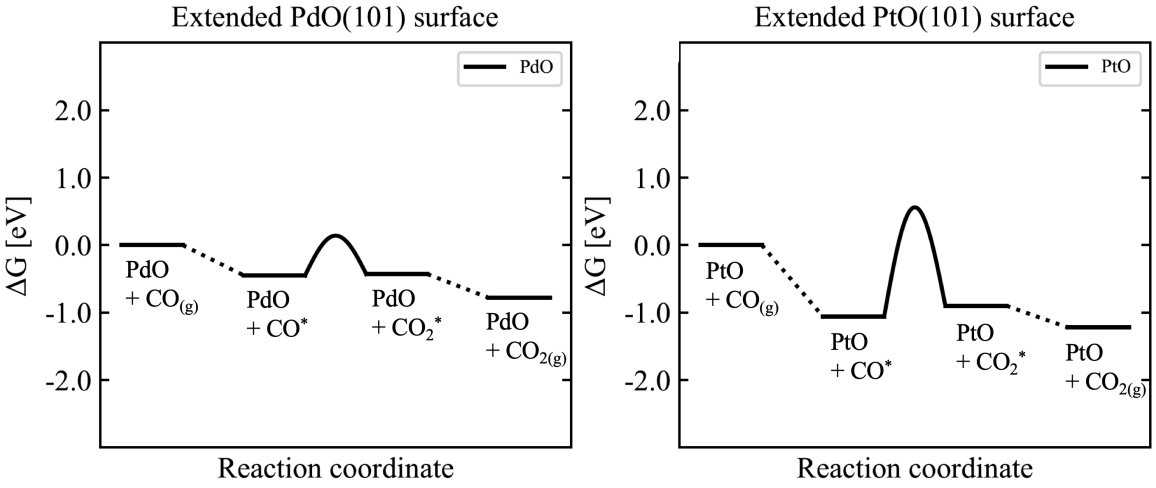

Figure 6.48.: Calculated Gibbs free energies of the structure-optimized CO oxidation elementary reaction steps on extended metal oxide surfaces as depicted in Figure 6.47 for PdO (upper row) and PtO (lower row) plotted against the reaction coordinate in a potential energy diagram. The Gibbs free energies are referenced to the extended noble metal oxide PdO and PtO crystal surface (101) in eV and at 423.15 K. The total energies, the ZPE and the entropies are listed in the Appendix in Table A.37.

atom adsorbed on the extended noble metal surface facets (100), (110), (111) and (211) in eV and at 423.15 K of the structure-optimized elementary steps depicted in Figure 6.44 for Pd and Figure 6.45 for Pt on and all four surface facets of the noble metal surfaces (111), (110), (100) and (211), respectively, relative to the stoichiometric pristine noble metal surfaces in eV and at 423.15 K. The Gibbs free energies are plotted in the potential energy diagram 6.46. The corresponding values are listed in Table 6.47. The $CO_{(g)}$ adsorption energies are exothermic in all cases despite high O^* coverage on the (101) surface of the oxides, with values of -0.45 eV for PdO and -1.06 eV for PtO. The resulting reaction barrier is 0.59 eV for PdO and 1.62 eV for PtO. The reaction energy barrier relative to $CO_{(g)}$ in the gas phase is 0.14 eV for PdO and 0.56 eV for PtO. The Bond length between the C^* and the O^* atom during the transition state is for the PdO surface 1.77 Å and 1.30 Å for the PtO surface. After the formation of $CO_2{}^*$ desorbs spontaneously. This CO oxidation follows an MvK mechanism, requiring lattice energy due to the crystal structure of the oxide to remove the adsorbed O^* atom from the surface. Therefore, the $CO_2{}^*$ molecule is initially coordinated at the emerging V_O defect. The desorption of the CO_2 molecule is exothermic in both cases, with values of -0.78 eV for PdO and -0.90 eV for PtO. The reaction energy for this elementary reaction is exothermic with -0.78 eV for CO oxidation on the PdO crystal and -1.22 eV on the PtO crystal of the (101) surfaces. The reaction barrier for PdO is minor; it can be considered that this reaction can indeed take place. Therefore, it can be considered that a partially oxidized nanometer crystal can indeed be an active species as a catalyst.

Table 6.16.: Calculated Gibbs free energies of the CO oxidation elementary reaction step on the on noble metal oxide surfaces of the structure-optimized elementary steps depicted in Figure 6.47 for Pd and Pt on all four surface facets of the noble metal surfaces (111), (110), (100) and (211), respectively, relative to the stoichiometric pristine noble metal oxide surfaces in eV and at 423.15 K. The potential energies are plotted in the potential energy diagram 6.48. The Bond length between the C^* and the O^* atom during the transition state is described as b.l. in Å at 0 K and included in gray letters. The bond angles in degree of the formed CO_2 molecules are given in gray letters.

	CO^* [eV]	$[CO\text{-}O]^\#$ [eV]	b.l. [Å]	$CO_2{}^*$ [eV]	CO_2 [eV]	angle [°]
CO oxidation via MvK Mechanism						
PdO(101)	-0.45	0.14	1.77	-0.43	-0.78	180
PtO(101)	-1.06	0.56	1.30	-0.90	-1.22	180

The corresponding adsorption energies were calculated and also listed in Table 6.47. These adsorption energies include the structural changes associated with the adsorption of a CO molecule. Plotting the stretching vibrations against the adsorption energies does not reveal any correlation. This, however, was expected, as previously mentioned, given that it is known that the CO molecule, due to the competition between electrostatic and covalent bond formation, does not exhibit linear scaling relations. This behavior is also exceptional compared to other adsorbates.

7. Analysis of Intrinsic chemical and electronic Properties by Scaling Relations

The field of theoretical catalysis uniquely enables systematic exploration of variations in potential catalyst structures at the electronic level through the application of quantum chemical methods. For this purpose, as reiterated in this work, a systematic bottom-up investigation of catalyst size is crucial. This investigation spans from single-atom catalysts, progressing to subnanometer clusters comprising 3 and 10 atoms, and culminating in nanometer-sized clusters approached by extended noble metal slabs. This approach is essential to identify a broad range of potential candidates. As former letters of Nørskov et al. have conceptualized as the universality principle of catalytic reactions, the bonding state and the transition state of the reactants forming the product can be correlated with a slope close to one.[162] The reaction activation energy and the stability of reaction intermediates as descriptors of the scaling relation lead to a reactant-independent relation between adsorption energies and catalytic activity. It is for that, that in this work the transition state structures and the adsorption site geometry are kept as similar as possible. By plotting these candidates and utilizing scaling relations, insights into their chemical and physical properties can be deduced. Subsequently, by combining two distinct scaling relations describing the activities of the catalysts under two competing aspects, a volcano plot can be interpreted to determine the regime of the most active species based on the discovered physical and chemical properties. In this section, we examine the structures of the transition states and categorize them into the respective species needed for analysis of reactivities in the following sections, using scaling relations. As consistently mentioned throughout this work, a strong emphasis was placed on making the configuration of transition states as similar as possible despite the different adsorption surfaces. Other surface geometries lead to alternative transition states, which may indeed exist within a similar energetic regime but result in a different category due to the alternative chemical environment. To minimize these deviations, we endeavored to maintain the electronic and physical properties of the catalyst surface as uniformly as possible. This systematic examination of catalyst surface activities aims to avoid comparing apples to oranges concerning geometric variations.

7.1. Structures of the Transition States of the O_2 Dissociation

In the following, we consider the dissociation of O_2 and establish scaling relations based on the calculated potential energies at single points along the reaction mechanism. In the case of the dissociation of O_2 on the noble metal, reference would be made to an LH mechanism, as it occurs within the reaction mechanism cycle of CO oxidation via an LH mechanism pathway. In the case of the regeneration of the O-defective catalyst, reference would be made to a corresponding MvK mechanism. The elementary steps for O_2 dissociation are shown in Equation 7.1.

$$O_{2(g)} + Kat \rightarrow O_2^* + Kat \rightarrow [O-O-Kat]^{\ddagger} \rightarrow 2O^* + Kat \tag{7.1}$$

Kat presents the heterogeneous catalyst as a surface onto which the $O_{2(g)}$ from the gas phase adsorbs to form $O_2{}^*$. Subsequently, the $O_2{}^*$ molecule undergoes a transition state $[O\text{-}O]^{\ddagger}$ for dissociation, leading to two dissociated $2O^*$ atoms, which remain adsorbed on the catalyst. In this section, we examine the structures of the transition states during the O_2 dissociation as studied in this work. In Figure 7.1 in the upper row, the transition states of O_2 dissociation on a stoichiometric ceria surfaces are considered. On the (100) and (111) ceria surfaces, the dissociating O atoms are located on top of the noble metal atom and have no further coordination to a Ce atom in the immediate vicinity. This is different on the (110) surface, where one of the O atoms is coordinated by a Ce atom. This latter circumstance arises because the noble metal atoms are embedded in a "tunnel", making them accessible only through close proximity to the surrounding Ce atoms. A thorough investigation of the reaction mechanism was conducted in Section 6.1.1. In Figure 7.1 in the bottom row,

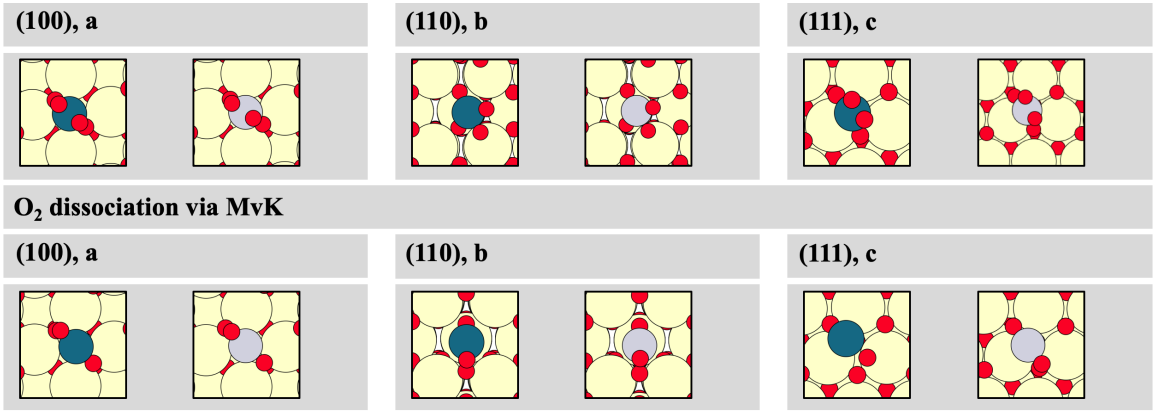

Figure 7.1.: Transition states of a O_2 dissociation on structure-optimized subnanometer clusters (1-4)CO^* + Pd_3 and (1-4)CO^* + Pt_3 via the MvK mechanism and O^* + Pd_3 and O^* + Pt_3 via the LH mechanism adsorbed on a CeO_2(111) surface. Red circles represent O atoms, large yellow circles denote Ce atoms, gray circles Pt atoms, and petrol circles represent Pd atoms.

the transition states of O_2 dissociation on the single-atom catalysts are investigated, which

are adsorbed on the V_O-defective ceria surfaces due to the absence of a surface lattice O_l. The dissociation of an O_2^* molecule occurs such that one O atom is adsorbed into theV_O defect, while the second atom along the single-atom catalyst continuously increases its bonding distance to the former O atom during the dissociation. The configurations of the transition states are constructed similarly on all three ceria surfaces (100), (110), and (111). A thorough investigation of the reaction mechanism was conducted in Section 6.1.2. In

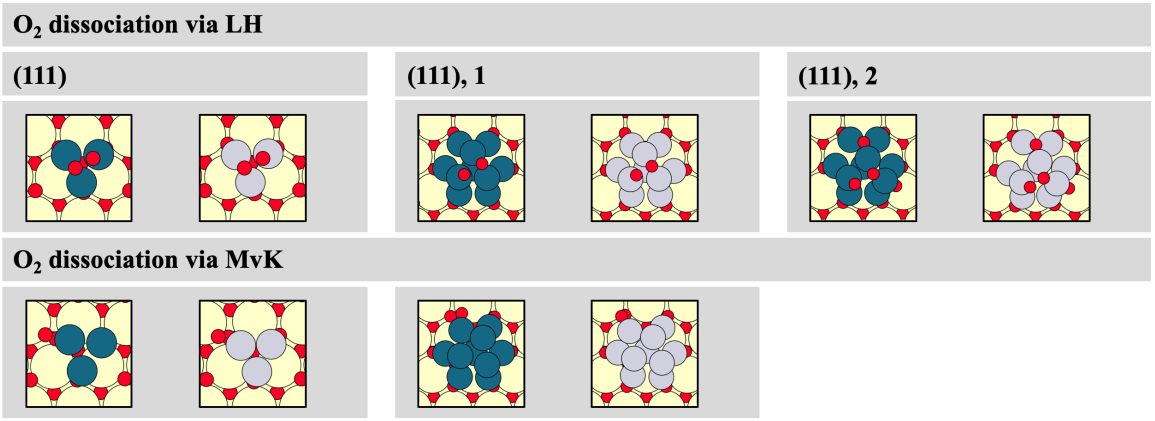

Figure 7.2.: Transition states of a O_2 dissociation on structure-optimized subnanometer clusters (1-4)CO-Pd_3 and (1-4)CO-Pt_3 via the MvK mechanism and Pd_3O and O^* + Pt_3 via the LH mechanism adsorbed on a CeO_2(111) surface. Red circles represent O atoms, large yellow circles denote Ce atoms, gray circles Pt atoms, and petrol circles represent Pd atoms.

Figure 7.2, the dissociations of O_2 molecules on the subnanometer clusters Pd_3, Pt_3, Pd_{10}, and Pt_{10}, as well as the oxidized $2O^*$ + Pd_{10} and $2O^*$ + Pt_{10} clusters that have already been oxidized by two O^* atoms, are depicted. The dissociation of the adsorbed O_2^* molecule occurs at the apex of the clusters, leading to coordination between the O^* atoms and three of the noble metal atoms. During the transition state, one O^* atom is coordinated atop one of the three noble metal atoms. In contrast, the other O atom is bridge-coordinated between the other two noble metal atoms. This configuration is consistent across all species depicted in this figure. For the Pd_3, Pt_3, Pd_{10}, and Pt_{10} clusters, the configuration of the clusters remains relatively unaffected by O_2 dissociation. However, this is different for the $2O^*$ + Pd_{10} and $2O^*$ + Pt_{10} clusters. Here, there is a deviation of the dissociating O_2^* molecules, with the apex of the cluster, composed of three noble metal atoms, slightly avoiding the other two O^* atoms adsorbed on the "leaves" of the flower-like structure on the side of the cluster. This could also be attributed to a strain effect. A thorough investigation of the reaction mechanism was conducted in Section 6.2.1 for the Pd_3 and Pt_3 subnanometer cluster, in Section 6.2.5 for the Pd_{10} and Pt_{10} and for the $2O^*$ + Pd_{10} and $2O^*$ + Pt_{10} subnanometer cluster. In Figure 7.3, the dissociations of O_2^* adsorbed on the extended metal surfaces of Pd and Pt on the surface facets (111), (110), (100) and (211) are depicted. The O_2 dissociation on the (111) and (211) surfaces is placed on the extended noble metal surfaces to gain the

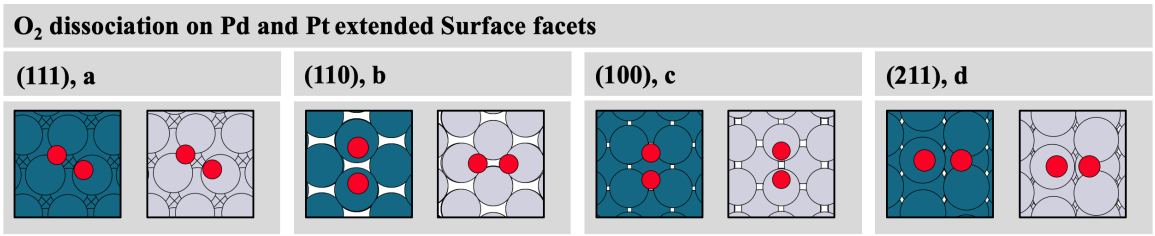

Figure 7.3.: Transition states of a O_2 dissociation on structure-optimized subnanometer clusters (1-4)CO^* + Pd_3 and (1-4)CO^* + Pt_3 via the MvK mechanism and O^* + Pd_3 and O^* + Pt_3 via the LH mechanism adsorbed on a CeO_2(111) surface. Red circles represent O atoms, gray circles Pt atoms, and petrol circles represent Pd atoms.

similar coordination between the dissociating $O_2{}^*$ molecule and three noble metal atoms as conducted on the apex of the subnanometer clusters. Here, it is evident that a direct size comparison between the subnanometer clusters and the nanometer clusters can be made by considering the extended surface facets as nanometer clusters. It is noteworthy that the O_2 dissociation on the (211) surface is considered here to occur on the terrace, which consists of three rows of noble metal atoms. This configuration is therefore directly comparable to that of the (111) surface. On the Pd(110) surface the O_2 dissociation is considered to occur at a short bridge, while for Pt, it is considered to occur at a long bridge. Regarding the (100) surface, there is also a difference between the Pd and Pt surfaces. On the Pd surface, the O_2 dissociation is bridge-coordinated for each O atom, while on the Pt surface, it is on-top coordinated for each O^* atom. The differences in configurations between the adsorption sites of the reactants on the noble metals arise from structural optimizations without intended influence.

7.1.1. Correlation of O_2 Dissociation and $2O^*$ Adsorption relative to $O_{2(g)}$

In Figure 7.4, the relationship between the energy of O_2 dissociation and the total energy of the resulting $2O^*$ atoms is depicted, both referenced relative to $O_{2(g)}$ in its gaseous phase. By aligning these energies to a common reference point, we establish a correlation between the transition state of O_2 molecule dissociation and the final states of the $2O^*$ atoms. As Figure 7.4 illustrates, there is indeed a linear correlation, which can be explained by a scaling relation of the spezies conducted. The transition states of the O_2 dissociations resemble those of the products, indicating that the driving force towards dissociation is present. This suggests that the electronic interactions of the catalyst with the O_2 molecule affect the eigenstates, leading to a preference for a dissociated configuration rather than the formation of the O_2 molecule bond.[198] The slope of the scaling relation is 0.69 for Pd and 0.81 for Pt. A lower scaling slope suggests that the activation barrier to the dissociated product increases less compared to the deduction in the gas phase. In other words, the bond-breaking step

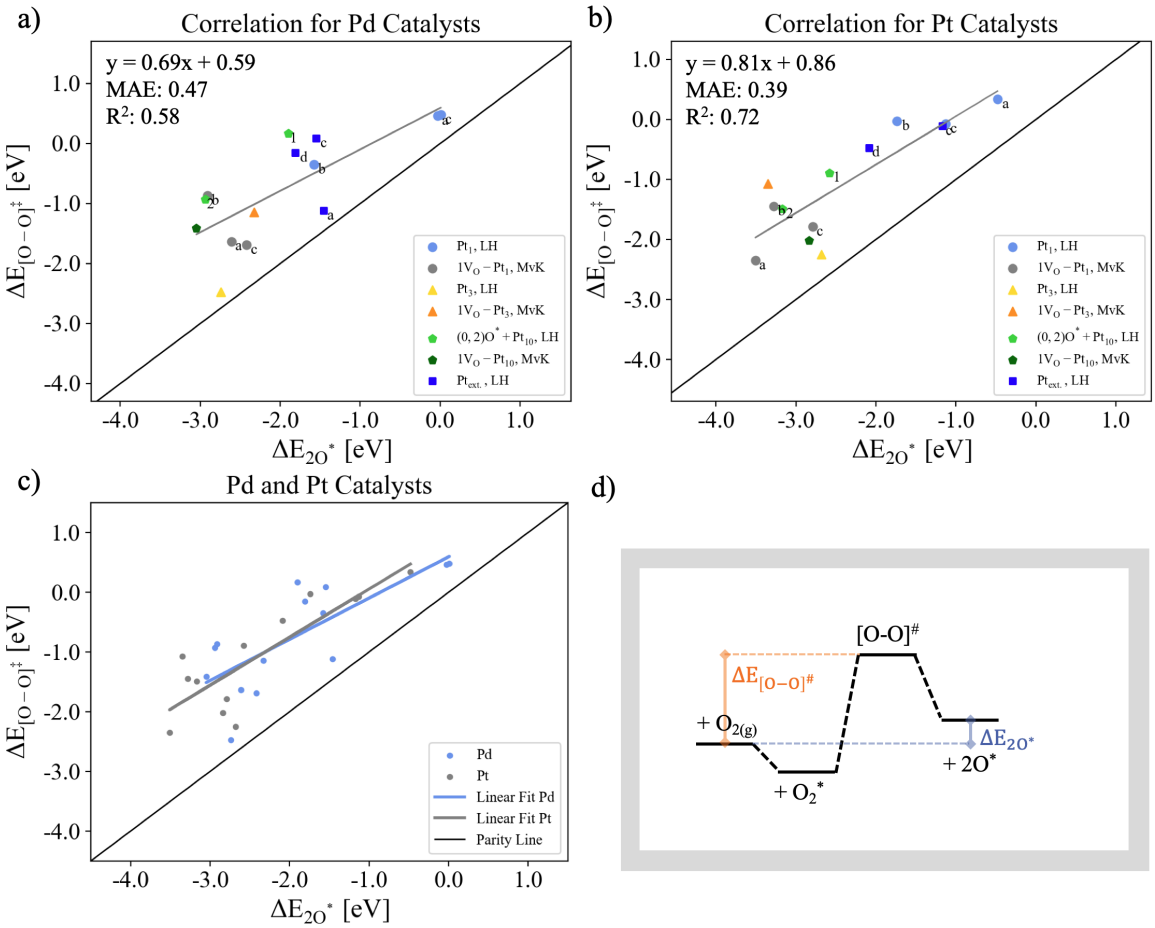

Figure 7.4.: The activation energy barrier $\Delta E_{[O\text{-}O]^{\ddagger}}$ of the O_2 dissociation is plotted against the $2O^*$ binding ΔE_{2O^*} relative to gas phase $O_{2(g)}$. Shown are Figure a) for Pd catalysts and b) for Pt catalysts. The parity line (black) and the linear fit of all species shown (grey) are plotted. The numbering corresponds to those of the figures presented in Section 7.1. Figure c) shows the combined plots of Pd (blue) and Pt (gray) catalysts. Figure d) illustrates the elementary reaction of O2 dissociation in a schematic Gibbs free energy diagram. The descriptors used for scaling relation are highlighted.

is less affected by the presence of the catalyst compared to the bond-forming step. This suggests that the transition state structure bears a closer resemblance to the $O_{2(g)}$ molecule affecting the reaction direction towards the initial state. Conversely, a higher scaling slope suggests that the activation barrier to the dissociated product increases more compared to the deduction in the gas phase. In this case, the bond-forming step is more affected by the presence of the catalyst compared to the bond-breaking step. This implies that the transition state structure more closely resembles the products. The binding strength of the $O_{2(g)}$ molecules is close enough to 1 in both cases to make the statement that the investigated catalysts are indeed active towards O_2 dissociation. The Gibbs free energies of the elementary step of O_2 dissociation on the varying sizes and shapes of the noble metals have been investigated in the corresponding sections on the activity of the noble metals

towards O_2 dissociation. The mean absolute error is quite high, with 0.47 for Pd and 0.39 for Pt catalysts. A higher coefficient of determination, expressed as the R^2 value, indicates a more optimal fit of the regression model to the dataset. This implies that a greater portion of the variance in the dependent variable, which is in this case the activation barrier to dissociated product ($\Delta E_{[O\text{-}O]^{\ddagger}}$ to ΔE_{2O^*}), can be elucidated by the independent variable, which is the presence of O_2 in the gas phase. With an R^2 value of 0.58 for Pd, it is inferred that 58% of the variability in the data on Pd catalysts can be accounted for by the regression model. For Pt, with an R^2 value of 0.72, the model explains a larger proportion of the data variance of 72%, suggesting an enhanced model fit to the dataset for Pt catalysts relative to Pd catalysts.

7.2. Structures of the Transition States of the CO Oxidation

In the preceding sections, the direction of the reaction was examined in terms of CO oxidation and consequent formation of CO_2. In this section, we will exclusively focus on the reverse reaction, namely CO_2 dissociation, to examine scaling relations. This choice is motivated by the discovery of linear scaling relations, as the activation energies for the dissociation of the CO_2 molecule correlate better with the resulting adsorbed CO molecule and O atom. This may be due to the configuration of the transition state, which is more similar to the dissociated products than an adsorbed $CO_2{}^*$ molecule. Consequently, when contemplating a scaling relation of the adsorbed $CO_2{}^*$ molecule, the diversity in catalyst sizes and shapes induces effects such as alterations in the geometry or angles of the molecule. As these factors are encompassed within a single correlation, the extensive range of catalyst sizes and shapes results in amplified deviations. The elementary steps for CO_2 dissociation are as follows:

$$CO_{2(g)} + Kat \rightarrow CO_2^* + Kat \rightarrow [CO - O - Kat]^{\ddagger} \rightarrow CO^* + O^* + Kat \tag{7.2}$$

Kat presents the heterogeneous catalyst as a surface onto which the $CO_{2(g)}$ from the gas phase adsorbs to form $CO_2{}^*$. Subsequently, the CO_2 molecule undergoes a transition state $[CO\text{-}O]^{\ddagger}$ for dissociation, leading to dissociated CO^* molecule and O^* atom, which remain adsorbed on the catalyst. In this section, we examine the structures of this reaction equation, which all catalysts studied in this work undergo. In Figure 7.5, the transition states of CO_2 dissociation on a stoichiometric ceria surface facets (100), (110) and (111) are considered. From left to right, here the O atoms surrounding the single-atom catalyst are reduced as they react via CO oxidation. The rows begin with two additional adsorbed O atoms, resulting in a formal oxidation state of +IV for the single atoms. Subsequently, this is reduced to an O atom with a formal oxidation state of +II, along with a stoichiometric ceria surface with a

formal oxidation state of 0. In the top row, the (100) surface of ceria is considered. Here, the

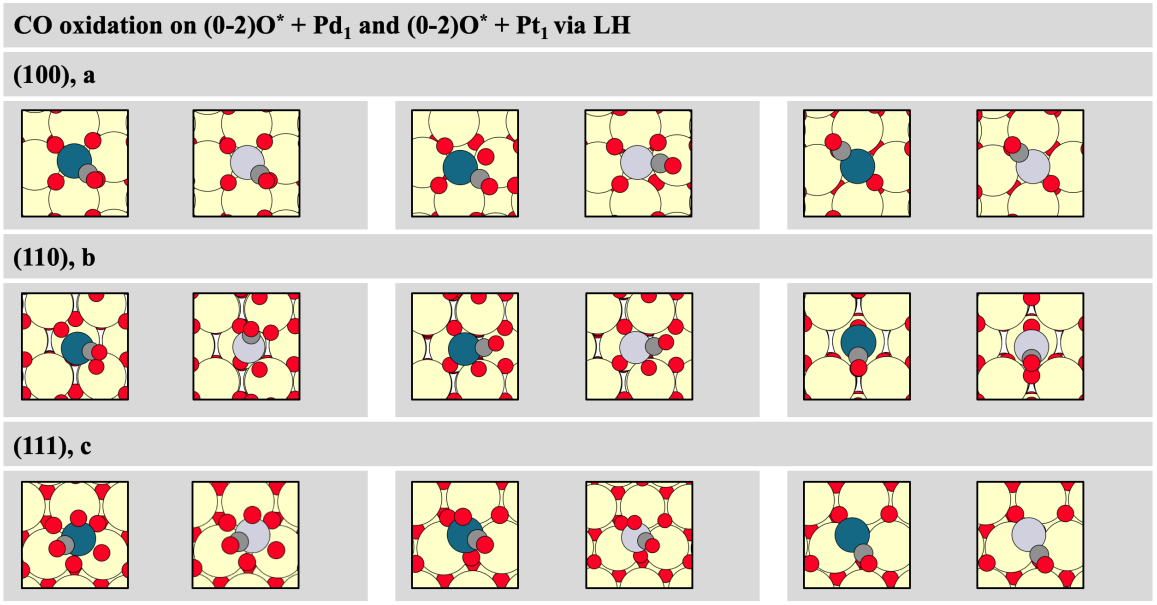

Figure 7.5.: Transition states of a CO_2 dissociation on structure-optimized subnanometer clusters (1-4)CO^*Pd_3 and (1-4)CO^*Pt_3 via the MvK mechanism and O^* + Pd_3 and O^* + Pt_3 via the LH mechanism adsorbed on a CeO_2(111) surface. Red circles represent O atoms, large yellow circles denote Ce atoms, dark gray circles represent C atoms, gray circles Pt atoms, and petrol circles represent Pd atoms.

single-atom catalysts, as discussed in Section 6.1, are embedded in square-planar pockets. The structures of CO_2 dissociation are similar for the +IV and 0 formal oxidation states are similar, with one of the O atoms being adsorbed into the vicinal anchoring corner. The CO molecule is only coordinated with the noble metal atom. The transition state occurs as the CO molecule detaches from the anchored O atom by increasing its angle to the surface. However, for the +II formal oxidation state, a different configuration occurs. The O atom and the CO molecule must overcome a Ce atom to dissociate, thus reaching the corners of the square-planar structure. In the middle row, the single-atom catalysts adsorbed on the (110) surface are depicted. For the formal oxidation state of +IV, the single noble metal atom displaces one of the previously square-planar O atoms to provide an adsorption site for the CO molecule. For the formal oxidation state of +II, an adsorption site is already available. In both cases, the transition state occurs outside the "tunnel" in the z-direction. For the formal oxidation state of 0, one of the O atoms from the bottom of the "tunnel" is utilized, resulting in a configuration change compared to the previous two oxidation states. However, the configurations are still quite similar overall, as the CO molecule is not coordinated with a Ce atom in any case and approaches the O atom in the z-direction. In the bottom row, the (111) surface of ceria is considered. Here, the transition states for all formal oxidation states occur in comparable configurations. The CO molecule is not coordinated with a Ce atom and migrates to one of the O atoms that are in a vicinal

position to the noble metal atom. In Figure 7.6, the transition states of the MvK mechanisms

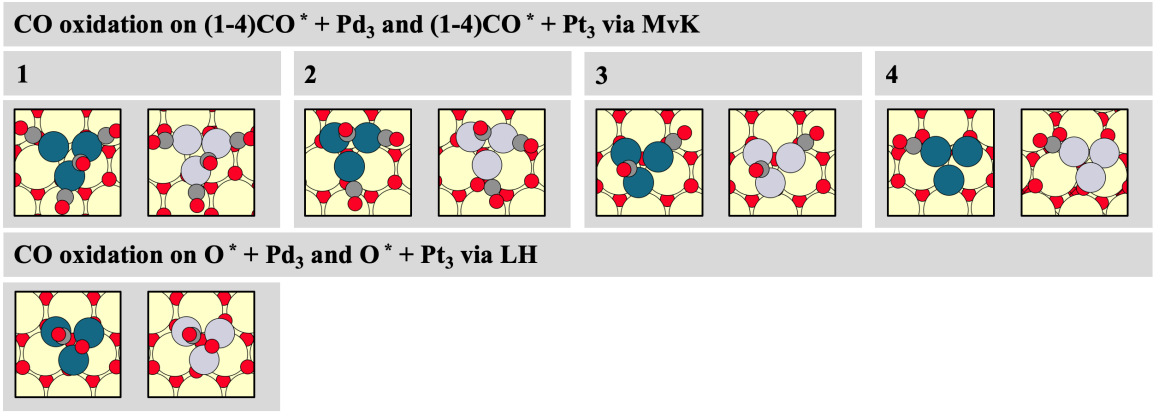

Figure 7.6.: Transition states of a CO_2 dissociation on structure-optimized subnanometer clusters (1-4)CO^* + Pd_3 and (1-4)CO^* + Pt_3 via the MvK mechanism and O^* + Pd_3 and O^* + Pt_3 via the LH mechanism adsorbed on a CeO_2(111) surface. Red circles represent O atoms, large yellow circles denote Ce atoms, dark gray circles represent C atoms, gray circles Pt atoms, and petrol circles represent Pd atoms.

and the LH mechanisms for CO_2 dissociation on a Pd_3 and Pt_3 subnanometer cluster are depicted. For the MvK mechanisms, care was taken to maintain the same configuration for the transition state by extracting an O atom from the ceria surface and migrating a CO molecule from the z-direction towards it. In the LH mechanism, this reaction occurs on top of the cluster. One O atom is coordinated with two of the three noble metal atoms, and the CO molecule is coordinated with the last one in an on-top position. In Figure 7.7,

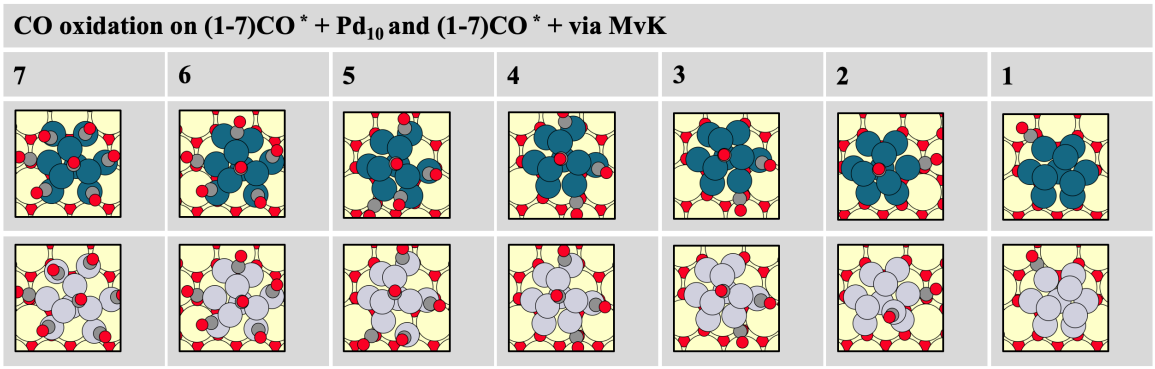

Figure 7.7.: Transition states of a CO_2 dissociation on structure-optimized subnanometer clusters (1-7)CO^* + Pd_{10} and (1-7)CO^* + Pt_{10} via the MvK mechanism adsorbed on a CeO_2(111) surface. Red circles represent O atoms, large yellow circles denote Ce atoms, dark gray circles represent C atoms, gray circles Pt atoms, and petrol circles represent Pd atoms.

the MvK mechanism for CO_2 dissociation on the (1-7)CO^* + Pd_{10} and (1-7)CO^* + Pt_{10} clusters, and the LH mechanism for CO_2 dissociation on the (1-4)O^* + Pd_{10} and (1-4)O^* + Pt_{10} clusters is shown. The MvK and LH mechanisms occur analogously to their respective mechanisms across all cases, and they are also analogous to those of the (1-4)CO^* + Pd_3

and (1-4)CO^* + Pt_3 clusters for the MvK mechanism and O^* + Pd_3 and O^* + Pt_3 clusters for the LH mechanism. However, in the case of the LH mechanisms, due to the mobility of the three apex noble metal atoms on the (1-4)O^* + Pd_{10} and (1-4)O^* + Pt_{10} clusters, a slight torsion occurred. The CO molecule is adsorbed in an on-top position for 3 and 4 adsorbed O atoms, while it is adsorbed in a bridge position for 2 and 1 O atoms. In

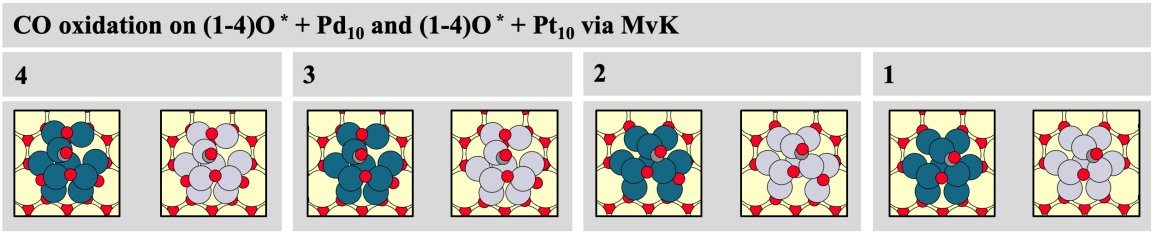

Figure 7.8.: Transition states of a CO_2 dissociation on structure-optimized subnanometer clusters (1-4)O^* + Pd_{10} and (1-4)O^* + Pt_{10} via the MvK mechanism adsorbed on a CeO_2(111) surface. Red circles represent O atoms, large yellow circles denote Ce atoms, dark gray circles represent C atoms, gray circles Pt atoms, and petrol circles represent Pd atoms.

Figure 7.9, the transition states of CO_2 dissociations on the extended metal surfaces (100), (110), (111), and (211) are depicted. In the top row a higher O loading is shown with an additional O atom present within the unit cell. In the middle row, a lower O loading is present, with only one O atom within the unit cell. The CO molecule and the O atom are bridge-bound for the (100) and (110) surfaces. For the (111) and (211) surfaces, the CO molecule is onto-bound, and the O atom is bridge-bound, with the three necessary noble metal atoms arranged in a triangular fashion. This configuration is analogous to the CO_2

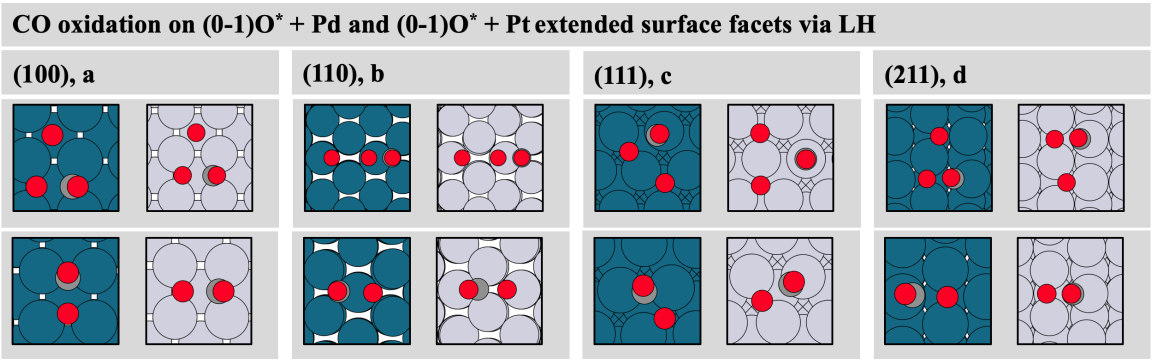

Figure 7.9.: Transition states of a CO_2 dissociation on structure-optimized extended metal surfaces of the Pd and Pt surface facets (100), (110), (111), and (211) via the MvK mechanism. Red circles represent O atoms, dark gray circles represent C atoms, gray circles Pt atoms, and petrol circles represent Pd atoms.

dissociations on the O^* + Pd_3 and O^* + Pt_3 clusters (1-4)O^* + Pd_{10} and (1-4)O^* + Pt_{10} cluster for the LH mechanism. Thus, these species are directly comparable to each other. The CO_2 dissociation on the metal oxides on the (101) surface is depicted in the bottom row. The transition state of CO_2 dissociation via the MvK mechanism occurs such that the CO

molecule, starting from an on-top position coordinated with a noble metal atom, migrates to an O atom situated in a bridge position between two noble metal atoms. This structure bears a resemblance to those of the subnanometer clusters for the MvK mechanism. In Figure

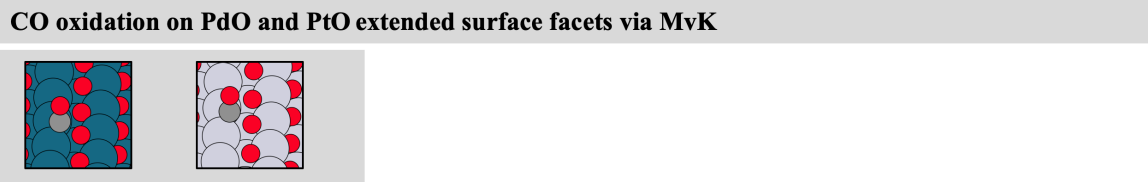

Figure 7.10.: Transition states of a CO_2 dissociation on structure-optimized extended metal oxide surfaces of the PdO and PtO surface facet (101) via the MvK mechanism. Red circles represent O atoms, dark gray circles represent C atoms, gray circles Pt atoms, and petrol circles represent Pd atoms.

7.10, the transition states on the noble metal oxides PdO and PtO with the surface facet (101) are depicted. As discussed in Section 6.3.4, the CO molecule migrates towards an surface O atom and undergoes an MvK mechanism for CO oxidation. The examination of the activity of noble metal oxides was conducted in this work to investigate the oxidized state of the noble metals. The extended oxide surfaces serve as an approximation to noble metal clusters of nanometer size. However, they can temporarily serve as a reference for oxidized sub-nanometer clusters for a preliminary assessment until more detailed studies regarding oxidized noble metals are conducted. It is important to reiterate that in the case of a noble metal oxide, the crystal structure represents that of an partially oxidized noble metal, and CO oxidation via an MvK mechanism induces an O lattice defect in the oxide PdO and PtO crystal. Surface adsorption of O atoms on subnanometer clusters and nanometer clusters undergoes CO oxidation via an LH mechanism.

7.2.1. Correlation of CO_2 Dissociation and CO_2 Adsorption relative to $CO_{2(g)}$

In Figure 7.11, the reaction energy barriers $\Delta E_{[CO\text{-}O]^{\ddagger}}$ of CO_2 dissociation are plotted against the dissociated products, the adsorbed CO^* molecule and the adsorbed O^* atom. The slope of the linear fit is 0.75 for the Pd catalysts and 0.81 for the Pt catalysts. These indicate how CO_2 dissociation changes relative to CO and O adsorption, with both quantities considered relative to $CO_{2(g)}$ in the gas phase. A slope of 0.75 for the Pd catalysts suggests that an increase in CO and O adsorption leads to an increase in CO_2 dissociation, with Pd having a moderate effect on dissociation. A higher slope of 0.81 for the Pt catalysts indicates that an increase in CO and O adsorption leads to a stronger increase in CO_2 dissociation, with Pt having a stronger effect on dissociation compared to Pd since the Pt catalysts bind the reactants more strongly. The MAE is 0.27 for Pd and 0.37 for Pt catalysts. These values were expected given the varying species. A higher coefficient of determination, expressed as the R^2 value, indicates a more optimal fit of the regression model to the dataset. This

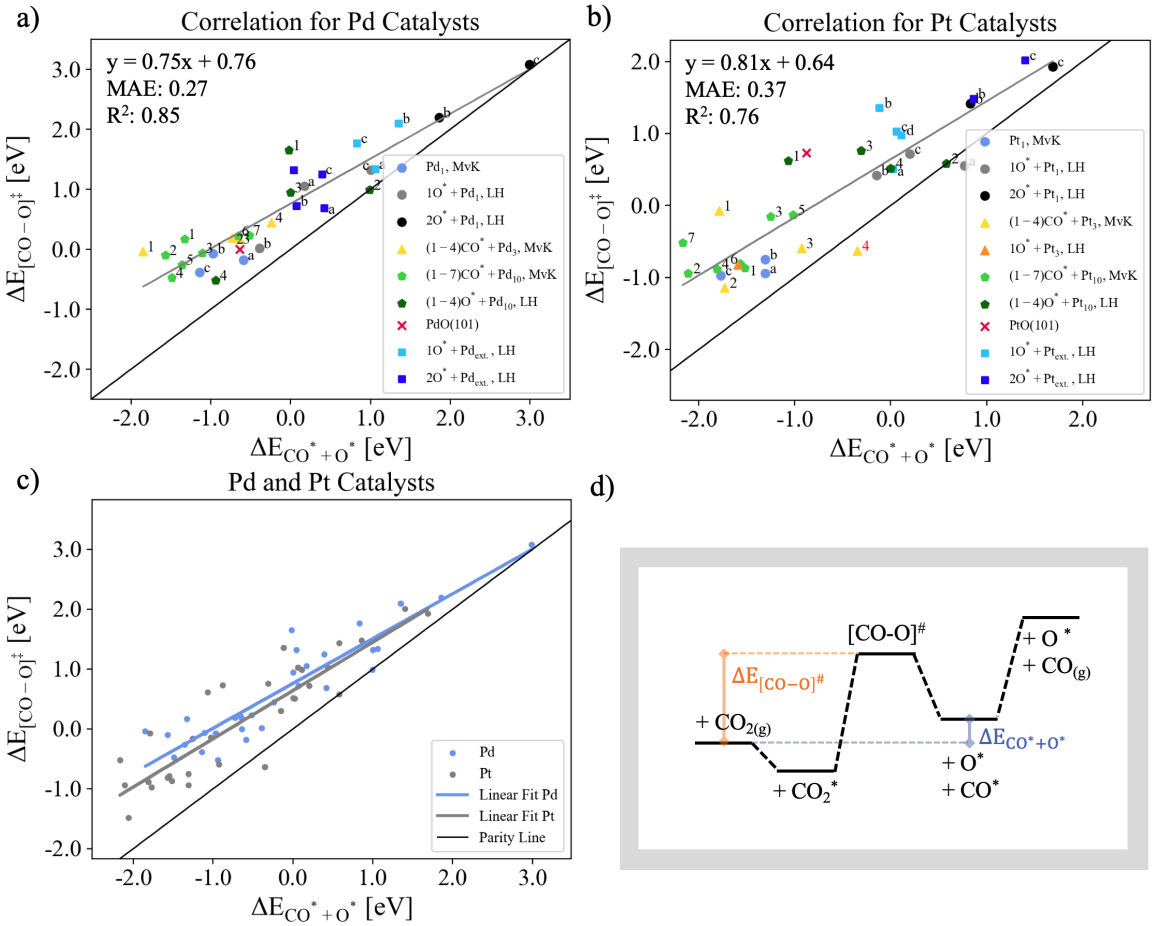

Figure 7.11.: The activation energy barrier $\Delta E_{[CO\text{-}O]^{\ddagger}}$ of the CO_2 dissociation is plotted against the $CO^* + O^*$ binding $\Delta E_{CO^* + O^*}$ relative to gas phase CO_2. Shown are Figure a) for Pd catalysts and b) for Pt catalysts. The parity line (black) and the linear fit of all species shown (grey) are plotted. The numbering corresponds to those of the figures presented in Section 7.2. Figure c) shows the combined plots of Pd (blue) and Pt (gray) catalysts. Figure d) illustrates the elementary reaction of CO_2 dissociation in a schematic Gibbs free energy diagram. The descriptors used for scaling relation are highlighted.

implies that a greater portion of the variance in the dependent variable, which is in this case the activation barrier to the dissociated product, can be elucidated by the independent variable, which is the presence of the catalyst, for Pd and Pt catalysts. With an R^2 value of 0.85 for Pd, it can be inferred that the regression model accounts for 85% of the variability in the data on Pd catalysts. Similarly, with an R^2 value of 0.76 for Pt, the model explains a significant proportion of the data variance. This indicates an improved model fit to the dataset for both Pd and Pt catalysts. When the two datasets of Pd and Pt catalysts are overlaid, it is evident that they are very close to each other. Consequently, the choice of the noble metal has a minor effect on the activity for CO_2 dissociation in correlation with CO and O adsorption. In general, it can also be stated that the MvK mechanisms for CO_2 dissociation tend to occur in the exothermic range compared to the LH mechanisms. This is

because CO_2 dissociation can regenerate an V_O defect on the ceria surface. Conversely, the LH mechanisms are more exothermic for CO_2 formation.

7.2.2. Correlation of CO_2 Dissociation and O Adsorption relative to $CO_{2(g)}$

A study by Ko et al. shows Brønsted-Evans-Polanyi relations for CO_2 dissociation.[310] They confirmed that the sum of adsorption energies of CO and O is linearly scaled not only with the adsorption energy of CO_2 but also with the reaction energy for the CO_2 dissociation. The

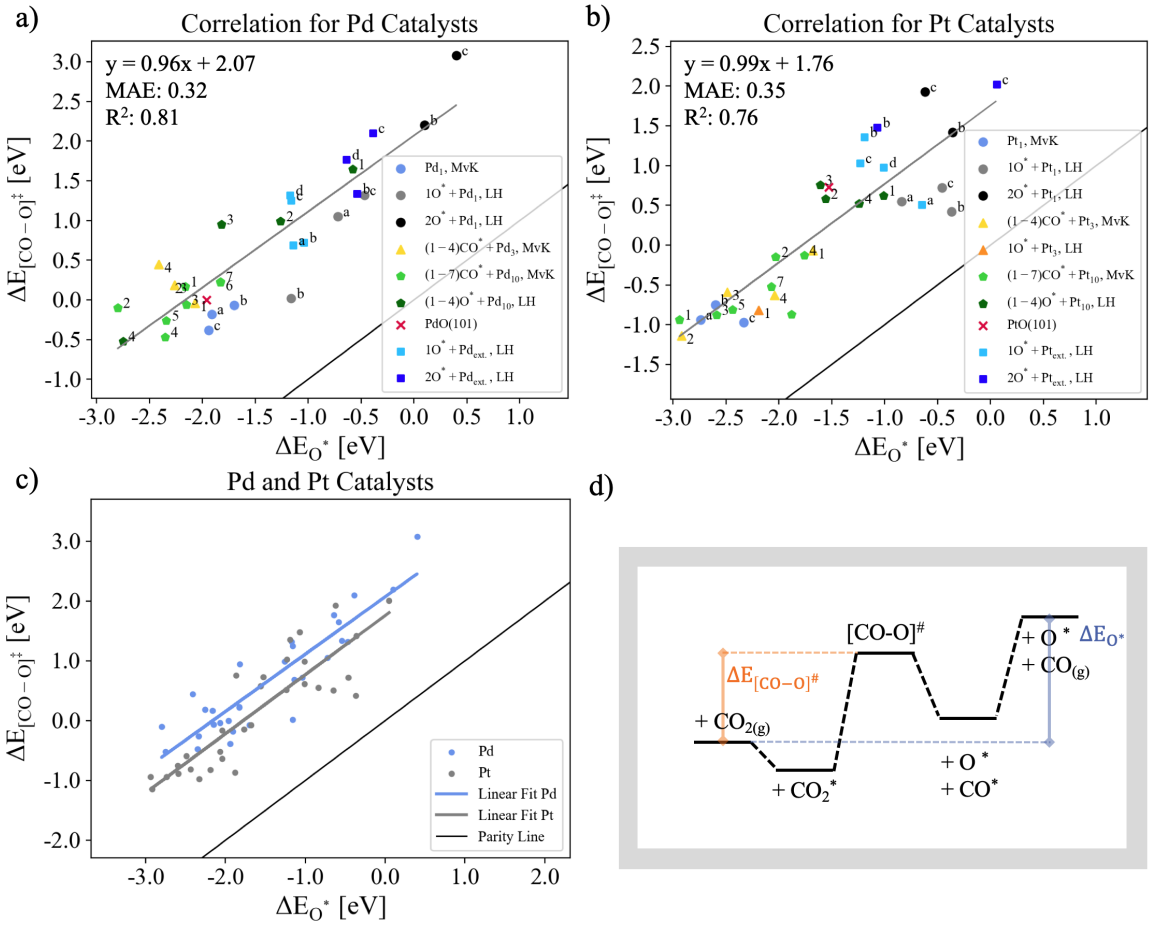

Figure 7.12.: The activation energy barrier $\Delta E_{[CO\text{-}O]^{\ddagger}}$ of the CO_2 dissociation relative to gas phase CO_2 is plotted against the O^* binding ΔE_{O^*} relative to gas phase O. Shown are Figure a) for Pd catalysts and b) for Pt catalysts. The parity line (black) and the linear fit of all species shown (grey) are plotted. The numbering corresponds to those of the figures presented in Section 7.2. Figure c) shows the combined plots of Pd (blue) and Pt (gray) catalysts. Figure d) illustrates the elementary reaction of CO_2 dissociation in a schematic Gibbs free energy diagram. The descriptors used for scaling relation are highlighted.

scaling relations shown in Figure 7.12 with a slope of 0.96 for Pd and 0.99 for Pt catalysts, indicate how the activation energy for CO_2 dissociation changes concerning the energy for O adsorption, both referenced relative to $CO_{2(g)}$ in the gas phase. A slope observed with Pt catalysts at 0.99, suggests that an increase in the energy for O adsorption results in a

proportionally larger increase in the activation energy for CO_2 dissociation. The slope of the scaling relation offers valuable insights into the impact of variations in the interaction strength of the catalysts with O atoms on the activation energy required for CO_2 dissociation, relative to alterations in O adsorption energy. This elucidates the relative significance of the bond-breaking and bond-forming steps within the overarching reaction mechanism. It can also be observed that the MvK mechanisms are located in the range of negative activation barriers relative to $CO_{2(g)}$ in the gas phase and the O adsorptions relative to $CO_{2(g)}$ in the gas phase. This is more pronounced for Pt than for Pd catalysts, which can be attributed to the property of Pt having a stronger O adsorption energy compared to Pd catalysts. Since the slope here is closer to 1 than the scaling relation in Section 7.2.1, it can be stated that the O adsorption has a stronger influence on the CO_2 dissociation than the CO adsorption. The MAE values are 0.32 for the Pd catalysts and 0.35 for the Pt catalysts. Considering the highly varied surface facets of the ceria substrate and the diverse scales of the active centers, these MAE values fall within an acceptable range. Additionally, the coefficient of determination R^2 is calculated as 0.81 for the Pd catalysts and 0.76 for the Pt catalysts. An R^2 value closer to 1 indicates a stronger correlation between the predicted and observed values. With R^2 values of 0.81 for Pd and 0.76 for Pt, the predictive models demonstrate a relatively high degree of accuracy in explaining the variance in CO_2 dissociation activity for both catalyst types. Overlaying the data points reveals that the Pd and Pt catalysts overall lie within a similar regime. The linear fits are nearly parallel to each other, with Pt closer to the parity line than Pd catalysts. This indicates that the Pt catalysts are more reactive towards CO_2 dissociation. Furthermore, it can be stated that there is indeed a scaling relation between the noble metal size scales and the adsorption energies. The general tendency suggests that CO_2 dissociation becomes more favorable with an increasing number of V_O defects present on the ceria surfaces as the O adsorption becomes stronger. If we reverse the direction of the reaction and consider CO_2 formation, this would imply that the LH mechanism is favored over the MvK mechanism. Therefore, CO_2 molecule formation is most favored on highly oxidized single-atom catalysts, followed by extended noble metal surfaces, and finally, subnanometer clusters, in descending order of preference.

7.3. Correlation of CO_2 Desorption and O Adsorption relative to $CO_{2(g)}$

In Figure 7.13, CO_2 desorption is plotted against O adsorption. These data could be overlaid on the plot in Figure 7.12 to create a volcano plot. However, both scaling relations are strongly dependent on reaction conditions, so any adjustment would introduce a shift that could alter a peak and potentially invalidate a statement. The red indices indicate that the

configuration change due to adsorption or desorption of the reactants has been included in the desorption energies. Therefore, the desorption energies are negative, which is unphysical

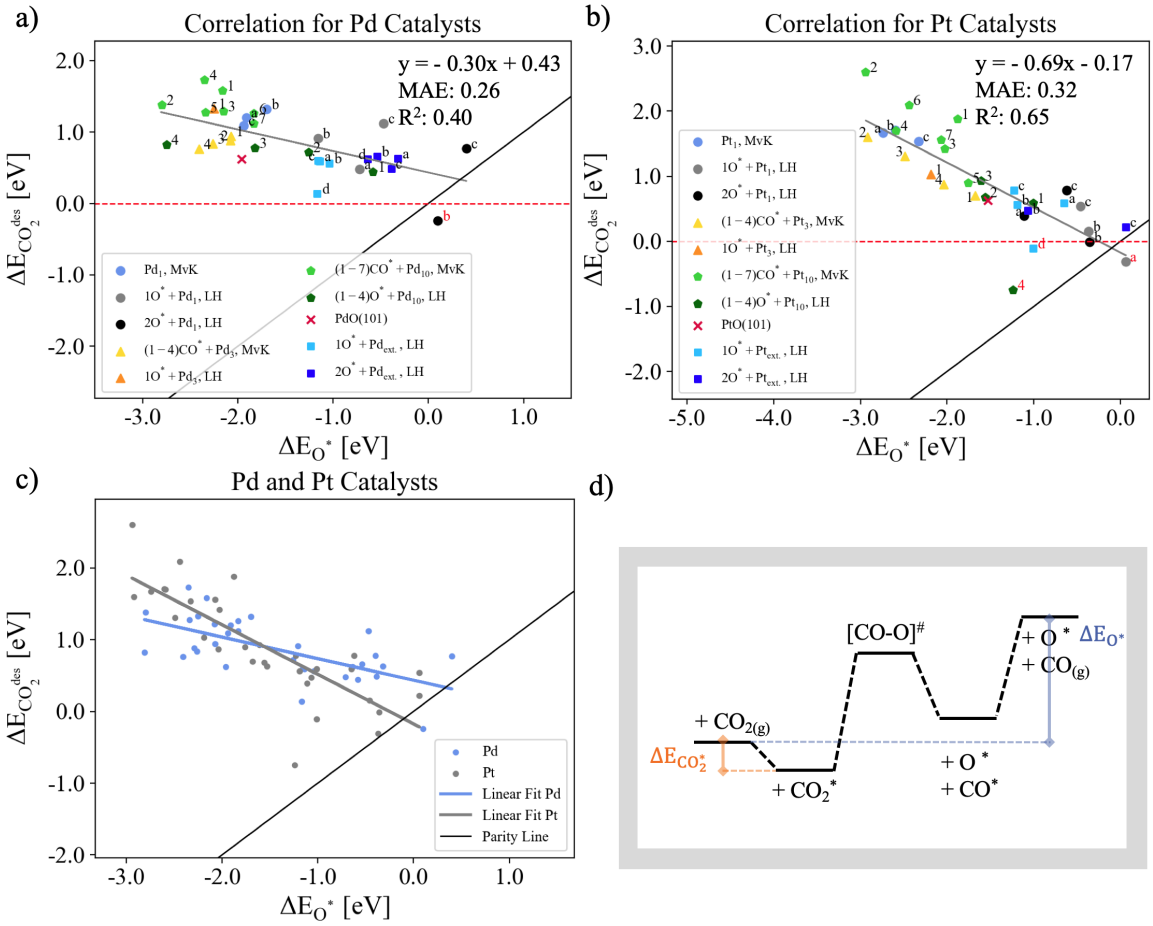

Figure 7.13.: The desorption energy $\Delta E_{CO_2}{}^{des}$ of the CO_2 molecule is plotted against the O^* binding relative to gas phase $CO_{2(g)}$. Shown are Figure a) for Pd catalysts and b) for Pt catalysts. The parity line (black) and the linear fit of all species shown (grey) are plotted. The numbering corresponds to those of the figures presented in Section 7.2. Figure c) shows the combined plots of Pd (blue) and Pt (gray) catalysts. Figure d) illustrates the elementary reaction of CO_2 dissociation in a schematic Gibbs free energy diagram. The descriptors used for scaling relation are highlighted. The species located below the red dashed line have negative desorption energies and are therefore not stable under reaction conditions.

at 0 K since entropy must always increase during desorption at 0 K. As shown in Figure 7.13 the slope of the Pd clusters is -0.30, while that of the Pt clusters is -0.69. These slopes indicate how $CO_2{}^*$ desorption changes relative to O adsorption, with both quantities correlated relative to $CO_{2(g)}$ in the gas phase. Conversely, a slope of -0.69 for Pt clusters indicates that an increase in O adsorption leads to a more significant decrease in $CO_2{}^*$ desorption. This suggests that the interaction between the Pt catalyst and O influences CO_2 desorption to a greater extent compared to the Pd catalysts, which exhibit a slope of -0.30. The interaction between the Pd catalyst and O results in a less pronounced decrease in $CO_2{}^*$ desorption energy. The MAE for Pd is 0.26, while for Pt it is 0.32, which are acceptably low

values considering the strong variety in morphology of the catalysts studied. An R^2 value of 0.40 for Pd and 0.65 for Pt suggests that a larger portion of the variability in the activation barrier to the dissociated product ($\Delta E_{[O\text{-}O]^{\ddagger}}$ to ΔE_{2O^*}) can be explained by the independent variable, the presence of $O_{2(g)}$ in the gas phase, for Pt compared to Pd. Thus, the regression model accounts for Pt a higher proportion with 65% of the variability in the data, indicating a more optimal fit of the model to the dataset. Conversely, for Pd, the model explains a lower proportion with 40% of the data variability, suggesting a less optimal fit relative to Pt. Overlaying the data points reveals that the Pd and Pt catalysts overall lie within a similar regime.

8. Conclusion

8.1. Spectroscopic Data of all Species investigated in this Work

Figure 8.1 represents the integration of all spectroscopic data collected in this study. This can serve as a guide for future investigations through experimental methods. When comparing the IR spectra found in the literature as shown in Section 1.6, it can be observed that the sizes of noble metal clusters affect the locality of the spectra. The carbonyl species $Pd_{c.}$ and $Pt_{c.}$ possess characteristic vibration frequencies. Single-atom catalysts, which arise from high dispersion of the noble metal catalysts on a ceria surface, are preferably found at high vibration frequencies. Subnanometer clusters, such as those of size Pd_3 and Pt_3, as well as Pd_{10} and Pt_{10}, are split both at high and low frequencies. In between, a gap is observed, which is particularly pronounced for Pt catalysts. Vibration frequencies around 1900 cm^{-1}

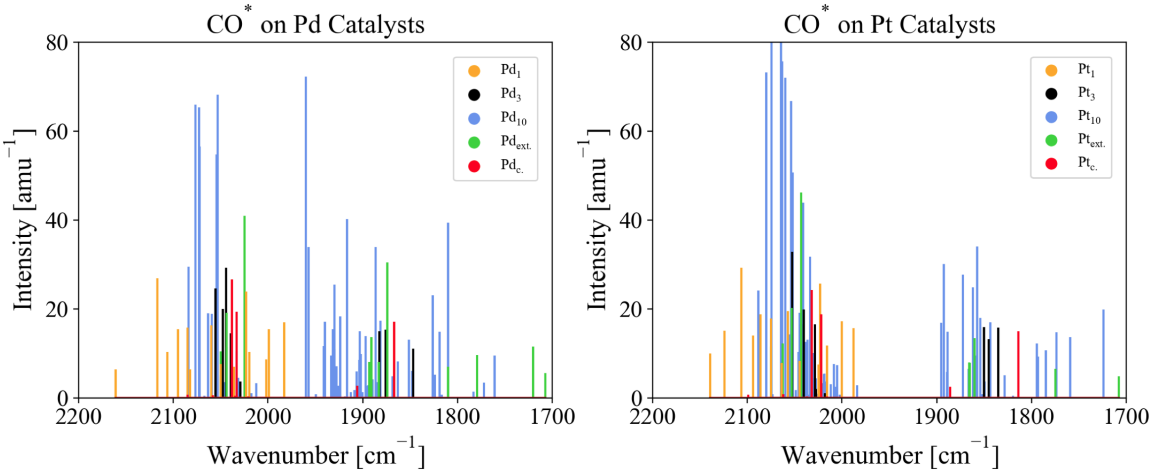

Figure 8.1.: Intensities plotted against the vibrational frequencies in cm^{-1} of adsorbed CO molecules on noble metal catalysts, which are themselves adsorbed on ceria surface facets at 0 K. The left side represents CO molecules adsorbed on Pd surfaces, while the right side shows Pt surfaces. The spectra are differentiated based on noble metal sizes: carbonyl species $Pd_{c.}$ and $Pt_{c.}$ (red), single-atom catalysts Pd_1 and Pt_1 (blue), subnanometer clusters with one layer Pd_3 and Pt_3 (black), subnanometer clusters with two layers Pd_{10} and Pt_{10}, and $Pd_{ext.}$, as well as nanometer-sized clusters approached by extended noble metal surfaces $Pt_{ext.}$ (orange).

can thus be attributed to both subnanometer clusters and extended metal surfaces, which

adsorb bridge-bound CO molecules. Frequencies between 1750 and 1800 cm^{-1} correspond to hollow site binding, which can be observed on both extended surfaces and subnanometer clusters. However, it is also evident that subnanometer clusters exhibit a broader distribution of frequencies around this range. The extended metal surfaces, which are an approximation of nanometer clusters, are split into three distinct bands. These indicate the presence of ontop, bridge, and hollow sites, which cause characteristic localizations of the spectra. The ontop sites are also within the range of single-atom catalysts, which are naturally bound ontop. The single-atom catalysts exhibit the widest distribution around the range of ontop-bound CO molecules, as the ceria surfaces (100), (110), and (111) were considered. The chemical environment of these surfaces induces a broader distribution of vibration spectra.

8.1.1. Identification of CO vibrational Frequencies on Pd_1 and Pt_1

The in-situ spectroscopic investigations conducted by Sarma et al. focused on CO and CO + O_2 reaction conditions, utilizing continuous gas flows to understand CO binding on catalysts synthesized through wet impregnation and precipitation methods.[268] By employing DRIFTS spectroscopy, they explored charged states and associated coordination environments of isolated supported noble metals with CO adsorption as the probing molecule. The strong reducing property of CO molecules prompted an investigation into structural and electronic changes at isolated active sites upon CO adsorption. Through in-situ XAS and DRIFTS experiments under reducing (1% CO) and oxidizing (1% CO + 1% O2) conditions over 1 hour, they tracked temporal evolution of various species. The obtained DRIFTS spectra were visualized in Figures 5.6 and 5.7 for CO and CO + O_2 atmospheres, respectively. Our calculated vibrational spectra, presented in Table 5.1, exhibit analogous vibrations to those reported in collaborative experimental data. The collaboration provided insights into CO adsorption behaviors on Pd and Pt sites, though noble metal size significantly influences vibrational spectra. For single-atom catalysts, species assignment relied on Table 5.1. Frequencies at 1985 and 1971 cm^{-1} for Pd and 2089 cm^{-1} for Pt did not align with pristine metal surfaces or single-atom catalysts, while those around 2061 cm^{-1} for Pd and 2096 cm^{-1} for Pt correlated with single-atom catalyst vibrations. Frequencies above 2100 cm^{-1} were attributed to formal +IV oxidation states, consistent with two O atoms adsorbed vicinally to noble metal atoms. In oxidizing conditions, frequencies shifted to higher values, with lower ones attributed to subnanometer clusters no longer present. Vibrational frequencies aligned with +II oxidation states for both Pd and Pt on ceria surfaces. Literature studies concurred with these observations, associating frequencies around 2095 cm^{-1} with single-site Pt species and 2090-2100 cm^{-1} with CO adsorption on small PtO_x clusters.[272] Additionally, UHV-IR spectroscopy by Maurer et al. depicted Pt single-atom catalysts and CeO_2 vibrations at 2179 and 2161 cm^{-1}, respectively, corroborating our findings.[69] While

species validation was not confirmed, the assumption that high oxidation states correspond to frequencies above 2100 cm^{-1} is plausible.

8.1.2. Identification of CO vibrational Frequencies on Pd_3, Pt_3, Pd_{10}, and Pt_{10} subnanometer Cluster

In Figure 5.6 in Section 5.2, the noble metals Pd and Pt were measured under reducing atmosphere conditions. The CO vibrational spectra exhibit lower frequencies, specifically 1971 and 1985 cm^{-1} for the Pd catalysts. These frequencies correspond analogously to those observed for Pd_1/CeO_2 on a (110) surface with one $1V_O$ or two $2V_O$ defects. However, for Pt, no spectra are found in this regime, raising doubts about the presence of single-atom catalysts. Referring to Table 5.32 in Section 5.6, where CO vibrational spectra on pristine Pd and Pt metal surfaces were calculated, no spectra can be assigned either. The spectra for Pd surfaces are around 2050 cm^{-1} for ontop sites, 1890 cm^{-1} for bridge sites, and 1700 to 1780 cm^{-1} for hollow sites, while for Pt surfaces, they are approximately 20 cm^{-1} higher for ontop and bridge positions, and consistent for hollow sites. The study of Spezzati et al.[28,142] observed similar trends for the Pd(111) surface. It could be speculated that these vibrational frequencies around 1970 to 1985 cm^{-1} should be attributed to subnanometer clusters. In Section 8.2.3 in the Appendix, these frequencies for subnanometer clusters are listed. They exhibit similar vibrational frequency ranges to those on pristine noble metal surfaces, with additional frequencies in the range of 1900 to 1960 cm^{-1} for Pd subnanometer clusters are assigned to bridge sites. Pt subnanometer clusters, on the other hand, have overall lower vibrational frequencies that do not fall within the aforementioned range. Based on the findings of this study, we would assign the observed spectra in Figure 5.6 to subnanometer clusters. The frequencies for Pt species, particularly at 2089 cm^{-1}, may also be attributed to subnanometer clusters, but distinguishing them from single-atom catalysts and pristine metal surfaces is challenging. Additionally, slightly lower frequencies around 1850 to 2050 cm^{-1} for bridge adsorbed CO molecules on the clusters would be expected. This assumption is supported by Table 1.1 in Section 1.6, which contains spectroscopic values from the literature. For instance, Spezzati et al. observed similar trends. Subnanometer clusters composed of 3 Pd atoms supported on ceria exhibited vibrational frequencies of 2062 cm^{-1} for ontop adsorption.[28,142] Partially oxidized subnanometer clusters of the same size showed slightly lower vibrations for bridge-adsorbed CO molecules, but comparable ones ranging from 1900 to 1950 cm^{-1}. Similar values were reported by Boronin et al.[30] and Salcedo et al.[10].

8.2. Activity of Pd_n and Pt_n Catalysts towards CO Oxidation and O_2 Dissociation

8.2.1. Activity towards O_2 Dissociation

As elucidated in Section 6.3.1, the adsorption energy is notably influenced by the adsorption site of the $O_{2(g)}$ molecule, identified as strain effects in a study by Dietze and Grönbeck, which impact the reactivity.[301] They noted in their study that compressive strain enhances bonding strength, while tensile strain diminishes the bond strength. The (111) and (211) surfaces can be compared with the reaction sites of the following subnanometer clusters. It can be noted here that the surface configuration indicates a tensile strain, resulting in lower adsorption energy as shown by a study of Dietze and Grönbeck.[301] In Figure 8.2, the O_2 dissociations determined in this study are plotted on different size scales of the noble metal supported on the ceria surface in a Gibbs free energy diagram. The LH and MvK mechanisms are considered in separate plots. The ceria surfaces chosen for the single-atom catalysts showed the highest activity, with the (110) surface for the LH mechanism and the (100) surface for the MvK mechanism. The Pd_3, Pt_3, Pd_{10}, and Pt_{10} subnanometer clusters are all supported on a (111) ceria surface. For the LH mechanism, it is evident that the Pd_3 and Pt_3 subnanometer clusters exhibit the highest activity towards O_2 dissociation according to Figure 8.2. It must still be emphasized that without considering both the reaction conditions and the entire reaction mechanism in a kinetic simulation study, no complete and definitive statements can be made. Within the scope of these studies, we can, after all, make initial impressions about the relative stabilities in relation to the activity. We have observed that the Pd_3 and Pt_3 clusters showing in Section 6.2.1 exhibit exceptional activity in O_2 dissociation compared to extended metal surfaces (111) and (211) approximating nanometer clusters and the Pd_{10} and Pt_{10} clusters as shown in Section 6.2.1 showcasing a subnanometer cluster consisting of two noble metal layer. For comparison, the single-atom catalysts adsorbed on a (111) surface can be considered. The adsorption of an $O_{2(g)}$ molecule on an already oxidized $2O^*$ + Pd_{10} cluster and $2O^*$ + Pt_{10} cluster results in exothermic adsorption energy for another $O_{2(g)}$ molecule, with values of -0.78 eV and -1.71 eV, respectively. The adsorption energies of the single-atom catalysts and the pre-oxidized subnanometer are for the Pd catalysts in the same range, but a significant difference can be seen for the Pt catalysts. Here, the adsorption energy is notably stronger on the pre-oxidized subnanometer cluster $2O^*$ + Pt_{10}. The adsorption energies of the $O_{2(g)}$ are slightly endothermic on the pristine noble metal surfaces even at low temperatures as 423.15 K, as shown here. Therefore, it can be concluded here that $O_{2(g)}$ molecule adsorption on a subnanometer cluster is preferred over a nanometer size cluster and accordingly, the reaction energy relative to $O_{2(g)}$ in the gas phase is significantly higher on the pristine metal surfaces. Consequently, a reaction does

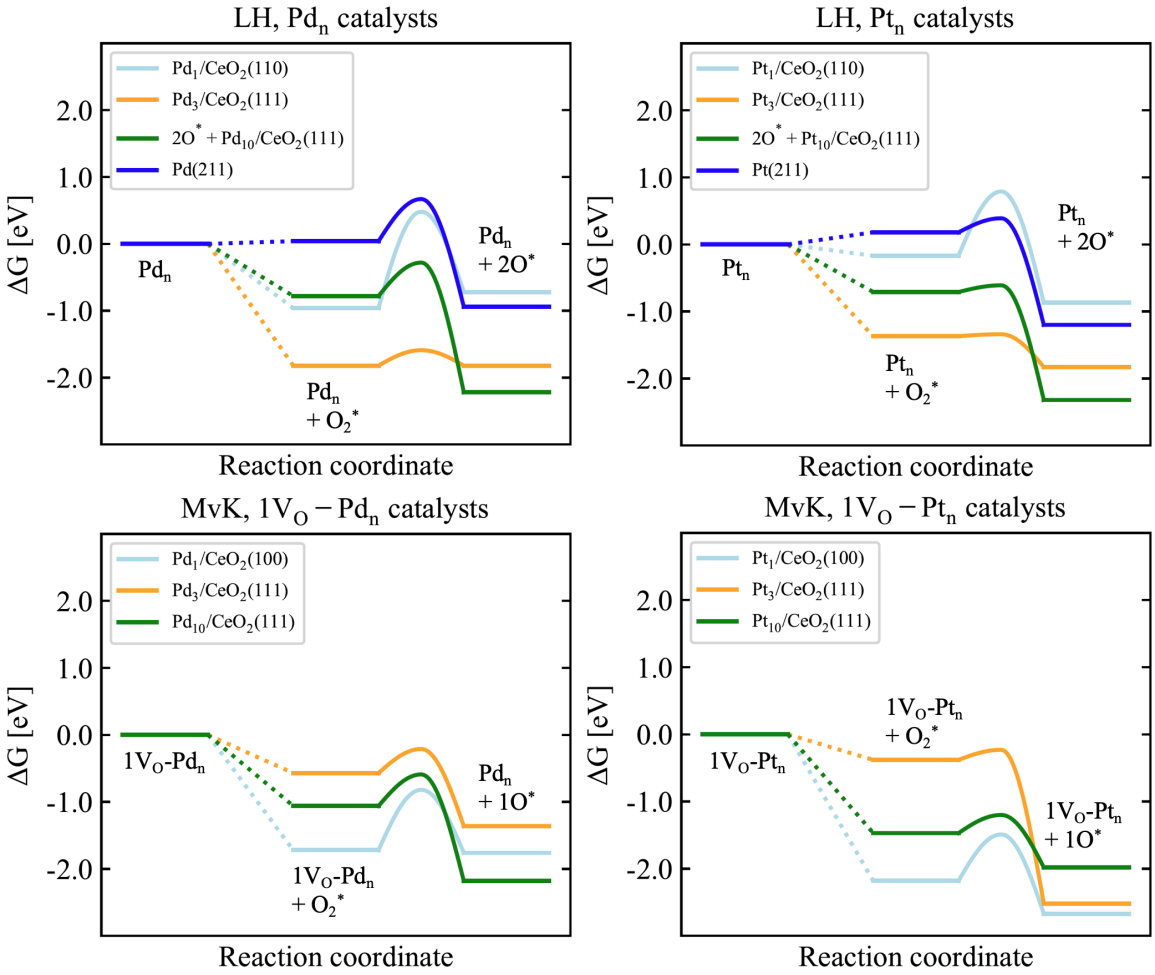

Figure 8.2.: Calculated Gibbs free energies of the structure-optimized O_2 dissociation elementary reaction steps for Pd and Pt clusters in varying sizes are plotted against the reaction coordinate in a potential energy diagram in eV at 423.15 K. Plotted here are the LH mechanisms (upper row) and MvK mechanisms (lower row) on single-atom catalysts Pd_1 and Pt_1 (sky blue), subnanometer clusters Pd_3, Pt_3 (orange), as well as Pd_{10} and Pt_{10} (green). For the LH mechanism, extended metal surfaces can also be considered (blue).

not occur on the pristine metal surfaces at 423.15 K, and adsorption becomes even less likely with increasing temperature. After $O_{2(g)}$ adsorption, the activation barrier on the reduced Pd_{10} cluster is 0.76 eV, while on the reduced Pt_{10} cluster, it is 0.44 eV. On the $2O^*$ + Pd_{10} cluster, this value is 0.50 eV, and on the $2O^*$ + Pt_{10} cluster, it is 0.10 eV. Consequently, the activation barriers are 0.32 eV smaller for Pt on the reduced cluster and 0.40 eV smaller on the pre-oxidized cluster. It also indicates that the barriers for the second O_2 dissociation are interestingly lower than those for the first by 0.26 eV for Pd und 0.35 eV for Pt. The reaction barrier for the first O_2 dissociation relative to $O_{2(g)}$ in the gas phase is 0.99 eV for the reduced Pd_{10} cluster and 0.06 eV for the reduced Pt_{10} cluster. The second O_2 dissociation

relative to $O_{2(g)}$ in the gas phase is -0.28 eV for the pre-oxidized $2O^*$ + Pd_{10} cluster and -0.61 eV for the $2O^*$ + Pt_{10} cluster, making it approximately 0.60 eV more exothermic than the reduced cluster counterparts. The reaction energy of the elementary step for the O_2 dissociation is -0.96 eV for the reduced Pd_{10} cluster, -1.61 eV for the reduced Pt_{10} cluster, -2.30 eV for the pre-oxidized $2O^*$ + Pd_{10} cluster, and -2.24 eV for the pre-oxidized $2O^*$ + Pt_{10} cluster. In summary, it can be stated that the second O_2 dissociation is likely, while the first one is not. Because of this, it makes sense to consider the pre-oxidized cluster for the LH mechanism in Figure 8.2. The adsorption energies on the pre-oxidized $2O^*$ + Pd_{10} cluster and the $2O^*$ + Pt_{10} cluster are significantly more exothermic with -0.78 eV and -0.71 eV, respectively. On the reduced ceria surface with one defect $1V_O$ is the most exothermic with -1.06 for the $1V_O$-Pd_{10} cluster and -1.47 eV for the $1V_O$-Pt_{10} cluster. This suggests that regeneration of the ceria surface at the interface with a noble metal cluster is indeed enhanced. On the extended noble metal surfaces, these values are all endothermic with 0.18 eV for Pd and 0.30 eV for Pt on the (111) surface, and slightly endothermic with 0.04 eV for Pd and 0.18 eV for Pt on the (211) surface. The adsorption configurations are identical for all mentioned species, involving three noble metal atoms and one of the O atoms in a bridge position between two of the three and on top of a third. A direct comparison is feasible, enabling us to elucidate a discernible size effect. The reaction barriers relative to $O_{2(g)}$ in the gas phase on the plain noble metals are comparable for the (111) surface, with 0.93 eV for Pd and 0.76 eV for Pt, for the Pd species. On the (211) surface, these are slightly less endothermic, with 0.67 eV for Pd and 0.39 eV for Pt. However, since adsorption on the extended noble metal surfaces is not favored, this reaction is not likely to occur at elevated temperatures. The activation barrier following $O_{2(g)}$ adsorption is 0.23 eV for the Pd_3 cluster and 0.03 eV for the Pt_3 cluster as presented in Section 6.2.1. The reaction barrier relative to $O_{2(g)}$ in the gas phase is significantly more negative for the Pd_3 cluster, with -1.59 eV, and for the Pt_3 cluster, with -1.34 eV, due to the strong adsorption energy of the $O_{2(g)}$ molecule and the low activation barrier, compared to the reduced Pd_{10} and Pt_{10} clusters. The difference in the reaction energies of O_2 dissociation on the Pd_3 and Pt_3 clusters compared to the Pd_{10} and Pt_{10} clusters and the extended noble metal surfaces, under the same configuration conditions, represent a size-effect that could significantly influence the activity of noble metals on ceria in the kinetics. The Pd_3 and Pt_3 subnanometer clusters are advantageous for the LH mechanism of O_2 dissociation. However, the size effect is more favorable for the $1V_O$-Pd_{10} and $1V_O$-Pt_{10} subnanometer clusters via the MvK mechanism. The single-atom catalyst on the (100) surface exhibits the highest activity compared to the subnanometer clusters via the MvK mechanism. Several experimental studies also support the assumption that highly dispersed noble metals exhibit increased activity. As indicated by an experimental study conducted by Gaenzler et al., Pt oxidation was predominantly

observed for small nanoparticles, particularly those smaller than 2 nm.[311] These smaller particles exhibit increased sensitivity to oxidation compared to their larger counterparts. The O transfer to Pt is facilitated at the noble metal-ceria interface[312], and ceria has a notable impact on the electronic structure of Pt[313]. However, it has remained unclear whether this is due to a quantum effect stemming from the small size of the clusters down to a low number of atoms or from the higher exposure of the interface between the noble metal and the support. Ultimately, it is assumed that both effects influence the activity of the noble metals. Based on the activity determined here regarding O_2 dissociation, it can be stated that the electronic effect only comes into play in the smallest subnanometer clusters. However, the occurrence of the Pd_3 and Pt_3 clusters or a single layer of the noble metals is assumed to be low. Single-atom catalysts, as depicted in Section 6.1.2 for a stoichiometric surface, cannot be directly compared here due to the diverse configuration of the adsorption site. Nevertheless, it can be stated that the activation of the O_2 molecule by adsorption on top of just one noble metal atom does not result in a significant increase in activity. It can be generally stated about the activation of the O_2 molecule that an O defect leads to a significant increase in activation. This was observed in single-atom catalysts in Section 6.1.2 as well as the subnanometer clusters Pd_{10} and Pt_{10} in Section 6.2.5. However, interestingly, this statement does not apply to the subnanometer clusters Pd_3 and Pt_3 in Section 6.2.1. Here, the O_2 dissociation on the stoichiometric surface is more active than on an O-defective surface. Additionally, the pre-oxidized subnanometer clusters $2O^*$ + Pd_{10} and $2O^*$ + Pt_{10} exhibit increased activity, evident in the regime of the O-defective surface.

8.2.2. Activity towards CO Oxidation

The study by Gaenzler et al. revealed for ceria-supported catalysts, that Pt particles covered by CO appear to represent a catalytically active state due to the involvement of Pt-CeO_2 interface sites in the reaction mechanism.[311] They concluded, that this different reaction path also explains the observed delay in Pt reoxidation during the light-off. These findings suggest the existence of the MvK mechanism pathway at the interface between the noble metal subnanometer clusters and the ceria surface.[25] The calculated activities obtained through first-principle methods in this study yield results consistent with these experimental findings as demonstrated in the scaling relations in Section 7.2.1. A study by Cargnello et al. demonstrated that the interface between the noble metal cluster and the ceria support exhibits higher activity compared to the noble metal surface away from the interface. The interface is further divided into two regions: the corners, characterized by relatively undercoordinated sites and representing possible corners at the interface of the cluster, and the perimeter, which consists of the row of noble metal atoms along the interface from one corner to another. Contrary to that, our studies reveal as demonstrated in Section 4.3.6 that O removal

from the ceria interface, even in the presence of a noble metal, is endothermic, even at elevated temperatures. In Figure 4.32 is it shown that the reduction of the ceria surface at the interface with the noble metal atoms Pd and Pt demands higher energy expenditure than the extended ceria surface. Interestingly, the removal of O on the sublayer positions is significantly less endothermic than a position in the nearest neighbor position to the noble metals. Various factors may play a role here, such as the bonding strength between the atoms or the electronic structure of the materials. A detailed explanation of these relationships requires further, detailed considerations involving the electron occupancy of the s- and p-orbitals, as well as the corresponding Fermi level. The species and activity trends found here can serve as initial input for any future studies. In summary, experimental studies have uncovered heightened activity in CO oxidation at the interface, likely due to an MvK mechanism. Notably, observations detailed in Section 4.2.3 and supported by literature in the introduction in Section 1.3.1 reveal that O defects in the sublayer are more stable than those at the interface. Moreover, reduction at the interface with noble metals is notably endothermic. These findings suggest that the reducibility of the ceria surface at the noble metal interface requires dynamic O migration, a process that ceria facilitates. However, even if the barrier of O removal of the ceria surface lattice is overcome, $CO_2{}^*$ desorption presents a challenge when it comes to the MvK mechanism. An observation of the Gibbs free energy diagrams presented in this work could lead to a conclusion that the transition states between CO adsorption and $CO_2{}^*$ desorption, and vice versa, are somewhat confined in a 'pot.' The initial species before CO or $CO_{2(g)}$ adsorption, for the forward and reverse reactions, respectively, lies above the adsorbed reactants, undergoing an elevated transition state for the reaction. In Figure 8.3, the most active species from this study for an LH mechanism and an MvK mechanism are summarized in a Gibbs free energy diagram for a reaction temperature of 423.15 K. The adsorption energies on extended noble metal surfaces range approximately between -0.40 eV and -0.85 eV on the Pd surfaces and -0.60 eV and -0.99 eV on the Pt surfaces. The adsorption energies of CO molecules on the Pd_{10} and Pt_{10} clusters are stronger than on the extended metal surfaces. While these are within the range of the adsorption energies on the pristine metal surfaces for the Pd cluster, they are significantly stronger for the Pt cluster. The CO adsorption energies on the single-atom catalysts with a formal oxidation state of 0, presented in Section 6.1.5, range from -0.51 eV to -1.01 eV for Pd single-atoms and from -0.34 eV to -1.22 eV for Pt single-atoms. The latter two values represent the (111) surface, which, in configurations, can still be compared more closely with those of subnanometer clusters Pd_{10} and Pt_{10} since they are in an ontop position and have no coordination to the ceria surface. Thus, the adsorption energy of single-atom catalysts in an ontop position is comparable to the adsorption energy on the first layer of subnanometer clusters directly at the interface with ceria. In comparison, the CO adsorption

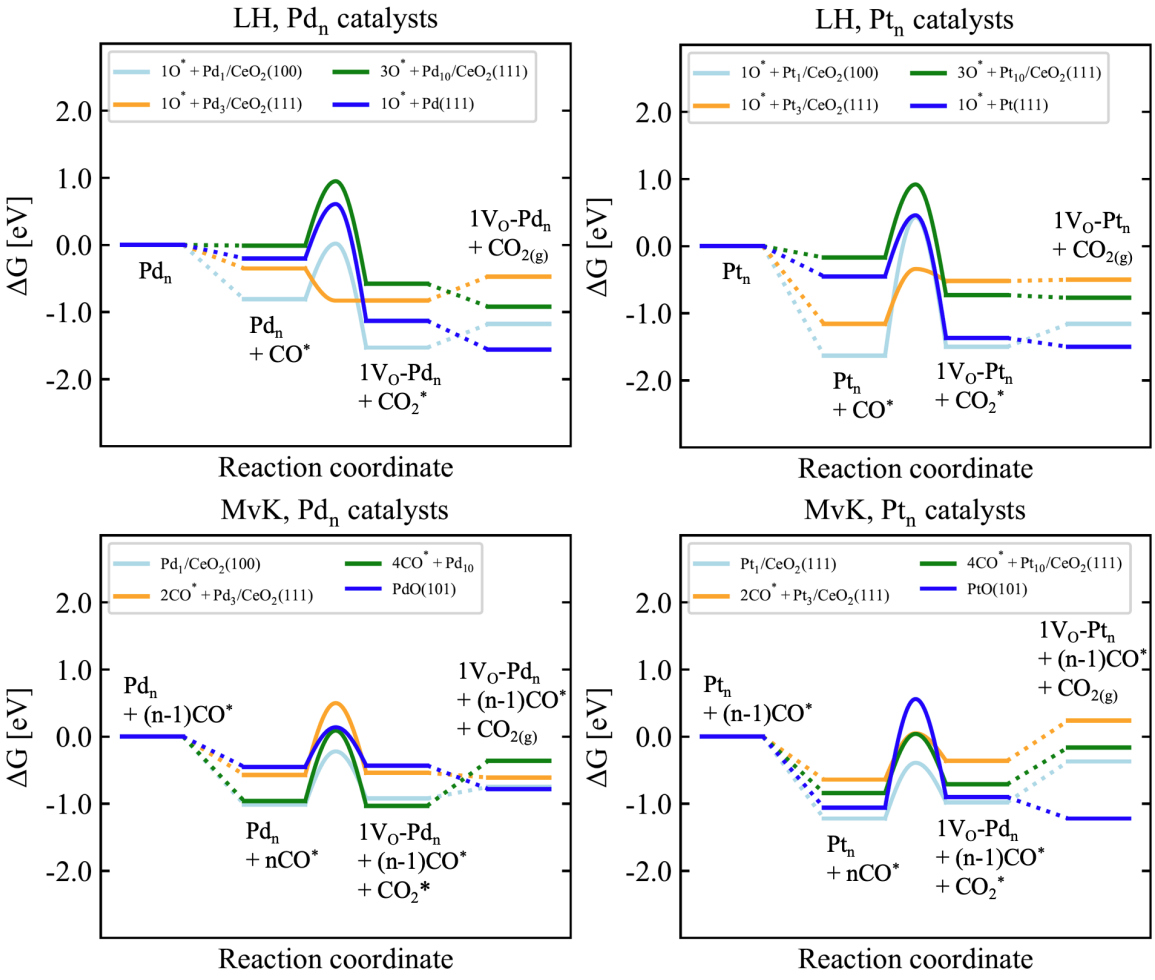

Figure 8.3.: Calculated Gibbs free energies of the structure-optimized CO oxidation elementary reaction steps for Pd and Pt clusters in varying sizes are plotted against the reaction coordinate plotted in a potential energy diagram in eV at 423.15 K. Plotted here are the LH mechanisms (upper row) and MvK mechanisms (lower row) on single-atom catalysts Pd_1 and Pt_1 (sky blue), subnanometer clusters Pd_3, Pt_3 (orange), as well as Pd_{10} and Pt_{10} (green). For the MvK mechanism, Extended metal oxide surfaces can also be considered (blue).

energies on the Pd_3 and Pt_3 clusters for (1-4)CO^* molecules, presented in Section 5.2.1, range from -0.57 eV and -1.54 eV for the Pd_3 cluster and -0.66 eV and -1.82 eV for the Pt_3 cluster with 1 and $2CO^*$ molecules, respectively. A higher CO coverage is unlikely under the given reaction conditions from 423.15 K to 723.15 K, as already investigated in the phase diagram in Section 5.2.1. According to the adsorption energies, it can be observed that those on the smaller Pd_3 or Pt_3 clusters with only one layer are comparable to those on the larger Pd_{10} or Pt_{10} clusters if the adsorption occurs on the first layer. For comparison, we considered adsorption ontop of the second layer of Pd_{10} and Pt_{10} clusters. This revealed that the adsorption of a CO molecule on an empty cluster is -0.03 eV for the

Pd cluster and 0.48 eV for the Pt cluster at a temperature of 423.15 K. Therefore, they are significantly endothermic for Pt and relatively neutral for Pd. The adsorption energies on the 2nd layer of subnanometer clusters are thus not comparable with those of the extended noble metal clusters, which still yielded exothermic adsorption energies for ontop positions on all surface facets (100), (110), (111) and (211). This suggests a size effect on the 2nd layer regarding the adsorption strength of a CO molecule in the ontop position. Regarding stabilities, the occurrence of these species is anyhow unlikely as diffusion towards bridge or hollow positions, which offer stronger adsorption energies, is favored. For the MvK mechanism, this "pot" is most pronounced for Pd_{10} and Pt_{10} clusters, less for single-atom catalysts. However, for Pd_3 and Pt_3 clusters, no such 'pot' exists. The CO_2 desorption is slightly exothermic, preventing an obstacle in the forward reaction, but the reverse reaction, CO_2 dissociation, is significantly hindered by an activation barrier without the compensation of a substantial adsorption energy. In addition to the noble metal size, insights into the activity concerning the chemical environment can be inferred when considering single-atom catalysts through the variation of different surface facets. A fully oxidized square planar structure of the single noble metal atoms, highly dispersed and adsorbed within a 'pocket' on the (100) surface, exhibits remarkably high reactivity for the $2O^*$ + Pd_1 and $2O^*$ + Pt_1 species. Moreover, the neutral barriers for Pd and the negative reaction barriers relative to CO in the gas phase for Pt also render them notably active. The noble metal atoms on the (111) surface are not embedded, neither in a 'pocket' nor a 'tunnel,' allowing them to swiftly transition between oxidation states by migrating on the ceria surface. The (110) surface consistently represents a favored structure, offering both free mobility and optimal anchoring for a highly dispersed state with available adsorption sites for the noble metal atoms. In summary, it can be stated that the reaction energy for the elementary reaction step of CO oxidation via the MvK mechanism is most exothermic for PdO and PtO (101) crystal surfaces. The activation barriers for CO oxidation via the MvK mechanism on the (1-4)CO^* + Pd_3 and (1-4)CO^* + Pt_3 clusters, as presented in Section 6.2.3, also exhibit a trend depending on the CO coverage. Starting from $4CO^*$ molecules and decreasing successively, the activation barriers are 0.75 eV, 0.85 eV, 1.06 eV, and 1.71 eV with only one CO molecule for the Pd_3 cluster, and -0.35 eV, 0.35 eV, 0.69 eV, and 1.69 eV with only one CO molecule for the Pt_3 cluster. The activation barriers for a cluster with only one layer of noble metal atoms are therefore in the same range. When compared to the pristine metal oxide (101) surfaces presented in Section 6.3.4, the barriers are also similarly high, with an activation barrier of 0.59 eV for PdO oxide and 1.62 eV for PtO oxide. The activation barriers of single-atom catalysts with a formal oxidation state of 0, presented in Section 6.1.5, exhibit activation barriers of 0.47 eV on the (100) ceria surface, 0.90 eV on the (110) ceria surface, and 0.78 eV on the (111) ceria surface for Pd. For the Pt noble metal atom,

the activation barriers are 0.40 eV on the (100) ceria surface, 0.55 eV on the (110) ceria surface, and 0.82 eV on the (111) ceria surface. These values are approximately 0.30-1.00 eV lower than those of the subnanometer clusters. The difference of 1.00 eV reflects an analogous surface structure to ceria with the (111) surface, making it directly comparable to that of the subnanometer clusters Pd_3 and Pt_3, and Pd_{10} and Pt_{10}. The reaction energy of the elementary step is exothermic via the LH mechanism for both noble metal clusters, measuring -0.47 eV for the Pd_3 cluster and -0.50 eV for the Pt_3 cluster. Via the MvK mechanism the reaction energy of the elementary step is exothermic for the Pd_3 cluster with -0.23 eV but endothermic for the Pt_3 cluster with 0.20 eV. The hindrance of $CO_2{}^*$ desorption is the primary factor contributing to the endothermic nature of the mechanism for the Pt cluster. The general statement can be made here that CO oxidation via the LH mechanism on the Pd_3 and Pt_3 clusters is indeed plausible. The barriers are comparable to those of fully oxidized single-atom catalysts. However, the oxidized Pd_1 and Pt_1 single-atom catalysts to the oxidation state of +IV with two $2O^*$ adsorbed, might not lead to increased activity due to the lack of their presence. The stability and likelihood of encountering these single-atom catalysts are significantly lower compared to the subnanometer clusters. In general, regarding the activation barriers after CO adsorption, it can be stated that the single metal atoms possess the lowest barriers, followed by the metal oxide surfaces (101) of the partially oxidized PdO and PtO crystals. These metal oxide surfaces could represent an oxidized nanometer cluster, which has undergone a crystalline configuration after O adsorption to assume the crystal structure of the oxides. The activation barriers after CO adsorption of the subnanometer clusters Pd_3 and Pt_3, as well as Pd_{10} and Pt_{10}, are uniformly about 0.30 eV higher. The reaction energy of the elementary step of the CO oxidation via the MvK mechanism is exothermic in all cases for the (1-4)CO^* + Pd_3 and (1-4)CO^* + Pd_3 subnanometer cluster, with -0.29 eV for a coverage of $4CO^*$ molecules, -0.44 eV for $3CO^*$ molecules, -0.61 eV for $2CO^*$ molecules, and -0.63 eV for one CO molecule for the Pd_3 cluster. For the Pt_3 cluster, the reaction energy of the elementary reaction step is -0.66 eV for a coverage of $4CO^*$ molecules, -0.21 eV for $3CO^*$ molecules, 0.24 eV for $2CO^*$ molecules, and -1.00 eV for one CO molecule. The CO_2 desorption at the Pd_{10} and Pt_{10} is endothermic in most cases as shown in Section 6.2.7, with values depending on the CO coverage, starting from $7CO^*$ molecules and decreasing successively with 0.17 eV, 0.30 eV, 0.29 eV, 0.68 eV, 0.23 eV, 0.41 eV, 0.61 eV for the Pd_{10} cluster and 0.50 eV, 0.94 eV, -0.25 eV, 0.55 eV, 0.16 eV, 1.44 eV, 0.90 eV for the Pt_{10} during the decrease of adsorbed CO molecules starting from $7CO^*$ molecules and ending with $1CO^*$ molecule. The $CO_2{}^*$ desorptions are thus in the same order of magnitude as those after CO oxidation via the MvK mechanism on single-atom catalysts based on the formal oxidation state of 0, as presented in Section 6.1.5. The desorption energies for the $CO_2{}^*$ molecule on Pd single-atom catalyst are 0.26 eV on

the (100) surface, 0.41 eV on the (110) surface, and 0.17 eV on the (111) surface. For Pt single-atom catalysts, the desorption energies are 0.69 eV on the (100) surface, 0.69 eV on the (110) surface, and 0.61 eV on the (111) surface. The desorption energies on the partially oxidized oxides PdO and PtO with (101) surfaces as shown in Section 6.3.4, however, are exothermic with -0.35 eV and -0.32 eV, respectively. The desorption barriers of $CO_2{}^*$ molecules after successful CO oxidation via the MvK mechanism on the (1-4)CO^* + Pd_3 and (1-4)CO^* + Pt_3 clusters as shown in Section 6.2.3 are slightly exothermic to neutral at a reaction temperature of 423.15 K on the Pd cluster, with -0.19 eV, -0.10 eV, -0.07 eV, and 0.01 eV as the CO coverage decreases from 4CO^* molecules to one CO molecule. For the Pt cluster, the desorption energy becomes endothermic at 2 and 3 CO coverages, with -0.10 eV, 0.29 eV, 0.60 eV, and -0.32 eV as the CO coverage decreases from 4CO^* molecules to one CO molecule. The $CO_2{}^*$ desorptions during CO oxidation via the MvK mechanism on (1-4)CO^* + Pd_3 and (1-4)CO^* + Pt_3 clusters are significantly more favorable for Pd, as they are even exothermic, and for Pt, they are not too high at a reaction temperature of 423.15 K. It is assumed that a higher reaction temperature of 723.15 K would further decrease the desorption energies. As can be well recognized here, considering the activities of the different size scales and oxidation states of the catalyst is quite a complex matter. Here too, it is necessary to conduct a kinetic study to untangle the high complexity and make it more structured.

8.2.3. Combined Scaling Relations resulting in a Volcano Plot

As generally known, the activity of a good catalyst can be attributed to the question of adsorption strengths, which ideally should be moderate. The current focus on exhaust after-treatment catalysts also centers on the scale of the noble metals. The scaling relations developed here can serve as a guide for identifying stable species and selecting those that are most active, thus identifying the most optimal catalysts. Therefore, it must be noted that a balance between adsorption strength and desorption capability leads to the optimal catalyst. However, catalytic activity hinges on reaction conditions, which can induce significant fluctuations within a combustion engine, resulting in dynamics among existing species. Factors influencing this activity include the adsorption strengths of reactants and the desorption strengths of products. Regarding reactant adsorption, the strength should be sufficient but not excessively strong to prevent poisoning by a monoatom or molecule, which could impede the adsorption of subsequent reactants. As for product desorption, it should be rapid and not overly strong to avoid hindering poisoning. Nevertheless, adsorption and desorption compete with each other concerning reaction conditions, surface structure, and the corresponding reaction mechanism. For instance, the MvK mechanism exhibits hindrance towards CO2 desorption. Extended noble metal surfaces, on the other hand, may

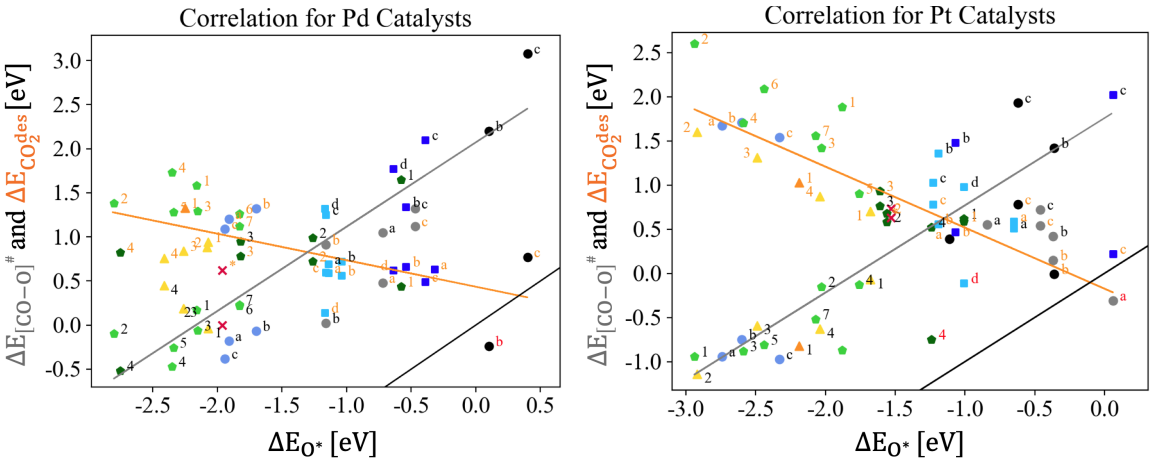

Figure 8.4.: The desorption energy $\Delta E_{CO_2{}^{des}}$ of the CO_2 molecule is plotted against the O^* binding relative to gas phase CO_2 (orange). Additionally, the activation energy barrier $\Delta E_{[CO\text{-}O]^{\ddagger}}$ of the CO_2 dissociation relative to gas phase CO_2 is plotted against the O^* binding ΔE_{O^*} relative to gas phase O (gray). The parity line (black) and the linear fit of all species shown are plotted. The numbering corresponds to those of the figures presented in Section 7.2. Species in red letters are not stable.

not face this issue but can result in low adsorption energies. Additionally, CO poisoning is a topic of discussion in the literature.[314,315] The volcano plot shown in Figure 8.4, which results from the overlay of two scaling relations, is only valid under the reaction conditions at 0 K and 0 bar. This is a reaction condition that is not realistic. A change in temperature as well as pressure would cause these scaling relations to shift relative to each other. However, we would like to visualize the overlay here once to provide a template for future considerations. Additionally, in theory, an initial examination of the most reactive species for both CO_2 dissociation and $CO_2{}^*$ desorption can be conducted. The numbering was already presented in Section 7.2.1 within the scaling relations, and corresponds to them. For better clarity, we have omitted it in Figure 8.4. The overlay of the scaling relations from Section 7.2.2 and Section 7.3 forms a volcano through the lower half of the cross. At the peak of this volcano, the species are located that induce the strongest CO and O adsorption possible, while simultaneously providing the weakest possible $CO_2{}^*$ desorption at the same location. Through these competing descriptors, the species that can satisfy both criteria can be identified here. The single-atom catalysts O^* + $Pd_1{}^{+II}/CeO_2(110)$ and $2O^*$ + $Pt_1{}^{+IV}/CeO_2(100)$ are located at the peak, as well as the subnanometer clusters $2O^*$ + Pd_{10} and (1-2)O^* + Pt_{10}, along with O^* + Pd and O^* + Pd low O loading specifically for the (100) and (110) surface facets. Interestingly, the subnanometer cluster $1CO^*$ + Pt_3 via the MvK mechanism is quite close to the cross. In contrast, the LH mechanism for $1O^*$ + Pt_3 is farther away. Similarly close to the cross is the PtO(101) crystal with the MvK mechanism. Thus, an oxidation state of +II for the single-atom catalysts, as expected, is among the most active species, as well as a subnanometer cluster of size 10 noble metal

atoms with low O surface loading, and extended noble metal surfaces with low O loading. The low O coverage on both the subnanometer clusters and the nanometer clusters (here approximated by extended noble metal surfaces) therefore makes sense, as a lower surface coverage by O atoms provides sufficient adsorption energy for the CO molecule. In general, it can be stated that both the LH and MvK mechanisms lie within a similar range. However, the LH mechanism with a low O loading is more active. It is important to emphasize once again that this only reflects a reaction temperature of 0 K and 0 bar. With an increase in temperature, the discussion should focus on other species. Another distinctive consideration, however, could focus on atmospheric pressure. A possible consideration would be that at a higher temperature, the scaling relation for CO_2 dissociation should increase to higher values, thus rising along the y-axis. This is because adsorption of the species becomes less favorable, resulting in barriers that increase relative to the gas phase. Conversely, the scaling relation for $CO_2{}^*$ desorption should decrease as desorption becomes increasingly favored. As a result, the scaling relation shifts relative to the scaling relation of $CO_2{}^*$ desorption in such a way that the subnanometer clusters (1-7)CO^* + Pd_{10} and (1-7)CO^* + Pt_{10} could lie at the cross. Consequently, the noble metal surfaces move away from the cross as temperatures increase. Conversely, an increase in pressure results in a realignment of the cross of both scaling relations towards the noble metal surfaces and the single-atom catalysts with an LH mechanism, moving away from the subnanometer clusters and single-atom catalysts that induce the MvK mechanism for CO oxidation. In this scenario, temperature and pressure would have opposite effects on the activities. As evident here, considerations regarding the reaction conditions that influence the overlay of scaling relations can indeed be beneficial. These scaling relations, which were established in this work, reflect the current state of research and can lead to new ideas, resulting in research findings that contribute to the optimization of catalysts.

Bibliography

[1] Fjodor M. Dostojewski. *Verbrechen und Strafe*. Trans. by Swetlana Geier. 7th ed. Frankfurt am Main: FISCHER Taschenbuch, 2008. ISBN: 9783596900107.

[2] Dietrich Stoltzenberg. "Fritz Haber, Carl Bosch und Friedrich Bergius—Protagonisten der Hochdrucksynthese". In: *Chemie in unserer Zeit* 33.6 (1999), pp. 359–364.

[3] F Haber and R Le Rossignol. "Über die technische Darstellung von Ammoniak aus den Elementen". In: *Zeitschrift für Elektrochemie und angewandte physikalische Chemie* 19.2 (1913), pp. 53–72.

[4] Timur Kandemir, Manfred Erwin Schuster, Anatoliy Senyshyn, Malte Behrens, and Robert Schlögl. "The Haber–Bosch Process Revisited: On the Real Structure and Stability of "Ammonia Iron" under Working Condition". In: *Angewandte Chemie International Edition* 52.48 (2013), pp. 12723–12726.

[5] Sara E Mikaloff Fletcher and Hinrich Schaefer. "Rising methane: A new climate challenge". In: *Science* 364.6444 (2019), pp. 932–933.

[6] David E Kissel et al. "The historical development and significance of the haber Bosch process". In: *Better Crops With Plant Food* 98.2 (2014), p. 31.

[7] Patrick Lott, Uwe Wagner, Thomas Koch, and Olaf Deutschmann. "Der Wasserstoffmotor–Chancen und Herausforderungen auf dem Weg zu einer dekarbonisierten Mobilitat". In: *Chem Ing Tech* 94 (2022), pp. 217–229.

[8] Kai F Kalz, Ralph Kraehnert, Muslim Dvoyashkin, Roland Dittmeyer, Roger Gläser, Ulrike Krewer, Karsten Reuter, and Jan-Dierk Grunwaldt. "Future challenges in heterogeneous catalysis: understanding catalysts under dynamic reaction conditions". In: *ChemCatChem* 9.1 (2017), pp. 17–29.

[9] Jens Kehlet Nørskov, Thomas Bligaard, Jan Rossmeisl, and Claus Hviid Christensen. "Towards the computational design of solid catalysts". In: *Nature chemistry* 1.1 (2009), pp. 37–46.

[10] Agustin Salcedo, Deniz Zengel, Florian Maurer, Maria Casapu, Jan-Dierk Grunwaldt, Carine Michel, and David Loffreda. "Identifying the Structure of Supported Metal Catalysts Using Vibrational Fingerprints from Ab Initio Nanoscale Models". In: *Small* (2023), p. 2300945.

[11] Matteo Maestri. “Escaping the trap of complication and complexity in multiscale microkinetic modelling of heterogeneous catalytic processes”. In: *Chemical Communications* 53.74 (2017), pp. 10244–10254.

[12] Bjarne Kreitz, Patrick Lott, Felix Studt, Andrew J Medford, Olaf Deutschmann, and C Franklin Goldsmith. “Automatisierte Generierung von Mikrokinetiken für heterogen katalysierte Reaktionen unter Berücksichtigung korrelierter Unsicherheiten”. In: *Angewandte Chemie* 135.39 (2023), e202306514.

[13] Karsten Reuter and Matthias Scheffler. “First-principles kinetic Monte Carlo simulations for heterogeneous catalysis: Application to the CO oxidation at Ru O 2 (110)”. In: *Physical Review B* 73.4 (2006), p. 045433.

[14] Karsten Reuter. “Ab initio thermodynamics and first-principles microkinetics for surface catalysis”. In: *Catalysis Letters* 146 (2016), pp. 541–563.

[15] Catherine Stampfl, HJ Kreuzer, SH Payne, and Matthias Scheffler. “Challenges in predictive calculations of processes at surfaces:. surface thermodynamics and catalytic reactions”. In: *Applied Physics A* 69 (1999), pp. 471–480.

[16] Robert J Farrauto. “Low-temperature oxidation of methane”. In: *Science* 337.6095 (2012), pp. 659–660.

[17] Yan-Yang Qin and Ya-Qiong Su. “A DFT study on heterogeneous Pt/CeO2 (110) single atom catalysts for CO oxidation”. In: *ChemCatChem* 13.17 (2021), pp. 3857–3863.

[18] Kathleen C Taylor. “Automobile catalytic converters”. In: *Catalysis*. Springer, 1984, pp. 119–170.

[19] Jan-Dierk Grunwaldt, Marek Maciejewski, Olav Sven Becker, Patrizia Fabrizioli, and Alfons Baiker. “Comparative study of Au/TiO2 and Au/ZrO2 catalysts for low-temperature CO oxidation”. In: *Journal of Catalysis* 186.2 (1999), pp. 458–469.

[20] Ib Chorkendorff and Johannes W Niemantsverdriet. *Concepts of modern catalysis and kinetics*. John Wiley & Sons, 2017.

[21] T Engel and G Ertl. “Elementary steps in the catalytic oxidation of carbon monoxide on platinum metals”. In: *Advances in catalysis*. Vol. 28. Elsevier, 1979, pp. 1–78.

[22] T Engel and G Ertl. “A molecular beam investigation of the catalytic oxidation of CO on Pd (111)”. In: *The Journal of Chemical Physics* 69.3 (1978), pp. 1267–1281.

[23] T Engel and G Ertl. “Surface residence times and reaction mechanism in the catalytic oxidation of CO on Pd (111)”. In: *Chemical Physics Letters* 54.1 (1978), pp. 95–98.

[24] Florian Maurer, Arik Beck, Jelena Jelic, Wu Wang, Stefan Mangold, Matthias Stehle, Di Wang, Paolo Dolcet, Andreas M Gänzler, Christian Kübel, et al. “Surface noble metal concentration on ceria as a key descriptor for efficient catalytic CO oxidation”. In: *ACS Catalysis* 12.4 (2022), pp. 2473–2486.

[25] Andreas M Gänzler, Maria Casapu, Dmitry E Doronkin, Florian Maurer, Patrick Lott, Pieter Glatzel, Martin Votsmeier, Olaf Deutschmann, and Jan-Dierk Grunwaldt. “Unravelling the different reaction pathways for low temperature CO oxidation on Pt/CeO2 and Pt/Al2O3 by spatially resolved structure–activity correlations”. In: *The Journal of Physical Chemistry Letters* 10.24 (2019), pp. 7698–7705.

[26] Ya-Qiong Su, Jin-Xun Liu, Ivo AW Filot, and Emiel JM Hensen. “Theoretical study of ripening mechanisms of Pd clusters on ceria”. In: *Chemistry of Materials* 29.21 (2017), pp. 9456–9462.

[27] Jin-Cheng Liu, Yang-Gang Wang, and Jun Li. “Toward rational design of oxide-supported single-atom catalysts: atomic dispersion of gold on ceria”. In: *Journal of the American Chemical Society* 139.17 (2017), pp. 6190–6199.

[28] Giulia Spezzati, Yaqiong Su, Jan P Hofmann, Angelica D Benavidez, Andrew T DeLaRiva, Jay McCabe, Abhaya K Datye, and Emiel JM Hensen. “Atomically dispersed Pd–O species on CeO2 (111) as highly active sites for low-temperature CO oxidation”. In: *Acs Catalysis* 7.10 (2017), pp. 6887–6891.

[29] Henrik Eliasson, Yubiao Niu, Richard E Palmer, Henrik Grönbeck, and Rolf Erni. “Support-facet-dependent morphology of small Pt particles on ceria”. In: *Nanoscale* (2023).

[30] Andrei I Boronin, Elena M Slavinskaya, Alberto Figueroba, Andrey I Stadnichenko, Tatyana Yu Kardash, Olga A Stonkus, Elizaveta A Fedorova, Valerii V Muravev, Valery A Svetlichnyi, Albert Bruix, et al. “CO oxidation activity of Pt/CeO2 catalysts below 0° C: platinum loading effects”. In: *Applied Catalysis B: Environmental* 286 (2021), p. 119931.

[31] H Conrad, G Ertl, J Koch, and EE Latta. “Adsorption of CO on Pd single crystal surfaces”. In: *Surface Science* 43.2 (1974), pp. 462–480.

[32] Gerhard Ertl. “Thermodynamics of gas-surface interactions”. In: *Pure and Applied Chemistry* 61.6 (1989), pp. 1001–1007.

[33] Petri Salo, Karoliina Honkala, Matti Alatalo, and Kari Laasonen. “Catalytic oxidation of CO on Pd (1 1 1)”. In: *Surface science* 516.3 (2002), pp. 247–253.

[34] DI Kochubey, SN Pavlova, BN Novgorodov, GN Kryukova, and VA Sadykov. “The influence of support on the low-temperature activity of Pd in the reaction of CO oxidation: 1. The structure of supported Pd”. In: *Journal of catalysis* 161.2 (1996), pp. 500–506.

[35] William E Kaden, William A Kunkel, Matt D Kane, F Sloan Roberts, and Scott L Anderson. “Size-dependent oxygen activation efficiency over Pd n/TiO2 (110) for the CO oxidation reaction”. In: *Journal of the American Chemical Society* 132.38 (2010), pp. 13097–13099.

[36] Matteo Cargnello, Vicky VT Doan-Nguyen, Thomas R Gordon, Rosa E Diaz, Eric A Stach, Raymond J Gorte, Paolo Fornasiero, and Christopher B Murray. “Control of metal nanocrystal size reveals metal-support interface role for ceria catalysts”. In: *Science* 341.6147 (2013), pp. 771–773.

[37] Bidyut Bikash Sarma, Florian Maurer, Dmitry E Doronkin, and Jan-Dierk Grunwaldt. “Design of Single-Atom Catalysts and Tracking Their Fate Using Operando and Advanced X-ray Spectroscopic Tools”. In: *Chemical Reviews* (2022).

[38] John Jones, Haifeng Xiong, Andrew T DeLaRiva, Eric J Peterson, Hien Pham, Sivakumar R Challa, Gongshin Qi, Se Oh, Michelle H Wiebenga, Xavier Isidro Pereira Hernández, et al. “Thermally stable single-atom platinum-on-ceria catalysts via atom trapping”. In: *Science* 353.6295 (2016), pp. 150–154.

[39] Jason A Farmer and Charles T Campbell. “Ceria maintains smaller metal catalyst particles by strong metal-support bonding”. In: *Science* 329.5994 (2010), pp. 933–936.

[40] Xavier Isidro Pereira-Hernández, Andrew DeLaRiva, Valery Muravev, Deepak Kunwar, Haifeng Xiong, Berlin Sudduth, Mark Engelhard, Libor Kovarik, Emiel JM Hensen, Yong Wang, et al. “Tuning Pt-CeO2 interactions by high-temperature vapor-phase synthesis for improved reducibility of lattice oxygen”. In: *Nature communications* 10.1 (2019), pp. 1–10.

[41] Andreas M Gänzler, Maria Casapu, Philippe Vernoux, Stéphane Loridant, Francisco J Cadete Santos Aires, Thierry Epicier, Benjamin Betz, Rüdiger Hoyer, and Jan-Dierk Grunwaldt. “Tuning the structure of platinum particles on ceria in situ for enhancing the catalytic performance of exhaust gas catalysts”. In: *Angewandte Chemie International Edition* 56.42 (2017), pp. 13078–13082.

[42] Andreas M Gänzler, Maria Casapu, Florian Maurer, Heike Störmer, Dagmar Gerthsen, Geraldine Ferre, Philippe Vernoux, Benjamin Bornmann, Ronald Frahm, Vadim Murzin, et al. “Tuning the Pt/CeO2 interface by in situ variation of the Pt particle size”. In: *ACS catalysis* 8.6 (2018), pp. 4800–4811.

[43] Hui Wang, Jin-Xun Liu, Lawrence F Allard, Sungsik Lee, Jilei Liu, Hang Li, Jianqiang Wang, Jun Wang, Se H Oh, Wei Li, et al. “Surpassing the single-atom catalytic activity limit through paired Pt-O-Pt ensemble built from isolated Pt1 atoms”. In: *Nature communications* 10.1 (2019), pp. 1–12.

[44] Venkatesh Botu, Rampi Ramprasad, and Ashish B Mhadeshwar. “Ceria in an oxygen environment: Surface phase equilibria and its descriptors”. In: *Surface science* 619 (2014), pp. 49–58.

[45] Xiansheng Li, Xing Wang, Ilia I Sadykov, Dennis Palagin, Olga V Safonova, Junhua Li, Arik Beck, Frank Krumeich, Jeroen A Van Bokhoven, and Luca Artiglia. “Temperature and Reaction Environment Influence the Nature of Platinum Species Supported on Ceria”. In: *ACS Catalysis* 11.21 (2021), pp. 13041–13049.

[46] Ya-Qiong Su, Long Zhang, Valery Muravev, and Emiel JM Hensen. “Lattice oxygen activation in transition metal doped ceria”. In: *Chinese Journal of Catalysis* 41.6 (2020), pp. 977–984.

[47] IS Shaplygin, GL Aparnikov, and VB Lazarev. “Preparation of palladium dioxide at high-pressure”. In: *Zhurnal Neorganicheskoi Khimii* 23.4 (1978), pp. 884–887.

[48] Walter J Moore Jr and Linus Pauling. “The crystal structures of the tetragonal monoxides of lead, tin, palladium, and platinum”. In: *Journal of the American Chemical Society* 63.5 (1941), pp. 1392–1394.

[49] Anubhav Jain, Shyue Ping Ong, Geoffroy Hautier, Wei Chen, William Davidson Richards, Stephen Dacek, Shreyas Cholia, Dan Gunter, David Skinner, Gerbrand Ceder, et al. “Commentary: The Materials Project: A materials genome approach to accelerating materials innovation”. In: *APL materials* 1.1 (2013).

[50] K-J Range, F Rau, U Klement, and AM Heyns. “β-PtO2: high pressure synthesis of single crystals and structure refinement”. In: *Materials research bulletin* 22.11 (1987), pp. 1541–1547.

[51] Atsushi Satsuma, Kaoru Osaki, Masatoshi Yanagihara, Junya Ohyama, and Kenichi Shimizu. “Activity controlling factors for low-temperature oxidation of CO over supported Pd catalysts”. In: *Applied Catalysis B: Environmental* 132 (2013), pp. 511–518.

[52] Abdul Hadi and Iskandar I Yaacob. “Synthesis of PdO/CeO2 mixed oxides catalyst for automotive exhaust emissions control”. In: *Catalysis Today* 96.3 (2004), pp. 165–170.

[53] Lian Meng, Ai-Ping Jia, Ji-Qing Lu, Liang-Feng Luo, Wei-Xin Huang, and Meng-Fei Luo. “Synergetic effects of PdO species on CO oxidation over PdO–CeO2 catalysts”. In: *The Journal of Physical Chemistry C* 115.40 (2011), pp. 19789–19796.

[54] Seung-Hoon Oh and Gar B Hoflund. “Chemical state study of palladium powder and ceria-supported palladium during low-temperature CO oxidation”. In: *The Journal of Physical Chemistry A* 110.24 (2006), pp. 7609–7613.

[55] Meng-Fei Luo, Zhi-Ying Pu, Mai He, Juan Jin, and Ling-Yun Jin. “Characterization of PdO/Ce0. 8Y0. 2O1. 9 catalysts for carbon monoxide and methane oxidation”. In: *Journal of Molecular Catalysis A: Chemical* 260.1-2 (2006), pp. 152–156.

[56] Adriana Trinchero, Anders Hellman, and Henrik Grönbeck. “Methane oxidation over Pd and Pt studied by DFT and kinetic modeling”. In: *Surface science* 616 (2013), pp. 206–213.

[57] Jens K Nørskov, Thomas Bligaard, Britt Hvolbæk, Frank Abild-Pedersen, Ib Chorkendorff, and Claus H Christensen. “The nature of the active site in heterogeneous metal catalysis”. In: *Chemical Society Reviews* 37.10 (2008), pp. 2163–2171.

[58] Jutta Rogal, Karsten Reuter, and Matthias Scheffler. “CO oxidation at Pd (100): A first-principles constrained thermodynamics study”. In: *Physical Review B* 75.20 (2007), p. 205433.

[59] Jutta Rogal, Karsten Reuter, and Matthias Scheffler. “First-principles statistical mechanics study of the stability of a subnanometer thin surface oxide in reactive environments: CO oxidation at Pd (100)”. In: *Physical review letters* 98.4 (2007), p. 046101.

[60] Zhiyao Duan and Graeme Henkelman. “CO oxidation on the Pd (111) surface”. In: *Acs Catalysis* 4.10 (2014), pp. 3435–3443.

[61] CJ Zhang and Peijun Hu. “CO oxidation on Pd (100) and Pd (111): A comparative study of reaction pathways and reactivity at low and medium coverages”. In: *Journal of the American Chemical Society* 123.6 (2001), pp. 1166–1172.

[62] Matthijs A Van Spronsen, Joost WM Frenken, and Irene MN Groot. “Surface science under reaction conditions: CO oxidation on Pt and Pd model catalysts”. In: *Chemical Society Reviews* 46.14 (2017), pp. 4347–4374.

[63] Ikuyo Nakai, Hiroshi Kondoh, Toru Shimada, Andrea Resta, Jesper N Andersen, and Toshiaki Ohta. “Mechanism of CO oxidation reaction on O-covered Pd (111) surfaces studied with fast x-ray photoelectron spectroscopy: Change of reaction path accompanying phase transition of O domains”. In: *The Journal of chemical physics* 124.22 (2006).

[64] Sang Hoon Kim, Javier Méndez, Joost Wintterlin, and Gerhard Ertl. “Enhanced reactivity of adsorbed oxygen on Pd (111) induced by compression of the oxygen layer”. In: *Physical Review B* 72.15 (2005), p. 155414.

[65] Javier Méndez, Sang Hoon Kim, Jorge Cerdá, Joost Wintterlin, and Gerhard Ertl. “Coadsorption phases of C O and oxygen on Pd (111) studied by scanning tunneling microscopy”. In: *Physical Review B* 71.8 (2005), p. 085409.

[66] BLM Hendriksen, SC Bobaru, and JWM Frenken. “Oscillatory CO oxidation on Pd (1 0 0) studied with in situ scanning tunneling microscopy”. In: *Surface Science* 552.1-3 (2004), pp. 229–242.

[67] Ninghua Fu, Xiao Liang, Xiaolu Wang, Tao Gan, Chenliang Ye, Zhi Li, Jin-Cheng Liu, and Yadong Li. “Controllable Conversion of Platinum Nanoparticles to Single Atoms in Pt/CeO2 by Laser Ablation for Efficient CO Oxidation”. In: *Journal of the American Chemical Society* 145.17 (2023), pp. 9540–9547.

[68] Albert Bruix, Yaroslava Lykhach, Iva Matolínová, Armin Neitzel, Tomáš Skála, Nataliya Tsud, Mykhailo Vorokhta, Vitalii Stetsovych, Klára Ševčíková, Josef Mysliveček, et al. “Auf dem Weg zu größtmöglicher Effizienz bei der katalytischen Nutzung von Edelmetallen: atomar dispergiertes Oberflächen-Platin”. In: *Angewandte Chemie* 126.39 (2014), pp. 10693–10698.

[69] Florian Maurer, Jelena Jelic, Junjun Wang, Andreas Gänzler, Paolo Dolcet, Christof Wöll, Yuemin Wang, Felix Studt, Maria Casapu, and Jan-Dierk Grunwaldt. “Tracking the formation, fate and consequence for catalytic activity of Pt single sites on CeO2”. In: *Nature Catalysis* 3.10 (2020), pp. 824–833.

[70] Yaroslava Lykhach, Albert Bruix, Stefano Fabris, Valérie Potin, Iva Matolínová, Vladimír Matolín, Jörg Libuda, and Konstantin M Neyman. “Oxide-based nanomaterials for fuel cell catalysis: the interplay between supported single Pt atoms and particles”. In: *Catalysis Science & Technology* 7.19 (2017), pp. 4315–4345.

[71] Joachim Paier, Christopher Penschke, and Joachim Sauer. “Oxygen defects and surface chemistry of ceria: quantum chemical studies compared to experiment”. In: *Chemical reviews* 113.6 (2013), pp. 3949–3985.

[72] Marta Boaro, Carla De Leitenburg, Giuliano Dolcetti, and Alessandro Trovarelli. "The dynamics of oxygen storage in ceria–zirconia model catalysts measured by CO oxidation under stationary and cycling feedstream compositions". In: *Journal of Catalysis* 193.2 (2000), pp. 338–347.

[73] Michael Nolan. "Charge compensation and Ce3+ formation in trivalent doping of the CeO2 (110) surface: the key role of dopant ionic radius". In: *The Journal of Physical Chemistry C* 115.14 (2011), pp. 6671–6681.

[74] Michael Nolan, Stephen C Parker, and Graeme W Watson. "The electronic structure of oxygen vacancy defects at the low index surfaces of ceria". In: *Surface Science* 595.1-3 (2005), pp. 223–232.

[75] Alessandro Trovarelli and Jordi Llorca. "Ceria catalysts at nanoscale: how do crystal shapes shape catalysis?" In: *ACS catalysis* 7.7 (2017), pp. 4716–4735.

[76] Alessandro Trovarelli. *Catalysis by ceria and related materials*. Vol. 2. World Scientific, 2002.

[77] Charles T Campbell and Charles HF Peden. "Oxygen vacancies and catalysis on ceria surfaces". In: *Science* 309.5735 (2005), pp. 713–714.

[78] TXT Sayle, SC Parker, and CRA Catlow. "The role of oxygen vacancies on ceria surfaces in the oxidation of carbon monoxide". In: *Surface Science* 316.3 (1994), pp. 329–336.

[79] Stefano Fabris, Gianpaolo Vicario, Gabriele Balducci, Stefano de Gironcoli, and Stefano Baroni. "Electronic and atomistic structures of clean and reduced ceria surfaces". In: *The Journal of Physical Chemistry B* 109.48 (2005), pp. 22860–22867.

[80] M Veronica Ganduglia-Pirovano, Juarez LF Da Silva, and Joachim Sauer. "Density-functional calculations of the structure of near-surface oxygen vacancies and electron localization on CeO 2 (111)". In: *Physical review letters* 102.2 (2009), p. 026101.

[81] M Veronica Ganduglia-Pirovano, Alexander Hofmann, and Joachim Sauer. "Oxygen vacancies in transition metal and rare earth oxides: Current state of understanding and remaining challenges". In: *Surface science reports* 62.6 (2007), pp. 219–270.

[82] Juarez LF Da Silva, M Veronica Ganduglia-Pirovano, Joachim Sauer, Veronika Bayer, and Georg Kresse. "Hybrid functionals applied to rare-earth oxides: The example of ceria". In: *Physical Review B* 75.4 (2007), p. 045121.

[83] Mailde S Ozorio, Karla F Andriani, and Juarez LF Da Silva. "A hybrid-DFT investigation of the Ce oxidation state upon adsorption of F, Na, Ni, Pd and Pt on the (CeO 2) 6 cluster". In: *Physical Chemistry Chemical Physics* 22.25 (2020), pp. 14099–14108.

[84] David R Mullins. “The surface chemistry of cerium oxide”. In: *Surface Science Reports* 70.1 (2015), pp. 42–85.

[85] Noemi Bosio, Andreas Schaefer, and Henrik Grönbeck. “Can oxygen vacancies in ceria surfaces be measured by O1s photoemission spectroscopy?” In: *Journal of Physics: Condensed Matter* 34.17 (2022), p. 174004.

[86] Zili Wu, Amanda KP Mann, Meijun Li, and Steven H Overbury. “Spectroscopic investigation of surface-dependent acid–base property of ceria nanoshapes”. In: *The Journal of Physical Chemistry C* 119.13 (2015), pp. 7340–7350.

[87] Stuart Turner, Sorin Lazar, Bert Freitag, Ricardo Egoavil, Johan Verbeeck, Stijn Put, Yvan Strauven, and Gustaaf Van Tendeloo. “High resolution mapping of surface reduction in ceria nanoparticles”. In: *Nanoscale* 3.8 (2011), pp. 3385–3390.

[88] Jan-Frederik Jerratsch, Xiang Shao, Niklas Nilius, Hans-Joachim Freund, Cristina Popa, M Veronica Ganduglia-Pirovano, Asbjörn M Burow, and Joachim Sauer. “Electron localization in defective ceria films: A study with scanning-tunneling microscopy and density-functional theory”. In: *Physical review letters* 106.24 (2011), p. 246801.

[89] M Veronica Ganduglia-Pirovano. “The non-innocent role of cerium oxide in heterogeneous catalysis: a theoretical perspective”. In: *Catalysis Today* 253 (2015), pp. 20–32.

[90] Fabio R Negreiros and Stefano Fabris. “Role of cluster morphology in the dynamics and reactivity of subnanometer Pt clusters supported on ceria surfaces”. In: *The Journal of Physical Chemistry C* 118.36 (2014), pp. 21014–21020.

[91] Adam D Mayernick and Michael J Janik. “Methane oxidation on Pd–Ceria: A DFT study of the mechanism over PdxCe1- xO2, Pd, and PdO”. In: *Journal of Catalysis* 278.1 (2011), pp. 16–25.

[92] Zongxian Yang, Gaixia Luo, Zhansheng Lu, Tom K Woo, and Kersti Hermansson. “Structural and electronic properties of NM-doped ceria (NM= Pt, Rh): a first-principles study”. In: *Journal of Physics: Condensed Matter* 20.3 (2007), p. 035210.

[93] Christian Spiel, Peter Blaha, Yuri Suchorski, Karlheinz Schwarz, and Günther Rupprechter. “CeO 2/Pt (111) interface studied using first-principles density functional theory calculations”. In: *Physical Review B* 84.4 (2011), p. 045412.

[94] Olaf Brummel, Fabian Waidhas, Firas Faisal, Roman Fiala, Mykhailo Vorokhta, Ivan Khalakhan, Martin Dubau, Alberto Figueroba, Gabor Kovacs, Hristiyan A Aleksandrov, et al. "Stabilization of small platinum nanoparticles on Pt–CeO2 thin film electrocatalysts during methanol oxidation". In: *The Journal of Physical Chemistry C* 120.35 (2016), pp. 19723–19736.

[95] Xiaohui Gao, Guangtao Yu, Lirong Zheng, Chunmei Zhang, Hui Li, Ting Wang, Pengda An, Min Liu, Xiaoqing Qiu, Wei Chen, et al. "Strong electron coupling from the sub-nanometer Pd clusters confined in porous ceria nanorods for highly efficient electrochemical hydrogen evolution reaction". In: *ACS Applied Energy Materials* 2.2 (2019), pp. 966–973.

[96] Thomas P Senftle, Adri CT Van Duin, and Michael J Janik. "Methane activation at the Pd/CeO2 interface". In: *Acs Catalysis* 7.1 (2017), pp. 327–332.

[97] G Ferré, M Aouine, F Bosselet, L Burel, FJ Cadete Santos Aires, C Geantet, S Ntais, F Maurer, M Casapu, J-D Grunwaldt, et al. "Exploiting the dynamic properties of Pt on ceria for low-temperature CO oxidation". In: *Catalysis Science & Technology* 10.12 (2020), pp. 3904–3917.

[98] Junjun Wang, Eric Sauter, Alexei Nefedov, Stefan Heißler, Florian Maurer, Maria Casapu, Jan-Dierk Grunwaldt, Yuemin Wang, and Christof Wöll. "Dynamic structural evolution of ceria-supported Pt particles: a thorough spectroscopic study". In: *The Journal of Physical Chemistry C* 126.21 (2022), pp. 9051–9058.

[99] Andreas M Gänzler, Maria Casapu, Florian Maurer, Heike Störmer, Dagmar Gerthsen, Geraldine Ferre, Philippe Vernoux, Benjamin Bornmann, Ronald Frahm, Vadim Murzin, et al. "Tuning the Pt/CeO2 interface by in situ variation of the Pt particle size". In: *Acs Catalysis* 8.6 (2018), pp. 4800–4811.

[100] Sheedeh Fouladvand, Stefan Schernich, Jörg Libuda, Henrik Grönbeck, Torben Pingel, Eva Olsson, Magnus Skoglundh, and Per-Anders Carlsson. "Methane oxidation over Pd supported on ceria–alumina under rich/lean cycling conditions". In: *Topics in Catalysis* 56 (2013), pp. 410–415.

[101] R Burch, PK Loader, and FJ Urbano. "Some aspects of hydrocarbon activation on platinum group metal combustion catalysts". In: *Catalysis today* 27.1-2 (1996), pp. 243–248.

[102] A Morlang, U Neuhausen, KV Klementiev, F-W Schütze, G Miehe, H Fuess, and ES Lox. "Bimetallic Pt/Pd diesel oxidation catalysts: Structural characterisation and catalytic behaviour". In: *Applied Catalysis B: Environmental* 60.3-4 (2005), pp. 191–199.

[103] Brou Albert Kouadio, Fuming Mei, Tao Li, and Lei Pang. “High performance Pd–Rh/YBaCo4O7/γ-Al2O3 three-way catalysts for gasoil engine”. In: *Journal of Taibah University for Science* 11.6 (2017), pp. 1306–1316.

[104] Alessandro Trovarelli, Carla De Leitenburg, Marta Boaro, and Giuliano Dolcetti. “The utilization of ceria in industrial catalysis”. In: *Catalysis today* 50.2 (1999), pp. 353–367.

[105] Serafin Bernal, Jan KASPAR, and Alessandro Trovarelli. “Recent progress in catalysis by ceria and related compounds”. In: *Catalysis today* 50.2 (1999).

[106] Alessandro Trovarelli. “Catalytic properties of ceria and CeO2-containing materials”. In: *Catalysis Reviews* 38.4 (1996), pp. 439–520.

[107] DC Sayle, TXT Sayle, SC Parker, CRA Catlow, and JH Harding. “Effect of defects on the stability of heteroepitaxial ceramic interfaces studied by computer simulation”. In: *Physical Review B* 50.19 (1994), p. 14498.

[108] DC Sayle, TXT Sayle, SC Parker, JH Harding, and CRA Catlow. “The stability of defects in the ceramic interfaces, MgOMgO and CeO2Al2O3”. In: *Surface science* 334.1-3 (1995), pp. 170–178.

[109] Michael Nolan, Sonja Grigoleit, Dean C Sayle, Stephen C Parker, and Graeme W Watson. “Density functional theory studies of the structure and electronic structure of pure and defective low index surfaces of ceria”. In: *Surface Science* 576.1-3 (2005), pp. 217–229.

[110] Dean C Sayle, C Richard A Catlow, John H Harding, Matthew JF Healy, S Andrada Maicaneanu, Stephen C Parker, Ben Slater, and Graeme W Watson. “Atomistic simulation methodologies for modelling the nucleation, growth and structure of interfaces”. In: *Journal of Materials Chemistry* 10.6 (2000), pp. 1315–1324.

[111] Thi XT Sayle, Stephen C Parker, and C Richard A Catlow. “Surface segregation of metal ions in cerium dioxide”. In: *The Journal of Physical Chemistry* 98.51 (1994), pp. 13625–13630.

[112] Alessandro Trovarelli. “Structural and oxygen storage/release properties of CeO2-based solid solutions”. In: *Comments on Inorganic Chemistry* 20.4-6 (1999), pp. 263–284.

[113] G Ranga Rao, Paolo Fornasiero, ROBERTA Di Monte, J Kašpar, Gilberto Vlaic, GABRIELE Balducci, S Meriani, G Gubitosa, A Cremona, and Mauro Graziani. “Reduction of NO over Partially Reduced Metal-Loaded CeO2–ZrO2Solid Solutions”. In: *Journal of Catalysis* 162.1 (1996), pp. 1–9.

[114] Arturo Martínez-Arias, Javier Soria, José C Conesa, Xosé L Seoane, Adolfo Arcoya, and Renato Cataluña. "NO reaction at surface oxygen vacancies generated in cerium oxide". In: *Journal of the Chemical Society, Faraday Transactions* 91.11 (1995), pp. 1679–1687.

[115] F Bozon-Verduraz and A Bensalem. "IR studies of cerium dioxide: influence of impurities and defects". In: *Journal of the Chemical Society, Faraday Transactions* 90.4 (1994), pp. 653–657.

[116] EA Kümmerle and G Heger. "The structures of C–Ce2O3+ δ, Ce7O12, and Ce11O20". In: *Journal of Solid State Chemistry* 147.2 (1999), pp. 485–500.

[117] Alessandro Trovarelli, Marta Boaro, Eliana Rocchini, Carla de Leitenburg, and Giuliano Dolcetti. "Some recent developments in the characterization of ceria-based catalysts". In: *Journal of Alloys and Compounds* 323 (2001), pp. 584–591.

[118] Friedrich Esch, Stefano Fabris, Ling Zhou, Tiziano Montini, Cristina Africh, Paolo Fornasiero, Giovanni Comelli, and Renzo Rosei. "Electron localization determines defect formation on ceria substrates". In: *Science* 309.5735 (2005), pp. 752–755.

[119] Vitalii Stetsovych, Federico Pagliuca, Filip Dvořák, Tomáš Duchoň, Mykhailo Vorokhta, Marie Aulická, Jan Lachnitt, Stefan Schernich, Iva Matolínová, Kateřina Veltruská, et al. "Epitaxial cubic Ce2O3 films via Ce–CeO2 interfacial reaction". In: *The journal of physical chemistry letters* 4.6 (2013), pp. 866–871.

[120] René Kopelent, Jeroen A van Bokhoven, Jakub Szlachetko, Jacinta Edebeli, Cristina Paun, Maarten Nachtegaal, and Olga V Safonova. "Catalytically active and spectator Ce3+ in ceria-supported metal catalysts". In: *Angewandte Chemie* 127.30 (2015), pp. 8852–8855.

[121] José J Plata, Antonio M Márquez, and Javier Fdez Sanz. "Electron mobility via polaron hopping in bulk ceria: a first-principles study". In: *The Journal of Physical Chemistry C* 117.28 (2013), pp. 14502–14509.

[122] Elizaveta A Derevyannikova, Tatyana Yu Kardash, Andrey I Stadnichenko, Olga A Stonkus, Elena M Slavinskaya, Valery A Svetlichnyi, and Andrei I Boronin. "Structural insight into strong Pt–CeO2 interaction: from single Pt atoms to PtO x clusters". In: *The Journal of Physical Chemistry C* 123.2 (2018), pp. 1320–1334.

[123] Stefano Fabris, Stefano de Gironcoli, Stefano Baroni, Gianpaolo Vicario, and Gabriele Balducci. "Reply to "Comment on 'Taming multiple valency with density functionals: A case study of defective ceria'"". In: *Physical Review B* 72.23 (2005), p. 237102.

[124] Lijun Wu, HJ Wiesmann, AR Moodenbaugh, RF Klie, Yimei Zhu, DO Welch, and M Suenaga. “Oxidation state and lattice expansion of CeO 2- x nanoparticles as a function of particle size”. In: *Physical Review B* 69.12 (2004), p. 125415.

[125] DG Lamas, RO Fuentes, IO Fábregas, ME Fernández de Rapp, GE Lascalea, JR Casanova, NE Walsöe de Reca, and Aldo Felix Craievich. “Synchrotron X-ray diffraction study of the tetragonal–cubic phase boundary of nanocrystalline ZrO2–CeO2 synthesized by a gel-combustion process”. In: *Journal of applied crystallography* 38.6 (2005), pp. 867–873.

[126] Masatomo Yashima, Kenji Morimoto, Nobuo Ishizawa, and Masahiro Yoshimura. “Diffusionless tetragonal–cubic transformation temperature in zirconia–ceria solid solutions”. In: *Journal of the American Ceramic Society* 76.11 (1993), pp. 2865–2868.

[127] Masatomo Yashima, Kenji Morimoto, Nobuo Ishizawa, and Masahiro Yoshimura. “Zirconia–ceria solid solution synthesis and the temperature–time–transformation diagram for the 1: 1 composition”. In: *Journal of the American Ceramic Society* 76.7 (1993), pp. 1745–1750.

[128] Asha Gupta, Anil Kumar, MS Hegde, and UV Waghmare. “Structure of Ce1-xSnxO2 and its relation to oxygen storage property from first-principles analysis”. In: *The Journal of chemical physics* 132.19 (2010).

[129] Changjun Zhang, Angelos Michaelides, David A King, and Stephen J Jenkins. “Anchoring sites for initial Au nucleation on CeO2 {111}: O vacancy versus Ce vacancy”. In: *The Journal of Physical Chemistry C* 113.16 (2009), pp. 6411–6417.

[130] J Zhang, ZC Kang, and L Eyring. “The binary higher oxides of the rare earths”. In: *Journal of alloys and compounds* 192.1-2 (1993), pp. 57–63.

[131] JM Leger, N Yacoubi, and J Loriers. “Synthese des monoxydes de cerium et de praesodyme”. In: *Materials Research Bulletin* 14.11 (1979), pp. 1431–1436.

[132] Maria M Branda, Christoph Loschen, Konstantin M Neyman, and Francesc Illas. “Atomic and electronic structure of cerium oxide stepped model surfaces”. In: *The Journal of Physical Chemistry C* 112.45 (2008), pp. 17643–17651.

[133] Georg Kresse, Peter Blaha, Juarez LF Da Silva, and M Veronica Ganduglia-Pirovano. “Comment on “Taming multiple valency with density functionals: A case study of defective ceria””. In: *Physical Review B* 72.23 (2005), p. 237101.

[134] John Hubbard. “Electron correlations in narrow energy bands”. In: *Proceedings of the Royal Society of London. Series A. Mathematical and Physical Sciences* 276.1365 (1963), pp. 238–257.

[135] John Hubbard. “The description of collective motions in terms of many-body perturbation theory. II. The correlation energy of a free-electron gas”. In: *Proceedings of the Royal Society of London. Series A. Mathematical and Physical Sciences* 243.1234 (1958), pp. 336–352.

[136] A Brooks Harris and Robert V Lange. “Single-particle excitations in narrow energy bands”. In: *Physical Review* 157.2 (1967), p. 295.

[137] Henk Eskes, Andrzej M Oleś, Marcel BJ Meinders, and Walter Stephan. “Spectral properties of the Hubbard bands”. In: *Physical Review B* 50.24 (1994), p. 17980.

[138] Ya-Qiong Su, Ivo AW Filot, Jin-Xun Liu, Ionut Tranca, and Emiel JM Hensen. “Charge transport over the defective CeO2 (111) surface”. In: *Chemistry of Materials* 28.16 (2016), pp. 5652–5658.

[139] Yang-Gang Wang, Donghai Mei, Jun Li, and Roger Rousseau. “DFT+ U study on the localized electronic states and their potential role during H2O dissociation and CO oxidation processes on CeO2 (111) surface”. In: *The Journal of Physical Chemistry C* 117.44 (2013), pp. 23082–23089.

[140] Uli Castanet, Cédric Feral-Martin, Alain Demourgues, Rachel L Neale, Dean C Sayle, Francesco Caddeo, Joseph M Flitcroft, Robert Caygill, Ben J Pointon, Marco Molinari, et al. “Controlling the $\{111\}/\{110\}$ surface ratio of cuboidal ceria nanoparticles”. In: *ACS applied materials & interfaces* 11.12 (2019), pp. 11384–11390.

[141] Bochuan Song, Shuxin Si, Asiye Soleymani, Yan Xin, and Helena E Hagelin-Weaver. “Effect of ceria surface facet on stability and reactivity of isolated platinum atoms”. In: *Nano Research* 15.7 (2022), pp. 5922–5932.

[142] Giulia Spezzati, Angelica D Benavidez, Andrew T DeLaRiva, Yaqiong Su, Jan P Hofmann, Shunsuke Asahina, Ezra J Olivier, Johannes H Neethling, Jeffrey T Miller, Abhaya K Datye, et al. “CO oxidation by Pd supported on CeO2 (100) and CeO2 (111) facets”. In: *Applied Catalysis B: Environmental* 243 (2019), pp. 36–46.

[143] Armin Neitzel, Alberto Figueroba, Yaroslava Lykhach, Tomas Skala, Mykhailo Vorokhta, Nataliya Tsud, Sascha Mehl, Klara Sevcikova, Kevin C Prince, Konstantin M Neyman, et al. “Atomically dispersed Pd, Ni, and Pt species in ceria-based catalysts: principal differences in stability and reactivity”. In: *The Journal of Physical Chemistry C* 120.18 (2016), pp. 9852–9862.

[144] Yaroslava Lykhach, Alberto Figueroba, Matteo Farnesi Camellone, Armin Neitzel, Tomáš Skála, Fabio R Negreiros, Mykhailo Vorokhta, Nataliya Tsud, Kevin C Prince, Stefano Fabris, et al. “Reactivity of atomically dispersed Pt 2+ species

towards H 2: model Pt–CeO 2 fuel cell catalyst". In: *Physical Chemistry Chemical Physics* 18.11 (2016), pp. 7672–7679.

[145] Alberto Figueroba, Gábor Kovács, Albert Bruix, and Konstantin M Neyman. "Towards stable single-atom catalysts: strong binding of atomically dispersed transition metals on the surface of nanostructured ceria". In: *Catalysis Science & Technology* 6.18 (2016), pp. 6806–6813.

[146] Zhaoming Fu, Bowen Yang, and Ruqian Wu. "Understanding the activity of single-atom catalysis from frontier orbitals". In: *Physical review letters* 125.15 (2020), p. 156001.

[147] Yang Lou, Yongping Zheng, Wenyi Guo, and Jingyue Liu. "Pt 1–O 4 as active sites boosting CO oxidation via a non-classical Mars–van Krevelen mechanism". In: *Catalysis Science & Technology* 11.10 (2021), pp. 3578–3588.

[148] Bing Liu, Jian Liu, Teng Li, Zhen Zhao, Xue-Qing Gong, Yu Chen, Aijun Duan, Guiyuan Jiang, and Yuechang Wei. "Interfacial effects of CeO2-supported Pd nanorod in catalytic CO oxidation: a theoretical study". In: *The Journal of Physical Chemistry C* 119.23 (2015), pp. 12923–12934.

[149] Yanru Wang, Jiamin Ma, Xiuyi Wang, Zheshan Zhang, Jiahan Zhao, Jie Yan, Yaping Du, Hongbo Zhang, and Ding Ma. "Complete CO Oxidation by O2 and H2O over Pt–CeO2- δ/MgO Following Langmuir–Hinshelwood and Mars–van Krevelen Mechanisms, Respectively". In: *ACS Catalysis* 11.19 (2021), pp. 11820–11830.

[150] Per-Anders Carlsson, Lars Österlund, Peter Thormählen, Anders Palmqvist, Erik Fridell, Jonas Jansson, and Magnus Skoglundh. "A transient in situ FTIR and XANES study of CO oxidation over Pt/Al2O3 catalysts". In: *Journal of Catalysis* 226.2 (2004), pp. 422–434.

[151] GS Zafiris and RJ Gorte. "Evidence for a second CO oxidation mechanism on Rh/ceria". In: *Journal of Catalysis* 143.1 (1993), pp. 86–91.

[152] Leo DeRita, Sheng Dai, Kimberly Lopez-Zepeda, Nicholas Pham, George W Graham, Xiaoqing Pan, and Phillip Christopher. "Catalyst architecture for stable single atom dispersion enables site-specific spectroscopic and reactivity measurements of CO adsorbed to Pt atoms, oxidized Pt clusters, and metallic Pt clusters on TiO2". In: *Journal of the American Chemical Society* 139.40 (2017), pp. 14150–14165.

[153] Lei Nie, Donghai Mei, Haifeng Xiong, Bo Peng, Zhibo Ren, Xavier Isidro Pereira Hernandez, Andrew DeLaRiva, Meng Wang, Mark H Engelhard, Libor Kovarik, et al. "Activation of surface lattice oxygen in single-atom Pt/CeO2 for low-temperature CO oxidation". In: *Science* 358.6369 (2017), pp. 1419–1423.

[154] C Doornkamp and V Ponec. “The universal character of the Mars and Van Krevelen mechanism”. In: *Journal of Molecular Catalysis A: Chemical* 162.1-2 (2000), pp. 19–32.

[155] C Kroger. “Zur Heterogenen Katalyse Binirer Gasreaktionen. II”. In: *Z. Anorg. Chem* 206 (1932), p. 289.

[156] K Klier, J Novakova, and P Jiru. “Exchange reactions of oxygen between oxygen molecules and solid oxides”. In: *Journal of Catalysis* 2.6 (1963), pp. 479–484.

[157] J Novakova. “Isotopic exchange of oxygen 18O between the gaseous phase and oxide catalysts”. In: *Catalysis Reviews* 4.1 (1971), pp. 77–113.

[158] Michel Boudart and Gérald Djéga-Mariadassou. *Kinetics of heterogeneous catalytic reactions*. Vol. 767. Princeton University Press, 2014.

[159] K Vasanth Kumar, K Porkodi, Rocha, and F. “Langmuir–Hinshelwood kinetics–a theoretical study”. In: *Catalysis Communications* 9.1 (2008), pp. 82–84.

[160] JN Bronsted. “Acid and Basic Catalysis.” In: *Chemical Reviews* 5.3 (1928), pp. 231–338.

[161] MG Evans and Michael Polanyi. “Inertia and driving force of chemical reactions”. In: *Transactions of the Faraday Society* 34 (1938), pp. 11–24.

[162] Jens K Nørskov, Thomas Bligaard, Ashildur Logadottir, S Bahn, Lars B Hansen, Mikkel Bollinger, H Bengaard, Bjørk Hammer, Z Sljivancanin, Manos Mavrikakis, et al. “Universality in heterogeneous catalysis”. In: *Journal of catalysis* 209.2 (2002), pp. 275–278.

[163] Zhi-Jian Zhao, Sihang Liu, Shenjun Zha, Dongfang Cheng, Felix Studt, Graeme Henkelman, and Jinlong Gong. “Theory-guided design of catalytic materials using scaling relationships and reactivity descriptors”. In: *Nature Reviews Materials* 4.12 (2019), pp. 792–804.

[164] BJKN Hammer and Jens K Nørskov. “Electronic factors determining the reactivity of metal surfaces”. In: *Surface science* 343.3 (1995), pp. 211–220.

[165] Bjørk Hammer and Jens Kehlet Nørskov. “Theoretical surface science and catalysis—calculations and concepts”. In: *Advances in catalysis*. Vol. 45. Elsevier, 2000, pp. 71–129.

[166] Adrian P Sutton. *Electronic structure of materials*. Clarendon Press, 1993.

[167] Jeff Greeley, Jens K Nørskov, and Manos Mavrikakis. “Electronic structure and catalysis on metal surfaces”. In: *Annual review of physical chemistry* 53.1 (2002), pp. 319–348.

[168] Hongliang Xin, Aleksandra Vojvodic, Johannes Voss, Jens K Nørskov, and Frank Abild-Pedersen. “Effects of d-band shape on the surface reactivity of transition-metal alloys”. In: *Physical Review B* 89.11 (2014), p. 115114.

[169] Alireza Khorshidi, James Violet, Javad Hashemi, and Andrew A Peterson. “How strain can break the scaling relations of catalysis”. In: *Nature Catalysis* 1.4 (2018), pp. 263–268.

[170] Gerhard Ertl. “Reaktionen an Oberflächen: vom Atomaren zum Komplexen (Nobel-Vortrag)”. In: *Angewandte Chemie* 120.19 (2008), pp. 3578–3590.

[171] Lin Li, Ask H Larsen, Nichols A Romero, Vitali A Morozov, Christian Glinsvad, Frank Abild-Pedersen, Jeff Greeley, Karsten W Jacobsen, and Jens K Nørskov. “Investigation of catalytic finite-size-effects of platinum metal clusters”. In: *The journal of physical chemistry letters* 4.1 (2013), pp. 222–226.

[172] Louis De Broglie. “Les principes de la nouvelle mécanique ondulatoire”. In: *Journal de Physique et le Radium* 7.11 (1926), pp. 321–337.

[173] Erwin Schrödinger. “Quantisierung als eigenwertproblem”. In: *Annalen der physik* 385.13 (1926), pp. 437–490.

[174] Ulrich Hohenester and Klaus Irgang. “Die Schrödingergleichung”. In: *Einführung in die Quantenmechanik: Für Studierende des Lehramts Physik*. Springer, 2023, pp. 69–88.

[175] Attila Szabo and Neil S Ostlund. *Modern quantum chemistry: introduction to advanced electronic structure theory*. Courier Corporation, 2012.

[176] Henry M Leicester. “Germain Henri Hess and the foundations of thermochemistry”. In: *Journal of chemical education* 28.11 (1951), p. 581.

[177] Marcus Elstner. *Physikalische Chemie I: Thermodynamik und Kinetik*. Springer-Verlag, 2017.

[178] Douglas R Hartree. “The wave mechanics of an atom with a non-Coulomb central field. Part I. Theory and methods”. In: *Mathematical Proceedings of the Cambridge Philosophical Society*. Vol. 24. 1. Cambridge university press. 1928, pp. 89–110.

[179] Frank Jensen. *Introduction to computational chemistry*. John wiley & sons, 2017.

[180] Pierre Hohenberg and Walter Kohn. “Inhomogeneous electron gas”. In: *Physical review* 136.3B (1964), B864.

[181] Walter Kohn. “Density-functional theory for excited states in a quasi-local-density approximation”. In: *Phys. Rev. A* 34 (2 Aug. 1986), pp. 737–741.

[182] Thomas Bayes. “LII. An essay towards solving a problem in the doctrine of chances. By the late Rev. Mr. Bayes, FRS communicated by Mr. Price, in a letter to John Canton, AMFR S”. In: *Philosophical transactions of the Royal Society of London* 53 (1763), pp. 370–418.

[183] Thomas Bayes. “XLIII. A letter from the late Reverend Mr. Thomas Bayes, FRS to John Canton, MA and FR S”. In: *Philosophical Transactions of the Royal Society of London* 53 (1763), pp. 269–271.

[184] George A Barnard and Thomas Bayes. “Studies in the history of probability and statistics: IX. Thomas Bayes’s essay towards solving a problem in the doctrine of chances”. In: *Biometrika* 45.3/4 (1958), pp. 293–315.

[185] C Bishop. “Pattern recognition and machine learning”. In: *Springer google schola* 2 (2006), pp. 531–537.

[186] Jess Wellendorff, Keld T Lundgaard, Andreas Møgelhøj, Vivien Petzold, David D Landis, Jens K Nørskov, Thomas Bligaard, and Karsten W Jacobsen. “Density functionals for surface science: Exchange-correlation model development with Bayesian error estimation”. In: *Physical Review B* 85.23 (2012), p. 235149.

[187] John C Snyder, Matthias Rupp, Katja Hansen, Klaus-Robert Müller, and Kieron Burke. “Finding density functionals with machine learning”. In: *Physical review letters* 108.25 (2012), p. 253002.

[188] John C Snyder, Matthias Rupp, Katja Hansen, Leo Blooston, Klaus-Robert Müller, and Kieron Burke. “Orbital-free bond breaking via machine learning”. In: *The Journal of chemical physics* 139.22 (2013).

[189] Jens Jørgen Mortensen, Kristen Kaasbjerg, Søren Lund Frederiksen, Jens Kehlet Nørskov, James P Sethna, and Karsten Wedel Jacobsen. “Bayesian error estimation in density-functional theory”. In: *Physical review letters* 95.21 (2005), p. 216401.

[190] Keld T Lundgaard, Jess Wellendorff, Johannes Voss, Karsten W Jacobsen, and Thomas Bligaard. “mBEEF-vdW: Robust fitting of error estimation density functionals”. In: *Physical Review B* 93.23 (2016), p. 235162.

[191] Michal Bajdich, Jens K Nørskov, and Aleksandra Vojvodic. “Surface energetics of alkaline-earth metal oxides: Trends in stability and adsorption of small molecules”. In: *Physical Review B* 91.15 (2015), p. 155401.

[192] Stefan Grimme. “Semiempirical GGA-type density functional constructed with a long-range dispersion correction”. In: *Journal of computational chemistry* 27.15 (2006), pp. 1787–1799.

[193] Matthieu Verstraete and Xavier Gonze. “Smearing scheme for finite-temperature electronic-structure calculations”. In: *Physical Review B* 65.3 (2001), p. 035111.

[194] Flaviano José dos Santos and Nicola Marzari. “Fermi energy determination for advanced smearing techniques”. In: *Physical Review B* 107.19 (2023), p. 195122.

[195] Matteo Cococcioni and Stefano De Gironcoli. “Linear response approach to the calculation of the effective interaction parameters in the LDA+ U method”. In: *Physical Review B* 71.3 (2005), p. 035105.

[196] W Heisenberg. “Über quantentheoretische Umdeutung kinematischer und mechanischer Beziehungen.” In: *Zeitschrift für Physik* 33.1 (1925), pp. 879–893.

[197] Jutta Rogal and Karsten Reuter. *Ab initio atomistic thermodynamics for surfaces: A primer*. Tech. rep. Max-planck-gesellschaft zur foerderung der wissenschaften ev berlin (germany . . ., 2006.

[198] Jens K Nørskov, Felix Studt, Frank Abild-Pedersen, and Thomas Bligaard. *Fundamental concepts in heterogeneous catalysis*. John Wiley & Sons, 2014.

[199] Max Trautz. “Das Gesetz der Reaktionsgeschwindigkeit und der Gleichgewichte in Gasen. Bestätigung der Additivität von Cv-3/2R. Neue Bestimmung der Integrationskonstanten und der Moleküldurchmesser”. In: *Zeitschrift für anorganische und allgemeine Chemie* 96.1 (1916), pp. 1–28.

[200] William Cudmore McCullagh Lewis. “XLI.—Studies in catalysis. Part IX. The calculation in absolute measure of velocity constants and equilibrium constants in gaseous systems”. In: *Journal of the Chemical Society, Transactions* 113 (1918), pp. 471–492.

[201] Jean Perrin. “Matière et lumière”. In: *Annales de Physique*. Vol. 9. 11. 1919, pp. 5–108.

[202] M Christine King and Keith J Laidler. “Chemical kinetics and the radiation hypothesis”. In: *Archive for History of Exact Sciences* (1984), pp. 45–86.

[203] Frederick A Lindemann, Svante Arrhenius, Irving Langmuir, NR Dhar, J Perrin, and WC McC Lewis. “Discussion on “the radiation theory of chemical action””. In: *Transactions of the Faraday Society* 17 (1922), pp. 598–606.

[204] Henry Eyring. “The theory of absolute reaction rates”. In: *Transactions of the Faraday Society* 34 (1938), pp. 41–48.

[205] Henry Eyring. “Viscosity, plasticity, and diffusion as examples of absolute reaction rates”. In: *The Journal of chemical physics* 4.4 (1936), pp. 283–291.

[206] Merdith G Evans and Michael Polanyi. “Some applications of the transition state method to the calculation of reaction velocities, especially in solution”. In: *Transactions of the Faraday Society* 31 (1935), pp. 875–894.

[207] MG Evans and M Polanyi. “On the introduction of thermodynamic variables into reaction kinetics”. In: *Transactions of the Faraday Society* 33 (1937), pp. 448–452.

[208] Georg Kresse and Jürgen Furthmüller. “Efficiency of ab-initio total energy calculations for metals and semiconductors using a plane-wave basis set”. In: *Computational materials science* 6.1 (1996), pp. 15–50.

[209] Georg Kresse and Jürgen Furthmüller. “Efficient iterative schemes for ab initio total-energy calculations using a plane-wave basis set”. In: *Physical review B* 54.16 (1996), p. 11169.

[210] Sune R Bahn and Karsten W Jacobsen. “An object-oriented scripting interface to a legacy electronic structure code”. In: *Computing in Science & Engineering* 4.3 (2002), pp. 56–66.

[211] Peter E Blöchl. “Projector augmented-wave method”. In: *Physical review B* 50.24 (1994), p. 17953.

[212] Georg Kresse and Daniel Joubert. “From ultrasoft pseudopotentials to the projector augmented-wave method”. In: *Physical review b* 59.3 (1999), p. 1758.

[213] PW Tasker. “The structure and properties of fluorite crystal surfaces”. In: *Le Journal de Physique Colloques* 41.C6 (1980), pp. C6–488.

[214] Jelena Jelic, Karsten Reuter, and Randall Meyer. “The role of surface oxides in NOx storage reduction catalysts”. In: *ChemCatChem* 2.6 (2010), pp. 658–660.

[215] RC Albers, Niels Egede Christensen, and Axel Svane. “Hubbard-U band-structure methods”. In: *Journal of Physics: Condensed Matter* 21.34 (2009), p. 343201.

[216] Min Huang and Stefano Fabris. “CO adsorption and oxidation on ceria surfaces from DFT+ U calculations”. In: *The Journal of Physical Chemistry C* 112.23 (2008), pp. 8643–8648.

[217] Stefano Fabris, Stefano de Gironcoli, Stefano Baroni, Gianpaolo Vicario, and Gabriele Balducci. “Taming multiple valency with density functionals: A case study of defective ceria”. In: *Physical Review B* 71.4 (2005), p. 041102.

[218] Christoph Loschen, Javier Carrasco, Konstantin M Neyman, and Francesc Illas. “First-principles LDA+ U and GGA+ U study of cerium oxides: Dependence on the effective U parameter”. In: *Physical Review B* 75.3 (2007), p. 035115.

[219] CWM Castleton, Jolla Kullgren, and Kersti Hermansson. “Tuning LDA+ U for electron localization and structure at oxygen vacancies in ceria”. In: *The Journal of chemical physics* 127.24 (2007).

[220] Yong Jiang, James B Adams, and Mark Van Schilfgaarde. “Density-functional calculation of CeO2 surfaces and prediction of effects of oxygen partial pressure and temperature on stabilities”. In: *The Journal of chemical physics* 123.6 (2005).

[221] Sergei L Dudarev, Gianluigi A Botton, Sergey Y Savrasov, CJ Humphreys, and Adrian P Sutton. “Electron-energy-loss spectra and the structural stability of nickel oxide: An LSDA+ U study”. In: *Physical Review B* 57.3 (1998), p. 1505.

[222] Hui-Ying Li, Hai-Feng Wang, Xue-Qing Gong, Yang-Long Guo, Yun Guo, Guanzhong Lu, and P Hu. “Multiple configurations of the two excess 4 f electrons on defective CeO 2 (111): origin and implications”. In: *Physical Review B* 79.19 (2009), p. 193401.

[223] José J Plata, Antonio M Márquez, and Javier Fdez Sanz. “Transport properties in the CeO2–x (111) surface: From charge distribution to ion-electron collaborative migration”. In: *The Journal of Physical Chemistry C* 117.48 (2013), pp. 25497–25503.

[224] Christopher WM Castleton, Amy Lee, and Jolla Kullgren. “Benchmarking density functional theory functionals for polarons in oxides: properties of CeO2”. In: *The Journal of Physical Chemistry C* 123.9 (2019), pp. 5164–5175.

[225] Zhong-Kang Han, Xinyi Duan, Xiaoyan Li, Dawei Zhang, and Yi Gao. “The dynamic interplay between water and oxygen vacancy at the near-surface of ceria”. In: *Journal of Physics: Condensed Matter* 33.42 (2021), p. 424001.

[226] Zhenpeng Hu and Horia Metiu. “Effect of dopants on the energy of oxygen-vacancy formation at the surface of ceria: Local or global?” In: *The Journal of Physical Chemistry C* 115.36 (2011), pp. 17898–17909.

[227] Nathan Daelman, Marçal Capdevila-Cortada, and Núria López. “Dynamic charge and oxidation state of Pt/CeO2 single-atom catalysts”. In: *Nature materials* 18.11 (2019), pp. 1215–1221.

[228] Julian Geiger, Albert Sabadell-Rendón, Nathan Daelman, and Núria López. “Data-driven models for ground and excited states for Single Atoms on Ceria”. In: *npj Computational Materials* 8.1 (2022), p. 171.

[229] AV Ruban, HL Skriver, and JK Nørskov. “Local equilibrium properties of metallic surface alloys”. In: *Chemical Physics of Solid Surfaces* 10.C (2002), pp. 1–29.

[230] A.V. Ruban, H.L. Skriver, and J.K. Nørskov. “Chapter 1 - Local equilibrium properties of metallic surface alloys”. In: *Surface Alloys and Alloys Surfaces*. Ed. by D.P. Woodruff. Vol. 10. The Chemical Physics of Solid Surfaces. Elsevier, 2002, pp. 1–29.

[231] David Anthony King. *The chemical physics of solid surfaces and heterogeneous catalysis*. Vol. 5. Elsevier, 2012.

[232] KPAH Huber. *Molecular spectra and molecular structure: IV. Constants of diatomic molecules*. Springer Science & Business Media, 2013.

[233] Ashriti Govender, Daniel Curulla Ferré, and JW Niemantsverdriet. “A density functional theory study on the effect of zero-point energy corrections on the methanation profile on Fe (100)”. In: *ChemPhysChem* 13.6 (2012), pp. 1591–1596.

[234] NV Skorodumova, Micael Baudin, and Kersti Hermansson. “Surface properties of CeO 2 from first principles”. In: *Physical Review B* 69.7 (2004), p. 075401.

[235] Micael Baudin, Mark Wójcik, and Kersti Hermansson. “Dynamics, structure and energetics of the (111),(011) and (001) surfaces of ceria”. In: *Surface science* 468.1-3 (2000), pp. 51–61.

[236] Patricia Pérez-Bailac, Pablo G Lustemberg, and M Verónica Ganduglia-Pirovano. “Facet-dependent stability of near-surface oxygen vacancies and excess charge localization at CeO2 surfaces”. In: *Journal of Physics: Condensed Matter* 33.50 (2021), p. 504003.

[237] H Nörenberg and GAD Briggs. “Defect formation on CeO2 (111) surfaces after annealing studied by STM”. In: *Surface science* 424.2-3 (1999), pp. L352–L355.

[238] SN Jacobsen, U Helmersson, R Erlandsson, Björn Skårman, and LR Wallenberg. “Sharp microfaceting of (001)-oriented cerium dioxide thin films and the effect of annealing on surface morphology”. In: *Surface science* 429.1-3 (1999), pp. 22–33.

[239] H Nörenberg and JH Harding. “The surface structure of CeO2 (0 0 1) single crystals studied by elevated temperature STM”. In: *Surface science* 477.1 (2001), pp. 17–24.

[240] Ya-Qiong Su, Yifan Wang, Jin-Xun Liu, Ivo AW Filot, Konstantinos Alexopoulos, Long Zhang, Valerii Muravev, Bart Zijlstra, Dionisios G Vlachos, and Emiel JM Hensen. “Theoretical approach to predict the stability of supported single-atom catalysts”. In: *ACS Catalysis* 9.4 (2019), pp. 3289–3297.

[241] Tianxiao Wu, Xiqiang Pan, Yibo Zhang, Zhenzhen Miao, Bin Zhang, Jingwei Li, and Xiangguang Yang. “Investigation of the redispersion of Pt nanoparticles on polyhedral ceria nanoparticles”. In: *The Journal of Physical Chemistry Letters* 5.14 (2014), pp. 2479–2483.

[242] Yaroslava Lykhach, Sergey M Kozlov, Tomáš Skála, Andrii Tovt, Vitalii Stetsovych, Nataliya Tsud, Filip Dvořák, Viktor Johánek, Armin Neitzel, Josef Mysliveček, et al. "Counting electrons on supported nanoparticles". In: *Nature materials* 15.3 (2016), pp. 284–288.

[243] Sergey M Kozlov and Konstantin M Neyman. "Effects of electron transfer in model catalysts composed of Pt nanoparticles on CeO2 (1 1 1) surface". In: *Journal of Catalysis* 344 (2016), pp. 507–514.

[244] Konstantin M Neyman and Sergey M Kozlov. "Quantifying interactions on interfaces between metal particles and oxide supports in catalytic nanomaterials". In: *NPG Asia Materials* 14.1 (2022), p. 59.

[245] Charlotte Vogt, Esther Groeneveld, Gerda Kamsma, Maarten Nachtegaal, Li Lu, Christopher J Kiely, Peter H Berben, Florian Meirer, and Bert M Weckhuysen. "Unravelling structure sensitivity in CO2 hydrogenation over nickel". In: *Nature Catalysis* 1.2 (2018), pp. 127–134.

[246] Charlotte Vogt and Bert M Weckhuysen. "The concept of active site in heterogeneous catalysis". In: *Nature Reviews Chemistry* 6.2 (2022), pp. 89–111.

[247] JF Hamilton and RC Baetzold. "Catalysis by Small Metal Clusters: Size-dependent catalytic activity can be correlated with changes in physical properties". In: *Science* 205.4412 (1979), pp. 1213–1220.

[248] Ryogo Kubo, Arisato Kawabata, and Shun-ichi Kobayashi. "Electronic properties of small particles". In: *Annual Review of Materials Science* 14.1 (1984), pp. 49–66.

[249] Michael Nolan, Joanne E Fearon, and Graeme W Watson. "Oxygen vacancy formation and migration in ceria". In: *Solid State Ionics* 177.35-36 (2006), pp. 3069–3074.

[250] HL Tuller and AS Nowick. "Small polaron electron transport in reduced CeO2 single crystals". In: *Journal of Physics and Chemistry of Solids* 38.8 (1977), pp. 859–867.

[251] A Pfau and KD Schierbaum. "The electronic structure of stoichiometric and reduced CeO2 surfaces: an XPS, UPS and HREELS study". In: *Surface Science* 321.1-2 (1994), pp. 71–80.

[252] H Nörenberg and GAD Briggs. "Defect structure of nonstoichiometric CeO 2 (111) surfaces studied by scanning tunneling microscopy". In: *Physical review letters* 79.21 (1997), p. 4222.

[253] DR Mullins, SH Overbury, and DR Huntley. "Electron spectroscopy of single crystal and polycrystalline cerium oxide surfaces". In: *Surface Science* 409.2 (1998), pp. 307–319.

[254] Michael A Henderson, CL Perkins, Mark H Engelhard, Suntharampillai Thevuthasan, and Charles HF Peden. “Redox properties of water on the oxidized and reduced surfaces of CeO2 (111)”. In: *Surface Science* 526.1-2 (2003), pp. 1–18.

[255] E Wuilloud, B Delley, W-D Schneider, and Y Baer. “Spectroscopic Evidence for Localized and Extended f-Symmetry States in Ce O 2”. In: *Physical review letters* 53.2 (1984), p. 202.

[256] Matthew A Panhans and RN Blumenthal. “A thermodynamic and electrical conductivity study of nonstoichiometric cerium dioxide”. In: *Solid State Ionics* 60.4 (1993), pp. 279–298.

[257] Claude Binet, Ahmed Badri, and Jean-Claude Lavalley. “A spectroscopic characterization of the reduction of ceria from electronic transitions of intrinsic point defects”. In: *The Journal of Physical Chemistry* 98.25 (1994), pp. 6392–6398.

[258] Vincent Perrichon, Ahmidou Laachir, Gérard Bergeret, Roger Fréty, Louise Tournayan, and Olivier Touret. “Reduction of cerias with different textures by hydrogen and their reoxidation by oxygen”. In: *Journal of the Chemical Society, Faraday Transactions* 90.5 (1994), pp. 773–781.

[259] Ya-Qiong Su, Ivo AW Filot, Jin-Xun Liu, and Emiel JM Hensen. “Stable Pd-doped ceria structures for CH4 activation and CO oxidation”. In: *ACS catalysis* 8.1 (2018), pp. 75–80.

[260] Zhongtian Mao, Pablo G Lustemberg, John R Rumptz, M Verónica Ganduglia-Pirovano, and Charles T Campbell. “Ni nanoparticles on CeO2 (111): energetics, electron transfer, and structure by Ni adsorption calorimetry, spectroscopies, and density functional theory”. In: *ACS Catalysis* 10.9 (2020), pp. 5101–5114.

[261] Zhansheng Lu and Zongxian Yang. “Interfacial properties of NM/CeO2 (111)(NM= noble metal atoms or clusters of Pd, Pt and Rh): a first principles study”. In: *Journal of Physics: Condensed Matter* 22.47 (2010), p. 475003.

[262] KM Neyman, C Inntam, VA Nasluzov, R Kosarev, and N Rösch. “Adsorption of d-metal atoms on the regular MgO (001) surface: Density functional study of cluster models embedded in an elastic polarizable environment”. In: *Applied Physics A* 78 (2004), pp. 823–828.

[263] V Musolino, A Selloni, and R Car. “Atomic and electronic structure of Cu clusters on MgO”. In: *Surface science* 402 (1998), pp. 413–417.

[264] K Michaelian, N Rendón, and IL Garzón. “Structure and energetics of Ni, Ag, and Au nanoclusters”. In: *Physical Review B* 60.3 (1999), p. 2000.

[265] Ilya V Yudanov, Stefan Vent, Konstantin Neyman, Gianfranco Pacchioni, and Notker Rösch. “Adsorption of Pd atoms and Pd4 clusters on the MgO (001) surface: a density functional study”. In: *Chemical physics letters* 275.3-4 (1997), pp. 245–252.

[266] Kristin Persson. *Materials Data on CeO (SG:225) by Materials Project*. An optional note. Feb. 2015. DOI: 10.17188/1187292.

[267] Albert Bruix, Annapaola Migani, Georgi N Vayssilov, Konstantin M Neyman, Jörg Libuda, and Francesc Illas. “Effects of deposited Pt particles on the reducibility of CeO 2 (111)”. In: *Physical Chemistry Chemical Physics* 13.23 (2011), pp. 11384–11392.

[268] Bidyut Bikash Sarma, Jelena Jelic, Dominik Neukum, Dmitry E Doronkin, Xiaohui Huang, Felix Studt, and Jan-Dierk Grunwaldt. “Tracking and understanding dynamics of atoms and clusters of late transition metals with in-situ DRIFT and XAS spectroscopy assisted by DFT”. In: *The Journal of Physical Chemistry C* 127.6 (2023), pp. 3032–3046.

[269] Matthew Kottwitz, Yuanyuan Li, Robert M Palomino, Zongyuan Liu, Guangjin Wang, Qin Wu, Jiahao Huang, Janis Timoshenko, Sanjaya D Senanayake, Mahalingam Balasubramanian, et al. “Local structure and electronic state of atomically dispersed Pt supported on nanosized CeO2”. In: *ACS Catalysis* 9.9 (2019), pp. 8738–8748.

[270] Hristiyan A Aleksandrov, Konstantin M Neyman, Konstantin I Hadjiivanov, and Georgi N Vayssilov. “Can the state of platinum species be unambiguously determined by the stretching frequency of an adsorbed CO probe molecule?” In: *Physical Chemistry Chemical Physics* 18.32 (2016), pp. 22108–22121.

[271] Yubing Lu, Shulan Zhou, Chun-Te Kuo, Deepak Kunwar, Coogan Thompson, Adam S Hoffman, Alexey Boubnov, Sen Lin, Abhaya K Datye, Hua Guo, et al. “Unraveling the intermediate reaction complexes and critical role of support-derived oxygen atoms in CO oxidation on single-atom Pt/CeO2”. In: *ACS Catalysis* 11.14 (2021), pp. 8701–8715.

[272] Joaquin Resasco, Leo DeRita, Sheng Dai, Joseph P Chada, Mingjie Xu, Xingxu Yan, Jordan Finzel, Sergei Hanukovich, Adam S Hoffman, George W Graham, et al. “Uniformity is key in defining structure–function relationships for atomically dispersed metal catalysts: the case of Pt/CeO2”. In: *Journal of the American Chemical Society* 142.1 (2019), pp. 169–184.

[273] Yifan Wang, Ya-Qiong Su, Emiel JM Hensen, and Dionisios G Vlachos. “Insights into supported subnanometer catalysts exposed to CO via machine-learning-enabled multiscale modeling”. In: *Chemistry of Materials* 34.4 (2022), pp. 1611–1619.

[274] Christoph Janiak, Hans-Jürgen Meyer, Dietrich Gudat, and Ralf Alsfasser. *Riedel Moderne Anorganische Chemie*. Walter de Gruyter, 2012.

[275] Andreas W Ehlers and Gernot Frenking. “Structures and bond energies of the transition-metal carbonyls M (CO) 5 (M= Fe, Ru, Os) and M (CO) 4 (M= Ni, Pd, Pt)”. In: *Organometallics* 14.1 (1995), pp. 423–426.

[276] Volker Jonas and Walter Thiel. “Theoretical study of the vibrational spectra of the transition metal carbonyls M (CO) 6 [M= Cr, Mo, W], M (CO) 5 [M= Fe, Ru, Os], and M (CO) 4 [M= Ni, Pd, Pt]”. In: *The Journal of chemical physics* 102.21 (1995), pp. 8474–8484.

[277] Jian Li, Georg Schreckenbach, and Tom Ziegler. “A reassessment of the first metal-carbonyl dissociation energy in M (CO) 4 (M= Ni, Pd, Pt), M (CO) 5 (M= Fe, Ru, Os), and M (CO) 6 (M= Cr, Mo, W) by a quasirelativistic density functional method”. In: *Journal of the American Chemical Society* 117.1 (1995), pp. 486–494.

[278] Gernot Frenking, Israel Fernández, Nicole Holzmann, Sudip Pan, Ingo Krossing, and Mingfei Zhou. “Metal–CO bonding in mononuclear transition metal carbonyl complexes”. In: *Jacs Au* 1.5 (2021), pp. 623–645.

[279] H Huber, P Kündig, M Moskovits, and Ga A Ozin. “Tetracarbonyls of Palladium and Platinum in Low Temperature Matrices”. In: *Nature Physical Science* 235.57 (1972), pp. 98–100.

[280] P Kündig, M Moskovits, and GA Ozin. “Matrix isolation laser Raman spectroscopy: a Raman and infrared spectral study including Raman polarisation data for the co-condensation reaction of Pd: Spectroscopic and structural data for the new tetra-carbonyls Pd (CO) 4 AND Pt (CO) 4”. In: *Journal of Molecular Structure* 14.1 (1972), pp. 137–144.

[281] JH Darling and JS Ogden. “Spectroscopic studies on matrix-isolated metal carbonyls. Part II. Infrared spectra and structures of Pd (CO) 4, Pd (CO) 3, Pd (CO) 2, and PdCO”. In: *Journal of the Chemical Society, Dalton Transactions* 10 (1973), pp. 1079–1085.

[282] Koichi Mogi, Yoshiko Sakai, Takaaki Sonoda, Qiang Xu, and Yoshie Souma. “Geometries and Electronic Structures of Group 10 and 11 Metal Carbonyl Cations,[M (CO) n] x+(M x+= Ni2+, Pd2+, Pt2+, Cu+, Ag+, Au+; n= 1- 4)”. In: *The Journal of Physical Chemistry A* 107.19 (2003), pp. 3812–3821.

[283] K Mogi, Y Sakai, T Sonoda, Q Xu, and Y Souma. “Geometry and electronic structure of binuclear metal carbonyl cations,[M2 (CO) 2] 2+ and [M2 (CO) 6] 2+(M= Ni, Pd, Pt)”. In: *Journal of Molecular Structure: THEOCHEM* 537.1-3 (2001), pp. 125–138.

[284] Jieming Cui, Xiaopeng Xing, Chaoxian Chi, Guanjun Wang, Zhipan Liu, and Mingfei Zhou. “Infrared Photodissociation Spectra of Mass-Selected Homoleptic Dinuclear Palladium Carbonyl Cluster Cations in the Gas Phase”. In: *Chinese Journal of Chemistry* 30.9 (2012), pp. 2131–2137.

[285] Daria Gashnikova, Florian Maurer, Miriam R Bauer, Sarah Bernart, Jelena Jelic, Mads Lützen, Carina B Maliakkal, Paolo Dolcet, Felix Studt, Christian Kübel, et al. “Lifecycle of Pd Clusters: Following the Formation and Evolution of Active Pd Clusters on Ceria During CO Oxidation by In Situ/Operando Characterization Techniques”. In: *ACS Catalysis* 14 (2024), pp. 14871–14886.

[286] Daria Gashnikova, Florian Maurer, Eric Sauter, Sarah Bernart, Jelena Jelic, Paolo Dolcet, Carina B Maliakkal, Yuemin Wang, Christof Wöll, Felix Studt, et al. “Highly Active Oxidation Catalysts through Confining Pd Clusters on CeO2 Nano-Islands”. In: *Angewandte Chemie International Edition* (2024), e202408511.

[287] Peter J Feibelman and DR Hamann. “Theory of H bonding and vibration on Pt (111)”. In: *Surface Science* 182.3 (1987), pp. 411–422.

[288] Catherine Stampfl and Matthias Scheffler. “Study of CO oxidation over Ru (0001) at high gas pressures”. In: *Surface science* 377 (1997), pp. 808–812.

[289] Peter J Feibelman. “d-electron frustration and the large fcc versus hcp binding preference in O adsorption on Pt (111)”. In: *Physical Review B* 56.16 (1997), p. 10532.

[290] Marek Gajdoš, Andreas Eichler, and Jürgen Hafner. “CO adsorption on close-packed transition and noble metal surfaces: trends from ab initio calculations”. In: *Journal of Physics: Condensed Matter* 16.8 (2004), p. 1141.

[291] A Föhlisch, M Nyberg, P Bennich, L Triguero, J Hasselström, O Karis, LGM Pettersson, and A Nilsson. “The bonding of CO to metal surfaces”. In: *The Journal of Chemical Physics* 112.4 (2000), pp. 1946–1958.

[292] Mark M Sadek and Lichang Wang. “Effect of adsorption site, size, and composition of Pt/Au bimetallic clusters on the CO frequency: a density functional theory study”. In: *The Journal of Physical Chemistry A* 110.51 (2006), pp. 14036–14042.

[293] E Shoko, MF Smith, and Ross H McKenzie. “Charge distribution near bulk oxygen vacancies in cerium oxides”. In: *Journal of Physics: Condensed Matter* 22.22 (2010), p. 223201.

[294] Ramzi Farra, Sabine Wrabetz, Manfred E Schuster, Eugen Stotz, Neil G Hamilton, Amol P Amrute, Javier Pérez-Ramírez, Núria López, and Detre Teschner. “Understanding CeO 2 as a Deacon catalyst by probe molecule adsorption and in situ infrared characterisations”. In: *Physical Chemistry Chemical Physics* 15.10 (2013), pp. 3454–3465.

[295] P Bazin, O Saur, JC Lavalley, M Daturi, and G Blanchard. “FT-IR study of CO adsorption on Pt/CeO 2: characterisation and structural rearrangement of small Pt particles”. In: *Physical Chemistry Chemical Physics* 7.1 (2005), pp. 187–194.

[296] Tatyana Tabakova, Flora Boccuzzi, Maela Manzoli, and Donka Andreeva. “FTIR study of low-temperature water-gas shift reaction on gold/ceria catalyst”. In: *Applied Catalysis A: General* 252.2 (2003), pp. 385–397.

[297] Marco Daturi, Claude Binet, Jean-Claude Lavalley, Anouk Galtayries, and Robert Sporken. “Surface investigation on Ce x Zr 1-x O 2 compounds”. In: *Physical Chemistry Chemical Physics* 1.24 (1999), pp. 5717–5724.

[298] IK Naik and Tseng-Ying Tien. “Small-polaron mobility in nonstoichiometric cerium dioxide”. In: *Journal of Physics and Chemistry of Solids* 39.3 (1978), pp. 311–315.

[299] Iskra Z Koleva, Hristiyan A Aleksandrov, and Georgi N Vayssilov. “Comparison of the Reactivity of Platinum Cations and Clusters Supported on Ceria or Alumina in Carbon Monoxide Oxidation”. In: *ACS Catalysis* 13.8 (2023), pp. 5358–5374.

[300] Mikkel Jørgensen and Henrik Gronbeck. “First-principles microkinetic modeling of methane oxidation over Pd (100) and Pd (111)”. In: *ACS Catalysis* 6.10 (2016), pp. 6730–6738.

[301] Elisabeth M Dietze and Henrik Grönbeck. “Structure-Dependent Strain Effects”. In: *ChemPhysChem* 21.21 (2020), pp. 2407–2410.

[302] Alexander Bogicevic, Johan Strömquist, and Bengt I Lundqvist. “First-principles diffusion-barrier calculation for atomic oxygen on Pt (111)”. In: *Physical Review B* 57.8 (1998), R4289.

[303] Joost Wintterlin, Rolf Schuster, and Gerhard Ertl. “Existence of a “Hot” Atom Mechanism for the Dissociation of O 2 on Pt (111)”. In: *Physical review letters* 77.1 (1996), p. 123.

[304] Peter J Feibelman, Bjørk Hammer, Jens Kehlet Nørskov, F Wagner, Matthias Scheffler, Roland Stumpf, R Watwe, and J Dumesic. “The co/pt (111) puzzle”. In: *The Journal of Physical Chemistry B* 105.18 (2001), pp. 4018–4025.

[305] DF Ogletree, MA Van Hove, and GA Somorjai. “LEED intensity analysis of the structures of clean Pt (111) and of CO adsorbed on Pt (111) in the c (4× 2) arrangement”. In: *Surface science* 173.2-3 (1986), pp. 351–365.

[306] GS Blackman, M-L Xu, DF Ogletree, MA Van Hove, and GA Somorjai. “Mix of molecular adsorption sites detected for disordered CO on Pt (111) by diffuse low-energy electron diffraction”. In: *Physical review letters* 61.20 (1988), p. 2352.

[307] H Hopster and H Ibach. “Adsorption of CO on Pt (111) and Pt 6 (111)×(111) studied by high resolution electron energy loss spectroscopy and thermal desorption spectroscopy”. In: *Surface Science* 77.1 (1978), pp. 109–117.

[308] H Steininger, S Lehwald, and H Ibach. “On the adsorption of CO on Pt (111)”. In: *Surface Science* 123.2-3 (1982), pp. 264–282.

[309] BE Hayden, K Kretzschmar, AM Bradshaw, and RG Greenler. “An infrared study of the adsorption of CO on a stepped platinum surface”. In: *Surface science* 149.2-3 (1985), pp. 394–406.

[310] Jeonghyun Ko, Byung-Kook Kim, and Jeong Woo Han. “Density functional theory study for catalytic activation and dissociation of CO2 on bimetallic alloy surfaces”. In: *The Journal of Physical Chemistry C* 120.6 (2016), pp. 3438–3447.

[311] Andreas M Gänzler, Benjamin Betz, Sina Baier-Stegmaier, Stéphanie Belin, Valérie Briois, Martin Votsmeier, and Maria Casapu. “Operando X-ray Absorption Spectroscopy Study During Conditioning of Pt-Based Catalysts and Its Implications for CO Oxidation”. In: *The Journal of Physical Chemistry C* 124.37 (2020), pp. 20090–20100.

[312] Georgi N Vayssilov, Yaroslava Lykhach, Annapaola Migani, Thorsten Staudt, Galina P Petrova, Nataliya Tsud, Tomáš Skála, Albert Bruix, Francesc Illas, Kevin C Prince, et al. “Support nanostructure boosts oxygen transfer to catalytically active platinum nanoparticles”. In: *Nature materials* 10.4 (2011), pp. 310–315.

[313] Albert Bruix, José A Rodriguez, Pedro J Ramírez, Sanjaya D Senanayake, Jaime Evans, Joon B Park, Dario Stacchiola, Ping Liu, Jan Hrbek, and Francesc Illas. “A new type of strong metal–support interaction and the production of H2 through the transformation of water on Pt/CeO2 (111) and Pt/CeO x/TiO2 (110) catalysts”. In: *Journal of the American Chemical Society* 134.21 (2012), pp. 8968–8974.

[314] Matthew T Darby, E Charles H Sykes, Angelos Michaelides, and Michail Stamatakis. "Carbon monoxide poisoning resistance and structural stability of single atom alloys". In: *Topics in catalysis* 61.5-6 (2018), pp. 428–438.

[315] Jilei Liu, Felicia R Lucci, Ming Yang, Sungsik Lee, Matthew D Marcinkowski, Andrew J Therrien, Christopher T Williams, E Charles H Sykes, and Maria Flytzani-Stephanopoulos. "Tackling CO poisoning with single-atom alloy catalysts". In: *Journal of the American Chemical Society* 138.20 (2016), pp. 6396–6399.

A. Appendix

A.1. Atoms and Molecules used throughout this Work

In this work, gas-phase species are utilized to employ ab initio thermodynamics and calculate Gibbs free energies and phase diagrams. In other cases, bulk-phase species are used to obtain a reference for the most stable bulk phase. The total energies are shown in Table A.1.

Table A.1.: The total energies calculated by structure optimization at 0 K in eV of atoms and molecules in the gas phase and in the bulk phase, which are used throughout this work. The entropy is calculated for a temperature of 423.15 K.

	E_{total} [eV]	ZPE [eV]	S [eV/T]
Gas phase species			
$Pd_{(g)}$	1.25		
$Pt_{(g)}$	2.24		
$O_{2(g)}$	-6.62	0.103	2.24E-03
$CO_{(g)}$	-12.09	0.138	2.16E-03
$CO_{2(g)}$	-18.02	0.202	2.43E-03
Bulk phase species			
$CeO_{2(bulk)}$	-73.47		
$Pd_{(bulk)}$	-1.97		
$Pt_{(bulk)}$	-3.11		

A.2. Pd and Pt Single-atom Catalysts adsorbed on stoichiometric Ceria surface facets

The total energies in Table A.2 were utilized to compute the surface energies $E_{surf.}$ of the ceria surface facets (100), (110) and (111) and the adsorption Gibbs free energies of one Pd atom E_{ads}(Pd) and one Pt atom E_{ads}(Pt) on the ceria surface facets (100), (110) and (111), as listed in Table 4.1 in Section 4.1. $E_{surf.}$ is calculated as presented in the methods section 3. The bulk phase E_{total}(bulk) contains 16 Ce atoms and 32 O atoms and the surface slabs contain the same number of elements for each surface facet. Thus, we consider 16 units with n=16. The surface area is determined by the use of the size of the unit cells in the POSCAR files.

Table A.2.: The total energies calculated by structure optimization at 0 K in eV for the stoichiometric ceria surfaces exhibiting all three surface facets (100), (110), and (111), and for adsorbed single-atom catalysts of the noble metals Pd and Pt, are illustrated in Figure 4.1.

	E_{total}(surface)	E_{total}(bulk)
Ceria surface facets		
CeO_2(100)	-280.18	-292.53
CeO_2(110)	-287.10	-292.53
CeO_2(111)	-288.72	-292.53
Pd_1 single-atom catalysts		
Pd_1/CeO_2(100)	-281.93	
Pd_1/CeO_2(110)	-287.94	
Pd_1/CeO_2(111)	-288.92	
Pt_1 single-atom catalysts		
Pt_1/CeO_2(100)	-283.53	
Pt_1/CeO_2(110)	-289.59	
Pt_1/CeO_2(111)	-289.81	

A.3. Nanometer Cluster theoretically approached by Extended Metal surfaces

The total energies in Table A.3 were utilized to compute the surface energies $E_{surf.}$ of the noble metal surface facets (100), (110), (111) and (211) of Pd and Pt crystals, as listed in Table 4.2 in Section 4.2. $E_{surf.}$ is calculated as presented in the methods section 3. The bulk phase E_{total}(bulk) contains 16 Ce atoms and 32 O atoms and the surface slabs contain the same number of elements for each surface facet. Thus, we consider 16 units with n=16 for the (100) and (111) surface facets, and 32 units with n=32 for the (100) and 24 units with n=24 for the (100). The surface area is determined by the use of the size of the unit cells in the POSCAR files.

Table A.3.: The total energies calculated by structure optimization at 0 K in eV for the noble metal surfaces exhibiting the surface facets (100), (110), (111) and (111) as illustrated in Figure 4.2

	E_{total}(surface)	E_{total}(bulk)
Pd surface facets		
Pd(100)	-25.36	-31.73
Pd(110)	-53.81	-63.46
Pd(111)	-26.63	-31.73
Pd(211)	-39.61	-47.60
Pt surface facets		
Pt(100)	-42.50	-49.81
Pt(110)	-88.50	-99.62
Pt(111)	-44.31	-49.81
Pt(211)	-66.54	-74.71

A.4. Ceria surface facets as the non-innocent Support for Pd and Pt as the Active Center

The total energies in Table A.4 were utilized to compute the adsorption energies of the O atom $\Delta G_{ads}(1O^*)$, the two O atoms $\Delta G_{ads}(2O^*)$, one O surface defect formation ΔG_{1V_O} and two O surface defect formation ΔG_{2V_O} on the ceria surface facets (100), (110) and (111), as illustrated in Figure 4.4 and listed in Table 4.3 in Section 4.2.1.

Table A.4.: The total energies calculated by structure optimization at 0 K in eV for Ceria surface facets with varying O adsorption and defect formation as illustrated in Figure 4.3. The entropy of the O atom involved in the reduction and oxidation processes is calculated for a temperature of 423.15 K.

	E_{total} [eV]	ZPE [eV]	S [eV/T]
CeO_2(100)			
$2V_O$	-270.47		
$1V_O$	-275.91	0.0574	1.45E-04
stoichiometric	-280.18	0.0576	1.27E-04
O^*	-282.39	0.0570	1.26E-04
$2O^*$	-284.47	0.0559	1.31E-04
CeO_2(110)			
$2V_O$	-275.61		
$1V_O$	-282.34	0.0610	1.05E-04
stoichiometric	-287.10	0.0605	1.04E-04
O^*	-289.00	0.0352	2.06E-04
$2O^*$	-290.75	0.0369	1.93E-04
CeO_2(111)			
$2V_O$	-277.71		
$1V_O$	-283.37	0.0586	1.09E-04
stoichiometric	-288.72	0.0580	1.10E-04
O^*	-290.12	0.0318	2.51E-04
$2O^*$	-	-	-

A.5. O defective and oxidized Pd and Pt Single-atoms adsorbed on Ceria surface facets

The total energies in Table A.5 were utilized to compute the adsorption energies of the O atom $\Delta G_{ads}(1O^*)$, the two O atoms $\Delta G_{ads}(2O^*)$, one O surface defect formation ΔG_{1V_O} and two O surface defect formation ΔG_{2V_O} on the ceria surface facets (100), (110) and (111) with a Pd or Pt single-atom catalyst adsorbed, as illustrated in Figure 4.7 and listed in Table 4.4 in Section 4.2.2.

Table A.5.: The total energies calculated by structure optimization at 0 K in eV for Ceria surface facets with varying O adsorption and defect formation as illustrated in Figure 4.5 for Pd_1 and 4.6 for Pt_1. The entropy of the O atom involved in the reduction and oxidation processes is calculated for a temperature of 423.15 K.

	E_{total} [eV]	ZPE [eV]	S [eV/T]
$Pd_1/CeO_2(100)$			
$2V_O$	-270.84		
$1V_O$	-276.72	0.0638	1.05E-04
stoichiometric	-281.93	0.0667	9.63E-05
O^*	-285.96	0.0647	9.68E-05
$2O^*$	-290.38	0.0717	8.42E-05
$Pt_1/CeO_2(100)$			
$2V_O$	-272.10		
$1V_O$	-277.48	0.0668	1.11E-04
stoichiometric	-283.53	0.0691	1.16E-04
O^*	-286.77	0.0693	9.41E-05
$2O^*$	-292.02	0.0728	8.57E-05
$Pd_1/CeO_2(110)$			
$2V_O$	-276.52		
$1V_O$	-282.93	0.0585	1.16E-04
stoichiometric	-287.94	0.0627	1.06E-04
O^*	-292.42	0.0667	1.06E-04
$2O^*$	-295.67	0.0562	1.79E-04
$Pt_1/CeO_2(110)$			
$2V_O$	-278.12		
$1V_O$	-283.68	0.0636	1.19E-04
stoichiometric	-289.59	0.0743	9.14E-05
O^*	-293.27	0.0701	1.35E-04
$2O^*$	-297.25	0.0629	2.11E-04
$Pd_1/CeO_2(111)$			
$2V_O$	-277.81		
$1V_O$	-283.66	0.0612	1.07E-04
stoichiometric	-288.92	0.0528	1.25E-04
O^*	-292.70	0.0599	1.39E-04
$2O^*$	-295.60	0.0555	1.82E-04
$Pt_1/CeO_2(111)$			
$2V_O$	-278.30		
$1V_O$	-284.17	0.0652	1.13E-04
stoichiometric	-289.81	0.0589	1.22E-04
O^*	-293.58	0.0653	1.29E-04
$2O^*$	-297.52	0.0631	1.67E-04

A.6. Migration of O Defect Formation into the Sublayer of Ceria

The total energies in Table A.6 were utilized to compute ceria surface facets with migrating O defects starting at the vicinity of Pd and Pt single-atom catalyst on the surface facets of ceria (100), (110), and (111) towards the bulk phase of the surfaces, as illustrated in Figure 4.9 and listed in Table 4.5 in Section 4.2.3.

Table A.6.: The total energies calculated by structure optimization at 0 K in eV for Ceria surface facets with migrating O defects starting at the vicinity of Pd and Pt single-atom catalyst on the surface facets of ceria (100), (110), and (111) towards the bulk phase of the surfaces. The numbering refers to the O layers of the ceria surface, with the first layer denoted as 1st, the second layer as 2nd, the third layer as 3rd, and the fourth layer as 4th as shown in Figure 4.8. The entropy of the migrating O atom is calculated for a temperature of 423.15 K.

	E_{total} [eV]	ZPE [eV]	S [eV/T]
$1V_O$-$Pd_1/CeO_2(100)$			
1st	-276.72	0.0638	1.05E-04
2nd	-276.02	0.0605	1.12E-04
3rd	-276.53	0.0619	1.12E-04
4th	-275.62	0.0676	9.19E-05
$1V_O$-$Pt_1/CeO_2(100)$			
1st	-277.48	0.0668	1.11E-04
2nd	-277.35	0.0704	9.58E-05
3rd	-277.74	0.0634	1.07E-04
4th	-276.89	0.0672	9.29E-05
$1V_O$-$Pd_1/CeO_2(110)$			
1st	-282.93	0.0585	1.16E-04
2nd	-282.71	0.0645	1.02E-04
3rd	-282.42	0.0618	1.05E-04
4th	-281.66	0.0654	9.57E-05
$1V_O$-$Pt_1/CeO_2(110)$			
1st	-283.68	0.0636	1.19E-04
2nd	-284.07	0.0694	9.47E-05
3rd	-283.68	0.0600	1.11E-04
4th	-283.37	0.0625	1.04E-04
$1V_O$-$Pd_1/CeO_2(111)$			
1st	-283.66	0.0612	1.07E-04
2nd	-283.56	0.0583	1.10E-04
3rd	-283.99	0.0725	8.02E-05
4th	-282.73	0.0679	8.94E-05
$1V_O$-$Pt_1/CeO_2(111)$			
1st	-284.17	0.0652	1.13E-04
2nd	-283.96	0.0621	1.05E-04
3rd	-284.51	0.0682	8.80E-05
4th	-283.54	0.0672	9.37E-05

A.7. Reduced and oxidized Pd and Pt Atoms as Substitutes for Ce Surface Atoms

The total energies in Table A.6 were utilized to compute Gibbs free energies of reduction by O defect formation and oxidation by O adsorption $\Delta G_{red/ox}$ relative to the stoichiometric but Ce defective ceria surface of single Pd or Pt atom as substitutes for Ce surface atoms on the two surface facets of ceria (110) and (111), as illustrated in Figure 4.12 and listed in Table 4.6 in Section 4.2.4.

Table A.7.: The total energies calculated by structure optimization at 0 K in eV for Adsorption energies of the first O atom $E_{ads}(1^{st}O)$, the second O atom $E_{ads}(2^{nd}O)$, the first O lattice defect formation $E_{form.}(V_O{}^{1st})$ and second O lattice defect formation $E_{form.}(V_O{}^{2nd})$ on the ceria surface facets (100), (110) and (111) with a single Pd or Pt atom adsorbed on the surface as shown in Figures 4.10 for Pd and 4.11 for Pt. The entropy of the O atom involved in the reduction and oxidation processes is calculated for a temperature of 423.15 K.

	E_{total} [eV]	ZPE [eV]	S [eV/T]
Pd_1/V_{Ce}-CeO_2(110)			
$2V_O$	-258.13		
$1V_O$	-264.44	0.0663	1.06E-04
stoichiometric	-269.74	0.0756	7.73E-05
O^*	-274.68	0.0688	8.70E-05
$2O^*$	-277.17	0.0672	8.98E-05
Pt_1/V_{Ce}-CeO_2(110)			
$2V_O$	-258.98		
$1V_O$	-265.67	0.0680	1.40E-04
stoichiometric	-270.86	0.0752	8.02E-05
O^*	-275.76	0.0707	8.30E-05
$2O^*$	-278.74	0.0646	9.50E-05
Pd_1/V_{Ce}-CeO_2(111)			
$2V_O$	-255.01		
$1V_O$	-260.22	0.0518	1.73E-04
stoichiometric	-266.22	0.0752	8.75E-05
O^*	-269.52	0.0518	1.73E-04
$2O^*$	-274.12	0.0577	1.28E-04
Pt_1/V_{Ce}-CeO_2(111)			
$2V_O$	-254.91		
$1V_O$	-261.45	0.0634	1.29E-04
stoichiometric	-267.31	0.0753	9.34E-05
O^*	-270.39	0.0651	1.00E-04
$2O^*$	-274.83	0.0593	1.21E-04

A.8. Nucleation Process onto Pd and Pt atoms as Substitutes for Ceria surface atoms

The total energies of the heterogeneous catalyst E_{total}(IS) before the adsorption of Pd_{10} and Pt_{10} as the initial state and after the adsorption of Pd_{10} and Pt_{10} E_{total}(FS) as the final state are listed in Table A.8. These were utilized to compute adsorption energies of the nucleation process as listed in Table 4.7 in Section 4.3.1. In the case of the oxidized $7O^*$ + Pd_{10} and $7O^*$ + Pt_{10} clusters, the entropies of the O atoms in the gas phase were calculated for a temperature of 423.15 K. The slabs of the surface consist of 4 layers in this case. The two lower layers are fixed, while the two upper layers used for surface calculations ware allowed to relax.

Table A.8.: The total energies calculated by structure optimization at 0 K in eV for adsorption energies E_{ads} of noble metal atoms from the gas phase forming Pd_{10} or Pt_{10} subnanometer clusters plotted against the number of $Pd_{nuc.}$ or $Pt_{nuc.}$ atoms as shown in Figure 4.19. E_{total}(IS) is the species before the adsorption and E_{total}(FS) after the adsorption.

	E_{total}(IS) [eV]	E_{total}(FS) [eV]
Adsorption of Pd_{10} onto Pd^{+IV}		
$2O^*$ + $1Pd_1$ + Pd_{10} + $1V_{Ce}$	-2588	-2601
$2O^*$ + $2Pd_1$ + Pd_{10} + $2V_{Ce}$	-2577	-2593
$2O^*$ + $3Pd_1$ + Pd_{10} + $3V_{Ce}$	-2567	-2583
Adsorption of Pt_{10} onto Pt^{+IV}		
$2O^*$ + $1Pt_1$ + Pt_{10} + $1V_{Ce}$	-2589	-2612
$2O^*$ + $2Pt_1$ + Pt_{10} + $2V_{Ce}$	-2580	-2605
$2O^*$ + $3Pt_1$ + Pt_{10} + $3V_{Ce}$	-2571	-2597
Adsorption of Pd_{10} onto Pd^0		
$1Pd_1$ + Pd_{10} + $1V_{Ce}$	-2581	-2591
$2Pd_1$ + Pd_{10} + $2V_{Ce}$	-2563	-2572
$3Pd_1$ + Pd_{10} + $3V_{Ce}$	-2544	-2556
Adsorption of Pt_{10} onto Pt^0		
$1Pt_1$ + Pt_{10} + $1V_{Ce}$	-2582	-2602
$2Pt_1$ + Pt_{10} + $2V_{Ce}$	-2565	-2583
$3Pt_1$ + Pt_{10} + $3V_{Ce}$	-2547	-2569
Adsorption of $7O^*$ + Pd_{10} onto Pd^{+IV}		
$1Pd_1$ + $7O^*$ + Pd_{10} + $1V_{Ce}$	-2588	-2632
$2Pd_1$ + $7O^*$ + Pd_{10} + $2V_{Ce}$	-2577	-2622
$3Pd_1$ + $7O^*$ + Pd_{10} + $3V_{Ce}$	-2567	-2614
Adsorption of $7O^*$ + Pt_{10} onto Pt^{+IV}		
$1Pt_1$ + $7O^*$ + Pt_{10} + $1V_{Ce}$	-2589	-2642
$2Pt_1$ + $7O^*$ + Pt_{10} + $2V_{Ce}$	-2580	-2635
$3Pt_1$ + $7O^*$ + Pt_{10} + $3V_{Ce}$	-2571	-2627
Adsorption of $7O^*$ + Pd_{10} onto Pd^0		
$1Pd_1$ + $7O^*$ + Pd_{10} + $1V_{Ce}$	-2581	-2622
$2Pd_1$ + $7O^*$ + Pd_{10} + $2V_{Ce}$	-2563	-2605
$3Pd_1$ + $7O^*$ + Pd_{10} + $3V_{Ce}$	-2544	-2587
Adsorption of $7O^*$ + Pt_{10} onto Pt^0		
$1Pt_1$ + $7O^*$ + Pt_{10} + $1V_{Ce}$	-2582	-2632
$2Pt_1$ + $7O^*$ + Pt_{10} + $2V_{Ce}$	-2565	-2616
$3Pt_1$ + $7O^*$ + Pt_{10} + $3V_{Ce}$	-2547	-2599

A.9. Atom Energy, integral Heat of Adsorption of Pd and Pt Clusters supported on Ceria and Charge Transfer forming Ce^{+III} Cations

The total energies in Table A.9 for Pd and A.10 for Pt are computed by the subnanometer clusters supported on the (111) surface of ceria, increasing in size from 1 atom to 61 atoms and categorized into shape classes as shown in Section 4.3.2. The total energies are utilized to compute the atom energy E_{atom} of each Pd bulk atom for different cluster shapes plotted against the cluster size shown in Figure 4.22 in Section 4.3.3, the integral heat of adsorption E_{heat} plotted against increasing cluster size as shown in Figure 4.23 in Section 4.3.4 and the quotient formed by the number of formed Ce^{+III} cations per number of interface noble metal atoms q_{chg}, plotted against cluster size shown in Figure 4.26 in Section 4.3.5.

Table A.9.: The total energies calculated by structure optimization at 0 K in eV for Pd subnanometer clusters in varying sizes as shown in Figure 4.20 in Section 4.3.2 and the atom energy E_{atom}, the integral heat of adsorption E_{heat}, the number of noble metal atoms at the interface to ceria n_{int}, and the number of reduced Ce ions Ce^{+III} induced by charge transfer for Pd subnanometer cluster.

Pd cluster	E_{total} [eV]	E_{atom} [eV]	E_{heat} [eV]	n_{int}	Ce^{+III}	q_{chg}
Extended ceria surface						
$CeO_2(111)$	-1278.64					
Pd_1	-1278.76	1.84	-1.38	1	1	1.00
Pd_2	-1279.30	1.64	-1.58	2	2	1.00
Pd_3	-1280.61	1.31	-1.91	3	2	0.67
Flower						
Pd_4	-1281.63	1.22	-2.00	3	1	0.33
Pd_{10}	-1290.36	0.80	-2.42	7	4	0.57
Pd_{11}	-1290.43	0.90	-2.32	7	4	0.57
Pd_{19}	-1302.07	0.73	-2.48	12	4	0.33
Pd_{24}	-1307.98	0.75	-2.47	12	5	0.42
Flakes						
Pd_{25}	-1309.23	0.74	-2.47	12	4	0.33
Pd_{26}	-1310.77	0.73	-2.49	13	4	0.31
Pd_{30}	-1316.45	0.71	-2.51	12	5	0.42
Triangle						
Pd_9	-1288.68	0.85	-2.37	6	3	0.50
Pd_{10}	-1289.47	0.88	-2.33	6	2	0.33
Pd_{16}	-1297.45	0.79	-2.43	10	3	0.30
Pd_{19}	-1301.03	0.79	-2.43	10	5	0.50
Pd_{25}	-1309.23	0.74	-2.47	15	5	0.33
Pd_{31}	-1317.43	0.72	-2.50	15	5	0.33
Pd_{36}	-1326.15	0.65	-2.57	21	6	0.29
Pd_{46}	-1341.28	0.61	-2.61	21	7	0.33

Heart						
Pd_{13}	-1293.53	0.82	-2.40	7	4	0.57
Pd_{22}	-1305.81	0.69	-2.53	12	5	0.42
Pd_{28}	-1311.92	0.78	-2.44	12	5	0.42
Pd_{33}	-1321.06	0.68	-2.54	18	6	0.33
Pd_{43}	-1335.88	0.64	-2.58	18	6	0.33
Pd_{61}	-1364.23	0.56	-2.65	25	7	0.28
Pyramid						
Pd_{30}	-1316.86	0.69	-2.53	18	6	0.33
Pd_{37}	-1326.94	0.66	-2.56	18	6	0.33
Pd_{43}	-1336.65	0.62	-2.60	25	6	0.24
Pd_{55}	-1355.74	0.57	-2.65	25	7	0.28
Balls						
Pd_{24}	-1306.79	0.79	-2.42	12	5	0.42
Pd_{30}	-1315.20	0.75	-2.47	18	5	0.28
Pd_{31}	-1316.71	0.74	-2.48	12	5	0.42
Pd_{34}	-1320.84	0.73	-2.49	12	5	0.42

Table A.10.: Total energies calculated by structure optimization at 0 K in eV for Pt subnanometer clusters in varying sizes as shown in Figure 4.21 in Section 4.3.2 and the atom energy E_{atom}, the integral heat of adsorption E_{heat}, the number of noble meal aotoms at the interface to ceria n_{int}, and the number of reduced Ce ions Ce^{+III} induced by charge transfer for Pt subnanometer cluster.

Pt cluster	E_{total} [eV]	E_{atom} [eV]	E_{heat} [eV]	n_{int}	Ce^{+III}	q_{chg}
Extended ceria surface						
$CeO_2(111)$	-1278.64					
Pt_1	-1279.25	2.50	-2.85	1	1	1.00
Pt_2	-1281.00	1.92	-3.42	2	2	1.00
Pt_3	-1282.94	1.67	-3.67	3	2	0.67
Flower						
Pt_4	-1285.74	1.33	-4.01	3	1	0.33
Pt_{10}	-1299.41	1.03	-4.31	7	4	0.57
Pt_{11}	-1300.83	1.09	-4.25	7	4	0.57
Pt_{19}	-1320.38	0.91	-4.43	12	4	0.33
Pt_{24}	-1332.10	0.88	-4.46	12	5	0.42
Flakes						
Pt_{25}	-1332.93	0.93	-4.41	12	3	0.25
Pt_{26}	-1336.47	0.88	-4.46	13	4	0.31
Pt_{30}	-1345.90	0.86	-4.48	10	3	0.30
Triangle						
Pt_9	-1297.52	1.01	-4.33	6	4	0.67
Pt_{10}	-1298.34	1.14	-4.21	6	2	0.33
Pt_{16}	-1313.10	0.95	-4.39	10	4	0.40
Pt_{19}	-1321.00	0.88	-4.47	10	5	0.50
Pt_{25}	-1334.97	0.85	-4.49	15	7	0.47
Pt_{31}	-1349.94	0.81	-4.54	15	8	0.53
Pt_{36}	-1363.08	0.76	-4.58	21	6	0.29
Pt_{46}	-1390.02	0.68	-4.66	21	7	0.33

Heart						
Pt_{13}	-1306.08	0.99	-4.35	7	4	0.57
Pt_{22}	-1327.50	0.88	-4.46	12	5	0.42
Pt_{28}	-1339.40	0.94	-4.41	12	5	0.42
Pt_{33}	-1354.29	0.81	-4.53	18	6	0.33
Pt_{43}	-1380.55	0.74	-4.61	18	7	0.39
Pt_{61}	-1428.17	0.65	-4.69	25	7	0.28
Pyramid						
Pt_{30}	-1346.28	0.85	-4.49	18	6	0.33
Pt_{37}	-1363.77	0.80	-4.54	18	7	0.39
Pt_{43}	-1380.41	0.74	-4.60	25	6	0.24
Pt_{55}	-1412.36	0.67	-4.67	25	7	0.28
Balls						
Pt_{24}	-1327.94	1.05	-4.29	12	5	0.42
Pt_{30}	-1343.51	0.94	-4.40	18	5	0.28
Pt_{31}	-1344.65	0.98	-4.37	12	5	0.42
Pt_{34}	-1352.93	0.92	-4.42	12	5	0.42

A.10. Reducibility of the Ceria Surface at the Interface to Pd_{10} and Pt_{10}

The total energies in Table A.11 were used to compute the desorption energies $G_{des}(O)$ of individual O atoms, as depicted in Figure 4.5 in Section 4.3.6. The slabs of the surface consist of 4 layers in this case. The two lower layers are fixed, while the two upper layers used for surface calculations were allowed to relax.

Table A.11.: The total energies calculated by structure optimization at 0 K in eV for structure-optimized configurations as shown in Figure 4.28 for the Pd cluster and 4.29 for the Pt cluster and as shown in Figure 4.30 for the Pd cluster and 4.31 for the Pt cluster.

	E_{total} [eV]	$G_{des}(O)$ [eV]
$CeO_2(111)$		
stoichiometric	-2598.51	
$1V_O$	-2593.80	0.42
$2V_O$	-2588.70	0.61
$3V_O$	-2583.82	0.61
$4V_O$	-2578.77	0.64
$5V_O$	-2573.46	0.72
$6V_O$	-2568.12	0.77
$7V_O$	-2563.76	0.67
Pd_{10}, nn		
stoichiometric	-2610.61	
$1V_O$	-2605.20	1.12
$2V_O$	-2599.54	1.24
$3V_O$	-2593.71	1.34
$4V_O$	-2587.83	1.40
$5V_O$	-2581.94	1.44
$6V_O$	-2575.67	1.53
$7V_O$	-2570.99	1.37

Pt_{10}, nn		
stoichiometric	-2619.19	
$1V_O$	-2614.06	0.84
$2V_O$	-2608.32	1.14
$4V_O$	-2596.95	1.27
$6V_O$	-2584.29	1.56
$7V_O$	-2579.44	1.39
Pd_{10}, sub		
stoichiometric	-2610.61	
$1V_O$	-2605.35	0.96
$2V_O$	-2600.32	0.85
$3V_O$	-2594.92	0.94
$4V_O$	-2589.97	0.87
$5V_O$	-2584.83	0.86
$6V_O$	-2579.32	0.92
Pt_{10}, sub		
stoichiometric	-2619.19	
$1V_O$	-2614.12	0.79
$2V_O$	-2609.00	0.80
$3V_O$	-2603.54	0.93
$4V_O$	-2598.53	0.87
$5V_O$	-2593.50	0.85
$6V_O$	-2587.80	0.94

A.11. CO Adsorption on Pd_3 or Pt_3 subnanometer Cluster

Table A.12.: The total energies calculated by structure optimization at 0 K in eV including ZPE and S of the averaged vibrational modes calculated for all adsorbed CO molecules for the calculation of full coverage with a total of 4 CO molecules adsorbed on the Pd_3 and Pt_3 clusters as shown in Figure 5.9 for the Pd_3 cluster and in Figure 5.10 for the Pt_3 cluster.

	E_{total} [eV]	ZPE [eV]	S [eV/T]
CO adsorption on the Pd_3/CeO_2 cluster			
stoichiometric	-1279.04		
$1CO^*$	-1293.53	0.210	3.57E-04
$2CO^*$	-1306.90	0.196	3.92E-04
$3CO^*$	-1320.00	0.195	2.99E-04
$4CO^*$	-1332.54	0.185	3.64E-04
CO adsorption on the Pt_3/CeO_2 cluster			
stoichiometric	-1281.67		
$1CO^*$	-1296.49	0.230	3.00E-04
$2CO^*$	-1310.01	0.213	2.41E-04
$3CO^*$	-1323.17	0.210	2.79E-04
$4CO^*$	-1336.19	0.206	2.52E-04

The total energies in Table A.12 were utilized to compute differential energies of structure-optimized Pd_3 and the Pt_3 cluster adsorbed on a $CeO_2(111)$ surface with the successive CO molecule adsorption ranging from 1 to 4 molecules is plotted against the number of adsorbed CO atoms as illustrated in Figure 5.11 and, in Figure 5.12, respectively, as listed in Table 5.2 in Section 5.2.1 or Pt_3 cluster.

A.12. O Adsorption on Pd_{10} and Pt_{10} subnanometer Cluster

The total energies in Table A.13 were utilized to compute differential energies of structure-optimized Pd_{10} and Pt_{10} clusters adsorbed on a $CeO_2(111)$ surface with a successive O atom adsorption ranging from 1 to 7 atoms is plotted against the number of adsorbed O atoms as illustrated in Figure 5.25 and in Figure 5.26, respectively, as listed in Table 5.25 in Section 5.4.

Table A.13.: The total energies calculated by structure optimization at 0 K in eV including ZPE and S of the averaged vibrational modes calculated for all adsorbed O atoms for the calculation of full coverage with a total of 7 O atoms adsorbed on the Pd_{10} and Pt_{10} clusters as shown in Figure 5.23 for the Pd_{10} cluster and in Figure 5.24 for the Pt_{10} cluster.

	E_{total} [eV]	ZPE [eV]	S [eV/T]
O adsorption on the Pd_{10}/CeO_2 cluster			
stoichiometric	-1288.96		
$1O^*$	-1292.85	0.033	3.02E-04
$2O^*$	-1297.42	0.064	1.02E-04
$3O^*$	-1302.55	0.074	8.25E-05
$4O^*$	-1307.18	0.074	8.22E-05
$5O^*$	-1312.14	0.080	7.27E-05
$6O^*$	-1316.40	0.080	7.53E-05
$7O^*$	-1320.86	0.081	7.40E-05
O adsorption on the Pt_{10}/CeO_2 cluster			
stoichiometric	-1297.54		
$1O^*$	-1301.86	0.042	2.23E-04
$2O^*$	-1306.74	0.064	1.08E-04
$3O^*$	-1311.66	0.073	9.35E-05
$4O^*$	-1316.19	0.073	8.97E-05
$5O^*$	-1321.54	0.081	7.34E-05
$6O^*$	-1325.80	0.083	7.26E-05
$7O^*$	-1331.16	0.073	8.95E-05

A.13. CO Adsorption on Pd_{10} and Pt_{10} Cluster

The total energies in Table A.14 were utilized to compute differential energies of structure-optimized Pd_{10} and Pt_{10} clusters adsorbed on a $CeO_2(111)$ surface with a successive CO molecule adsorption ranging from 1 to 12 molecules is plotted against the number of adsorbed CO atoms as illustrated in Figure 5.16 and in Figure 5.17, respectively, as listed in Table 5.4 in Section 5.3.

Table A.14.: The total energies calculated by structure optimization at 0 K in eV including ZPE and S of the averaged vibrational modes calculated for all adsorbed CO molecules for the calculation of full coverage with a total of 12 CO molecules adsorbed on the Pd_{10} and Pt_{10} clusters as shown in Figure 5.14 for the Pd_{10} cluster and in Figure 5.15 for the Pt_{10} cluster.

	E_{total} [eV]	ZPE [eV]	S [eV/T]
CO adsorption on the Pd_{10}/CeO_2 cluster			
stoichiometric	-1290.36		
CO^*	-1304.21	0.198	5.66E-04
$2CO^*$	-1317.97	0.203	4.52E-04
$3CO^*$	-1331.57	0.202	4.96E-04
$4CO^*$	-1345.40	0.200	4.42E-04
$5CO^*$	-1359.05	0.200	4.17E-04
$6CO^*$	-1372.59	0.198	5.12E-04
$7CO^*$	-1385.82	0.200	4.77E-04
$8CO^*$	-1398.35	0.198	4.72E-04
$9CO^*$	-1410.80	0.198	5.23E-04
$10CO^*$	-1423.26	0.192	5.17E-04
$11CO^*$	-1435.68	0.196	4.84E-04
$12CO^*$	-1448.28	0.210	4.84E-04
CO adsorption on the Pt_{10}/CeO_2 cluster			
stoichiometric	-1299.41		
CO^*	-1313.73	0.211	4.24E-04
$2CO^*$	-1328.00	0.211	4.47E-04
$3CO^*$	-1341.99	0.217	4.55E-04
$4CO^*$	-1355.76	0.221	4.40E-04
$5CO^*$	-1369.25	0.218	3.84E-04
$6CO^*$	-1383.06	0.221	4.63E-04
$7CO^*$	-1397.32	0.222	4.50E-04
$8CO^*$	-1410.03	0.219	4.39E-04
$9CO^*$	-1423.42	0.220	4.46E-04
$10CO^*$	-1435.25	0.212	4.69E-04
$11CO^*$	-1448.77	0.214	4.85E-04
$12CO^*$	-1461.21	0.210	4.85E-04

A.14. Correlation of Oxidation State and CO stretching Vibrational Frequency

The total energies in Table A.15 were calculated by structure optimization structure-optimized Pd_1 and Pt_1 single-atom catalysts with one CO molecule adsorbed varying ceria surface facets (100), (110) and (111) given in 4.5 for Pd and 4.6 for Pt and plotted in Figure 5.13 in Section 5.2.2.

Table A.15.: The total energies, vibrational frequencies, and Bader charges were calculated through structure optimization at 0 K in eV for the spectroscopic data obtained through DFT calculations.

	$E_{total}(M_1)$ [eV]	$E_{total}(CO_{adsorbed})$ [eV]	Bader Charge Analysis
Pd_1/V_{Ce}-CeO_2(100)			
$2V_O$	-270.84	-284.06	10.60
$1V_O$	-276.72	-291.21	10.07
stoichiometric	-281.93	-295.32	9.56
O^*	-285.96	-299.79	9.20
$2O^*$	-290.38		8.82
Pt_1/V_{Ce}-CeO_2(100)			
$2V_O$	-272.10	-285.43	11.08
$1V_O$	-277.48	-292.84	10.20
stoichiometric	-283.53	-296.82	9.46
O^*	-286.77	-301.42	9.23
$2O^*$	-292.02	-304.44	8.66
Pd_1/V_{Ce}-CeO_2(110)			
$2V_O$	-276.52	-289.77	10.83
$1V_O$	-282.93	-297.61	10.15
stoichiometric	-287.94	-301.92	9.63
O^*	-292.46	-306.35	9.02
$2O^*$	-295.67	-308.62	8.76
Pt_1/V_{Ce}-CeO_2(110)			
$2V_O$	-278.12	-291.11	11.16
$1V_O$	-283.68	-299.22	10.29
stoichiometric	-289.59	-303.01	9.50
O^*	-293.27	-307.75	9.10
$2O^*$	-297.25	-310.77	8.66
Pd_1/V_{Ce}-CeO_2(111)			
$2V_O$	-277.81	-292.71	10.06
$1V_O$	-283.66	-297.94	10.00
stoichiometric	-288.92	-302.82	9.78
O^*	-292.70	-305.94	9.02
$2O^*$	-295.60	-307.73	8.75
Pt_1/V_{Ce}-CeO_2(111)			
$2V_O$	-278.30	-294.24	10.52
$1V_O$	-284.17	-299.32	10.12
stoichiometric	-289.81	-303.96	9.61
O^*	-293.58	-307.63	8.97
$2O^*$	-297.52	-309.92	8.55

A.15. Vibrational Frequencies of adsorbed CO Molecules on Pd_3 and Pt_3

The total energies in Table A.16 were calculated by structure optimization structure-optimized Pd_3 and Pt_3 subnanometer cluster covered by CO molecules ranging from 1 to 4 CO molecules. The computed intensities and vibrational frequencies are plotted in Figure 5.13 in Section 5.2.2.

Table A.16.: The total energies, vibrational frequencies, and Bader charges were calculated through structure optimization at 0 K in eV of the structures given in Figure 5.9 for the Pd_3 cluster and in Figure 5.10 for the Pt_3 cluster in Section 5.2.1. The CO molecules can adsorb on ontop (o), bridge (b), and hollow (h) sites.

Pd_3 and Pt_3 cluster									
Pd_3					Pt_3				
nCO^*	E_{total}	coord.	f [cm^{-1}]	I [amu^{-1}]	nCO^*	E_{total}	coord.	f [cm^{-1}]	I [amu^{-1}]
$1CO^*$	-1293.53	o	2044	29.3	1	-1296.49	o	2053	32.9
$2CO^*$	-1306.90	b	1876	15.4	2	-1310.01	b	1850	16.0
		o	2039	14.5			o	2029	16.5
$3CO^*$	-1320.00	h	1882	15.0	3	-1323.17	b	1835	15.8
		o	2035	0.0			o	2029	4.4
		o	2048	20.0			o	2043	16.6
$4CO^*$	-1332.54	b	1847	11.1	4	-1336.19	b	1845	13.17
		o	2029	3.7			o	2018	1.02
		o	2045	0.0			o	2028	2.04
		o	2055	24.6			o	2041	19.91

A.16. Vibrational Frequencies of adsorbed CO Molecules on Pd_{10} and Pt_{10}

The total energies in Table A.17 and continued in A.18 were calculated by structure optimization structure-optimized Pd_{10} and Pt_{10} subnanometer cluster covered by CO molecules ranging from 1 to 12 molecules. The computed intensities and vibrational frequencies are plotted in Figure 5.18, 5.19, 5.20 and 5.21 in Section 5.3.1. These total energies were utilized to calculate the differential Gibbs free energies and phase diagrams as shown in Figure 5.16 and 5.17, respectively. The total energies are utilized to compute the atom energy E_{atom} of each Pd bulk atom for different cluster shapes plotted against the cluster size shown in Figure 4.22 in Section 4.3.3, the integral heat of adsorption E_{heat} plotted against increasing cluster size as shown in Figure 4.23 in Section 4.3.4 and the quotient formed by the number of formed Ce^{+III} cations per number of interface noble metal atoms q_{chg}, plotted against cluster size shown in Figure 4.26 in Section 4.3.5.

Table A.17.: The total energies, vibrational frequencies, and Bader charges were calculated through structure optimization at 0 K in eV of the structures given in Figure 5.14 for the (1-12)O^* + Pd_{10} cluster and in Figure 5.15 for the (1-12)O^* + Pt_{10} cluster in Section 5.3. The CO molecules can adsorb on ontop (o), bridge (b), and hollow (h) sites.

CO vibrational frequencies									
Pd_{10}					Pt_{10}				
nCO^*	E_{total}	coord.	f [cm^{-1}]	I [amu^{-1}]	nCO^*	E_{total}	coord.	f [cm^{-1}]	I [amu^{-1}]
$1CO^*$	-1304.21	b	1881	17.44	$1CO^*$	-1313.73	b	1854	18.01
$2CO^*$	-1317.97	b	1882	1.44	$2CO^*$	-1328.00	b	1852	0.89
		b	1887	33.87			b	1857	34.06
$3CO^*$	-1331.57	b	1878	8.88	$3CO^*$		b	1858	9.47
		b	1890	1.29			b	1873	27.76
		b	1907	34.65			o	2045	19.18
$4CO^*$	-1345.40	h	1787	11.73	$4CO^*$	-1355.76	b	1866	10.70
		b	1861	8.03			b	1874	19.97
		b	1899	10.46			o	2010	15.96
		b	1918	24.68			o	2041	29.42
$5CO^*$	-1359.05	h	1761	9.52	$5CO^*$	-1369.25	h	1851	12.99
		b	1863	8.25			b	1868	5.75
		b	1890	4.13			b	1874	18.43
		b	1900	1.29			b	2020	8.02
		b	1917	40.25			b	2023	32.58
$6CO^*$	-1372.59	h	1819	14.91	$6CO^*$	-1370.63	h	1794	12.24
		b	1904	8.55			b	1895	16.88
		b	1918	0.17			b	2027	1.00
		b	1930	11.00			b	2031	7.82
		b	1931	15.51			b	2040	1.34
		b	1957	33.98			b	2054	66.79
$7CO^*$	-1385.82	h	1851	13.06	$7CO^*$	-1397.32	h	1793	9.26
		b	1919	0.37			b	1889	14.87
		b	1926	2.68			b	2019	5.42
		b	1931	1.05			b	2032	1.44
		b	1941	11.67			b	2038	12.64
		b	1949	0.79			b	2044	0.26
		b	1960	72.21			b	2060	72.04
$8CO^*$	-1398.35	b	1885	3.52	$8CO^*$	-1410.03	h	1785	10.66
		b	1902	9.89			b	1889	5.82
		b	1910	0.04			b	1984	2.91
		b	1933	9.53			o	2005	7.34
		b	1940	17.11			o	2030	10.17
		b	2033	10.53			o	2033	31.81
		o	2048	0.21			o	2044	2.84
		o	2054	54.77			o	2052	50.71

Table A.18.: The total energies, vibrational frequencies, and Bader charges were calculated through structure optimization at 0 K in eV of the structures given in Figure 5.23 for the Pd_{10} cluster and in Figure 5.24 for the Pt_{10} cluster in Section 5.3.1. The CO molecules can adsorb on ontop (o), bridge (b), and hollow (h) sites.

CO vibrational frequencies									
Pd_{10}					Pt_{10}				
nCO*	E_{total}	coord.	f [cm^{-1}]	I [amu^{-1}]	nCO*	E_{total}	coord.	f [cm^{-1}]	I [amu^{-1}]
9CO*	-1410.80	b	1894	2.88	9CO*	-1423.42	b	1828	5.07
		b	1902	0.89			b	1866	6.60
		b	1909	1.84			o	2012	3.11
		b	1926	0.02			o	2017	3.64
		b	1930	25.52			o	2028	2.24
		o	2031	4.48			o	2034	0.39
		o	2038	7.72			o	2043	3.84
		o	2060	18.90			o	2052	1.03
		o	2072	56.49			o	2064	113.84
10CO*	-1423.26	h	1816	0.66	10CO*	-1435.25	b	1862	24.84
		h	1826	23.10			o	1992	0.27
		b	1896	2.77			o	2010	0.15
		b	1907	5.91			o	2019	5.35
		b	1928	7.14			o	2020	0.11
		o	2033	0.42			o	2024	7.17
		o	2037	0.51			o	2032	0.21
		o	2054	3.14			o	2046	10.32
		o	2067	0.51			o	2064	0.75
		o	2073	65.31			o	2074	84.89
11CO*	-1435.68	h	1824	5.25	11CO*	-1448.77	b	1819	0.53
		b	1907	0.10			b	1844	17.04
		b	1912	1.36			o	2008	2.48
		b	1924	18.38			o	2020	0.43
		o	2013	3.33			o	2020	3.31
		o	2032	1.12			o	2028	4.35
		o	2043	0.11			o	2039	3.46
		o	2046	1.32			o	2040	0.24
		o	2050	5.17			o	2055	14.25
		o	2054	6.08			o	2073	0.79
		o	2084	29.57			o	2080	73.26
12CO*	-1448.28	b	1848	6.10	12CO*	-1461.21	h	1773	14.73
		b	1868	4.90			b	1850	3.66
		b	1903	15.03			o	2003	0.73
		o	1924	0.53			o	2016	0.29
		o	2018	1.13			o	2028	1.93
		o	2028	0.12			o	2030	1.67
		o	2030	0.23			o	2036	0.76
		o	2046	3.63			o	2043	5.04
		o	2050	4.73			o	2049	1.79
		o	2054	0.00			o	2053	0.00
		o	2063	19.04			o	2063	75.75
		o	2077	65.93			o	2088	24.16

Table A.19.: Total energies and spectroscopic data of the structure-optimized mono- and dimer Pd and Pt species with two or three co-adsorbed CO molecules forming adsorbed carbonyl species and gas phase species as shown in Figure 5.22 in Section 5.3.

	$E_{total}(CO_{ads})$ [eV]	f [cm^{-1}]	I [amu^{-1}]	$E_{total}(CO_{(g)})$ [eV]	f [cm^{-1}]	I [amu^{-1}]
Pd						
$2CO^{*}$ + $Pd_1/CeO_2(111)$	-1303.84	2005	0.03	-26.27	2021	0.32
		2033	19.46		2085	0.76
$3CO^{*}$ + $Pd_2/CeO_2(111)$	-1318.33	1867	17.19	-40.27	1906	2.74
		2029	0.01		2035	0.44
		2038	26.71		2058	0.64
Pt						
$2CO^{*}$ + $Pt_1/CeO_2(111)$	-1305.08	1988	0.16	-27.53	2016	0.33
		2022	18.82		2099	0.71
$3CO^{*}$ + $Pt_2/CeO_2(111)$	-1320.86	1814	15.04	-42.58	1886	2.49
		2019	0.00		2037	0.35
		2032	24.23		2062	0.84

A.17. Validation of Sizes and Shapes of subnanometer Cluster

The total energies in Table A.20 were calculated by structure optimization of the Pd_3, Pd_{19}, Pd_{30}, $Pd_{30,fcc}$ and $Pd_{30,hcp}$ subnanometer cluster. The computed intensities and vibrational frequencies are plotted in Figure 5.18, 5.19, 5.20 and 5.21 in Section 5.4.

Table A.20.: The total energies were calculated through structure optimization at 0 K in eV of the structures given in Figure 5.27 in Section 5.5.

Pd Subnanometer Cluster				
Pd_3	Pd_{19}	Pd_{30}	$Pd_{30}O_{15,fcc}$	$Pd_{30}O_{13,,hcp}$
-1268.38	-1290.49	-1305.34	-1372.28	-1359.35

A.18. CO Molecules adsorbed on the Extended Pd and Pt surface facets

The total energies in Table A.21 were calculated by structure optimization structure-optimized Pd and Pt surface facets (111), (110), (100), and (211) covered by one CO molecule in one unit cell. The computed intensities and vibrational frequencies are plotted in Figure 5.32 and the vibrational frequencies are plotted against the adsorption energies as shown in Figure 5.33 in Section 5.6.

Table A.21.: Spectroscopic data obtained through DFT calculations. The species under investigation here refer to the structures of pristine metal surfaces given in 5.30 for Pd and 5.31 for Pt in Section 5.6 The CO molecules can adsorb on ontop, bridge, and hollow sites.

	$E_{total}(CO_{ads})$ [eV]	$E_{total}(CO_g)$ [eV]
	Pd_{10}	Pt_{10}
CO Molecules adsorbed on extended Pd and Pt surfaces		
(111)	-26.57	-44.22
(110)	-53.64	-88.42
(100)	-25.22	-42.48
(211)	-39.47	-66.52
CO^* adsorbed on the (111) facet		
ontop	-39.79	-57.99
bridge	-40.17	-
hollow	-40.31	-58.05
CO^* adsorbed on the (110) facet		
ontop	-67.07	-102.48
bridge	-67.39	-102.42
hollow	-67.38	-
CO^* adsorbed on the (100) facet		
ontop	-38.58	-56.16
bridge	-39.12	-56.24
hollow	-38.89	-55.68
CO^* adsorbed on the (211) facet		
ontop	-53.04	-80.19
bridge	-53.37	-80.20
hollow	-53.35	-

A.19. O_2 Dissociation on $Pd_1{}^0$ and $Pt_1{}^0$ via LH Mechanism

The total energies in Table A.22 were calculated by structure optimization of the reaction mechanism of an O_2 dissociation on Pd_1 and Pt_1 single-atom catalysts adsorbed on the stoichiometric (111), (110) and (100) ceria surface facets. The total energies are utilized to calculate the Gibbs free energy diagrams in Figure 6.3 and listed in Table 6.10 in Section 6.1.1.

Table A.22.: The total energies were calculated through structure optimization at 0 K in eV of the structures given in Figure 6.1 for Pd_1 and in Figure 6.2 for Pt_1 single-atom catalysts in Section 6.1.1 in eV including ZPE and S of the reactants.

	E_{total} [eV]	ZPE [eV]	S [eV/T]
O_2 Dissociation on $Pd_1{}^0$ and $Pt_1{}^0$			
$Pd_1/CeO_2(100)$	-281.93	0.067	9.63E-05
$Pd_1/CeO_2(110)$	-287.94	0.063	1.06E-04
$Pd_1/CeO_2(111)$	-288.92	0.054	1.22E-04
$Pt_1/CeO_2(100)$	-283.53	0.069	1.16E-04
$Pt_1/CeO_2(110)$	-289.59	0.074	9.14E-05
$Pt_1/CeO_2(111)$	-289.81	0.059	1.22E-04
O_2 Adsorption			
$O_2{}^*$ + $Pd_1/CeO_2(100)$	-289.51	0.200	5.00E-04
$O_2{}^*$ + $Pd_1/CeO_2(110)$	-296.32	0.199	5.09E-04
$O_2{}^*$ + $Pd_1/CeO_2(111)$	-297.08	0.191	3.91E-04
$O_2{}^*$ + $Pt_1/CeO_2(100)$	-290.89	0.208	4.09E-04
$O_2{}^*$ + $Pt_1/CeO_2(110)$	-297.17	0.199	4.88E-04
$O_2{}^*$ + $Pt_1/CeO_2(111)$	-297.74	0.197	5.17E-04
Transition states			
O-O-$Pd_1/CeO_2(100)^‡$	-288.09	0.193	4.00E-04
O-O-$Pd_1/CeO_2(110)^‡$	-294.91	0.202	4.63E-04
O-O-$Pd_1/CeO_2(111)^‡$	-295.05	0.164	3.55E-04
O-O-$Pt_1/CeO_2(100)^‡$	-289.80	0.206	4.20E-04
O-O-$Pt_1/CeO_2(110)^‡$	-296.23	0.201	4.58E-04
O-O-$Pt_1/CeO_2(111)^‡$	-296.50	0.185	5.02E-04
Oxidized Species			
$2O^*$ + $Pd_1/CeO_2(100)$	-288.58	0.165	5.54E-04
$2O^*$ + $Pd_1/CeO_2(110)$	-296.14	0.192	3.69E-04
$2O^*$ + $Pd_1/CeO_2(111)$	-295.52	0.174	4.41E-04
$2O^*$ + $Pt_1/CeO_2(100)$	-290.63	0.195	4.44E-04
$2O^*$ + $Pt_1/CeO_2(110)$	-297.94	0.208	3.45E-04
$2O^*$ + $Pt_1/CeO_2(111)$	-297.56	0.188	4.53E-04

A.20. O_2 Dissociation on $1V_O$-$Pd_1^{-\delta}$ and $1V_O$-$Pt_1^{-\delta}$ via MvK Mechanism

The total energies in Table A.23 were calculated by structure optimization of the reaction mechanism of an O_2 dissociation on $1V_O$-Pd_1 and $1V_O$-Pt_1 single-atom catalysts adsorbed on the O defective $1V_O$ (111), (110) and (100) ceria surface facets. The total energies are utilized to calculate the Gibbs free energy diagrams in Figure 6.6 and listed in Table 6.2 in Section 6.1.2.

Table A.23.: The total energies were calculated through structure optimization at 0 K in eV of the structures given in Figure 6.4 for $1V_O$-Pd_1 and in Figure 6.5 for $1V_O$-Pt_1 single-atom catalysts in Section 6.1.2 in eV including ZPE and S of the reactants.

	E_{total} [eV]	ZPE [eV]	S [eV/T]
O_2 dissociation on $1V_O$-$Pd_1^{-\delta}$ and $1V_O$-$Pt_1^{-\delta}$			
$1V_O$-Pd_1/CeO_{2n-1}(100)	-276.72		
$1V_O$-Pd_1/CeO_{2n-1}(110)	-282.93		
$1V_O$-Pd_1/CeO_{2n-1}(111)	-283.66		
$1V_O$-Pt_1/CeO_{2n-1}(100)	-277.48		
$1V_O$-Pt_1/CeO_{2n-1}(110)	-283.68		
$1V_O$-Pt_1/CeO_{2n-1}(111)	-284.17		
O_2 adsorption			
$1O_2^*$ + $1V_O$-Pd_1/CeO_{2n-1}(100)	-285.91	0.140	2.93E-04
$1O_2^*$ + $1V_O$-Pd_1/CeO_{2n-1}(110)	-291.25	0.132	3.16E-04
$1O_2^*$ + $1V_O$-Pd_1/CeO_{2n-1}(111)	-292.58	0.131	2.50E-04
$1O_2^*$ + $1V_O$-Pt_1/CeO_{2n-1}(100)	-287.17	0.150	2.47E-04
$1O_2^*$ + $1V_O$-Pt_1/CeO_{2n-1}(110)	-292.38	0.147	2.78E-04
$1O_2^*$ + $1V_O$-Pt_1/CeO_{2n-1}(111)	-293.22	0.134	2.34E-04
Transition states of the O_2 dissociation			
[O-O-$1V_O$-Pd_1/CeO_{2n-1}(100)]‡	-284.97	0.116	3.29E-04
[O-O-$1V_O$-Pd_1/CeO_{2n-1}(110)]‡	-290.42	0.081	3.83E-04
[O-O-$1V_O$-Pd_1/CeO_{2n-1}(111)]‡	-291.96	0.089	2.56E-04
[O-O-$1V_O$-Pt_1/CeO_{2n-1}(100)]‡	-286.45	0.104	1.96E-04
[O-O-$1V_O$-Pt_1/CeO_{2n-1}(110)]‡	-291.75	0.095	2.43E-04
[O-O-$1V_O$-Pt_1/CeO_{2n-1}(111)]‡	-292.58	0.116	2.16E-04
Oxidized species			
$1O^*$ + Pd_1/CeO_2(100)	-285.94	0.123	2.83E-04
$1O^*$ + Pd_1/CeO_2(110)	-292.46	0.135	2.17E-04
$1O^*$ + Pd_1/CeO_2(111)	-292.70	0.118	2.58E-04
$1O^*$ + Pt_1/CeO_2(100)	-287.61	0.129	3.20E-04
$1O^*$ + Pt_1/CeO_2(110)	-293.58	0.135	2.41E-04
$1O^*$ + Pt_1/CeO_2(111)	-293.58	0.131	2.45E-04

A.21. CO Oxidation at $2O^* + Pd_1^{+IV}$ and $2O^* + Pt_1^{+IV}$ via LH Mechanism

The total energies in Table A.24 were calculated by structure optimization of the reaction mechanism of an CO oxidation on $2O^* + Pd_1^{+IV}$ and $2O^* + Pt_1^{+IV}$ single-atom catalysts adsorbed on the (111), (110) and (100) ceria surface facets. The total energies are utilized to calculate the Gibbs free energy diagrams in Figure 6.9 and listed in Table 6.3 in Section 6.1.3.

Table A.24.: The total energies were calculated through structure optimization at 0 K in eV of the structures given in Figure 6.7 for $2O^* + Pd_1^{+IV}$ and in Figure 6.8 for $2O^* + Pt_1^{+IV}$ single-atom catalysts in Section 6.1.3 in eV including ZPE and S of the reactants.

	E_{total} [eV]	ZPE [eV]	S [eV/T]
CO oxidation at $2O^* + Pd_1^{+IV}$ and $2O^* + Pt_1^{+IV}$			
$2O^* + Pd_1/CeO_2(100)$	-290.38	0.213	2.64E-04
$2O^* + Pd_1/CeO_2(110)$	-295.67	0.189	4.23E-04
$2O^* + Pd_1/CeO_2(111)$	-295.60	0.174	4.34E-04
$2O^* + Pt_1/CeO_2(100)$	-292.02	0.220	2.63E-04
$2O^* + Pt_1/CeO_2(110)$	-297.25	0.194	3.19E-04
$2O^* + Pt_1/CeO_2(111)$	-297.52	0.187	4.57E-04
CO adsorption			
$CO^* + 1O^* + Pd_{12}/CeO_2(100)$	sp.		
$CO^* + 1O^* + Pd_{12}/CeO_2(110)$	-308.62	0.385	6.44E-04
$CO^* + 1O^* + Pd_{12}/CeO_2(111)$	-307.73	0.363	7.30E-04
$CO^* + 1O^* + Pt_{12}/CeO_2(100)$	-304.44	0.423	6.70E-04
$CO^* + 1O^* + Pt_{12}/CeO_2(110)$	-310.77	0.416	7.08E-04
$CO^* + 1O^* + Pt_{12}/CeO_2(111)$	-309.92	0.406	7.06E-04
Transition states of the CO oxidation			
$1O^* + [CO\text{-}O\text{-}Pd_1/CeO_2(100)]^{\ddagger}$	sp.		
$1O^* + [CO\text{-}O\text{-}Pd_1/CeO_2(110)]^{\ddagger}$	-308.29	0.397	7.03E-04
$1O^* + [CO\text{-}O\text{-}Pd_1/CeO_2(111)]^{\ddagger}$	-307.63	0.453	8.45E-04
$1O^* + [CO\text{-}O\text{-}Pt_1/CeO_2(100)]^{\ddagger}$	sp.		
$1O^* + [CO\text{-}O\text{-}Pt_1/CeO_2(110)]^{\ddagger}$	-310.18	0.443	7.01E-04
$1O^* + [CO\text{-}O\text{-}Pt_1/CeO_2(111)]^{\ddagger}$	-309.68	0.467	8.90E-04
CO_2 adsorbed			
$CO_2^* + 1O^* + Pd_1/CeO_2(100)$	-305.15	0.469	7.16E-04
$CO_2^* + 1O^* + Pd_1/CeO_2(110)$	-310.24	0.430	7.50E-04
$CO_2^* + 1O^* + Pd_1/CeO_2(111)$	-311.49	0.444	7.48E-04
$CO_2^* + 1O^* + Pt_1/CeO_2(100)$	-306.01	0.480	6.90E-04
$CO_2^* + 1O^* + Pt_1/CeO_2(110)$	-311.59	0.450	7.01E-04
$CO_2^* + 1O^* + Pt_1/CeO_2(111)$	-312.38	0.446	7.62E-04
Reduced species			
$1O^* + Pd_1/CeO_2(100)$	-285.94	0.123	2.83E-04
$1O^* + Pd_1/CeO_2(110)$	-292.46	0.135	2.17E-04
$1O^* + Pd_1/CeO_2(111)$	-292.70	0.118	2.58E-04
$1O^* + Pt_1/CeO_2(100)$	-287.61	0.129	3.20E-04
$1O^* + Pt_1/CeO_2(110)$	-293.58	0.135	2.41E-04
$1O^* + Pt_1/CeO_2(111)$	-293.58	0.131	2.45E-04

A.22. CO Oxidation at Pd_1^{+II} and Pt_1^{+II} via MvK Mechanism

The total energies in Table A.25 were calculated by structure optimization of the reaction mechanism of the CO oxidation on $1O^* + Pd_1^{+II}$ and $1O^* + Pt_1^{+II}$ single-atom catalysts adsorbed on the (111), (110) and (100) ceria surface facets. The total energies are utilized to calculate the Gibbs free energy diagrams in Figure 6.12 and listed in Table 6.4 in Section 6.1.4.

Table A.25.: The total energies were calculated through structure optimization at 0 K in eV of the structures given in Figure 6.10 for $1O^* + Pd_1^{+II}$ and in Figure 6.11 for $1O^* + Pt_1^{+II}$ single-atom catalysts in Section 6.1.4 in eV including ZPE and S of the reactants.

	E_{total} [eV]	ZPE [eV]	S [eV/T]
CO oxidation at Pd_1^0 and Pt_1^{+II}			
$1O^* + Pd_1/CeO_2(100)$	-285.96	0.135	1.84E-04
$1O^* + Pd_1/CeO_2(110)$	-292.42	0.138	2.01E-04
$1O^* + Pd_1/CeO_2(111)$	-292.70	0.118	2.58E-04
$1O^* + Pt_1/CeO_{2n}(100)$	-286.77	0.136	1.86E-04
$1O^* + Pt_1/CeO_{2n}(110)$	-293.27	0.131	3.40E-04
$1O^* + Pt_1/CeO_{2n}(111)$	-293.58	0.131	2.45E-04
CO adsorption			
$CO^* + 1O^* + Pd_1/CeO_2(100)$	-299.79	0.354	3.59E-04
$CO^* + 1O^* + Pd_1/CeO_2(110)$	-306.35	0.358	5.36E-04
$CO^* + 1O^* + Pd_1/CeO_2(111)$	-305.94	0.326	4.77E-04
$CO^* + 1O^* + Pt_1/CeO_2(100)$	-301.42	0.381	4.15E-04
$CO^* + 1O^* + Pt_1/CeO_2(110)$	-307.75	0.370	5.18E-04
$CO^* + 1O^* + Pt_1/CeO_2(111)$	-307.63	0.354	6.64E-04
Transition states of the CO oxidation			
$[CO\text{-}O\text{-}Pd_1/CeO_{2n}(100)]^‡$	-298.91	0.338	4.27E-04
$[CO\text{-}O\text{-}Pd_1/CeO_{2n}(110)]^‡$	-305.95	0.384	4.86E-04
$[CO\text{-}O\text{-}Pd_1/CeO_{2n}(111)]^‡$	-305.62	0.330	6.28E-04
$[CO\text{-}O\text{-}Pt_1/CeO_{2n}(100)]^‡$	-300.10	0.308	5.27E-04
$[CO\text{-}O\text{-}Pt_1/CeO_{2n}(110)]^‡$	-307.18	0.384	4.86E-04
$[CO\text{-}O\text{-}Pt_1/CeO_{2n}(111)]^‡$	-307.11	0.380	6.09E-04
CO_2 adsorbed			
$CO_2^* + Pd_1/CeO_2(100)$	-300.43	0.404	6.58E-04
$CO_2^* + Pd_1/CeO_2(110)$	-306.88	0.372	6.06E-04
$CO_2^* + Pd_1/CeO_2(111)$	-308.06	0.385	7.77E-04
$CO_2^* + Pt_1/CeO_2(100)$	-301.24	0.373	4.91E-04
$CO_2^* + Pt_1/CeO_2(110)$	-307.76	0.381	5.44E-04
$CO_2^* + Pt_1/CeO_2(111)$	-308.37	0.386	5.91E-04
Reduced species			
$Pd_1/CeO_2(100)$	-281.93	0.067	9.63E-05
$Pd_1/CeO_2(110)$	-287.94	0.063	1.06E-04
$Pd_1/CeO_2(111)$	-288.92	0.054	1.22E-04
$Pt_1/CeO_2(100)$	-283.53	0.069	1.16E-04
$Pt_1/CeO_2(110)$	-289.59	0.074	9.14E-05
$Pt_1/CeO_2(111)$	-289.81	0.059	1.22E-04

A.23. CO Oxidation at Pd_1^0 and Pt_1^0 via MvK Mechanism

The total energies in Table A.26 were calculated by structure optimization of the reaction mechanism of an CO oxidation on Pd_1^0 and Pt_1^0 single-atom catalysts adsorbed on the (111), (110) and (100) ceria surface facets. The total energies are utilized to calculate the Gibbs free energy diagrams in Figure 6.15 and listed in Table 6.5 in Section 6.1.5.

Table A.26.: The total energies were calculated through structure optimization at 0 K in eV of the structures given in Figure 6.13 for $1O^*$ + $Pd^0{}_1$ and in Figure 6.14 for $Pt^0{}_1$ single-atom catalysts in Section 6.1.5 in eV including ZPE and S of the reactants.

	E_{total} [eV]	ZPE [eV]	S [eV/T]
CO oxidation at Pd_1^0 and Pt_1^0			
$Pd_1/CeO_2(100)$	-281.93	0.067	9.63E-05
$Pd_1/CeO_2(110)$	-287.94	0.063	1.06E-04
$Pd_1/CeO_2(111)$	-288.92	0.054	1.22E-04
$Pt_1/CeO_2(100)$	-283.53	0.069	1.16E-04
$Pt_1/CeO_2(110)$	-289.59	0.074	9.14E-05
$Pt_1/CeO_2(111)$	-289.81	0.059	1.22E-04
CO adsorption			
CO^* + $Pd_1/CeO_2(100)$	-295.32	0.269	5.27E-04
CO^* + $Pd_1/CeO_2(110)$	-301.92	0.269	4.45E-04
CO^* + $Pd_1/CeO_2(111)$	-302.82	0.256	5.08E-04
CO^* + $Pt_1/CeO_2(100)$	-296.82	0.291	4.30E-04
CO^* + $Pt_1/CeO_2(110)$	-303.01	0.290	4.18E-04
CO^* + $Pt_1/CeO_2(111)$	-303.96	0.275	4.55E-04
Transition states of the CO oxidation			
$[CO\text{-}O\text{-}1V_O\text{-}Pd_1/Ce_nO_{2n\text{-}1}(100)]^‡$	-294.92	0.259	3.49E-04
$[CO\text{-}O\text{-}1V_O\text{-}Pd_1/Ce_nO_{2n\text{-}1}(110)]^‡$	-301.02	0.249	4.04E-04
$[CO\text{-}O\text{-}1V_O\text{-}Pd_1/Ce_nO_{2n\text{-}1}(111)]^‡$	-302.06	0.243	4.20E-04
$[CO\text{-}O\text{-}1V_O\text{-}Pt_1/Ce_nO_{2n\text{-}1}(100)]^‡$	-296.44	0.274	3.18E-04
$[CO\text{-}O\text{-}1V_O\text{-}Pt_1/Ce_nO_{2n\text{-}1}(110)]^‡$	-302.45	0.269	3.70E-04
$[CO\text{-}O\text{-}1V_O\text{-}Pt_1/Ce_nO_{2n\text{-}1}(111)]^‡$	-303.16	0.263	3.73E-04
CO_2 adsorbed			
CO_2^* + $1V_O\text{-}Pd_1/Ce_nO_2(100)$	-295.94	0.312	5.14E-04
CO_2^* + $1V_O\text{-}Pd_1/Ce_nO_2(110)$	-302.27	0.309	5.83E-04
CO_2^* + $1V_O\text{-}Pd_1/Ce_nO_2(111)$	-302.78	0.310	5.39E-04
CO_2^* + $1V_O\text{-}Pt_1/Ce_nO_2(100)$	-297.17	0.318	4.21E-04
CO_2^* + $1V_O\text{-}Pt_1/Ce_nO_2(110)$	-303.41	0.313	3.20E-04
CO_2^* + $1V_O\text{-}Pt_1/Ce_nO_2(111)$	-303.74	0.318	5.26E-04
Reduced species			
$1V_O\text{-}Pd_1/Ce_nO_2(100)$	-276.72		
$1V_O\text{-}Pd_1/Ce_nO_2(110)$	-282.93		
$1V_O\text{-}Pd_1/Ce_nO_2(111)$	-283.66		
$1V_O\text{-}Pt_1/Ce_nO_2(100)$	-277.48		
$1V_O\text{-}Pt_1/Ce_nO_2(110)$	-283.68		
$1V_O\text{-}Pt_1/Ce_nO_2(111)$	-284.17		

A.24. O_2 Dissociation on Pd_3 and Pt_3 Clusters via the LH and the MvK Mechanism

The total energies in Table A.27 were calculated by structure optimization of the reaction mechanism of an O_2 dissociation on Pd_3, Pt_3, $1V_O$-Pd_3 and $1V_O$-Pt_3 subnanometer cluster adsorbed on the stoichiometric (111) ceria surface facet and O defective (111) ceria surface facet $1V_O$. The total energies are utilized to calculate the Gibbs free energy diagrams in Figure 6.18 and listed in Table 6.6 in Section 6.2.1.

Table A.27.: The total energies were calculated through structure optimization at 0 K in eV of the structures given in Figure 6.16 for Pd_3 and in Figure 6.17 for Pt_3 subnanometer cluster in Section 6.2.1 in eV including ZPE and S of the reactants.

	E_{total} [eV]	ZPE [eV]	S [eV/T]
O_2 dissociation on $Pd_3/CeO_2(111)$ and $Pt_3/CeO_2(111)$			
Pd_3	-1279.04		
$1V_O$-Pd_3	-1273.66		
Pt_3	-1281.67		
$1V_O$-Pt_3	-1276.68		
nO adsorption			
O_2^* + Pd_3	-1288.39	0.159	1.89E-04
O_2^* + $1V_O$-Pd_3	-1281.81	0.116	3.50E-04
O_2^* + Pt_3	-1290.58	0.150	1.81E-04
O_2^* + $1V_O$-Pt_3	-1284.54	0.132	2.61E-04
Transition states			
$[O\text{-}O\text{-}Pd_3]^‡$	-1288.13	0.115	1.74E-04
$[O\text{-}O\text{-}1V_O\text{-}Pd_3]^‡$	-1281.42	0.089	2.32E-04
$[O\text{-}O\text{-}Pt_3]^‡$	-1290.54	0.129	1.46E-04
$[O\text{-}O\text{-}1V_O\text{-}Pt_3]^‡$	-1284.37	0.096	2.36E-04
CO_2 adsorption			
$2O^*$ + Pd_3	-1288.39	0.159	1.90E-04
$1O^*$ + Pd_3	-1282.61	0.129	2.14E-04
$2O^*$ + Pt_3	-1290.97	0.137	3.01E-04
$1O^*$ + Pt_3	-1286.65	0.125	3.26E-04

A.25. CO Oxidation on $1O^*$ + Pd_3 and $1O^*$ + Pt_3 Cluster via LH and MvK Mechanism

The total energies in Table A.27 were calculated by structure optimization of the reaction mechanism of the CO oxidation on $1O^*$ + Pd_3 and $1O^*$ + Pt_3 subnanometer cluster adsorbed on the stoichiometric (111) ceria surface facet and O defective (111) ceria surface facet $1V_O$. The total energies are utilized to calculate the Gibbs free energy diagrams in Figure 6.21 and listed in Table 6.7 in Section 6.2.2.

Table A.28.: The total energies were calculated through structure optimization at 0 K in eV of the structures given in Figure 6.19 for O^* + Pd_3 and in Figure 6.20 for O^* + Pt_3 subnanometer cluster in Section 6.2.2 in eV including ZPE and S of the reactants.

	E_{total} [eV]	ZPE [eV]	S [eV/T]
CO oxidation on $1O^*$ + Pd_3 and $1O^*$ + Pt_3			
$1O^*$ + Pd_3	-1284.60	0.073	8.63E-05
$1O^*$ + Pd_3	-1284.60	0.073	8.63E-05
$1O^*$ + Pt_3	-1287.17	0.053	1.32E-04
$1O^*$ + Pt_3	-1287.17	0.059	1.53E-04
CO adsorption			
CO^* + $1O^*$ + Pd_3	-1297.87	0.274	4.45E-04
CO^* + $1O^*$ + Pd_3	-1297.87	0.274	4.45E-04
CO^* + $1O^*$ + Pt_3	-1301.28	0.278	4.67E-04
CO^* + $1O^*$ + Pt_3	-1301.28	0.278	4.67E-04
Transition states			
$[CO\text{-}O\text{-}Pd_3]^‡$	sp.		
$[CO\text{-}O\text{-}1V_O\text{-}Pd_3]^‡$	-1297.13	0.232	5.55E-04
$[CO\text{-}O\text{-}Pt_3]^‡$	-1300.52	0.280	3.35E-04
$[CO\text{-}O\text{-}1V_O\text{-}Pt_3]^‡$	-1300.21	0.252	4.08E-04
CO_2 adsorption			
CO_2^* + Pd_3	-1298.40	0.307	4.02E-04
CO_2^* + $1V_O\text{-}Pd_3$	-1297.89	0.306	3.17E-04
CO_2^* + Pt_3	-1300.72	0.315	3.57E-04
CO_2^* + $1V_O\text{-}Pt_3$	-1300.75	0.318	4.10E-04
nO adsorption			
Pd_3	-1279.04		
$1V_O\text{-}Pd_3$	-1278.80		
Pt_3	-1281.67		
$1V_O\text{-}Pt_3$	-1280.98		

A.26. CO Oxidation on (1-4)O^* + Pd_3 and a (1-4)O^* + Pt_3 Cluster via MvK Mechanism

The total energies in Table A.29 were calculated by structure optimization of the reaction mechanism of an CO oxidation on (1-4)CO^* + Pd_3 and (1-4)CO^* + Pt_3 subnanometer cluster adsorbed on the stoichiometric (111) ceria surface facet along with a CO^* coverage ranging from 1 to 4 CO molecules.. The total energies are utilized to calculate the Gibbs free energy diagrams in Figure 6.24 and listed in Table 6.8 in Section 6.2.3.

Table A.29.: The total energies were calculated through structure optimization at 0 K in eV of the structures given in Figure 6.22 for O^* + Pd_3 and in Figure 6.23 for O^* + Pt_3 subnanometer cluster in Section 6.2.3 in eV including ZPE and S of the reactants.

	E_{total} [eV]	ZPE [eV]	S [eV/T]
CO oxidation on (1-4)O^* + Pd_3 and a (1-4)O^* + Pt_3			
$3CO^*$ + Pd_3	-1320.00	0.062	1.07E-04
$2CO^*$ + Pd_3	-1306.90	0.061	1.12E-04
$1CO^*$ + Pd_3	-1293.53	0.058	1.21E-04
Pd_3/CeO_2	-1279.04	0.058	1.17E-04
$3CO^*$ + Pt_3	-1323.17	0.059	1.10E-04
$2CO^*$ + Pt_3	-1310.01	0.061	1.19E-04
$1CO^*$ + Pt_3	-1296.49	0.057	1.52E-04
Pt_3/CeO_2	-1281.67	0.058	1.53E-04
CO adsorption			
$4CO^*$ + Pd_3	-1332.54	0.233	5.45E-04
$3CO^*$ + Pd_3	-1320.00	0.252	4.99E-04
$2CO^*$ + Pd_3	-1306.90	0.246	7.18E-04
$1CO^*$ + Pd_3	-1293.53	0.273	4.14E-04
$4CO^*$ + Pt_3	-1336.71	0.300	3.05E-04
$3CO^*$ + Pt_3	-1323.17	0.270	4.38E-04
$2CO^*$ + Pt_3	-1310.01	0.266	6.28E-04
$1CO^*$ + Pt_3	-1296.49	0.291	3.97E-04
Transition states			
$3CO^*$ + $[CO\text{-}O\text{-}1V_O\text{-}Pd_3]^‡$	-1331.85	0.234	4.01E-04
$2CO^*$ + $[CO\text{-}O\text{-}1V_O\text{-}Pd_3]^‡$	-1319.16	0.232	4.25E-04
$1CO^*$ + $[CO\text{-}O\text{-}1V_O\text{-}Pd_3]^‡$	-1305.98	0.235	3.66E-04
$[CO\text{-}O\text{-}1V_O\text{-}Pd_3]^‡$	-1291.72	0.232	5.55E-04
$3CO^*$ + $[CO\text{-}O\text{-}1V_O\text{-}Pt_3]^‡$	-1336.47	0.257	3.74E-04
$2CO^*$ + $[CO\text{-}O\text{-}1V_O\text{-}Pt_3]^‡$	-1322.82	0.256	3.95E-04
$1CO^*$ + $[CO\text{-}O\text{-}1V_O\text{-}Pt_3]^‡$	-1309.42	0.255	3.47E-04
$[CO\text{-}O\text{-}1V_O\text{-}Pt_3]^‡$	-1294.77	0.257	3.89E-04
CO_2 adsorption			
$3CO^*$ + $CO_2{}^*$ + $1V_O$-Pd_3	-1333.06	0.311	4.80E-04
$2CO^*$ + $CO_2{}^*$ + $1V_O$-Pd_3	-1320.19	0.311	4.87E-04
$1CO^*$ + $CO_2{}^*$ + $1V_O$-Pd_3	-1307.04	0.310	4.65E-04
$CO_2{}^*$ + $1V_O$-Pd_3	-1292.63	0.306	5.05E-04
$3CO^*$ + $CO_2{}^*$ + $1V_O$-Pt_3	-1336.71	0.317	4.45E-04
$2CO^*$ + $CO_2{}^*$ + $1V_O$-Pt_3	-1323.54	0.311	3.16E-04
$1CO^*$ + $CO_2{}^*$ + $1V_O$-Pt_3	-1309.88	0.317	3.79E-04
$CO_2{}^*$ + $1V_O$-Pt_3	-1295.40	0.304	3.11E-04
Reduced species			
$3CO^*$ + $1V_O$-Pd_3/CeO_2	-1314.28		
$2CO^*$ + $1V_O$-Pd_3/CeO_2	-1301.33		
$1CO^*$ + $1V_O$-Pd_3/CeO_2	-1288.14		
$1V_O$-Pd_3/CeO_2	-1273.66		
$3CO^*$ + $1V_O$-Pt_3/CeO_2	-1317.82		
$2CO^*$ + $1V_O$-Pt_3/CeO_2	-1304.22		
$1CO^*$ + $1V_O$-Pt_3/CeO_2	-1290.26		
$1V_O$-Pt_3/CeO_2	-1276.68		

A.27. CO Oxidation on Pd_3 and Pt_3 Cluster via MvK Mechanism including the Effect of Ceria Reduction

The total energies in Table A.30 were calculated by structure optimization of the reaction mechanism of the CO oxidation on O^* + Pd_3 and O^* + Pt_3 subnanometer cluster adsorbed on the O defective (111) ceria surface facet. The total energies are utilized to calculate the Gibbs free energy diagrams in Figure 6.28 and listed in Table 6.9 in Section 4.2.3.

Table A.30.: The total energies were calculated through structure optimization at 0 K in eV of the structures given in Figure 6.26 for O^* + Pd_3 with the reaction to occur at a Ce^{+III} ion and at a Ce^{+IV} ion, in Figure 6.27 for O^* + Pt_3 with the reaction to occur at a Ce^{+III} ion and at a Ce^{+IV} ion in Section 4.2.3 in eV including ZPE and S of the reactants.

	E_{total} [eV]	ZPE [eV]	S [eV/T]
CO Oxidation on Ce^{+III} and on Ce^{+IV}			
$O^*1V_{O,vic}$-$Pd_3O/Ce^{+III}O_2$	-2600.58	0.070	8.49E-05
$O^*1V_{O,vic}$-$Pd_3O/Ce^{+IV}O_2$	-2600.58	0.072	8.09E-05
$1V_{O,vic}$-$Pt_3O/Ce^{+III}O_2$	-2602.82	0.070	8.51E-05
$1V_{O,vic}$-$Pt_3O/Ce^{+IV}O_2$	-2602.80	0.071	8.32E-05
O Migration			
$1V_{O,sub}$-$Pd_3O/Ce^{+III}O_2$	-2600.97	0.058	1.28E-04
$1V_{O,sub}$-$Pd_3O/Ce^{+IV}O_2$	-2600.97	0.057	1.35E-04
$1V_{O,sub}$-$Pt_3O/Ce^{+III}O_2$	-2603.65	0.064	1.43E-04
$1V_{O,sub}$-$Pt_3O/Ce^{+IV}O_2$	-2603.77	0.068	1.35E-04
CO adsorption			
$1V_{O,sub}$-$Pd_3O/Ce^{+III}O_2$	-2614.27	0.253	3.51E-04
$1V_{O,sub}$-$Pd_3O/Ce^{+IV}O_2$	-2614.31	0.254	3.38E-04
$1V_{O,sub}$-$Pt_3O/Ce^{+III}O_2$	-2617.65	0.274	3.16E-04
$1V_{O,sub}$-$Pt_3O/Ce^{+IV}O_2$	-2617.46	0.267	1.85E-04
Transition States			
$[CO\text{-}O\text{-}1V_{O,vic}\text{-}1V_{O,sub}\text{-}Pd_3O/Ce^{+III}O_2]^‡$	-2613.99	0.232	5.55E-04
$[CO\text{-}O\text{-}1V_{O,vic}\text{-}1V_{O,sub}\text{-}Pd_3O/Ce^{+IV}O_2]^‡$	-2613.20	0.240	4.87E-04
$[CO\text{-}O\text{-}1V_{O,vic}\text{-}1V_{O,sub}\text{-}Pt_3O/Ce^{+III}O_2]^‡$	-2617.16	0.251	4.01E-04
$[CO\text{-}O\text{-}1V_{O,vic}\text{-}1V_{O,sub}\text{-}Pt_3O/Ce^{+IV}O_2]^‡$	-2616.20	0.256	5.47E-04
CO_2 Adsorbed			
$CO_2{}^*$ + $1V_{O,vic}$-$1V_{O,sub}$-$Pd_3O/Ce^{+III}O_2$	-2614.54	0.321	3.08E-04
$CO_2{}^*$ + $1V_{O,vic}$-$1V_{O,sub}$-$Pd_3O/Ce^{+IV}O_2$	-2613.87	0.310	5.27E-04
$CO_2{}^*$ + $1V_{O,vic}$-$1V_{O,sub}$-$Pt_3O/Ce^{+III}O_2$	-2617.47	0.336	2.78E-04
$CO_2{}^*$ + $1V_{O,vic}$-$1V_{O,sub}$-$Pt_3O/Ce^{+IV}O_2$	-2616.70	0.312	2.53E-04
CO_2 Desorption			
$Pd_3O/Ce^{+III}O_2$	-2595.37		
$Pd_3O/Ce^{+IV}O_2$	-2595.46		
$Pt_3O/Ce^{+III}O_2$	-2597.72		
$Pt_3O/Ce^{+IV}O_2$	-2597.82		

A.28. O_2 Dissociation on Pd_{10} and Pt_{10} Cluster via LH and MvK mechanism

The total energies in Table A.31 were calculated by structure optimization of the reaction mechanism of an O_2 dissociation on reduced subnanometer cluster Pd_{10}, Pt_{10}, pre-oxidized subnanometer cluster $2O^*$ + Pd_{10}, $2O^*$ + Pt_{10} adsorbed on the (111) ceria surface facet and reduced $1V_O$-Pd_3 and $1V_O$-Pt_3 subnanometer cluster adsorbed on O defective (111) ceria surface facet $1V_O$. The total energies are utilized to calculate the Gibbs free energy diagrams in Figure 6.31 and listed in Table 6.10 in Section 6.2.5.

Table A.31.: The total energies were calculated through structure optimization at 0 K in eV of the structures given in Figure 6.29 for Pd_{10}, $2O^*$ + Pd_{10} and $1V_O$-Pd_3 cluster and in Figure 6.30 for Pt_{10}, $2O^*$ + Pt_{10} and $1V_O$-Pt_3 cluster in Section 6.2.5 in eV including ZPE and S of the reactants.

	E_{total} [eV]	ZPE [eV]	S [eV/T]
Pd_{10} and Pt_{10} cluster			
Pd_{10}	-1288.96		
$2O^*$ + Pd_{10}	-1297.43		
$1V_O$-Pd_{10}	-1283.49		
Pt_{10}	-1297.54		
$2O^*$ + Pt_{10}	-1306.71		
$1V_O$-Pt_{10}	-1292.35		
nO adsorption			
$O_2{}^*$ + Pd_{10}	-1296.16	0.119	3.54E-04
$O_2{}^*$ + $2O^*$ + Pd_{10}	-1305.46	0.150	8.47E-04
$O_2{}^*$ + $1V_O$-Pd_{10}	-1292.00	0.122	3.02E-04
$O_2{}^*$ + Pt_{10}	-1305.51	0.126	2.79E-04
$O_2{}^*$ + $2O^*$ + Pt_{10}	-1314.92	0.138	2.01E-04
$O_2{}^*$ + $1V_O$-Pt_{10}	-1301.30	0.129	2.70E-04
Transition states			
$[O\text{-}O\text{-}Pd_{10}]^‡$	-1295.41	0.095	2.76E-04
$2O^*$ + $[O\text{-}O\text{-}Pd_{10}]^‡$	-1304.97	0.116	7.40E-04
$[O\text{-}O\text{-}1V_O\text{-}Pd_{10}]^‡$	-1291.51	0.082	2.50E-04
$[O\text{-}O\text{-}Pt_{10}]^‡$	-1305.04	0.102	2.11E-04
$2O^*$ + $[O\text{-}O\text{-}Pt_{10}]^‡$	-1314.82	0.117	1.67E-04
$[O\text{-}O\text{-}1V_O\text{-}Pt_{10}]^‡$	-1300.99	0.093	2.57E-04
$2O^*$ Adsorbed			
$2O^*$ + Pd_{10}	-1297.48	0.130	2.03E-04
$4O^*$ + Pd_{10}	-1306.98	0.138	6.19E-04
$1O^*$ + Pd_{10}	-1293.16	0.123	2.22E-04
$2O^*$ + Pt_{10}	-1306.24	0.117	3.70E-04
$4O^*$ + Pt_{10}	-1316.49	0.136	2.99E-04
$1O^*$ + Pt_{10}	-1301.81	0.120	2.50E-04

A.29. CO Oxidation on (1-4)O^* + Pd_{10} and (1-4)O^* + Pt_{10} via LH Mechanism

The total energies in Table A.32 were calculated by structure optimization of the reaction mechanism of a CO oxidation on (1-4)O^* + Pd_{10} and (1-4)O^* + Pt_{10} subnanometer cluster adsorbed on the stoichiometric (111) ceria surface facet along with an O^* coverage ranging from 1 to 4 O atoms. The total energies are utilized to calculate the Gibbs free energy diagrams in Figure 6.34 and listed in Table 6.11 in Section 6.2.6.

Table A.32.: The total energies were calculated through structure optimization at 0 K in eV of the structures given in Figure 6.32 for (1-4)O^* + Pd_{10} and in Figure 6.33 for (1-4)O^* + Pt_{10} cluster in Section 6.2.6 in eV including ZPE and S of the reactants.

	E_{total} [eV]	ZPE [eV]	S [eV/T]
CO oxidation on (1-4)O^* + Pd_{10} and (1-4)O^* + Pt_{10}			
$4O^*$ + Pd_{10}	-1307.18	0.078	7.18E-05
$3O^*$ + Pd_{10}	-1302.55	0.073	8.25E-05
$2O^*$ + Pd_{10}	-1297.42	0.061	1.10E-04
$1O^*$ + Pd_{10}	-1292.85	0.053	1.32E-04
$4O^*$ + Pt_{10}	-1316.19	0.082	6.77E-05
$3O^*$ + Pt_{10}	-1311.47	0.049	1.53E-04
$2O^*$ + Pt_{10}	-1306.74	0.063	1.08E-04
$1O^*$ + Pt_{10}	-1301.86	0.049	1.53E-04
CO adsorption			
CO^* + $4O^*$ + Pd_{10}	-1320.09	0.279	5.14E-04
CO^* + $3O^*$ + Pd_{10}	-1315.44	0.266	5.04E-04
CO^* + $2O^*$ + Pd_{10}	-1311.65	0.266	3.34E-04
CO^* + $1O^*$ + Pd_{10}	-1307.00	0.261	3.43E-04
CO^* + $4O^*$ + Pt_{10}	-1329.66	0.303	4.45E-04
CO^* + $3O^*$ + Pt_{10}	-1325.06	0.288	4.61E-04
CO^* + $2O^*$ + Pt_{10}	-1321.29	0.279	4.99E-04
CO^* + $1O^*$ + Pt_{10}	-1316.63	0.288	4.16E-04
Transition states			
$3O^*$ + $[CO\text{-}O\text{-}Pd_{10}]^‡$	-1319.66	0.248	4.22E-04
$2O^*$ + $[CO\text{-}O\text{-}Pd_{10}]^‡$	-1314.49	0.247	4.07E-04
$1O^*$ + $[CO\text{-}O\text{-}Pd_{10}]^‡$	-1309.88	0.240	3.66E-04
$[CO\text{-}O\text{-}Pd_{10}]^‡$	-1305.33	0.226	4.17E-04
$3O^*$ + $[CO\text{-}O\text{-}Pt_{10}]^‡$	-1329.15	0.268	3.32E-04
$2O^*$ + $[CO\text{-}O\text{-}Pt_{10}]^‡$	-1324.00	0.265	3.54E-04
$1O^*$ + $[CO\text{-}O\text{-}Pt_{10}]^‡$	-1319.31	0.265	1.93E-04
$[CO\text{-}O\text{-}Pt_{10}]^‡$	-1315.25	0.224	5.00E-04
CO_2 Adsorbed			
$CO_2{}^*$ + $3O^*$ + Pd_{10}	-1319.96	0.309	2.84E-04
$CO_2{}^*$ + $2O^*$ + Pd_{10}	-1316.14	0.305	2.82E-04
$CO_2{}^*$ + $1O^*$ + Pd_{10}	-1311.59	0.319	6.67E-04
$CO_2{}^*$ + Pd_{10}	-1307.41	0.294	4.73E-04
$CO_2{}^*$ + $3O^*$ + Pt_{10}	-1328.92	0.308	3.80E-04
$CO_2{}^*$ + $2O^*$ + Pt_{10}	-1325.68	0.318	3.88E-04
$CO_2{}^*$ + $1O^*$ + Pt_{10}	-1320.43	0.303	5.68E-04
$CO_2{}^*$ + Pt_{10}	-1316.15	0.300	3.92E-04

Reduced species	
$3O^* + Pd_{10}$	-1301.12
$2O^* + Pd_{10}$	-1297.43
$1O^* + Pd_{10}$	-1293.02
Pd_{10}	-1288.96
$3O^* + Pt_{10}$	-1311.65
$2O^* + Pt_{10}$	-1306.71
$1O^* + Pt_{10}$	-1301.81
Pt_{10}	-1297.54

A.30. CO Oxidation on (1-7)CO^* + Pd_{10} and (1-7)CO^* + Pt_{10} Cluster via MvK Mechanism

The total energies in Table A.32 were calculated by structure optimization of the reaction mechanism of an CO oxidation on (1-7)CO^* + Pd_{10} and (1-7)CO^* + Pt_{10} subnanometer cluster adsorbed on the stoichiometric (111) ceria surface facet along with a CO^* coverage ranging from 1 to 7 CO molecules. The total energies are utilized to calculate the Gibbs free energy diagrams in Figure 6.37 and listed in Table 6.12 in Section 6.2.7.

Table A.33.: The total energies were calculated through structure optimization at 0 K in eV of the structures given in Figure 6.32 for (1-7)CO^* + Pd_{10} and in Figure 6.33 for (1-7)CO^* + Pt_{10} subnanometer cluster in Section 6.2.7 in eV including ZPE and S of the reactants.

	E_{total} [eV]	ZPE [eV]	S [eV/T]
CO oxidation on (1-7)CO^* + Pd_{10} and (1-7)CO^* + Pt_{10}			
$6CO^* + Pd_{10}$	-1371.12	0.057	1.16E-04
$5CO^* + Pd_{10}$	-1357.58	0.057	1.14E-04
$4CO^* + Pd_{10}$	-1343.84	0.062	1.07E-04
$3CO^* + Pd_{10}$	-1329.99	0.062	1.07E-04
$2CO^* + Pd_{10}$	-1316.32	0.063	1.05E-04
$1CO^* + Pd_{10}$	-1302.84	0.060	1.11E-04
Pd_{10}	-1288.96	0.057	1.16E-04
$6CO^* + Pt_{10}$	-1381.44	0.065	1.06E-04
$5CO^* + Pt_{10}$	-1367.59	0.058	1.17E-04
$4CO^* + Pt_{10}$	-1353.63	0.065	1.03E-04
$3CO^* + Pt_{10}$	-1339.70	0.065	1.03E-04
$2CO^* + Pt_{10}$	-1325.77	0.065	1.04E-04
$1CO^* + Pt_{10}$	-1311.89	0.063	1.08E-04
Pt_{10}	-1297.54	0.058	1.20E-04
nCO adsorption			
$7CO^* + Pd_{10}$	-1384.52	0.259	4.48E-04
$6CO^* + Pd_{10}$	-1371.12	0.247	3.86E-04
$5CO^* + Pd_{10}$	-1357.58	0.255	3.55E-04
$4CO^* + Pd_{10}$	-1343.84	0.260	4.95E-04
$3CO^* + Pd_{10}$	-1329.99	0.260	4.35E-04
$2CO^* + Pd_{10}$	-1316.32	0.261	2.63E-04
$1CO^* + Pd_{10}$	-1302.84	0.260	4.79E-04

$7CO^{*} + Pt_{10}$	-1396.25	0.282	3.60E-04
$6CO^{*} + Pt_{10}$	-1381.44	0.275	4.19E-04
$5CO^{*} + Pt_{10}$	-1367.59	0.276	3.71E-04
$4CO^{*} + Pt_{10}$	-1353.63	0.287	4.19E-04
$3CO^{*} + Pt_{10}$	-1339.70	0.275	4.09E-04
$2CO^{*} + Pt_{10}$	-1325.77	0.274	3.89E-04
$1CO^{*} + Pt_{10}$	-1311.89	0.275	3.66E-04
Transition states			
$6CO^{*} + [CO\text{-}O\text{-}1V_O\text{-}Pd_{10}]^{\ddagger}$	-1383.77	0.235	4.21E-04
$5CO^{*} + [CO\text{-}O\text{-}1V_O\text{-}Pd_{10}]^{\ddagger}$	-1370.25	0.240	3.69E-04
$4CO^{*} + [CO\text{-}O\text{-}1V_O\text{-}Pd_{10}]^{\ddagger}$	-1356.48	0.235	4.42E-04
$3CO^{*} + [CO\text{-}O\text{-}1V_O\text{-}Pd_{10}]^{\ddagger}$	-1342.83	0.239	3.73E-04
$2CO^{*} + [CO\text{-}O\text{-}1V_O\text{-}Pd_{10}]^{\ddagger}$	-1328.94	0.234	4.16E-04
$1CO^{*} + [CO\text{-}O\text{-}1V_O\text{-}Pd_{10}]^{\ddagger}$	-1314.85	0.234	4.05E-04
$[CO\text{-}O\text{-}1V_O\text{-}Pd_{10}]^{\ddagger}$	-1301.34	0.234	3.92E-04
$6CO^{*} + [CO\text{-}O\text{-}1V_O\text{-}Pt_{10}]^{\ddagger}$	-1394.60	0.253	3.68E-04
$5CO^{*} + [CO\text{-}O\text{-}1V_O\text{-}Pt_{10}]^{\ddagger}$	-1380.67	0.251	3.63E-04
$4CO^{*} + [CO\text{-}O\text{-}1V_O\text{-}Pt_{10}]^{\ddagger}$	-1366.71	0.248	4.23E-04
$3CO^{*} + [CO\text{-}O\text{-}1V_O\text{-}Pt_{10}]^{\ddagger}$	-1352.71	0.247	3.56E-04
$2CO^{*} + [CO\text{-}O\text{-}1V_O\text{-}Pt_{10}]^{\ddagger}$	-1338.60	0.252	3.38E-04
$1CO^{*} + [CO\text{-}O\text{-}1V_O\text{-}Pt_{10}]^{\ddagger}$	-1324.60	0.244	4.47E-04
$[CO\text{-}O\text{-}1V_O\text{-}Pt_{10}]^{\ddagger}$	-1311.25	0.250	3.45E-04
O surface defects $1V_O$			
$6CO^{*} + CO_2 + 1V_O\text{-}Pd_{10}$	-1385.16	0.303	4.81E-04
$5CO^{*} + CO_2 + 1V_O\text{-}Pd_{10}$	-1371.72	0.306	4.54E-04
$4CO^{*} + CO_2 + 1V_O\text{-}Pd_{10}$	-1357.50	0.312	3.69E-04
$3CO^{*} + CO_2 + 1V_O\text{-}Pd_{10}$	-1344.00	0.307	4.26E-04
$2CO^{*} + CO_2 + 1V_O\text{-}Pd_{10}$	-1330.08	0.305	4.19E-04
$1CO^{*} + CO_2 + 1V_O\text{-}Pd_{10}$	-1316.13	0.307	4.22E-04
$CO_2 + 1V_O\text{-}Pd_{10}$	-1303.09	0.309	4.14E-04
$6CO^{*} + CO_2 + 1V_O\text{-}Pt_{10}$	-1395.59	0.317	3.55E-04
$5CO^{*} + CO_2 + 1V_O\text{-}Pt_{10}$	-1381.95	0.312	3.97E-04
$4CO^{*} + CO_2 + 1V_O\text{-}Pt_{10}$	-1367.47	0.310	4.08E-04
$3CO^{*} + CO_2 + 1V_O\text{-}Pt_{10}$	-1353.52	0.310	4.21E-04
$2CO^{*} + CO_2 + 1V_O\text{-}Pt_{10}$	-1339.77	0.316	3.67E-04
$1CO^{*} + CO_2 + 1V_O\text{-}Pt_{10}$	-1326.26	0.311	3.83E-04
$CO_2 + 1V_O\text{-}Pt_{10}$	-1312.25	0.309	4.17E-04
Reduced species			
$6CO^{*} + 1V_O\text{-}Pd_{10}$	-1366.03		
$5CO^{*} + 1V_O\text{-}Pd_{10}$	-1352.45		
$4CO^{*} + 1V_O\text{-}Pd_{10}$	-1338.20		
$3CO^{*} + 1V_O\text{-}Pd_{10}$	-1324.33		
$2CO^{*} + 1V_O\text{-}Pd_{10}$	-1310.86		
$1CO^{*} + 1V_O\text{-}Pd_{10}$	-1296.73		
$1V_O\text{-}Pd_{10}$	-1283.49		
$6CO^{*} + 1V_O\text{-}Pt_{10}$	-1376.06		
$5CO^{*} + 1V_O\text{-}Pt_{10}$	-1361.84		
$4CO^{*} + 1V_O\text{-}Pt_{10}$	-1348.56		
$3CO^{*} + 1V_O\text{-}Pt_{10}$	-1333.80		
$2CO^{*} + 1V_O\text{-}Pt_{10}$	-1320.43		
$1CO^{*} + 1V_O\text{-}Pt_{10}$	-1305.64		
$1V_O\text{-}Pt_{10}$	-1292.35		

A.31. O_2 Dissociation on pristine noble Metal surfaces of Pd and Pt via LH Mechanism

The total energies in Table A.32 were calculated by structure optimization of Pd and Pt surface facets (111), (110), (100), and (211). The total energies are utilized to calculate the Gibbs free energy diagrams in Figure 6.40 and listed in Table 6.13 in Section 6.3.1.

Table A.34.: The total energies were calculated through structure optimization at 0 K in eV of the structures given in Figure 6.38 for Pd surface facets and in Figure 6.39 for Pt surface facets in Section 6.3.1 in eV including ZPE and S of the reactants.

	E_{total} [eV]	ZPE [eV]	S [eV/T]
O_2 dissociation on pristine noble metal surfaces			
Pd(100)	-25.36		
Pd(110)	-53.81		
Pd(111)	-26.63		
Pd(211)	-39.61		
Pt(100)	-42.50		
Pt(110)	-88.50		
Pt(111)	-44.31		
Pt(211)	-66.54		
O_2 adsorption			
O_2^* + Pd(100)	-33.26	0.139	2.12E-04
O_2^* + Pd(110)	-61.51	0.139	2.97E-04
O_2^* + Pd(111)	-33.93	0.136	2.71E-04
O_2^* + Pd(111)	-47.05	0.134	2.68E-04
O_2^* + Pt(100)	-49.95	0.142	3.08E-04
O_2^* + Pt(110)	-96.50	0.130	3.70E-04
O_2^* + Pt(111)	-51.46	0.142	2.34E-04
O_2^* + Pt(211)	-73.84	0.134	2.47E-04
Transition states of the O_2 dissociation			
$[O\text{-}O\text{-}(100)]^‡$	-33.10	0.108 1.64E-04	
$[O\text{-}O\text{-}(110)]^‡$	sp.	-	-
$[O\text{-}O\text{-}(111)]^‡$	-33.16	0.098 2.31E-04	
$[O\text{-}O\text{-}(211)]^‡$	-46.38	0.095 2.82E-04	
$[O\text{-}O\text{-}Pt(100)]^‡$	sp.	-	-
$[O\text{-}O\text{-}Pt(110)]^‡$	-95.99	0.109	2.72E-04
$[O\text{-}O\text{-}Pt(111)]^‡$	-51.04	0.109	1.93E-04
$[O\text{-}O\text{-}Pt(211)]^‡$	-73.63	0.105	1.99E-04
Oxidized species			
$2O^*$ + Pd(100)	-33.43	0.102	2.80E-04
$2O^*$ + Pd(110)	-62.02	0.118	3.19E-04
$2O^*$ + Pd(111)	-34.80	0.141	1.73E-04
$2O^*$ + Pd(211)	-48.04	0.132	2.32E-04
$2O^*$ + Pt(100)	-51.22	0.149	1.78E-04
$2O^*$ + Pt(110)	-97.37	0.115	2.12E-04
$2O^*$ + Pt(111)	-52.10	0.138	1.82E-04
$2O^*$ + Pt(211)	-75.25	0.139	1.99E-04

A.32. CO Oxidation on Extended Pd and Pt noble Metal surfaces with high O^* loading via LH Mechanism

The total energies in Table A.35 were calculated through structure optimization of Pd and Pt surface facets (111), (110), (100), and (211) with two $2O^*$ atoms pre-adsorbed within one unit cell of the slab, reflecting a high O loading. The total energies are utilized to calculate the Gibbs free energy diagrams in Figure 6.43 and listed in Table 6.14 in Section 6.3.2.

Table A.35.: The total energies were calculated through structure optimization at 0 K in eV of the structures given in Figure 6.41 for Pd surface facets and in Figure 6.42 for Pt surface facets in Section 6.3.2 in eV including ZPE and S of the reactants.

	E_{total} [eV]	ZPE [eV]	S [eV/T]
CO oxidation with high O^* loading			
Pd(100)	-33.43	0.051	1.38E-04
Pd(110)	-62.02	0.059	1.60E-04
Pd(111)	-34.80	0.072	8.20E-05
Pd(211)	-48.04	0.064	1.41E-04
Pt(100)	-51.22	0.075	8.85E-05
Pt(110)	-97.37	0.058	2.05E-04
Pt(111)	-52.10	0.074	8.02E-05
Pt(211)	-75.25	0.071	1.07E-04
CO adsorption			
CO^* + Pd(100)	-46.43	0.245	3.22E-04
CO^* + Pd(110)	-75.12	0.252	4.22E-04
CO^* + Pd(111)	-47.77	0.258	5.43E-04
CO^* + Pd(211)	-61.28	0.259	4.23E-04
CO^* + Pt(100)	-64.07	0.282	4.08E-04
CO^* + Pt(110)	-110.16	0.246	2.92E-04
CO^* + Pt(111)	-65.46	0.282	4.33E-04
CO^* + Pt(211)	-88.49	0.276	3.50E-04
Transition states of the CO oxidation			
$[CO\text{-}O\text{-}Pd(100)]^{\ddagger}$	-46.45	0.248	3.31E-04
$[CO\text{-}O\text{-}Pd(110)]^{\ddagger}$	-74.85	0.224	3.63E-04
$[CO\text{-}O\text{-}Pd(111)]^{\ddagger}$	-47.01	0.247	4.08E-04
$[CO\text{-}O\text{-}Pd(211)]^{\ddagger}$	-60.34	0.253	3.44E-04
$[CO\text{-}O\text{-}Pt(100)]^{\ddagger}$	-63.70	0.250	3.09E-04
$[CO\text{-}O\text{-}Pt(110)]^{\ddagger}$	-109.54	0.224	3.53E-04
$[CO\text{-}O\text{-}Pt(111)]^{\ddagger}$	-64.85	0.267	3.16E-04
$[CO\text{-}O\text{-}Pt(211)]^{\ddagger}$	-87.59	0.262	3.60E-04
CO_2 adsorbed			
CO_2^* + Pd(100)	-48.45	0.313	5.32E-04
CO_2^* + Pd(110)	-76.85	0.321	6.01E-04
CO_2^* + Pd(111)	-49.61	0.315	7.40E-04
CO_2^* + Pd(211)	-62.74	0.320	6.13E-04
CO_2^* + Pt(100)	-65.41	0.322	5.77E-04
CO_2^* + Pt(110)	-111.48	0.311	5.62E-04
CO_2^* + Pt(111)	-67.09	0.310	3.45E-04
CO_2^* + Pt(211)	-89.55	0.323	8.86E-04

Extended noble metal surfaces	
Pd(100)	-29.81
Pd(110)	-58.17
Pd(111)	-31.10
Pd(211)	-44.09
Pt(100)	-46.46
Pt(110)	-93.00
Pt(111)	-48.84
Pt(211)	-70.86

A.33. CO Oxidation on Extended Pd and Pt noble Metal surfaces with low O* loading via LH Mechanism

The total energies in Table A.36 were calculated through structure optimization of Pd and Pt surface facets (111), (110), (100), and (211) with two 2O* atoms pre-adsorbed within one unit cell of the slab, reflecting a high O loading. The total energies are utilized to calculate the Gibbs free energy diagrams in Figure 6.46 and listed in Table 6.15 in Section 6.3.3.

Table A.36.: The total energies were calculated through structure optimization at 0 K in eV of the structures given in Figure 6.44 for Pd surface facets and in Figure 6.45 for Pt surface facets in Section 6.3.3 in eV including ZPE and S of the reactants.

	E_{total} [eV]	ZPE [eV]	S [eV/T]
CO oxidation with low O* loading			
O* + Pd(100)	-29.81	0.047	1.46E-04
O* + Pd(110)	-58.17	0.064	9.79E-05
O* + Pd(111)	-31.10	0.070	8.47E-05
O* + Pd(211)	-44.09	0.069	8.58E-05
O* + Pt(100)	-46.46	0.059	1.14E-04
O* + Pt(110)	-93.00	0.062	1.70E-04
O* + Pt(111)	-48.84	0.074	7.78E-05
O* + Pt(211)	-70.86	0.070	8.57E-05
CO adsorption			
CO* + O* + Pd(100)	-42.96	0.266	3.89E-04
CO* + O* + Pd(110)	-71.76	0.262	3.85E-04
CO* + O* + Pd(111)	-44.27	0.261	3.14E-04
CO* + O* + Pd(211)	-57.59	0.276	4.58E-04
CO* + O* + Pt(100)	-60.49	0.269	3.72E-04
CO* + O* + Pt(110)	-106.64	0.254	4.52E-04
CO* + O* + Pt(111)	-62.27	0.282	2.95E-04
CO* + O* + Pt(211)	-84.45	0.285	3.86E-04
Transition states of the CO oxidation			
[CO-O-Pd(100)]‡	-42.69	0.239	3.45E-04
[CO-O-Pd(110)]‡	-71.12	0.223	3.71E-04
[CO-O-Pd(111)]‡	-43.41	0.243	3.92E-04
[CO-O-Pd(211)]‡	-56.31	0.237	3.69E-04
[CO-O-Pt(100)]‡	-60.01	0.242	3.24E-04
[CO-O-Pt(110)]‡	-105.16	0.233	3.62E-04
[CO-O-Pt(111)]‡	-61.30	0.259	3.93E-04
[CO-O-Pt(211)]‡	-83.57	0.255	3.97E-04

CO_2 adsorbed			
CO_2^* + Pd(100)	-43.97	0.326	6.99E-04
CO_2^* + Pd(110)	-72.39	0.309	4.18E-04
CO_2^* + Pd(111)	-45.25	0.312	3.04E-04
CO_2^* + Pd(211)	-57.78	0.302	4.46E-04
CO_2^* + Pt(100)	-61.11	0.322	5.75E-04
CO_2^* + Pt(110)	-107.08	0.304	1.93E-04
CO_2^* + Pt(111)	-63.11	0.312	5.66E-04
CO_2^* + Pt(211)	-84.45	0.312	5.66E-04
Reduced species			
Pd(100)	-25.36		
Pd(110)	-53.81		
Pd(111)	-26.63		
Pd(211)	-39.61		
Pt(100)	-42.50		
Pt(110)	-88.50		
Pt(111)	-44.31		
Pt(211)	-66.54		

A.34. CO Oxidation on Extended Metal Oxide surfaces

The total energies in Table A.37 were calculated through structure optimization of Pd and Pt surface facets (111), (110), (100), and (211) with two $2O^*$ atoms pre-adsorbed within one unit cell of the slab, reflecting a high O loading. The total energies are utilized to calculate the Gibbs free energy diagrams in Figure 6.48 and listed in Table 6.16 in Section 6.3.4.

Table A.37.: The total energies were calculated through structure optimization at 0 K in eV of the structures given in Figure 6.47 for Pd surface facets and in Figure 6.45 for Pt surface facets in Section 6.3.4 in eV including ZPE and S of the reactants.

	E_{total} [eV]	ZPE [eV]	S [eV/T]
CO oxidation on metal oxide surfaces			
PdO(101)	-95.25	0.080	7.00E-05
PtO(101)	-107.03	0.086	6.33E-05
CO adsorption			
CO^* + PdO(101)	-108.65	0.279	3.59E-04
CO^* + PtO(101)	-121.10	0.305	2.49E-04
Transition states of the CO oxidation			
$[CO\text{-}O\text{-}1V_O\text{-}Pd_nO_{n-1}(101)]^‡$	-108.01	0.262	4.25E-04
$[CO\text{-}O\text{-}1V_O\text{-}Pt_nO_{n-1}(101)]^‡$	-119.48	0.319	2.56E-04
CO_2 adsorbed			
CO_2^* + $Pd_nO_{n-1}(101)$	-108.63	0.327	4.64E-04
CO_2^* + $Pt_nO_{n-1}(101)$	-120.84	0.326	5.06E-04
Reduced species			
$Pd_nO_{n-1}(101)$	-89.99		
$Pt_nO_{n-1}(101)$	-102.19		

A.35. Supercell Slabs of the Heterogeneous Catalysts

In this section, the supercells of the heterogeneous catalysts investigated in this work are presented.

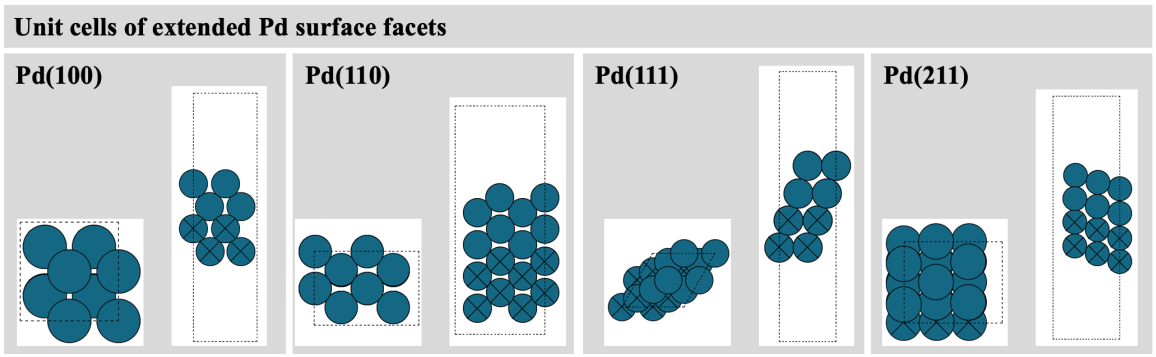

Figure A.1.: Visualization of the supercells for calculating the Pd crystal extended surface facets (100), (110), (111) and (211). Red circles represent O, and petrol circles indicate Pd atoms.

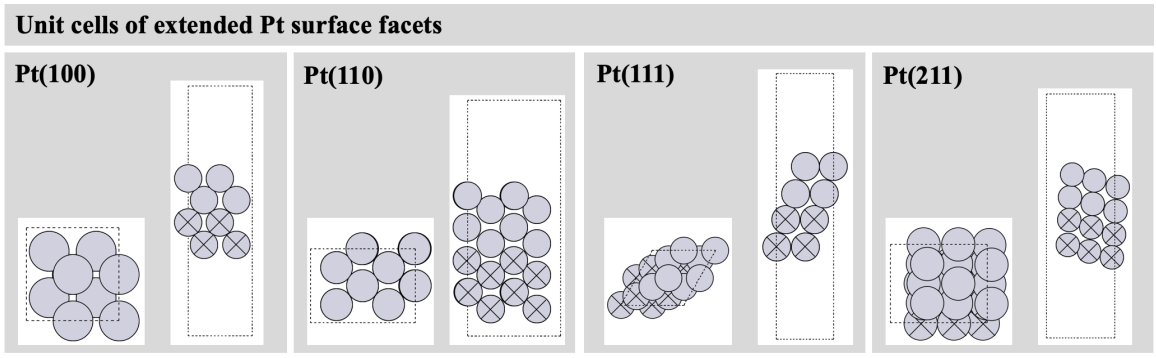

Figure A.2.: Visualization of the supercells for calculating the Pt crystal extended surface facets (100), (110), (111) and (211). Red circles represent O, and gray circles indicate Pt atoms.

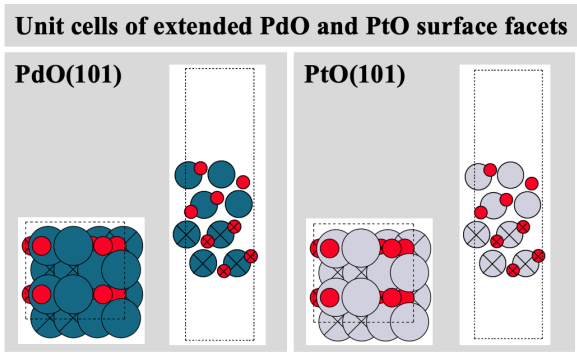

Figure A.3.: Visualization of the supercells for calculating thePdO and PtO extended surface facets (101). Red circles represent O, petrol circles Pt atoms, and gray circles indicate Pt atoms.

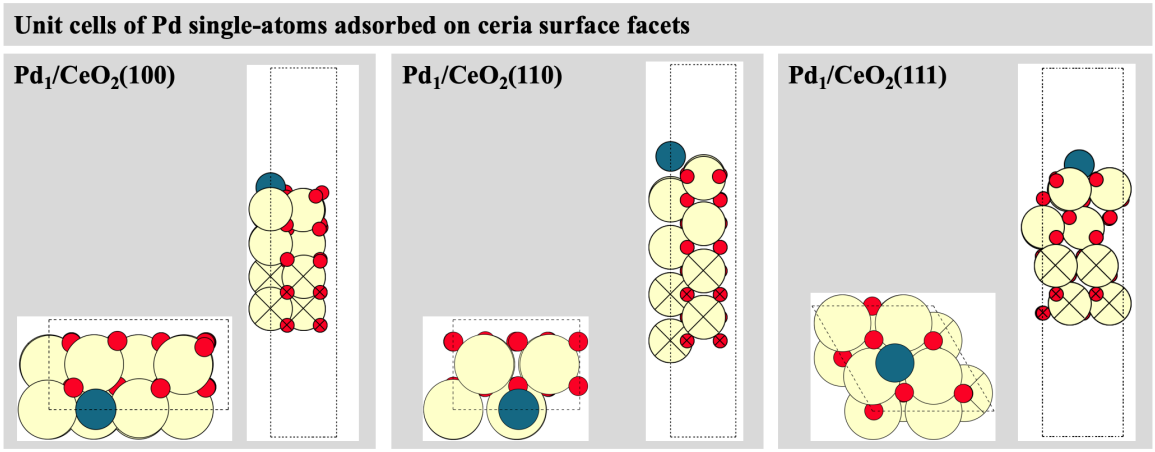

Figure A.4.: Visualization of the supercells for calculating the Pd single-atom catalyst adsorbed on the ceria surface facets (100), (110), and (111). Red circles represent O, and petrol circles indicate Pd atoms.

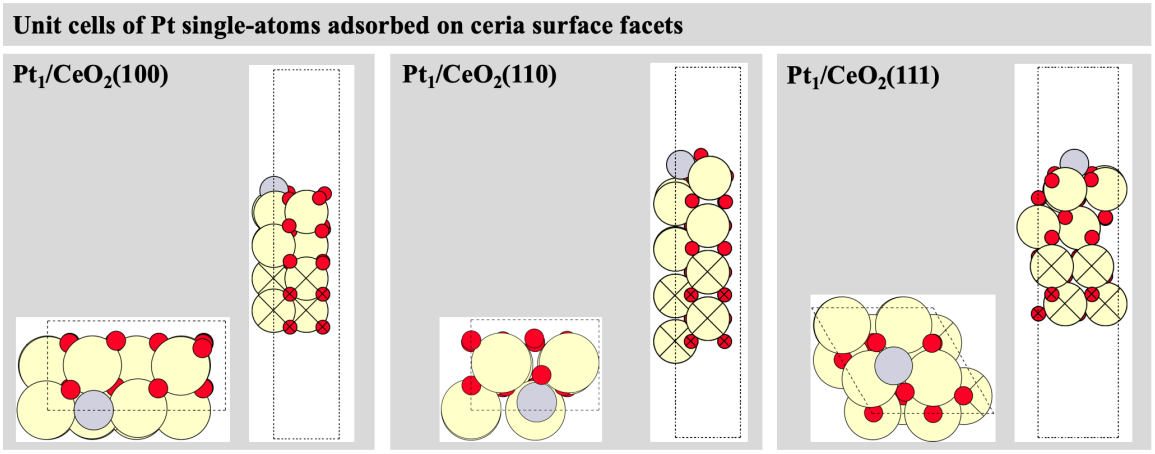

Figure A.5.: Visualization of the supercells for calculating the Pt single-atom catalyst adsorbed on the ceria surface facets (100), (110), and (111). Red circles represent O, and gray circles indicate Pt atoms.

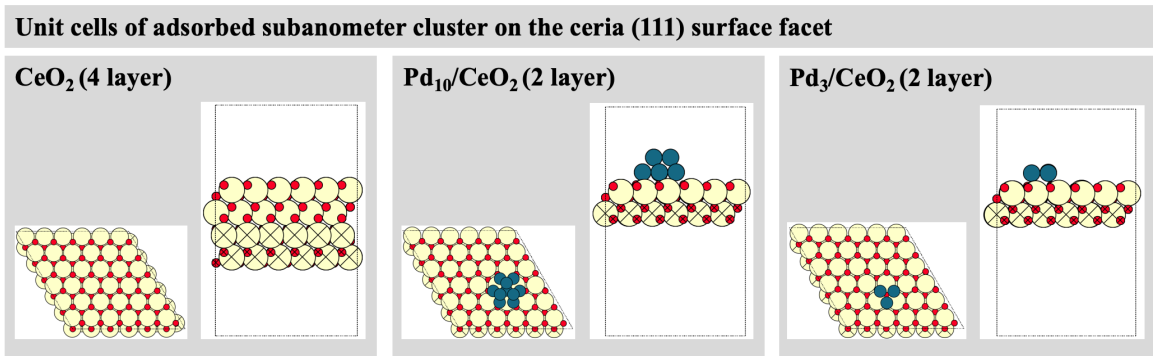

Figure A.6.: Visualization of the supercells for calculating the ceria crystal extended surface facets (100), (110), (111) and (211). Red circles represent O, and yellow circles indicate Ce atoms.

A.36. Comment on the Configurations of $2O^*$ + Pd_1 and $2O^*$ + Pt_1 Single-atom Catalysts

In this section, various 2O* configurations for Pd_1 and Pt_1 are presented.

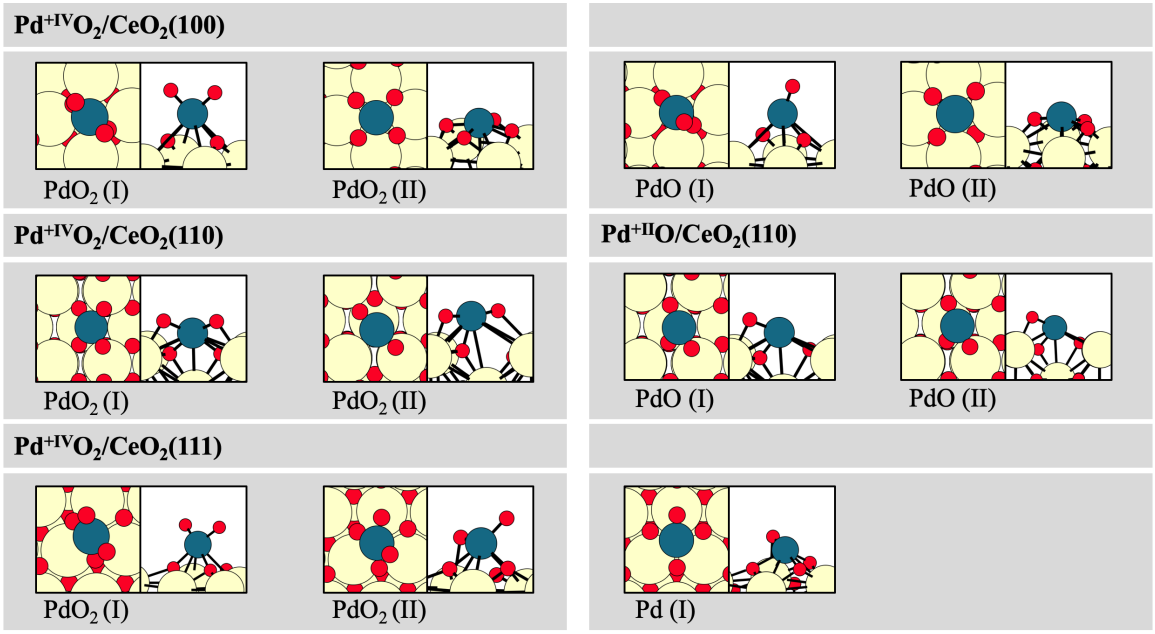

Figure A.7.: Metastable structures formed after O_2 dissociation are described with (I). The structures available for CO oxidation $2O^*$ + Pd_1 are described with (II). Red circles indicate O atoms, yellow circles Ce atoms, and petrol circles Pd atoms.

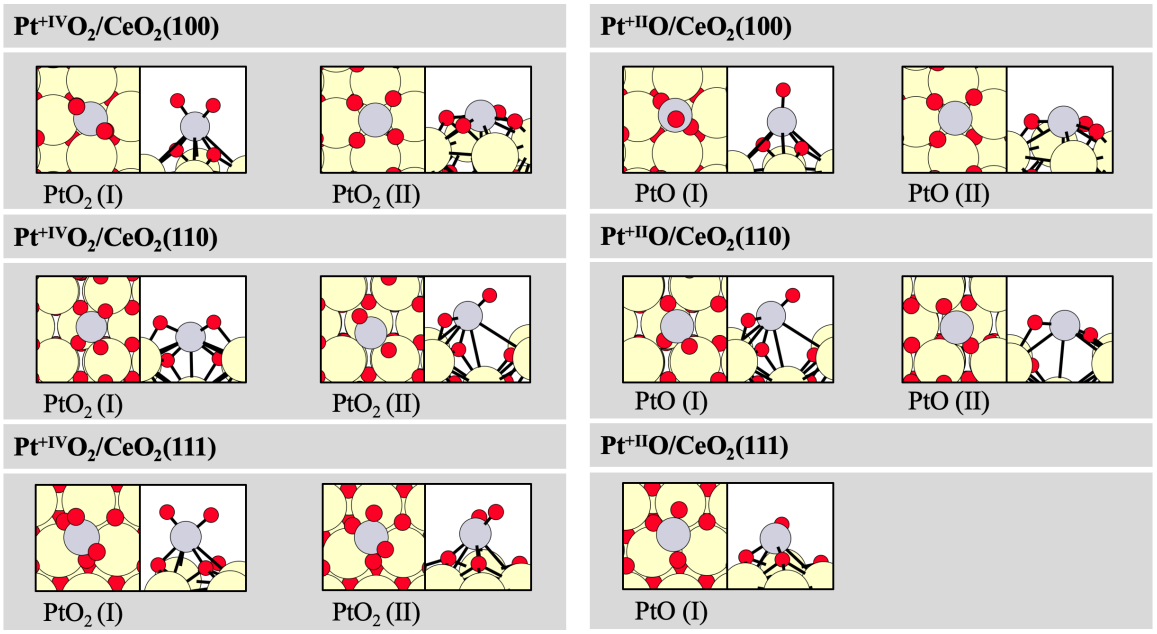

Figure A.8.: Metastable structures formed after O_2 dissociation are described with (I). The structures available for CO oxidation $2O^* + Pt_1$ are described with (II). Red circles indicate O atoms, yellow circles Ce atoms, and gray circles Pt atoms.

Acknowledgements

This study and my work were funded by the Deutsche Forschungsgemeinschaft (DFG, German Research Foundation) through SFB 1441 - TrackAct for "Tracking the Active Site in Heterogeneous Catalysis for Emission Control" (project ID 426888090) within project B4. I would like to express my gratitude to Prof. Dr. Jan-Dirk Grunwaldt, Prof. Dr. Olaf Deutschmann, and Prof. Dr. Felix Studt for making this research project possible. I would also like to especially thank Prof. Dr. Karin Fink for her continuous professional and academic support. I extend my thanks to Dr. Daria Gashnikova, Dr. Florian Maurer, and Dr. Jelena Jelic for their academic assistance. Further support was provided by the Research Training Group (RTG) 2450 - Tailored Scale-Bridging Approaches to Computational Nanoscience, funded by the DFG and led by Prof. Dr. Markus Elstner, for which I am deeply grateful for the inspiration in Physical Chemistry and Theoretical Chemistry during my studies, which shaped and fundamentally developed my scientific thinking. I am very grateful for the support and funding of the research by the Helmholtz Association of German Research Centres e. V., which supports research at KIT. The computations were performed on the High Performance Computers (HPC) which are supported by the state of Baden-Württemberg through bwHPC and the German Research Foundation (DFG) through grant no INST 40/575-1 FUGG (JUSTUS 2 cluster) and bwUniCluster (2.0). Further information about my research can be found using my ORCID ID 0000-0001-5722-7634. My data related to the calculations published here will be made available after the successful publication of the articles related to this work and this work itself at KITopen. I also have a profile on GitHub, https://github.com/SarahBernart, where I regularly publish codes.

Persönliche Danksagung

Ich schrieb diese Arbeit stets im Gedenken an meine Tante Prof. Dr. Yvonne Bernart und zu Ehren meines Urgroßonkels Prof. Dr. Emanuel Bernart, die mir vom Himmel auf Erden in meinen schwierigsten Zeiten Rückhalt und Stärke gaben.

Ich bin stolz, bereits die dritte Person in direkter Folge zu sein, um meinem Großvater Walter Bernart Recht zu tun.

Im Gedenken an meinen Großvater Chongrak Tantrakul und Großonkel Santi Settaphong habe ich mich unbeugsam und rechtschaffen gezeigt. Im Gedenken an meine Großmutter Gudrun geb. Pisenek habe ich meine Stärke nicht verkommen lassen.

Ich danke meinen Liebsten, Christopher Balleis, Misa und Asuna of Brightshine, Orapim und Suntaree Tantrakul sowie Diana, Michaela und Dr. Wolfgang Bernart, für ihre stetige Verbundenheit.